Transactions of the ASME®

Transactions of the ASME, Journal of Fluids Engineering (ISSN 0098-2202) is published quarterly (Mar., June, Sept., Dec.) by The American Society of Mechanical Engineers, Three Park Avenue, New York, NY 10016. Periodicals postage paid at New York, NY and additional mailing offices.
POSTMASTER: Send address changes to Transactions of the ASME, Journal of Fluids Engineering, c/o THE AMERICAN SOCIETY OF MECHANICAL ENGINEERS, 22 Law Drive, Box 2300, Fairfield, NJ 07007-2300.
CHANGES OF ADDRESS must be received at Society headquarters seven weeks before they are to be effective. Please send old label and new address.
STATEMENT from By-Laws. The Society shall not be responsible for statements or opinions advanced in papers or ... printed in its publications (B7.1, Par. 3).

INDEXED by Applied Mechanics Reviews and Engineering Information, Inc. Canadian Goods & Services Tax Registration #126148048.

Journal of Fluids Engineering

Published Quarterly by The American Society of Mechanical Engineers

VOLUME 123 • NUMBER 1 • MARCH 2001

(Contents continued on inside back cover)

This journal is printed on acid-free paper, which exceeds the ANSI Z39.48-1992 specification for permanence of paper and library materials. ♾™
♻ 85% recycled content, including 10% post-consumer fibers.

Journal of Fluids Engineering Volume 123, Number 1 MARCH 2001

TECHNICAL BRIEFS

ANNOUNCEMENTS

Journal of Fluids Engineering

Editorial

I would like to start this editorial by expressing my gratitude to three Associate Editors who have recently completed their three-year terms. Professor Peter Bradshaw has provided his unparalleled experience and expertise in all aspects of turbulent flows, particularly in turbulence modeling. Professor David Williams has been our expert in boundary layers, wakes, flow structures in separated flows and wakes as well as flow control. Dr. Frederic K. Wasden has provided a unique perspective that combines industrial experience in the chemical engineering industry and a background in multiphase flows, interfaces, liquid films and related nonlinear dynamics. The valuable service of the Associate Editors is critical for the success and reputation of a journal. Besides the essential technical knowledge, the job requires a considerable investment of time, and the willingness to perform tasks which are not always a pleasure (such as nagging referees to provide reviews in a timely manner, ''harassing'' authors to complete revisions and negotiating conflicting reviews). This service and support are greatly appreciated.

Four new Associate Editors are joining us. Addressing the increasing flux of papers involving numerical simulations, three of the new Associate Editors are experts in computational fluid dynamics (CFD). Dr. Edward Graf is presently the head of the Computational Development Group at Flowserve Pump Division. He has almost thirty years of experience in studying a wide variety of problems in aerodynamic, hydraulic and acoustic design as well as in design of advanced turbomachines. Dr. Graf is also a recipient of a Distinguished Inventor Award from his company and has authored papers in turbomachinery, CFD and cavitation.

Dr. Ismail Celik is presently a professor of Mechanical and Aerospace Engineering in West Virginia University. His field of expertise is in CFD including heat transfer, multiphase flow, combustion, numerical uncertainty, turbulence modeling and application of variety of commercial CFD codes. He has a substantial record of publications and has been active in the Fluid Engineering Division of ASME, including organization of conferences and chairing the Coordinating Group on CFD. Dr. Celik has also been Fulbright Senior Lecturer and has considerable experience in consulting.

Dr. Jeffrey Marshall is an Associate Professor of Mechanical Engineering at the University of Iowa. He specializes in vortex dynamics, fluid-structure interactions, vortex turbulence and two-phase turbulent flows. He has made substantial contribution to the development and application of Lagrangian computational methods and has published extensively in his field of expertise.

The fourth new Associate Editor, Dr. Ajay Prasad, will enhance our ability to review papers involving state of the art experimental techniques and their application to flows in complex geometries. Dr. Prasad is an Associate Professor in the Department of Mechanical Engineering at the University of Delaware. He is predominantly an experimentalist with substantial experience in development and application of Particle Image Velocimetry (PIV). Among other projects, he has contributed to development of stereo-PIV and has applied his expertise to study the flow in the nasal cavity. We are excited about the diverse experience of the new additions to our team and are certain that they will contribute to the quality of JFE.

In the March issue, we traditionally recognize the contributions of the many referees who have donated their time and expertise to the Journal by providing reviews of submitted manuscripts. Their thoughtful assistance to the authors and editors alike has served to maintain the excellence of our publication.

This issue contains 21 articles dealing with a variety of subjects. Five papers focus on turbulence modeling and simulations. Chaouat uses Reynolds stress models to simulate channel flows with spanwise rotation and wall injection. Secundov et al. generalize the ν_t-92 turbulence model for shear-free and stagnation point flows, and Durbin et al. introduce a formulation to apply the two-layer κ-ε model to rough surfaces. Modeling of laminar-turbulent transition for high free-stream turbulence is the topic of the paper by Steelant and Dick, and a brief by Tangemann and Gretler introduces an expression for the primary stress combined with an algebraic stress model to compute the flow in a wall jet.

Two papers focus on flows driven by electrical/magnetic forces. Liu et al. study the stability of an electrically driven flow between concentric cylinders. Chamkha develops a two-phase fluid-particle model for a laminar hydro-magnetic flow of a particulate suspension with gravity.

Multiphase flows are the subject of four additional papers. An experimental study modeling 2-D leakage jet cavitation as a simplified model for tip-leakage flows is presented by Watanabe et al. Waniewski et al. measure experimentally the entrainment of air by bow waves, Flynn et al. perform simulations of human exposure to aerosols, and Fossa examines the structure of air-water flows in horizontal pipes.

Four papers deal with flows in complex geometries. Dong et al. perform measurements within a pump passage in an automotive torque converter, and a piezoelectric valve-less pump is modeled by Ullmann. The flow, forces and pressure around gurney flaps, fitted to a double-element wing, are studied by Jeffrey et al., and laminar flow in a channel with longitudinal tubes is studied theoretically in a technical brief by Wang. Experimental studies involving simpler geometries are the subject of three additional papers. The forces and pressure on a diffuser in ground effects are studied by Senior and Zhang. Near wall measurements of a turbulent impinging slot jet are described by Zhe and Modi, and experiments within a plane turbulent surface jet in shallow tailwater are reported by Ead and Rajaratnam.

Compressible flows and compressibility effects are the subject of three papers. Johansen et al. introduce a data reduction algorithm for multi-hole pressure probes in compressible subsonic flow fields. Chung reports on experiments focusing on the interaction of an impinging shock wave and an expansion fan at a Mach number of 1.28, and Ben-Dor et al. study numerically the reflection of shock waves from wedges in dust-gas suspensions.

J. Katz
Editor

Simulations of Channel Flows With Effects of Spanwise Rotation or Wall Injection Using a Reynolds Stress Model

Bruno Chaouat
Senior Scientist,
ONERA, Computational Fluid Dynamics and Aeroacoustics Department,
Chatillon 92322, France

Simulations of channel flows with effects of spanwise rotation and wall injection are performed using a Reynolds stress model. In this work, the turbulent model is extended for compressible flows and modified for rotation and permeable walls with fluid injection. Comparisons with direct numerical simulations or experimental data are discussed in detail for each simulation. For rotating channel flows, the second-order turbulence model yields an asymmetric mean velocity profile as well as turbulent stresses quite close to DNS data. Effects of spanwise rotation near the cyclonic and anticyclonic walls are well observed. For the channel flow with fluid injection through a porous wall, different flow developments from laminar to turbulent regime are reproduced. The Reynolds stress model predicts the mean velocity profiles, the transition process and the turbulent stresses in good agreement with the experimental data. Effects of turbulence in the injected fluid are also investigated. [DOI: 10.1115/1.1343109]

Introduction

For engineering applications, calculations of turbulent flows are generally performed with a first-order closure turbulence model based on two transport equations. However, standard two-equation models using the Boussinesq hypothesis have been incapable of accurately predicting flows where the normal Reynolds stresses play an important role, e.g., in flows with strong effects of streamline curvature, system rotation, wall injection or adverse pressure gradient. In turbomachinery, the system rotation affects both mean motion, turbulence intensity and turbulence structure. For instance, due to the Coriolis force, a channel flow subjected to a spanwise rotation becomes asymmetric with a turbulence activity which is much reduced to the cyclonic side compared with the anticyclonic side, as observed experimentally by Johnson et al. [1] and also reproduced by direct numerical simulations by Kristoffersen and Anderson [2] and more recently by Lamballais et al. [3]. This kind of rotating flow is important for the turbomachinery industry. Indeed, in order to improve the performance of jet aircrafts, it is necessary to obtain an accurate description of the flow structure in the different parts of the engine. In solid rocket propulsion [4], the mass transfer which results from the propellant combustion modifies the shear stress distribution across the flow in comparison with the shear stress of wall-bounded flow. The internal flow in solid rocket motor, which is produced by mass injection, plays an important role in ballistics prediction. Modeling such flows is a difficult task because different regimes from laminar to turbulent can be observed in these motor chambers due to the transition behavior of the mean axial velocity.

The turbulence model used for the closure of the Reynolds averaged Navier-Stokes equations must be able to predict accurately such complex flows. In this aim, Reynolds stress models have been proposed in the past decade. Contrary to first-order turbulence models, the Coriolis terms associated with system rotation are included in the second-moment closures. Exact production terms appear as sources (or sinks) in the transport equations for the individual Reynolds stress components. In the RSM formulation, the pressure-strain correlation term forms a pivotal role by incorporating history and nonlocal effects of the flow. This term has been modeled by assuming homogeneous flows that are near equilibrium [5] and recent developments in this direction have been made [6]. For calculations of complex wall-bounded turbulent flows, a wall reflection term has been incorporated in the model for reproducing the logarithmic region of the turbulent boundary layer [7]. In the usual approach, the modeled wall reflection term requires a variety of *ad hoc* wall damping functions which depend on the distance normal to the wall [8,9]. Durbin [10] has recently proposed an alternative route of a relaxation approach in which an elliptic equation is introduced and interpreted as an approximation of the wall effects. For simulating complex flows, it appears that Reynolds stress models, which take into account these recent developments, are a good compromise between large eddy simulations, that require very large computing time, and first-order closure models, which are not able to predict flows accurately.

In this work, the model developed by Launder and Shima [11] has been selected because it has predicted flows fairly despite that its formulation is simpler than those of other models [12]. It contains only a few empirical terms and thus is a good candidate to handle a large variety of flows. This model is extended for compressible flows, adapted for rotation and for permeable walls with fluid injection. Comparison with data of direct numerical simulations for nonrotating [13] and rotating [3] channel flows, and with experimental data for channel flows with wall injection [14] are discussed in details. In addition, the Lumley representation of the second and third invariant of the Reynolds stress anisotropy tensor is considered for analyzing the solutions trajectories.

Governing Equations

Turbulent flow of a viscous fluid is considered. As in the usual treatments of turbulence, the flow variable ξ is decomposed into ensemble Reynolds mean and fluctuating parts as $\xi=\bar{\xi}+\xi'$. In the present case, the Favre-averaged is used for compressible fluid so that the variable ξ can be written as $\xi=\tilde{\xi}+\xi''$ with the particular properties $\tilde{\xi''}=0$ and $\overline{\rho\xi''}=0$ where ρ is the mass density. These relations imply that $\tilde{\xi}=\overline{\rho\xi}/\bar{\rho}$. The Reynolds average of the

Contributed by the Fluids Engineering Division for publication in the JOURNAL OF FLUIDS ENGINEERING. Manuscript received by the Fluids Engineering Division January 17, 2000; revised manuscript received November 16, 2000. Associate Editor: P. Bradshaw.

Navier-Stokes equations produces in Favre variables the following forms of the mass, momentum, and energy equations in a rotation frame of reference Ω:

$$\frac{\partial \overline{\rho}}{\partial t} + \frac{\partial}{\partial x_j}(\overline{\rho}\widetilde{u}_j) = 0 \tag{1}$$

$$\frac{\partial}{\partial t}(\overline{\rho}\widetilde{u}_i) + \frac{\partial}{\partial x_j}(\overline{\rho}\widetilde{u}_i\widetilde{u}_j) = \frac{\partial \overline{\Sigma}_{ij}}{\partial x_j} - 2\epsilon_{ijk}\overline{\rho}\Omega_j\widetilde{u}_k \tag{2}$$

$$\frac{\partial}{\partial t}(\overline{\rho}\widetilde{E}) + \frac{\partial}{\partial x_j}(\overline{\rho}\widetilde{E}\widetilde{u}_j) = \frac{\partial}{\partial x_j}(\overline{\Sigma}_{ij}\widetilde{u}_i) + \frac{\partial}{\partial x_j}\left(\overline{\sigma_{ij}u_i''} - \frac{1}{2}\widetilde{\overline{\rho}u_k''u_k''u_j''}\right) - \frac{\partial \overline{q}_j}{\partial x_j} \tag{3}$$

where u_i, E, Σ_{ij}, σ_{ij}, q_i, ϵ_{ijk} are, respectively, the velocity vector, the total energy, the total stress tensor, the viscous stress tensor, the total heat flux vector, and the permutation tensor. The mean stress tensor $\overline{\Sigma}_{ij}$ is composed by the mean modified pressure which includes the centrifugal force potential $\overline{p}^* = \overline{p} - \frac{1}{2}\overline{\rho}|\Omega \times \mathbf{x}|^2$, the mean viscous stress $\overline{\sigma}_{ij}$, and the turbulent stress $\overline{\rho}\tau_{ij}$ as follows:

$$\overline{\Sigma}_{ij} = -\overline{p}^*\delta_{ij} + \overline{\sigma}_{ij} - \overline{\rho}\tau_{ij} \tag{4}$$

In this expression, the tensor $\overline{\sigma}_{ij}$ takes the usual form:

$$\overline{\sigma}_{ij} = \overline{\mu}\left(\frac{\partial \overline{u}_i}{\partial x_j} + \frac{\partial \overline{u}_j}{\partial x_i}\right) - \frac{2}{3}\overline{\mu}\frac{\partial \overline{u}_k}{\partial x_k}\delta_{ij} \tag{5}$$

and the Favre-averaged Reynolds stress tensor is:

$$\tau_{ij} = \widetilde{u_i''u_j''} \tag{6}$$

where the quantity μ is the molecular viscosity. The mean heat flux $\overline{q}_i$ is composed by the laminar and turbulent flux contributions:

$$\overline{q}_i = -\overline{\kappa}\frac{\partial \overline{T}}{\partial x_i} + \overline{\rho}\widetilde{h''u_i''} \tag{7}$$

where T, h, and κ are the temperature, the specific enthalpy, and the thermal conductivity, respectively. Closure of the mean flow equations is necessary for the turbulent stress $\overline{\rho}\widetilde{u_i''u_j''}$, the molecular diffusion $\overline{\sigma_{ij}u_i''}$, the turbulent transport of the turbulent kinetic energy $\overline{\rho}\widetilde{u_k''u_k''u_j''}$, and the turbulent heat flux $\overline{\rho}\widetilde{h''u_i''}$.

Turbulence Model

The Favre-averaged correlation tensor $\tau_{ij} = \widetilde{u_i''u_j''}$ is computed by means of Reynolds stress model. In this study, the model of Launder and Shima [11] has been considered and extended to compressible flows using the Favre-averaged. The turbulent model has been also modified to simulate rotating flows. For this, the Coriolis force has been incorporated in the Reynolds stress transport equation and the pressure-strain correlation has been developed in a form-invariant under Galilean transformation. This has consisted in replacing the mean vorticity tensor $\overline{\omega}_{ij}$ of usual form,

$$\overline{\omega}_{ij} = \frac{1}{2}\left(\frac{\partial \overline{u}_i}{\partial x_j} - \frac{\partial \overline{u}_j}{\partial x_i}\right) \tag{8}$$

which appears in the modeled pressure-strain term, by the absolute mean vorticity tensor defined as $\overline{W}_{ij} = \overline{\omega}_{ij} + \epsilon_{mji}\Omega_m$, where Ω is the angular velocity vector. So that the pressure-strain term takes the following form:

$$\begin{aligned}\Phi_{ij} = &-c_1\overline{\rho}\epsilon a_{ij} + \tfrac{4}{3}c_2\overline{\rho}k\overline{S}_{ij} \\ &+ c_2\overline{\rho}k(a_{ik}\overline{S}_{jk} + a_{jk}\overline{S}_{ik} - \tfrac{2}{3}a_{mn}\overline{S}_{mn}\delta_{ij}) \\ &+ c_2\overline{\rho}k(a_{ik}\overline{W}_{jk} + a_{jk}\overline{W}_{ik})\end{aligned} \tag{9}$$

where k is the turbulent kinetic energy, $a_{ij} = (\tau_{ij} - \frac{2}{3}k\delta_{ij})/k$ is the anisotropic tensor, $\overline{S}_{ij}$ is the mean rate of strain defined as:

$$\overline{S}_{ij} = \frac{1}{2}\left(\frac{\partial \overline{u}_i}{\partial x_j} + \frac{\partial \overline{u}_j}{\partial x_i}\right) \tag{10}$$

ϵ is the dissipation rate and c_1 and c_2 are functions dependent on the second and third invariants $A_2 = a_{ij}a_{ji}$, $A_3 = a_{ij}a_{jk}a_{ki}$. Then, Eq. (9) is rewritten with respect to the Reynolds stress τ_{ij} and the mean velocity gradient $\partial \overline{u}_i/\partial x_j$ in order to obtain a more compact form for the slow and rapid contributions, Φ_{ij}^1, Φ_{ij}^2 of the pressure-strain correlations [15] such as $\Phi_{ij} = \Phi_{ij}^1 + \Phi_{ij}^2$. Expressions of these quantities are the following:

$$\Phi_{ij}^1 = -c_1\overline{\rho}\epsilon a_{ij} \tag{11}$$

$$\Phi_{ij}^2 = -c_2\left(P_{ij} + \tfrac{1}{2}P_{ij}^R - \tfrac{1}{3}P_{kk}\delta_{ij}\right) \tag{12}$$

where P_{ij} is the production by the mean flow:

$$P_{ij} = -\overline{\rho}\tau_{ik}\frac{\partial \widetilde{u}_j}{\partial x_k} - \overline{\rho}\tau_{jk}\frac{\partial \widetilde{u}_i}{\partial x_k} \tag{13}$$

and P_{ij}^R is the production generated by the rotation:

$$P_{ij}^R = -2\overline{\rho}\Omega_p(\epsilon_{jpk}\tau_{ki} + \epsilon_{ipk}\tau_{kj}) \tag{14}$$

Due to these considerations, the modeled transport equation of the Reynolds stress tensor takes the form as follows:

$$\begin{aligned}\frac{\partial}{\partial t}(\overline{\rho}\tau_{ij}) + \frac{\partial}{\partial x_k}(\overline{\rho}\tau_{ij}\widetilde{u}_k) = &P_{ij} + P_{ij}^R - \frac{2}{3}\overline{\rho}\epsilon\delta_{ij} + \Phi_{ij}^1 \\ &+ \Phi_{ij}^2 + \Phi_{ij}^w + J_{ijk}\end{aligned} \tag{15}$$

where:

$$\begin{aligned}\Phi_{ij}^w = &c_1^w\frac{\overline{\rho}\epsilon}{k}\left(\tau_{kl}n_kn_l\delta_{ij} - \frac{3}{2}\tau_{ki}n_kn_j - \frac{3}{2}\tau_{kj}n_kn_i\right)f_w \\ &+ c_2^w\left(\Phi_{kl}^2n_kn_l\delta_{ij} - \frac{3}{2}\Phi_{ik}^2n_kn_j - \frac{3}{2}\Phi_{jk}^2n_kn_i\right)f_w\end{aligned} \tag{16}$$

$$J_{ijk} = \frac{\partial}{\partial x_k}\left(\overline{\mu}\frac{\partial \tau_{ij}}{\partial x_k} + c_s\overline{\rho}\frac{k}{\epsilon}\tau_{kl}\frac{\partial \tau_{ij}}{\partial x_l}\right) \tag{17}$$

The terms on the right-hand side of Eq. (15) are identified as production by the mean flow, dissipation rate, slow redistribution, rapid redistribution, wall reflection, and diffusion. The wall reflection term has been introduced in the model in order to take into account the pressure fluctuations from a rigid wall. The functions c_1, c_2, c_1^w, c_2^w are empirically calibrated as: $c_1 = 1 + 2.58AA_2^{1/4}(1 - \exp(-(0.0067R_t)^2))$, $c_2 = 0.75A^{1/2}$, $c_1^w = -\frac{2}{3}c_1 + 1.67$, $c_2^w = \max(\frac{2}{3}c_2 - 1/6, 0)/c_2$ where $A = 1 - 9/8(A_2 - A_3)$ is the flatness coefficient parameter and $R_t = k^2/\nu\epsilon$ is the turbulent Reynolds number. In expression (16), $f_w = 0.4k^{3/2}/\epsilon x_n$ is a function dependent of the normal distance to the wall x_n and n is the normal to the wall. The coefficient c_s takes the value of 0.22. The dissipation rate ϵ of expression (15) is computed by means of the following transport equation which takes the form as:

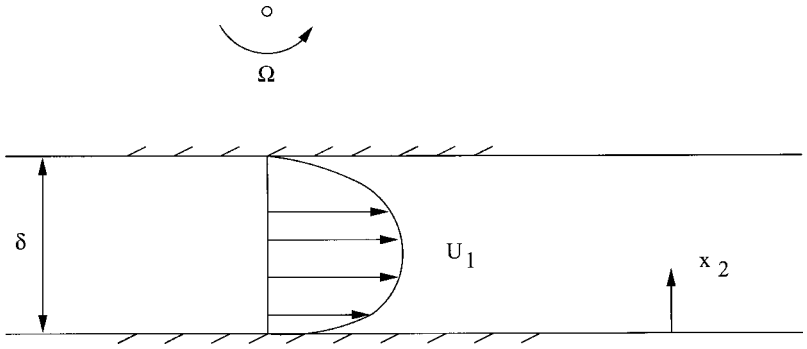

Fig. 1 Schematic of fully-developed turbulent channel flow in a rotating frame

$$\frac{\partial}{\partial t}(\overline{\rho}\overline{\epsilon})+\frac{\partial}{\partial x_j}(\overline{\rho}\widetilde{u}_j\overline{\epsilon})=\frac{\partial}{\partial x_j}\left(\overline{\mu}\frac{\partial\overline{\epsilon}}{\partial x_j}+c_\epsilon\overline{\rho}\frac{\overline{k}}{\overline{\epsilon}}\tau_{jl}\frac{\partial\overline{\epsilon}}{\partial x_l}\right)-(c_{\epsilon1}+\psi_1+\psi_2)\overline{\rho}\frac{\overline{\epsilon}}{\overline{k}}\tau_{ij}\frac{\partial\widetilde{u}_j}{\partial x_i}-c_{\epsilon2}\overline{\rho}\frac{\widetilde{\epsilon}\overline{\epsilon}}{\overline{k}} \tag{18}$$

with $c_{\epsilon1}=1.45$, $c_{\epsilon2}=1.9$, $c_\epsilon=0.18$ where

$$\widetilde{\epsilon}=\epsilon-2\nu\left(\frac{\partial\sqrt{k}}{\partial x_n}\right)^2 \tag{19}$$

The function ψ_1 in Eq. (18) is defined as:

$$\psi_1=1.5A\left(\frac{P_{ii}}{2\overline{\rho}\overline{\epsilon}}-1\right) \tag{20}$$

and has the effect of reducing the turbulence length scale. Relative to the model of Shima [16], the function ψ_1 has been modified to simulate flows with fluid injection through a porous wall. The reason is that this function can reach too large values, in comparison with the standard value $c_{\epsilon1}$, when flows are far from equilibrium. Due to these considerations, the function ψ_1 has been bounded, $|\psi_1|<0.125c_{\epsilon1}$. This has the effects to prevent too early laminarization of flows. On the other hand, the function ψ_2 has been reduced to zero because of its empirical character which alters the rationale formulation of the dissipation rate equation.

Regarding the molecular diffusion and the turbulent transport terms, a gradient hypothesis has been considered:

$$\overline{\sigma_{ij}u_i''}-\frac{1}{2}\overline{\rho\widetilde{u_k''u_k''u_j''}}=\left(\overline{\mu}+c_s\overline{\rho}\frac{\overline{k}}{\overline{\epsilon}}\tau_{jk}\right)\frac{\partial k}{\partial x_j} \tag{21}$$

For the heat transfer, the turbulent flux is computed by means of the k and ϵ variables:

$$\widetilde{h''u_i''}=-\frac{c_\mu k^2}{\epsilon}\frac{c_p}{P_{r_t}}\frac{\partial\overline{T}}{\partial x_i} \tag{22}$$

where c_p and P_{r_t} are the specific heat at constant pressure and the turbulent Prandtl number, respectively. The coefficient c_μ takes the standard value 0.09.

Realizability Conditions for the RSM Model. The Reynolds stress tensor τ_{ij} computed by the modeled transport equation (15) must satisfy the realizability conditions which imply non-negative values of the three principal invariants [17] I_i that appear in the characteristic polynomial $P(\lambda)=\lambda^3-I_1\lambda^2+I_2\lambda-I_3$ of the matrix formed by the components τ_{ij}. It is easier to examine the question of realizability in a coordinate system aligned with the principal axes of the Reynolds stress tensor. For practical reasons, it is also more convenient to analyze the weak form of realizability [17] which requires that when a principal Reynolds stress component vanishes, its time derivative must be positive. This ensures that negative energy component cannot occur when this constraint is satisfied. Although the basis of the principal axes of the Reynolds stress tensor is rotating in time, Speziale et al. [18] have shown that the first derivative constraint takes the same formulation in the principal axes. So that the modeled transport equation (15) of the turbulent stress component $\tau_{(\alpha\alpha)}$ can be written as:

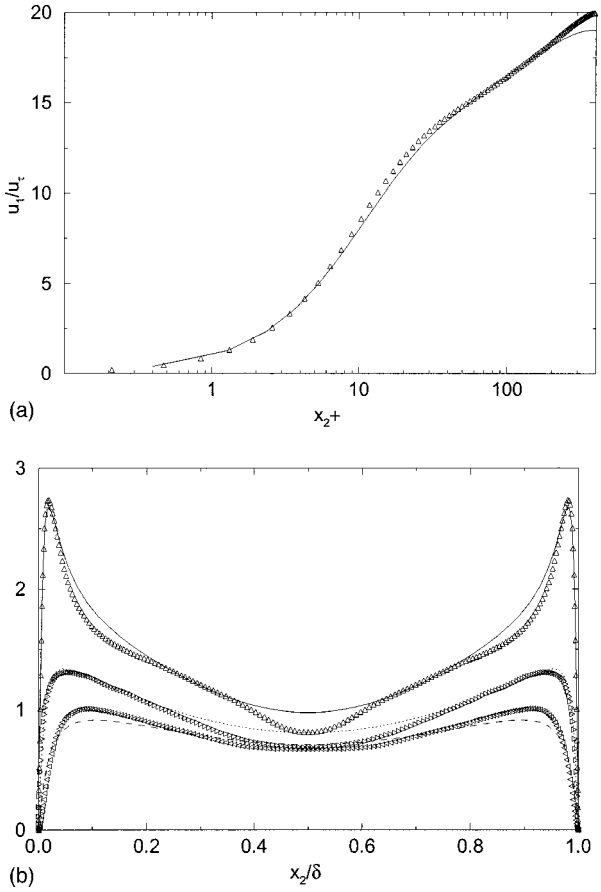

Fig. 2 (*a*) Mean velocity profile $\overline{u_1}/u_\tau$ in logarithmic coordinates; △: DNS; solid-line: RSM. (*b*) Root-mean square velocity fluctuations normalized by the wall shear velocity in global coordinates; Symbols: DNS data; lines: RSM; $(\widetilde{u_1''u_1''})^{1/2}/u_\tau$: △, solid-line; $(\widetilde{u_2''u_2''}R_\tau=395)^{1/2}/u_\tau$: ◁, dashed-line; $(\widetilde{u_3''u_3''})^{1/2}/u_\tau$: ▷, dotted-line.

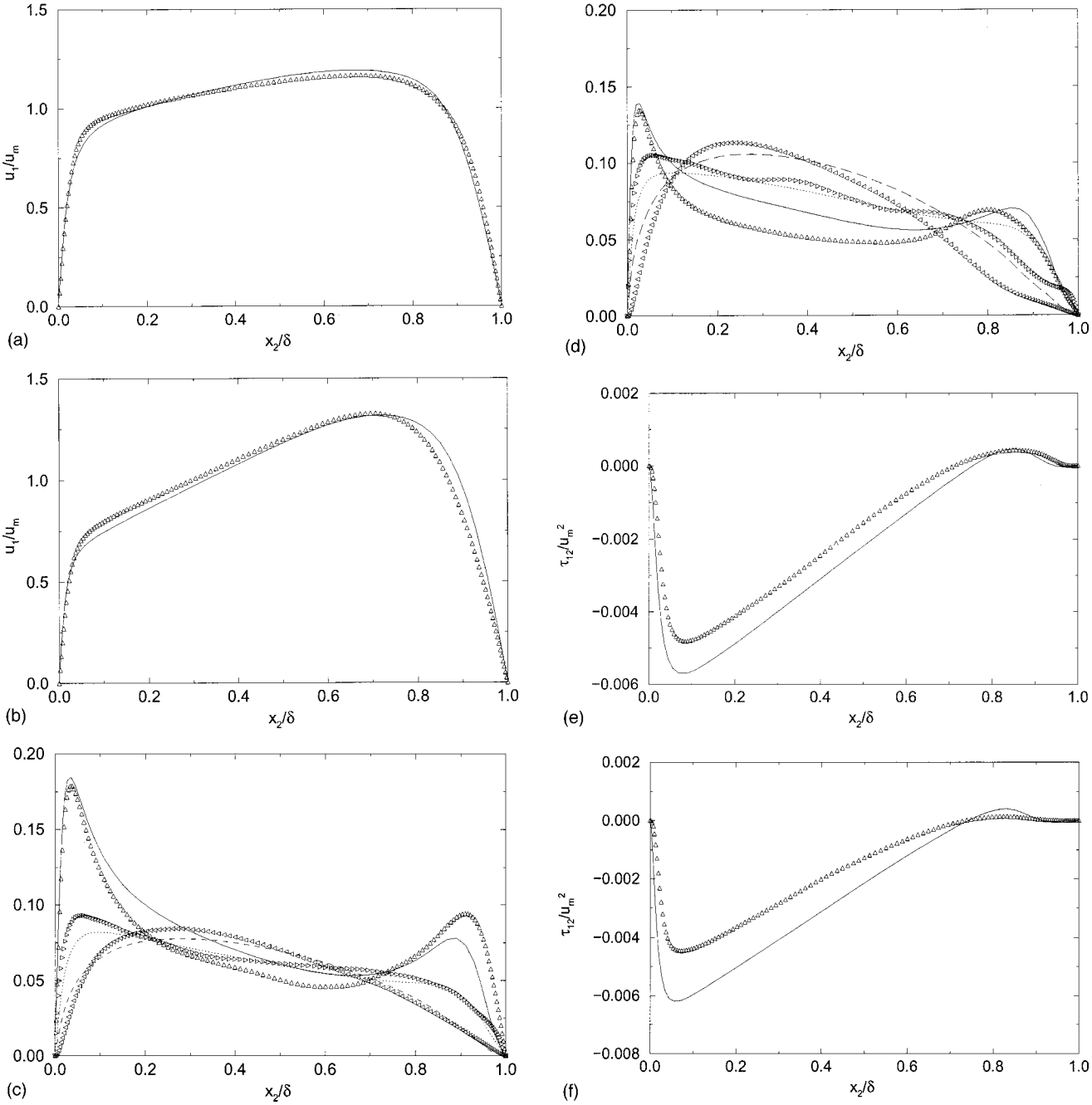

Fig. 3 (***a***), (***b***) **Mean velocity profile $\bar{u}_1/u_m$ in global coordinates; △: DNS; solid-line: RSM.** (***c***), (***d***) **Root-mean square velocity fluctuations normalized by the bulk velocity; Symbols: DNS data; lines: RSM;** $(\widetilde{u_1''u_1''})^{1/2}/u_m$**: △, solid-line;** $(\widetilde{u_2''u_2''})^{1/2}/u_m$**: ◁, dashed-line;** $(\widetilde{u_3''u_3''})^{1/2}/u_m$**: ▷, dotted-line.** (***e***), (***f***) **Turbulent Reynolds shear stress normalized by the bulk velocity in global coordinates** $\widetilde{u_1''u_2''}/u_m^2$**; △: DNS; solid-line: RSM.** (***a***, (***c***), (***e***)**:** $R_\tau=162$, $R_o=18$; (***b***), (***d***), (***f***)**:** $R_\tau=162$, $R_o=6$.

$$\overline{\rho}\frac{d\tau_{(\alpha\alpha)}}{dt}=P_{(\alpha\alpha)}+P^R_{(\alpha\alpha)}-\frac{2}{3}\overline{\rho}\epsilon-c_1\overline{\rho}\frac{\epsilon}{k}\left(\tau_{(\alpha\alpha)}-\frac{2}{3}k\right)$$
$$-c_2\left(P_{(\alpha\alpha)}+\frac{1}{2}P^R_{(\alpha\alpha)}-\frac{1}{3}P_{\alpha\alpha}\right) \quad (23)$$

where the Einstein summation convention is suspended for indices which lies within parentheses. The diffusion term as well as the reflection term are not considered. When the component stress $\tau_{(\alpha\alpha)}$ vanishes, it can be shown that the production terms $P_{(\alpha\alpha)}$ and $P^R_{(\alpha\alpha)}$ are zero so that the weak realizability conditions implies:

$$c_1 \geqslant 1-c_2\frac{P_{\alpha\alpha}}{2\overline{\rho}\overline{\epsilon}} \quad (24)$$

Due to the expressions of the coefficients c_1 and c_2, Eq. (24) is verified when the production term $P_{\alpha\alpha}$ of the turbulent kinetic energy is positive. This corresponds to the usual case of flow physics and therefore ensures the satisfaction of the weak realizability constraint.

Nonrotating Channel Flow

Numerical simulation of fully developed turbulent channel flow is compared with data of direct numerical simulation [13] for the

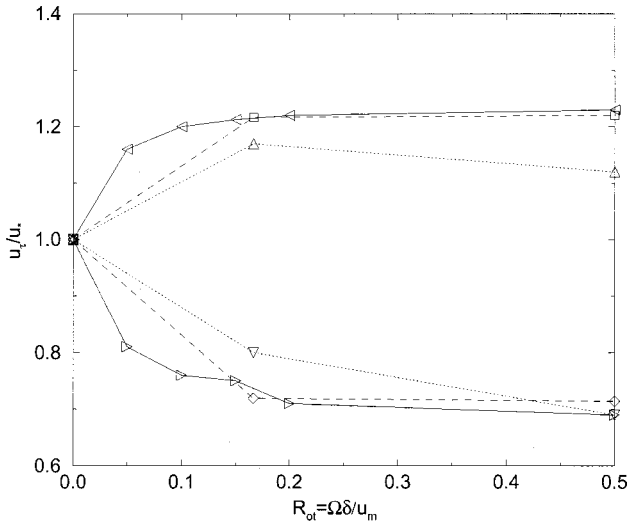

Fig. 4 Variation with the rotation number $R_{ot}=\Omega\delta/u_m$ of the normalized cyclonic and anticyclonic friction velocities. Solid-line, ◁, ▷: DNS results from Kristoffersen et al. [2]; dotted-line, △, ▽: DNS results from Lamballais et al. [3]; dashed-line, □, ◇: present RSM results.

Reynolds number $R_\tau=u_\tau\delta/2\nu=395$, based on the averaged friction velocity u_τ and the channel width $\delta/2$ (see Fig. 1 with $\Omega=0$). Other useful definitions of the Reynolds number include those based on the mean centerline velocity $R_c=u_c\delta/\nu$ and the bulk velocity $R_m=u_m\delta/\nu$. In the present case, RSM results can be compared with DNS data computed for incompressible flow because the Mach number takes a low value. The closure equation (22) hasn't influenced the numerical results due to the fact that the temperature is almost uniform. Figure 2(*a*) describes the dimensionless velocity profile $\overline{u_1}/u_\tau$ in wall coordinates $x_2^+=x_2u_\tau/\nu$ in order to illustrate the logarithmic region. The velocity follows very well the DNS data but the logarithmic profile is not completely resolved in the center of the channel. The ratio of the centerline velocity to the bulk velocity takes the value 1.13, quite close to DNS result, 1.15. Excellent agreement with Dean's correlation of $u_c/u_m=1.28R_m^{-0.0116}=1.15$ is also obtained. The value of the skin friction coefficient computed by Dean's suggested correlation $c_f=0.073R_m^{-0.25}=6.80$ agrees well the DNS result, 6.70. Figure 2(*b*) shows the axial, normal, and spanwise turbulence intensities normalized by the wall-shear velocity $(\widetilde{u_i''u_i''})^{1/2}/u_\tau$ ($i=1,2,3$), versus the global coordinates x_2/δ. The Reynolds stress model provides good agreement with the DNS data. In particular, the peak of the streamwise turbulence intensity in the wall region is well captured.

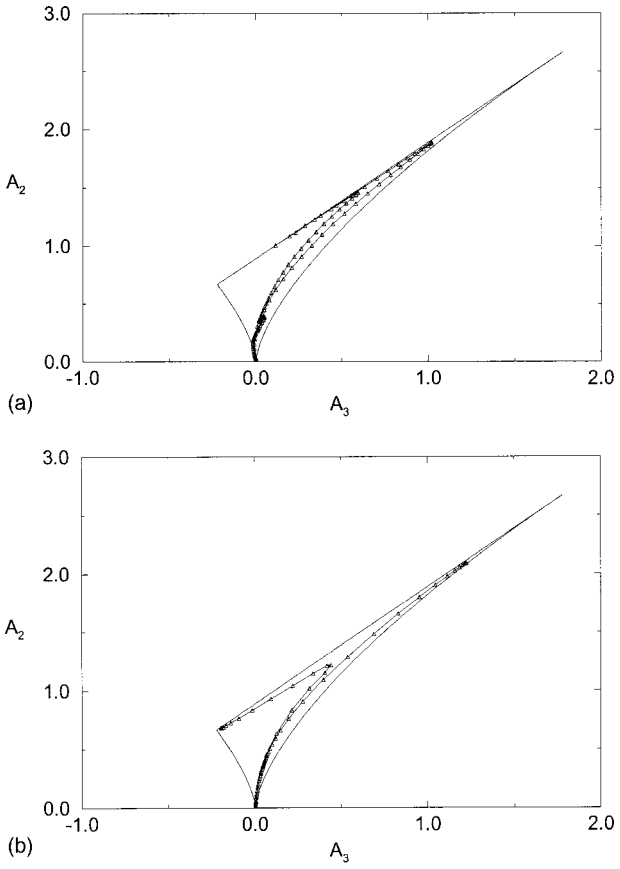

Fig. 5 Solution trajectories in fully developed rotating channel flow projected onto the second-invariant/third-invariant plane (*a*) DNS; (*b*) RSM.

Rotating Channel Flows

Numerical simulations of rotating channel flows are performed for the Reynolds number $R_\tau=162$, based on the friction velocity u_τ which is defined as $u_\tau=\sqrt{\frac{1}{2}(u_{\tau c}^2+u_{\tau a}^2)}$ where $u_{\tau c}$ and $u_{\tau a}$ are, respectively, the friction velocities on the cyclonic and anticyclonic walls. The Reynolds number based on the bulk velocity takes the value $R_m=5000$. For this application, different values of the Rossby number $R_0=3u_m/\delta\Omega$ are considered, $R_0=18$ and $R_0=6$, respectively. These values correspond to moderate and high rotation regimes. The vector rotation considered is along the spanwise direction x_3 as indicated in Fig. 1. Figures 3(*a*),(*b*) show the mean dimensionless velocity profiles normalized by the bulk velocity $\overline{u_1}/u_m$ versus the global coordinates for both rotationre-

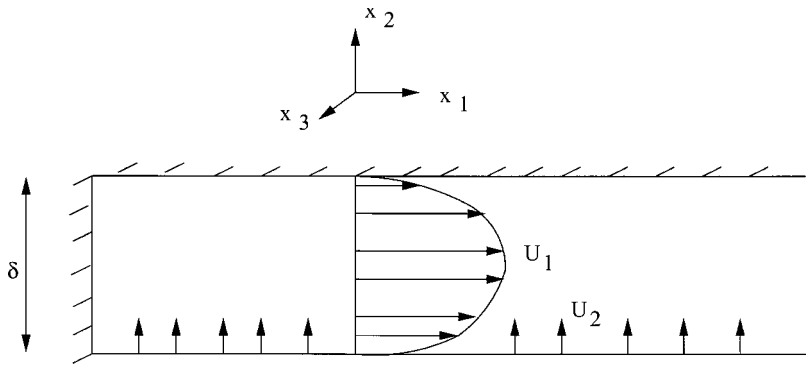

Fig. 6 Schematic of channel flow with fluid injection

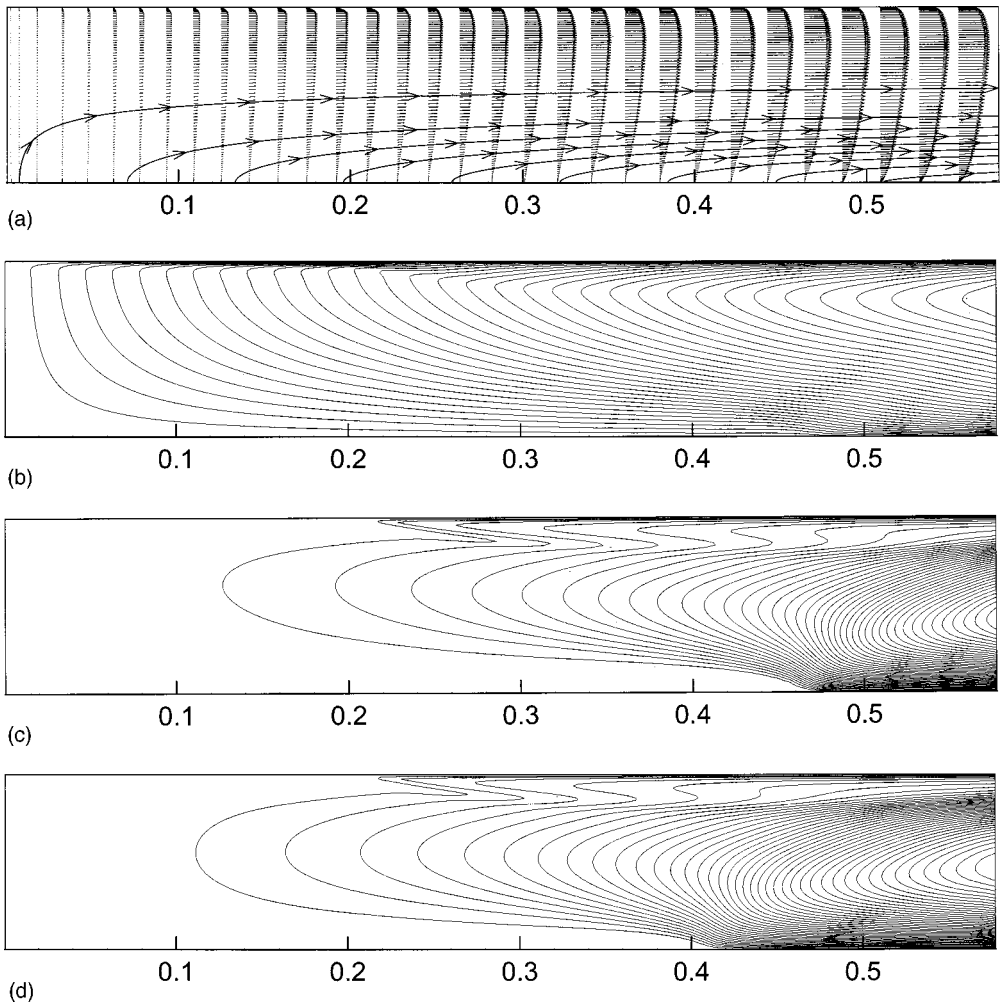

Fig. 7 (*a*) Streamlines and mean flow velocity field; $\sigma_s=0.2$. (*b*) Mach number contours; $\triangle=0.01$; $\sigma_s=0.2$. (*c*), (*d*) Contours of turbulent Reynolds number $R_t=k^2/\nu\epsilon$; $\triangle=110$; (*c*): $\sigma_s=0.2$; $0<R_t<4000$. (*d*): $\sigma_s=0.5$; $0<R_t<4200$.

gimes. These figures illustrate the asymmetric character of the flow because of the rotation effects. For both rotation regimes, an excellent agreement between the RSM simulations and DNS data of Lamballais et al. [3] is observed. For these rotating flows, it is of interest to note that the mean component $\overline{u_1}$ of the velocity is only affected by the Coriolis term through the turbulent shear stress τ_{12} which appears in the momentum equation (2). For $k-\epsilon$ model with a Boussinesq hypothesis, it is a simple matter to show that the mean velocity profile remains perfectly symmetric. For both simulations performed at $R_0=18$ and $R_0=6$, one can notice that the mean velocity profile exhibits a linear region of constant shear stress. The computation indicates that the slope of the mean velocity gradient $\partial\overline{u_1}/\partial x_2$ is approximately equal to $2\Omega_3$, and corresponds to a nearly-zero mean spanwise absolute vorticity vector, i.e., $\overline{W}_3=\overline{\omega}_3+2\Omega_3\approx 0$ where $\omega_i=\epsilon_{ijk}\partial u_k/\partial x_j$ represents the vorticity vector, as already noticed experimentally by Johnston et al. [1]. By considering the Richardson number defined as:

$$R_i=\frac{-\Omega_3(S_{12}-\Omega_3)}{S_{12}^2} \tag{25}$$

it can be mentioned that this particular portion of the profile represents a region of neutral stability $R_i\approx 0$. On the cyclonic side, the flow is stabilized since the Richardson number R_i is positive whereas negative values on the anticyclonic wall imply that the rotation destabilizes the flow [19]. Figures 3(*c*),(*d*) show the evolutions of the axial, normal, and spanwise turbulence intensities normalized by the bulk velocity $(\widetilde{u_i''u_i''})^{1/2}/u_m$ $(i=1,2,3)$ versus the global coordinates x_2/δ for both rotation regimes. The model predicts Reynolds turbulent stresses in excellent agreement with DNS data [3] for the moderate rotation regime $R_0=18$. For the higher rotation $R_0=6$, a very good agreement is also observed with the DNS data although the turbulence intensity is slightly overpredicted in the cyclonic wall region. The distribution of the turbulence fluctuations differs appreciably in the nonrotating and rotating cases. When the rotation rate is increased, the turbulence activity is more reduced for the cyclonic wall than for the anticyclonic wall. This suggests that the turbulence on the cyclonic side may originate from interaction with turbulent anticyclonic side. Due to the rotation, the flow anisotropy is modified. Near the anticyclonic side, the intensity of the streamwise velocity fluctuations $(\widetilde{u_1''u_1''})^{1/2}/u_m$ decreases with the rotation rate whereas the intensities of the normal and spanwise velocity fluctuations $(\widetilde{u_2''u_2''})^{1/2}/u_m$, $(\widetilde{u_3''u_3''})^{1/2}/u_m$ are increased. On the other hand, it can be observed a monotonic decrease of the root-mean square velocity components $(\widetilde{u_i''u_i''})^{1/2}/u_m$ $(i=1,2,3)$ near the cyclonic channel side. Figures 3(*e*), (*f*) show the Reynolds shear stress normalized by the bulk velocity $\widetilde{u_1''u_2''}/u_m^2$ in global coordinates for

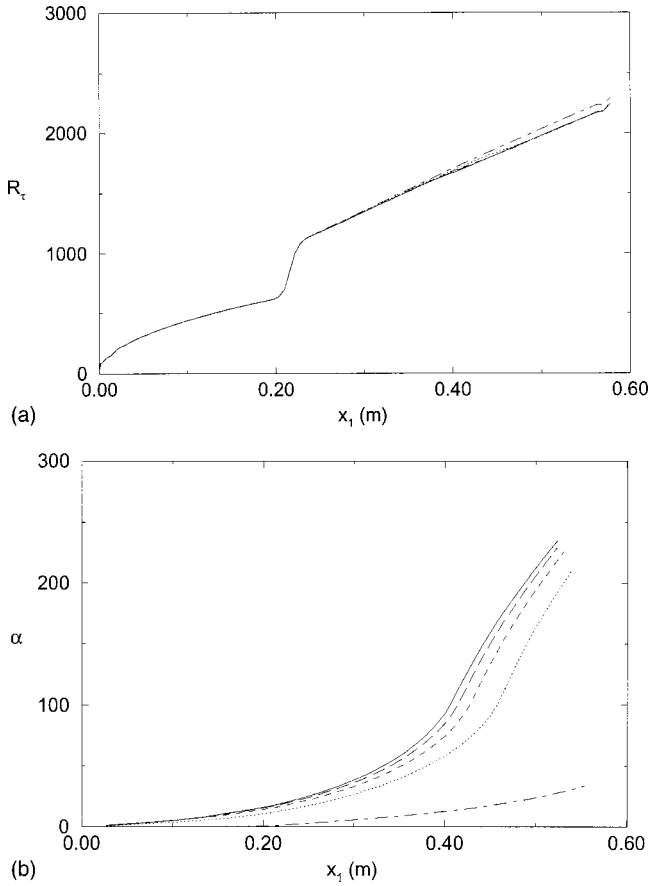

Fig. 8 Axial variations of turbulent coefficients for different values of the injection parameter σ_s. (*a*) Reynolds number R_τ; (*b*) coefficient α. Dot-dashed-line: $\sigma_s=0.1$; dotted-line: $\sigma_s=0.2$; dashed-line: $\sigma_s=0.3$; long-dashed-line: $\sigma_s=0.4$; solid-line: $\sigma_s=0.5$.

both Rossby numbers. The asymmetric character of the flow is well illustrated. Figure 4 describes the evolution of the normalized friction velocities on the cyclonic and anticyclonic walls u_τ/u_* versus the number rotation $R_{0t}=\Omega\delta/u_m=3/R_0$. The quantity u_* is the friction velocity in the absence of rotation. The present results produced by the Reynolds stress model appear to be quite close to DNS data of Kristoffersen and Andersson [2] but slightly overpredicted near the anticyclonic wall in comparison with data of Lamballais et al. [8] Figure 5 shows the solution trajectories projected onto the plane formed by the second invariant and third invariant for the DNS simulation and RSM prediction. The solution trajectories are computed along a straight line normal to the walls in a cross section of the channel. It can be seen that the trajectories produced by the model remain inside the curvilinear triangle which is the realizable region, and agree well with the DNS trajectories. Due to rotation, the trajectories are not symmetric when moving from the anticyclonic wall toward the cyclonic wall.

Channel Flows With Wall Injection

The objective is to investigate the flow in a channel with appreciable fluid injection through a permeable wall as indicated in Fig. 6. The wall injection is encountered in the combustion induced flowfields in solid propellant rocket motors (SRM). It is known that the flow in a channel with wall injection evolves significantly with respect to the distance from the front wall. Different regimes of flow are observed depending on the injection Reynolds number $R_s=\rho_s u_s\delta/\mu$, defined with the injection density ρ_s, the velocity u_s, the dynamics viscosity μ, at the porous surface, and with the height δ of the planar channel. In the first regime, the velocity field is developed in accordance with the laminar theory. The second flow regime is characterized by the development of turbulence and is affected by the transition process of the mean axial velocity when a critical turbulence threshold is attained. Simulations of channel flows with wall injection using a first-order closure model have provided different predictions of the transition process and overpredicted turbulence levels by about 300 percent and 200 percent in the post-transition of the flow [20–22]. Simulations using a second-order closure model with an algebraic relation for the turbulence macro-length scale were performed by Beddini [23]. Experimental data of Yamada et al. [24] were overpredicted by about 200 percent but a reasonable agreement with the data of Dunlap et al. [25] was obtained by generating pseudo-turbulence at the porous surface. These previous numerical results show that channel flows with wall injection present physics phenomena that are difficult to reproduce by simulations. A recent specific experimental setup has been realized at ONERA for investigating the characteristics of injection driven flows. The planar experimental facility is composed of a parallelepipedic channel bounded by a lower porous plate. Values of the duct length and the channel height are, respectively, $L=58.1$ cm and $\delta=1.03$ cm. Cold air at 303 K is injected with a uniform mass flow rate $\mathrm{m}=2.619\,\mathrm{kg/m^2s}$ through a porous material of porosities, 8 μm or 18 μm. The injection velocities are fixed by the local pressure in the channel. In accordance with the operating conditions of the experimental setup, the pressure at the head-end of the channel is $p_0=1.5$ bar wheras the exit pressure is $p_e=1.374$ bar. Due to the mass conservation equation, the flow Reynolds number $R_m=\rho_m u_m\delta/\mu$ based on the bulk density ρ_m and the bulk velocity u_m varies linearly versus the axial distance of the channel so that it can be computed as $R_m=mx_1/\mu$. It ranges from zero to the approximate value 9×10^4. The injection Reynolds number is close to 1600. Experiments have been carried out by Avalon [14].

Different boundary conditions are applied in the computational domain. For the impermeable walls, no slip on velocity and constant temperature are required. Zero turbulent kinetic energy and the wall dissipation rate value $\epsilon_w=2\nu(\partial\sqrt{k}/\partial x_n)^2$ are specified. For the permeable wall, the inflow boundary condition requires a constant mass flow rate at the same temperature. Experimental investigations [14,26] of injected air from porous plate indicate that some stationary velocity fluctuations appear in the flow and that the disturbance amplitude increases with increasing injection velocity. Due to this situation, the turbulence fluctuations at the porous surface can be related to the mean injected velocity by means of a coefficient defined as $\sigma_s=(\widetilde{u_2''u_2''}/u_s^2)^{1/2}$ to be parametrically investigated. Other correlations such as $\widetilde{u_1''u_1''}$ or $\widetilde{u_3''u_3''}$ are smaller than the normal velocity fluctuations $\widetilde{u_2''u_2''}$ of the injected flow. In this work, several simulations are performed for investigating the influence of turbulence in injected fluid, $\sigma_s=0.1$, 0.2, 0.3, 0.4, and 0.5. For injection of low turbulence intensity, the reasonable wall dissipation ϵ_w is also imposed at the porous surface. Another point to emphasize concerns the pressure fluctuations. Considering that the permeable wall does not reflect the pressure fluctuations, the term Φ_{ij}^w of Eq. (15) is reduced to zero in the normal direction to the permeable wall. The slow and rapid pressure-strain correlation terms Φ_{ij}^1 and Φ_{ij}^2 of Eqs. (11) and (12) have not been modified. The reason is that the functions c_1 and c_2 in that modeled terms are dependent of the flow turbulent variables, such as the anisotropy tensor a_{ij} or the Reynolds number R_t, and are automatically modified by the nature of the flow. No more modifications are necessary because the local effects of flowfield anisotropy near wall are incorporated in the modeled term [11] $\Phi_{ij}-\frac{2}{3}\overline{\rho\epsilon}\delta_{ij}$.

Figure 7(*a*) shows the streamlines and the mean velocities of the flowfield. Strong effects of the streamlines curvature are observed near the porous wall due to the fluid injection. The veloci-

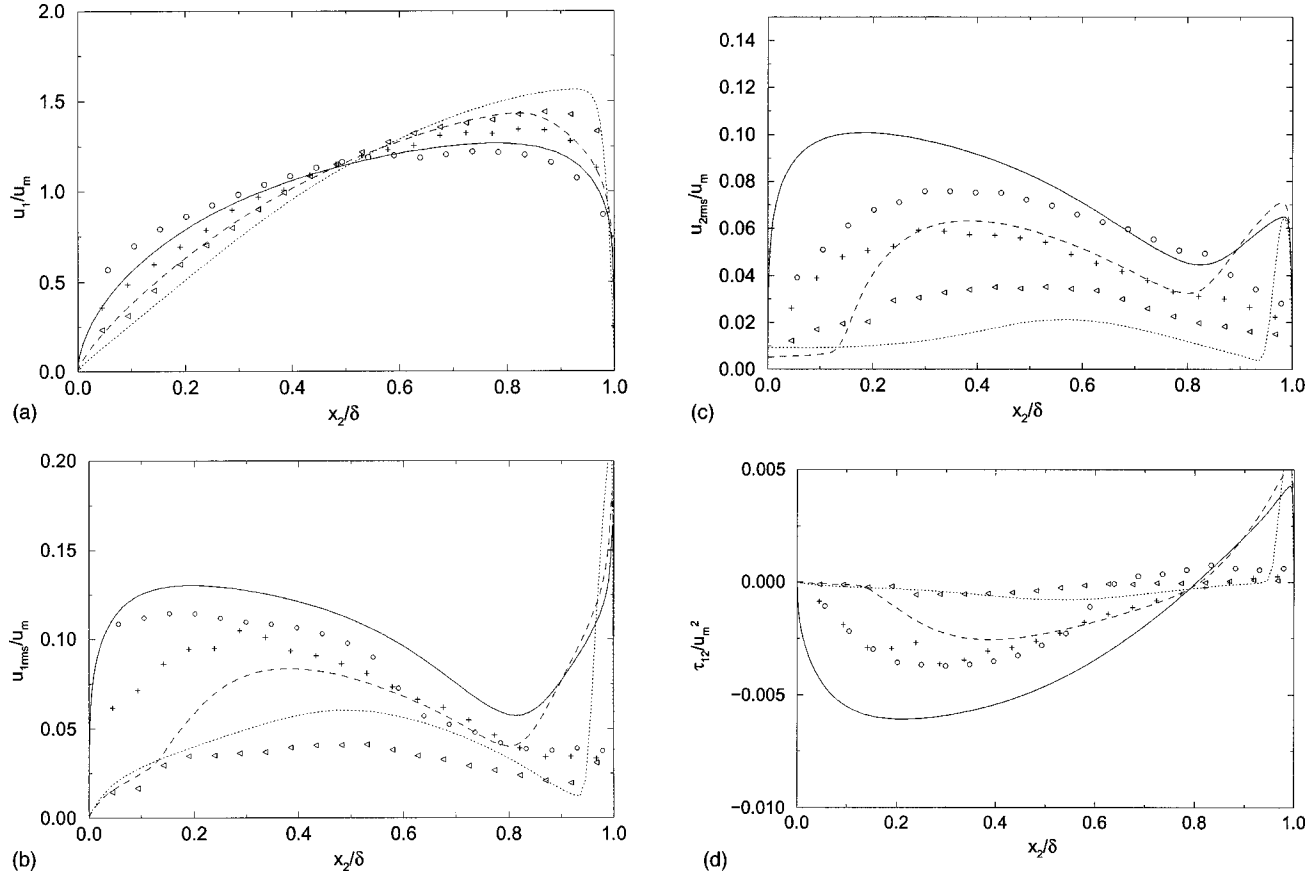

Fig. 9 (*a*) **Mean dimensionless velocity profiles.** (*b*) **Root-mean square velocity fluctuations normalized by the bulk velocity** $(\widetilde{u_1''u_1''})^{1/2}/u_m$. (*c*) $(\widetilde{u_2''u_2''})^{1/2}/u_m$. (*d*) $\widetilde{u_1''u_2''}/u_m^2$. $\sigma_s=0.2$. **Symbols: experimental data; lines: RSM.** $x_1=22$ **cm:** ◁, **dotted-line; 40 cm: +, dashed-line; 57 cm:** ○, **solid-line.**

ties increase rapidly in the boundary layer generated by the rigid wall. Figure 7(*b*) illustrates the Mach number contours of the channel flow. High resolution of the steady-state computational flowfield can be observed through the regular behavior of the contour lines. The Mach number ranges from zero in the head-end of the channel to approximately 0.33 in the exit section.

Several simulations have been performed to investigate the influence of the turbulence injection. As could be expected, the turbulence transition is affected by the pseudoturbulence injected through the porous wall. Figures 7(*c*), (*d*) show the contours of the turbulent Reynolds number $R_t=k^2/\nu\epsilon$ for different values of the injection parameter. The turbulence is first developed in the impermeable wall region and after in the permeable wall region. Increase of pseudo-turbulence intensity can anticipate the flow transition near the permeable wall but has no effect on the flow in the impermeable wall region. Figure 8(*a*) shows the evolution of the Reynolds number $R_\tau=u_\tau\delta/2\nu$ based on the averaged friction velocity u_τ versus the longitudinal distance of the channel. The average friction velocity is defined as $u_\tau=\sqrt{\frac{1}{2}(u_{\tau w}^2+u_{\tau m}^2)}$ where $u_{\tau w}$ and $u_{\tau m}$ are the friction velocities computed on the impermeable and permeable walls, respectively. The rapid rise of the Reynolds number, which occurs in the first part of the channel at 0.2 m, corresponds to the flow transition near the impermeable wall region. Figure 8(*b*) shows the evolutions of the integral turbulent coefficient

$$\alpha=\frac{c_\mu}{\mu\delta}\int_0^\delta\frac{\overline{\rho}k^2}{\epsilon}dx_2 \tag{26}$$

for different values of the injection parameter σ_s. The rise of the coefficient α figure out the transition locations of the turbulent flow. It can be noticed that the low initial turbulence injection for $\sigma_s=0.1$ is too small to trigger the transition regime. It appears that the flow turbulence intensity remains insensitive to the injected turbulence level when such level is large. Figure 9(*a*) shows the dimensionless mean velocity profiles normalized by the bulk velocity $\overline{u_1}/u_m$ in global coordinates x_2/δ for $\sigma_s=0.2$. The general shapes of the profiles present a good agreement with experimental data. The flatness of the curves is attributed to the turbulent effects which increase when moving to the exit section of the channel. Figures 9(*b*), (*c*), (*d*) show the evolutions of the streamwise, normal, and cross turbulent velocity fluctuations normalized by the bulk velocity, $(\widetilde{u_1''u_1''})^{1/2}/u_m$, $(\widetilde{u_2''u_2''})^{1/2}/u_m$, $(\widetilde{u_1''u_2''})/u_m^2$, for $\sigma_s=0.2$ in different sections of the channel located at $x_1=22$ cm, 40 cm, and 57 cm. In a general way, it can be observed that the levels of the Reynolds stresses of the flow are fairly reproduced by the RSM model although that minor discrepancy with the experimental data appears for the last section. The disagreement near the impermeable side must be attributed to the experimental data which are altered by the hot wire probe which is introduced through the impermeable wall. Figures 10(*a*),(*b*) show the normal velocity fluctuations $(\widetilde{u_2''u_2''})^{1/2}/u_m$, in different cross sections for the RSM and the $k-\epsilon$ model of Myong and Kasagi [27]. The $k-\epsilon$ model overpredicts the turbulent stresses by about 300 percent.

Conclusion

Numerical flow field simulations for the nonrotating fully developed channel flow, the rotating channel flows and the channel flows with wall injection have been performed using a Reynolds stress model. Comprehensive comparisons with DNS data or ex-

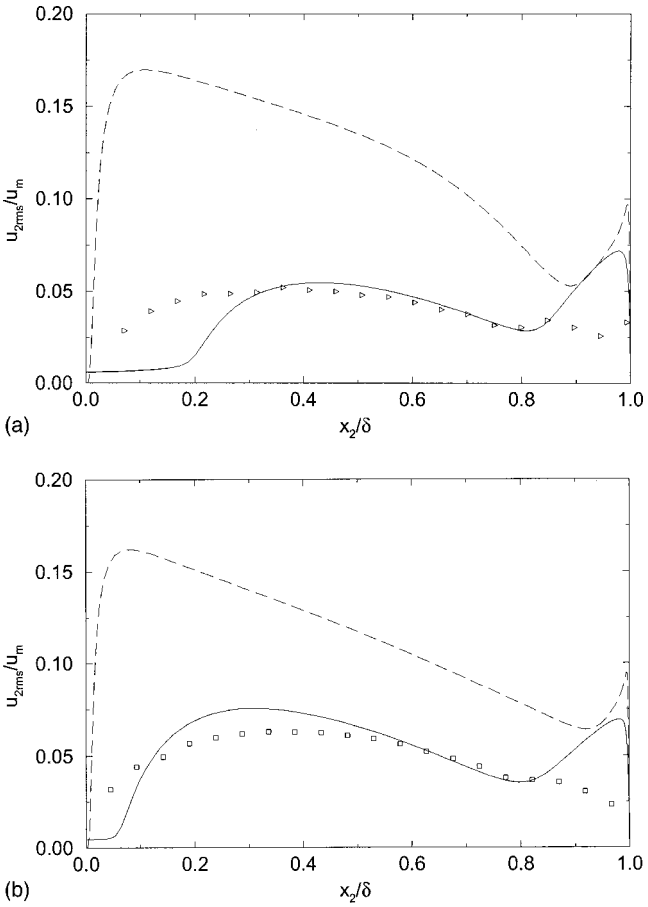

Fig. 10 Root-mean square velocity fluctuations normalized by the bulk velocity $(\widetilde{u_2''u_2''})^{1/2}/u_m$. $\sigma_s=0.2$. Symbols: experimental data; solid-line: RSM; dashed-line: $k-\epsilon$. (*a*) 35 cm: ▷; (*b*) 45 cm: □.

perimental data for each encountered configuration have been presented. It has been demonstrated that the model which has been extended for compressible flows and modified for system rotation and wall injection predicts accurately the flows. For rotating channel flows, the RSM model yields asymmetric mean velocity and turbulent stresses in very good agreement with the DNS data. For the channel flow with fluid injection through a permeable wall, different flow regimes from laminar to turbulent as well as the transition of the mean velocity profile, have been reproduced in accordance with the experimental data. Because of the presence of permeable and impermeable walls, the development of turbulence occurs at two different locations in the channel. Effects of pseudo-turbulence in injected fluid through the porous surface have also been investigated.

References

[1] Johnston, J. P., Halleen, R. M., and Lezius, D. K., 1972, ''Effects of Spanwise Rotation on the Structure of Two-Dimensional Fully Developed Turbulent Channel Flow,'' J. Fluid Mech., **56**, pp. 533–557.

[2] Kristoffersen, R., and Andersson, H. I., 1973, ''Direct simulations of low-Reynolds-number turbulent flow in a rotating channel,'' J. Fluid Mech., **256**, pp. 163–197.

[3] Lamballais, E., Métais, O., and Lesieur, M., 1998, ''Spectral-Dynamic Model for Large-Eddy Simulations of Turbulent Rotating Flow,'' Theor. Comput. Fluid Dyn., **12**, pp. 149–177.

[4] Chaouat, B., 1997, ''Flow Analysis of a Solid Propellant Rocket Motor with Aft Fins,'' J. Propul. Power, **13**, No. 2, pp. 194–196.

[5] Launder, B. E., Reece, G. J., and Rodi, W., 1975, ''Progress in the Development of a Reynolds Stress Turbulence Closure,'' J. Fluid Mech., **68**, pp. 537–566.

[6] Speziale, C. G., Sarkar, S., and Gatski, T. B., 1991, ''Modelling the Pressure-Strain Correlation of Turbulence: an Invariant Dynamical Systems Approach,'' J. Fluid Mech., **227**, pp. 245–272.

[7] Gibson, M. M., and Launder, B. E., 1978, ''Ground Effects on Pressure Fluctuations in the Atmospheric Boundary Layer,'' J. Fluid Mech., **86**, pp. 491–511.

[8] So, R. M., Lai, Y. G., and Zhang, H. S., 1991, ''Second Order Near Wall Turbulence Closures: a Review,'' AIAA J., **29**, No. 11, pp. 1819–1835.

[9] Hanjalic, K., Hadzic, I., and Jakilic, S., 1999, ''Modeling Turbulent Wall Flows Subjected to Strong Pressure Variations,'' ASME J. Fluids Eng., **121**, pp. 57–64.

[10] Durbin, P. A., 1993, ''A Reynolds Stress Model for Near-Wall Turbulence,'' J. Fluid Mech., **249**, pp. 465–498.

[11] Launder, B. E., and Shima, N., 1989, ''Second Moment Closure for the Near Wall Sublayer: Development and Application,'' AIAA J., **27**, No. 10, pp. 1319–1325.

[12] Pettersson, B. A., and Andersson, H. I., 1997, ''Near Wall Reynolds Stress Modelling in Non-inertial Frames of Reference,'' Fluid Dyn. Res., **19**, pp. 251–276.

[13] Moser, R., Kim, D., and Mansour, N., 1999, ''Direct Numerical Simulation of Turbulent Channel Flow up to $R_\tau=590$,'' Phys. Fluids, **11**, No. 4, pp. 943–945.

[14] Avalon, G., 1998, ''Flow Instabilities and Acoustic Resonance of Channels with Wall Injection,'' AIAA Paper 98-3218, July, In 34th AIAA/ASME/SAE/ASEE Joint Propulsion Conference and Exhibit.

[15] Chaouat, B., 1999, ''Numerical Simulations of Fully Developed Channel Flows Using k-ϵ, Algebraic and Reynolds Stress Models,'' AIAA Paper 99-0158, Jan., In 37th AIAA Aerospace Sciences Meeting and Exhibit.

[16] Shima, N., 1993, ''Prediction of Turbulent Boundary Layers with a Second-moment Closure: Part I-Effects of Periodic Pressure Gradient, Wall Transpiration and Free-stream Turbulence. Part II-Effects of Streamline Curvature and Spanwise Rotation,'' ASME J. Fluids Eng., **115**, pp. 56–69.

[17] Schumann, U., 1977, ''Realizability of Reynolds Stress Turbulence Models,'' Phys. Fluids, **20**, No. 5, pp. 721–725.

[18] Speziale, C. G., Abid, R., and Durbin, P. A., 1994, ''On the Realisability of Reynolds Stress Turbulence Closures,'' J. Sci. Comput., **9**, No. 4, pp. 369–403.

[19] Tritton, D. J., 1992, ''Stabilization and destabilization of turbulent shear flow in a rotating fluid,'' J. Fluid Mech., **241**, pp. 503–523.

[20] Sviridenkov, A. A., and Yagodkin, V. I., 1976, ''Flows in the Initial Sections of Channels with Permeable Walls,'' Fluid Dyn., **11**, pp. 43–48.

[21] Sabnis, J. S., Madabhushi, R. K., Gibeling, H. J., and Donald, H. M., 1989, ''On the Use of $k-\epsilon$ Turbulence Model for Computation of Solid Rocket Internal Flows,'' AIAA Paper 89-2558, July, in 25th AIAA/ASME/SAE/ASEE Joint Propulsion Conference and Exhibit.

[22] Chaouat, B., 1997, ''Computation using $k-\epsilon$ Model with Turbulent Mass Transfer in the Wall Region,'' 11th *Symposium on Turbulence Shear Flows*, Vol. 2, pp. 2.71–2.76.

[23] Beddini, R. A., 1986, ''Injection-Induced Flows in Porous-Walled Ducts,'' AIAA J., **11**, No. 6, pp. 1766–1773.

[24] Yamada, K., Goto, M., and Ishikawa, N., 1976, ''Simulative Study on the Erosive Burning of Solid Rocket Motors,'' AIAA J., **14**, No. 9, pp. 1170–1176.

[25] Dunlap, R., Willoughby, P. G., and Hermsen, R. W., 1974, ''Flowfield in the Combustion Chamber of a Solid Propellant Rocket Motor,'' AIAA J., **12**, No. 10, pp. 1440–1443.

[26] Ramachandran, N., Heaman, J., and Smith, A., 1992, ''An Experimental Study of the Fluid Mechanics Associated with Porous Walls,'' AIAA Paper 92-0769, Jan., in 30th Aerospace Sciences Meeting and Exhibit.

[27] Myong, H., and Kasagi, N., 1990, ''A New Approach to the Improvement of $k-\epsilon$ Turbulence Model for Wall-Bounded Shear Flows,'' JSME Int. J., **33**, No. 1, pp. 63–72.

A. N. Secundov
Professor,
Scientific and Research Center "Ecolen,"
2 Ul. Aviamotornaya,
111250, Moscow, Russia

M. Kh. Strelets
Professor

A. K. Travin
Research Scientist

Federal Scientific Center "Applied Chemistry,"
14 Dobrolyubov Ave.,
197198, St. Petersburg, Russia

Generalization of ν_t-92 Turbulence Model for Shear-Free and Stagnation Point Flows

The one-equation, eddy-viscosity transport model of Gulyaev, Kozlov, and Secundov, ν_t-92, is modified and supplemented by an equation for the turbulence length scale. The advantages of the model developed here are demonstrated by computing a shear-free ''boundary layer'' on a flat plate, and the flow and heat transfer near the forward stagnation line of a circular cylinder. Both cases are known to be challenging for conventional turbulence models. [DOI: 10.1115/1.1341196]

Introduction

Although the relatively simple turbulence models based on the scalar eddy-viscosity concept are far from perfect, they are still capable of predicting a rather wide range of aerodynamic and industrial shear flows. A distinguishing physical feature of such flows is that their turbulent length scale is proportional to the characteristic size of a shear layer. However, in many flows of practical interest, most of all in internal flows, the level of turbulence is significant everywhere, not only in the regions of high mean velocity gradients (shear layers). Two typical examples of such flows are the so-called shear-free boundary layer, and the flow in the vicinity of the forward stagnation point/line of bluff bodies. In both cases the length scale of the turbulence is set solely by the external turbulence. Apparently, any model that claims to predict such flows should describe properly not only the turbulence in shear layers but, also, the interaction of the high external turbulence with the solid walls.

The ''shear-free boundary layer,'' i.e., the boundary layer on a flat plate moving with a velocity equal to that of the turbulent free stream, has been studied in a number of works (see, for instance [1–4]). A specific feature of that flow determined in those studies is that the shear-free boundary layer thickness, Δ, scales with the length scale of the external turbulence, $L_e(t)$, and does not depend on its intensity (at high Reynolds number, the second, viscous, length scale of this flow, $(t\nu)^{1/2}$, is much less than $L_e(t)$ and so plays only a minor role). The simplest, one-equation, turbulence models (e.g., ν_t-92 model [5] and S-A model [6]) cannot describe that behavior since they do not contain any information on the free-stream turbulence length scale. Two-equation models and, in particular, the most widely used k-ε model, do in principle provide such a possibility. However, they also fail to predict the character of the near-wall variation of turbulent quantities in the shear-free boundary layer observed in the experiments and in the DNS studies. As shown in [7], the k-ε model, applied to shear-free boundary layers at high Reynolds numbers, predicts that both k and ε vary outside the viscous sublayer as the square root of the distance to the wall, d: $k \sim d^{1/2}$, $\varepsilon \sim d^{1/2}$. As a result, the turbulence length scale L, proportional to $k^{3/2}/\varepsilon$, varies like $d^{1/4}$, whereas experiment and DNS suggest that $k \sim d^0$, $\varepsilon \sim d^{-1}$ and $L \sim d^1$.

The flow near the forward stagnation line of a circular cylinder has also been studied theoretically and experimentally in a number of works. Both the rapid distortion theory of Hunt [8] and experiments [9,10] show that, along with a viscous boundary layer with a thickness proportional to $1/\mathrm{Re}^{1/2}$, another, much thicker, boundary layer exists near the stagnation line. All the turbulence quantities experience significant variations across this layer whose thickness, Δ, is proportional to the length scale of the external turbulence: $\Delta \sim L_e$. So, just as for the shear-free boundary layer, Δ does not depend upon the external turbulence intensity. This very important feature cannot be captured by relatively simple one- and two-equation turbulence models. The failure is caused by the dominant role of the convective terms in the models' transport equations which makes the ''secondary'' boundary layer drastically thinner than in experiments. One of the negative consequences of that deficiency is a significant overestimate (by a factor of 2 or even 3) of the heat flux at the stagnation point. Quite similar effects are typical not only of the cylinder and other bluff bodies, but also of impinging jets (e.g., [11]).

The two flows considered are the simplest examples of a wide class of turbulent flows where a length scale of external turbulence plays a dominant role and, as demonstrated in the above analysis, the conventional eddy-viscosity turbulence models become invalid. Note that the advanced Reynolds Stress Models (RSM), usually considered as computationally expensive but much more capable than the simple eddy-viscosity models, suffer from the same weakness. Although formally RSM include all the production terms for the whole Reynolds stress tensor, they use a local approximation for those stresses as well as for the pressure strain tensor. However, the pressure field can be described accurately only on the basis of the integral of a Poisson equation, and in this sense RSM are inferior to the rapid distortion theory. In addition, a crucial element of any RSM is a transport equation for some turbulence quantity (ω, ε, etc.) that provides a turbulence length scale and, therefore, the RSM automatically inherits some drawbacks of the corresponding transport equations. The authors are aware of only one work [12] reporting a successful resolution of the ''large turbulence length scale'' issue. However, the model used in this work (the four-equation model of Durbin [13]) is much more complicated than one- and two-equation models.

In the present work, we outline a generalization of the one-equation eddy-viscosity transport turbulence model ν_t-92 [5] that makes it applicable to flows where for some reason the turbulence length scale does not scale with the shear layer thickness. The generalization includes an additional equation for the turbulence scale, L. Other than that, some minor alterations of the original terms of the eddy-viscosity transport equation are made, aimed at improving model performance for the shear-free boundary layer. Finally, more serious modifications are suggested, associated with

Contributed by the Fluids Engineering Division for publication in the JOURNAL OF FLUIDS ENGINEERING. Manuscript received by the Fluids Engineering Division April 1, 2000; revised manuscript received October 3, 2000. Associate Editor: P. Bradshaw.

a new parameter, Φ, that increases the role of the ''elliptic'' terms of the model and improves predictions of the stagnation point flow.

Modified ν_t-92 Transport-Equation for Eddy Viscosity

The ν_t-92 model that is the parent of the model we are suggesting in the present study is a one-equation model formulated directly for the eddy viscosity ν_t:

$$\partial\nu_t/\partial t+u_i\partial\nu_t/\partial x_i=(1/\rho)\partial/\partial x_i[\rho(C_0\nu_t+\nu)\partial\nu_t/\partial x_i]+(1/\rho)\times(\partial\nu_t/\partial x_i)\cdot\partial/\partial x_i\{\rho[(C_0-C_1)\nu_i-\nu]\}+P_\nu-D_\nu. \quad (1)$$

Here, u_i are the Favre-averaged velocity components, ν is the kinematic viscosity of the fluid, and the difference between the production and dissipation terms is defined as follows:

$$P_\nu-D_\nu=C_2F_2\{\nu_t\Gamma_1+A_1\nu_t^{4/3}\Gamma_2^{2/3}+A_2[(\nu_t+\nu)\Gamma_1]^{1/2}N_1\}+C_3\nu_t(\partial^2\nu_t/\partial x_i^2+N_2)-C_4\nu_t[\partial\langle U_i\rangle/\partial x_i+abs(\partial\langle U_i\rangle/\partial x_i)]-C_5\Gamma_1^2/a^2-[C_6\nu_t(N_1d+\nu_w)+C_7F_1\nu\nu_t]/d^2 \quad (2)$$

Here, a is the speed of sound, d is the closest distance to the solid wall modified to account for the effect of wall roughness, $d=d_w+0.1k_s$, d_w, where d_w is the real wall-distance, k_s is the effective height of the sand roughness, and ν_w is the eddy viscosity at the wall. At a smooth surface it is equal to zero and at a rough one is defined from the homogeneous boundary condition $(\partial\nu_t/\partial n)_w=0$.

The functions F_1 and F_2 in (2) are defined as:

$$F_1=(N_1d_w+0.4C_8\nu)/(\nu_t+C_8\nu+\nu_w),\quad F_2=(\chi^2+1.3\chi+0.2)/(\chi^2-1.3\chi+1.0),\quad \chi=\nu_t/(7\nu) \quad (3)$$

Finally, relations for the quantities Γ_1, Γ_2, N_1, and N_2 are as follows:

$$\Gamma_1^2=\partial u_i/\partial x_j(\partial u_i/\partial x_j+\partial u_j/\partial x_i),\quad \Gamma_2^2=(\partial^2u_i/\partial x_k^2)(\partial^2u_i/\partial x_k^2),\quad N_1^2=(\partial\nu_t/\partial x_i)^2,\quad N_2^2=(\partial N_1/\partial x_i)^2 \quad (4)$$

The empirical constants of the model are:

$$A_1=-0.5,\ A_2=4.0,\ C_0=0.8,\ C_1=1.6,\ C_2=0.1,\ C_3=4.0,\ C_4=0.35,\ C_5=3.5,\ C_6=2.9,\ C_7=31.5,\ C_8=0.1. \quad (5)$$

For the shear-free boundary layer, DNS and experiment suggest the following functional relations between local values of the eddy viscosity ν_t, and turbulence length scale L, and their free-stream values, $\nu_{te}(t)$ and $L_e(t)$:

$$\nu_t=\nu_{te}f(d/L_e),\quad L=L_e\varphi(d/L_e). \quad (6)$$

Such relations can be satisfied, for instance, if the eddy viscosity obeys the following equation:

$$\nu_t\partial^2\nu_t/\partial x_k^2+\nu_tN_1/L-\nu_tN_1/d=0. \quad (7)$$

Similar to other semi-empirical turbulence models, Eq. (1) contains, as an important element, an ''equilibrium'' relation that can be obtained by neglecting the convective, production, and molecular diffusion terms in (1) and (2):

$$C_0\nu_t\partial^2\nu_t/\partial x_i^2+C_1N_1^2-C_6\nu_tN_1/d=0. \quad (8)$$

From a comparison of (7) with (8), one can see that they have some common features and, consequently, (8) can be presented in a form of the following, more general, ''equilibrium'' relation for the eddy viscosity:

$$b_1\nu_t\partial^2\nu_t/\partial x_k^2+b_2\nu_tN_1/L-b_3\nu_tN_1/d=0, \quad (9)$$

where b_1, b_2, and b_3 are new empirical constants (note that when deriving (9) from (8) it is assumed that $N_1\approx\nu_t/d$) in a turbulent boundary layer.

Considering the equilibrium relation (9), a modified eddy-viscosity transport equation (1) can be written as follows

$$\partial\nu_t/\partial t+u_i\partial\nu_t/\partial x_i=[C_0(1+\Phi)\nu_t+\nu]\partial^2\nu_t/\partial x_i^2+P_\nu^M-D_\nu^M, \quad (10)$$

where the difference between the production and dissipation terms, $P_\nu^M-D_\nu^M$, is given by

$$P_\nu^M-D_\nu^M=C_2F_2\{\nu_t\Gamma_1+A_1\nu_t(\nu_t+\beta\nu)(\nu_t+\nu)^{-2/3}\Gamma_2^{2/3}+A_2[(\nu_t+\nu)\Gamma_1]^{1/2}N_1\}+C_3\nu_t(\partial^2\nu_t/\partial x_i^2+N_2)+C_1(1+\Phi)\nu_tN_1/L/(1+0.1L^2\Gamma_1/(\nu_t+\nu))-C_4\nu_t[\partial\langle U_i\rangle/\partial x_i+abs(\partial\langle U_i\rangle/\partial x_i)]-C_5\nu_t^2\Gamma_1^2/a^2-\{C_6(1+c\Phi)\nu_t(N_1d+\nu_w)+C_7F_1\nu\nu_t\}/d^2. \quad (11)$$

As seen from a comparison of (1), (2) with (10), (11), the major difference between the original and modified equations is associated with the diffusion and destruction terms, and also with an additional production term (with the coefficient C_1). The latter term contains a new variable, turbulence length scale, L, and describes generation of the eddy viscosity due to its spatial nonuniformity, characterized by the quantity N_1. A new parameter $\Phi=K(L^2/\nu_t)\partial L/\partial x_iS_{ik}\partial L/\partial x_k$ (whose meaning is explained in more detail in the next section) is essential only in the vicinity of the stagnation point and results in an increase of the ''elliptic'' terms in both the ν_t and L equations.

In addition, in the course of calibration of the new model some of the empirical constants of the original ν_t-92 transport equation (1) have been somewhat changed (a set of new constants is presented below, after formulation of the equation for turbulence length scale, L). Also, in order to improve the model performance as applied to a near-wall boundary layer with a streamwise pressure gradient, the term of the model with the second derivative of the velocity, Γ_2, is slightly modified (a parameter β is introduced).

Role of Large Scales in Turbulence Transport

The major peculiarity of the flow near a forward stagnation point, already mentioned in the Introduction, is a significant alteration of the turbulence characteristics from those in the ''free stream'' far upstream of the body. Experimental studies (e.g., [10]), show that the turbulence length scale varies along the critical streamline in accordance with the following law:

$$L=L_eF(d/L_e). \quad (12)$$

This law does not involve the free-stream turbulence intensity, $(u'/U)_e$, which means that convection of turbulence in this flow is negligible.

Another mechanism that could be responsible for the strong propagation of the disturbances in the upstream direction observed in the experiments is turbulent diffusion. However, in the vicinity of the stagnation point, the ratio of the diffusion and convective terms of the k-transport equation can be evaluated as $(k_e)^{1/2}/U_e(L_e/D)$, where D is the curvature diameter at the stagnation point. It is clear that this ratio is of the order of, or less than, one, so diffusion of turbulence in the vicinity of the stagnation point is also relatively weak, and the only remaining mechanism that could explain the phenomenon mentioned above is a fluctuating pressure signal, propagating in all directions instantaneously (in the incompressible fluid) or with the speed of sound (in the compressible gas). Note that exactly this mechanism plays a major role in rapid distortion theory [8], which achieves a fair agreement with experiments. However, such pressure signals exist in any turbulent flow, including the shear flows that can be predicted quite accurately by a wide range of existing turbulent mod-

els. So, the question arises why the same models fail to predict the flow near the forward stagnation point. This can be explained as follows.

In typical shear flows the convection, diffusion, and ''elliptic'' propagation of turbulence caused by the pressure signals are of approximately the same order of magnitude. However, as mentioned in the Introduction, the length scale of the turbulence, L, in all such flows (jets, wakes, boundary layers, etc.) is relatively small: L is either significantly less than, or of the same order as, the thickness of the shear layer, δ. Therefore, turbulence propagation due to the pressure fluctuations, though it does take place, does not produce a crucial effect, since it changes the turbulence only within small regions whose size is of order L. In simple turbulence models those changes are accounted for indirectly and rather crudely, or are not accounted for at all. For instance, in one-equation models such as the ν_t-92 and S-A models, the effects of the pressure signals are modeled by introducing a minimum wall distance, d, into the destruction terms of the eddy-viscosity transport equations. In this context it might be noted that the desire to eliminate d (see, for instance, the studies [13,14]) is based mostly on invariance restrictions or numerical considerations rather than on other physical reasons.

The flow near the forward stagnation point/line, as stated many times earlier, can have a much larger length scale of turbulence than a shear flow. For instance, for the circular cylinder, the free-stream turbulence length scale, L_e, can be two orders of magnitude larger than the thickness of the viscous near-wall boundary layer in the vicinity of the stagnation line: $L_e \gg D/Re^{1/2}$. In many cases, L_e can be even larger than the curvature diameter D at the stagnation point. The latter circumstance is very important since exactly the value of that diameter defines the thickness of the dynamic boundary layer where the mean flow velocity is varying from its free-stream value to zero. Precisely for this reason the role of the pressure signals in the turbulence transport in such flows becomes a dominant one and cannot be accounted for by the simple ways applicable for shear flows. Note that, depending on the L_e/D ratio, the incoming turbulence can either increase due to the ''stretching'' of its vortices, or decrease due to the ''blocking'' effect [8].

So the difference between ''typical shear flows'' and shear-free or mixed flows can be considered as a crucial difference of their length scales, resulting in a quite different role for the pressure signals. A quantitative criterion of that difference might be the ratio L_e/δ or L_e/D, depending on whether δ or D defines the size of the boundary layer. However, these parameters are not local and, in addition, suffer some vagueness since L_e can experience some, though not significant, spatial variation. For this reason, in the context of the role of the pressure signals, a more objective criterion of the size of the turbulence length scale is the gradient of the length scale, $\partial L/\partial x_k$.

In shear flows, the ratio of the Reynolds shear stress and the turbulence kinetic energy, $(\nu_t \partial U/\partial y)/k$, is known to be roughly constant, about 0.3. In terms of ν_t and L this is equivalent to $(L^2 \partial U/\partial y)/\nu_t \approx 10$. Considering that in shear flows the gradient of L, $\partial L/\partial x_k$, is very small (less than 0.1), it seems to be natural to suggest an invariant combination of L^2/ν_t, the mean strain tensor S_{ik}, and the tensor $(\partial L/\partial x_i, \partial L/\partial x_k)$ in the form of the criterion Φ introduced above and defined as

$$\Phi = K(L^2/\nu_t)\partial L/\partial x_i S_{ik} \partial L/\partial x_k \tag{13}$$

K being an empirical constant of order unity.

It should be noted that Φ reaches its maximum when the mean strain tensor S_{ik} is aligned with the tensor $(\partial L/\partial x_i, \partial L/\partial x_k)$. This is exactly what we have at a stagnation point, where the role of elliptic effects (pressure signals) should be most important. For ''simple'' shear flows (boundary layer, shear layer) this is not the case, and so $\Phi \ll 1$, even if the length scale of turbulence in the free-stream, L_e, is large. That is exactly what one should expect, since it is well known that external turbulence only slightly affects boundary layer characteristics. Also, in the boundary layer the role of convective turbulence transport is not significant while the ''elliptic'' term is of the same order as the production and dissipation and remains important even if Φ is small.

Transport Equation for the Turbulence Length Scale

The modified eddy-viscosity transport equation (10) contains a new parameter, turbulence length scale, L. In order to define it we use an L-transport equation based on the well-known ideas outlined, in particular, in the work [7]. This equation reads:

$$\begin{aligned}\partial L/\partial t + u_i \partial L/\partial x_i = [k_0(1+\Phi)\nu_t + \nu]\partial^2 L/\partial x_i^2 + k_1(1+\Phi)G\nu_t/L \\ + k_2 \nu_t/L - 1/3L\,\partial U_i/\partial x_i - k_3 L \nu_t \Gamma_1/(\nu_t+\nu) \\ - k_4(1+\Phi)G\nu_t L/d^2.\end{aligned} \tag{14}$$

Here $G^2 = (\partial L/\partial x_i)^2$ and $k_0 - k_4$ are empirical constants.

The first term in the right-hand side of (14) is a diffusion term and the second and third terms describe an increase of turbulence length scale caused by viscous effects. The fourth term accounts for the effect of compressibility (it is equal to zero in a divergence-free mean velocity field). Finally, the fifth and sixth terms describe a decrease of the length scale caused by mean-flow non-uniformity and by the closeness to a solid wall. Note that the terms of (14) associated with the ''elliptic'' equilibrium relation (9) contain the factor $(1+\Phi)$.

The empirical constants of the resulting two-equation model (10), (14) were obtained on the basis of comparison with experimental data on the standard boundary layer flows. Their tentative values, which might be slightly changed after fine-tuning on a wider range of experimental data, are:

$$A_l = -0.5,\ A_2 = 4.0.$$

$$C_0 = 0.8,\ C_1 = 2.6,\ C_2 = 0.1,\ C_3 = 4.0,\ C_4 = 0.35,\ C_5 = 3.5,$$

$$C_6 = 3.3,\ C_7 = 26,\ C_8 = 0.2 + (0.035\beta)^2,$$

$$\beta = 10,\ C_9 = 0.1,\ K = 0.3,\ k_0 = 0.1,\ k_1 = 1.6,\ k_2 = 1.0,$$

$$k_3 = 0.1,\ k_4 = 2.6.$$

The boundary conditions for the ν_t-L model (10), (14) are imposed as follows. At the solid wall the eddy viscosity, ν_t, and the turbulence length scale, L, are set to zero. A free stream value of ν_t can be computed from the given free-stream turbulence characteristics. For instance, if the turbulence intensity, $Tu = k^{1/2}/U_e$, and length scale L_e are known, ν_t can be estimated as $\nu_{te} \approx 0.2 U_e Tu L_e$.

Results and Discussion

The ν_t-L model capabilities were first evaluated in the sample near-wall boundary layers, mixing layers, and plane and round jets. In all those cases it gave results rather close to those of the original ν_t-92 model. It should be noted, however, that for those ''canonical'' flows the new model performs somewhat worse than the original model (the capabilities of the latter are demonstrated in [5,15,16]). For instance, for the plane mixing layer the new model predicts a noticeable although minor variation of the quantity $L(y/x)/X$ (X is the size of the computational domain), i.e., the model does not provide a strictly self-similar solution. In addition, with the new model the shape of the velocity profile slightly depends on the free-stream turbulence length scale. To reduce this effect, the free-stream value of L being imposed as a boundary condition to the L-transport equation should satisfy the constraint $L_e > X$. Thus, even though for typical shear flows the new model achieves a much higher accuracy than that of the standard $k-\varepsilon$ model (the inaccuracy of the latter can reach 100 percent; see, for example, [17]), it still cannot be considered as an improved version of the ν_t-92 model for such flows. Its major goal is to show in principle the possibility of developing a simple eddy-viscosity

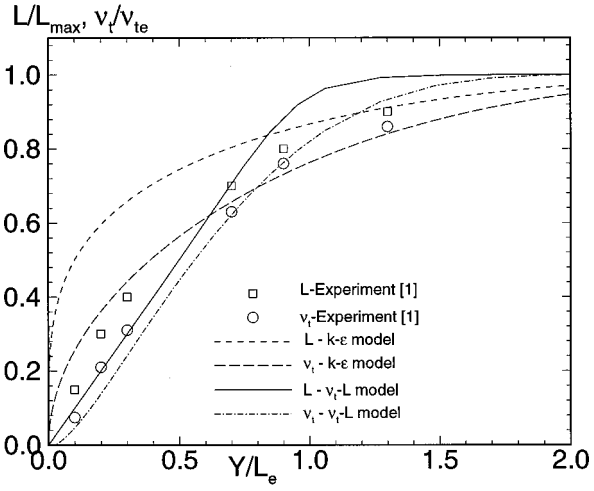

Fig. 1 Eddy viscosity and turbulence length scale profiles in the shear-free boundary layer

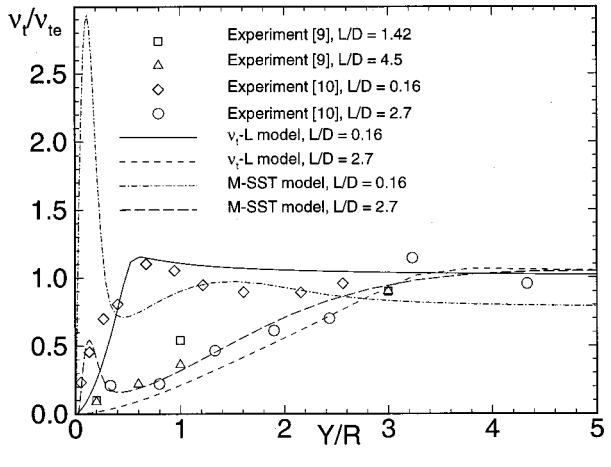

Fig. 3 Eddy viscosity distributions along the symmetry plane upstream of the stagnation point of the circular cylinder

model capable of predicting shear-free flows and stagnation-point flows. That capability is illustrated below on the two flows mentioned in the Introduction.

The first one is the shear-free ''boundary layer'' on a flat plate. It has a quasi-self-similar solution with the thickness of the near-wall layer (a layer where the turbulent flow characteristics ν_t and L change from their free-stream to their wall values) proportional to $L_e(x)$. This solution was obtained with the use of a parabolic (boundary layer type) solver by streamwise integration until the flow parameters effectively ceased to vary in the coordinates $\nu_t/\nu_{te}(x)=F_\nu(y/L_e(x))$. Exactly that solution is used to compare the predictions obtained with different turbulence models with the experimental data. In addition, to perform such a comparison, we need a relation between turbulence length scale and other turbulent quantities. In the present study we have used the relation $L=5\nu_t/\sqrt{k}$, which provides a coincidence of the scales given by different turbulence models for the usual near-wall turbulent boundary layer. In Fig. 1 we compare the profiles of the turbulence length scale and eddy viscosity measured in the experiments with those computed with the use of the ν_t-L and standard, low Reynolds number, $k-\varepsilon$ model of Jones and Launder [18]. In the experiments [1] the length scale was determined via the spectral functions at the zero frequency limit. Then the eddy viscosity has been computed as $\nu_t\sim L\sqrt{\langle\nu'^2\rangle}$. One can see that the ν_t-L model does capture the effect of the wall on turbulence, especially on its length scale, in a manner that is qualitatively correct and more accurate than with the $k-\varepsilon$ model. As mentioned above, the latter gives a solution $L\sim y^{1/4}$ near the wall, while the ν_t-L model predicts a more realistic behavior $L\sim y$. Figure 2 shows a comparison of the computed and measured profiles of the wall-normal velocity fluctuation, ν'/ν'_e. Again, a tangible superiority of the ν_t-L model is observed. It should be emphasized that this superiority is caused only by the use of the additional equation for L and by replacing the term $(C_0-C_1)N_1^2$ in (1) by the term $C_1\nu_tN_1/L$ in (11): The remaining changes from the original model are not essential as far as shear-free flows are concerned.

The second flow we have considered is the evolution of free-stream turbulence in the vicinity of the forward stagnation line of a circular cylinder. The computations were performed with an incompressible 2D Reynolds Averaged Navier-Stokes solver based on an implicit fifth order upwind scheme [19]. Along with the ν_t-L model, computations have been carried out with the $k-\omega$ model of Menter [20] (M-SST model) that is today considered one of the most accurate two-equation models for aerody-

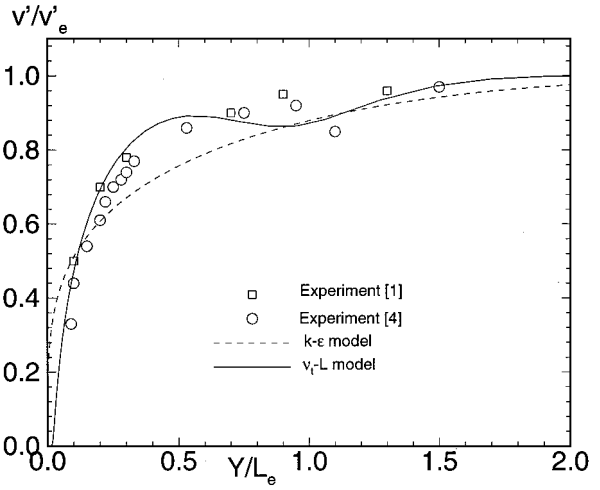

Fig. 2 Normal velocity fluctuation profiles in the shear-free boundary layer

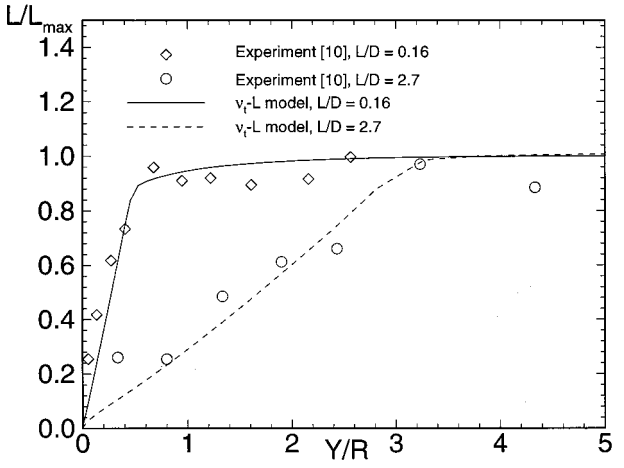

Fig. 4 Turbulence length scale distributions along the symmetry plane upstream of the stagnation point of the circular cylinder

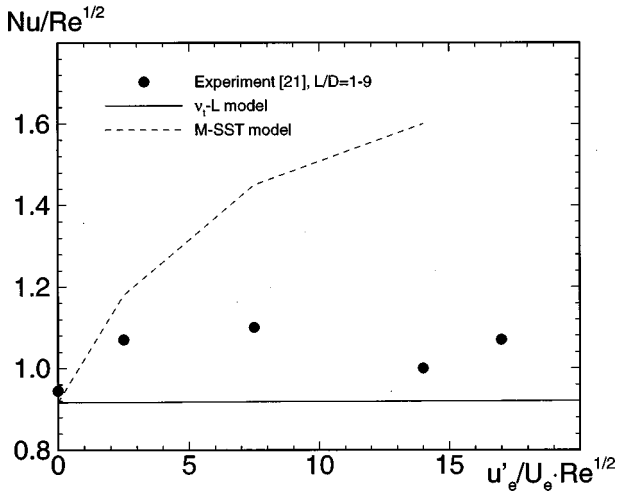

Fig. 5 Effect of free-stream turbulence on heat transfer at the stagnation point of the circular cylinder

namic flows. In Figs. 3, 4 we compare the two models' predictions with each other and with the experimental data [9,10].

Figure 3 shows eddy viscosity distributions for different values of the ratio of the free-stream turbulence length scale to cylinder diameter, D. One can see a significant superiority of the $\nu_t - L$ model over M-SST in terms of the eddy viscosity prediction. In particular, the M-SST model predicts sharp peaks of eddy viscosity in the vicinity of the stagnation point that are not observed in the experiment. In addition, the $\nu_t - L$ model gives good predictions of the experimental distributions of turbulence length scale (see Fig. 4).

One of our most important goals for the $\nu_t - L$ model was an improvement of the prediction of heat transfer at a stagnation point, which is known to be one of the challenging issues for current turbulence models. Experimental studies (see, for instance, [10]) show that the effect of external turbulence on the heat transfer is large at moderate and small turbulence scales, $L_e/D < 0.5$, while at large values of turbulence scale ($L_e/D > 1-2$) this effect becomes negligible. Figure 5 shows that, unlike the experiment, the M-SST model predicts a significant increase in heat transfer rate in the latter range (note that a similar deficiency is typical of the original $\nu_t - 92$ model). The $\nu_t - L$ model, as was hoped, adjusts its behavior quite correctly and agrees fairly well with the Nusselt number measured in the experiment [21].

Conclusions

A new approach is suggested, providing for a more complete account of the effect of turbulence length scale (''elliptic'' mechanism of turbulence propagation) in the framework of simple eddy-viscosity turbulence models. Using this approach, the one-equation turbulence model $v_t - 92$ is modified and supplemented by an additional equation for turbulence length scale, which results in a new, two-equation $v_t - L$ model. The latter has been shown to be applicable to a wider range of turbulent flows than conventional two-equation models. In particular, its advantages over both the $k-\varepsilon$ and the $k-\omega$ M-SST models are demonstrated for the shear-free boundary layer on a flat plate and for the flow and heat transfer in the vicinity of the forward stagnation point of a circular cylinder. Both flows are known to be challenging for conventional turbulence models due to the significant nonlocal effect of the external turbulence length-scale.

Acknowledgments

The work was supported by the Russian Fundamental Research Foundation (grants no. 98-01-00153 and no. 97-02-16492.) and by Boeing Operation International Inc. The authors are grateful to Dr. Ph. Spalart for his helpful discussions.

References

[1] Thomas, N. H., and Hancock, P. E., 1977, ''Grid Turbulence Near a Moving Wall,'' J. Fluid Mech., **82**, Part 3, pp. 481–496.
[2] Hunt, J. C. R., and Graham, J. M., 1978, ''Free-Stream Turbulence Near Plane Boundaries,'' J. Fluid Mech., **84**, Part 2, pp. 209–235.
[3] Perot, B., and Moin, P., 1995, ''Shear-Free Turbulent Boundary Layers. Part I. Physical Insights into Near-Wall Turbulence,'' J. Fluid Mech., **295**, pp. 199–227.
[4] Aronson, D., Johansson, A. V., and Lofdahl, L., 1997, ''Shear-Free Turbulence Near a Wall,'' J. Fluid Mech., **338**, pp. 363–385.
[5] Gulyaev, A., Kozlov, V., and Secundov, A., 1993, ''A Universal One-Equation Model for Turbulent Viscosity,'' Fluid Dyn., **28**, No. 4, pp. 485–494 (translation from Russian).
[6] Spalart, P. R., and Allmaras, S. R., 1994, ''A One-Equation Turbulence Model for Aerodynamic Flows,'' La Recherche Aerospatiale, No. 1, pp. 5–21.
[7] Secundov, A. N., 1997, ''Turbulence Model for Description of Interaction between Boundary Layer and Large-Scale External Turbulence,'' Fluid Dyn., **32**, No. 2, pp. 204–211 (translation from Russian).
[8] Hunt, J. C. R., 1973, ''A Theory of Turbulent Flow Round Two-Dimensional Bluff Bodies,'' J. Fluid Mech., **61**, pp. 625–706.
[9] Britter, R. E., Hunt, J. C. R., and Mumford, J. C., 1979, ''The Distortion of Turbulence by a Circular Cylinder,'' J. Fluid Mech., **92**, Part 2, pp. 269–301.
[10] Maslov, V. P., Mineev, B. I., Pichkov, K. N., Secundov, A. N., Vorobiev, A. N., Strelets, M. Kh., and Travin, A. K., 1999, ''Effect of Free-Stream Turbulence Intensity and Length Scale on Heat Transfer at the Leading Edge of Turbine Blade,'' ASME Paper 99-GT-423.
[11] Ashforth-Frost, S., and Jambunathan, K., 1996, ''Numerical prediction of semi-confined jet impingement and comparison with experimental data,'' Int. J. Numer. Methods Fluids, **23**, pp. 295–306.
[12] Behnia, M., Parneix, S., and Durbin, P. A., 1997, ''Accurate modeling of impinging jet heat transfer,'' Stanford/NASA Ames Center for Turbulence Research, Annual Research Briefs, pp. 149–164.
[13] Durbin, P. A., 1995, ''Separated Flow Computations with the k-ε-ν'^2 Model,'' AIAA J., **33**, No. 4, pp. 659–664.
[14] Launder, B. E., and Li, S. P., 1994, ''On the elimination of wall topography parameters from second-moment closure,'' Phys. Fluids, **6**, pp. 999–1006.
[15] Shur, M., Strelets, M., Zaikov, L., Gulyaev, A., Kozlov, V., and Secundov, A., 1995, ''Comparative Numerical Testing of One- and Two-Equation Turbulence Models for Flows with Separation and Reattachment,'' AIAA Paper, AIAA-95-0863 (note that in this paper the factor 0.1 in the roughness allowance, given after Eq. (3) of the present paper, was misprinted as 0.01).
[16] Vasiliev, V. I., Volkov, D. V., Zaitsev, S. A., and Lyubimov, D. A., 1997, ''Numerical Simulation of Channel Flows by a One-Equation Turbulence Model,'' ASME J. Fluids Eng., **119**, pp. 885–892.
[17] Bardina, J. E., Huang, P. G., and Coakley, T. J., 1998, ''Turbulence Modeling Validation, Testing and Development,'' NASA Technical Memoranda No. 110446.
[18] Jones, W. P., and Launder, B. E., 1973, ''The Calculation of Low-Reynolds-Phenomena with Two-Equation Model of Turbulence,'' Int. J. Heat Mass Transf., **16**, pp. 1119–1130.
[19] Rogers, S. E., and Kwak, D., 1990, ''An Upwind Differencing Scheme for the Time-Accurate Incompressible Navier-Stokes Equations,'' AIAA J., **28**, No. 2, pp. 253–262.
[20] Menter, F. R., 1993, ''Zonal Two Equation k-ω Turbulence Models for Aerodynamic Flows,'' AIAA Paper, AIAA 93-2906.
[21] Wang, H. P., Goldstein, R. J., and Olson, S. J., 1998, ''Effect of High Free Stream Turbulence with Large Length Scale on Blade Heat/Mass Transfer,'' ASME Paper 98-GT-107.

P. A. Durbin
G. Medic
J.-M. Seo
J. K. Eaton
S. Song

Mechanical Engineering Department,
Stanford University,
Stanford, CA 94305-3030

Rough Wall Modification of Two-Layer $k-\varepsilon$

A formulation is developed to apply the two-layer $k-\varepsilon$ model to rough surfaces. The approach involves modifying the ℓ_ν formula and the boundary condition on k. A hydrodynamic roughness length is introduced and related to the geometrical roughness through a calibration procedure. An experiment has been conducted to test the model. It provides data on flow over a ramp with and without surface roughness.
[DOI: 10.1115/1.1343086]

1 Introduction

Surface roughness can have a profound effect on heat transfer to surfaces beneath turbulent flow. The viscous sublayer adjacent to a smooth wall presents a high impedance to transport to and from the surface. Protrusions that penetrate the viscous layer increase transfer rates between the surface and the fluid. They do so by generating irregular, turbulent motion and by extending the surface into the flow. Incorporating rough wall capability into computational methods is a considerable practical need. The present paper is in the vein of providing a practical extension to an existing, popular turbulence model.

From an operational perspective, the influence of surface irregularities must be represented indirectly through a mathematical scheme. The rough surface is replaced by an effective, smooth surface on which modified boundary conditions are imposed. Influences of roughness are represented by a quantity called the hydrodynamic roughness length. Hydrodynamic roughness modifies a turbulence model in order to reproduce averaged effects of the true roughness upon the mean flow and upon the turbulence. The exact prescription of hydrodynamic roughness is, therefore, a function of the turbulence model.

The $k-\varepsilon$ model is widely used in computational fluid dynamics; that is the motive for adopting it here. One could debate whether $k-\varepsilon$ is the most effective model available; probably it is not. A notable flaw is its inability to describe the near-wall zone. The two-layer approach [1] seems to be the most promising method to fix that flaw. It generally gives more accurate flow predictions than other schemes [2], such as wall functions or 'low Reynolds number' modifications. It is well suited to our present purposes; but it is worth noting that the procedure to treat roughness described herein can be applied to other models.

Many aerodynamic and heat transfer applications require a model that is valid for the whole range from smooth, to intermediately rough, to fully rough walls. The high pressure turbine blade is the application that provided an immediate motivation for the present work. In the course of their lifetime blades are subject to erosion by impinging combustor air. The roughened surface experiences an increased rate of heat transfer from the gas stream [3].

Models for roughness have a long history. A good survey of the literature is provided by Raupauch et al. [4]. Both engineering and meterological concerns are covered. The authors state that in the engineering approach the log-law is modified by an additive roughness function, while in the meteorological approach it is represented by a roughness length. In the present paper we refer to the latter as the hydrodynamic roughness length, to distinguish it from the true, geometrical roughness. However, we have to disagree with the distinction made in [4] between the engineering and meteorological approaches. Present concern is with engineering problems, but we make use of both the additive form and of the hydrodynamic roughness length.

The additive form is simply [5] $U/u_*=1/\kappa\log(y_+)+B_r$. Data on the additive coefficient (B_r) as a function of roughness height constitute the empirical input to the present formulation. A long-standing method used in engineering closure is to modify a mixing length prescription by adding a hydrodynamic roughness length to the wall distance [6]: e.g., $\ell=\kappa(y+y_0)$. The present model is of a different form, but y_0 is made use of. Finally, the present two-layer formulation requires a modified k boundary condition. The rough wall version of the $k-\omega$ model [6] shares this feature of incorporating roughness into the boundary condition, although in that case it is in the ω-boundary condition.

This list of methodologies is not meant to be exhaustive; it cites approaches that bear on the present paper. Other methods to represent roughness include adding body forces [7].

2 The Two-Layer Formulation

The formulation begins by reviewing the two-layer method. It consists in patching together the $k-\ell$ and $k-\varepsilon$ models. The standard model equation for turbulent kinetic energy is

$$\partial_t k+\mathbf{U}\cdot\boldsymbol{\nabla}k=2\nu_T|\mathbf{S}|^2-\varepsilon+\boldsymbol{\nabla}\cdot((\nu+\nu_T)\boldsymbol{\nabla}k) \tag{1}$$

where $S_{ij}=1/2(\partial_j U_i+\partial_i U_j)$ is the rate of strain tensor and ν_T is the eddy viscosity. It is used in both the $k-\ell$ and $k-\varepsilon$ formulations.

In the $k-\varepsilon$ model equation (1) is supplemented by

$$\partial_t\varepsilon+\mathbf{U}\cdot\boldsymbol{\nabla}\varepsilon=\frac{2C_{\varepsilon1}\nu_T|\mathbf{S}|^2-C_{\varepsilon2}\varepsilon}{T}+\boldsymbol{\nabla}\cdot\left(\left(\nu+\frac{\nu_T}{\sigma_\varepsilon}\right)\boldsymbol{\nabla}\varepsilon\right) \tag{2}$$

where the turbulent time-scale is $T=k/\varepsilon$ and the eddy viscosity is

$$\nu_T=C_\mu kT. \tag{3}$$

The standard model constants are

$$C_{\varepsilon1}=1.44;\quad C_{\varepsilon2}=1.92;\quad \sigma_\varepsilon=1.3;\quad C_\mu=0.09.$$

In the $k-\ell$ model, the dissipation rate is represented by

$$\varepsilon=\frac{k^{3/2}}{\ell_\varepsilon} \tag{4}$$

and the eddy viscosity is

$$\nu_T=C_\mu\sqrt{k}\ell_\nu. \tag{5}$$

These supplement the k-equation (1). The VonDriest form for the length scales will be adopted here:

$$\ell_\varepsilon=C_\ell y_{\text{eff}}(1-e^{-R_y/A_\varepsilon});\quad \ell_\nu=C_\ell y_{\text{eff}}(1-e^{-R_y/A_\nu}). \tag{6}$$

Contributed by the Fluids Engineering Division for publication in the JOURNAL OF FLUIDS ENGINEERING. Manuscript received by the Fluids Engineering Division May 8, 2000; revised manuscript received November 17, 2000. Associate Editor: J. Lasheras.

$R_y = y_{\text{eff}}\sqrt{k}/\nu$ is a wall-distance Reynolds number in which, for smooth walls, y_{eff} is distance from the wall. It subsequently will be modified by adding the hydrodynamic roughness to the wall distance. The log-layer solution requires that $C_\ell = \kappa/C_\mu^{3/4}$ where κ is the VonKarman constant. The widely accepted value of $\kappa = 0.41$ gives $C_\ell = 2.5$. The requirement that $k \to \varepsilon y^2/2\nu$ as $y \to 0$ gives $A_\varepsilon = 2C_\ell = 5.0$ [1].

There is only one free constant, A_ν. We have selected the value $A_\nu^0 = 62.5$ for use with the two-layer formulation. That value gave very good agreement between C_f versus R_θ predictions and experiments for zero pressure gradient, flat plate boundary layers.

The two-layer formulation consists simply of using (5) and (4) near a wall, and switching abruptly to (3) and (2) at a patching point. The patching point is defined as the location where the damping function $1 - e^{-R_y/A_\nu^0}$ equals 0.95; i.e., where $y = \log(20)A_\nu^0\nu/\sqrt{k}$.

3 Modifications for Roughness

Roughness has the effect of disrupting the viscous sublayer. We define the y-origin to be where the mean velocity is extrapolated to zero: that is $U(y=0)=0$, by definition. This location of $y=0$ need not be the effective origin for the turbulent kinetic energy. In fact, for a fully rough wall, the log-layer extends to the origin, at which point k cannot vanish. By definition U is of the form

$$U = \frac{u_*}{\kappa}\log[(y+y_0)/y_0]$$

under fully rough conditions. Then the eddy viscosity is $\nu_T = u_*^2/\partial_y U = u_*\kappa(y+y_0)$. Hence, the turbulence has an effective origin at $-y_0$. This shifted origin could be considered as a definition of the hydrodynamic roughness, y_0.

In Eq. (6) let $y_{\text{eff}} = y + y_0$. This will accommodate the effective origin of the turbulence—provided that y_0 is appropriately specified. Just modifying y_{eff} does not accommodate the fully rough condition, that the log-law extends to $y=0$; the damping function should also be deleted. A_ε is sufficiently small that the ℓ_ε damping has little effect under fully rough conditions: so, invoking ''occam's razor,'' we will leave it as. However A_ν is not small; it must be reduced with roughness. The data cited by [4] give the criterion $r_+ > 90$ for fully rough flow. Here the non-dimensional parameter r_+ is defined as ru_*/ν where r is the geometrical roughness height. The simple, linear interpolation

$$A_\varepsilon = \max[1, A_\nu^0(1 - r_+/90)] \tag{7}$$

has the desired effect of deleting the damping. The lower limit of 1 was used, instead of 0, in the *max* function to avoid division by zero. Now, when $r_+ > 90$, $\ell_\nu = C_\ell(y+y_0)$. The well known log-layer solution [8] $k = u_*^2/\sqrt{C_\mu}$ gives $\nu_T = u_*\kappa(y+y_0)$, as desired.

If the log-layer is indeed to extend to the origin of y under fully rough conditions, the boundary condition on k must become $k(0) = u_*^2/\sqrt{C_\mu}$. But on a smooth wall $k(0)=0$. Again, a simple interpolation is used; however, in this case is it quadratic. The boundary condition on k is

$$k(0) = \frac{u_*^2}{\sqrt{C_\mu}}\min[1; (r_+/90)^2]. \tag{8}$$

The reason for quadratic interpolation is that the dissipation formula (4) gives

$$\varepsilon(y=0) \to \frac{\nu k(0)}{y_0^2 C_\ell A_\varepsilon} \to \frac{u_*^4}{\nu C_\ell A_\varepsilon\sqrt{C_\mu}}\left(\frac{r_+}{90y_0}\right)^2$$

as y_0, $r_+ \to 0$. The use of quadratic interpolation leads to a finite, non-zero value for $\varepsilon(0)$ in the smooth wall limit.

The formula

$$u_*^2 = (\nu + \nu_T)\partial_y U|_0 \tag{9}$$

for the surface stress completes the roughness formulation. At least, it would complete the formulation if y_0 were known as a function of the geometrical roughness r. y_0 is not a physical length; it is an artifice added to produce a suitable mean velocity.

4 Hydrodynamic Roughness

Surface protrusions will increase the drag force exerted by the wall on the flow. In a channel flow with given pressure drop, the increased drag would decrease the mass flux and the centerline velocity. The additive constant, B, in the log-law should therefore be decreased by roughness. Assume that the roughness is of the random, sandgrain, variety. The log-law can be written

$$U = u_*(1/\kappa\log[y_+] + B + \Delta B_r(r_+)) \tag{10}$$

where r_+ was defined above equation (7). The function $\Delta B_r(r_+)$ represents the alteration of the additive constant by roughness. The function $\Delta B_r(r_+)$ has been measured experimentally by Nikuradse; [5] fit the curve

$$\left.\begin{array}{lll} \Delta B_r = 0 & ; & r_+ < 2.25 \\ \Delta B_r = \xi(8.5 - B - 1/\kappa\log(r_+)) & ; & 2.25 \leqslant r_+ \leqslant 90 \\ \Delta B_r = 8.5 - B - 1/\kappa\log(r_+) & ; & r_+ > 90 \end{array}\right\} \tag{11}$$

through his measurements. This formula is broken into three regions: effectively smooth, transitionally rough, and fully rough. The interpolation function ξ in (11) is

$$\xi = \sin\left(\frac{\pi/2\log[r_+/2.25]}{\log[90/2.25]}\right)$$

which increases from 0 to 1 through the transitionally rough range $2.25 \leqslant r_+ \leqslant 90$. Under fully rough conditions (11) and (10) give

$$U/u_* = 1/\kappa\log(y/r) + 8.5.$$

While Eqs. (11) are fit to data on sandgrain roughness, other roughness geometries only alter the transitional range. Ligrani and Moffat [5] discuss the case of hemispherical roughness.

The rough wall law (10) is commonly represented by

$$U = \frac{u_*}{\kappa}\log[y/z_0]$$

where

$$z_0 \equiv re^{-(\kappa B_r + \log(r_+))}$$

can be called the hydrodynamic roughness length. In the fully rough regime, $r_+ > 90$, the last of (11) gives $z_0 = r/e^{8.5\kappa} = .031r$—the hydrodynamic roughness length is a small fraction of the geometrical roughness size. In the smooth wall regime, $r_+ < 2.5$, $z_0 = e^{-\kappa B}\nu/u_*$, which recovers the smooth wall log-law. We have used $B = 5.5$ for the smooth wall additive constant.

The two-layer roughness model is to be solved along with the usual mean flow equation

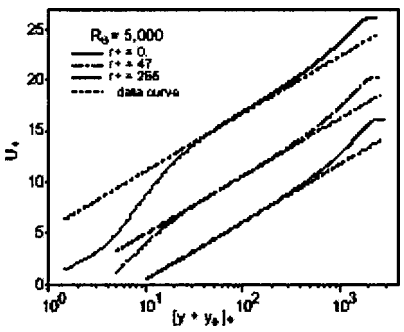

Fig. 1 Computed log layers compared to data correlation

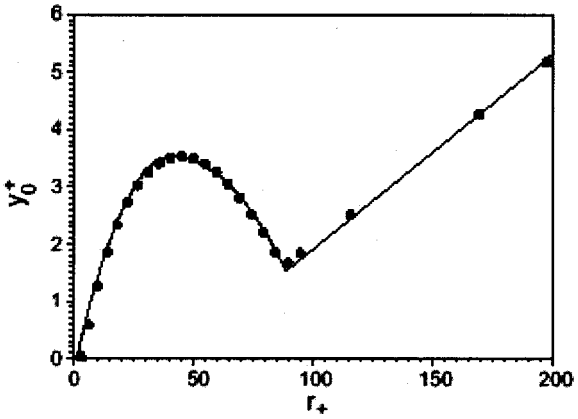

Fig. 2 Calibration curve for hydrodynamic roughness

$$\partial_t \mathbf{U} + \mathbf{U}\cdot\nabla\mathbf{U} = -1/\rho\nabla p + \nabla\cdot((\nu+\nu_T)[{}^t\nabla U + \nabla U]) \quad (12)$$

for incompressible flow. To calibrate the model, a zero pressure gradient, boundary layer approximation

$$U\partial_x U + V\partial_y V = \partial_y((\nu+\nu_T)\partial_y U)$$

is solved, along with the two-layer $k-\varepsilon$ equations. The solution is a function of r_+ and y_0^+. A boundary layer at the representative Reynolds number of $R_\theta = 5{,}000$ was computed. The range $100 < y_+ < 160$ was used as a sample of the velocity in the logarithmic region. In that region, we define the computed additive constant by

$$\Delta B_{comp}(r_+, y_0^+) = U_+ - (1/\kappa \log[y_+] + B),$$

averaged over the sample points. Equating this to the experimental data (11) provides an implicit equation

$$\Delta B_{comp}(r_+, y_0^+) = \Delta B_r(r_+) \quad (13)$$

that was solved to find y_0^+ as a function of r_+. Because ΔB_{comp} is only known through a boundary layer solution, the boundary layer code was put into a loop and Eq. (13) was solved by Newton iteration. Figure 1 contains a few comparisons between the computed boundary layer profile and the formula of [5] after the iterations had converged: this simply illustrates the manner in which y_0 was found.

The solution for y_0^+ as a function of r_+ obtained by the above procedure is shown in Fig. 2. The circles are values computed by the Newton iterations. The solid line was fit through those values to give a continuous calibration curve.

5 Tests of the Model

The roughness formulation was tested by computing the experiment of Coleman and Moffat [9]. The experiments were on a flat plate boundary layer subjected to acceleration of the free-stream. Both rough and smooth wall data were measured. The acceleration parameter was defined as $K_r \equiv (rdU_\infty/dx)/U_\infty$. Data sets are for $K_r = 0$, 1.5×10^{-4}, 2.9×10^{-4}. The inlet condition in the computations is a fully developed, zero pressure gradient boundary layer at the experimental inlet R_θ. The fully developed state implicitly specifies profiles of U, k and ε. For the three pressure gradients, the inlet Reynolds numbers were $R_\theta = 2{,}200$; 3,740 and 2,320, respectively.

Figure 3 includes the measured values of r_+. The roughness consisted of close packed hemispheres. The equivalent sandgrain roughness height of the hemispheres was constant and equal to 0.31 in. All the data are near to fully rough. Under fully rough conditions, the shape of the roughness elements becomes irrelevant. The other data in Fig. 3 consist of the skin friction coefficient and Stanton number. Because of the pressure gradient, the Reynolds analogy between heat transfer and skin friction, $St \approx 1/2C_f$, does not hold.

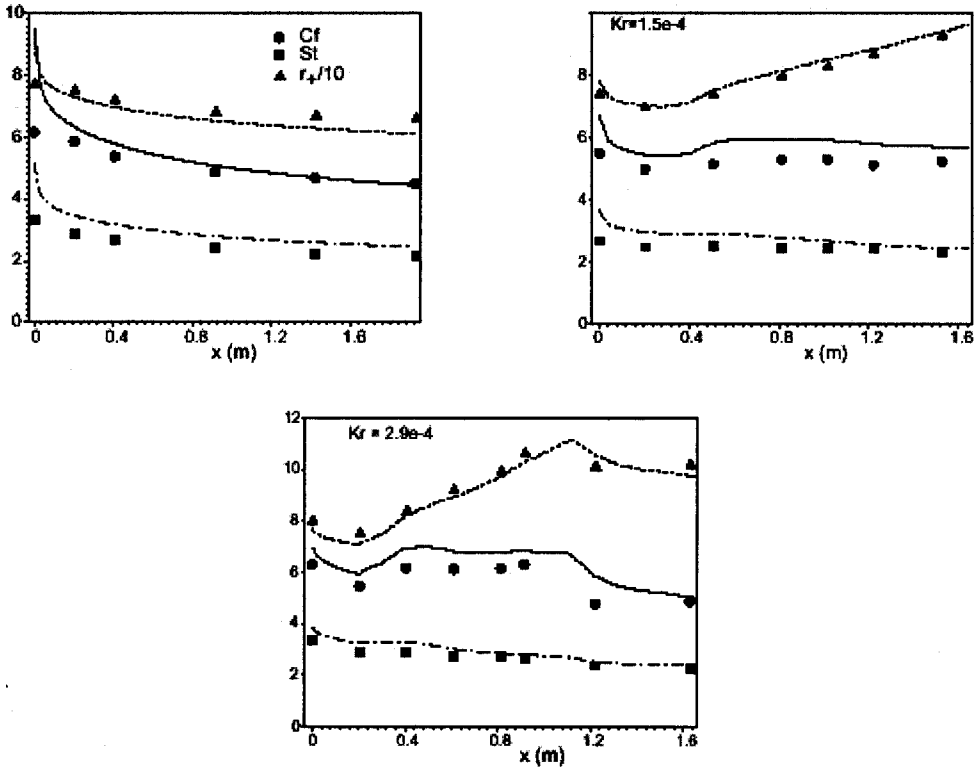

Fig. 3 Rough wall in zero and favorable pressure gradients. Clockwise from upper left: $k_r = 0$, $K_r = 1.5\times10^{-4}$, $K_r = 2.9\times10^{-4}$, ▲ = $r_+/10$, ■ = St, ● = C_f.

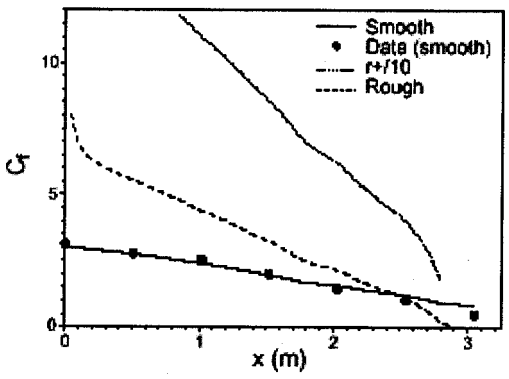

Fig. 4 Predicted effect of adverse pressure gradient on smooth and rough wall

The agreement of the model solution to the data in Fig. 3 is generally quite good. The computations used the experimental free stream velocity, $U_\infty(x)$, which was available at the measurement stations. The pressure gradient was computed from a parabolic fit through the velocity data. Therefore, the input pressure gradient was piecewise linear; this is why the computed curves appear to be irregular. The level of agreement between model and data is sufficient to initially validate the present roughness formulation.

A curious phenomenon was observed when the model was applied to an adverse pressure gradient boundary layer. The smooth wall case of Schubauer and Spangenberg [10] was computed with a rough wall. Roughness initially increased the skin friction, but subsequently caused it to decline more steeply than on a smooth wall, and the boundary layer separated. This thought experiment is shown in Fig. 4. On further consideration, the behavior is quite plausible: roughness thickens the boundary layer and makes the near-wall region more susceptible to flow reversal.

Experimental data on roughness induced separation are not available; so the prediction that roughness can provoke separation inspired us to conduct a new experiment. An existing ramp was installed in the test section of the wind tunnel described in [11]. The geometry is shown in Fig. 5 with a computational grid.

First, mean flow profiles were measured above the smooth-walled model. Then the segment from the inlet to the bottom of the ramp was covered with sandpaper and rough wall data were obtained. The lower wall of the windtunnel, downstream of the ramp, was left smooth.

For computations, and in the results to be presented, the curved section of the ramp is taken to be the unit of length and the origin is placed at the top of the ramp. Hence the ramp extends from $x=0$ to $x=1$. In these units, the inlet of the computational domain is at $x=-2$, and the exit is at $x=4.7$. The height of the inlet is 1.87 and it extends from $y=0$ to $y=1.87$. After the end of the ramp the lower wall has dropped to $y=-0.294$ in these units.

Under smooth conditions, the inlet momentum thickness Reynolds was $R_\theta=3{,}400$, while under rough conditions it was 3,800. The roughness height was constant; at the inlet $r_+=360$. Of course, at separation $r_+=0$, so the full range from fully rough to smooth occurs in this flow. At the computational inlet a fully developed boundary layer, with the appropriate thickness was prescribed for the calculation. It was obtained from a separate computation using a boundary layer code. The upper wall also was provided an inlet boundary layer having $R_\theta=3{,}400$.

The geometry in Fig. 5 is such that separation will occur before the foot of the ramp at $x=1$ in the smooth wall case. So the geometry is not ideal for demonstrating the predicted ability of roughness to cause separation, but it can be seen from the data in Fig. 6 that separation occurs earlier and is more extensive when the ramp is covered with sandpaper.

At the first three locations of Fig. 6 the rough wall model shows better agreement to data than the smooth wall calculation. However, both are in good agreement and illustrate the larger velocity defect of a rough wall layer. Separation onset is seen to occur upstream of $x=0.74$ over the rough wall, where the smooth wall flow is just on the verge of separation. At $x=1$ both cases are separated, but when the wall is rough the separation bubble is higher. The qualitative prediction of roughness induced separation is substantiated by these experiments and the agreement between predictions and data is not bad. It should be noted that the model was developed before the experiment was conducted—indeed it was the model prediction that motivated the measurements.

The final test case is the ''sand dune'' experiment of [12]. This experiment is an open channel flow over an artificial dune, consisting of a backward facing ramp. More precisely, over a train of two-dimensional ramps, identical in size and shape. This configuration allows the introduction of a periodic condition in the axial direction, reducing the problem to the single dune presented in Fig. 7. The dune bed has the equivalent sand-grain roughness height $k_s/d=0.0055$.

We will concentrate on the case designated in [12] as T6: water depth $d=0.292m$, with $L=1.6m$ and $h=0.08m$ (Fig. 7). With this depth, the water surface can be treated as a plane, free-slip boundary. The Reynolds number based on the bulk velocity and water depth d is $R_d=1.75\times10^5$. Computations of this configuration have been presented previously by [13], who utilized the $k-\omega$ model, with the rough wall boundary condition proposed by Wilcox [8]. Patel and Yoon [13] used a computational grid consisting in 82 stream-wise points and 69 cross-stream points, whereas we have used 160 stream-wise points and 50 cross-stream points. In both cases, the distance of the first grid point from the bed was approximately at $10^{-6}d$, corresponding to $y_+\leqslant0.25$. In both analyses, the free surface was assumed to be a plane of symmetry. Computed streamlines are included in Fig. 7. They display a region of separated flow along the ramp, with reattachment downstream, on the horizontal lower wall.

Figure 8 presents a comparison of friction coefficient C_f to the experimental data and to the $k-\omega$ computations (transcribed from

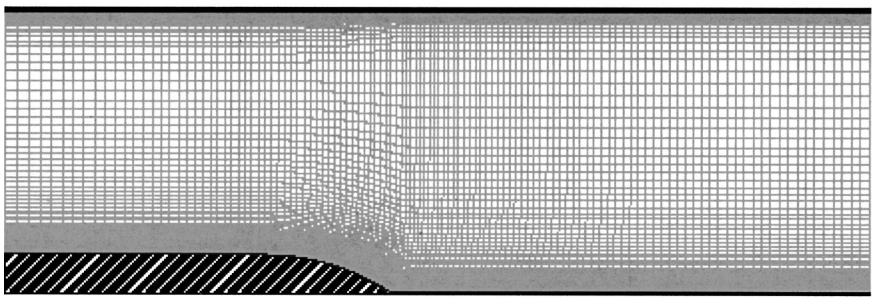

Fig. 5 Ramp geometry for present experiment

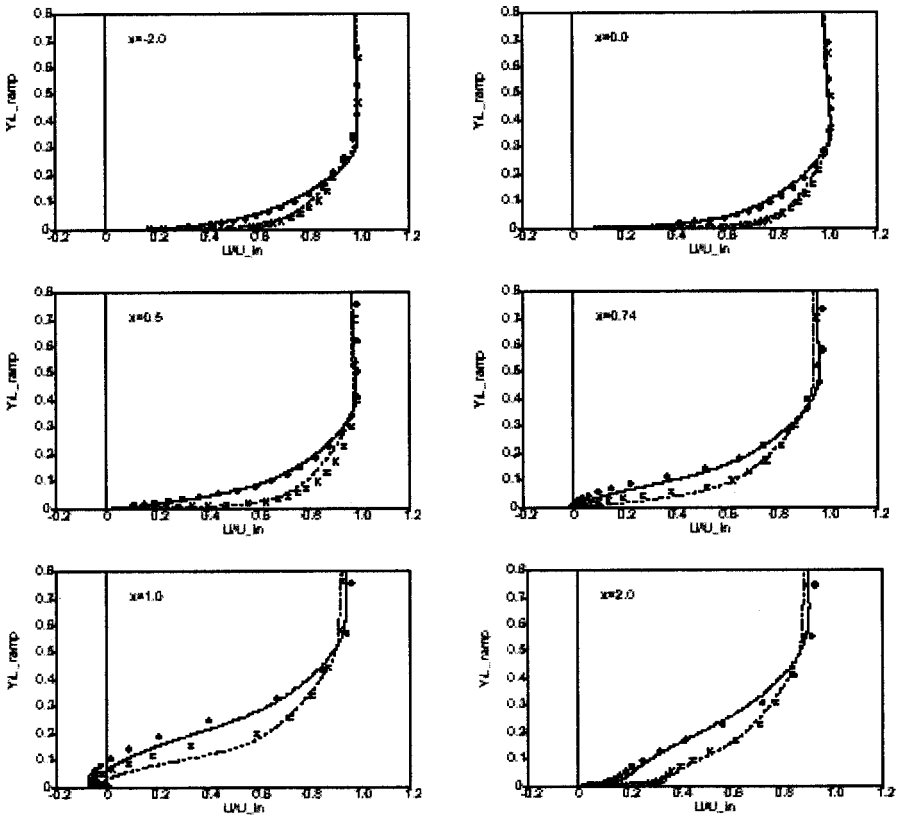

Fig. 6 Profiles of *U* velocity component at various downstream positions. Experiment ●, rough wall; ×, smooth wall. Computation ——, rough wall; ----, smooth wall.

[13]). A smooth wall computation with the two-layer $k-\varepsilon$ model is also shown. The introduction of roughness slightly increases the predicted recirculation region, but the largest effect is after reattachment. The roughness model brings C_f predictions to the correct level. Both turbulence models are in agreement with the data.

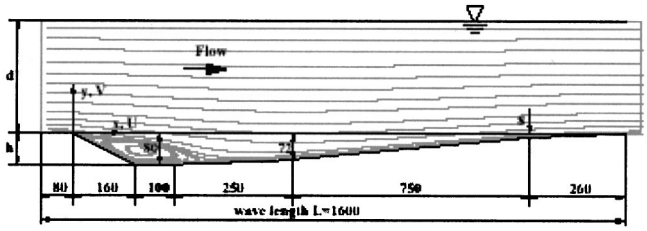

Fig. 7 Flow domain for sand dune test case. Dimensions are in mm. The lighter lines show streamlines of the separated flow over the roughened ramp.

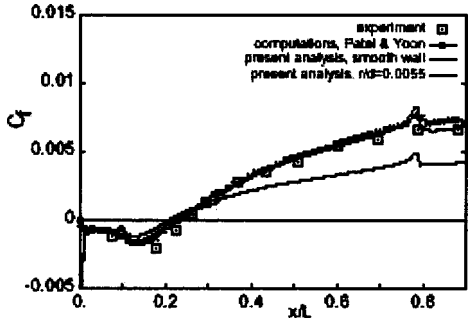

Fig. 8 Friction coefficient on lower wall. □, experiment; ——, present; -X--, $k-\omega$; ·····, smooth wall.

Finally, we compare velocity profiles from the roughness simulation to data at measurement stations 4 ($x=0.13L$), 7 ($x=0.27L$) and 14 ($x=0.7L$). The *x*-locations are measured from the inlet, corresponding to the diagram, Fig. 7. The magnitude of the backflow in the separated region is seen to be predicted correctly by the upper left panel of Fig. 9. *U*-velocity profiles at the other locations are also in satisfactory agreement to the data. The *V*-profiles in Fig. 10 also agree well with experiments, except near the wall at station 7. This is on the flat bottom wall, shortly after

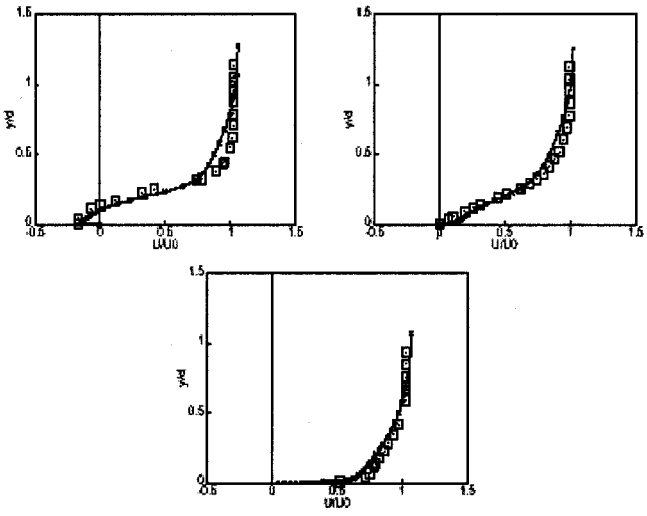

Fig. 9 U-velocity profiles at stations 4, 7, and 14, proceeding clockwise from the upper left. Lines are computations, squares are experiment.

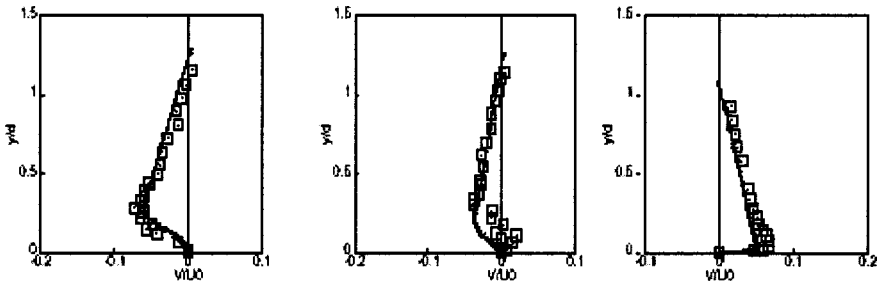

Fig. 10 V-velocity profiles at stations 4, 7, and 14. Lines are computations, squares are experiment.

reattachment. It may indicate a slight misprediction of the reattachment location. Note, however, that the values of V are an order of magnitude less than U.

6 Conclusion

The overall objective, to develop a rough wall formulation for the two-layer $k-\varepsilon$ model has been met. The basic method consists of inserting a hydrodynamic roughness length into the equations and modifying the k boundary condition to interpolate between the fully rough and smooth limits. The success of the method depends on a calibration procedure that relates hydrodynamic roughness, y_0 to the true, geometric roughness, r. The data selected here are for sandgrain roughness. Other roughness geometries would produce an altered calibration curve in the regime of intermediate roughness. The basic approach of modifying the smooth wall formulation, then calibrating y_0 by iterating on boundary layer solutions, could be applied to other models.

Model predictions of roughness induced separation motivated an experiment to verify this behavior. The experiment was conducted in an existing facility and consisted of comparing rough and smooth wall flow over a backward facing ramp. The predicted behavior was confirmed.

Acknowledgment

We gratefully acknowledge support from General Electric Aircraft Engines and from the Office of Naval Research, contract N00014-99-1-0300-P0001.

References

[1] Chen, C.-J., and Patel, V.-C., 1988, ''Near-wall turbulence models for complex flows including separation,'' AIAA J., **26**, pp. 641–648.
[2] Rodi, W., 1991, ''Experience using two-layer models combining the $k-\varepsilon$ model with a one-equation model near the wall'' AIAA paper 91-0609.
[3] Bogard, D. G., Schmidt, D. L., and Tabbtta, M., 1998, ''Characterization and laboratory simulation of turbine airfoil surface roughness and associated heat transfer,'' ASME J. Turbomach., **120**, pp. 337–342.
[4] Raupauch, M. R., Antonia, R. A., and Rajagopalan, S., 1991, ''Rough-wall turbulent boundary layers,'' Appl. Mech. Rev., **44**, pp. 1–25.
[5] Ligrani, P. M., and Mǿffat, R. J., 1986, ''Structure of transitionally rough and fully rough turbulent boundary layers,'' J. Fluid Mech., **162**, pp. 69–98.
[6] Kays, W. M., and Crawford, M. E., 1993, *Convective Heat and Mass Transfer*, 3rd ed., McGraw-Hill, NY.
[7] Taylor, R. P., Coleman, H. W., and Hodge, B. K., 1985, ''Prediction of turbulent rough-wall skin friction using a discrete element approach,'' ASME J. Fluids Eng., **107**, pp. 251–257.
[8] Wilcox, D. C., 1993, *Turbulence Modeling for CFD*, DCW inc.
[9] Coleman, H. W., Moffat, R. J., and Kays, W. M., 1976, Momentum and energy transport in the accelerated fully rough turbulent boundary layer, Report **HMT-24**, Dept. of Mech. Eng., Stanford University.
[10] Kline, S. J., Morkovin, M. V., Sovran, G. and Cockrell, D. J., eds., 1968, *Computation of Turbulent Boundary Layers*, v. 1, AFOSR-IFP-Stanford conference.
[11] DeGraaff, D. B., and Eaton, J. K., 2000, ''Reynolds number scaling of the turbulent boundary layer on a flat plate and on swept and unswept bumps,'' J. Fluid Mech., **422**, pp. 319–386.
[12] Mierlo, M. C. L. M., and De Rytter, J. C. C., 1988, ''Turbulence measurements above artificial dunes,'' Report, Q789, Delft Hydraulics Laboratory, Netherlands.
[13] Patel, V. C., and Yoon, J. Y., 1995, ''Application of turbulence models to separated flow over rough surfaces,'' ASME J. Fluids Eng., **117**, pp. 234–241.

J. Steelant
Marie-Curie Research Fellow
European Space Research
and Technology Centre,
Aerothermodynamics Section,
Noordwijk, The Netherlands

E. Dick
Professor
Department of Flow,
Heat and Combustion,
University of Gent,
Gent, Belgium

Modeling of Laminar-Turbulent Transition for High Freestream Turbulence

To simulate transitional skin friction or heat transfer, the conditionally averaged Navier-Stokes equations are used. To describe the diffusion of freestream turbulence into the boundary layer and the intermittent laminar-turbulent flow behavior during transition, a turbulence weighting factor τ is used. A transport equation is presented for this τ-factor including convection, diffusion, production, and sink terms. In combination with the conditioned Navier-Stokes equations, this leads to an accurate calculation of flow characteristics within the transitional layer. The method is validated on transitional skin friction and heat transfer measurements, respectively on a flat plate and in a linear turbine cascade. [DOI: 10.1115/1.1340623]

Introduction

In contrast to natural transition which emanates from the breakdown of amplified disturbances within the boundary layer, bypass transition is caused by the freestream turbulence affecting the pretransitional (pseudo-laminar) layer both by diffusion and by pressure fluctuations [1]. If the freestream turbulence is high enough, i.e., $Tu \geqslant 1$ percent, the transition happens far further upstream than what would be expected for natural transition. Also, the transition length is shorter and is directly related to the turbulence level.

The diffusion of turbulent eddies into the boundary layer prior to the transition onset has an intermittent character and is first localized in the outer part of the laminar boundary layer. This process has also been observed experimentally by Gostelow and Blunden [2] in the early stage of transition. They measured an intermittency in the outer layer of the boundary layer, which was clearly higher than in the near wall region, i.e., $y/\delta < 0.4$. Intermittent behavior is also seen during the transition where the flow in the boundary layer is characterized by distinct turbulent and laminar phases alternating in function of time. The intermittent behavior during transition has been quantified by the intermittency factor γ. This factor is the relative fraction of time during which the flow is turbulent at a certain position. It evolves from 0 percent at the transition point up to 100 percent at the end of transition.

The same relative fraction of time can be taken to quantify the intermittent behavior of the diffusing turbulent eddies in the pseudo-laminar boundary layer. This parameter, called here the ''freestream factor'' ω, is 0 percent near the wall and tends to 100 percent in the freestream.

Conditioned Averages

Global time averaging used for classical turbulence modeling is not valid in intermittently changing flows. To describe the transitional zone and the outer layer zone, it is necessary to use conditional time averaging. These averages are taken during the fraction of time the flow is laminar or turbulent, respectively. As we are only interested in the state of the flow, i.e., laminar or turbulent, at a certain position, it is sufficient to use a turbulence weighting factor $\tau(x,y)$, which is the sum of the intermittency factor $\gamma(x,y)$ and the freestream factor $\omega(x,y)$:

$$\tau(x,y) = \gamma(x,y) + \omega(x,y). \tag{1}$$

As a consequence, this factor τ incorporates two effects: first, the diffusion of freestream turbulent eddies into the boundary layer and second, the transport and growth of the turbulent spots during transition. Hence, this factor is 0 percent in the vicinity of the wall within the pretransitional boundary layer, and 100 percent in the freestream and inside a fully turbulent boundary layer.

The global mean and rms-values can be evaluated with the conditional averaging techniques derived in earlier work [3] but now based on the turbulence weighting factor τ:

$$\tilde{u} = (1-\tau)\tilde{u}_l + \tau\tilde{u}_t,$$

$$\widetilde{u'^2} = (1-\tau)\widetilde{u_l'^2} + \tau\widetilde{u_t'^2} + \tau(1-\tau)(\tilde{u}_l - \tilde{u}_t)^2, \tag{2}$$

where $\tilde{u}$ denotes the global Favre average of the x-velocity component, $\tilde{u}_l$ and $\tilde{u}_t$, respectively, the Favre averages during the laminar and turbulent phase. Fluctuating quantities are denoted by single accents.

An obvious advantage of the τ-factor, in contrast with the γ-factor, is the ability to end up with turbulent flow quantities in the freestream prior to transition. At such a position, τ is set at 100 percent while γ is set at 0 percent. In the absence of laminar fluctuations, the averages lead to $\tilde{u} = \tilde{u}_t$ and $\widetilde{u'^2} = \widetilde{u_t'^2}$ when using the τ-factor and $\tilde{u} = \tilde{u}_l$ and $\widetilde{u'^2} = 0$ when using the γ-factor. Clearly, only when the τ-factor is applied, one obtains the right turbulent freestream values. Although experiments indicate the existence of laminar fluctuations during the laminar state, their modeling is not straightforward. Therefore, they are neglected in the present study.

Applying the conditional averaging technique to the Navier-Stokes equations leads to a set of laminar and turbulent equations for mass, momentum and energy [3,4]. These conditioned equations differ from the original Navier-Stokes equations by the presence of source terms which are functions of the turbulence weighting factor τ:

$$\frac{\partial \overline{U}_l}{\partial t} + \frac{\partial \overline{F}_l}{\partial x} + \frac{\partial \overline{G}_l}{\partial y} = \frac{\partial \overline{F}_{vl}}{\partial x} + \frac{\partial \overline{G}_{vl}}{\partial y} + S_l^\tau,$$

$$\frac{\partial \overline{U}_t}{\partial t} + \frac{\partial \overline{F}_t}{\partial x} + \frac{\partial \overline{G}_t}{\partial y} = \frac{\partial \overline{F}_{vt}}{\partial x} + \frac{\partial \overline{G}_{vt}}{\partial y} + S_t^\tau.$$

The laminar and turbulent continuity equations are, respectively:

Contributed by the Fluids Engineering Division for publication in the JOURNAL OF FLUIDS ENGINEERING. Manuscript received by the Fluids Engineering Division June 26, 2000; revised manuscript received October 13, 2000. Associate Editor: P. Bradshaw.

$$\frac{\partial \overline{\rho}_l}{\partial t}+\frac{\partial \overline{\rho}_l \widetilde{u}_l}{\partial x}+\frac{\partial \overline{\rho}_l \widetilde{v}_l}{\partial y}=S^{\tau}_{l,\rho}=\frac{1}{2(1-\tau)}S^{\tau}_{\rho},$$

$$\frac{\partial \overline{\rho}_t}{\partial t}+\frac{\partial \overline{\rho}_t \widetilde{u}_t}{\partial t}+\frac{\partial \overline{\rho}_t \widetilde{v}_t}{\partial y}=S^{\tau}_{t,\rho}=\frac{1}{2\tau}S^{\tau}_{\rho},$$

with

$$S^{\tau}_{\rho}=(\overline{\rho}_l-\overline{\rho}_t)\frac{\partial \tau}{\partial t}+(\overline{\rho}_l \widetilde{u}_l-\overline{\rho}_t \widetilde{u}_t)\frac{\partial \tau}{\partial x}+(\overline{\rho}_l \widetilde{v}_l-\overline{\rho}_t \widetilde{v}_t)\frac{\partial \tau}{\partial y}.$$

The momentum and energy equations have similar expressions. All source terms become zero when τ approaches zero or one. In order to close the equation, τ has to be determined. The factor τ has a spatial distribution which largely depends on the conditions of the mean flow and the boundary layer. For simple cases, one can derive an algebraic expression. For more general flows, a transport equation is more appropriate.

Transport Equation for τ

Since the evolution of τ depends on the diffusion of the freestream turbulence, on the one hand, and on the transport and growth of the turbulent spots, on the other hand, the differential model should certainly include convection, diffusion, and production terms. Since the presence of the wall prohibits the existence of large scale eddies and hence damps the influence of turbulent eddies, a dissipation term has been added. A general transport equation for τ can be cast in the following form:

$$\frac{\partial \overline{\rho}\widetilde{u}\tau}{\partial x}+\frac{\partial \overline{\rho}\widetilde{v}\tau}{\partial y}=D_{\tau}+P_{\tau}-E_{\tau}, \tag{3}$$

where D_{τ} is the diffusion term, P_{τ} the production term, and E_{τ} the dissipation term. The terms $\widetilde{u}$ and $\widetilde{v}$ are global mean values of the velocity components.

Diffusion. Prior to transition, the turbulence factor τ reduces to the freestream factor ω as the intermittency factor $\gamma=0$. The boundary conditions of τ or ω are such that $\tau=100$ percent in the freestream and 0 percent at the wall prior to the transition point. To the knowledge of the authors, no detailed experiments are available on the intermittent behavior of freestream turbulence affecting the edge of the laminar boundary layer. Hence, the normal variation of the freestream factor ω cannot be modeled using experiments. Therefore we postulate that the effect of freestream turbulence on the underlying boundary layer is similar in the pretransitional region and in the posttransitional region. For the latter, it is known that $\tau=1$. The variation of the intermittency in the normal direction for turbulent boundary layers was correlated by Klebanoff as

$$\gamma(y)=\frac{1}{1+5\left(\frac{y}{\delta}\right)^6}. \tag{4}$$

Using Eq. (1) the freestream factor should then be:

$$\omega=1-\gamma. \tag{5}$$

For ease of analysis (see later), the function (4) is approximated by an exponential law:

$$\gamma(y)=\exp\left[-C\left(\frac{y}{\delta}\right)^n\right],$$

where C and n are to be determined. A best global fit is obtained for $n=4$ and $C=2$. A better fit near the wall is obtained with $n=6$ and $C=4$ and near the edge with $n=2$ and $C=2$. Based on Eq. (5), the evolution of the freestream factor ω can be described as:

$$\omega(y)=1-\exp\left[-\left(\frac{y}{\delta_{\omega}}\right)^n\right], \tag{6}$$

with $\delta_{\omega}=C^{-1/n}\delta$.

As mentioned previously, the variation of $\omega(y)$ is determined by a diffusion process. As $\tau(y)=\omega(y)$ for a pretransitional boundary layer, Eq. (3), in combination with the continuity equation, reduces to:

$$\frac{\partial \overline{\rho}\widetilde{u}\tau}{\partial x}+\frac{\partial \overline{\rho}\widetilde{v}\tau}{\partial y}=\overline{\rho}\widetilde{v}\frac{\partial \tau}{\partial y}=D_{\tau}. \tag{7}$$

The term D_{τ}, controlling the diffusion of turbulent eddies from the freestream toward the wall, needs to be modeled. In its most general form, this term can be written as:

$$D_{\tau}=\frac{\partial}{\partial x_i}\left[\mu_{\tau}\frac{\partial \tau}{\partial x_i}\right],$$

where μ_{τ} needs to be defined. The diffusion coefficient is postulated to be proportional to the molecular viscosity μ:

$$\mu_{\tau}=\mu f(\tau).$$

Equation (7) then results in:

$$\frac{\partial}{\partial y}\left[\mu f\frac{\partial \tau}{\partial y}\right]=\overline{\rho}\widetilde{v}\frac{\partial \tau}{\partial y}. \tag{8}$$

Taking as a first approximation $\overline{\rho}\widetilde{v}$ as constant, Eq. (8) can be integrated resulting in

$$\mu f\frac{\partial \tau}{\partial y}-\overline{\rho}\widetilde{v}\tau=C_0.$$

From Eqs. (4) and (5) it follows that at the wall $\tau=0$ and $\partial\tau/\partial y=0$. This implies $C_0=0$. The function f is then

$$f=\frac{\overline{\rho}\widetilde{v}\tau}{\mu\frac{\partial \tau}{\partial y}}.$$

From Eq. (6) it follows

$$\frac{\partial \tau}{\partial y}=\frac{n}{\delta_{\omega}}\left(\frac{y}{\delta_{\omega}}\right)^{n-1}\exp\left[-\left(\frac{y}{\delta_{\omega}}\right)^n\right].$$

Also, from Eq. (6), one obtains

$$\left(\frac{y}{\delta_{\omega}}\right)^n=-\ln(1-\tau).$$

This allows writing the derivative $\partial\tau/\partial y$ in function of τ:

$$\frac{\partial \tau}{\partial y}=\frac{n(1-\tau)}{\delta_{\omega}}[-\ln(1-\tau)]^{(n-1)/n}.$$

Hence, the function $f(\tau)$ is:

$$f=\frac{\widetilde{v}}{n\widetilde{u}_{\infty}}\frac{\overline{\rho}\widetilde{u}_{\infty}\delta_{\omega}}{\mu}\frac{\tau}{1-\tau}[-\ln(1-\tau)]^{-(n-1)/n}.$$

The limit for $\tau\to 0$ results in $f=0$. The obtained expression is, however, not valid for $\tau\to 1$. In order to remove the singularity for τ close to 1, we take as expression for f:

$$f=C_1 f_{\mu_{\tau}}\frac{\overline{\rho}\widetilde{u}_{\infty}\delta_{\omega}}{\mu}[-\ln(1-\tau)]^{-(n-1)/n}.$$

The near-wall function $f_{\mu_{\tau}}$ should ensure that close to a solid wall the function f approaches 0. Hence the diffusion coefficient can be written as:

$$\mu_{\tau}=\mu C_1 f_{\mu_{\tau}}\frac{\overline{\rho}\widetilde{u}_{\infty}\delta_{\omega}}{\mu}[-\ln(1-\tau)]^{-(n-1)/n}. \tag{9}$$

Dissipation. During the transition and close to the wall, the τ-factor should reduce to the intermittency factor γ. Since a zero normal variation of the intermittency γ is generally assumed near the wall, this property should also hold for the turbulence weighting factor τ. Therefore, the sink term E_τ is constructed such that this property can be obtained automatically during transition. Based on the ideas from the work of Cho and Chung [5], the product of normal derivatives of velocity amplitude and τ will yield this property. Therefore, the term E_τ is chosen to be proportional to

$$E_\tau \sim \frac{\partial}{\partial n}\left[\frac{\tilde{c}^2}{\tilde{c}_\infty^2}\right]\frac{\partial \tau}{\partial n} \sim \frac{\tilde{c}}{\tilde{c}_\infty^2}\frac{\partial \tilde{c}}{\partial n}\frac{\partial \tau}{\partial n},$$

with $\tilde{c}=\sqrt{\tilde{u}^2+\tilde{v}^2}$ the amplitude of the global velocity vector and n the wall normal direction. As can be verified, the proportionality factor should have the dimension of a viscosity. The diffusion coefficient for the turbulence weighting factor is used, resulting in:

$$E_\tau = C_3 \mu_\tau \frac{\tilde{c}}{\tilde{c}_\infty^2}\frac{\partial \tilde{c}}{\partial n}\frac{\partial \tau}{\partial n}$$

where C_3 still needs to be defined.

Production. In previous work [3,4], a production term P_γ was derived for the calculation of the intermittency factor γ by means of a transport equation:

$$\frac{\partial \bar{\rho}\tilde{u}\gamma}{\partial x}+\frac{\partial \bar{\rho}\tilde{v}\gamma}{\partial y}=P_\gamma.$$

As the normal derivative of τ vanishes near the wall, the E_τ-term, as well as the diffusion, disappear near the wall. As a consequence, the production term P_τ should then reduce to the production term P_γ:

$$P_\tau = 2\, f_\tau (1-\tau)\sqrt{-\ln(1-\tau)}\,\beta\bar{\rho}\tilde{c}.$$

This production term is set to zero on the wall prior to the transition point. The damping function f_τ models the distributed breakdown. For $\tau > 0.45$ the function $f_\tau = 1$, and for $\tau < 0.45$ it is given by:

$$f_\tau = 1-\exp[-1.735\tan(5.45\tau-0.95375)-2.2].$$

The function β accounts for the turbulent spot growth:

$$\beta = \sqrt{\hat{n}\sigma(K,Tu)}\frac{\tilde{c}_\infty}{\nu}$$

$$\hat{n}\sigma = f_K 1.25\, 10^{-11} Tu_\infty^{7/4}. \tag{10}$$

A modification of previous work [3,4] is the use of the local turbulence intensity Tu_∞ in the correlation (10). This leads to a better agreement with the experiments. To determine the local Tu_∞, one can extract it from the local freestream turbulence kinetic energy k_∞ calculated by the turbulence model. For general flow situations, however, it is sometimes very hard to define k_∞, e.g., in turbine cascades. To estimate the local freestream Tu_∞, a simple algebraic correlation is proposed. Examining different sets of experimental data, the reduction of the freestream k_∞ is little affected by the dissipation within the transitional zone. It is, however, primarily affected by acceleration and deceleration. Hence, the transport equation for the freestream turbulence reduces to:

$$\frac{dU_\infty k_\infty}{dx}=0 \tag{11}$$

As $k_\infty \sim Tu_\infty^2 U_\infty^2$, the expression (11) results after integration into:

$$Tu_\infty = Tu_{le,\infty}\left(\frac{U_{le,\infty}}{U_\infty}\right)^{3/2}. \tag{12}$$

A second adaptation to the expression (10) is the definition of the pressure parameter f_K. From the experimental data of Gostelow et al. [6] the authors observed that the pressure gradient has a small effect on the spot growth during the initial phase of the transitional zone. This phase is characterized by the distributed breakdown. Based on this observation, the pressure parameter f_K is relaxed by using the distributed breakdown parameter f_τ:

$$f_K = 1+f_\tau(\mathrm{PRC}-1),$$

where PRC expresses the pressure influence on the spot growth. The same correlations given in previous work are still used to account for this pressure influence:

$$\mathrm{PRC}=\begin{cases}(474 Tu_{le,\infty}^{-2.9})^{[1-\exp(2\times 10^6 K)]} & K<0,\\ 10^{-3227K^{0.5985}} & K>0,\end{cases} \tag{13}$$

with $K=\nu/U_\infty^2(dU_\infty/dx)$ the incompressible pressure gradient parameter and $Tu_{le,\infty}$ the local turbulence intensity at the entrance plane.

The production term obtained so far, is directly applicable to incompressible transitional flows. In transonic flows, on the contrary, compressibility and the presence of shock waves effect the length of the transitional zone considerably, which should be dealt with by the spot growth parameter (10). Unfortunately, there is only limited open literature about these effects on the spot growth.

Qualitatively, increasing the Mach number results into a lengthening of the transition zone and a retarding of the onset. However, a large discrepancy among the different correlations exists when this effect is quantified. Narasimha [7] suggests the ratio of the transition length Δx to the onset location x_s to be independent of Mach number whereas $\mathrm{Re}_{x_s} \sim [1+0.38M^{0.6}]$. This suggests that the spot growth is correlated to the Mach number as:

$$\hat{n}\sigma_M = \hat{n}\sigma_{\mathrm{inc}}[1+0.38M^{0.6}]^{-2}, \tag{14}$$

where $\hat{n}\sigma_{\mathrm{inc}}$ is the incompressible spot production parameter given by Eq. (10) and $\hat{n}\sigma_M$ the parameter including the Mach effect. This correlation means a decrease of the spot growth, by a factor 1.9 at $M=1$. The analysis of Chen and Tyson [8] based on low freestream turbulence flows, indicates a lower influence corresponding to a decrease of about 1.16 at $M=1$. On the other hand, Boyle and Simon [9], however, suggest a drastic influence of Mach number resulting in a factor of approximately 6 at $M=1$. From numerically obtained results on turbine guidevanes (to be discussed later), the authors experienced a too low Mach number influence when using Eq. (14). On the other hand, the Mach influence suggested by Boyle and Simon resulted into a too large impact on the spot production rate with a too long transition length as a consequence. Based on this experience, the authors found the relation

$$\hat{n}\sigma_M = \hat{n}\sigma_{\mathrm{inc}}[1+0.58M^{0.6}]^{-2}, \tag{15}$$

to be more realistic, at least for the considered test cases. At $M=1$, it corresponds to a decrease with a factor of 2.5. The large discrepancy in the different correlations suggests that there is a fundamental need for more experimental data to better understand the influence of Mach number in the range of 0.5–1.5. Within the calculation, the local Mach number M is obtained from the total and static pressure assuming an isentropic relation.

The influence of the pressure gradient on the spot production parameter is considered not to be altered directly by the compressibility. The correlations given by (13) are still valid but the definition of the acceleration parameter needs to be extended for compressible flows. For incompressible flow a constant parameter K_{inc} corresponds with a flow through a wedge shaped channel. One can then prove that K can be written in function of geometrical parameters as:

$$K_{\mathrm{inc}} = \frac{\nu}{U_\infty^2}\frac{dU_\infty}{dx} = \frac{\nu tg\alpha}{U_0 h_0}, \tag{16}$$

with α the wedge angle, U_0 and h_0 the velocity and height at the inlet. If the second formulation of K in expression (16) is taken as a basis, a compressible flow through a wedge shaped geometry results then, after some algebra, into the following compressible definition of K_M:

$$K_M = -\frac{\mu_\infty}{\rho_\infty^2 U_\infty^3}|1-M^2|\frac{dp}{dx}.$$

Analyzing transitional experiments, the presence of a shock wave reveals a sharp increase toward turbulent values downstream of the shock with a shortening of the transition zone as a result. To model the influence of a shock wave on a transitional flow, it is necessary to quantify this effect on the spot production parameter. The presence of a local strong adverse pressure gradient is certainly not sufficient to model this sharp transition. Another driving parameter is the freestream turbulence intensity. From the DNS-work of Lee et al. [10,11] it is clear that the freestream turbulence level definitely increases due to the presence of a shock. Lee et al. remarked also that both a spatial and physical distinction can be made related to the increase of the velocity fluctuations. An initially straight shock evolves into a distorted front when turbulence is introduced into the freestream. The resulting shock zone has now a certain thickness which extends over a distance of about 2.5 times the turbulence length scale. Hence the streamwise component in the shock zone contains ''intermittency'' effects due to the unsteady distortions of the shock front. The corresponding Tu_∞-level within the shock zone increases with a factor of 5 or more. Downstream of the shock zone, the turbulence level is not contaminated by the aforementioned intermittency effects. The increase is much smaller and is mainly due to the pressure work. The Tu_∞-level raises approximately with a factor of 1.2–1.3.

For the test cases discussed below, the shock zone thickness is of the order of 1 cm. Since the transition length is generally comparable with the shock zone thickness for turbine cascades, the corresponding high Tu_∞-level is considered by the authors as the prime cause of the sudden growth of the turbulent spots. To incorporate the shock wave effect within the correlations of the transition model, the turbulence intensity Tu_∞, obtained with Eq. (12), is corrected downstream of the shock and put at $Tu_\infty = 15$ percent. This model is only a first attempt to describe roughly the shock wave effect. Clearly, more experiments or DNS calculations are necessary to better understand the underlying physics and to come up with more physical models. A similar correction to Eq. (12) is applied in the wake region. In the vicinity of shear layers the *Tu*-levels typically raise to 20 percent or higher. In this region, the level is set at $Tu_\infty = 20$ percent.

Transport Equation. Although the effects of freestream and intermittency factors have been modeled separately, it would, however, be convenient to combine the modeled terms to end up with one single transport equation for τ. This combination certainly leads to mutual influences which we presently neglect. This means, for instance, the acceptance that the transitional diffusion process is similar to the pretransitional diffusion process. We propose the following transport equation for τ:

$$\frac{\partial \overline{\rho}\widetilde{u}\tau}{\partial x} + \frac{\partial \overline{\rho}\widetilde{v}\tau}{\partial y} = \frac{\partial}{\partial x_i}\left[\mu_\tau \frac{\partial \tau}{\partial x_i}\right] + P_\tau - C_3 \mu_\tau \frac{\tilde{c}}{\tilde{c}_\infty^2}\frac{\partial \tilde{c}}{\partial n}\frac{\partial \tau}{\partial n}.$$

The premultiplying factors still have to be defined. The factor $\overline{\rho}\widetilde{u}_\infty \delta_\omega / \mu$ in expression (9) can be written as

$$\frac{\overline{\rho}\widetilde{u}_\infty \delta_\omega}{\mu} \sim \frac{\overline{\rho}\widetilde{u}_\infty \delta}{\mu} \sim \mathrm{Re}_\delta.$$

To have an idea of the Reynolds number, we take the value at the transition point as representative. With $\mathrm{Re}_{\delta_s} \sim \mathrm{Re}_{\theta_s}$ combined with Eq. (17) (see below), this factor $\overline{\rho}\widetilde{u}_\infty \delta_\omega / \mu \sim Tu_{le}^{-.69}$.

By use of several numerical experiments, the different factors have been determined to obtain best agreement with the ''reverse'' Klebanoff function:

$$C_3 = 2.5$$

$$\mu_\tau = 33 f_{\mu_\tau} \mu Tu_{le,\infty}^{-0.69} [-\ln(1-\tau)]^{-5(1-\tau)/6}$$

$$\text{with } f_{\mu_\tau} = 1 - \exp\left[-256\left(\frac{y c_\infty}{\nu}\right)^2\right].$$

One might observe that the exponent $n - 1/n$ is replaced by $5(1-\tau)/6$. Originally $n=4$ was taken and gave reasonable results. As the fit with the Klebanoff function is better for $n=6$ near the wall ($\tau = 0$) and for $n=1$ in the freestream ($\tau = 1$), a linear variation was taken as a first attempt to model this behavior. Although this variation was not taken into account during the analysis, the authors found a better agreement both near the wall and further away.

Transition Onset. The start of transition can be defined as the most upstream location where turbulent spots are generated. Physically, the generation of turbulent spots is not located on one single line, but is spread over a certain distance. This means that a distributed breakdown occurs. Mayle [12] proposed a correlation for the onset using intermittency data,

$$\mathrm{Re}_{\theta_{t,\mathrm{inc}}} = 420 Tu_{le,\infty}^{-.69}, \tag{17}$$

which however gives the location at the maximum spot generation rate. As the present model takes into account the distributed breakdown, a new correlation is proposed. In previous work [3], the width of the breakdown was determined to be:

$$\mathrm{Re}_{\Delta x} = 2[\mathrm{Re}_x(\gamma = 0.2) - \mathrm{Re}_x(\gamma = 0.01)]$$

$$= \frac{0.744}{\sqrt{\hat{n}\sigma_{x_s}}} = 210508 Tu_{le,\infty}^{-7/8}.$$

The wall boundary condition for τ is set to zero upstream of the position:

$$\mathrm{Re}_{x_{s,\mathrm{inc}}} = \mathrm{Re}_{x_{t,\mathrm{inc}}} - 0.5\,\mathrm{Re}_{\Delta x}$$

$$= \frac{\mathrm{Re}_{\theta_{t,\mathrm{inc}}}^2}{0.664^2} - 0.5\,\mathrm{Re}_{\Delta x}$$

$$= 400094 Tu_{le,\infty}^{-1.38} - 105254 Tu_{le,\infty}^{-7/8}. \tag{18}$$

Beyond this onset, the wall value of τ is determined by the transport equation. As an expression in $\mathrm{Re}_{\theta_{s,\mathrm{inc}}}$ is more general to define the transition onset, the expression (18) is converted by the laminar boundary layer relation:

$$\mathrm{Re}_{\theta_{s,\mathrm{inc}}} = 0.664\sqrt{\mathrm{Re}_{x_{s,\mathrm{inc}}}}.$$

With increasing Mach number, all experiments indicate that the transition onset shifts downstream at any given turbulence level. The following correlation is suggested by Narasimha [7] based on experiments with a wide range of turbulence levels ($0.3 < Tu < 3$ percent):

$$\mathrm{Re}_{\theta_{s,M}} = \sqrt{1 + 0.38M^{0.6}}\,\mathrm{Re}_{\theta_{s,\mathrm{inc}}},$$

where the start of transition with compressibility effect, given by $\mathrm{Re}_{\theta_{s,M}}$, is related to the incompressible value $\mathrm{Re}_{\theta_{s,\mathrm{inc}}}$ in combination with the local Mach number M.

Test Cases. The above equations are first validated with experimental data obtained from transitional flows over adiabatic flat plates with sharp leading edges [13]. The test case, denoted as T3A, has zero pressure gradient (ZPG). The second test case, denoted as T3C1, has a pressure distribution similar to an aft loaded turbine blade (see Fig. 1). The specifications of the differ-

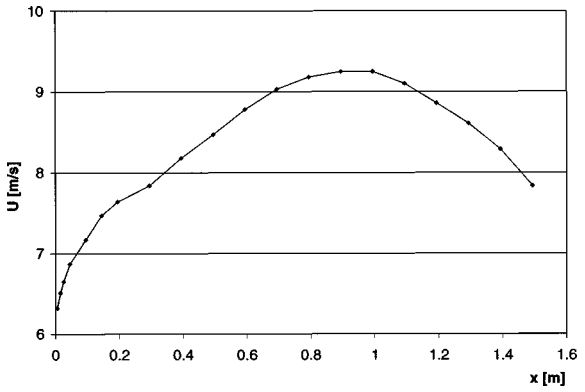

Fig. 1 Velocity distribution for T3C1

ent test cases are given in Table 1 where U_i stands for the oncoming velocity and Tu_{le} for the turbulence level at the leading edge.

The capability of the present transition model is also demonstrated on a turbine guidevane operating at typical design conditions. This guidevane has been experimentally investigated by Arts et al. [14] in order to understand the influence of Mach number, turbulence intensity, and Reynolds number on the transitional heat transfer distribution. The blade profile has a chord of 67.647 mm and a pitch to chord ratio of 0.85. The total inlet temperature is set at approximately $T_{01}=420$ K. The wall temperature is considered to be at a nearly constant level of 300 K during the measurement. To validate the present transition model, three different test cases are considered which are described in Table 2. The incoming turbulence level Tu_i is measured 55 mm upstream of the leading edge plane. As no length scale or dissipation was measured, the turbulence level at the leading edge Tu_{le} is estimated by the correlation of Roach [15],

$$Tu = 80\left(\frac{x}{d}\right)^{-5/7}$$

where the rod diameter is $d=3$ mm.

The computational domain consists of two blocks. The first is a O-grid with 433 nodes along the blade and 73 nodes normal to the blade. The first point is situated at a location $y^+<1$. The second block is a H-grid of 217×49 nodes and is placed in line with the outlet angle. Figure 2 shows the geometry and the location of the different blocks.

The equations are solved in their steady-state form by a relaxation procedure. A vertex-centered finite volume discretization is based on a second-order upwind formulation in combination with a minmod-limiter. The Yang-Shih low-Reynolds k-ε turbulence model is used. Full details of the numerical method are given in Steelant and Dick [16].

Table 1 Description of the flat plate test cases

Case	$U_i(m/s)$	$Tu_{le}(\%)$
T3A	5.00	3.14
T3C1	6.12	7.78

Table 2 Description of the turbine test cases

Case	$M_{2,is}$	$Tu_i(\%)$	$Tu_{le}(\%)$	$Re_{c,2}$
MUR239	0.922	6	4.52	2.10^6
MUR245	0.924	4	3.34	2.10^6
MUR241	1.089	6	4.52	2.10^6

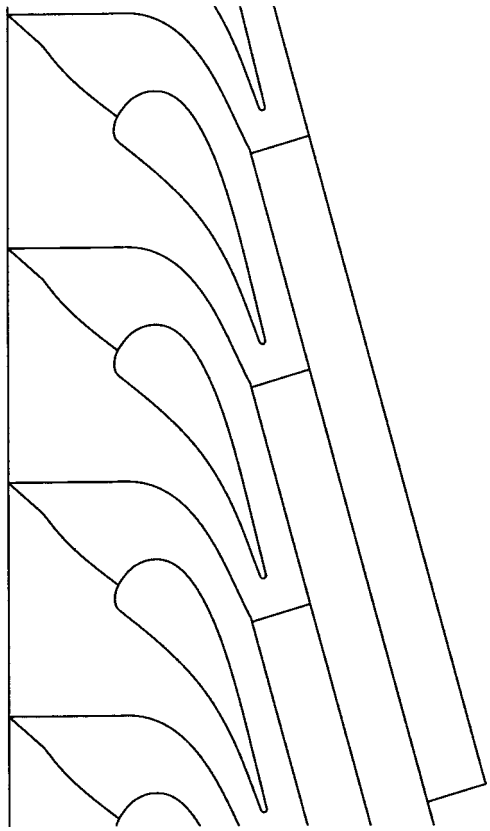

Fig. 2 Geometry with location of the different blocks: C-grid around turbine blade, H-grid along the outlet angle

Transition Results

For the T3A case, the evolution of τ in the streamwise direction on the wall is given in Fig. 3 (full line) together with the experimental values of the intermittency factor γ represented by '$\times$'-signs. The correspondence is extremely good. In Fig. 4, the normal variation of τ prior to the transition onset is compared to the inverse of the Klebanoff law:

$$\omega(y) = 1 - \frac{1}{1+5\left(\frac{y}{\delta}\right)^6}.$$

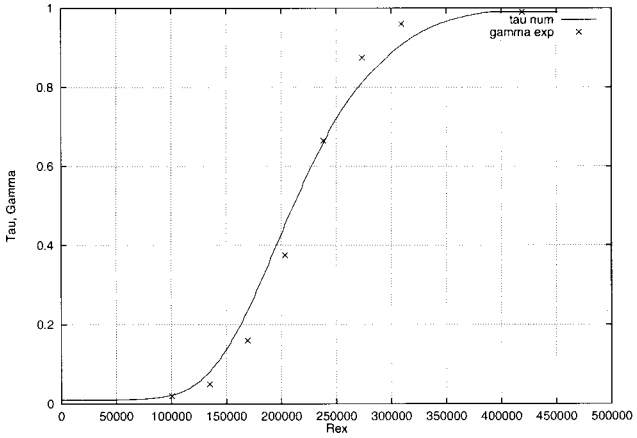

Fig. 3 Evolution of τ along the wall for T3A compared with experimental γ values

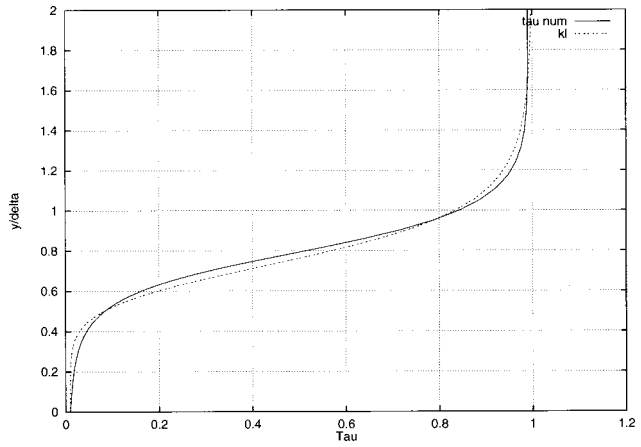

Fig. 4 Normal variation of τ prior to the transition point for T3A compared with the suggested free stream factor

Also here the agreement is very good. These results clearly show that the modeling of the diffusion and the growth of the turbulent spots is well described by the present transport equation for τ.

Figure 5 gives the τ-evolution for T3C1. The symbols do not correspond here to experimentally measured intermittency data. They were derived from the measured skin friction using the linear combination of laminar and turbulent skin friction correlations. Despite this approximation, it gives a good idea about the expected γ-distribution. The numerically obtained τ-distribution near the wall corresponds very well with the experimentally derived data.

In Fig. 6, the skin friction C_f of the two test cases are shown as functions of Re_x. The lower line in the C_f plot represents the exact Blasius' solution given by $C_f = 0.664/\sqrt{\mathrm{Re}_x}$. The upper line represents the relation for the turbulent skin friction: $C_f = 0.445/\ln^2(0.06\,\mathrm{Re}_x)$. The determination of the skin friction from experimentally measured velocity profiles is quite delicate. For a fully turbulent boundary layer, the friction velocity is determined by fitting the log-law (Clauser technique) with a corresponding uncertainty of 5 percent–10 percent. During transition, this method cannot be used. Therefore the linear law $u^+ = y^+$ of the viscous sublayer is used instead with a larger uncertainty of 10 percent up to 25 percent as consequence [17]. The C_f-values obtained by this technique are given by '×'-signs. The C_f-evolution can also be obtained by using the integral momentum equation and the measured θ, H and U_e:

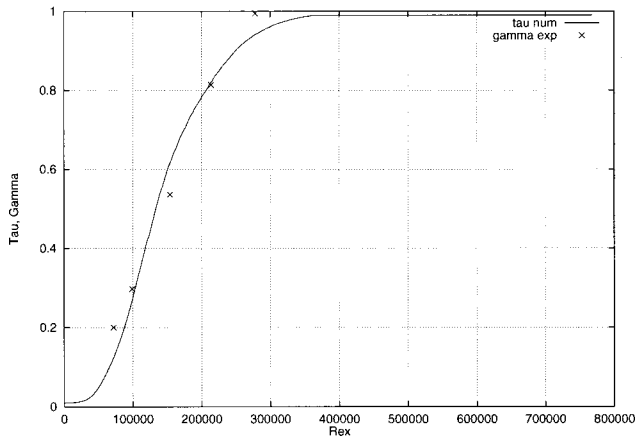

Fig. 5 Evolution of τ along the wall for T3C1

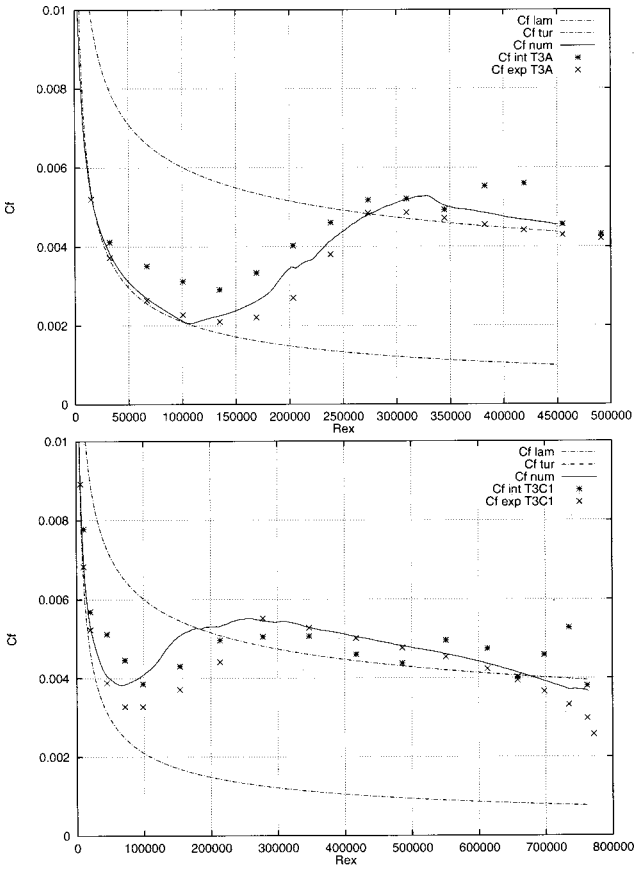

Fig. 6 Skin friction coefficient for T3A (top) and T3C1 (bottom)

$$\frac{C_f}{2} = \frac{d\theta}{dx} + (2+H)\,\frac{\theta}{U_e}\,\frac{dU_e}{dx}.$$

The corresponding values are given by '∗'-symbols. The predicted C_f-evolution is given by the full line. It is seen that both the transition point and length are very close to the experiments and are within the above mentioned uncertainty bands.

The experimental evolution of the shape factor, given in Fig. 7, already starts to deviate upstream of the transition point from the laminar value 2.59. This effect is more dominant at higher turbulence levels. This drop is mainly due to the diffusion of the turbulent eddies from the main flow toward the wall. Moreover, at very high turbulence levels (e.g., T3C1), these eddies induce fluctuations in the laminar portion of the flow with corresponding Reynolds stresses. These stresses slightly modify the Blasius velocity profile resulting in a further drop of the shape factor prior to transition. The numerically obtained shape factors have a slightly slower drop due to the absence of laminar fluctuations in the calculations.

Figure 8 shows for the T3A-case the profiles of the global streamwise velocity fluctuation u' at three positions during transition: near the start, the middle and the end. The global streamwise Reynolds normal stress $\widetilde{u'^2}$ is, with the usual approximation $(\widetilde{u'^2} = \tilde{k})$ given by

$$\widetilde{u'^2} = \tau\tilde{k}_t + \tfrac{1}{2}\tau(1-\tau)[(\tilde{u}_t - \tilde{u}_l)^2 + (\tilde{v}_t - \tilde{v}_l)^2],$$

where $\tilde{k}_t$ is the turbulence kinetic energy during the turbulent phase. The term $(1-\tau)\tilde{k}_l$ is dropped as the laminar fluctuations are neglected in the present calculations. This results in a lower peak than measured near the start of transition. The use of a turbulence weighting factor now results in a nonzero turbulence level in the freestream before and in the beginning of the transition

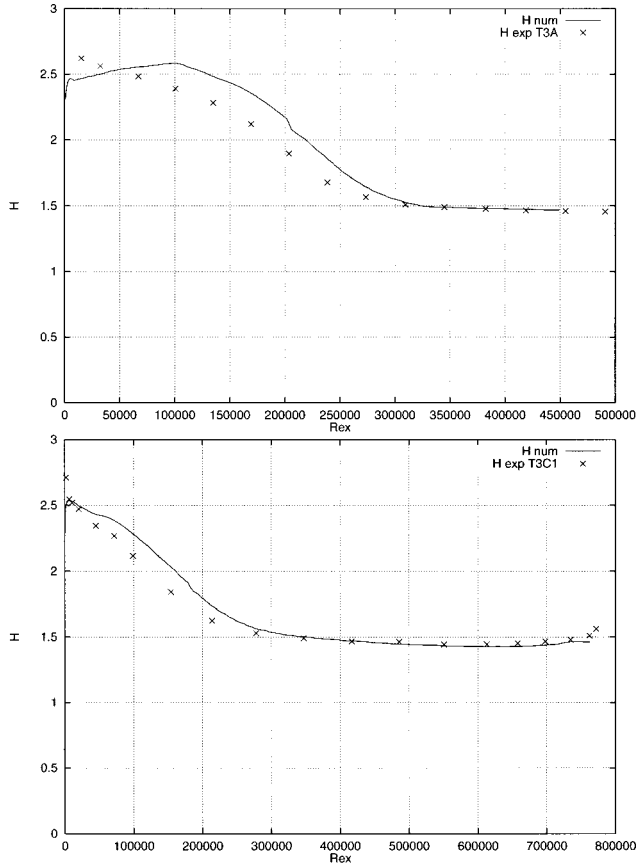

Fig. 7 Shape factor for T3A (top) and T3C1 (bottom)

zone in contrast to using the intermittency factor γ with no normal variation [3,4]. The difference in the calculated and measured freestream *Tu*-level is entirely due to the inability of the underlying k-ε equations to model correctly the decay of the turbulence in the freestream. The typical high peak (15 percent up to 20 percent) in the middle of the transition zone is predicted very well. Near the end, the peak drops off faster, toward the value of approximately 10 percent for a fully developed turbulent boundary layer, than is obtained in the experiments. A possible explanation is a too-large turbulence dissipation produced by the turbulence k-ε model.

The present transition model on turbine test case MUR239 results in the heat transfer and intermittency distributions given in Fig. 9. The heat transfer coefficient and the intermittency factor on the pressure side are placed on the left-hand side, while those on the suction side are placed on the right-hand side. The overall distribution agrees very well with the experimental results, which is mainly due to the correct prediction of the evolution of the turbulence weighting factor near the wall. The predicted heat transfer rate in the pretransitional boundary layer is generally lower than the experimental values both on the suction and pressure side. At high freestream turbulence, velocity fluctuations are induced in the boundary layer prior to transition. This inherently results in higher heat transfer rates [18]. This mechanism is, however, not incorporated in the present model. A possible method dealing with freestream turbulence effects is the model proposed by Volino [19]. Here, pure laminar values are obtained which are almost identical to the low *Tu*-level data ($Tu=1$ percent). The fully turbulent level is higher than the experimental level. This can be attributed to the underlying turbulence model. The near-wall distribution of the turbulence weighting factor τ, which corresponds with the intermittency factor γ, indicates that the transition is almost completed on the suction side (dashed line in Fig.

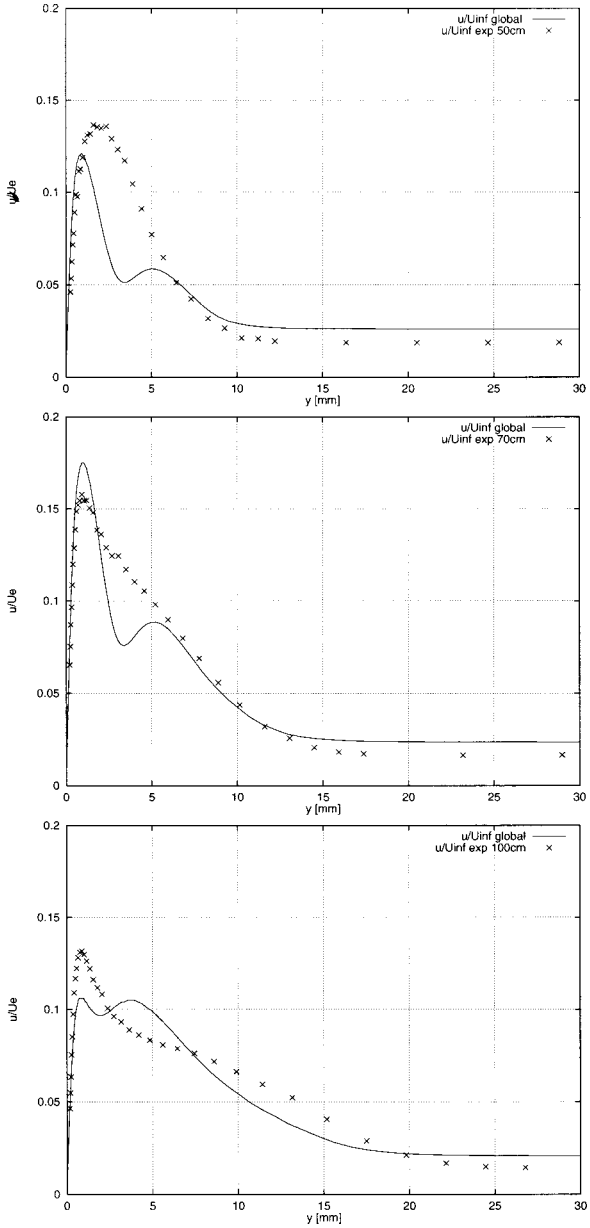

Fig. 8 $\sqrt{u'^2}/Ue$ for T3A at Re_x=169200 (top), Re_x=238400 (middle) and at Re_x=344700 (bottom)

9). On the pressure side, the transition is not completed, as the intermittency reaches about 70 percent near the trailing edge. The isentropic Mach number distribution is given in Fig. 10 together with the only available experimental results taken at slightly different Mach numbers ($M_{2,is}=0.875$ and 1.02).

Lowering only the turbulence level to 4 percent (MUR245) reduces the spot production parameter such that a shock wave appears within the transition zone (Fig. 11). The sudden rise in heat transfer is very well predicted but it ends with a too-large overshoot. On the pressure side, the intermittency evolution is lower than in the previous case due to the lower turbulence level. On the suction side, however, the intermittency undergoes a steep increase downstream of the shock. This leads to a shorter transition zone ending before the trailing edge. The corresponding isentropic Mach number distribution is given in Fig. 12 and differs slightly on the suction side from the result in Fig. 10. The pres-

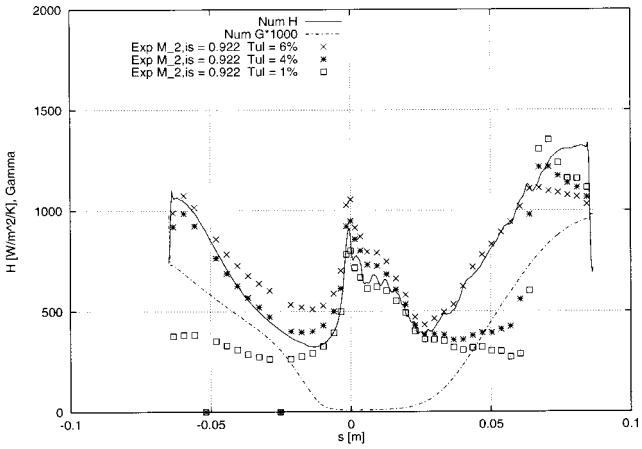

Fig. 9 Heat transfer distribution for MUR239 (Tu_i = 6 percent); full line: calculated heat transfer, dashed line: intermittency (× 1000), symbols: experiments (other Tu_i also shown)

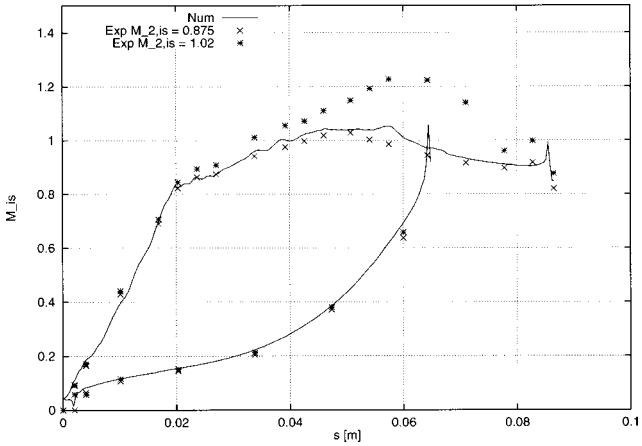

Fig. 10 Isentropic Mach number distribution for MUR239; full line: calculated, symbols: experiment

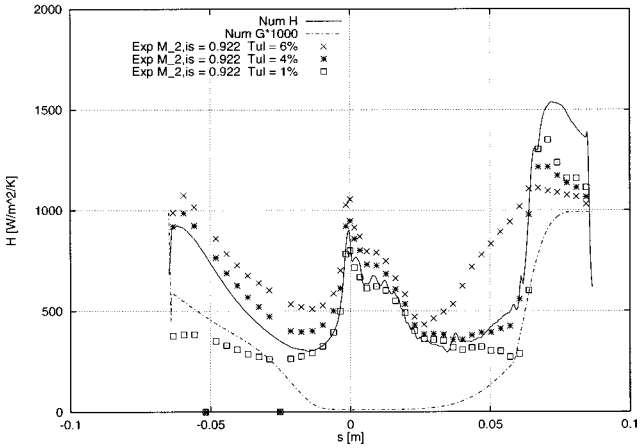

Fig. 11 Heat transfer distribution for MUR245 (Tu_i = 4 percent); full line: calculated heat transfer, dashed line: intermittency (× 1000), symbols: experiments (other Tu_i also shown)

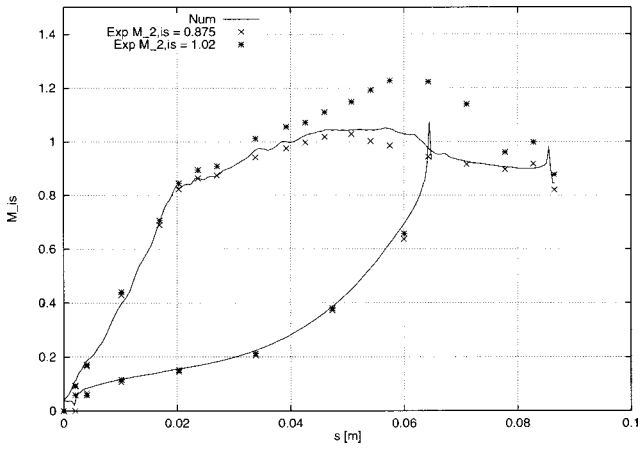

Fig. 12 Isentropic Mach number distribution for MUR245; full line: calculated, symbols: experiment

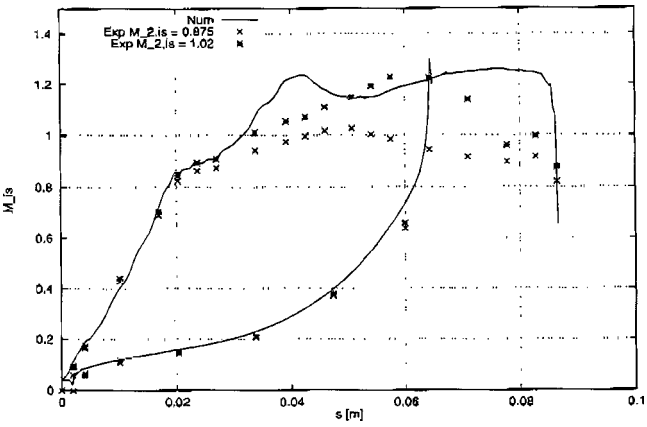

Fig. 13 Isentropic Mach number distribution for MUR241; full line: calculated, symbols: experiments

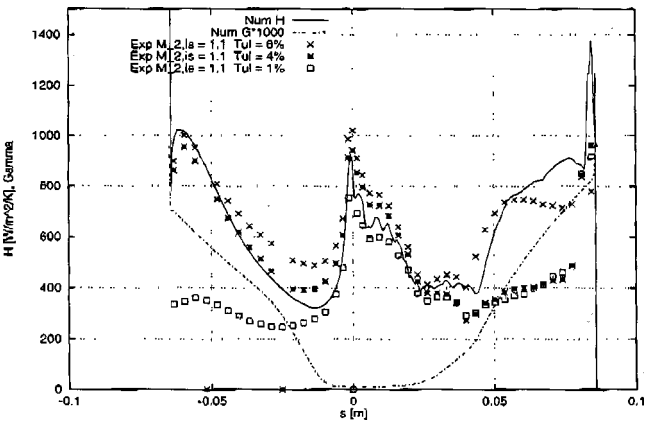

Fig. 14 Heat transfer distribution for MUR241 (legend see Fig. 9)

ence of a thinner, laminar layer allows a longer persistence of the low pressure region than in the MUR239 case ending with a shock wave.

Increasing the outlet isentropic Mach number from $M_{2,is}=0.922$ in MUR239 to $M_{2,is}=1.089$ in MUR241, results in a lower pressure distribution on the suction side but has little or no effect on the pressure side (Fig. 13). The higher acceleration in the region $s=30$ to 40 mm compared to MUR239 decreases the spot growth resulting in $\gamma=15$ percent at position $s=40$ mm instead of the 26 percent value in the MUR239 case (Fig. 14). The deceleration from $s=40$ to 50 mm increases the spot growth again with a sharp rise in heat transfer as a consequence. The slightly accelerated region further downstream attenuates this rise. Near the aft, the heat transfer rate ends with a peak due to the presence of a shock at the trailing edge. On the pressure side the intermittency distribution is almost identical to MUR239 due to the identical pressure distribution.

Conclusion

The use of conditioned Navier-Stokes equations in combination with a transport equation for the ''turbulence weighting factor'' allows the calculation of transitional skin friction and heat transfer distributions. The numerically obtained results are in good correspondence with the experimental data. Besides pressure gradient and turbulence level, the effect of compressibility needs to be taken into account to assure the correct prediction of both the transition onset and length. The present model, however, does not allow the prediction of the higher turbulence kinetic energy or the higher heat transfer rate in the pretransitional boundary layer. This pleads for a further extension of the model to incorporate the physics of the freestream pressure fluctuations affecting the underlying boundary layer.

Acknowledgments

The work reported here was granted under contract G.0283.96 by the Flemish Science Foundation (F.W.O.). The work is also related to research activities, undertaken in the European Space Agency's Facilities, in the framework of a fellowship granted through the Training and Mobility of Researchers Programme financed by the European Community.

The authors especially wish to thank Prof. T. Arts, Prof. R. Mayle and Prof. T. Wang for their helpful discussions during the course of this work.

Nomenclature

C_f = skin friction, $\tau_w/(\rho_w U_\infty^2/2)$
d = rod diameter of turbulence grid [m]
f_K = pressure parameter
f_τ = distributed breakdown parameter
F, G = convective flux vectors
F_v, G_v = diffusive flux vectors
H = shape factor
k = turbulence kinetic energy [m^2/s^2]
K = acceleration parameter
M = local Mach number
n = direction normal to the wall
$\hat{n}\sigma$ = spot growth parameter
PRC = pressure correction parameter for $\hat{n}\sigma$
Re_x = Reynolds number, $\rho_\infty U_\infty x/\mu_\infty$
Re_θ = momentum thickness Reynolds number
s = distance along the blade surface starting at the leading edge stagnation point [m]
S = source term
Tu = turbulence intensity, $100\sqrt{k_\infty}/U_\infty$ (percent)
$\tilde{u}=\overline{\rho u}/\overline{\rho}$ = global Favre time averaged velocity [m/s]
$\tilde{u}_t$ = averaged velocity during turbulent state [m/s]
$\tilde{u}_l$ = averaged velocity during laminar state [m/s]
u', v' = fluctuating velocity components [m/s]
γ = intermittency factor
δ = boundary layer thickness [m]
μ = dynamic viscosity [kg/m/s]
ε = turbulence dissipation [m^2/s^3]
ν = kinematic viscosity [m^2/s]
ρ = density [kg/m^3]
τ = turbulence weighting factor
θ = momentum thickness [m]
ω = freestream factor

Subscripts

0 = total value
1 = inlet value
2 = outlet value
i = inlet
inc = incompressible
is = isentropic
l = laminar state
le = leading edge
s = start of transition ($\gamma=1$ percent)
t = turbulent state
w = wall value
M = with Mach number effect
∞ = freestream

Superscripts

$\tilde{}$ = conditioned Favre-average
$\bar{}$ = conditioned Reynolds-average

References

[1] Mayle, R. E., and Schulz, A., 1997, ''The Path to Predicting Bypass Transition,'' ASME J. Turbomach., **119**, pp. 405–411.
[2] Gostelow, J. P., and Blunden, A. R., 1989, ''Investigations of Boundary Layer Transition in an Adverse Pressure Gradient,'' ASME J. Turbomach., **111**, pp. 366–375.
[3] Steelant, J., and Dick, E., 1996, ''Modelling of Bypass Transition with Conditioned Navier-Stokes Equations coupled to an Intermittency Equation,'' Int. J. Numer. Methods Fluids, **23**, pp. 193–220.
[4] Steelant, J., and Dick, E., 1996, ''Calculation of Transition in Adverse Pressure Gradient Flow by Conditioned Equations,'' ASME 96-GT-160.
[5] Cho, R., and Chung, M. K., 1992, ''A k-ε-γ equation turbulence model,'' J. Fluid Mech., **237**, pp. 301–322.
[6] Gostelow, J. P., Blunden, A. R., and Walker, G. J., 1994, ''Effects of Free-Stream Turbulence and Adverse Pressure Gradients on Boundary Layer Transition,'' ASME J. Turbomach., **116**, pp. 392–404.
[7] Narasimha, R., 1985, ''The Laminar-Turbulent Transition Zone in the Boundary Layer,'' Prog. Aerosp. Sci., **22**, pp. 29–80.
[8] Chen, K. K., and Tyson, N. A., 1971, ''Extension of Emmons' Spot Theory to Flows on Blunt Bodies,'' AIAA J., **9**, pp. 821–825.
[9] Boyle, R. J., and Simon, F. F., 1996, ''Mach Number Effects on Turbine Blade Transition Length Prediction,'' ASME-Paper 98-GT-367.
[10] Lee, S., Lele, S. K., and Moin, P., 1993, ''Isotropic Turbulence Interacting with a Weak Shock Wave,'' J. Fluid Mech., **251**, and corrigendum 264:373–374, 1994, pp. 533–562.
[11] Lee, S., Lele, S. K., and Moin, P., 1997, ''Interaction of Isotropic Turbulence with Shock Waves: Effect of Shock Strength,'' J. Fluid Mech., **340**, pp. 225–247.
[12] Mayle, R. E., 1991, ''The Role of Laminar-Turbulent Transition in Gas Turbine Engines,'' ASME J. Turbomach., **113**, pp. 509–537.
[13] Savill, A. M., 1992, ''A synthesis of T3 Test Case Predictions,'' *Numerical Simulation of Unsteady Flows and Transition to Turbulence*, O. P. et al., ed., Cambridge University Press, pp. 404–442.
[14] Arts, T., de Rouvroit, L. M., and Rutherford, A. W., 1990, ''Aero-Thermal Investigation of a Highly Loaded Transonic Linear Turbine Guide Vane Cascade,'' Tech. Rep. TN-174, Von Karman Institute.
[15] Roach, P. E., 1989, ''The Generation of Nearly Isotropic Turbulence by means of Grids,'' Heat Fluid Flow, **8**, No. 2, pp. 82–92.
[16] Steelant, J., and Dick, E., 1994, ''A Multigrid Method for the Compressible Navier-Stokes Equations Coupled to the $k-\varepsilon$ Turbulence Equations,'' Int. J. Numer. Methods Heat Fluid Flow, **4**, No. 2, pp. 99–113.
[17] Keller, F. J., and Wang, T., 1993, ''Flow and Thermal Structures in Heated Transitional Boundary Layers with and without Streamwise acceleration,'' Tech. rep., Clemson University, Department of Mechanical Engineering.
[18] Mayle, R. E., Dullenkopf, K., and Schulz, A., 1998, ''The Turbulence that Matters,'' ASME J. Turbomach., **120**, pp. 402–409.
[19] Volino, R. J., 1998, ''A New Model for Free-Stream Turbulence Effects on Boundary Layers,'' ASME J. Turbomach., **120**, pp. 613–620.

Stability of the Base Flow to Axisymmetric and Plane-Polar Disturbances in an Electrically Driven Flow Between Infinitely-Long, Concentric Cylinders

J. Liu

G. Talmage

Department of Mechanical and Nuclear Engineering,
The Pennsylvania State University,
University Park, PA 16802-1412

J. S. Walker

Department of Mechanical and Industrial Engineering,
The University of Illinois,
Urbana, IL 61801

The method of normal modes is used to examine the stability of an azimuthal base flow to both axisymmetric and plane-polar disturbances for an electrically conducting fluid confined between stationary, concentric, infinitely-long cylinders. An electric potential difference exists between the two cylinder walls and drives a radial electric current. Without a magnetic field, this flow remains stationary. However, if an axial magnetic field is applied, then the interaction between the radial electric current and the magnetic field gives rise to an azimuthal electromagnetic body force which drives an azimuthal velocity. Infinitesimal axisymmetric disturbances lead to an instability in the base flow. Infinitesimal plane-polar disturbances do not appear to destabilize the base flow until shear-flow transition to turbulence. [DOI: 10.1115/1.1335497]

I Introduction

We have used the method of normal modes to treat the stability of an electromagnetically driven swirling flow with respect to two types of infinitesimal disturbances. An electrically conducting liquid is confined to the radial gap between two concentric, stationary, infinitely long, circular cylinders, as shown in Fig. 1. There is an externally applied, uniform, steady, axial magnetic field. An external power source produces a constant voltage difference between the two concentric cylinders, which are perfect electrical conductors. The voltage difference drives a radial electric current through the liquid, and this current interacts with the axial magnetic field to produce an azimuthal electromagnetic body force (EMBF) which drives the swirling flow. The azimuthal flow interacts with the axial magnetic field to produce a radial induced electric field which partially cancels the static electric field due to the externally applied voltage difference, so that the azimuthal velocity and the radial electric current are intrinsically coupled in the base flow. For cylindrical coordinates, r^*, θ, z^* with the z^* axis along the centerline of the two concentric cylinders, the externally applied magnetic field is $B_0\hat{\mathbf{z}}$, where the asterisk denotes a dimensional variable, B_0 is the magnetic flux density, and $\hat{\mathbf{r}}, \hat{\theta}, \hat{\mathbf{z}}$ are unit vectors for the cylindrical coordinates. The voltage of the outer cylinder minus that of the inner cylinder is $\Delta\phi$. Both B_0 and $\Delta\phi$ can be positive or negative, so that the swirling flow can be in the positive or negative θ direction. We normalize the liquid velocity with $\Delta\phi/LB_0$, where L is the radial distance between the two cylinders, so that the dimensionless azimuthal base-flow velocity $v_{\theta 0}(r)$ is positive for all combinations of B_0 and $\Delta\phi$. The dimensionless coordinates r and z are normalized by L. Moving radially outward, $v_{\theta 0}$ increases from zero at $r=R$ to a maximum $v_{\theta 0\,\max}$ at $r=r_{\max}$ and then decreases to zero at $r=(R+1)$.

This configuration and magnetic field orientation are of significance to homopolar devices, which are high-current, low-voltage DC electromechanical energy converters that operate in the presence of magnetic fields. Typically, solid copper disks (or rotors) are mounted on a shaft, and the tip of each rotor is shrouded by a stationary copper surface (or stator). Sliding electrical contacts, which provide low-resistance current paths between the rotor tips and shrouding stators, carry DC current between the outer periphery of each rotor and stator surface. A liquid metal in the narrow gap between the rotor tip and concentric stator surface replaces silver graphite brushes to act as a sliding electrical contact. Details of the application for liquid metal homopolar devices have been detailed by Stevens et al. [1]. The ratio of the axial length scale to the radial length scale in the narrow gap region is on the order of 30. Therefore, the central region of the liquid metal sliding electrical contact behaves in a manner similar to that of two infinitely long concentric cylinders. Instability issues of a liquid metal sliding electrical contact involve both that of a rotating inner surface and that of an electrically driven flow. While the instability associated with that of a rotating inner cylinder has been explored, the instability associated with an electrically driven flow has not.

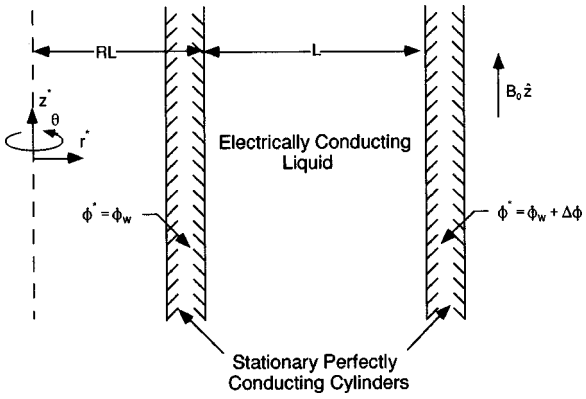

Fig. 1 Schematic of the electrically driven flow problem

Contributed by the Fluids Engineering Division for publication in the JOURNAL OF FLUIDS ENGINEERING. Manuscript received by the Fluids Engineering Division March 6, 2000; revised manuscript received September 7, 2000. Associate Editor: Y. Tsujimoto.

Therefore, before coupling both effects, each should be understood in turn. In this work, only the effect of the electrically driven flow on stability will be considered. As to the magnetic field configuration, a purely axial magnetic field orientation is favored over a skewed magnetic field orientation since there are eddy current losses associated with a radial component of the magnetic field [2].

There are some similarities between our stability problem and the classical Taylor-Couette problem, where a liquid is confined to the radial gap between two concentric, infinitely long, circular cylinders, and a swirling flow is generated by the rotation of one or both cylinders about their centerline. An inviscid linear stability analysis indicates that the Taylor-Couette flow without a magnetic field is stable or unstable for $\alpha>0$ or $\alpha<0$, respectively, where $\alpha=d(r|v_{\theta 0}|)/dr$ is the gradient of the absolute angular momentum per unit mass in the base flow [[3], Chapter 3]. With viscosity, the Taylor-Couette flow is only prone to instability where $\alpha<0$. Taylor [4] distinguished between two cases: (1) corotation with both cylinders rotating in the same direction or one cylinder at rest, so that α is either positive or negative over the entire radial gap, and (2) counter-rotation with the two cylinders rotating in opposite azimuthal directions, so that $\alpha<0$ for $R\leqslant r<r_\alpha$ and $\alpha>0$ for $r_\alpha<r\leqslant(R+1)$. Here, $r=r_\alpha$ when $\alpha=0$. For our base flow, $\alpha>0$ for $R\leqslant r<r_\alpha$, and $\alpha<0$ for $r_\alpha<r\leqslant(R+1)$, where r_α is always slightly larger than $r_{\max}$. Thus our base flow is similar to the Taylor-Couette counter-rotation case in that α has different signs in two parts of the radial gap, but our instability-prone region with $\alpha<0$ is near the outer cylinder, while that for the Taylor-Couette counter-rotation case is near the inner cylinder.

The effects of an externally applied, uniform, steady, axial magnetic field on the Taylor-Couette instability were first considered by Chandrasekhar [5], who used the narrow-gap approximation, i.e., an asymptotic solution for $R\gg1$. The role of the uniform, axial magnetic field in the Taylor-Couette problem is quite different from its role in our problem. For the Taylor-Couette problem, the base-flow azimuthal velocity is entirely independent of an axial magnetic field, while the steady, axisymmetric flow perturbations considered by Chandrasekhar [5] interact with the magnetic field to generate electric current circulations. The Joulean heating associated with the perturbation electric currents augments the viscous dissipation to stabilize the flow. The stabilizing effect of a uniform axial magnetic field on Taylor-Couette flow predicted by Chandrasekhar [5] was verified experimentally by Donnelly and Ozima [6]. For our electromagnetically driven base flow, there is no flow without a magnetic field. As the magnetic field strength is increased, the base-flow velocity increases until the induced electric field becomes comparable to the static electric field.

Weinstein [7] considered the Taylor-Couette problem with a three-dimensional magnetic field which altered the radial variation of the base-flow azimuthal velocity, but we only consider our flow with an axial magnetic field. Chandrasekhar [8] and Roberts [9] showed that a uniform axial magnetic field has a more stabilizing effect in the Taylor-Couette problem when the cylinders are perfect electrical conductors than it does when they are electrical insulators. Chang and Sartory [10] provided a physical explanation of the increased magnetic stabilization with conducting cylinders. Since our cylinders must impose a voltage difference across the liquid and provide the electric current driving the base flow, only perfectly conducting cylinders are considered here.

Roberts [9] considered the Taylor-Couette problem with a finite radial gap, i.e., for a finite value of R. For a stationary outer cylinder with $R=19$, i.e., with the liquid in $19\leqslant r\leqslant20$, his results agreed well with the narrow-gap results of Chandrasekhar [5,8] for $R\gg1$. Soundalgekar et al. [11] treated the Taylor-Couette problem with electrically insulating cylinders, with a uniform axial magnetic field, and with an arbitrary radial gap. Their results show that the effects of changing R depend on the magnetic field strength. For example, for counter-rotation with the angular velocity of the inner cylinder equal to ten times that of the outer cylinder, (1) the Taylor-Couette flow for $R=19$ is more stable than that for $R=0.111$ when the magnetic field strength is below a certain value, and (2) the flow for $R=19$ is less stable than that for $R=0.111$ when the field strength is greater than this value.

With one exception, all the studies mentioned so far only considered axisymmetric perturbations in the linear stability analysis of Taylor-Couette flow with or without a magnetic field. Based on experimental data, Roberts [9] conjectured that for sufficiently strong magnetic fields, the most unstable mode might be nonaxisymmetric, but his numerical results indicated that the most unstable mode was steady and axisymmetric for all cases he considered. Recently, Chen and Chang [12] showed that in certain situations, the most unstable mode is unsteady and nonaxisymmetric for Taylor-Couette flow with an axial magnetic field. For our electrically driven flow, we have considered two types of infinitesimal perturbations to the azimuthal base flow. First, we considered axisymmetric perturbations, i.e., we set the azimuthal wave number equal to zero, and we found the axial wave number for the most unstable mode for each magnetic field strength and radial gap. The most unstable axisymmetric mode was always steady. Second, we considered plane-polar perturbations, i.e., we set the axial wave number equal to zero, and we searched for any azimuthal wave number with an unstable mode. Our motivation for treating plane-polar modes parallels that of Roberts [9]: the azimuthal perturbation vorticity in an axisymmetric mode is strongly damped by an axial magnetic field, while the axial perturbation vorticity in a plane-polar mode acts as a generator on open circuit, i.e., a static electric field develops to cancel the induced electric field due to the perturbation velocity so that there is no electric current and no magnetic damping. Again, paralleling Roberts [9] we found no unstable plane-polar modes short of the shear-flow transition to turbulence.

Richardson [13] presented a linear stability analysis of a swirling flow which is closer to our electromagnetically driven flow than Taylor-Couette flow is. He treated the flow inside a single infinitely long cylinder due to a rotating magnetic field, which is a very weak transverse magnetic field that rotates about the centerline of the cylinder at some constant angular velocity and drives a steady, azimuthal flow whose velocity is much less than the radius times the field's angular velocity. The single cylinder corresponds to $R=0$. Like our base flow, his $v_{\theta 0}$ increases from zero at $r=0$ to a maximum at $r=r_{\max}$ and then decreases back to zero at $r=1$, so that $\alpha>0$ for $0\leqslant r<r_\alpha$ and $\alpha<0$ for $r_\alpha<r\leqslant1$, i.e., the region prone to a Taylor-Couette type instability is close to the periphery of the liquid region. There are two major differences between our problem and that treated by Richardson [13]. First, for his base-flow r_α is very close to one so that the instability prone region represents a very small fraction of the radial gap. For our problem with a narrow gap, the profile is parabolic so that r_α is slightly more than $(R+0.5)$ and nearly half the radial gap is prone to instability, i.e., $r_\alpha=19.502$ for $R=19$ with the liquid in $19\leqslant r\leqslant20$. As the gap width increases relative to the inner cylinder radius, the region with $\alpha<0$ decreases slightly, but remains close to half the gap, i.e., $r_\alpha=1.528$ for $R=1$ with the liquid in $1\leqslant r\leqslant2$. Second, the only role of the magnetic field in Richardson's problem is to produce a steady azimuthal body force which drives the base flow, and there is no magnetic damping of perturbations. As noted earlier for our problem, a significant axial magnetic field is needed to drive the base flow so that there is always magnetic damping of perturbations.

II General Governing Equations and Boundary Conditions

In cylindrical coordinates with no gravitational effects, the dimensionless governing equations are

$$N^{-1}\left(\frac{Dv_r}{Dt}-\frac{v_\theta^2}{r}\right)=-\frac{\partial p}{\partial r}+j_\theta + \mathrm{Ha}^{-2}\left(\nabla^2 v_r-\frac{v_r}{r^2}-\frac{2}{r^2}\frac{dv_\theta}{\partial\theta}\right), \quad (1a)$$

$$N^{-1}\left(\frac{Dv_\theta}{Dt}+\frac{v_r v_\theta}{r}\right)=-\frac{1}{r}\frac{\partial p}{\partial\theta}-j_r + \mathrm{Ha}^{-2}\left(\nabla^2 v_\theta-\frac{v_\theta}{r^2}+\frac{2}{r^2}\frac{\partial v_r}{\partial\theta}\right), \quad (1b)$$

$$N^{-1}\frac{Dv_z}{Dt}=-\frac{\partial p}{\partial z}+\mathrm{Ha}^{-2}\nabla^2 v_z, \quad (1c)$$

$$\frac{\partial v_r}{\partial r}+\frac{v_r}{r}+\frac{1}{r}\frac{\partial v_\theta}{\partial\theta}+\frac{\partial v_z}{\partial z}=0, \quad (1d)$$

$$\frac{\partial j_r}{\partial r}+\frac{j_r}{r}+\frac{1}{r}\frac{\partial j_\theta}{\partial\theta}+\frac{\partial j_z}{\partial z}=0 \quad (1e)$$

$$j_r=-\frac{\partial\phi}{\partial r}+v_\theta, \quad (1f)$$

$$j_\theta=-\frac{1}{r}\frac{\partial\phi}{\partial\theta}-v_r, \quad (1g)$$

and

$$j_z=-\frac{\partial\phi}{\partial z}, \quad (1h)$$

where

$$\frac{D}{Dt}=\frac{\partial}{\partial t}+v_r\frac{\partial}{\partial r}+\frac{v_\theta}{r}\frac{\partial}{\partial\theta}+v_z\frac{\partial}{\partial z}$$

and

$$\nabla^2=\frac{\partial^2}{\partial r^2}+\frac{1}{r}\frac{\partial}{\partial r}+\frac{1}{r^2}\frac{\partial}{\partial\theta}+\frac{\partial^2}{\partial z^2}.$$

Equations (1*a–c*) are the radial, azimuthal, and axial components of the Navier-Stokes equations, respectively. Conservation of mass and charge are given by Eqs. (1*d*, *e*), respectively. Equations (1*f–h*) are the radial, azimuthal, and axial components of Ohm's law for a moving conductor, respectively. The variables v_r, v_θ, and v_z denote the radial, azimuthal, and axial components of the velocity vector, respectively. The pressure is denoted by p, and ϕ is the electric potential function. The electric current density in the radial, azimuthal, and axial directions are j_r, j_θ, and j_z, respectively. Finally, there are two dimensionless parameters: the Hartmann number and the interaction parameter, which are defined as $\mathrm{Ha}=B_0L\sqrt{\sigma/\mu}$ and $N=\sigma B_0^3L^2/\rho(\Delta\phi)$, respectively. Here, ρ is the density of the fluid, μ is its molecular viscosity, σ is the electrical conductivity, $\Delta\phi$ is the electric potential difference across the radial gap, and B_0 is the magnetic flux density. The Hartmann number represents the square root of the ratio of the EMBF to the viscous effects, and the interaction parameter is the ratio of the EMBF to the inertial effects. The nondimensionalizations used to establish Eqs. (1*a–h*) are

$$r^*=Lr,\quad z^*=Lz,\quad t^*=\frac{L^2B_0}{(\Delta\phi)}t,$$

$$\vec{v}^*=\frac{(\Delta\phi)}{LB_0}\vec{v},\quad \vec{J}^*=\frac{\sigma(\Delta\phi)}{L}\vec{J}$$

$$\phi^*=\phi_w+(\Delta\phi)\phi,\quad \text{and}\quad p^*=\sigma(\Delta\phi)B_0p,$$

where an asterisk denotes a dimensional variable. The dimensional electric potential of the inner wall is given by ϕ_w, and L represents the dimensional radial gap width.

The walls of both cylinders are solid, stationary, perfect electric conductors. Therefore, the appropriate boundary conditions with respect to the velocity and the electric potential function are

$$\vec{v}=\phi=0,\ \text{at}\ r=R$$

$$\vec{v}=0,\ \ \phi=1\ \ \text{at}\ \ r=R+1.$$

The governing equations together with the boundary conditions form a well-posed problem with parameters *R*, *N*, and *Ha*.

For a linear stability analysis, we will use the method of normal modes, in which a disturbance is superposed on a base flow solution denoted by the subscript 0. Here, the base flow solution is

$$j_{r0}=\frac{K}{r},$$

$$v_{\theta0}=\mathrm{Ha}^2K\left[\frac{r}{2}\ln r+\left(r-\frac{(R+1)^2}{r}\right)\frac{R^2}{2(2R+1)}\ln(R) -\left(r-\frac{R^2}{r}\right)\frac{(R+1)^2}{2(2R+1)}\ln(R+1)\right],$$

$$p_0=\frac{v_{\theta0}^2}{Nr},$$

$$\phi_0=\mathrm{Ha}^2K\left\{\frac{r^2}{4}\ln r-\frac{R^2}{4}\ln R-\frac{r^2-R^2}{8} +\left[\frac{r^2-R^2}{2}-(R^2+1)^2\ln\left(\frac{r}{R}\right)\right]\frac{R^2}{2(2R+1)}\ln R -\left[\frac{r^2-R^2}{2}-R^2\ln\left(\frac{r}{R}\right)\right]\frac{R^2}{2(2R+1)}\ln(R+1)\right\}-k\ln(r/R),$$

where

$$K^{-1}=\mathrm{Ha}^2\left\{-\frac{2R+1}{8}+\frac{R^2(R+1)^2}{2(2R+1)}\left[\ln\left(\frac{R+1}{R}\right)\right]^2\right\}-\ln\left(\frac{R+1}{R}\right),$$

with $K<0$ for $0<\mathrm{Ha}<\infty$ and $1<(R+1)/R<\infty$, and $v_{r0}=v_{z0}=j_{\theta0}=j_{z0}=0$.

The disturbance is assumed to be of the form,

$$\phi_1(r)e^{[i(n\theta+kz-\lambda t)]}, \quad (2a)$$

$$p_1(r)e^{[i(n\theta+kz-\lambda t)]}, \quad (2b)$$

$$\vec{v}_1(r)e^{[i(n\theta+kz-\lambda t)]}, \quad (2c)$$

$$\vec{J}_1(r)e^{[i(n\theta+kz-\lambda t)]}, \quad (2d)$$

where the amplitude of the disturbance, e.g., $\phi_1(r)$, is complex. The real, integer azimuthal wave number is denoted by n; k is the real axial wave number; and $\lambda=\lambda_r+i\lambda_i$, where λ_r is the circular frequency, and λ_i is the attenuation/amplification factor. If $\lambda_i<0$, then the disturbance will attenuate or decay. If $\lambda_i>0$, then the disturbance will be amplified or grow. And, if $\lambda_i=0$, then the disturbance will oscillate: it will neither decay nor grow.

The linearized disturbance equations are obtained by substituting the base flow variables together with the disturbance variables [Eqs. (2)] into Eqs. (1), subtracting out the base flow equations, and then neglecting any term in which two or more disturbance quantities appear:

$$N^{-1}\left[-i\lambda v_{r1}+\frac{in}{r}v_{\theta0}v_{r1}-\frac{2}{r}v_{\theta0}v_{\theta1}\right]+\frac{dp_1}{dr} =j_{\theta1}+\mathrm{Ha}^{-2}\left[\frac{d^2v_{r1}}{dr^2}+\frac{1}{r}\frac{dv_{r1}}{dt}-\frac{(1+n^2)}{r^2}v_{r1} -k^2v_{r1}-\frac{2in}{r^2}v_{\theta1}\right], \quad (3a)$$

$$N^{-1}\left[-i\lambda v_{\theta 1}+\frac{in}{r}v_{\theta 0}v_{\theta 1}+\left(\frac{dv_{\theta 0}}{dr}+\frac{v_{\theta 0}}{r}\right)v_{r1}\right]+\frac{in}{r}p_1$$
$$=-j_{r1}+\mathrm{Ha}^{-2}\left[\frac{d^2v_{\theta 1}}{dr^2}+\frac{1}{r}\frac{dv_{\theta 1}}{dr}-\frac{(1+n^2)}{r^2}v_{\theta 1}-k^2v_{\theta 1}+\frac{2in}{r^2}v_{r1}\right], \quad (3b)$$

$$N^{-1}\left[-i\lambda v_{z1}+\frac{in}{r}v_{\theta 0}v_{z1}\right]+ikp_1=\mathrm{Ha}^{-2}\left[\frac{d^2v_{z1}}{dr^2}+\frac{1}{r}\frac{dv_{z1}}{dr}-\frac{n^2}{r^2}v_{z1}-k^2v_{z1}\right], \quad (3c)$$

$$\frac{dv_{r1}}{dr}+\frac{v_{r1}}{r}+\frac{in}{r}v_{\theta 1}+ikv_{z1}=0, \quad (3d)$$

$$\frac{dj_{r1}}{dr}+\frac{j_{r1}}{r}+\frac{in}{r}j_{\theta 1}+ikj_{z1}=0, \quad (3e)$$

$$j_{r1}=-\frac{d\phi_1}{dr}+v_{\theta 1}, \quad (3f)$$

$$j_{\theta 1}=-\frac{in}{r}\phi_1-v_{r1}, \quad (3g)$$

$$j_{z1}=-ik\phi_1, \quad (3h)$$

with $v_{r1}=v_{\theta 1}=v_{z1}=j_{r1}=j_{\theta 1}=j_{z1}=\phi_1=0$, at $r=R$ and at $r=R+1$.

Rather than consider the full problem, we will consider the two limit cases. At one extreme is the problem that is closely related to the classical Taylor-Couette instability. With $k>0$ and $n=0$, the disturbance is axisymmetric and toroidal (Taylor) vortices whose axes are aligned with θ appear. This flow will be strongly damped by an axial magnetic field. At the other extreme with $k=0$ and $n>0$, the axes of the vortices are aligned with z, and the disturbance is plane-polar. There is zero EMBF opposing the disturbance modes in this case. As a consequence of the alignment of the vortices either with the azimuthal axis or with the vertical axis, the critical mode will change from $k>0$ and $n=0$ for $\mathrm{Ha}\ll 1$ to $k=0$ and $n>0$ for $\mathrm{Ha}\gg 1$. We will begin by considering the axisymmetric disturbance.

III The Axisymmetric Disturbance: $k>0$ and $n=0$

III.A Analytical Formulation. With $n=0$, the azimuthal variation of the disturbance is zero, so that the disturbance is axisymmetric. Equations (3) reduce to:

$$N^{-1}\left[-i\lambda v_{r1}-\frac{2}{r}v_{\theta 0}v_{\theta 1}\right]=-\frac{dp_1}{dr}+j_{\theta 1}+\mathrm{Ha}^{-2}\left[\frac{d^2v_{r1}}{dr^2}+\frac{1}{r}\frac{dv_{r1}}{dr}-\left(\frac{1}{r^2}+k^2\right)v_{r1}\right], \quad (4a)$$

$$N^{-1}\left[-i\lambda v_{\theta 1}+\left(\frac{dv_{\theta 0}}{dr}+\frac{v_{\theta 0}}{r}\right)v_{r1}\right]=-j_{r1}+\mathrm{Ha}^{-2}\left[\frac{d^2v_{\theta 1}}{dr^2}+\frac{1}{r}\frac{dv_{\theta 1}}{dr}-\left(\frac{1}{r^2}+k^2\right)v_{\theta 1}\right], \quad (4b)$$

$$-i\lambda v_{z1}N^{-1}=kp_1+\mathrm{Ha}^{-2}\left[\frac{d^2v_{z1}}{dr^2}+\frac{1}{r}\frac{dv_{z1}}{dr}-k^2v_{z1}\right], \quad (4c)$$

$$\frac{dv_{r1}}{dr}+\frac{v_{r1}}{r}+ikv_{z1}=0, \quad (4d)$$

$$\frac{dj_{r1}}{dr}+\frac{j_{r1}}{r}+ikj_{z1}=0, \quad (4e)$$

$$j_{r1}=-\frac{d\phi_1}{dr}+v_{\theta 1}, \quad (4f)$$

$$j_{\theta 1}=-v_{r1}, \quad (4g)$$

$$j_{z1}=-ik\phi_1, \quad (4h)$$

with

$$v_{r1}=v_{\theta 1}=v_{z1}=0 \text{ at } r=R \quad (5a)$$

$$j_{r1}=j_{\theta 1}=j_{z1}=\phi_1=0 \text{ at } r=R \quad (5b)$$

$$v_{r1}=v_{\theta 1}=v_{z1}=0 \text{ at } r=R+1 \quad (5c)$$

$$j_{r1}=j_{\theta 1}=j_{z1}=\phi_1=0 \text{ at } r=R+1. \quad (5d)$$

From Eq. (4*g*) we see that the azimuthal electric current density $j_{\theta 1}$, due to the induced electric field, produces an EMBF that opposes the radial component of the disturbance velocity v_{r1}, and results in damping of the disturbance. The system of equations given by Eqs. (4*a–h*) can be further reduced to two unknowns, $v_{r1}(r)$ and $j_{r1}(r)$, as follows. From Eqs. (4*d*, *e*), v_{z1} and j_{z1} can be written in terms of v_{r1} and j_{r1}, respectively:

$$v_{z1}=\frac{i}{k}\left[\frac{dv_{r1}}{dr}+\frac{v_{r1}}{r}\right] \quad (6a)$$

and

$$j_{z1}=\frac{i}{k}\left[\frac{dj_{r1}}{dr}+\frac{j_{r1}}{r}\right]. \quad (6b)$$

To relate ϕ_1 to j_{r1}, introduce Eq. (4*h*) into Eq. (6*b*):

$$\phi_1=-\frac{1}{k^2}\left[\frac{dj_{r1}}{dr}+\frac{j_{r1}}{r}\right]. \quad (7)$$

By substituting Eq. (7) into Eq. (4*f*) a relation between $v_{\theta 1}$ and j_{r1} is established,

$$v_{\theta 1}=j_{r1}-\frac{1}{k^2}\left[\frac{d^2j_{r1}}{dr^2}+\frac{1}{r}\frac{dj_{r1}}{dr}-\frac{j_{r1}}{r^2}\right]. \quad (8)$$

If v_{z1} is replaced in Eq. (4*c*) by $i/k[dv_{r1}/dr+v_{r1}/r]$ from Eq. (6*a*), then p_1 is known in terms of v_{r1}:

$$p_1=\frac{\mathrm{Ha}^{-2}}{k^2}\left[\frac{d^3v_{r1}}{dr^3}+\frac{2}{r}\frac{d^2v_{r1}}{dr^2}-\left(\frac{1}{r^2}+k^2\right)\frac{dv_{r1}}{dr}+\left(\frac{1}{r^3}-\frac{k^2}{r}\right)v_{r1}\right]+\frac{i\lambda}{k^2}N^{-1}\left[\frac{dv_{r1}}{dr}+\frac{1}{r}v_{r1}\right]. \quad (9)$$

The governing equation for v_{r1} is established by substituting Eqs. (4*g*), (8), and (9) into Eq. (4*a*):

$$-i\lambda\,\mathrm{Re}\left[\frac{d^2v_{r1}}{dr^2}+\frac{1}{r}\frac{dv_{r1}}{dr}-\left(k^2+\frac{1}{r^2}\right)v_{r1}\right]=\frac{d^4v_{r1}}{dr^4}+\frac{2}{r}\frac{d^3v_{r1}}{dr^3}-\left(2k^2+\frac{3}{r^2}\right)\frac{d^2v_{r1}}{dr^2}-\left(2k^2-\frac{3}{r^2}\right)\frac{dv_{r1}}{dr}+\left(k^4+\mathrm{Ha}^2k^2+\frac{2k^2}{r^2}-\frac{3}{r^4}\right)v_{r1}+\frac{2}{r}\mathrm{Re}\,v_{\theta 0}\left[\frac{d^2j_{r1}}{dr^2}+\frac{1}{r}\frac{dj_{r1}}{dr}-\left(k^2+\frac{1}{r^2}\right)j_{r1}\right], \quad (10)$$

with

$$v_{r1}=0 \quad \text{at} \quad r=R \quad \text{and at} \quad r=R+1. \tag{11a}$$

$$\frac{dv_{r1}}{dr}=0 \quad \text{at} \quad r=R \quad \text{and at} \quad r=R+1. \tag{11b}$$

Here, $\mathrm{Re}=\mathrm{Ha}^2/N=\rho\Delta\phi/\mu B_0$. The second boundary condition, Eq. (11*b*), comes from the continuity equation [Eq. (4*d*)] with $v_{z1}=0$ at $r=R$ and at $r=R+1$.

To obtain a governing equation for j_{r1}, substitute Eq. (8) into Eq. (4*b*) to replace $v_{\theta 1}$ with terms involving j_{r1}:

$$\begin{aligned}-i\lambda\,\mathrm{Re}&\left[\frac{d^2j_{r1}}{dr^2}+\frac{1}{r}\frac{dj_{r1}}{dr}-\left(k^2+\frac{1}{r^2}\right)j_{r1}\right]\\&=\frac{d^4j_{r1}}{dr^4}+\frac{2}{r}\frac{d^3j_{r1}}{dr^3}-\left(2k^2+\frac{3}{r^2}\right)\frac{d^2j_{r1}}{dr^2}\\&\quad-\left(2k^2-\frac{3}{r^2}\right)\frac{1}{r}\frac{dj_{r1}}{dr}+\left(k^4+\mathrm{Ha}^2k^2+\frac{2k^2}{r^2}-\frac{3}{r^4}\right)j_{r1}\\&\quad+\mathrm{Re}\,k^2\left[\frac{dv_{\theta 0}}{dr}+\frac{v_{\theta 0}}{r}\right]v_{r1}.\end{aligned} \tag{12}$$

From conservation of charge, Eq. (4*e*),

$$\frac{dj_{r1}}{dr}+\frac{j_{r1}}{r}=0, \quad \text{at} \quad r=R \quad \text{and at} \quad r=R+1. \tag{13a}$$

A second boundary condition for the radial disturbance electric current density component can be found through Eq. (8), with $v_{\theta 1}=0$ at $r=R$ and at $r=R+1$:

$$\frac{d^2j_{r1}}{d^2r}+\frac{1}{r}\frac{dj_{r1}}{dr}-\left(k^2+\frac{1}{r^2}\right)j_{r1}=0.$$

A more compact form of this boundary condition is found by adding and subtracting the term j_{r1}/r^2 to the above equation, then applying Eq. (13*a*) to obtain:

$$\frac{d^2j_{r1}}{dr^2}-\left(k^2+\frac{2}{r^2}\right)j_{r1}=0, \quad \text{at} \quad r=R \quad \text{and at} \quad r=R+1. \tag{13b}$$

III.B Numerical Formulation. Equations (10) and (12) together with the boundary conditions [Eqs. (11) and (13)] form an eigenvalue problem whose parameters are: R, which is a measure of the gap width; k, the axial wave number; Re, the Reynolds number; and Ha, the Hartmann number. (Note that when R is large, the gap width is narrow.) To establish the neutral stability curve, choose values for R, k, and Ha, then determine Re such that the imaginary portion of the eigenvalue, λ_i, is zero. To this end, a collocation technique is used in which the unknowns are represented by Chebyshev polynomials [[14], pp. 65–70]. Since the Chebyshev polynomials are defined on the interval from -1 to $+1$, the radial coordinate r will be redefined as:

$$\zeta=2r-(2R+1)$$

such that ζ is between ± 1 when $r=R$ and $R+1$, respectively. This coordinate transformation is applied to Eqs. (10–13). Both the disturbance velocity v_{r1} and the disturbance electric current density j_{r1} are now represented by Chebyshev polynomials which are functions of ζ,

$$v_{r1}(\zeta)=\sum_{s=0}^{S+2} a_sT_s(\zeta) \quad \text{and} \quad j_{r1}(\zeta)=\sum_{s=0}^{S+2} b_sT_s(\zeta)$$

where a_s and b_s are unknown coefficients, $T_s(\zeta)$ denotes a Chebyshev polynomial of order s,

$$T_s(\zeta)=\cos[s\arccos(\zeta)], \quad \text{with} \quad 0\leqslant\arccos(\zeta)\leqslant\pi,$$

and $(S+2)$ represents the highest-order polynomial. The series representation is substituted into the transformed version of Eqs. (10), (13) and the boundary conditions to obtain:

$$-i\lambda\,\mathrm{Re}\sum_{s=0}^{S+2} Q2_{s,j}a_s=\sum_{s=0}^{S+2} Q4_{s,j}a_s+\frac{2}{r}\mathrm{Re}\,v_{\theta 0}(r_j)\sum_{s=0}^{S+2} Q2_{s,j}b_s \tag{14a}$$

$$-i\lambda\,\mathrm{Re}\sum_{s=0}^{S+2} Q2_{s,j}b_s=\sum_{s=0}^{S+2} Q4_{s,j}b_s+\frac{\mathrm{Re}\,k^2}{r_j}\frac{d[r_jv_{\theta 0}(r_j)]}{dr}\sum_{s=0}^{S+2} T_s(\zeta_j)a_s \tag{14b}$$

$$\sum_{\substack{s=0\\ s\ \text{even}}}^{S+2} a_s=0 \tag{14c}$$

$$\sum_{\substack{s=1\\ s\ \text{odd}}}^{S+1} a_s=0 \tag{14d}$$

$$\sum_{\substack{s=0\\ s\ \text{even}}}^{S+2} s^2a_s=0 \tag{14e}$$

$$\sum_{\substack{s=1\\ s\ \text{odd}}}^{S+1} s^2a_s=0 \tag{14f}$$

$$\sum_{s=0}^{S+2} b_s\left[\frac{2s^2}{(a-1)}+\frac{1}{a}\right]=0 \tag{14g}$$

$$\sum_{s=0}^{S+2} (-1)^sb_s\left[\frac{2s^2}{(a-1)}-1\right]=0 \tag{14h}$$

$$\sum_{s=0}^{S+2} b_s\left[\frac{4s^2(s^2-1)}{3(a-1)}-k^2-\frac{2}{a}\right]=0 \tag{14i}$$

$$\sum_{s=0}^{S+2} (-1)^sb_s\left[\frac{4s^2(s^2-1)}{3(a-1)}-k^2-2\right]=0 \tag{14j}$$

where

$$Q2_{s,j}=\frac{4}{(a-1)^2}T_s''(\zeta_j)+\frac{2}{(a-1)r_j}T_s'(\zeta_j)-\left(k^2+\frac{1}{r_j^2}\right)T_s(\zeta_j),$$

$$\begin{aligned}Q4_{s,j}&=\frac{16}{(a-1)^4}T_s^{iv}(\zeta_j)+\frac{16}{(a-1)^3r_j}T_s'''(\zeta_j)\\&\quad-\frac{4}{(a-1)^2}\left(2k^2+\frac{3}{r_j^2}\right)T_s''(\zeta_j)+\frac{2}{(a-1)}\\&\quad+\left(2k^2-\frac{3}{r_j^2}\right)T_s'(\zeta_j)+\left(k^4+\mathrm{Ha}^2k^2+\frac{2k^2}{r_j^2}-\frac{3}{r_j^4}\right)T_s(\zeta_j),\end{aligned}$$

and $j=1,2,\cdots,(S-1)$ are associated with the collocation points. Equations (14*a*,*b*) must be satisfied at the $(S-1)$ collocation points, which are given by $\zeta_j=\cos(j\pi/S)$, $j=1,2,\cdots,(S-1)$. For a given R and Ha this system of equations, Eqs. (14*a–j*), is solved through the MSIMSL subroutine DGVLCG to determine when λ_i is zero, at which point the flow is neutrally stable. The results presented here are with $S=26$.

An alternative solution technique was used to check the results from the eigenvalue solver. Here, the system of equations, Eqs. (10–13), was solved with a collocation method in conjunction with a Crank-Nicolson technique to determine whether the solu-

tion attenuates or amplifies with time. This technique is described by Morthland and Walker [15]. Unlike the previous approach, any disturbance $q_1(r)e^{-i\lambda t}$ is replaced by $q_1(r,t)$, and the coefficients in the Chebyshev polynomial representation are functions of time:

$$v_{r1}(\zeta,t)=\sum_{s=0}^{S+2} a_s(t)T_s(\zeta) \quad \text{and} \quad j_{r1}(\zeta,t)=\sum_{s=0}^{S+2} b_s(t)T_s(\zeta).$$

Therefore, $\partial v_{r1}(\zeta,t)/\partial t=\sum_{s=0}^{S+2}[(a_s^m-a_s^{m-1})/\Delta t]T_s(\zeta)$, where $a_s^m=a_s(t_m)$ at the current time step t_m and $a_s^{m-1}=a_s(t_m-\Delta t)$ is at the previous time step. The governing equations [Eqs. (10) and (12)] and boundary conditions, when the Crank-Nicolson technique is applied, can be written as:

$$\sum_{s=0}^{S+2} a_s^m\left[Q2_{s,j}-\frac{\Delta t}{2\,\mathrm{Re}}Q4_{s,j}\right]+\sum_{s=0}^{S+2} b_s^m\left[-\frac{\Delta t}{r_j}v_{\theta 0}(r_j)Q2_{2,j}\right]$$
$$=\sum_{s=0}^{S+2} a_s^{m-1}\left[Q2_{s,j}+\frac{\Delta t}{2\,\mathrm{Re}}Q4_{s,j}\right]$$
$$+\sum_{s=0}^{S+2} b_s^{m-1}\left[\frac{\Delta t}{r_j}v_{\theta 0}(r_j)Q2_{s,j}\right]$$

$$\sum_{s=0}^{S+2} a_s^m\left\{-\frac{\Delta t}{2}\frac{k^2}{r_j}\frac{d[r_j v_{\theta 0}(r_j)]}{dr}T_s(\zeta_j)\right\}$$
$$+\sum_{s=0}^{S+2} b_s^m\left[Q2_{s,j}-\frac{\Delta t}{2\,\mathrm{Re}}Q4_{s,j}\right]$$
$$=\sum_{s=0}^{S+2} a_s^{m-1}\left\{\frac{\Delta t}{2}\frac{k^2}{r_j}\frac{d[r_j v_{\theta 0}(r_j)]}{dr}T_s(\zeta_j)\right\}$$
$$+\sum_{s=0}^{S+2} b_s^{m-1}\left[Q2_{s,j}+\frac{\Delta t}{2\,\mathrm{Re}}Q4_{s,j}\right]$$

$$\sum_{\substack{s=0\\ s\ \text{even}}}^{S+2} a_s^m=\sum_{\substack{s=1\\ s\ \text{odd}}}^{S+1} a_s^m=\sum_{\substack{s=0\\ s\ \text{even}}}^{S+2} s^2a_s^m=\sum_{\substack{s=1\\ s\ \text{odd}}}^{S+1} s^2a_s^m=0,$$

$$\sum_{s=0}^{S+2} b_s^m\left[\frac{2s^2}{(a-1)}+\frac{1}{a}\right]=\sum_{s=0}^{S+2}(-1)^s b_s^m\left[\frac{2s^2}{(a-1)}-1\right]$$
$$=\sum_{s=0}^{S+2} b_s^m\left[\frac{4s^2(s^2-1)}{3(a-1)}-k^2-\frac{2}{a}\right]$$
$$=\sum_{s=0}^{S+2}(-1)^s b_s^m\left[\frac{4s^2(s^2-1)}{3(a-1)}-k^2-2\right]=0.$$

The coefficients a_s^m and b_s^m are to be determined. For small Hartmann numbers, the time step was set to $\Delta t=0.1$, with larger steps possibly resulting in immediate divergence of the solution, and smaller steps converging to the same results as $\Delta t=0.1$. For large Hartmann numbers, however, the time step must be smaller, varying as $O(Ha^{-2})$. As time increases, the coefficients initially increase in value, then decrease if the base flow is stable for a particular disturbance. Otherwise, the coefficients continue to increase. In either case, there is no evidence that any of the coefficients oscillate with time. The largest coefficient appeared to be a_2. Therefore, to determine whether a particular set of parameters leads to an instability, an amplification-attenuation factor, G, is defined: $G=a_2^{200}/a_2^{175}$. Results using other definitions, such as $G=a_2^{400}/a_2^{350}$, did not produce significantly different results. If $G<1$, then the solution decays, indicating that for that particular set of parameters, the results are stable. If $G>1$, the flow is unstable. There were no significant differences for S approximately between 20 and 30, depending on the parameters. However, for S greater than approximately 45, the results were not reliable.

Both the eigenvalue technique and the Crank-Nicolson solution were in good agreement.

III.C Axisymmetric Results and Discussion. Before presenting the results for the problem described by Eqs. (10–13), consider the inviscid case. As noted in the introduction, if viscous effects are neglected in Eqs. (10) and (13), then stability hinges on the sign of the gradient of the absolute angular momentum per unit mass, $\alpha=d(r|v_{\theta 0}|)/dr$ [3]. If α is negative, then the flow is unstable. This is indeed the case here, where for any given value of R and Ha, there is a region in the flow field for which α is negative. This region of instability occurs nearer the outer cylinder at $r=R+1$ rather than the inner one at $r=R$.

One may anticipate that α will play a role in the stability of the viscous flow as well. Therefore, it is necessary to consider both $v_{\theta 0}$ and α. If $v_{\theta 0}$ and α are normalized with respect to $v_{\theta 0_{\max}}$, the maximum base flow azimuthal velocity, and the radial coordinate is normalized by $R+1$, then for a given value of R all plots collapse onto each other regardless of Ha, as shown in Figs. 2 (*a*, *b*) for $R=4.0$ and 0.25. As R is decreased, the radial gap width increases, and the radial electric current is more concentrated at the inner radius than at the outer one, so that there is a larger azimuthal body force near the inner cylinder. As seen in Figs. 2 (*a*, *b*), this skews the parabolic profile so that $v_{\theta 0_{\max}}$ moves toward the inner cylinder resulting in a decrease of $(r_{\max}-R)$ and an increase of $(r_\alpha-R)$. Here, $r_{\max}=4.481$ for $R=4.0$, and $r_{\max}=0.637$ for $R=0.25$. And, $\alpha=0$ when

$$r=r_\alpha=\exp\left[\frac{R^2}{2R+1}\ln\left(\frac{R+1}{R}\right)+\ln(R+1)-\frac{1}{2}\right],$$

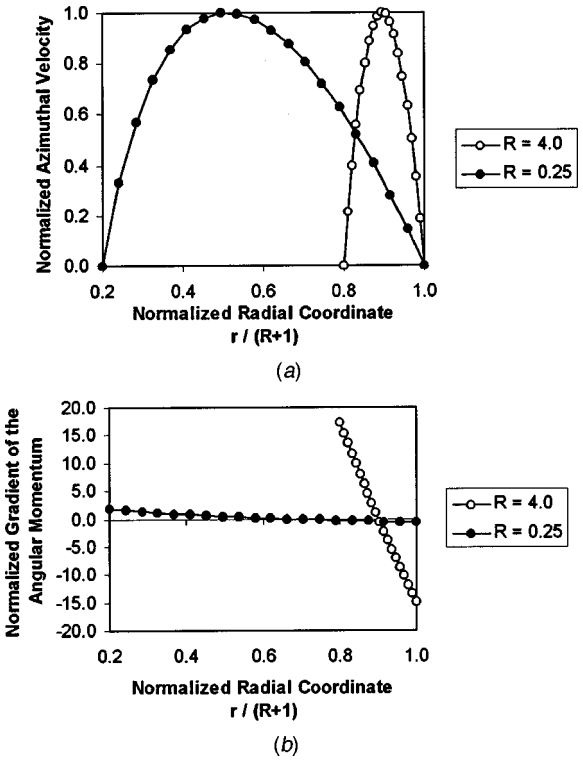

Fig. 2 (*a*) Normalized base flow azimuthal velocity versus the normalized radial coordinate; (*b*) normalized gradient of the base flow angular momentum versus the normalized radial coordinate

Table 1 The maximum base flow azimuthal velocity with $r_{max}=4.481$ when $R=4.0$ and $r_{max}=0.637$ when $R=0.25$

R	4.0	0.25
Ha	$v_{\theta 0max}$	$v_{\theta 0max}$
3.162	0.680	0.582
10.0	1.338	1.290
31.62	1.482	1.468

Table 2 The critical wave number and critical Reynolds number for given Ha and R

R	4.0		0.25	
Ha Hartmann Number	k	Re	k	Re
3.162	16.775	212.66	1.156	171.21
10.0	18.367	210.61	1.249	139.01
31.62	14.632	922.60	1.055	580.19

which for $R=4.0$ occurs at $r\cong 4.51$ and for $R=0.25$ at $r\cong 0.811$. Therefore, assuming that $\alpha<0$ is a necessary condition for instability, the unstable region for $R=4.0$ is approximately 49 percent of the entire flow domain, and when $R=0.25$, approximately 44 percent of the flow domain is sensitive to infinitesimal axisymmetric disturbances. Consequently, a slightly larger portion of the flow domain should be unstable for $R=4.0$ than for $R=0.25$. Note that with $R=4.0$ the gap width is narrower than when $R=0.25$.

The maximum base flow azimuthal velocity is presented in Table 1. Two trends are apparent from Table 1: (1) as Ha increases, $v_{\theta 0_{max}}$ increases for both $R=4.0$ and $R=0.25$ towards a maximum of approximately 1.50 and 1.49, respectively; and (2) for a given Ha, $v_{\theta 0_{max}}$ is larger for $R=4.0$ than for $R=0.25$. Regarding the first trend, Ha can be viewed as a measure of the strength of the magnetic field. As Ha increases, the base-flow velocity increases until the induced electric field becomes comparable to the static electric field. Beyond this Ha the maximum velocity does not change. The second trend can be understood by considering two capacitor plates separating a material with a known resistivity. For a given voltage difference across the plates, as the gap between the plates increases, the resistance increases, and the net current decreases. The same is true here. For a given $\Delta\phi$ the radial current decreases as R decreases, the radial gap widens leading to a reduced EMBF and a smaller maximum velocity.

For small Ha, one typical neutral stability curve is shown in Fig. 3 for $R=4.0$ and Ha=0.025. This figure is reminiscent of the neutral stability curves found in the Benard-Rayleigh problem. The disturbance attenuates when (k,Re) values lie to the left of the neutral stability curve, indicating that the base flow is stable with respect to that particular disturbance. The base flow is unstable with respect to a given disturbance when (k,Re) values lie to the right of the neutral stability curve. Table 2 lists the critical wave number, k_{cr}, and the critical Reynolds number, Re_{cr}, for $R=4.0$ and 0.25 with Ha=3.162, 10.0, and 31.62. (These values of Ha correspond to $Q=\mathrm{Ha}^2=10$, 100, and 1000, which is often the parameter used in the literature.) The critical wave number, k_{cr}, initially increases as Ha increases, then decreases. An increase in k_{cr} corresponds to a decrease in the wave length of the disturbance. The behavior of k_{cr} with ln(Ha) is illustrated in Fig. 4 for $R=4.0$. Here, k is essentially constant until Ha≈1, then increases linearly until Ha≅28.75, at which point k decreases as Ha increases. The relationship between k_{cr} and Ha is similar for $R=0.25$. To better understand why k_{cr} behaves in this manner, consider Figs. 5–7 with $R=4.0$ and Ha=28.5, 28.75, and 29. In these figures, we observe that there are two competing wave numbers, with the base flow being more sensitive to the wave number at the smaller Re. This is a bifurcation: with Ha below some value, here that value is approximately 28.75, the base flow is more sensitive to infinitesimal axisymmetric disturbances at larger wave numbers (or shorter wave lengths), and for Ha above some value, the base flow is more sensitive to disturbances at smaller wave numbers (or larger wave lengths). At this point, we are not able to explain why this is so.

For a different perspective, consider the effective Reynolds number, $\mathrm{Re}^*=v^*_{\theta 0_{max}}L/\nu=v_{\theta 0_{max}}\mathrm{Re}$. From Table 3 we observe that as Ha increases, Re* also increases, indicating that the base flow becomes less sensitive to infinitesimal axisymmetric disturbances as the magnetic-field strength increases. Furthermore, it becomes clear that for the narrower radial gap, $R=4.0$, the base flow is more stable than with the wider radial gap, $R=0.25$. This suggests that the effect of the walls is to stabilize the flow.

Next, consider the stream lines for $R=0.25$ with Ha=3.162 and 31.62. Both the abscissa and the ordinate have been rescaled, with the abscissa being $\xi=r-R$, and the ordinate being $2\pi z/k_{cr}$.

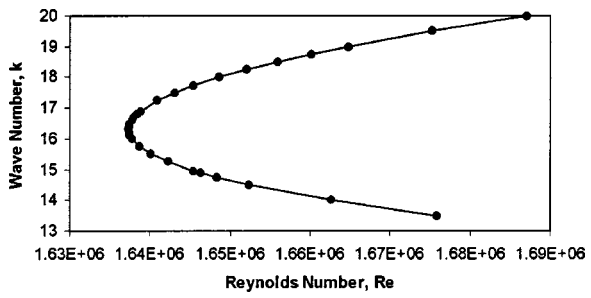

Fig. 3 Neutral stability curve for Ha=0.025 and $R=4.0$

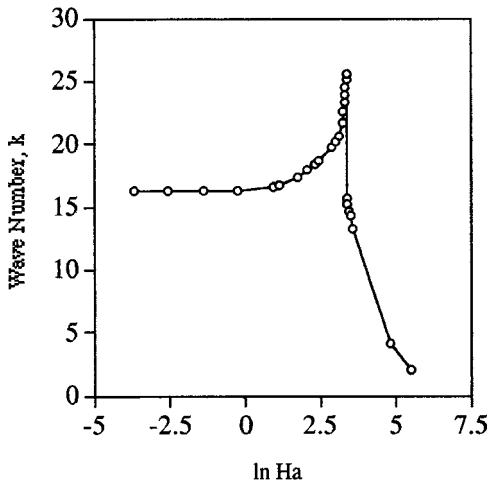

Fig. 4 Wave number as a function of ln (Ha) for $R=4.0$

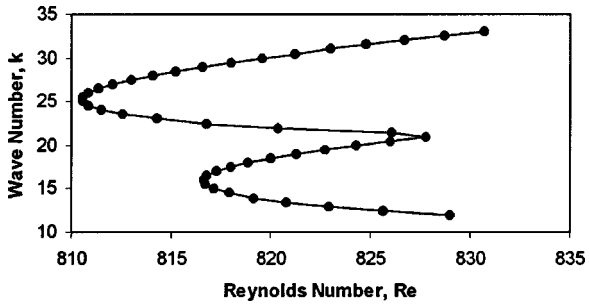

Fig. 5 Neutral stability curve for Ha=28.5 and $R=4.0$

Therefore, at the inner cylinder, when $r=R$, $\xi=0$; and at the outer cylinder, when $r=R+1$, $\xi=1$. Here, the critical wavelength is related to the critical wave number: $\lambda_{cr}=2\pi/k_{cr}$. Therefore, with $R=0.25$, $\lambda_{cr}=5.435$ and $\lambda_{cr}=5.956$ for Ha=3.162 and 31.62, respectively. In Fig. 8, we observe that the meridional flow forms into horizontal nodal planes. Between each pair of nodal planes, there is a strong clockwise (or counterclockwise) circulation near the outer cylinder and a much weaker counterclockwise (or clockwise) circulation near the inner cylinder. Between the adjacent pair of nodal planes, the circulations are opposite: if a strong counterclockwise cell occurs near the outer cylinder, then in the adjacent nodal plane, there will be a strong clockwise cell near the outer cylinder. Taylor [[4], p. 327] made note of these cells, attributing them to the fact that the surface along which the velocity was zero separated the radial gap into two regions. However, he was quick to point out that the edges of these cells did not meet at the zero velocity surface. In our case, there is no zero velocity surface within the radial gap. However, there is a surface along which α is zero. From Fig. 8, it is apparent that the edge of the cells do not meet at the $\alpha=0$ surface. For small Ha, the circulation near the outer cylinder extends over a large portion of the radial domain and is much stronger than that near inner cylinder. Further evidence of this is seen in the real and imaginary components of the amplitude of the radial component of the disturbance velocity, $v_{r1}(r)$, Fig. 9. The imaginary part of v_{r1} is essentially zero when Ha=3.162. The real part of v_{r1} illustrates that there are two cells,

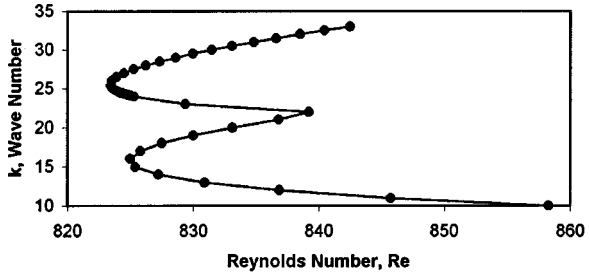

Fig. 6 Neutral stability curve for Ha=28.75 and $R=4.0$

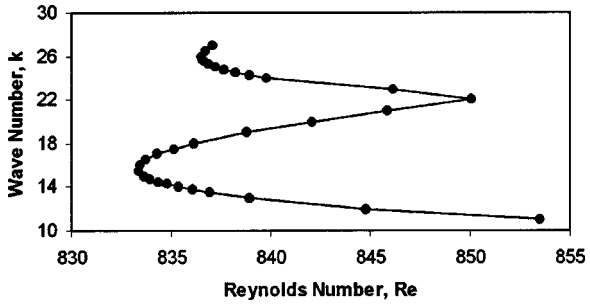

Fig. 7 Neutral stability curve for Ha=29 and $R=4.0$

Table 3 The critical wave number and effective Reynolds number, $Re^*=v^*_{\theta 0_{max}}L/\nu$, for given Ha and R

R	4.0		0.25	
Ha Hartmann Number	k	Re^*	k	Re^*
3.162	16.775	144.53	1.156	99.69
10.0	18.367	281.87	1.249	179.27
31.62	14.632	1367.30	1.055	851.76

the stronger of the cells, near the outer cylinder, extends over a larger portion of the radial domain. As Ha increases, the radial extent of the cell near the outer cylinder decreases, and the inner cells increase in both radial extent and magnitude. The axial extent of the cells initially decreases with Ha, then increases after bifurcation. After bifurcation, the cells become distorted, Fig. 10. The strong clockwise (or counterclockwise) outer circulation between one pair of nodal planes connects with the weaker clock-

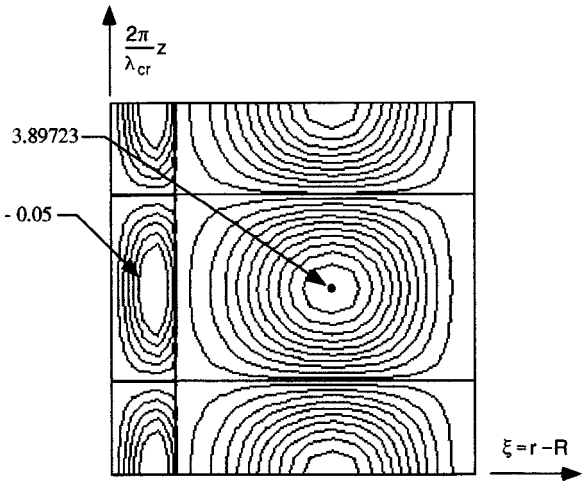

Fig. 8 Stream lines for Ha=3.162 and $R=0.25$. The contour interval for the right cell is 0.37, with the maximum occurring at the center of the cell. The contour interval for the left cell is 0.1, with the absolute maximum value occurring at the center of the cell.

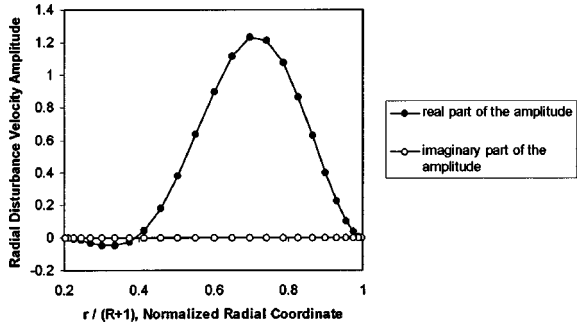

Fig. 9 Amplitude of the radial disturbance velocity as a function of the normalized radial coordinate for Ha=3.162 and $R=0.25$

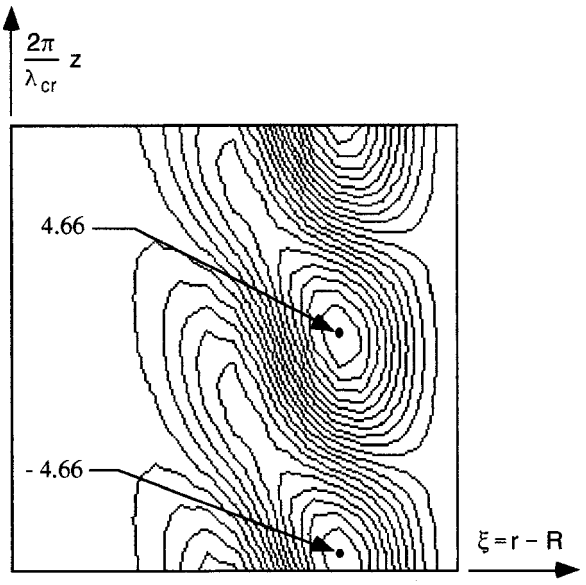

Fig. 10 Stream lines for Ha=31.62 and $R=0.25$. The contour interval is 0.44.

wise (counterclockwise) inner circulation from the adjacent nodal plane. Therefore, the circulations cross the original nodal planes, creating a new nodal surface which is neither horizontal nor vertical. This behavior is reflected in the real and imaginary parts of v_{r1}, where the imaginary part is now substantial and out of phase with the real part of v_{r1}, Fig. 11. The results presented in Figs. 8–11 illustrate the bifurcation: the nodal surfaces undergo a transition from horizontal to skewed for Ha above a critical value.

A very similar pattern is seen when $R=4.0$. However, for Ha $=3.162$ the meridional flow consists of one cell which fills the entire radial gap (not shown here). Therefore, a larger portion of the flow domain is unstable when $R=4.0$ than when $R=0.25$, as anticipated when we considered the influence of α. As Ha increases and the cell near $r=R+1$ contracts radially, a second, weaker cell forms near the inner cylinder. Its circulation is opposite to that of the main cell at the outer cylinder. Here, too, the horizontal nodal surfaces are skewed upon bifurcation.

To summarize these results, the disturbances arise near the outer cylinder, where the flow is most unstable. These disturbances then spread radially inwards toward the inner cylinder. However, as Ha increases, the EMBF opposes the radial spread of the disturbances, so that their radial extent decreases. This stabilizing effect of the magnetic field is also seen through Re*, which increases with Ha. In addition, the flow with $R=4.0$, a narrower gap, is more stable to infinitesimal axisymmetric disturbances

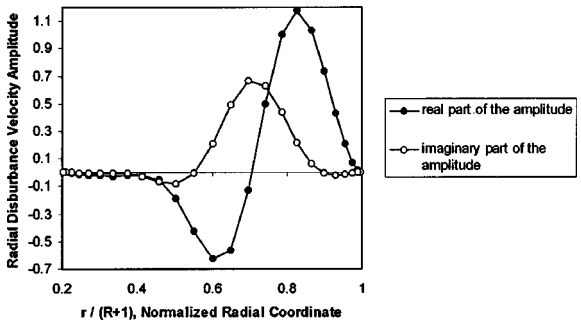

Fig. 11 Amplitude of the radial disturbance velocity as a function of the normalized radial coordinate for Ha=31.62 and $R=0.25$

than the flow with $R=0.25$, a wider gap. Finally, we observed a bifurcation in which the nodal pattern changes from horizontal to skewed.

IV Plane-Polar Instability: $k=0$ and n>0

In this case, the variation is in the azimuthal direction. Therefore, should an instability exist, the disturbance vortices would have their axes aligned with the z axis. Here, we only consider Ha$\gg$1, and the base flow azimuthal velocity is independent of Ha:

$$v_{\theta 0}=\hat{K}\left[\frac{r}{2}\ln r+\left(r-\frac{(R+1)^2}{r}\right)\frac{R^2}{2(2R+1)}\ln(R)-\left(r-\frac{R^2}{r}\right)\frac{(R+1)^2}{2(2R+1)}\ln(R+1)\right], \tag{15}$$

where $\hat{K}^{-1}=-(2R+1)/8+[R^2(R+1)^2/2(2R+1)][\ln(R+1/R)]^2$. The disturbance electric current density vector is zero, as is the axial component of the disturbance velocity: $j_{r1}=j_{\theta 1}=j_{z1}=v_{z1}=0$. Equations (3) can reduced to a single equation in terms of one unknown, v_{r1}. The disturbance quantities, $v_{\theta 1}$ and p_1, then can be determined from Eqs. (3*d*) and (3*b*), respectively.

To understand these statements, observe that from Eq. (3*h*), with $k=0$, $j_{z1}=0$. The azimuthal component of Ohm's law, Eq. (3*g*), can be written as

$$\phi_1=\frac{ir}{n}(j_{\theta 1}+v_{r1}). \tag{16}$$

Take the first derivative of Eq. (16) with respect to r and substitute the result into Eq. (3*f*) to obtain

$$j_{r1}=-\frac{i}{n}\left(r\frac{dj_{\theta 1}}{dr}+j_{\theta 1}\right), \tag{17}$$

where the velocity components have been eliminated through the use of Eq. (3*d*). To generate an equation in terms of $j_{\theta 1}$, Eq. (17) is substituted into Eq. (3*e*) to obtain,

$$r^2\frac{d^2j_{\theta 1}}{dr^2}+3r\frac{dj_{\theta 1}}{dr}+(1-n^2)j_{\theta 1}=0,$$

or $j_{\theta 1}=c_1r^{(1+n)}+c_2r^{(1-n)}$, where c_1 and c_2 are constants to be determined by the boundary conditions. When the boundary conditions are applied, $j_{\theta 1}=0$ at $r=R$ and $r=R+1$, both constants are zero, and $j_{\theta 1}=0$ everywhere. With $j_{\theta 1}=0$, Eq. (3*e*) simplifies to $(1/r)d(rj_{r1})/dr=0$, which, after the boundary conditions are applied, indicates that $j_{r1}=0$ everywhere. Therefore, with $j_{r1}=j_{\theta 1}=j_{z1}=0$, there is no EMBF in the disturbance equations.

As a consequence, Eq. (3*c*) has only one unknown, v_{z1}, which appears in each term. That equation is homogeneous as are the boundary conditions. Therefore, the axial component of the disturbance velocity is zero. From continuity, Eq. (3*d*),

$$v_{\theta 1}=\frac{i}{n}\left(r\frac{dv_{r1}}{dr}+v_{r1}\right). \tag{18}$$

If Eq. (18) is substituted into Eq. (3*b*), then a relation for p_1 in terms of $v_{\theta 0}$ and v_{r1} is obtained:

$$\mathrm{Ha}^2p_1=n^{-2}\left[r^2\frac{d^3v_{r1}}{dr^3}+4r\frac{d^2v_{r1}}{dr^2}+(1-n^2)\frac{dv_{r1}}{dr}-(1-n^2)\frac{v_{r1}}{r}\right]+\frac{i\,\mathrm{Re}}{n^2}\left[(\lambda r^2-nv_{\theta 0})\frac{dv_{r1}}{dr}+\left(\lambda r+nr\frac{dv_{\theta 0}}{dr}\right)v_{r1}\right] \tag{19}$$

With Eq. (19) and the continuity equation applied to Eq. (3*a*), the governing equation for v_{r1} is established:

$$
\begin{aligned}
i\,\mathrm{Re}\Bigg\{ & r(\lambda r - n v_{\theta 0})\frac{d^2 v_{r1}}{dr^2} + 3(\lambda r - n v_{\theta 0})\frac{dv_{r1}}{dr} \\
& + \left[\lambda(1-n^2) + \frac{n}{r}(n^2-2)v_{\theta 0} + n\frac{dv_{\theta 0}}{dr} + nr\frac{d^2 v_{\theta 0}}{dr^2}\right] v_{r1}\Bigg\} \\
& + r^2\frac{d^4 v_{r1}}{dr^4} + 6r\frac{d^3 v_{r1}}{dr^3} + (5-2n^2)\frac{d^2 v_{r1}}{dr^2} \\
& - \frac{(1+2n^2)}{r}\frac{dv_{r1}}{dr} + \frac{(1-n^2)^2}{r^2} v_{r1} = 0
\end{aligned} \tag{20}
$$

with $v_{r1} = dv_{r1}/dr = 0$, at $r = R$ and $r = R+1$, where $\mathrm{Re} = \mathrm{Ha}^2/N = \rho(\Delta\phi)/\mu B_0$ is the Reynolds number. From Eq. (20) we observe that the magnetic field has no direct effect in this two-dimensional, ordinary hydrodynamic stability problem. The only roles of the magnetic field are: (1) to interact with j_{r0} to produce $v_{\theta 0}$, and (2) to force a shift to modes with $k = 0$.

Equation (20) together with the boundary conditions forms an eigenvalue problem: given R and Re, determine λ such that Eq. (20) and its boundary conditions are satisfied. Here, too, a collocation technique is used in which v_{r1} is represented by Chebyshev polynomials:

$$
v_{r1}(\zeta) = \sum_{s=0}^{S+2} a_s T_s(\zeta),
$$

where the terms have been defined in Section III.B. The series representation is substituted into the transformed version of Eq. (20) and the boundary conditions to obtain:

$$
\begin{aligned}
\sum_{s=0}^{S+2} a_n \Bigg\{ & \frac{16 r_j^2}{(a-1)^4} T_s^{iv}(\zeta_j) + \frac{48 r_j}{(a-1)^3} T_s'''(\zeta_j) + \frac{4(5-2n^2)}{(a-1)^2} T_s''(\zeta_j) - \frac{2(1+2n^2)}{r_j(a-1)} T_s'(\zeta_j) + \frac{(1-n^2)^2}{r_j^2} T_s(\zeta_j) \\
& + i\,\mathrm{Re}\Bigg[\frac{4 r_j[\lambda r_j - n v_{\theta 0}(r_j)]}{(a-1)^2} T_s''(\zeta_j) + \frac{6[\lambda r_j - n v_{\theta 0}(r_j)]}{(a-1)} T_s'(\zeta_j) + \frac{(1-n^2)^2}{r_j^2} \\
& \times \left\{ \lambda[1-n^2] + \frac{n}{r_j}[n^2-2] v_{\theta 0}(r_j) + n\frac{dv_{\theta 0}(r_j)}{dr} + nr\frac{d^2 v_{\theta 0}(r_j)}{dr^2} \right\} T_s(\zeta_j) \Bigg] \Bigg\} = 0
\end{aligned} \tag{21}
$$

and

$$
\sum_{\substack{s=0 \\ s\ \text{even}}}^{S+2} a_s = 0 \tag{22a}
$$

$$
\sum_{\substack{s=1 \\ s\ \text{odd}}}^{S+1} a_s = 0 \tag{22b}
$$

$$
\sum_{\substack{s=2 \\ s\ \text{even}}}^{S+2} a^s s_s = 0 \tag{22c}
$$

$$
\sum_{\substack{s=1 \\ s\ \text{odd}}}^{S+1} a_s = 0. \tag{22d}
$$

Equation (21) must be satisfied at the $(S-1)$ collocation points, which are given by $\zeta_j = \cos(j\pi/S)$, $j = 1,2,\ldots,(S-1)$. For a given R and Re, this system of equations, Eqs. (21) and (22), is solved as in Section III.B through the MSIMSL subroutine DGVLCG.

Before considering the results for Eqs. (21) and (22), it should be noted that there are four possible flows that can be considered: inviscid, small-gap; viscous, small-gap; inviscid with finite-gap; and viscous with finite-gap. Equations (21) and (22) include both viscous and curvature effects. For the small gap, $R \gg 1$. The base flow azimuthal velocity reduces to $v_{\theta 0} = -6x(x-1)$, where $x = r - R$, and Eq. (20) reduces to the Orr-Sommerfeld equation with a real wave number. Using the collocation technique together with the MSIMSL subroutine DGVLCG, the results were in good agreement with the results presented by Orszag [16] for the Poiseuille velocity profile. When this problem is treated as inviscid by assuming $\mathrm{Re} \to \infty$, the equation further reduces to the Rayleigh equation, and there is no tendency toward instability for any wave number. This is in agreement with the Rayleigh inflection point theorem, which states that, given an inviscid parallel flow, a necessary condition for instability is that the base flow velocity has an inflection point. The velocity distribution given by $v_{\theta 0} = -6x(x-1)$ has no inflection point, therefore the flow should be stable.

When the problem is treated as inviscid with a finite gap, there is no tendency toward instability for any wave number with $R = 1$ and 1/9. It should be noted there is an inflection point in this velocity distribution, Eq. (15), which would indicate that the flow could become unstable. However, a necessary condition for instability is no longer the Rayleigh inflection point theorem, which is based on the inviscid Orr-Sommerfeld equation. A necessary condition here is that: $d[(1/r)d(rv_\theta)/dr]/dr$ must change sign somewhere on the open interval $r \in (R, R+1)$. This condition is not met by the velocity distribution given in Eq. (15). Therefore, no instability should be anticipated. Note that this condition is a necessary condition not a sufficient condition.

When viscosity is introduced, for a purely hydrodynamic flow, the problem is known as the Dean problem [17]. The important parameters are: R, a measure of the gap width; Re, the Reynolds number; and n, the azimuthal wave number which assumes integer values. As the outer radius increases, the maximum value of the azimuthal velocity decreases, as can be seen from Table 4, where $r_{\max}$ is the location of the maximum base azimuthal velocity, $v_{\theta 0_{\max}}$. This would lead one to anticipate that the flow would be more stable as the outer radius increases.

For the range of Reynolds numbers tested with $R = 4.0$, 2.0, 1.0, 0.25 and 1/9 and n between 1.0 and 10.0, the imaginary portion of the eigenvalue did not pass through zero. One example is shown in Fig. 12 with $R = 1/9$ and $n = 10.0$. In Fig. 12 the Reynolds number ranges from 9×10^5 and 9×10^6, and as Re increases, the magnitude of the imaginary portion of the eigenvalue decreases towards zero. The imaginary portion of the eigenvalue is essentially zero when $\mathrm{Re} = 1.59 \times 10^7$, indicating that an instability does exist. However, for such a large value of Re, the flow is most likely turbulent. If the Reynolds number is defined in terms of the maximum velocity, then $\mathrm{Re}^* = v^*_{\theta 0_{\max}} L/\nu$, and $\lambda_i \approx 0$ at $\mathrm{Re}^* = 2.35 \times 10^7$. For some values of R, Re* was as small as $O(10^5)$.

Table 4 Maximum base azimuthal velocity and its location for given values of *R*

R	r_{max}	$v_{\theta_{max}}$
4.0	4.481	1.4999
2.0	2.467	1.4996
1.0	1.444	1.4988
0.25	0.637	1.4908
0.111	0.475	1.4795

Therefore, it appears as though the flow undergoes a transition to turbulence rather than passing through some intermediate stable state.

V Conclusions

We have considered the stability of an electrically driven flow to infinitesimal axisymmetric and plane-polar disturbances using the method of normal modes. Here, the flow is confined between two concentric, stationary, infinitely long, circular cylinders. A voltage difference is maintained across the radial gap, creating a radial electric current. In the presence of an axial magnetic field, an azimuthal electromagnetic body force arises which induces an azimuthal base flow.

This flow is similar to a Taylor-Couette flow with counter-rotating cylinders. In both a Taylor-Couette flow and an electrically driven flow, the base flow does undergo an instability to a new state in which circulation cells appear. However, the region of instability for a Taylor-Couette flow is nearer the inner cylinder, and for an electrically driven flow the region of instability is nearer the outer cylinder. Were an axial magnetic field included in the Taylor-Couette problem, as was considered by Chandrasekhar [5], its effect on the flow would be different from its effect in the electrically driven flow problem. In the Taylor-Couette problem, the magnetic field does not have an impact on the azimuthal base flow, while in the electrically driven flow problem, there would be no flow in the absence of an axial magnetic field. We have observed that the base flow becomes increasingly stable to infinitesimal axisymmetric disturbances as Ha increases or as R decreases. Recall that an increase in Ha represents an increase in the magnetic field strength, and a decrease in *R* corresponds to an increase in the radial gap width. For the electrically driven flow subjected to an infinitesimal axisymmetric disturbance, depending on the radial gap width and the strength of the magnetic field, there may be one cell in a given horizontal plane which extends over the entire radial gap width or two cells, circulating in opposite directions that together occupy the entire radial gap width. Cells which are vertically aligned have oppose sense of circulation—one being counterclockwise and the other clockwise. For sufficiently large Ha, two cells that rotate in the same sense from vertically adjacent planes combine to form a new cell which is no longer horizontal but rather skewed. This shift in modes from horizontal to skewed constitutes a bifurcation.

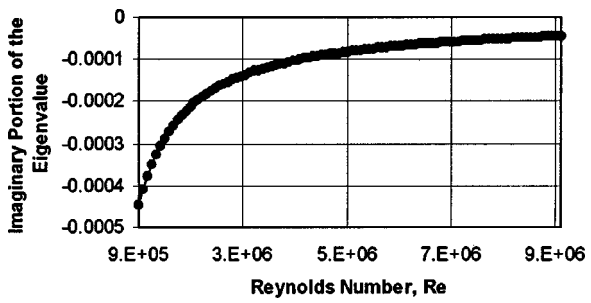

Fig. 12 Imaginary portion of the eigenvalue as a function of Re for $n=10.0$ and $R=1/9$

It had been anticipated that an infinitesimal plane polar disturbance would given rise to an instability in which vortices would be arranged around the centerline of the cylinders and their axes aligned with the *z* axis. However, for an infinitesimal plane-polar disturbance, the base flow does not appear to undergo an instability to a new state until the flow undergoes transition to turbulence.

Acknowledgments

The authors would like to express their deepest appreciation to Mary Grace Williams for her insightful comments and suggestions. This research was supported by the U.S. National Science Foundation under Grant CTS-9321876 and Grant DMS-9512483.

Nomenclature

a_s = coefficient associated with the *s*-order Chebyshev polynomial in the series representation of the disturbance radial velocity component
b_s = coefficient associated with the *s*-order Chebyshev polynomial in the series representation of the disturbance radial current density component
B_0 = dimensional applied magnetic flux density
G = amplication/attenuation factor
Ha = Hartmann number, $B_0 L\sqrt{\sigma/\mu}$
j_r = radial electric current density component
j_θ = azimuthal electric current density component
j_z = axial electric current density component
k = real axial wave number
L = dimensional radial distance between the two cylinders
n = real, integer azimuthal wave number
N = interaction parameter, $\sigma B_0^3 L^2/\rho(\Delta\phi)$
p = pressure
r = radial coordinate
r_{max} = radial location at which $v_{\theta 0}$ assumes its maximum value
r_α = radial location at which $\alpha=0$
R = radius of the inner cylinder
Re = Reynolds number, $\mathrm{Ha}^2/N=\rho\Delta\phi/\mu B_0$
Re* = effective Reynolds number, $v_{\theta 0_{max}}\mathrm{Re}$
$S+2$ = highest-order Chebyshev polynomial
t = time
T_s = Chebyshev polynomial of order *s*
v_r = radial velocity component
v_θ = azimuthal velocity component
v_z = axial velocity component
z = axial coordinate
α = parameter associated with stability, $d(r|v_{\theta 0}|)/dr$
$\Delta\phi$ = electric potential difference across the radial gap
ζ = transformed coordinate, $2r-(2R+1)$
ζ_j = collocation point

θ = azimuthal coordinate
λ = $\lambda_r + i\lambda_i$, where λ_r is the circular frequency, and λ_i is the attenuation/amplification factor
μ = molecular viscosity
ξ = rescaled radial coordinate used to plot the stream lines, $r-R$
ρ = density
σ = electrical conductivity
ϕ = electric potential function
ϕ_w = the dimensional electric potential of the inner cylinder wall

Subscripts/Superscripts

cr = critical value
j = index associated with the collocation points
m = index associated with the time
s = order of the Chebyshev polynomials
0 = base flow quantity
1 = disturbance quantity
* = dimensional quantity

References

[1] Stevens, H. O., Superczynski, M. J., Doyle, T. J., Harrison, J. H., and Messinger, H., 1976 ''Superconducting machinery for naval ship propulsion,'' *IEEE Transactions on Magnetics Applications Superconducting Conference*, **13**, No. 1, pp. 269–274.

[2] Talmage, G., Mazumder, S., Brown, S. H., and Sondergaard, N. A., 1995, ''Viscous and Joulean power losses in liquid-metal sliding electrical contacts with finite electrically conducting electrodes,'' IEEE Transactions on Energy Conversion, **10**, No. 4, pp. 634–644.

[3] Drazin, P. G., and Reid, W. H. 1991, *Hydrodynamic Stability*, Cambridge University Press.

[4] Taylor, G. I., 1923, ''Stability of a viscous liquid contained between two rotating cylinders,'' Proc. R. Soc. London, Ser. A, **A223**, pp. 289–343.

[5] Chandrasekhar, F. R. S., 1953, ''The stability of viscous flow between rotating cylinders in the presence of a magnetic field,'' Proc. R. Soc. London, Ser. A, **216**, pp. 293–309.

[6] Donnelly, R. J., and Ozima, M., 1962, ''Experiments on the stability of flow between rotating cylinders in the presence of a magnetic field,'' Proc. R. Soc. London, Ser. A, **266**, pp. 272–286.

[7] Weinstein, M., 1990, ''An analytical solution of the basic Couette flow affected by a three-dimensional magnetic field,'' J. Franklin Inst., **327**, No. 1, pp. 13–24.

[8] Chandrasekhar, F. R. S., 1961, *Hydrodynamic and Hydomagnetic Stability*, Dover, New York, p. 411.

[9] Roberts, P. H., 1964, ''The stability of hydromagnetic Couette flow,'' Proc. Cambridge Philos. Soc., **60**, pp. 635–651.

[10] Chang, T. S., and Sartory, W. K., 1967, ''On the onset of instability by oscillatory modes in hydromagnetic Couette flow,'' Proc. R. Soc. London, Ser. A, **301**, pp. 451–471.

[11] Soundalgekar, V. M., Ali, M. A., and Takhar, H. S., 1994, ''Hydromagnetic stability of dissipative Couette flow: wide-gap problem,'' International Journal of Energy Research, **18**, pp. 689–695.

[12] Chen, C.-K., and Chang, M. H., 1998, ''Stability of hydromagnetic dissipative Couette flow with non-axisymmetric disturbance,'' J. Fluid Mech., **366**, pp. 135–158.

[13] Richardson, A. T., 1974, ''On the stability of a magnetically driven rotating fluid flow,'' J. Fluid Mech., **63**, No. 3, pp. 593–605.

[14] Canuto, C., Hussaini, M. Y., Quarteroni, A., and Zang, T. A., 1998, *Spectral Methods in Fluids Dynmaics*. Springer-Verlag, New York.

[15] Morthland, T. E., and Walker, J. S., 1999, ''Instability of dynamic thermocapillary liquid layers with magnetic fields,'' J. Fluid Mech., **382**, pp. 87–108.

[16] Orszag, S. A., 1971, ''Accurate solution of the Orr-Sommerfeld stability equation,'' J. Fluid Mech., **50**, No. 4, pp. 689–703.

[17] Gibson, R. D., and Cook, A. E., 1974, ''The stability of curved channel flow,'' Quarterly J. Mech. Appl. Math., **27**, No. 2, pp. 139–150.

On Two-Dimensional Laminar Hydromagnetic Fluid-Particle Flow Over a Surface in the Presence of a Gravity Field

Ali J. Chamkha
Department of Mechanical and Industrial Engineering,
Kuwait University,
P.O. Box 5969,
Safat, 13060, Kuwait

A continuum two-phase fluid-particle model accounting for particle-phase stresses and a body force due to the presence of a magnetic field is developed and applied to the problem of two-dimensional laminar hydromagnetic flow of a particulate suspension over a horizontal surface in the presence of a gravity field. Analytical solutions for the velocity distributions and the skin-friction coefficients of both phases are reported. Two cases of wall hydrodynamic (velocity) conditions corresponding to stationary and oscillatory velocity distributions are considered. Numerical evaluations of the analytical solutions are performed and the results are reported graphically to elucidate special features of the solutions. The effects of the particle-phase stresses and the magnetic field are illustrated through representative results for the horizontal velocity profiles, fluid-phase displacement thickness, and the complete skin-friction coefficient for various combinations of the physical parameters. It is found that the presence of the magnetic field increases the fluid-phase skin-friction coefficient for various particulate volume fraction levels while the presence of the particle-phase viscous stresses reduces it for various particle-to-fluid density ratios. [DOI: 10.1115/1.1343460]

Introduction

Deposition of solid particles from flowing fluid/solid suspensions on surfaces is an important process in various natural and engineering applications. Some possible applications include deep-bed and membrane filtration, separation of proteins, viruses, antibodies, and vaccines, atmospheric pollution, and microbial and cell transport in living systems (Yiantsios and Karabelas [1]). There have been considerable research work done on particulate deposition in laminar flows such as the reviews by Jia and Williams [2] and van de Ven [3]. Sedimentation effects for particle sizes close to one micron or larger are reported by Yao et al. [4]. Adamczyk and van de Ven [5,6] have considered particulate deposition in rectilinear flows over flat surfaces. Marmur and Ruckenstein [7] have reported on the process of cells deposition on a flat plate. Apazidis [8,9] has analyzed the velocity and temperature distributions of two-dimensional laminar flows of a particulate suspension in the presence of a gravity field. More recently, Dahlkid [10] has considered the motion of Brownian particles and sediment on an inclined plate. This work was done in relation to the process of separation of proteins, viruses, antibodies, and vaccines. Yiantsios and Karabelas [1] has studied the effect of gravity on the deposition of micron-sized particles on smooth surfaces. Their work was focused on particulate deposition from liquid suspensions with the main motivation being fouling of heat transfer or filtration equipment by suspended particles.

In many fluid-particle flows, the fluid phase may be electrically conducting and the particle-phase concentration may be high. In an environment where a magnetic field is present, these effects play an important role in altering the flow characteristics. Particle-phase viscosity effects in particulate suspensions are especially important in multiphase systems consisting of high solid particulate concentration in liquids and gases. Particle-phase viscosity is needed to model particle-particle interaction. It can be thought of as arising naturally from the averaging processes used to derive continuum equations describing either a system exhibiting turbulent fluctuations (see, for instance, Chen and Wood [11]) or a system containing discrete elements (see, for instance, Drew and Segal [12]). Also, it is often employed to facilitate numerical solutions. Particle-phase viscous effects have been investigated previously by many investigators (see, for instance, Gidaspow [13], Tsuo and Gidaspow [14], and Gadiraju et al., [15]).

In the present work, a simple two-phase model is employed in which the suspension is assumed to be somewhat dense in the sense that inter-particle collision exists and that this is accounted for by endowing the particle phase by an artificial viscosity. The fluid phase is considered to be Newtonian and electrically conducting but the particles and the surface are assumed to be electrically nonconducting and that the magnetic Reynolds number is assumed to be small. The particle phase is assumed to have uniform density distribution and is made of spherical particles having one size. The present work is a direct generalization of the work reported by Apazidis [8] on the flow characteristics of particle-fluid flow past a horizontal plate in the presence of a gravity field.

Governing Equations

Consider unsteady laminar hydromagnetic flow of a two-phase particulate suspension over a horizontal infinite surface in the presence of a gravity field. The surface is coincident with the half plane $y=0$, $x\geq 0$ and the flow above the surface is a uniform stream in the x-direction parallel to the surface with both phases being in equilibrium. A magnetic field with uniform strength is applied in the y-direction normal to the flow direction. Owing to the density difference between both the fluid and particle phases, a separational motion in which heavy particles falling from the flow form a layer of dense sediment on the surface while the continuous fluid phase moves in the opposite upward direction is introduced. This settling process has been called sedimentation (Wallis [16]). According to Kynch [17] and later by Apazidis [8], the vertical sedimentation of solid particles may proceed in three different ways depending on the shape of the curve of the total particle flow rate versus the volume fraction of particles in the

Contributed by the Fluids Engineering Division for publication in the JOURNAL OF FLUIDS ENGINEERING. Manuscript received by the Fluids Engineering Division November 4, 1999; revised manuscript received November 27, 2000. Associate Editor: J. Eaton.

suspension. Apazidis [8] has considered the case when a direct shock from the initial value of the particulate volume fraction α to the final fully settled value α_M is formed at the interface of the mixture and the settled particles with maximum packing existing at the surface. The fluid phase is assumed to be Newtonian and electrically conducting while the particle phase and the surface are assumed to be electrically nonconducting. The particle phase is assumed to be somewhat dense so that particle-phase stresses are considered important and is made up of spherical solid particles having one size and with a uniform density distribution. The particle Reynolds number is assumed to be less than unity so that the force interaction between the phases is limited to the linear Stokes drag force. Also, the magnetic Reynolds number is assumed to be small so that the induced magnetic field is neglected. In addition, no electric field is assumed to exist and the Hall effect is neglected. The assumption of small magnetic Reynolds number uncouples the flow equations from Maxwell's equations (see, Cramer and Pai [18]). Based on the above assumptions and treating the particle phase as a continuum (Marble [19]), the governing equations for this investigation can be written as

$$-\frac{\partial \alpha}{\partial t}+\frac{\partial}{\partial y}((1-\alpha)v)=0 \tag{1}$$

$$(1-\alpha)\rho\left(\frac{\partial u}{\partial t}+v\frac{\partial u}{\partial y}\right)=(1-\alpha)\mu\frac{\partial^2 u}{\partial y^2}-\frac{9}{2}f(\alpha)\frac{\mu}{a^2}(u-u_p)-(1-\alpha)\sigma B_0^2(u-u_\infty) \tag{2}$$

$$(1-\alpha)\rho\left(\frac{\partial v}{\partial t}+v\frac{\partial v}{\partial y}\right)=(1-\alpha)\left(\mu\frac{\partial^2 v}{\partial y^2}-\frac{\partial p}{\partial y}-\rho g\right)-\frac{9}{2}f(\alpha)\frac{\mu}{a^2}(v-v_p) \tag{3}$$

for the fluid phase and

$$\frac{\partial \alpha}{\partial t}+\frac{\partial}{\partial y}(\alpha v_p)=0 \tag{4}$$

$$\alpha\rho_p\left(\frac{\partial u_p}{\partial t}+v_p\frac{\partial u_p}{\partial y}\right)=\alpha\mu_p\frac{\partial^2 u_p}{\partial y^2}+\frac{9}{2}f(\alpha)\frac{\mu}{a^2}(u-u_p) \tag{5}$$

$$\alpha\rho_p\left(\frac{\partial v_p}{\partial t}+v_p\frac{\partial v_p}{\partial y}\right)=\alpha\left(\mu_p\frac{\partial^2 v_p}{\partial y^2}-\frac{\partial p}{\partial y}-\rho_p g\right)+\frac{9}{2}f(\alpha)\frac{\mu}{a^2}(v-v_p) \tag{6}$$

for the particle phase where t is time and y is the vertical distance; u, v, and p are the fluid-phase x-component of velocity, y-component of velocity, and pressure, respectively; α, ρ, μ, and σ are the volume fraction of particles and the fluid-phase density, dynamic viscosity, and electrical conductivity, respectively; a, g, B_0, and u_∞ are the particle radius, gravitational acceleration, magnetic induction and the free stream velocity, respectively. A subscript p indicates a property associated with the particle phase.

Equations (1)–(6) are supplemented by the function $f(\alpha)$ which is reported by Tam [20] and employed later by Apazidis [8] such that

$$f(\alpha)=\frac{\alpha(4+3(8\alpha-3\alpha^2)^{1/2}+3\alpha)}{(2-3\alpha)^2} \tag{7}$$

It is worth noting that $f(\alpha)$ represents a correction factor for the Stokes drag force on a single spherical particle and accounts for finite volume fraction of the particle phase.

For convenience, the following equations

$$\eta=\frac{y}{a},\quad \tau=\frac{ga\gamma}{\nu}t,\quad u=\frac{ga^2\gamma}{\nu}U,\quad u_p=\frac{ga^2\gamma}{\nu}U_p \tag{8}$$

$$v=\frac{ga^2\gamma}{\nu}V,\quad v_p=\frac{ga^2\gamma}{\nu}V_p,\quad p=-\rho g y(1-\gamma P)$$

are substituted into Eqs. (1)–(6) to yield

$$-\frac{\partial \alpha}{\partial \tau}+\frac{\partial}{\partial \eta}((1-\alpha)V)=0 \tag{9}$$

$$\mathrm{Re}\left(\frac{\partial U}{\partial \tau}+V\frac{\partial U}{\partial \eta}\right)=\frac{\partial^2 U}{\partial \eta^2}-\frac{9}{2}\frac{f(\alpha)}{(1-\alpha)}(U-U_p)-M^2(U-U_\infty) \tag{10}$$

$$\mathrm{Re}\left(\frac{\partial V}{\partial \tau}+V\frac{\partial V}{\partial \eta}\right)=\frac{\partial^2 V}{\partial \eta^2}+P-\frac{9}{2}\frac{f(\alpha)}{(1-\alpha)}(V-V_p) \tag{11}$$

$$\frac{\partial \alpha}{\partial \tau}+\frac{\partial}{\partial \eta}(\alpha V_p)=0 \tag{12}$$

$$\gamma\,\mathrm{Re}\left(\frac{\partial U_p}{\partial \tau}+V_p\frac{\partial U_p}{\partial \eta}\right)=\beta\frac{\partial^2 U_p}{\partial \eta^2}+\frac{9}{2}\frac{f(\alpha)}{\alpha}(U-U_p) \tag{13}$$

$$\gamma\,\mathrm{Re}\left(\frac{\partial V_p}{\partial \tau}+V_p\frac{\partial V_p}{\partial \eta}\right)=\beta\frac{\partial^2 V_p}{\partial \eta^2}+P-1+\frac{9}{2}\frac{f(\alpha)}{\alpha}(V-V_p) \tag{14}$$

where

$$\gamma=\frac{\rho_p}{\rho},\quad \mathrm{Re}=\frac{ga^3\gamma}{\nu^2},\quad \nu=\frac{\mu}{\rho},\quad M^2=\frac{\sigma B_0^2 a^2}{\mu},\quad U_\infty=\frac{u_\infty \nu}{ga^2\gamma},\quad \beta=\frac{\mu_p}{\mu} \tag{15}$$

are the particle-to-fluid density ratio, Reynolds number based on the particle diameter, kinematic viscosity, square of the Hartmann number, dimensionless freestream velocity, particle to fluid viscosity ratio, respectively. It should be mentioned that if M and β are formally equated to zero in Eqs. (9)–(14), the continuity and momentum equations reported by Apazidis [9] will be recovered except the factor 9/2 which is mistakenly missing from his equations.

As explained by Apazidis [8], one of the possible ways that the vertical sedimentation of solid particles may proceed is when a direct shock from the initial particle concentration value to the final fully settled concentration is formed at the interface of a mixture and maximally concentrated dispersed phase settled at the horizontal solid surface. Since this case is quite common and is easier to analyze than the other possible ways in which the particle concentration is non-uniform, it is considered in this work and the volume fraction of particles in the mixture is assumed constant. With this, Eqs. (9) and (12) give

$$\frac{\partial V}{\partial \eta}=\frac{\partial V_p}{\partial \eta}=0 \tag{16}$$

Also, with the assumption of zero volumetric flux in the vertical direction as in the case of batch sedimentation (Wallis [16]), one may write

$$\alpha V_p+(1-\alpha)V=0 \tag{17}$$

Furthermore, assuming that the vertical motion of both phases due to the gravity field has reached its stationary state ($\partial V_p/\partial \tau=\partial V/\partial \tau=0$) and using Eqs. (11), (14), and (17) result in the following vertical components of the velocity fields of both phases:

$$V=\frac{2}{9}\frac{\alpha^2(1-\alpha)}{f(\alpha)},\quad V_p=-\frac{2}{9}\frac{\alpha(1-\alpha)^2}{f(\alpha)} \tag{18}$$

The interface vertical velocity can be shown to be

$$V_i = \frac{2}{9}\frac{\alpha^2(1-\alpha)^2}{(\alpha_M-\alpha)f(\alpha)} \tag{19}$$

where α_M (≈ 0.6 for spherical particles) is the volume fraction of particles in the dense sediment near the surface (see Apazidis [8]).

The x-momentum equations (10) and (13) governing the horizontal velocity distributions of both phases (U and U_p) can be transformed by using a new coordinate system which moves upwards with the interface velocity V_i such that

$$\eta^* = \eta - V_i\tau \tag{20}$$

to yield

$$\mathrm{Re}\left[\frac{\partial U}{\partial \tau} + (V-V_i)\frac{\partial U}{\partial \eta^*}\right] = \frac{\partial^2 U}{\partial \eta^{*2}} - \frac{9}{2}\frac{f(\alpha)}{(1-\alpha)}(U-U_p) - M^2(U-U_\infty) \tag{21}$$

$$\gamma\,\mathrm{Re}\left[\frac{\partial U_p}{\partial \tau} + (V_p-V_i)\frac{\partial U_p}{\partial \eta^*}\right] = \beta\frac{\partial^2 U_p}{\partial \eta^{*2}} + \frac{9}{2}\frac{f(\alpha)}{\alpha}(U-U_p) \tag{22}$$

Analytical Results

Analytical solutions for the particulate suspension flow behavior of the problem under consideration are obtained for two physical cases. The first case is that of steady hydromagnetic two-phase flow over an infinite surface while the second case deals with hydromagnetic two-phase flow due to an oscillating infinite surface.

Case 1: Steady Hydromagnetic Two-Phase Flow Over an Infinite Surface. For this case the x-momentum equations of both phases (21) and (22) (with the asterisks being dropped) and the appropriate boundary conditions can be written as

$$\mathrm{Re}\left[(V-V_i)\frac{dU}{d\eta}\right] = \frac{d^2U}{d\eta^2} - \frac{9}{2}\frac{f(\alpha)}{(1-\alpha)}(U-U_p) - M^2(U-U_\infty) \tag{23}$$

$$\gamma\,\mathrm{Re}\left[(V_p-V_i)\frac{dU_p}{d\eta}\right] = \beta\frac{d^2U_p}{d\eta^2} + \frac{9}{2}\frac{f(\alpha)}{\alpha}(U-U_p) \tag{24}$$

$$\eta = 0: \quad U = 0, \tag{25a}$$

$$U_p = S\frac{dU_p}{d\eta} \tag{25b}$$

$$\eta = \infty: \quad U = U_\infty, \tag{25c}$$

$$U_p = U_\infty \tag{25d}$$

where S is a dimensionless wall particulate slip factor. It should be noted that while the exact boundary condition to be satisfied by a particle phase at a surface is not well understood at present, the form used in Eq. (25b) is borrowed from rarefied gas dynamics and has been used by several previous authors (see, for instance, Soo [21] and Chamkha [22]).

Equations (23) and (24) can be combined into a fourth-order ordinary differential equation in terms of U_p. This is done by solving for U from Eq. (24) and then substituting the result into Eq. (23) to yield

$$\beta\Gamma_1\frac{d^4U_p}{d\eta^4} - \Gamma_1[\mathrm{Re}(V-V_i)\beta + \Gamma_2]\frac{d^3U_p}{d\eta^3} - [1-\Gamma_1\Gamma_2\,\mathrm{Re}(V-V_i) + \beta(\Delta + M^2\Gamma_1)]\frac{d^2U_p}{d\eta^2} + [\mathrm{Re}(V-V_i) + \Gamma_2(\Delta + M_2\Gamma_1)]\frac{dU_p}{d\eta} + M^2U_p = M^2U_\infty \tag{26}$$

where

$$\Gamma_1 = \frac{2}{9}\frac{\alpha}{f(\alpha)}, \quad \Gamma_2 = \gamma\,\mathrm{Re}(V_p-V_i), \quad \Delta = \frac{\alpha}{1-\alpha} \tag{27}$$

Inviscid Particle Phase ($\beta=0$). For this situation, Eq. (26) reduces to

$$N_1\frac{d^3U_p}{d\eta^3} + N_2\frac{d^2U_p}{d\eta^2} + N_3\frac{dU_p}{d\eta} + N_4U_p = -N_4U_\infty \tag{28}$$

where

$$N_1 = \Gamma_1\Gamma_2, \quad N_2 = 1-\Gamma_1\Gamma_2\,\mathrm{Re}(V-V_i)$$
$$N_3 = \mathrm{Re}(V_i-V) - \Gamma_2(\Delta + M^2\Gamma_1), \quad N_4 = -M^2 \tag{29}$$

Three boundary conditions are needed to solve Eq. (28). These are given by Eqs. (25a,c,d). Equation (25b) is ignored since for $\beta=0$, the particle-phase momentum equation becomes a first-order differential equation and only one boundary condition (25d) is needed.

Without going into detail, it can be shown that the general solution of Eq. (28) subject to the boundary conditions can be written as

$$U_p = U_\infty\left[1 - \frac{1}{(1-\Gamma_1\Gamma_2\lambda_1)}\exp(-\lambda_1\eta)\right] \tag{30}$$

where λ_1 is the absolute value of the only negative real root of the characteristic equation:

$$N_1\lambda^3 + N_2\lambda^2 + N_3\lambda + N_4 = 0 \tag{31}$$

With the solution of U_p being known, Eqs. (23) or (24) can be solved for U to give

$$U = U_\infty[1-\exp(-\lambda_1\eta)] \tag{32}$$

It should be mentioned that the physical solution of Eq. (28) requires that the characteristic equation (31) has two positive real roots and one negative real root. More than one negative root makes the problem to be underdetermined. While there is no analytical method to show the existence of two positive and one negative roots for Eq. (31), this condition was satisfied in all the results obtained for this case. It can be shown that as $M\to 0$ in Eqs. (30) and (32), the solutions of Apazidis [8] are recovered provided that his parameters are related properly to those of the present work. It is an interesting fact that the form of the solution for a nonzero magnetic field is the same as that without a magnetic field. The effects of the magnetic field are all contained in changes of the real characteristic root λ_1.

Figure 1 presents the effects of the Hartmann number M, the particle Reynolds number Re and the particle-phase volume fraction α on the fluid-phase displacement thickness of the viscous layer $1/\lambda_1$ for a density ratio $\gamma=1000$. It is observed that increases in the values of Re causes the viscous boundary layer close to the surface to decrease as a result of convection of momentum toward the interface between the particulate suspension and the layer of sediment at the bottom. Application of a magnetic field normal to the flow direction for the problem considered gives rise to a motive force acting in the flow direction which tends to aid the flow along the horizontal surface. This causes both the fluid- and particle-phase horizontal velocities to increase and their viscous boundary layers to decrease. These behaviors are evident from the decreases in $1/\lambda_1$ as the Hartmann number M increases shown in Fig. 1. From other results not presented herein for brevity, it was observed that the velocity profiles of both phases increase while their displacement thicknesses decrease (see Fig. 1) as the particle-phase volume fraction increases. In addition, these velocities separate in the vicinity of the surface for low values of α and that this separation close to the surface reduces as α increases. This behavior is associated with the fact that, for large density differences between the phases as employed in Fig. 1, the particle-

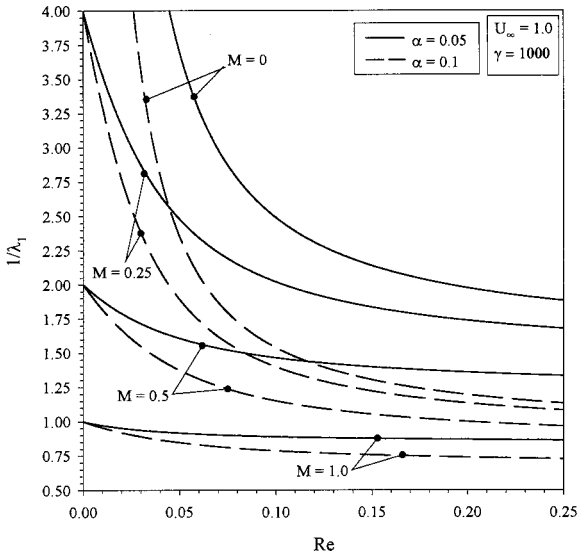

Fig. 1 Effects of *M*, Re, and α on the fluid-phase displacement thickness

phase inertia prevents the adjustment of the horizontal velocity of the particle phase to that of the fluid phase causing a nonzero particle-phase horizontal velocity at the interface.

Figure 2 shows the magnitude of the velocity difference ($U_p - U$) at $\eta=0$ (or the particle-phase velocity at the interface since the fluid-phase velocity there vanishes due to the no-slip condition) versus Re and for various values of M and γ. It is observed that, for the parametric conditions used, the interface velocity difference increases as Re increases. This is associated with the increase in the velocities of both phases as Re increases mentioned above. Also, the velocity difference at $\eta=0$ is predicted to be lower for $\gamma=100$ than for $\gamma=1000$ as explained above. The effect of the magnetic field is seen to increase the velocity difference at the interface.

Viscous Particle Phase ($\beta\neq 0$). For this particular case, Eq. (26) has the following characteristic equation:

$$N_{11}s^4+N_{22}s^3+N_{33}s^2+N_{44}s+N_{55}=0 \tag{33}$$

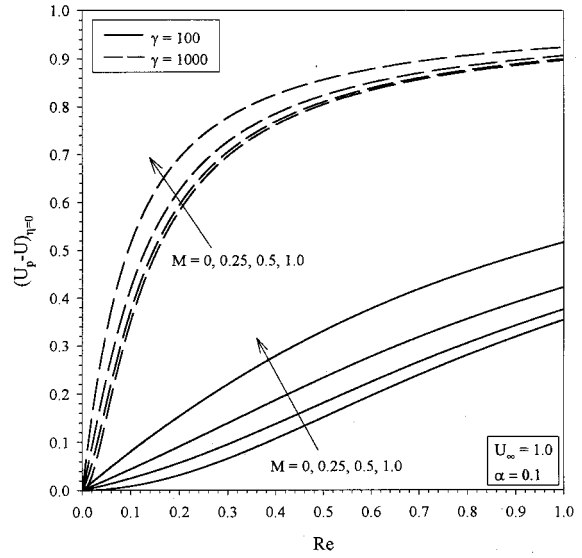

Fig. 2 Effects of *M*, Re, and γ on the velocity difference at the interface

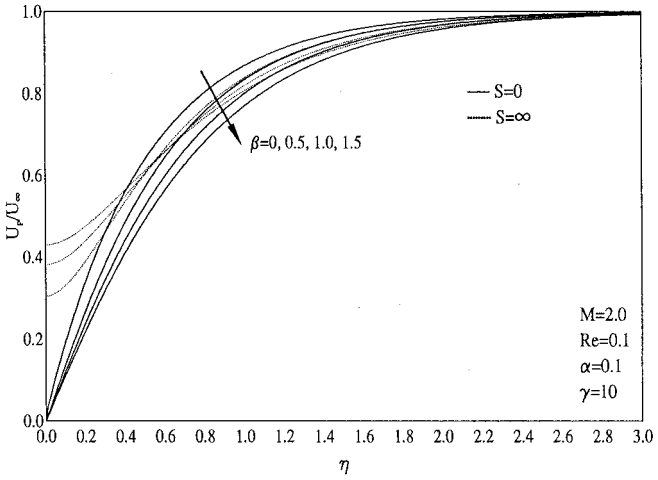

Fig. 3 Effects of *S* and β on particle-phase velocity profiles

where

$$N_{11}=\beta\Gamma_1,\quad N_{22}=-\mathrm{Re}(V-V_i)\Gamma_1\beta-\Gamma_1\Gamma_2$$
$$N_{33}=-1+\Gamma_1\Gamma_2\,\mathrm{Re}(V-V_i)-\beta(\Delta+M^2\Gamma_1) \tag{34}$$
$$N_{44}=\mathrm{Re}(V-V_i)+\Gamma_2(\Delta+M^2\Gamma_1),\quad N_{55}=M^2$$

The physical solution of Eq. (33) requires that it has two negative and two positive real roots. Without going into detail, the general solutions for U_p and U can be written as

$$U_p=U_\infty+C_1\exp(-s_1\eta)+C_2\exp(-s_2\eta) \tag{35}$$

$$U=U_\infty+C_1M_1\exp(-s_1\eta)+C_2M_2\exp(-s_2\eta) \tag{36}$$

where C_1 and C_2 are arbitrary constants, s_1 and s_2 are the absolute values of the two negative roots of Eq. (33) and

$$M_1=1-\Gamma_1\beta s_1^2-\Gamma_1\Gamma_2 s_1,\quad M_2=1-\Gamma_1\beta s_2^2-\Gamma_1\Gamma_2 s_2 \tag{37}$$

The constants C_1 and C_2 are determined by application of the boundary conditions (25) and can be shown to be

$$C_1=\frac{U_\infty(x_2-M_2)}{(x_1M_2-x_2M_1)};\quad C_2=\frac{U_\infty(x_1-M_1)}{(x_2M_1-x_1M_2)}; \tag{38}$$

where

$$x_1=1+Ss_1,\quad x_2=1+Ss_2 \tag{39}$$

Figure 3 displays the influence of the viscosity ratio β on the particle-phase horizontal velocity U_p for the two cases of no particle wall slip ($S=0$) and perfect particulate wall slip ($S=\infty$). For the case of no slip ($S=0$), it is apparent that the velocity component U_p is zero at the interface between the mixture and the sediment layer as it should be. On the other hand, U_p is nonzero for the case where the particles undergo perfect slip at the interface. The presence of a particle-phase viscosity in the model causes increases in the effective viscosity of the mixture. This, in turn, produces retardation in the motion of the particle phase. This slower motion of the particle phase causes the fluid phase to move slower as well because of the interphase drag force between the fluid and the particle phases. Thus, further increases in the particle-phase viscosity produce further decreases in the motions of both the fluid and the particle phases for the case of no particulate wall slip. However, for the case of perfect particulate wall slip, the reductions in the particle-phase horizontal velocity due to increases in the particle-phase viscosity occur everywhere above the surface except in the immediate vicinity of the interface where

the particle-phase horizontal velocity tends to increase as β increases. These behaviors are evident from Fig. 3.

Case 2: Hydromagnetic Two-Phase Flow due to an Oscillating Infinite Surface. For this case the fluid-phase wall velocity has the dimensionless form

$$U = U_0 \cos(\omega\tau) \tag{40}$$

where U_0 and ω are the amplitude and the frequency of wall velocity oscillation.

It should be noted here that the layer of sediment settling on the surface is assumed to be stationary with respect to its horizontal motion. Therefore, it performs harmonic oscillations in the horizontal direction as that of the surface. Far from the surface, the flow is at rest. This is represented by

$$U(\tau,\infty) = U_p(\tau,\infty) = 0 \tag{41}$$

The general unsteady equations (21) and (22) are solved subject to Eqs. (40) and (41) for $U(\tau,\eta)$ and $U_p(\tau,\eta)$ by assuming

$$U(\tau,\eta) = U_0 \cos(\omega\tau + \delta\eta)\exp(-m\eta) \tag{42}$$

$$U_p(\tau,\eta) = [D_1 \cos(\omega\tau + \delta\eta) + D_2 \sin(\omega\tau + \delta\eta)]\exp(-m\eta) \tag{43}$$

where δ, D_1, D_2, and m are constants which make Eqs. (21) and (22) subject to Eqs. (40) and (41) identically satisfied by the solutions (42) and (43). It should be noted that these solutions represent two damped transverse waves propagating into the mixture's interior. The depth of penetration of these waves is dependent on both the wave velocity and wavelength which are functions of the particle Reynolds number Re, particle volume fraction α, density ratio γ, frequency of oscillations ω, Hartmann number M, and the viscosity ratio β. This is in direct contrast with the single-phase flow case for which the depth of penetration is only a function of the fluid viscosity and the frequency of surface oscillations. These behaviors will be shown in the graphical results for this case. Also, it is understood that the particle-phase velocity solution given by Eq. (43) applies for both cases of inviscid and viscous particle phase and that the particle-phase wall condition (25*b*) is not imposed.

Substitution of Eqs. (42) and (43) into Eqs. (21) and (22) results in two equations of the general form:

$$P_1 \cos(\omega\tau + \beta\eta) + P_2 \sin(\omega\tau + \beta\eta) = 0 \tag{44}$$

where P_1 and P_2 are functions of the constants δ, D_1, D_2, and m. Equating P_1 and P_2 of each of the obtained two equations to zero results in the following system of equations:

$$\mathrm{Re}(V - V_i)m + m^2 - \delta^2 - \frac{9}{2}\frac{f(\alpha)}{(1-\alpha)}\left(1 - \frac{D_1}{U_0}\right) - M^2 = 0 \tag{45}$$

$$\mathrm{Re}\,\omega + \mathrm{Re}(V - V_i)\delta + 2m\delta + \frac{9}{2}\frac{f(\alpha)}{(1-\alpha)}\frac{D_2}{U_0} = 0 \tag{46}$$

$$\gamma\,\mathrm{Re}[mD_1 - D_2\omega - (V_p - V_i)D_2\delta] - \beta D_1\delta^2 - 2mD_2\delta\beta + \beta m^2 D_1 + \frac{9}{2}\frac{f(\alpha)}{\alpha}(U_0 - D_1) = 0 \tag{47}$$

$$\gamma\,\mathrm{Re}[D_1\omega + mD_2 + (V_p - V_i)D_1\delta] - \beta D_2\delta^2 + 2mD_1\delta\beta + \beta m^2 D_2 - \frac{9}{2}\frac{f(\alpha)}{\alpha}D_2 = 0 \tag{48}$$

Equations (45)–(48) represent four nonlinear algebraic equations with four unknowns (δ, D_1, D_2, and m) which must be solved numerically. For fast convergence of the solutions, the following procedure is followed. First, Eqs. (45) and (46) are solved for D_1 and D_2 in terms of δ and m, respectively. Second, the obtained expressions for D_1 and D_2 are then substituted into Eq. (48) which produces a quadratic equation in m with the coefficients containing the constant δ. For an assumed value of δ and given values of the involved physical parameters, the roots of this quadratic equation which are real and of opposite signs can be obtained. Therefore, the negative root is chosen and its absolute value is the needed value of m. With the value of m being known for the assumed δ, the constants D_1 and D_2 can then be determined from Eqs. (45) and (46) as mentioned above. Finally, the values of m, D_1, and D_2 are substituted into Eq. (47) which is then solved for δ. As long as $\delta_{\text{assumed}} \neq \delta_{\text{obtained}}$, the same iteration procedure continues until convergence is achieved within a prescribed acceptable error.

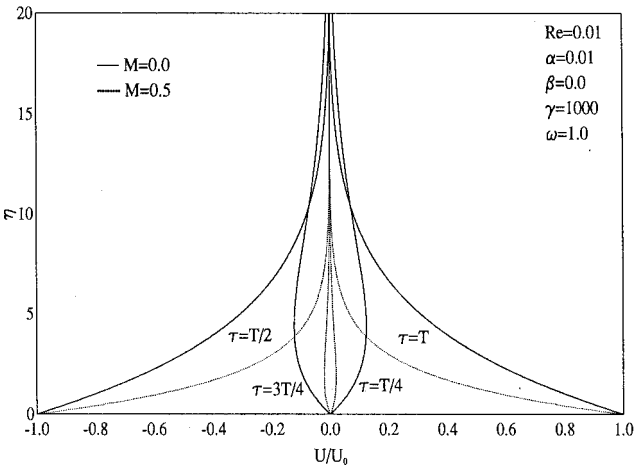

Fig. 4 Effects of *M* on fluid-phase periodic velocity distribution

Results based on the solutions of U and U_p given by Eqs. (42) and (43) are displayed in Figs. 4–6 to illustrate the influence of the Hartmann number M and the viscosity ratio β.

Figures 4 and 5 display the effects of the Hartmann number M on the fluid- and particle-phase periodic horizontal velocity distributions in air-particle flow for Re=0.01, α=0.01, β=0 and ω=1.0, respectively. As in the case of a stationary wall, the effect of the magnetic field increases both the fluid- and particle-phase horizontal velocities (for $\tau = T/2$ and $\tau = 3T/4$) while it produces lower horizontal velocity distributions for both phases (for $\tau = T$ and $\tau = T/4$). It is also observed from these figures that the magnetic field effect speeds up the approach of both phases to the free stream hydrodynamic conditions existing far above the surface.

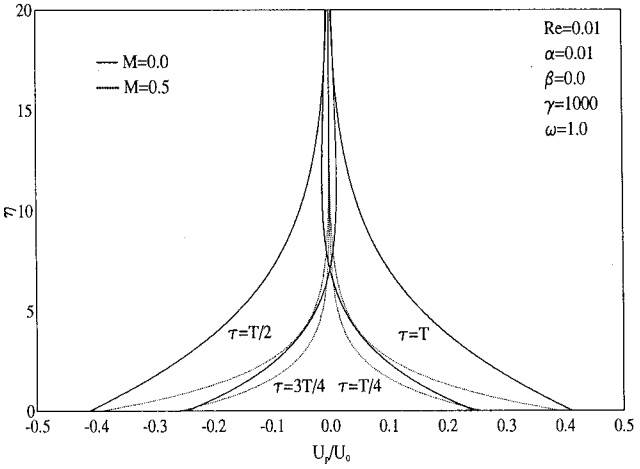

Fig. 5 Effects of *M* on particle-phase periodic velocity distribution

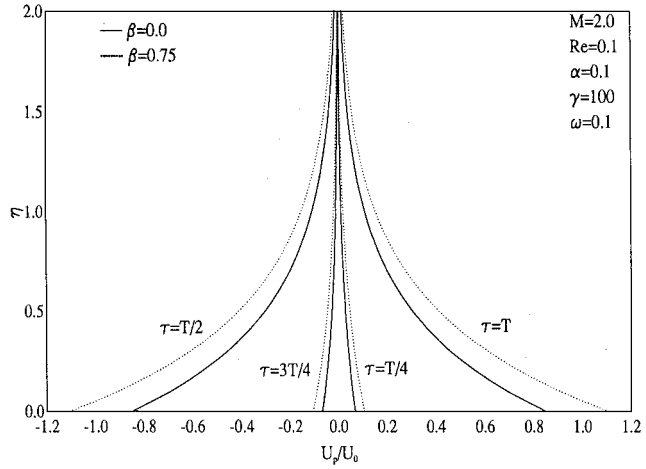

Fig. 6 Effects of β on particle-phase periodic velocity distribution

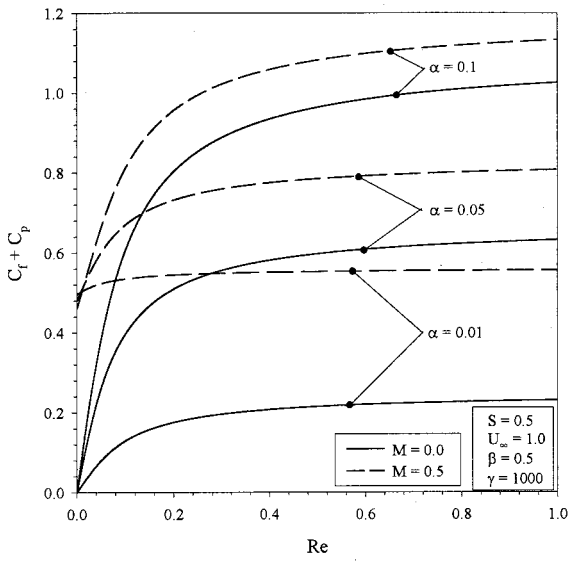

Fig. 7 Effects of *M*, Re and α on the complete skin-friction coefficient

Figure 6 displays the effects of the viscosity ratio β on the particle-phase horizontal velocity component U_p/U_0. It is predicted that U_p/U_0 increases for $\tau=T$ and $\tau=T/4$ and decreases for $\tau=T/2$ and $\tau=3T/4$ due to increases in the values of β and that the wall velocity exceeds that of the amplitude of oscillations of the surface. The effect of β on the fluid-phase horizontal velocity component U/U_0 for this case was found to be insignificant. Again, it should be noted that in the absence of the magnetic field ($M=0$) and the viscosity ratio ($\beta=0$), the results of Apazidis [8] for the problem of two-phase flow due to an oscillating infinite surface are obtained provided that his parameters are properly related to those reported in this work.

Skin-Friction Coefficients. Of special interest for this problem are skin-friction coefficients of both phases. The shear stresses for the fluid and the particle phases at the interface between the particulate suspension and the layer of sediment on the surface can be defined, respectively, as follows:

$$\tau_f=(1-\alpha)\mu\left.\frac{\partial u}{\partial y}\right|_{y=0}=(1-\alpha)\frac{\mu g a\gamma}{\nu}\left.\frac{\partial U}{\partial \eta}\right|_{\eta=0},$$

$$\tau_p=\alpha\mu_p\left.\frac{\partial u_p}{\partial y}\right|_{y=0}=\alpha\frac{\mu_p g a\gamma}{\nu}\left.\frac{\partial U_p}{\partial \eta}\right|_{\eta=0} \tag{49}$$

The dimensionless skin-friction coefficients for both the fluid and the particle phases can be written, respectively, as

$$C_f=\frac{\tau_f}{\rho g a\gamma}=(1-\alpha)\left.\frac{\partial U}{\partial \eta}\right|_{\eta=0},\quad C_p=\frac{\tau_p}{\rho g a\gamma}=\alpha\beta\left.\frac{\partial U_p}{\partial \eta}\right|_{\eta=0} \tag{50}$$

For the case of steady hydromagnetic two-phase flow over an infinite surface, Eqs. (50) take on the respective forms:

$$C_f=(1-\alpha)U_\infty\lambda_1,\quad C_p=0 \tag{51}$$

for the inviscid particle phase case, and

$$C_f=-(1-\alpha)(C_1s_1M_1+C_2s_2M_2),\quad C_p=-\alpha\beta(C_1s_1+C_2s_2) \tag{52}$$

for the viscous particle phase case.

Figure 7 illustrates the influence of the parameters *M*, α, and Re on the complete skin-friction coefficient (C_f+C_p) at the interface between the fluid-particle mixture and the sediment layer on the surface for the case of a viscous particle phase ($\beta\neq0$). Inspection of Fig. 1 shows that both the fluid-phase viscous boundary layer close to the interface and that of the particle phase decrease causing the wall slopes of the fluid- and particle-phase horizontal velocity profiles to increase as either of *M*, α, or Re increases. This has the direct effect of increasing the complete skin-friction coefficient as shown in Fig. 7.

Figure 8 depicts the influence of all of the density ratio γ, viscosity ratio β, and the particulate wall slip parameter *S* on the complete skin-friction coefficient (C_f+C_p). In general, individual results for C_f and C_p which are not presented herein show that they increase with increasing values of γ and that the values of C_f decrease while the values of C_p increase with increasing values of β resulting in a net increase in the complete skin-friction coefficient. The increase in the values of C_p as β increases is related to the definition of C_p as being directly proportional to β. Also, in this figure, two situations of no particulate wall slip ($S=0$) and some particulate wall slip ($S=0.5$) are shown. It is predicted that as *S* increases, the wall slope of the fluid-phase velocity increases while that of the particle phase decreases caus-

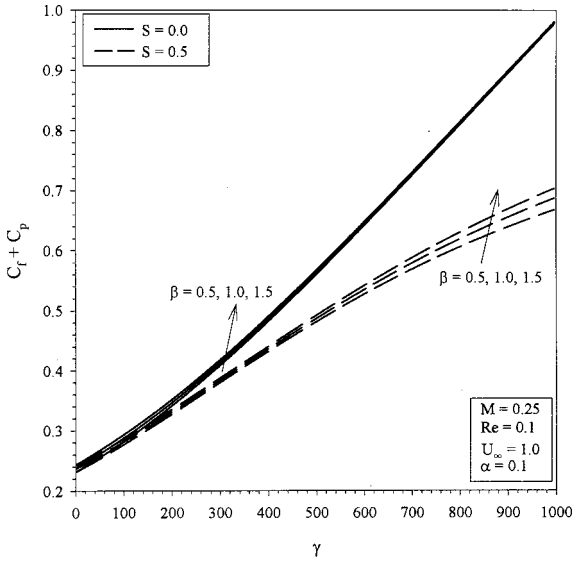

Fig. 8 Effects of *S*, β and γ on the complete skin-friction coefficient

ing respective increases and decreases in the values of C_f and C_p. As a result, the complete skin-friction coefficient is lower for $S=0.5$ than that for $S=0$.

Conclusion

This work was focused on the problem of hydromagnetic particulate suspension flow over a horizontal impermeable surface in the presence of a gravity field. The particle phase was assumed to be somewhat dense and, as a consequence, it was endowed by an artificial viscosity. A boundary condition borrowed from rarefied gas dynamics allowing for general situations of particulate wall slip conditions was employed. Analytical solutions for the velocity distributions and the skin-friction coefficients of both phases were obtained for stationary and periodic wall velocity conditions. Representative results for various parametric conditions were presented graphically to elucidate interesting features of the solutions. It was found that the presence of a magnetic field increased the motion of the mixture along the surface with increased values in the fluid-phase skin-friction coefficient. On the other hand, while the presence of a particle-phase viscosity increased the skin-friction coefficient for the particle phase, it produced reductions in the fluid-phase skin-friction coefficient. Allowing the particle phase to undergo a certain amount of slip at the interface between the layer of sediment and the mixture caused increases in the fluid-phase skin-friction coefficient and decreases in the particle-phase skin-friction coefficient. It is hoped that the present work be used as a vehicle for understanding other particle-phase stress models and other body force effects.

Nomenclature

a = particle radius
B_0 = magnetic induction
C_f = fluid-phase skin-friction coefficient ($C_f=(1-\alpha)\partial U/\partial\eta|_{\eta=0}$)
C_p = particle-phase skin-friction coefficient ($C_p=\alpha\beta\partial U_p/\partial\eta|_{\eta=0}$)
f = correction factor defined by Eq. (7)
g = gravitational acceleration
M = Hartmann number ($M^2=\sigma B_0^2 a^2/\mu$)
p = fluid-phase pressure
P = dimensionless fluid-phase reduced pressure
Re = particle Reynolds number ($\mathrm{Re}=ga^3\gamma/\nu^2$)
S = dimensionless particle-phase wall slip factor
t = time
u = fluid-phase x-component of velocity
U = dimensionless fluid-phase horizontal velocity ($U=\nu/(ga^2\gamma)u$)
v = fluid-phase y-component of velocity
V = dimensionless fluid-phase normal velocity ($V=\nu/(ga^2\gamma)v$)
x = distance along the surface
y = distance normal to the surface

Greek Symbols

α = volume fraction of particles
β = particle-to-fluid viscosity ratio ($\beta=\mu_p/\mu$)
α_m = dense sediment particulate volume fraction ($\alpha_m\simeq 0.6$)
η = dimensionless vertical distance ($\eta=y/a$)
γ = particle-to-fluid density ratio ($\gamma=\rho_p/\rho$)
μ = fluid-phase dynamic viscosity
ν = fluid-phase kinematic viscosity
ω = frequency of oscillation of wall velocity
ρ = fluid-phase density
σ = fluid-phase electrical conductivity
τ = dimensionless time ($\tau=ga\gamma/\nu t$)
τ_f = fluid-phase shear stress at the interface defined by Eqs. (49)
τ_p = particle-phase shear stress at the interface defined by Eqs. (49)

Subscripts

i = interface
p = particle phase
∞ = free stream

References

[1] Yiantsios, S. G., and Karabelas, A. J., 1998, ''The effect of gravity on the deposition of micron-sized particles on smooth surfaces,'' Int. J. Multiphase Flow, **24**, pp. 283–293.
[2] Jia, X., and Williams, R. A., 1990, ''Particle/deposition at a charged solid/liquid interface,'' Chem. Eng. Commun., **91**, pp. 127–198.
[3] Ven van de, T. G. M., 1989, *Colloidal Hydrodynamics*, Academic Press, London.
[4] Yao, K. M., Habibian, M. T., and O'Melia, C. R., 1971, ''Water and waste water filtration: concepts and applications,'' Environ. Sci. Technol., **5**, pp. 1105–1112.
[5] Adamczyk, Z., and van de Ven, T. G. M., 1981, ''Deposition of particles under external forces in laminar flow through parallel-plate and cylindrical channels,'' J. Colloid Sci., **80**, pp. 340–356.
[6] Adamczyk, Z., and van de Ven, T. G. M., 1982, ''Particle transfer to a plate in uniform flow,'' Chem. Eng. Sci., **37**, pp. 869–880.
[7] Marmur, A., and Ruckenstein, E., 1986, ''Gravity and cell adhesion,'' J. Colloid Interface Sci., **114**, pp. 261–266.
[8] Apazidis, N., 1985, ''On two-dimensional laminar flows of a particulate suspension in the presence of a gravity field,'' Int. J. Multiphase Flow, **11**, pp. 657–698.
[9] Apazidis, N., 1990, ''Temperature distribution and heat transfer in a particle-fluid flow past a heated horizontal plate,'' Int. J. Multiphase Flow, **16**, pp. 495–513.
[10] Dahlkild, A. A., 1997, ''The motion of Brownian particles and sediment on an inclined plate,'' J. Fluid Mech., **337**, pp. 25–47.
[11] Chen, C. P., and Wood, P. E., 1986, ''Turbulence closure modeling of the dilute gas-particle axisymmetric jet,'' AIChE J., **32**, pp. 163–166.
[12] Drew, D. A., and Segal, L. A., 1971, ''Analysis of fluidized beds and foams using averaged equations,'' Stud. Appl. Math., **50**, pp. 233–252.
[13] Gidaspow, D., 1986, ''Hydrodynamics of fluidization and heat transfer: super computer modelling,'' Appl. Mech. Rev., **39**, pp. 1–23.
[14] Tsuo, Y. P., and Gidaspow, D., 1990, ''Computation of flow patterns in circulating fluidized beds,'' AIChE J., **36**, pp. 888–896.
[15] Gadiraju, M., Peddieson, J., and Munukutla, S., 1992, ''Exact solutions for two-phase vertical pipe flow,'' Mech. Res. Commun., **19**, pp. 7–13.
[16] Wallis, G. B., 1969, *One-dimensional Two-phase Flow*, McGraw-Hill, New York.
[17] Kynch, G. J., 1952, ''A theory of sedimentation,'' Trans. Faraday Soc., **48**, pp. 166–176.
[18] Cramer, K. R., and Pai, S.-I., 1973, *Magnetofluid Dynamics for Engineers and Applied Physicists*, Scripta Publishing Company, Washington, D.C.
[19] Marble, F. E., 1970, ''Dynamic of dusty gases,'' Annu. Rev. Fluid Mech., **2**, pp. 397–446.
[20] Tam, K. W., 1969, ''The drag on a cloud of spherical particles in low Reynolds number flow,'' J. Fluid Mech., **38**, pp. 537–546.
[21] Soo, S. L., 1989, *Particulates and Continuum Multiphase Fluid Dynamics*, Hemisphere Publishing, New York, pp. 282 and 292.
[22] Chamkha, A. J., 1996, ''Compressible dusty-gas boundary-layer flow over a flat surface,'' ASME J. Fluids Eng., **118**, pp. 179–185.

Satoshi Watanabe
Associate Professor
Faculty of Engineering,
Kyushu University,
6-10-1 Hakozaki, Higashi-ku,
Fukuoka 812-8581 Japan

Hiraku Seki
Graduate Student

Seiji Higashi
Graduate Student

Kazuhiko Yokota
Research Associate

Yoshinobu Tsujimoto
Professor

Graduate School of Engineering Science,
Osaka University,
1-3 Machikaneyama, Toyonaka,
Osaka 560-8531 Japan

Modeling of 2-D Leakage Jet Cavitation as a Basic Study of Tip Leakage Vortex Cavitation

As the first step of the study of cavitation in the tip leakage flow in turbomachinery, experimental and numerical investigations on characteristics of 2-D leakage jet cavitation are conducted. The experiments using 2-D model apparatus are carried out for three values of initial pressure and for three values of tip clearance. The numerical methods are constructed by combining the vortex method with three types of cavity models. Through the comparisons with the experiments, it is found that one of the models, which takes account of the effects of cavity behavior on the ambient flow, simulate the location and the size of the cavity fairly well in spite of its simplicity. [DOI: 10.1115/1.1340634]

Introduction

Liquid fuel and oxidizer turbopumps for rocket engines are usually operated under cavitating condition with quite high rotational speed to attain high pressure performance with their minimum size and weight. Under such conditions, inducers easily fall into the unstable operation with severe cavitation instabilities such as cavitation surge (Young [1]) and rotating cavitation (Kamijo et al. [2]). These cavitation instabilities have been found to be caused by the positive mass flow gain factor, meaning that the cavity volume increases if the flow rate is decreased (Young [1] and Tsujimoto et al. [3]). Thus, it is important to predict the cavitation characteristics such as mass flow gain factor and cavitation compliance. The latter is defined as the cavity volume increase due to the unit inlet pressure decrease.

Cavitation occurring in inducers can be classified into two types—blade cavitation and tip leakage cavitation. The former has been extensively studied, and it has made it possible to predict theoretically the values of mass flow gain factor and cavitation compliance (Brennen [4] and Otsuka et al. [5]). On the contrary, tip leakage cavitation is caused by the leakage flow driven by the pressure difference between pressure and suction sides. It occurs mainly in the low pressure region in the vortex core formed by rolling up of the shear layer between tip leakage flow and main flow, and also in the low pressure region of the shear layer. A large amount of tip vortex cavitation is generally found in real inducers. However, only a few studies have focused on the understanding of basic characteristics of tip leakage cavitation. The tip leakage cavitation sometimes has a very complicated structure with not only the tip vortex cavitation but also the cavitation in the shear layer. In the present study, we consider the simple case only with the tip vortex cavitation, which is also observed in real situations with larger tip clearance.

Rains [6] first proposed applying the slender body approximation to the tip leakage vortex, in which three-dimensional tip leakage flow is simulated by a two-dimensional unsteady cross flow. This method is further applied by Chen et al. [7] and examined by comparisons with experiments. However, the effects of cavity development are not included in these studies.

In the present study, as the first step of the study of three-dimensional tip leakage cavitation, numerical and experimental investigations on a two-dimensional leakage jet cavitation are carried out. Several two-dimensional analytical methods are proposed and examined by two-dimensional experiments. In the experimental study, the behavior of cavity in the tip leakage flow, especially its growing process and movement, is investigated by using two-dimensional apparatus. The numerical study uses a vortex method which includes the effect of cavity growth. Three simple models are proposed for the tip leakage cavitation. These models are validated through the comparisons with experiments, mainly focusing on the effects of the downstream pressure and the thickness of tip leakage jet on the cavity behavior.

Experimental Apparatus and Procedure

Figure 1 shows the experimental apparatus. It consists mainly of a small two-dimensional water tank with 20 mm depth and a wall representing the blade with a small clearance at one end. The tip of the wall is rounded to prevent the cavity in the clearance. On the left-hand side of the wall (upstream side), a vertically movable piston is placed on the bottom of the tank. On the other side (downstream side), an air chamber is placed. The initial pressure is adjusted by using a vacuum pump. The tip leakage flow is induced by (i) lowering the internal pressure at least below the ambient pressure, (ii) pulling out the piston and keeping the displacement to 10 mm from the wall, (iii) releasing the piston. Then, the piston is driven by the pressure difference across it, and a certain amount of water is injected downstream until the piston collides on the lower wall. The cavity initiated in the vortex core rapidly grows as long as the leakage jet lasts, and shrinks just after the collision of the piston on the casing wall. In the present study, we focus only on the growth phase because the collapse phase is not a natural one.

The velocity of the tip leakage flow, the unsteady downstream pressure, and the cavity behavior such as the trajectory and the size of cavity, are observed in the experiments. The velocity of the tip leakage flow can be estimated by taking the time derivative of

Contributed by the Fluids Engineering Division for publication in the JOURNAL OF FLUIDS ENGINEERING. Manuscript received by the Fluids Engineering Division March 22, 2000; revised manuscript received October 13, 2000. Associate Editor: J. Katz.

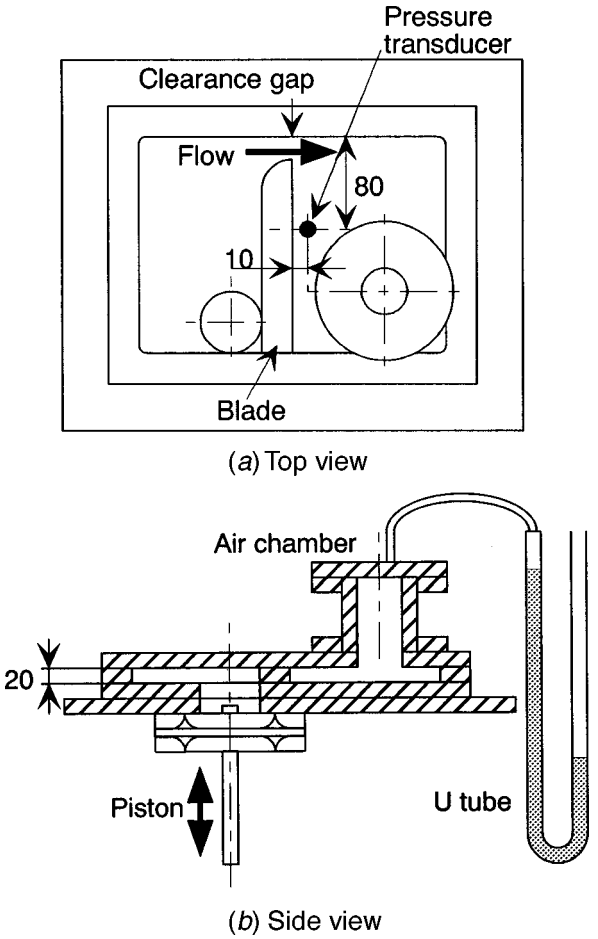

Fig. 1 Experimental apparatus

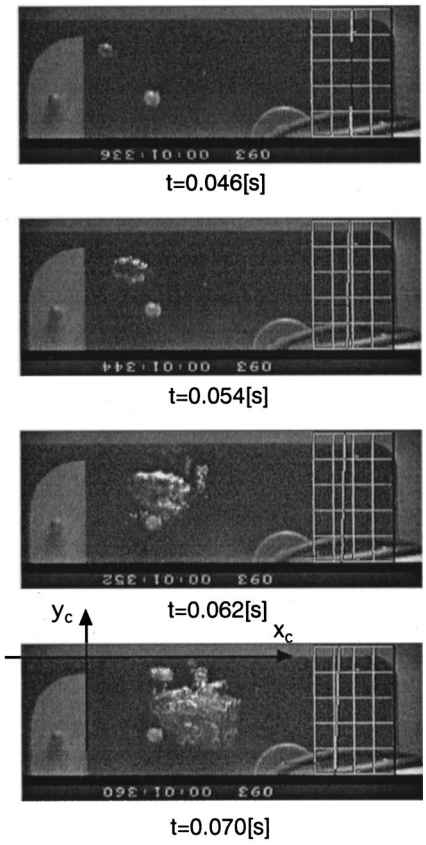

Fig. 2 Example of pictures of cavitation in the two-dimensional tip leakage flow (τ=6.2 [mm], P_0=5 [kPa])

the displacement of the piston which is measured by a gap sensor. The unsteady downstream pressure is measured by a pressure transducer at the location shown in Fig. 1(*a*). Because it was found that the pressure transducer had a different gage factor at large negative pressure, a calibration was made at negative pressure by using a U-tube manometer filled with mercury. The trajectory of the cavity and the cavity size are estimated from the high-speed video pictures (500 frames/s). It was found from the video pictures taken from the side that the cavity is almost two-dimensional and cylindrical except just after the inception of the cavity. The cavity initiates near the upper wall, but grows rapidly mainly to the spanwise direction. Then, the cavity becomes almost cylindrical and grows gradually to the radial direction. So we evaluate the cavity size by the area viewed from the top and the trajectory of the cavity by the location of the center of cavity. Figure 2 shows examples of the high-speed video pictures. The cavity is observed clearly enough for the estimation of the size and the location of the cavity.

Experiments were made for various values of the initial pressure P_0 and the tip clearance τ. The initial pressure was set by adjusting the pressure in the air chamber using a vacuum pump. It should be noted that, by changing the tip clearance τ, the velocity of the tip leakage flow varies in accordance with the variation of the tip clearance.

Distilled water is used and is sufficiently deaerated to avoid the influence of inpurities as much as we can. We have confirmed that we can diminish the influence of the water quality on the growth of the cavity by deaerating the tested water for more than 6 hours. However, the cavitation inception might be very sensitive to the water quality, so we abandoned getting to the study on the cavitation inception.

The repeatability is also confirmed by carrying out the same experiment several times for the same condition. In this paper, results are averaged with three to five samples for each condition. Table 1 summarizes the experimental conditions. Initial downstream pressure is represented by nominal values with real values shown in the parenthesis. Vapor pressure is estimated from the water temperature.

Uncertainties for each measurement are estimated as follows. The uncertainty in the velocity of the leakage flow is less than 5 percent of the velocity because it depends mainly on the uncertainty of the initial displacement of the piston. The piston can be set to be 10.0 [mm] with the error less than 0.5 [mm]. The uncertainty in the pressure depends mainly on the calibration using the U-tube filled with mercury. The error for reading the height of the mercury column is less than 0.5 [mm], which results in the uncertainty in the pressure of 0.1 [kPa] at most. The cavity behavior, especially the cavity size, is difficult to measure accurately from the high-speed video pictures. Results obtained in the present

Table 1 Experimental Conditions

	Clearance, τ [mm]	Initial pressure, P_0 [kPa]	Vapour pressure, p_v [kPa]
Case 1	6.2	5 (5.1)	1.7
Case 2		7 (6.9)	1.7
Case 3		9 (9.2)	1.7
Case 4	4.4	5 (5.0)	1.5
Case 5	9.6	5 (4.5)	1.5

study might contain the error of 5 percent. The location of the center of the cavity can be estimated with the error less than 1 [mm] if the center of the cavity is clearly identified. It should be noted that the time resolution in the estimations of cavity behavior is 2 [ms], which comes from the frame rate of the high-speed video camera, 500 [frames/s].

There should be a certain similitude to generalize the characteristics of leakage cavitation, and the results should be shown in the nondimensional form. However, we could not find any nondimensional parameters with the small number of our trail data. So, hereafter, the results are represented in the dimensional form.

Analysis by Vortex Method

Fundamental Flow Field. As shown in Fig. 3, the two-dimensional tip leakage flow field can be modeled by a source distribution q_J representing the tip leakage jet and discrete free vortices Γ_k representing the shear layer, which are released from the tip of the blade. The effects of walls far downstream are ignored for simplicity. Tip leakage vortices Γ_k are released for each time step corresponding to the temporal jet velocity. The velocity induced by the growth of the cavity is represented by a free source whose strength is determined from the cavity growth, as described in the following section. Thus, the velocity field at the time $t=n\Delta t$ can be represented as the total of the complex potential induced by (i) the source distribution of tip leakage jet q_J, (ii) the free vortices Γ_k representing the shear layer, and (iii) the source q_B representing the cavity. Boundary conditions on the upper wall and the blade can be satisfied by introducing the mirror images of singularities. Denoting the complex potentials of (i)–(iii) by W_J, W_V, and W_B, the complex potential can be represented as follows.

$$W=W_J+W_V+W_B \tag{1}$$

The complex potential representing the tip leakage jet W_J can be represented by distributing the constant source q_J between $y=-\tau$ and τ along the y-axis.

$$W_J=\int_{-\tau}^{\tau}\frac{q_J}{2\pi}\ln(z-i\eta)d\eta$$

$$=\frac{q_J}{2\pi}[(z-i\tau)\ln(z-i\tau)-(z+i\tau)\ln(z+i\tau)] \tag{2}$$

where $q_J=2U_J(t)$ with $U_J(t)$ denoting the velocity of the tip leakage jet.

The complex potential of free vortices W_V can be represented as follows.

$$W_V=\sum_{k=1}^{n}\frac{i\Gamma_k}{2\pi}[\ln(z-z_k)+\ln(z+z_k)-\ln(z-z_k^*)-\ln(z+z_k^*)] \tag{3}$$

where z_k is the location of the free vortex Γ_k and * denotes the complex conjugate. The strength of the vortices Γ_k is determined from the leakage velocity at $t=k\Delta t$ as $\Gamma_k=[U_J(k\Delta t)]^2\Delta t/2$, and it is introduced at the location of $(\Delta x_k,-\tau)$ where $\Delta x_k=U_J(k\Delta t)\Delta t/2$.

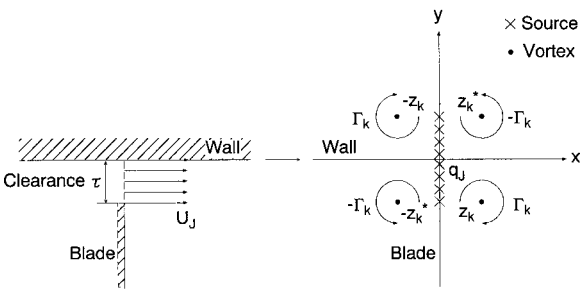

Fig. 3 Model for present calculation

The complex potential W_B representing the cavity growth is represented as follows by assuming that the cavity is cylindrical.

$$W_B=\frac{q_B}{2\pi}[\ln(z-z_B)+\ln(z+z_B)+\ln(z-z_B^*)+\ln(z+z_B^*)] \tag{4}$$

where z_B is the center of cavity. The strength of source q_B is represented by $q_B=2\pi RdR/dt$, where $R(t)$ is the radius of cavity.

The free vortices Γ_k and the free source q_B are convected on the free velocity which can be obtained by taking z-derivative of the complex potential of Eq. (1). The cavity radius R and the growth rate dR/dt are still unknown for the determination of the flow field.

Evaluation of Cavity Growth. It is assumed that the cavity initiates at the location where the pressure first becomes lower than the vapor pressure p_v. It is also assumed that the cavity consists of a single small spherical or cylindrical bubble. We introduce here three types of cavity model (I)–(III), and only the model (III) considers the effect of cavity growth on the flow field through the complex potential of W_B.

(I) The cavity size is simply estimated from the area where the pressure is lower than the vapor pressure p_v.

(II) We assume that a single spherical cavity initiates at the location of the minimum pressure $p_{\min}$. The radius of spherical cavity R is determined by the following Rayleigh-Plesset equation with the minimum pressure $p_{\min}$.

$$R\frac{d^2R}{dt^2}+\frac{3}{2}\left(\frac{dR}{dt}\right)^2=-\frac{p_{\min}-p_v}{\rho} \tag{5}$$

Then, the cavity size is evaluated as the base area of a cylinder with its height of 20 mm (= channel height) with the same volume as that of spherical bubble obtained above.

(III) Here, we derive the equation for the growth of cylindrical cavity from the unsteady version of Bernoulli equation. Applying it between the cavity surface C $(z=z_B+Re^{i\theta})$ and the location of the pressure measurement $(z=z_\infty)$, and then assuming that the pressure on the cavity surface equals the vapor pressure, we can obtain the following equation.

$$\left[\mathrm{Re}\left(\frac{\partial W_B}{\partial t}\right)+\frac{1}{2}w_Bw_B^*+\frac{1}{2}(w_Bw_{J+V}^*+w_B^*w_{J+V})\right]_{z=z_\infty}^{C}=\frac{p_\infty'-p_v}{\rho} \tag{6}$$

where

$$\frac{p_\infty'}{\rho}=\frac{p_\infty}{\rho}-\left[\mathrm{Re}\left(\frac{\partial W_{J+V}}{\partial t}\right)+\frac{1}{2}w_{J+V}w_{J+V}^*\right]_{z=z_\infty}^{C} \tag{7}$$

and [ ] in Eqs. (6) and (7) means to subtract the value at $z=z_\infty$ from the value on the cavity surface C. Moreover, $W_{J+V}=W_J+W_V$ and $w_{J+V}=w_J+w_V$ with $w_{J,V,B}=\partial W_{J,V,B}/\partial z$ denoting the velocities induced by the leakage jet, the free vortices and the free source, respectively. The pressure p_∞' is a virtual pressure on the cavity surface, obtained by subtracting pure effects of the leakage jet and the free vortices from the downstream pressure p_∞. Because we assume a small cylindrical cavity, we can estimate the values of W_{J+V} and w_{J+V} at the center of cavity instead of those on the cavity surface.

We assume here that the distances between the free source representing the cavity and its mirror images are sufficiently small compared with that between the cavity and the location of pressure measurement. Moreover, we approximate the moving velocity of the cavity by w_{J+V}. Combining Eqs. (4) and (6) with the relation of $q_B=2\pi RdR/dt$, it can be easily found that the highest order time-derivative of cavity radius is included as Rd^2R/dt^2 in

the first term of the left-hand side of Eq. (6). Then we can represent Eq. (6) as follows, which determines the cavity growth.

$$\frac{d^2R}{dt^2} = f\left(R, \frac{dR}{dt}, z_B, z_\infty, w_{J+V}, \frac{p'_\infty - p_v}{\rho}\right) \tag{8}$$

The cavity size is evaluated as the area of circle with its radius of R.

In all calculations, the experimental values of the velocity of the tip leakage jet $U_J(t)$ and the downstream pressure p_∞ at the pressure tap shown in Fig. 1 are used. The initial radius of the cavity is set to be 0.005 [mm] after confirming that its influence can be seen only for a few time steps just after the inception. The time increment is set to be $\Delta t = 0.39$ [μs]. It is also confirmed that the result of the calculation by the model (III) with the smaller time increment shows that the global behavior does not largely change although the cavity initiates earlier.

Results and Discussions

Comparisons Among Calculations. Here, to examine the validity of the numerical models (I)–(III), the comparisons among the numerical results and also with the experimental result are made for the case with the initial pressure of $P_0 = 5$ [kPa] and the tip clearance of $\tau = 6.2$ [mm]

Figure 4 shows the time histories of the cavity behavior obtained by the experiment and the three numerical models. As shown in Fig. 4(*a*), the trajectory of the center of cavity is well simulated by all calculations. Figure 4(*b*) shows the time history of the cavity size. It can be seen that the result calculated with the model (III) agrees well with the experimental one while the cavity size is over-estimated in the calculations with the models (I) and (II). The reason can be related with the distribution of the discrete vortices. As shown in Fig. 5(*a*), in the calculations with the models (I) and (II), the discrete vortices shed from the tip are gather-

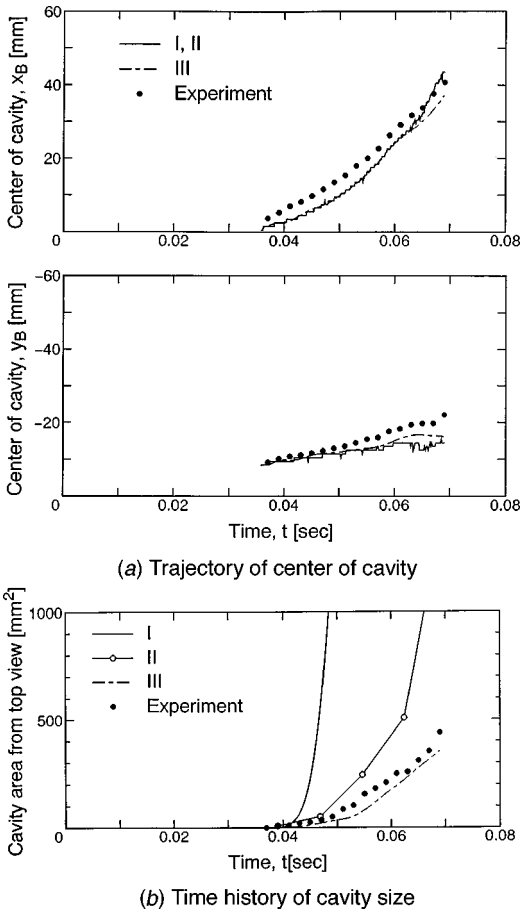

Fig. 4 Comparisons of cavity behavior between calculations (I)–(III) and experiment ($\tau = 6.2$ [mm], $P_0 = 5$ [kPa]. Uncertainties in the location of center of cavity and cavity size are 1 [mm] and 20 [mm^2], respectively).

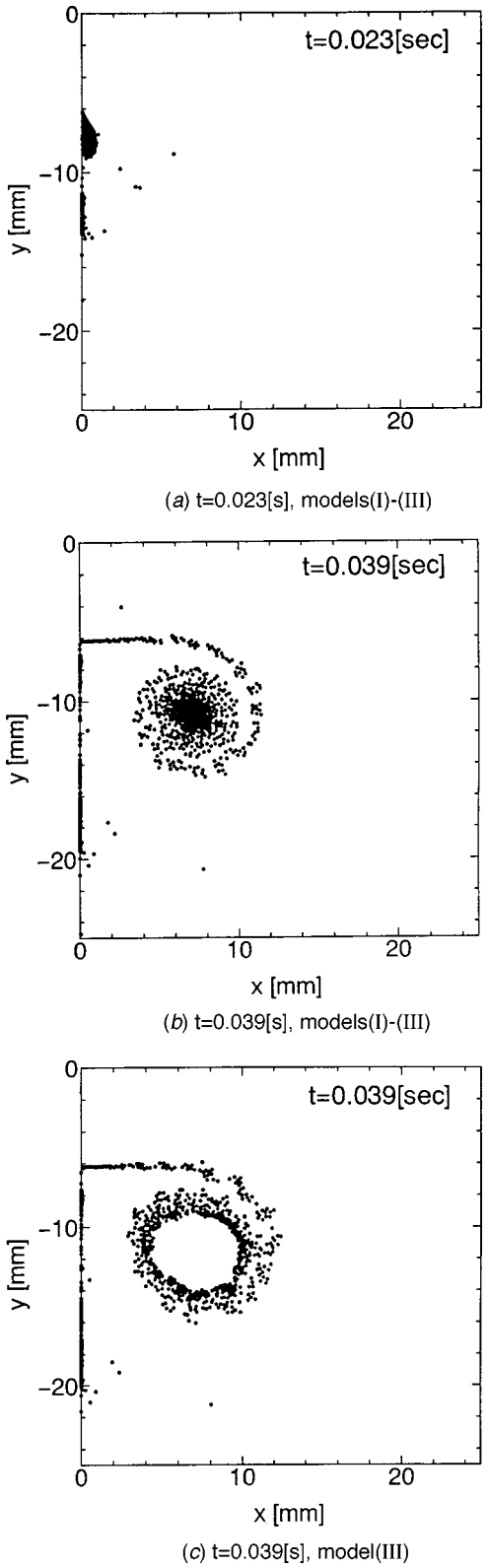

Fig. 5 Comparisons of distributions of discrete vortices between calculations (I)–(II) and (III) ($\tau = 6.2$ [mm], $P_0 = 5$ [kPa])

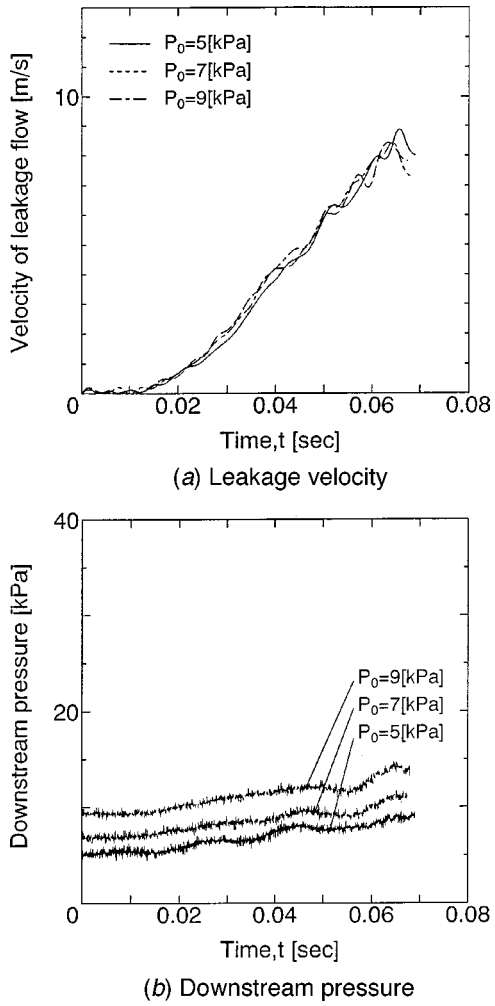

Fig. 6 Time histories of leakage velocity and downstream pressure (τ=6.2 [mm], P_0=5, 7 and 9 [kPa]. Uncertainties in the leakage velocity and downstream pressure are 0.5 [m/s] and 0.1 [kPa], respectively).

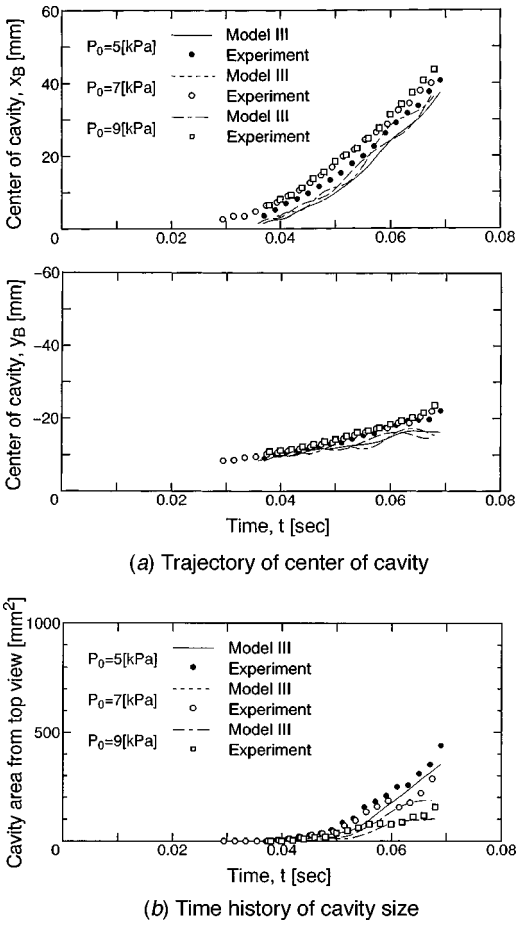

Fig. 7 Influence of downstream pressure on cavity behavior (τ=6.2 [mm], P_0=5, 7 and 9 [kPa]. Uncertainties in the location of center of cavity and cavity size are 1 [mm] and 20 [mm^2], respectively).

ing at the center of vortex core, and the pressure there continues to decrease even after the inception of the cavity. Thus, the cavity grows rapidly with the decreasing minimum pressure. On the other hand, in the calculation with model (III), the discrete vortices around the center of vortex core are scattered due to the cavity growth, and the pressure there does not decrease so much with the sparse population of vortices, resulting in the gradual cavity growth.

Because the model (III) is found to simulate the cavity behavior the best, discussions below are made based on the results of the calculation with model (III).

Influence of Downstream Pressure on Cavity Behavior. In this section, to examine the influence of the downstream pressure on the cavity behavior, experiments under various initial pressure conditions were carried out. Also, the calculations using the model (III) were made and validated through the comparisons with the experimental results.

Figure 6 shows the time histories of the velocity of the tip leakage jet and the downstream pressure obtained by the experiments under various initial pressure conditions (P_0=5,7,9 [kPa]) for the case with the tip clearance of τ=6.2 [mm]. From the time history of leakage velocity shown in Fig. 6(*a*), we can see that the leakage velocity is almost independent of the initial pressure. On the other hand, the curves of the downstream pressure are parallel with each other for all conditions. The leakage velocity was expected to be almost independent of the initial pressure in the present study because the piston is driven by the pressure difference between the initial pressure (5–9 kPa) and the ambient pressure (100 kPa) which for the present apparatus was minimally varied. It should be noted that this independence might be only seen in the present experimental apparatus and not applicable to many 3-D flow situations.

Figure 7 shows the experimental and numerical results of the cavity behavior under the same conditions as in Fig. 6. The calculation is made with the model (III). From the trajectory of the center of the cavity shown in Fig. 7(*a*), we can see that the experimental and numerical results are in reasonable agreement although the cavity initiates earlier and moves a little faster in the experiments than in the calculations. It is unknown what causes these discrepancies in the time scale offsets when using the numerical model. Figure 7(*b*) shows the time histories of cavity size. As is easily imagined, it can be seen in both experimental and numerical results that the cavity becomes larger for the case with the lower initial pressure. The present numerical model (III) can fairly well simulate the influence of the downstream pressure on the behavior of the tip leakage cavitation.

Influence of Tip Clearance on Cavity Behavior. It is interesting and desirable to examine the influence of both the tip leakage velocity and the gap of the tip clearance on the behavior of the cavity. However, our experimental setup cannot change them independently. So, in this section, we examine the cavity behavior experimentally for the cases with three values of the tip clearance gap. We should note that the leakage flow velocity also varies

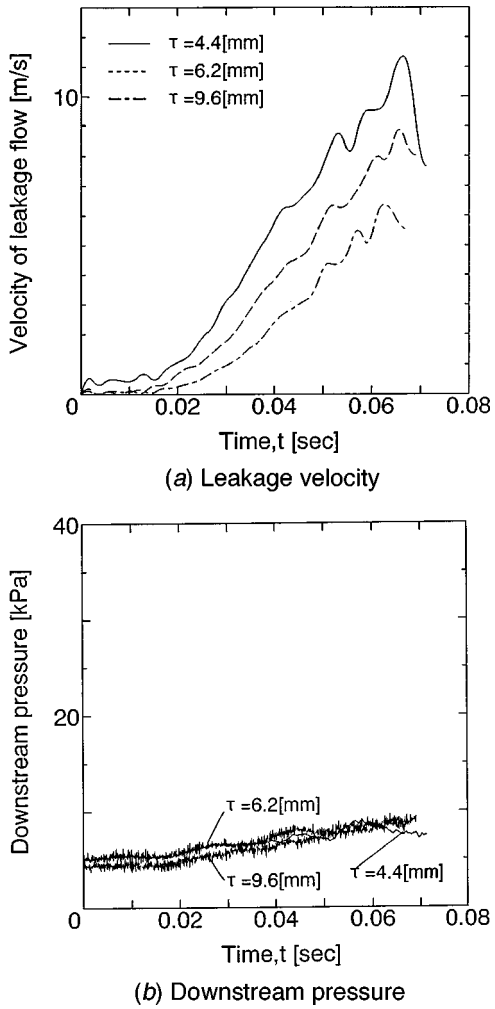

Fig. 8 Time histories of leakage velocity and downstream pressure (τ=4.4, 6.2 and 9.6 [mm], P_0=5 [kPa]. Uncertainties in the leakage velocity and downstream pressure are 0.5 [m/s] and 0.1 [kPa], respectively).

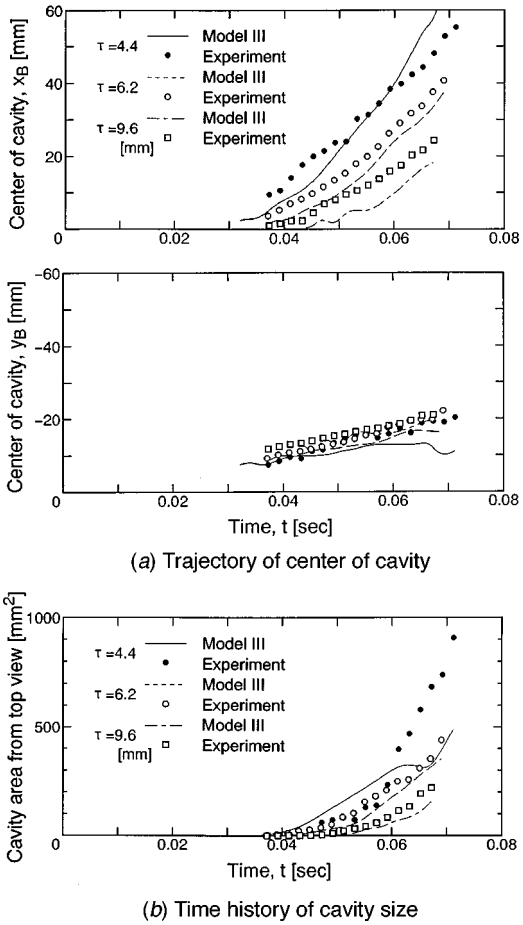

Fig. 9 Influence of tip clearance τ on cavity behavior (τ=4.4, 6.2 and 9.6 [mm], P_0=5 [kPa]. Uncertainties in the location of center of cavity and cavity size are 1 [mm] and 50 [mm^2], respectively).

with the variation of the tip clearance gap. The calculations using the model (III) were also carried out and compared with the experimental results.

Figure 8 shows the time histories of the velocity of the tip leakage jet and the downstream pressure obtained by the experiments with various tip clearance of τ=4.4, 6.2 and 9.6 [mm]. The initial pressure is set to be P_0=5 [kPa]. From the time history of the leakage velocity shown in Fig. 8(*a*), we can see that the leakage velocity is larger for the smaller tip clearance. It was confirmed that the displacement of the piston, which drives the tip leakage flow, did not change very much depending on the tip clearance. The time history of the downstream pressure is almost independent on the tip clearance as shown in Fig. 8(*b*).

Figure 9 shows the experimental and numerical results of the cavity behavior under the same conditions as in Fig. 8. From the trajectory of the center of the cavity shown in Fig. 9(*a*), we can see that the cavity moves faster for the cases with the smaller tip clearance. This is simply because the leakage velocity is larger with the smaller tip clearance. Figure 9(*b*) shows the time histories of the cavity size. We can see that the cavity is larger for the case with the smaller tip clearance. It is conjectured that the large velocity of the tip leakage jet due to the small clearance makes the tip vortex stronger. This results in the lower minimum pressure and in the larger tip vortex cavity. It is also shown that the present numerical model simulates the behavior of the cavity well until the size of cavity becomes quite large compared to the tip clearance. However, the discrepancies with the experiments are more remarkable when the cavity is larger. This is considered to be the limitation of the application of the numerical model based on the assumption of small cylindrical cavity.

Conclusion

Results obtained in the present study can be summarized as follows.

1 A simple numerical model based on the assumption of single small cylindrical cavity (Model III) is proposed to simulate the two-dimensional tip leakage jet cavitation.

2 Higher initial pressure makes the cavity smaller simply because the pressure around the cavity becomes higher in this case. The proposed numerical model (III) succeeded in simulating this tendency.

3 The cavity is smaller for the case of larger tip clearance in the system examined. This is caused by smaller tip leakage jet velocity. This tendency is also simulated by the proposed numerical model.

The numerical model proposed in the present study is found to be able to simulate the two-dimensional cavitation in tip leakage vortex. The present 2-D unsteady model should be adapted to simulate 3-D steady tip leakage cavitation by applying a slender body approximation as proposed by Rains [6]. The authors are currently completing this adaption.

Nomenclature

f = function representing cavity growth, defined in Eq. (8)
i = imaginary unit
P_0 = initial pressure in experiments
$p_{\min}$ = minimum pressure in the flow field
p_v = vapor pressure
p_∞ = downstream pressure
p'_∞ = virtual pressure, defined in Eq. (7)
q = strength of source
R = radius of cavity
t = time
x, y = coordinates
U_j = velocity of tip leakage jet
W = complex potential
w = complex conjugate velocity
z = complex coordinate, $=x+iy$
Δt = time increment
Δx = location of introduction of new vortices
Γ = strength of vortices
ρ = density
τ = tip clearance

Superscript

$*$ = complex conjugate

Subscripts

B = values concerning source representing cavity development
J = values concerning tip leakage jet
k = index of vortices
V = values concerning vortices
∞ = values at pressure tap

References

[1] Young, W. E., 1972, ''Study of Cavitating Inducer Instabilities, Final Report,'' NASA-CR-123939.
[2] Kamijo, K., Yoshida, M., and Tsujimoto, Y., 1993, ''Hydraulic and Mechanical Performance of LE-7 LOX Pump Inducer,'' AIAA Journal of Propulsion and Power, **9**, No. 6, pp. 819–826.
[3] Tsujimoto, Y., Kamijo, K., and Yoshida, Y., 1993, ''A Theoretical Analysis of Rotating Cavitation in Inducers,'' ASME J. Fluids Eng., **115**, pp. 135–141.
[4] Brennen, C. E., 1978, ''Bubbly Flow Model for the Dynamic Characteristics of Cavitating Pumps,'' J. Fluid Mech., **89**, pp. 223–240.
[5] Otsuka, S., Tsujimoto, Y., Kamijo, K., and Furuya, O., 1996, ''Frequency Dependence of Mass Flow Gain Factor and Cavitation Compliance of Cavitating Inducers,'' ASME J. Fluids Eng., **118**, pp. 400–408.
[6] Rains, D. A., 1954, ''Tip Clearance Flows in Axial Compressors and Pumps,'' California Institute of Technology, Hydrodynamic and Mechanical Engineering laboratories Report No. 5.
[7] Chen, G. T., Greitzer, E. M., Tan, C. S., and Marble, F. E., 1991, ''Similarity Analysis of Compressor Tip Clearance Flow Structure,'' ASME J. Turbomach., **113**, pp. 260–271.

T. A. Waniewski
Research Scientist,
Naval Hydrodynamics Division,
Science Applications International Corporation,
10260 Campus Point Dr., M/S C4,
San Diego, CA 92121

C. E. Brennen
Professor of Mechanical Engineering

F. Raichlen
Professor of Civil and
Mechanical Engineering

Division of Engineering
and Applied Science,
California Institute of Technology,
Mail Code 104-44
Pasadena, CA 91125

Measurements of Air Entrainment by Bow Waves

This paper describes measurements of the air entrained in experiments simulating the breaking bow wave of a ship for Froude numbers between two and three. The experiments and the characteristics of the wave itself are detailed in T. Waniewski, 1999, ''Air Entrainment by Bow Waves; Ph.D. theses, Calif. Inst. of Tech.'' The primary mechanism for air entrainment is the impact of the plunging wave jet, and it was observed that the air bubbles were entrained in spatially periodic bubble clouds. The void fraction and bubble size distributions were measured in the entrainment zone. There were indications that the surface disturbances described in Waniewski divide the plunging liquid jet sheet into a series of plunging jets, each of which produces a bubble cloud.
[DOI: 10.1115/1.1340622]

1 Introduction

To our knowledge, there are no records in the literature of void fraction and bubble size distribution measurements beneath breaking bow waves in the field, probably because this type of experiment would be exceedingly difficult and costly. There have been, however, studies which measure void fraction and bubble size distributions beneath other types of plunging breaking waves including white caps, and two-dimensional and three-dimensional plunging waves created in laboratory wave tanks. An early example is the measurement of bubble size distributions under white caps by Blanchard and Woodcock [1]. Later, sets of void fraction measurements were made by Lamarre and Melville for two-dimensional plunging waves [2], three-dimensional plunging waves [3], and white caps [4] using impedance-based void fraction instrumentation. They observed that wave breaking creates a bubble cloud which can have a void fraction as high as 30–40 percent. This cloud, primarily comprised of millimeter sized bubbles, then degasses rapidly leaving behind a diffuse plume of microbubbles. Bubble production rates and size distribution measurements for the larger bubbles were made by Cipriano and Blanchard [5] and Loewen et al. [6], among others. Bubble populations in fresh and salt water were compared in studies such as Cartmill and Su [7] and Loewen et al. [6]; bubble plumes in fresh water contain a larger number of smaller bubbles than those in salt water.

Bow waves are continuously breaking plunging waves, and Chanson and Cummings [8] found that the air entrainment process for plunging, breaking waves is similar to that for an inclined plunging jet in cross flow. Studies concerning gas entrainment by plunging liquid jets are summarized in a recent review by Bińk [9] show that the nature of the air entrainment process depends on a number of parameters including the flow rate, jet surface turbulence, and jet geometry. Chanson and Cummings [10] use the information from these works to predict the volume rate of air entrainment, bubble sizes, and bubble penetration depth for plunging breakers and demonstrate good comparison with the experimental field data.

Lamarre and Melville [2] showed that the air entrainment process is closely coupled with the breaking wave dynamics, but virtually all of the investigations described above focus on ''two-dimensional'' wave breaking and there is little information on the highly three-dimensional processes which occur in breaking bow waves. The research presented herein used a three-dimensional simulated bow wave, described by Waniewski [11], which allowed for detailed examination of the wave breaking and air entrainment processes. One set of experiments were performed in a 40 m long recirculating flume and are referred to herein as the large flume experiments. The waves were created by a deflecting plate mounted at an angle to the oncoming supercritical flow in the flume. The Froude number of these flows was limited by the flume and ranged from two to three.

2 Experimental Equipment

The 40 m flume is 109 cm wide and 61 cm deep with 1.3 cm thick tempered glass sidewalls and a stainless steel bottom plane to within ± 2.5 mm. It was filled with city tap water at about 23°C. Flow rate, Q, is measured using a venturi meter and the depth, d, is measured with a point gage. The maximum discharge is approximately 0.394 m^3/s. To create a super-critical flow, a 20.3 cm high two-dimensional spillway section was installed at the upstream end of the flume, downstream of a 8.1 m long reservoir. The test section is located approximately 24 m (or over 200 depths for the flows investigated) downstream of the spillway. This location ensured a fully developed flow and also gave the air bubbles entrained in the flow downstream of the deflecting plate the maximum time to settle out. Here, a 75 cm long by 50 cm high lucite plate was mounted at an angle θ to the oncoming flow to simulate a wedge shaped hull with half angle θ. The plate's leading edge was machined to a sharp edge and displaced 12 cm from the flume sidewall to reduce the effect of the boundary layer on the wall of the flume. A steady breaking wave, similar to that observed at the bow of a ship, is created as the flow rides up on the plate.

An impedance based void fraction meter (IVFM) was developed to measure the void fraction, α, in these high speed, unsteady, multiphase flows. The IVFM probe, based on a design by Chanson [12] consisted of two concentric stainless steel electrodes, as shown in Fig. 1. The probe tip was aligned with the direction of the bubble velocity, and its small dimensions allowed it to respond to individual bubbles. The impedance across the two electrodes, which increased with void fraction, was mainly resistive for excitation frequencies below the megahertz level. The electronics were designed to detect a 1 mm diameter bubble moving at 2 m/s; therefore, the minimum frequency response required was 4 kHz. The present experiments used 500 kHz excitation at

Contributed by the Fluids Engineering Division for publication in the JOURNAL OF FLUIDS ENGINEERING. Manuscript received by the Fluids Engineering Division June 4, 1999; revised manuscript received October 17, 2000. Associate Editors: M. Sommerfeld and J. Katz.

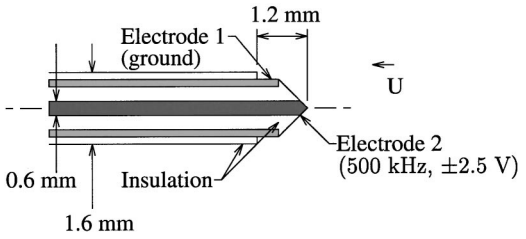

Fig. 1 Cross sectional view of the IVFM probe (not to scale).

the level of ±2.5 V applied to the inner electrode, and the outer electrode was grounded. The output was low-pass filtered with a cutoff of 40 kHz and demodulated to provide a DC signal proportional to the local void fraction.

Single bubble tests were conducted to determine the sensitivity of the IVFM probe to bubble position. The probe was mounted in a tank of water with the tip pointing downward. Single bubbles were intermittently released from a stainless steel tube installed several centimeters below the probe. The bubbles were of uniform 5 mm diameter just before release and deformed as they traveled upward as shown in Fig. 2. The high speed video camera and the IVFM data acquisition system were triggered simultaneously at time $t=0$ ms. Figure 3 shows the voltage signal corresponding to the images shown in Fig. 2. Correlation of numerous images and voltage signals like these confirmed that a large negative voltage pulse is produced each time a bubble impacted the probe. The pulse width was defined as the time difference between the two crossings of a particular voltage level. The pulse amplitude and width were sensitive to the lateral location of the bubble at impact and this relationship is defined in Waniewski [11].

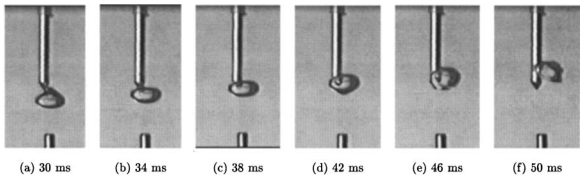

Fig. 2 Frames from high speed video of the single bubble tests showing the IVFM probe tip above the tube which released the bubbles. The time is noted beneath each frame.

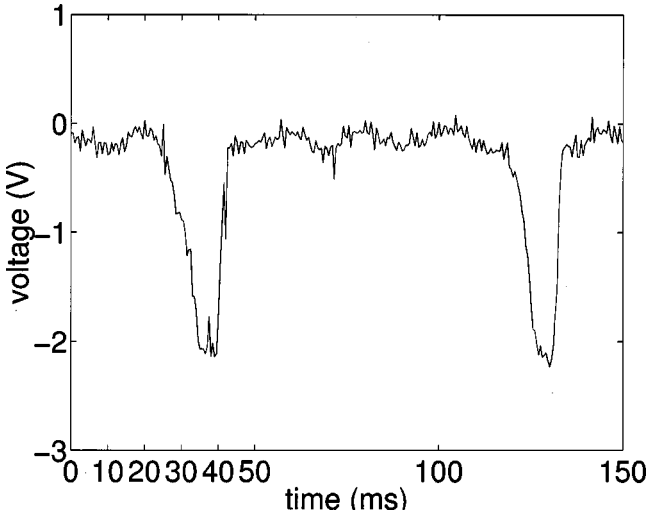

Fig. 3 Typical IVFM signal from the single bubble tests; the frames from the corresponding high speed video are shown in Fig. 2.

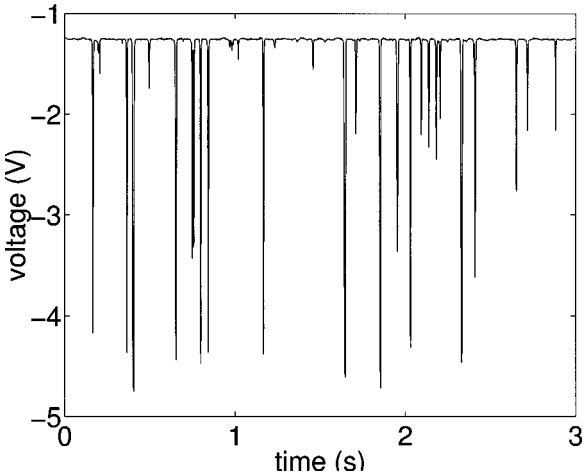

Fig. 4 Typical IVFM signal from the calibration experiments. A voltage of −1.2 V occurs when no air bubbles are touching the probe tip, and each large negative pulse corresponds to an air bubble encounter.

A vertical two-phase flow facility (see Kytomaa [13]) was used to calibrate the IVFM. It included a 10.2 cm working section with an air injector at the lower end. The injector produced air bubbles of uniform diameter of roughly 5 mm. Two static pressure taps located 1.1 m apart, and approximately equally spaced above and below the downward-pointing IVFM probe, were connected to an inverted manometer. The reading from this manometer provided the steady-state void fraction, α. The IVFM signal was sampled at 2 kHz; a typical signal corresponding to $\alpha=4.31$ percent is shown in Fig. 4. High speed videos confirmed that each pulse corresponded to the impact of a bubble on the probe tip. The IVFM signals were digitally processed using a fourth order Butterworth filter with a cutoff frequency of 1 kHz. Forward and reverse filtering were used to prevent phase distortion, and the mean noise level was subtracted from each signal to compensate for any drift in the IVFM electronics.

The void fraction was calculated from the processed signal using a procedure suggested by Ishii [14] for Eulerian time averaging of two phase flow mixtures. The phases are designated by the subscript k where $k\in\{1,2\}$. The state density function, M_k, for the *kth* phase at location x and time t is defined as taking a value of unity when the *kth* phase is detected and zero when it is absent. The time averaged phase density function or void fraction, α_k, is then given by

$$\alpha_k(x_o,t_o)=\lim_{\delta\to 0}\frac{1}{\Delta t}\int_{[\Delta t]}M_k(x_o,t)dt \tag{1}$$

where δ is the interfacial region thickness (assumed to be small), x_o is a reference location, and t_o is a reference time. The time interval Δt is fixed and large enough to smooth out local variations in flow properties. Since the actual electronic output was not a simple binary signal, it was necessary to use a threshold output value to convert it to either a zero or unit value of $M_k(x,t)$ so that α could be calculated (Waniewski [11]). Similar methods have been used by other researchers using conductivity probes to measure void fraction (see, for example, Teyssedou et al. [15]).

The calibration was repeated on four different days, and a typical calibration curve is shown in Fig. 5. The void fractions were estimated using three different IVFM signal thresholds. A threshold of −0.75 V gave the best agreement, especially at the lower void fractions as can be seen in Fig. 5.

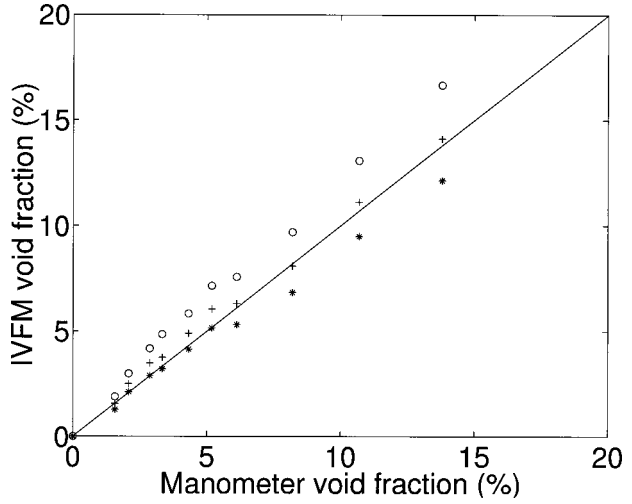

Fig. 5 Calibration data for the IVFM from the bubbly column facility. The different groups of points were produced by processing the same data set using different thresholds; (○) for threshold=−0.50 V, (+) for threshold=−0.75 V, and (*) for threshold=−1.00 V. A linear curve fit for the data corresponding to threshold=−0.75 V also is shown.

3 Experimental Observations

The air entrainment process in the large flume experiments could be observed best when the laboratory was darkened and a stroboscope was positioned to provide a high intensity and short duration, 0.5 μs, light pulse through the window in the bottom of the test section (Waniewski [11]). Observations of the bubbles were made through the glass sidewall of the flume and both direct inspection and high speed movies and videos showed the primary source of air entrainment resulted from the impact of the plunging wave jet on the passing water flow. The resulting splash forms droplets which reimpact causing further entrainment, but this secondary entrainment mechanism will not be addressed here (see, for example, Prosperetti and Oguz [16]).

The plunging wave jet entrained air in ''bursts,'' forming approximately spherical clouds of bubbles visible beneath the free surface. This observation is similar to that of Chanson and Cummings [8] in their experiments on a planar supported jet. For high jet impact velocities (4–8 m/s) they reported a thin layer of air entering the flow at the impact point, adding that the ''air pockets are entrained by discontinuous gusts at the lower end of the air layer.'' In the present experiments, high speed videos revealed that the bubble clouds had a diameter of about 5–10 cm and were comprised of bubbles which were more tightly packed at the center of the cloud than at the edges. Moreover, the formation of these clouds was spatially periodic so that a train of bubble clouds could be observed beneath the free surface at any particular moment in time. A typical photograph of bubble clouds is shown in Fig. 6. Photographs of individual bubbles within the bubble clouds were obtained using a telephoto lens, and though most of the bubbles appeared to be 1–5 mm in diameter, larger finger-like pockets of air also were observed. These did not persist in the clouds; either they were broken up into smaller bubbles by the turbulent flow or they rose to the free surface. Finally, the clouds grew in size as they were convected downstream.

4 Void Fraction and Bubble Size Measurements

For void fraction measurements beneath the simulated bow wave, the IVFM probe was mounted on the carriage described in Waniewski [11]. Measurements were taken at a series of locations in the impact line region of the bow wave plunging jet; one such traverse is shown in Fig. 7. A preliminary series of experiments

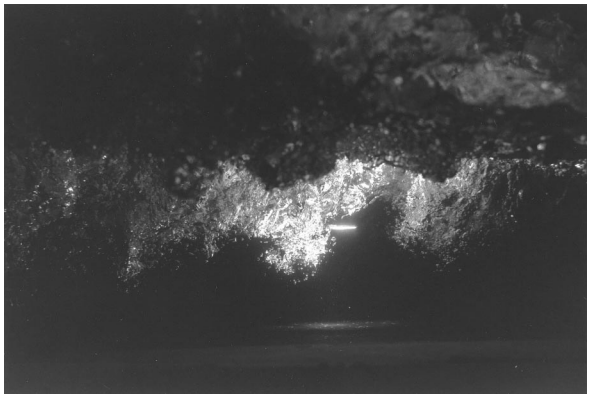

Fig. 6 Photograph of bubble clouds passing by the IVFM probe, the tip of which is visible in the center. The flow is from right to left with $\theta=25°$, $\phi=0°$, $U=2.47$ m/s, $d=7.39$ cm, and F=2.90.

verified the IVFM signal (see Waniewski [11] for details); a typical signal is presented in Fig. 8. Next, the repeatability of the results was tested. A set of nine IVFM signals were sampled at 20 kHz for 3.2 s at one location under the same circumstances. These had a mean void fraction of 3.2 percent and showed a standard deviation of 0.8 percent thus demonstrating repeatability. Subse-

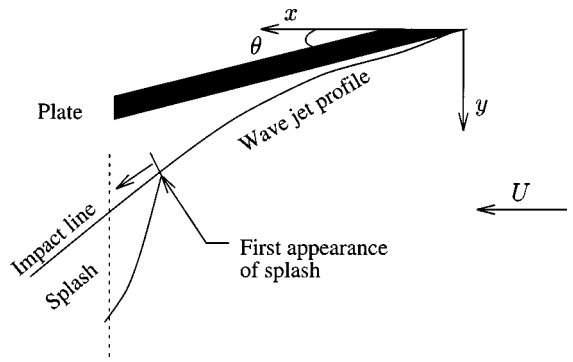

Fig. 7 Schematic diagram of the planform of the flow with a typical IVFM traverse (···) indicated.

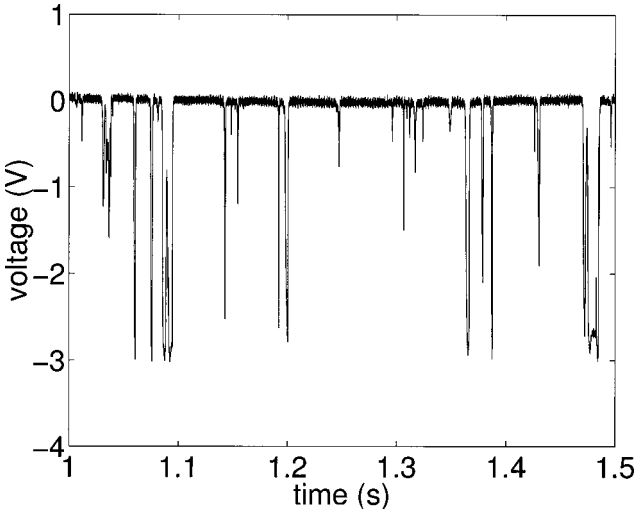

Fig. 8 A typical signal from the IVFM located several centimeters beneath the bow wave plunging jet: $\theta=26°$, $U=2.39$ m/s, $d=6.47$ cm, F=3.00, and $\alpha=6.5$ percent.

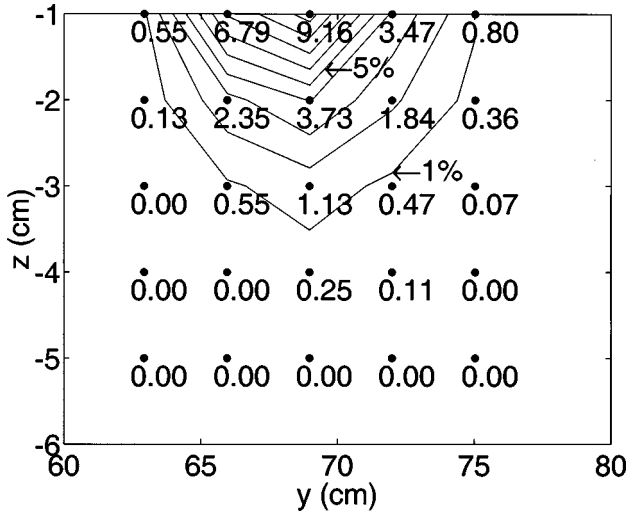

Fig. 9 Local, averaged void fractions beneath the bow wave plunging jet for a traverse at $x=91.2$, and for $\theta=26°$, $\phi=0°$, $U=2.48$ m/s, $d=7.89$ cm, and F=2.82. The IVFM measurement locations are marked (●) and labeled with the void fraction (percent). Nine equally spaced contour levels ($\Delta\alpha=1$ percent) also are shown.

quent measurements were repeated only three times for each location; the mean of the three is reported hereafter.

An example of time-averaged, ensemble-averaged, void fraction data for a traverse as viewed from downstream is shown in Fig. 9. The leading edge of the deflecting plate is located at $(x,y)=(0,0)$ and the upstream free surface is located at $z=0$. Void fraction contours were constructed and highlight the trends in the data. Because the free surface was unsteady, it was not possible to estimate the void fraction at locations above $z=-1$ cm without the free surface dipping below the probe or the probe entraining air. In addition, there is a surface proximity effect for this type of void fraction instrumentation which is described in Lamarre and Melville [3].

Figure 10 shows the void fraction contours for sets of traverses and confirms observations from the high speed video. First, the bubble clouds are shown to be roughly circular in cross section and grow as they convect downstream. Second, the bubbles are more tightly packed at the cloud center than at the edges. The center of the cloud, the region with greatest void fraction, was located directly beneath the impacting jet.

The void fraction mappings in Fig. 10 also were used to calculate the total volume of air entrained at particular streamwise locations. The areas between pairs of consecutive void fraction contours were calculated and multiplied by the void fraction in those regions. A trapezoidal summation of these terms gave the total volume of air, V_{air}, per unit streamwise distance. Note that this is a conservative estimate, since the void fraction was greater than 10 percent for some regions within the cloud but could not be measured accurately. The results for the traverses of Fig. 10 are included in Fig. 11 where $x^*=0$ corresponds to the origin of the impact line. The data for the two sets of flow conditions appear to be consistent with one another despite the slight offset which was within the repeatability of the experiments. Moreover, the data clearly shows that the quantity of air contained in the bubble clouds increases with the distance downstream of the impact line origin. The slope of the quadratic fit in Fig. 11 was used to calculate the volume rate of air entrainment, Q_{air}, for a given bubble cloud where

$$Q_{\text{air}}=Ud_c\frac{dV_{\text{air}}}{dx^*}$$

and d_c is the diameter of the bubble cloud. At location $x^*=10$ cm, typical clouds were 7 cm in diameter and the above expression yielded a Q_{air} of 62 cm^3/s.

The same IVFM signals were used to produce bubble chord distributions for the bubbles which comprised the bubble clouds. The typical dimension of the individual bubbles was represented by a quantity called the bubble chord, l, calculated using $l=U\Delta T$ where ΔT is an individual pulse width in the IVFM signal. Note that since very small bubbles remain spherical, this chord should be close to the bubble diameter. Similar bubble chord calculations for a dual tip conductivity probe are described by Chanson [17] Bubble chord histograms were compiled using bin size of 2 mm. Separate measurements at the same location demonstrated that the histograms were repeatable (Waniewski [11]).

Figure 12 presents typical bubble chord histograms for bubble clouds that passed through the traverse shown in Fig. 10(*d*). Note that most of the bubble chords were 1–7 mm, consistent with the high speed video observations of the size of the individual bubbles. Note also that the number of bubbles in this size range increased from the edge to the center of the cloud and from the bottom to the top of the cloud. Larger pockets of air existed in the center of the cloud near the free surface, giving rise to the larger bubble chords registered at those locations.

5 Frequency of Bubble Cloud Encounters

As described in Section 3, the formation of the bubble clouds was observed to be spatially periodic. Since the clouds convect downstream with the mean flow velocity, they pass a particular location at some specific frequency. High speed video of the bubble clouds was used to estimate this frequency of cloud encounters with the IVFM probe. Each frame of the video was examined, and it was noted whether or not a bubble cloud was present at the probe tip. Frequencies of cloud encounters for flow conditions similar to those in Fig. 8 were between 7 and 14 Hz.

A signal processing technique was implemented to extract the same information from the IVFM signals. This required a quantitative definition of a cloud, and so it was assumed that two bubbles located 1 cm or less apart belong to the same bubble cloud since the clouds were about 10 cm in diameter. If two bubbles are separated by 1 cm in the streamwise direction and move at the mean flow velocity then the time delay between the two bubbles as they impact the IVFM probe tip can be calculated. The IVFM signal was processed using an algorithm which searched for successive pulses caused by individual bubble impacts occurring within this time delay. Figure 13 shows the result of this cloud detection algorithm for a typical IVFM signal. The lower graph shows the reciprocal of the time delay, or frequency of individual bubble impacts with the IVFM probe, as a function of time. To count the clouds, a particular individual bubble impact frequency was chosen as a threshold. Since the mean flow velocity was 2.39 m/s, a threshold of 200 s^{-1} implied that two bubbles belonging to the same cloud could have had a maximum separation distance of 1.2 cm. This threshold also is shown in the lower graph, and a cloud was counted for each local maximum greater than 200 s^{-1}. Note that this technique does not count bubble clouds for which only a single bubble impacted the probe tip; therefore, it gives a lower bound for the frequency of bubble cloud encounters.

The frequency of bubble cloud encounters as a function of depth also was explored (Waniewski [11]). Since the bottom edge of the bubble clouds was lower in void fraction, there was a greater chance at larger depths that only a single bubble would impact the IVFM probe and the algorithm would not count the cloud because the same threshold was maintained for all depths. Hence, the cloud frequency decreased with depth. Near the surface, the typical cloud frequencies measured were 15 Hz as illustrated by Fig. 13; this frequency is similar to those obtained earlier from the high speed video. When compared with the frequency of

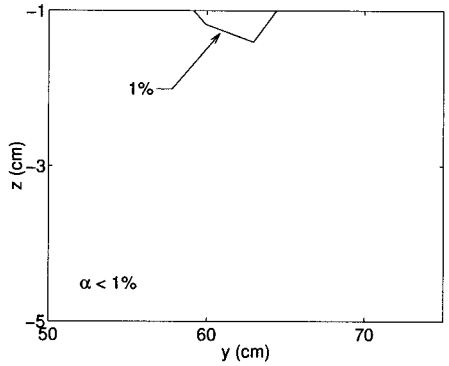

(a) $x = 73.4$ cm, $x^* = 4.4$ cm; plunging jet impacts at $y \approx 63$ cm.

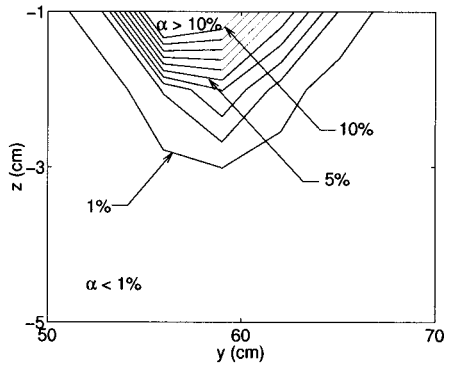

(b) $x = 70.8$ cm, $x^* = 17.8$ cm; plunging jet impacts at $y \approx 56$ cm.

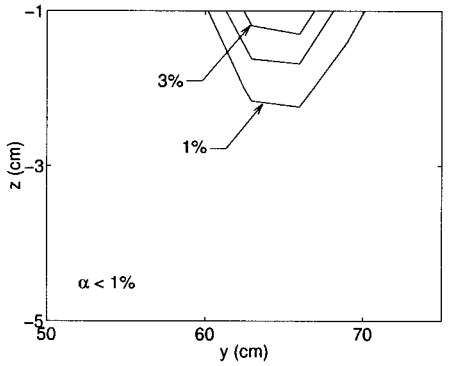

(c) $x = 81.0$ cm, $x^* = 12.0$ cm; plunging jet impacts at $y \approx 65$ cm.

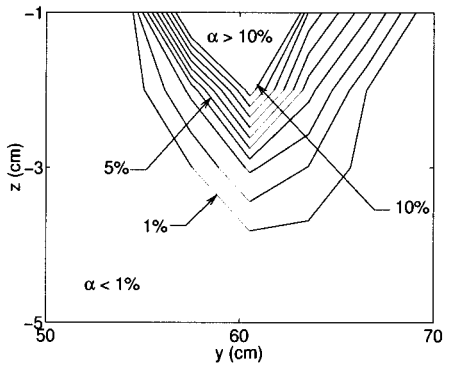

(d) $x = 75.9$ cm, $x^* = 22.9$ cm; plunging jet impacts at $y \approx 60$ cm.

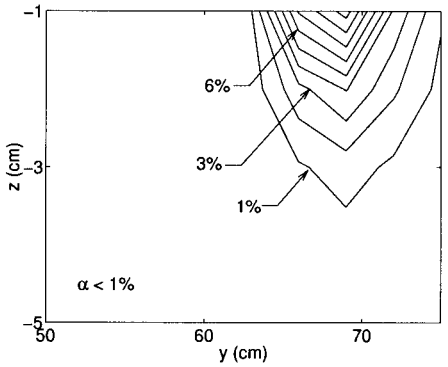

(e) $x = 91.2$ cm, $x^* = 22.2$ cm; plunging jet impacts at $y \approx 69$ cm.

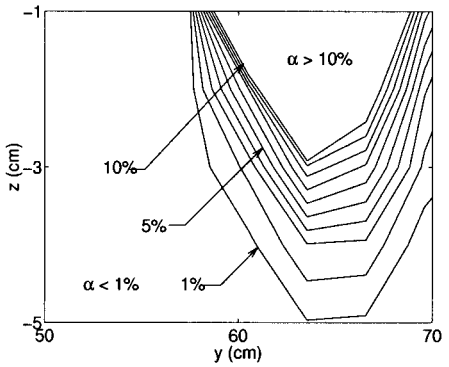

(f) $x = 84.2$ cm, $x^* = 31.2$ cm; plunging jet impacts at $y \approx 64$ cm.

Fig. 10 Local, averaged void fractions for six different traverses: (*a*), (*c*), and (*e*) for the flow conditions specified in Fig. 9 and (*b*), (*d*), and (*f*) for $\theta = 26°$, $\phi = 0°$, $U = 2.39$ m/s, $d = 6.47$ cm, and F=3.00. Ten equally spaced contour levels ($\Delta\alpha = 1$ percent) are shown.

impact by individual bubbles on the IVFM probe, the number of individual bubble impacts per cloud was calculated to be between three and five.

6 Discussion of Bubble Cloud Formation

Surface disturbances exist on the plunging face of the bow wave because of various flow instabilities, and each surface disturbance leads to an individual plunging jet. These individual jets may or may not break up into a string of droplets before impact. As discussed in Waniewski [11], the individual jets are convected downstream with the mean flow velocity and each entrains air at the point where it impacts the lower water surface. Observations of the bubble clouds beneath the free surface show small bubble clouds formed at the first location where the plunging wave jet

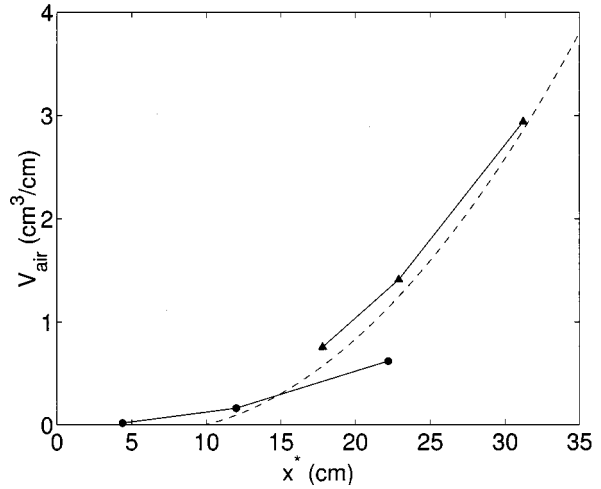

Fig. 11 Total volume of air entrained per unit streamwise distance as a function of distance from the origin of the impact line, x^*; (●) for the traverses of Fig. 10(*a*), (*c*), and (*e*) and (▲) for those of Fig. 10(*b*), (*d*), and (*f*). A quadratic curve fit (- -) also is shown.

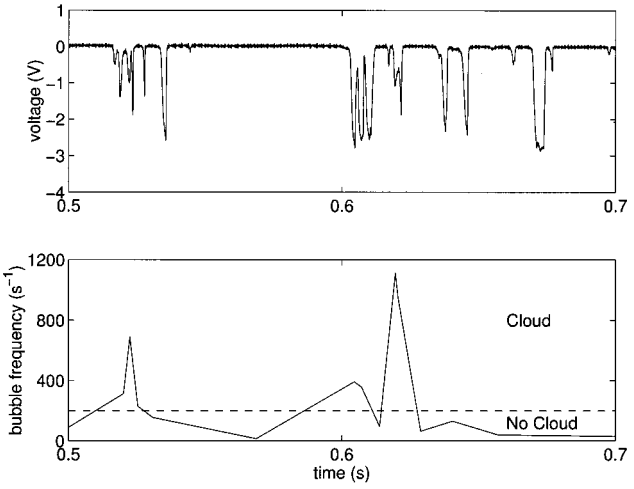

Fig. 13 Detail of signal processing technique. Upper: raw IVFM signal. Lower: cloud detection algorithm output, frequency of individual bubble impacts, from the IVFM signal.

impacts the free surface. These clouds grow in size (observed in high speed video and measured by IVFM) and increase in void fraction (measured by IVFM) as they convect downstream in a direction which follows the impact line of the bow wave.

On the basis of these observations, a mechanism for air entrainment is proposed and is shown schematically in Fig. 14. Each of the individual plunging wave jets entrains air into its own bubble cloud. These jet-cloud structures convect downstream with the mean flow velocity; therefore, the distance between successive surface disturbances determines the distance between bubble clouds. This is consistent with the visual observations of the clouds since dividing the mean flow velocity by the spacing between the disturbances yields the same 20 Hz frequency manifest in the bubble cloud train. Cross-correlations of the IVFM and wave gage signals also seemed to support this hypothesis (Waniewski [11]). In addition, the void fraction increases with downstream distance since more bubbles are injected over time. Simultaneously, the cloud size increases with downstream distance as a result of turbulent mixing.

We now compare the typical rate of air entrainment measured in these experiments, 62 cm^3/s (see Section 4), with that which might be expected using existing theories. Van de Sande and Smith [18] model air entrainment by low velocity (2–5 m/s) turbulent water jets plunging into a quiescent pool of water and obtain:

$$Q_{\text{air}} = 0.021 \frac{d_j^{3/2} U_j^2 l_j^{1/3}}{\sin(\beta)} \ m^3/s \tag{2}$$

where Q_{air} is the volume rate of air entrainment, d_j is the jet diameter, U_j is the jet velocity, l_j is the jet length, and β is the jet impingement angle. Using the experimental data presented in Waniewski [11]: $d_j = 3.8$ cm, $U_j = 2.3$ m/s, $l_j = 23$ cm, and $\beta = 58°$, Eq. (2) yields a Q_{air} of 600 cm^3/s. This discrepancy with the measured 62 cm^3/s, was expected. Figure 10 shows that most of the air exists in the >10 percent core and in the $-1 < z < 0$ cm surface layer; however, this air was not included in the 62 cm^3/s. The void fraction in the core was approximated as 10 percent and no approximation was made for the air in the surface layer. The error from these approximations could well account for the difference. On the other hand, it is likely that the air in the core and surface layer out-gasses to the surface quite quickly and the measured Q_{air} of 62 cm^3/s is a better indication of the bubble entrainment which persists further downstream.

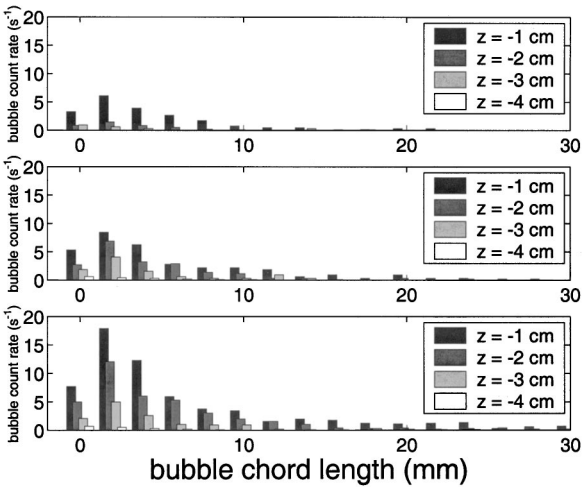

Fig. 12 Bubble chord histograms from bubble clouds observed at $x = 75.9$ cm for different elevations. Upper: $y = 66.6$ cm. Middle: $y = 63.5$ cm. Lower: $y = 60.5$.

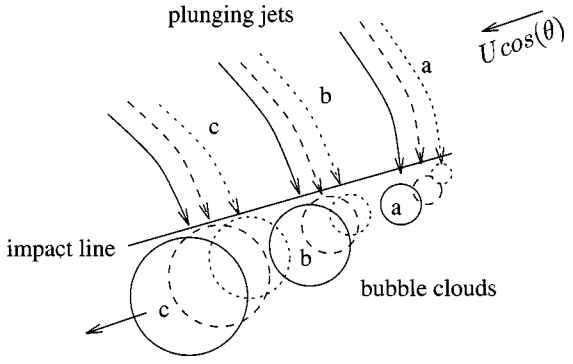

Fig. 14 Schematic diagram of the proposed air entrainment mechanism. A time series of plunging jets and bubble clouds is depicted; (···) for $t = 0$, (- -) for $t = \Delta t$, and (—) for $t = 2\Delta t$.

One of the uses of these data and/or model would be to improve the two-phase flow computations around surface ships. In the absence of such input, Carrica et al. [19] assumed that for an arbitrary area near the bow, a mixture of water and air with a void fraction of 10 percent entered the flow with a constant downward velocity. They further assumed the bubble size distribution measured by Cartmill and Su [7]. The present paper would suggest the following improvements. The location of the air entrainment should be along the impact line only, and the void fraction as a function of the distance along the impact line should be specified consistent with the present data. A similarly consistent bubble size distribution from an average of experimental measurements should be used. Even though the size distributions were seen to vary with location in the present study, most of the bubble chords were between 1 and 7 mm. The velocity of these bubbles entering the flow at the free surface should be the vector sum of the plunging wave jet velocity and the downstream velocity as described in Waniewski [11]. As more detailed models became appropriate, the periodicity observed in the bubble clouds could be included.

7 Conclusions

The primary mechanism for air entrainment in the present bow wave experiments was the impact of the plunging wave jet. Observations of the air entrainment process were made during experimental simulations of a bow wave in a flume which used a high speed video camera with a synchronized strobe lamp. An impedance based void fraction meter (IVFM) was developed specifically to measure void fraction and bubble size distributions beneath this breaking wave.

It was observed that the air is entrained in spatially periodic bubble clouds, approximately 5–10 cm in diameter. The IVFM signals were processed using a cloud detection algorithm to find the rate of bubble cloud encounters. For depths between 1 and 3 cm beneath the free surface, the bubble cloud rates varied from 5–20 Hz. The bubble cloud void fraction could exceed 10 percent in the center of the cloud, and the bubble chords for the bubbles comprising the clouds were between 1 and 7 mm. Void fraction mappings for different flow cross sections beneath the wave were generated, and the bubble chord distributions were calculated for these locations. The void fraction mappings were used to estimate the quantity of air entrained at different streamwise locations. It was found that for a given flow condition, the void fraction increases with the distance traveled along the impact line.

In addition, it appears that the frequency of the surface disturbances, described in detail in Waniewski [11], controls the frequency of the bubble clouds. The surface disturbances divide the plunging liquid jet sheet into a series of individual plunging jets, and each jet entrains air into its own bubble cloud beneath the free surface. This is supported by comparison of the predicted volume rate of air entrainment, Q_{air}, for a plunging liquid jet with the experimentally evaluated Q_{air} for a bubble cloud.

Acknowledgments

The authors wish to acknowledge the assistance of Mr. Hai Vu in developing the IVFM and the support of the Office of Naval Research under grant number N00014-94-1-1210, technical monitor Dr. Edwin Rood.

Nomenclature

d = upstream depth or model draft (m)
d_c = bubble cloud diameter (cm)
$\mathbf{F}$ = Froude number based on upstream conditions, $\mathbf{F} = U/\sqrt{gd}$
g = gravitational acceleration (m/s^2)
l = bubble chord length (mm)
Q = volume flow rate (m^3/s)
t = time (s)
U = upstream velocity (m/s)
V_{air} = total volume of air per unit streamwise distance (cm^3/cm)
x = streamwise coordinate (cm)
x^* = streamwise coordinate measured from impact line origin (cm)
y = cross stream coordinate (cm)
z = vertical coordinate (cm)
α = void fraction (percent)
ΔT = pulse width (s)
ϕ = dihedral angle (degrees)
θ = wedge half angle (degrees)

References

[1] Blanchard, D. C., and Woodcock, A. H., 1957, ''Bubble Formation and Modification in the Sea and its Meteorological Significance,'' Tellus, **9**, No. 2, pp. 145–158.
[2] Lamarre, E., and Melville, W. K., 1991, ''Air Entrainment and Dissipation in Breaking Waves,'' Nature (London), **351**, pp. 469–472.
[3] Lamarre, E., and Melville, W. K., 1994, ''Void fraction measurements and sound-speed fields in bubble plumes generated by breaking waves,'' J. Acoust. Soc. Am., **95**, No. 3, pp. 1317–1328.
[4] Lamarre, E., and Melville, W. K., 1992, ''Instrumentation for the Measurement of Void-Fraction in Breaking Waves: Laboratory and Field Results,'' IEEE J. Ocean Eng., **17**, No. 2, pp. 204–215.
[5] Cipriano, R. J., and Blanchard, D. C., 1981, ''Bubble and Aerosol Spectra Produced by a Laboratory Breaking Wave,'' J. Geophys. Res., **86**, pp. 8085–8092.
[6] Loewen, M. R., O'Dor, M. A., and Skafel, M. G., 1996, ''Bubbles Entrained by Mechanically Breaking Waves,'' J. Geophys. Res., **101**, pp. 20759–20769.
[7] Cartmill, J. W., and Su, M. Y., 1993, ''Bubble size distribution under saltwater and freshwater breaking waves,'' Dyn. Atmos. Oceans, **20**, pp. 25–31.
[8] Chanson, H., and Cummings, P. D., 1994, ''Modeling Air Entrainment in Plunging Breakers,'' Int. Symp.: Waves-Physical and Numerical Modeling, Vancouver, Canada, June.
[9] Bińi, A. K., 1993, ''Gas entrainment by plunging liquid jets,'' Chem. Eng. Sci., **48**, No. 21, pp. 3585–3630.
[10] Chanson, H., and Cummings, P. D., 1994, ''Effects of plunging breakers on the gas contents in the ocean,'' Mar. Technol. Soc. J., **28**, No. 3, pp. 22–32.
[11] Waniewski, T. A., 1999, ''Air Entrainment by Bow Waves,'' Ph.D. thesis, Calif. Instit. of Tech.
[12] Chanson, H., 1988, ''A study of air entrainment and aeration devices on a spillway model,'' Ph.D. thesis, Univ. of Canterbury.
[13] Kytomaa, H. K., 1987, ''Stability of the Structure in Multicomponent Flow,'' Ph.D. thesis, Calif. Instit. of Tech., Pasadena, CA.
[14] Ishii, M., 1975, *Thermo-Fluid Dynamic Theory of Two-Phase Flow*, Eyrolles, Paris.
[15] Teyssedou, A., Tapucu, A., and Lortie, M., 1988, ''Impedance probe to measure local void fraction profiles,'' Rev. Sci. Instrum., **59**, No. 4, pp. 631–638.
[16] Prosperetti, A., and Oguz, H. N., 1993, ''The impact of drops on liquid surfaces and the underwater noise of rain,'' Annu. Rev. Fluid Mech., **25**, pp. 577–602.
[17] Chanson, H., 1995, ''Air Bubble Entrainment in Free-Surface Turbulent Flows,'' Tech. rept. CH46/95. Univ. of Queensland, June.
[18] Van de Sande, E., and Smith, J. M., 1976, ''Jet break-up and air entrainment by low velocity turbulent water jets,'' Chem. Eng. Sci., **31**, pp. 219–224.
[19] Carrica, P. M., Bonetto, F., Drew, D., and Lahey, Jr., R. T., 1998, ''A Polydisperse Approach to the Two-Phase Flow Around a Ship,'' Third Int. Conf. on Multiphase Flow, Lyon, France, June.

Numerical Simulation of Human Exposure to Aerosols Generated During Compressed Air Spray-Painting in Cross-Flow Ventilated Booths

Michael R. Flynn
Department of Environmental Sciences and Engineering, University of North Carolina, Chapel Hill, NC 27599-7400

Eric D. Sills
North Carolina Supercomputing Center, PO Box 12889, RTP, NC 27709-2889

This paper examines the use of computational fluid dynamics as a tool for predicting human exposure to aerosols generated during compressed air spray painting in cross-flow ventilated booths. Wind tunnel experiments employing a mannequin and non-volatile oil provide data to evaluate the numerical predictions. Fidap (v8.01) is used to calculate the velocity field and particle trajectories, while in-house codes were developed to post-process the trajectory data into mass concentrations, size distributions, transfer efficiency, and over-spray generation rates. The predicted dimensionless breathing-zone concentration of 0.13±23 percent is in agreement with the measured value of 0.13±15 percent given the uncertainties involved in such comparisons. Computational fluid dynamics is a powerful tool capable of providing useful information to occupational hygiene engineers involved in controlling human exposures to toxic airborne contaminants.
[DOI: 10.1115/1.1340636]

Keywords: Computational Fluid Dynamics, Spray Painting, Ventilation, Exposure Modeling, Aerosols, Occupational Hygiene

Introduction

Predicting human exposure to toxic airborne contaminants in the workplace is important from both the epidemiological-assessment, and engineering-control perspectives. To estimate dose-response relationships between inhaled contaminants and disease incidence, retrospective epidemiological studies must differentiate human exposures based upon historical records. The absence of robust models that quantitatively relate these records to exposure ultimately attenuates the power of such studies. Occupational hygiene engineers, confronted with the design of ventilation systems to minimize human exposures, need modeling tools to assist in the optimization of such controls. In addition, EPA Premanufacture Notification (PMN) and OSHA legislation make it incumbent upon industry to estimate and control employee exposures to toxic airborne contaminants.

Despite the advent of sophisticated computational fluid dynamics (CFD) software, and powerful computers, there have been relatively few studies (Heinonen et al. [1], Kulmala et al. [2], Flynn and Sills [3]) to explore critically their application to these types of problems. The resources required to simulate the complex, unsteady, three-dimensional, turbulent flows that arise in occupational environments are significant, and judicious approximations are needed. The approach presented here begins by constructing a conceptual model of reality, i.e., human exposure to total mass generated during spray painting. The difference between reality, as evaluated with field sampling, and the conceptual model, based upon dimensional analysis and wind tunnel studies, defines an error that characterizes the adequacy of the conceptual model. Subsequently, numerical simulation is conducted based upon a simple representation of the wind tunnel experiments used to develop the conceptual model. The difference between the numerical results and the wind tunnel experiments defines a second error, which evaluates the adequacy of the numerical approximations. By partitioning the uncertainties in this manner it is possible to identify whether refinements in the conceptual model or the numerical approach will most improve simulations of human exposure.

Contributed by the Fluids Engineering Division for publication in the JOURNAL OF FLUIDS ENGINEERING. Manuscript received by the Fluids Engineering Division March 22, 2000; revised manuscript received October 13, 2000. Associate Editor: L. Mondy.

Background

A recent paper (Flynn et al. [4]) summarizes the conceptual model described above and presents a simple mathematical model of human exposure to total mass generated during the compressed air spray painting of a flat plate in a cross-flow ventilated booth. As summarized in Eq. (1), this model predicts a dimensionless breathing zone concentration as a function of an air momentum flux ratio and worker orientation,

$$\log_{10}\left(\frac{CHUD}{\dot{m}_0}\right) = \alpha + \Delta\left(\frac{F_g}{F_m}\right)^{\gamma} \tag{1}$$

C is the total mass concentration in the breathing zone, solid, liquid, and vapor.

U is the average air velocity in the cross-flow spray booth.

H and D are the height and breadth of the worker.

$\dot{m}_0$ is the over-spray mass generation rate.

F_g and F_m are the momentum flux of air from the gun, and through the projected area of the mannequin, respectively.

α, Δ, and γ are constants that depend upon geometry and the angle of orientation, Θ, of the spray gun and the booth airflow (see Fig. 1).

$$\frac{F_g}{F_m} = \frac{K}{HDU^2} \tag{2}$$

where,

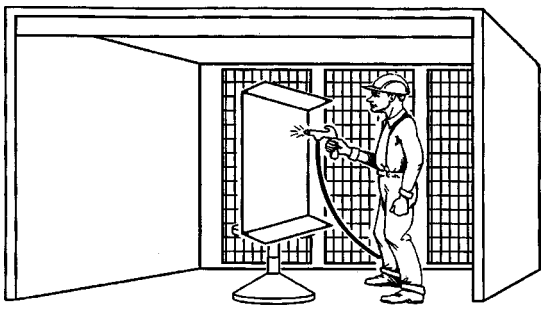

90° ORIENTATION

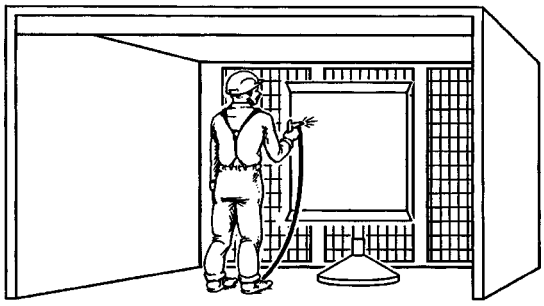

180° ORIENTATION

Fig. 1 The reality being simulated: compressed air spray painting of a flat plate in a cross-flow ventilated booth, Θ=90 and 180 deg

$$K=\frac{\rho_n A_n V_n^2+(p_n-p_{\text{atm}})A_n}{\rho_{\text{atm}}}+\frac{\rho_f A_f V_f^2+(p_f-p_{\text{atm}})A_f}{\rho_{\text{atm}}} \quad (3)$$

K is the kinematic momentum flux of air from the spray gun, p is pressure, V is the air velocity, and A is the exit area. The n and f subscripts denote the nozzle atomization airflow and nozzle fan airflow (used to shape the spray pattern) respectively, atm indicates atmospheric conditions. The over-spray mass generation rate, ($\dot{m}_o$) is related to the liquid (paint) flow rate ($\dot{m}_L$) by the transfer efficiency (η_T) as follows:

$$\dot{m}_o=\dot{m}_L(1-\eta_T) \quad (4)$$

The major result of the empirical work was to evaluate α, Δ, and γ for the two orientations over a representative range of momentum flux ratios using data from scale model wind tunnel studies. Greater exposure occurs in the 90 deg orientation relative to the 180 deg case, for most real-world spray paint applications. A field evaluation of this model was performed (Carlton and Flynn [5]) with eight spray painters sampled for a total of 55 tasks. The mean measured exposure for the eight workers was 129 mg/m^3 with a 95 percent confidence interval of [70–188] mg/m^3. The corresponding predicted mean exposure was 85 mg/m^3 with a 95 percent confidence interval of [76–93] mg/m^3 indicating that the model worked well for the limited flat-plate geometry for which it was intended, despite a bias to under predict. This suggested that the approximations employed in developing the model were reasonable, and that the wind-tunnel data would be useful for evaluating CFD simulations of exposure.

The wide variety of work piece geometry, and ventilation configurations (e.g., downdraft booths) encountered in real spray applications limits the dimensional analysis–conceptual model approach. Numerical simulation provides a more flexible tool with extension to complex geometry, time-dependent flows, and volatile aerosols. A recent paper (Flynn and Sills [3]) presents preliminary CFD simulations of the wind tunnel studies confirming the orientation effect observed in both laboratory, and field studies (Carlton and Flynn [5], Heitbrink et al. [6]). Those simulations employed coarse approximations, and although the exposure rankings were correct, there was not good quantitative agreement between the predictions and experimental data. The objective of this work is to improve the numerical approximations, and to examine the ability of CFD models to make accurate estimates of aerosol exposure. An analysis of some of the more significant sources of uncertainty is presented.

Experimental Methods

The laboratory wind tunnel experiments employed a nonvolatile oil in lieu of paint, and a stationary mannequin. Despite these limitations, application to moving workers with volatile paints was reasonably successful—details are reported in (Carlton and Flynn [7,8]). One set of experiments, designed to reflect typical working conditions, is selected for comparison with numerical simulation and is summarized here briefly. The dependent variables of interest are: (1) the breathing-zone mass concentration; (2) the associated aerosol size distribution; and (3) the transfer efficiency of the spraying process. A mannequin holding a Spray Systems 1/4 J nozzle was placed in a 1.524 m square wind tunnel and oriented 90 deg to a flat plate. The nozzle was 0.203 m from the plate and operated at a gauge air pressure of 345 kPa (50 psig). A liquid (corn oil) mass flow ($\dot{m}_L$) of 0.00283 kg/s was used, and the wind tunnel air speed was 0.478 m/s. Figure 2 is a photograph of this particular set-up looking into the wind-tunnel.

The 1/4 J nozzle is a coaxial, air-blast atomizer similar in design to a conventional spray paint gun, but operated without the ''fan-air'' which is used to shape the spray pattern in actual spray-paint guns. The 1/4 J nozzle and corn oil system was selected since information about the spray size distribution was available from an empirical study (Kim and Marshall [9]). For the transfer efficiency comparisons, data was also used from a study (Tan and Flynn [10]) employing an HVLP (High Volume Low Pressure) spray gun which operated at the same momentum flux as the 1/4 J described above, but was positioned 0.254 m from the plate to match the simulation. This spray gun had fan-air as well. It should be noted that because an ''arm'' is not included in the simulation the distance of the nozzle to the plate is not quite the same for the 1/4 J nozzle. Breathing-zone concentration and particle size measurements were made only for the 1/4 J nozzle. Table 1 presents a summary of the relevant parameters.

Transfer efficiency is defined here as the fraction of liquid mass sprayed that deposits on the object. This was measured by mass balance by removing what had impacted on the flat plate. The breathing zone concentrations and size distributions were measured using open-face and closed-face 37 mm filter cassettes re-

Fig. 2 Photo of the experimental setup: mannequin in wind tunnel with 37-mm open-face cassette located in mouth

Table 1 Experimental and numerical parameters

	Experimental Values	Simulation Values
D (m) mannequin (cylinder) diameter	0.2	0.2
H (m) mannequin (cylinder) height	1.04	1.016
s (m) characteristic length of nozzle (jet)	0.0015	0.0127
Z_p (m) nozzle – to –plate distance	0.203 (¼ J) 0.254 (HVLP)	0.254
L_t length of (tunnel) (m)	2.44	5.0
W_t width of tunnel (m)	1.52	1.524
H_t height of tunnel (m)	1.52	1.524
H_p height of plate (m)	1.02	1.016
W_p width of plate (m)	0.66	0.66
U_j nozzle (jet) velocity (m/s)	sonic	129.5
U tunnel velocity(m/s)	0.478	0.478
m_a nozzle (jet) mass flow of air (kg/s)	0.002	0.014
m_t tunnel mass flow of air (kg/s)	1.33	1.33
m_L (kg/s) liquid mass flow	0.00285	N/A
F_g/F_m momentum flux ratio	18	18

spectively, both operating at 2.0 L/m. The aspiration losses of large particles inherent in the use of these cassettes are a major source of uncertainty in comparisons with the numerical results. They are addressed here by correcting the numerical predictions according to empirical equations developed by Vincent [11].

Numerical Methods

The three-step numerical procedure outlined in (Flynn and Sills [3]) is employed here. First the steady, three-dimensional, air velocity field is calculated. Subsequently, aerosol particles of appropriate size are introduced at the center of the jet face, moving at the air speed, and tracked through the flow field assuming they do not influence the air velocity field in any way. Others (Hicks [12]) have employed this decoupling of the liquid and gas phases in spray-painting simulations by introducing the particles downstream of the atomization (near nozzle) region. However, recent studies (Flynn et al. [4], Tan and Flynn [3]) suggest that due to the relatively low momentum flux of liquid relative to gas present in most spray paint applications that including the aerosol along with an equivalent momentum air jet is also a good representation of the process. Finally, the aerosol trajectories are converted into predictions of transfer efficiency, breathing-zone mass concentration, and size distributions for comparison to the empirical data. The first two-steps are accomplished with FIDAP (v8.01). Conversion of the particle trajectories to concentrations and transfer efficiency is accomplished through algorithms developed in-house.

To represent the mannequin in the wind tunnel a circular cylinder of height H, and diameter D, is used. A square orifice on the surface of this cylinder of side length, s, represents the spray nozzle as a jet of air. The face of this nozzle is at a distance, Z_p, from the plate. The 1/4 J nozzle used in the experiments has an exit airflow area of 0.0225 cm^2 and the velocity is sonic for the pressures employed. This work uses an incompressible flow calculation with a larger orifice, but equivalent momentum, to approximate the compressible-flow, high-pressure spraying operation. A comparison of experimental and computational length, velocity, and mass flow scales is given in Table 1.

Air Velocity Field. The equations selected to model the airflow are the steady state, incompressible, turbulent, Navier-Stokes equations with the standard two-equation k-e model. These equations are:

$$\nabla \cdot \mathbf{u} = 0 \tag{5}$$

Table 2 Boundary conditions for Eqs. (2)–(5)

	Tangential Velocity (m/s)	Normal Velocity (m/s)	Stress	Turbulence kinetic energy $(m/s)^2$	Turbulence dissipation $(m^2)/(s^3)$
Inlet	0	0.478	-	0.00343	0.00705
Outlet	-	-	0	$\partial k/\partial n = 0$	$\partial \varepsilon/\partial n = 0$
Jet Face	0	129.5	-	40.3	97331.6
Solid Surfaces	0	0	-	0.	0

$$\mathbf{u}\cdot\nabla\mathbf{u} = \nabla\cdot\left[\frac{\mu+\mu_t}{\rho}(\nabla\mathbf{u}+\nabla\mathbf{u}^{\mathrm{T}})\right] - \frac{1}{\rho}\nabla p \tag{6}$$

$$\rho(\mathbf{u}\cdot\nabla k) = \nabla\cdot\left(\mu+\frac{\mu_t}{\sigma_k}\nabla k\right) + \mu_t\Phi - \rho\varepsilon \tag{7}$$

$$\rho(\mathbf{u}\cdot\nabla\varepsilon) = \nabla\cdot\left(\mu+\frac{\mu_t}{\sigma_\varepsilon}\nabla\varepsilon\right) + c_1\frac{\varepsilon}{k}\mu_t\Phi - c_2\rho\frac{\varepsilon^2}{k} \tag{8}$$

where:

$$\mu_t = \rho c_\mu \frac{k^2}{\varepsilon} \tag{9}$$

The constants are:

$$c_\mu = 0.09; \quad \sigma_k = 1.00; \quad \sigma_\varepsilon = 1.30; \quad c_1 = 1.44; \quad c_2 = 1.92.$$

Together with the boundary conditions specified in Table 2, these equations are solved using a segregated approach with pressure projection. Streamline upwinding is used with the cell Reynolds number relaxation scheme. This approach is reported to be very nearly second order accurate (Fidap Manual [13]). The criterion for terminating the nonlinear iterations is the simultaneous convergence of the relative error norm to below 0.001 for each of the six variables.

Aerosol Trajectories. Particles are tracked according to a generalized drag equation:

$$\frac{\mathbf{dv}}{dt} = \frac{\mathbf{u}-\mathbf{v}}{\tau} + \frac{\rho_p-\rho_a}{\rho_p}\mathbf{g} \tag{10}$$

Table 3 Input particle size distributions

Size Range in micrometers	Midpoint (μm) Input to FIDAP	Mass fraction in interval for ¼ J and (HVLP)
0-5	2.5	0.0274 (0.0295)
5-10	7.5	0.0314 (0.0342)
10-15	12.5	0.0356 (0.0390)
15-20	17.5	0.0399 (0.0439)
20-25	22.5	0.0440 (0.0486)
25-30	27.5	0.0478 (0.0528)
30-35	32.5	0.0512 (0.0563)
35-40	37.5	0.0538 (0.0589)
40-45	42.5	0.0556 (0.0602)
45-50	47.5	0.0563 (0.0602)
50-55	52.5	0.0560 (0.0590)
55-60	57.5	0.0546 (0.0565)

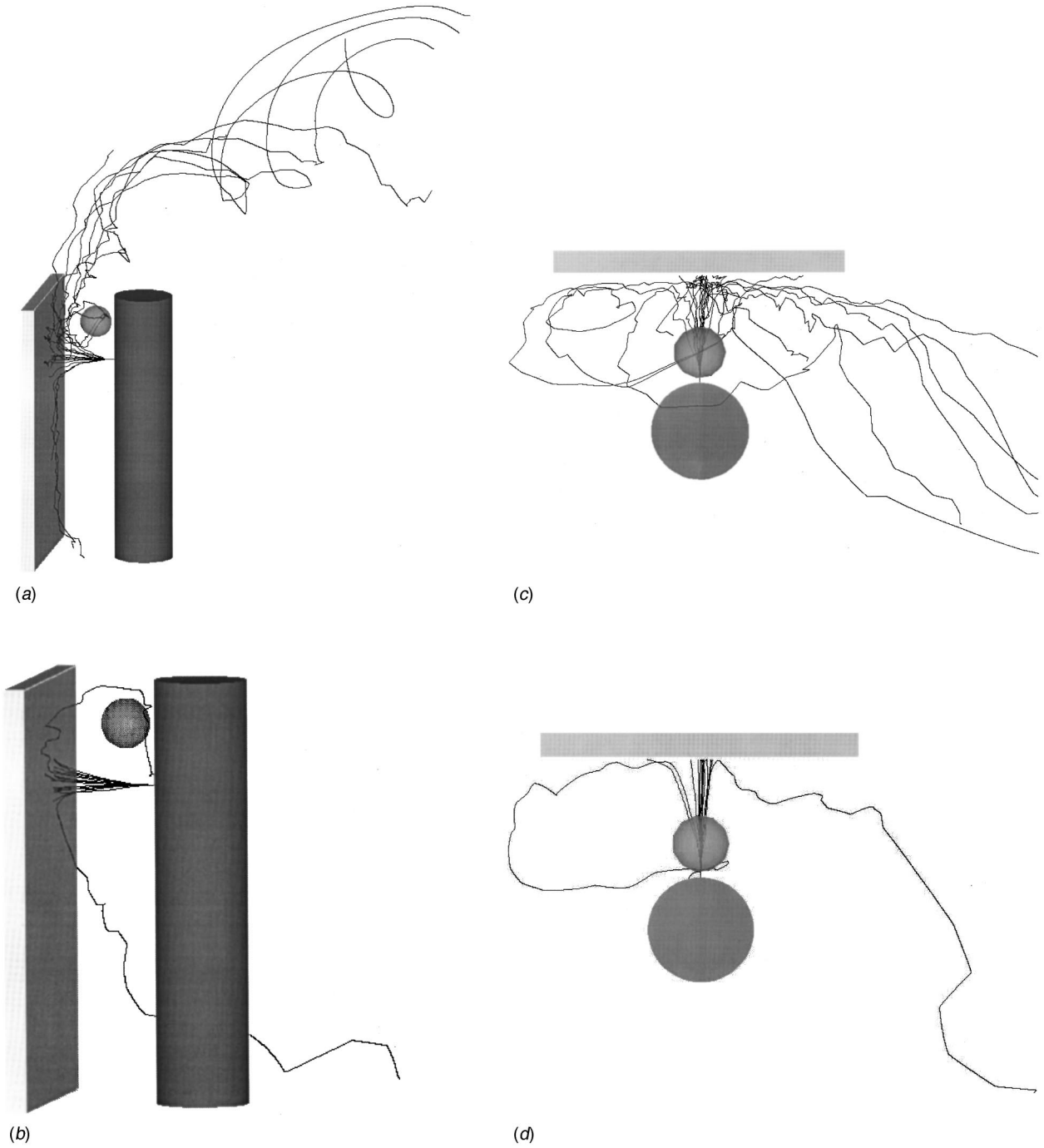

Fig. 3 Particle trajectories for the 90 deg orientation, in each case the small sphere depicts the breathing zone volume. Side views (*a*) 27.5 μm diameter particles, and (*b*) 52.5 μm diameter particles. Top-down views (*c*) 27.5 μm diameter particles, and (*d*) 52.5 μm diameter particles, booth airflow is from left to right.

where:

$$\tau = \frac{4\rho_p D_p^2}{3\mu C_D \mathrm{Re}_p} \tag{11}$$

and,

$$C_D = \frac{24}{\mathrm{Re}_p}(1 + 0.15\,\mathrm{Re}_p^{0.687}) \tag{12}$$

$$\mathrm{Re}_p = \frac{D_p|\mathbf{u}-\mathbf{v}|\rho_a}{\mu} \tag{13}$$

where:
u is the air velocity vector.
v is the particle velocity vector.
Re_p is the particle Reynolds number.
C_D is the particle drag coefficient.
D_p is the diameter of the aerosol particle.
τ is the particle relaxation time.
ρ_a *and* ρ_p are the density of the air and particle, respectively.

The input particle size distribution is determined from the empirical equations of Kim and Marshall [9] who specifically examined the 1/4 J nozzle, and oleic acid (corn oil) used here. A dis-

crete representation of the size distribution, based on 5 μm intervals was used with the midpoint as input to FIDAP. The mass fractions associated with each size interval are used to determine transfer efficiency and concentration. Table 3 presents the discrete representation of the particle size distribution for the experimental conditions described above, and also includes mass fractions for the HVLP gun based on the appropriate experimental conditions. The upper size limit of 60 μm was selected since it was observed during the simulations that all particles greater than this size impacted on the plate and did not contribute to exposure. All of the mass over 60 μm is included in the simulated prediction of transfer efficiency.

Equation (10) is integrated with an implicit option available in FIDAP, i.e., the Backward-Euler method. Turbulent displacement of the particle is included via a random number subroutine. This is accomplished according to a stochastic model based on the method of Gosman and Ioannides [14]. The interaction of each particle with a fluid eddy is limited to the lesser of the eddy lifetime or the time it takes the particle to traverse the eddy.
FIDAP creates an output file containing the endpoints of each increment on each particle trajectory, along with the value of the time step. This information is used to calculate transfer efficiency, breathing zone concentration, and particle size distributions, as described below.

Transfer Efficiency and Concentration. The formula for the calculation of mass concentration in the breathing zone, based on particle trajectories determined from the computed velocity field, is (Heinsohn [15]):

$$C = \sum_{i=1}^{N} \frac{\dot{m}_i t_i}{V_{bz}} \tag{14}$$

where, $\dot{m}_i$ is the mass flow rate associated with the ith trajectory, V_{bz} is the breathing zone volume, t_i is the residence time for the ith trajectory in V_{bz}, and N is the total number of trajectories. An in-house code (Flynn and Sills [3]) was used to calculate concentration inside a spherical breathing zone of volume of 0.000905 m^3. This sphere was positioned to coincide with the location of the filter used in the experiment. The algorithm identifies the proportion of each trajectory increment that lies within the numerical breathing zone and sums the time spent within this zone. This provides the information for exposure and size distribution calculations.

An additional part of the in-house, post-processing algorithm determines the number of aerosol particles impacting on the object. Transfer efficiency for a given size particle is obtained as the ratio of particles impacting on the object to the total number used for that size. Size-specific over-spray generation rates are obtained directly from this information.

Parameters governing the accuracy of the numerical solution are the size of the time step (Δt), the total time the particles are tracked (T), the input size distribution (Ψ), the mesh refinement, and the number of particles input in each size interval. Previous work (Flynn and Sills [3]) suggests that a value for the time step may be selected according to Eq. (15),

$$\Delta t = 0.1 \frac{Z_p}{U_j} \tag{15}$$

For the simulations here $\Delta t = 0.0002$ second, and a total time of 30 seconds, or 3 nominal wind-tunnel volume air-changes, was found to be adequate. Figure 3 shows an illustration of trajectories for two different size particles, 27.5 μm and 52.5 μm. The larger particles impact the plate while the smaller ones escape, some passing through the spherical breathing zone.

Results and Uncertainty Analysis

Five different meshes of increasing refinement, identified m1–m5, were employed. All meshes were generated using FIGEN by projecting paved meshes over various vertical increments. Table 4 presents a summary of the meshes giving the number of elements along various mesh edges in addition to the total number of nodes. NELX, NELY and NELZ are the number of elements along the edges of the domain representing the wind tunnel, while NELOF and NELCF are the number of elements on the face of the object (flat plate) and the cylinder face (front of worker) respectively. Figure 4 shows various views of the m3 mesh. Initially, a solution vector consisting of the velocity components, turbulence kinetic energy, and dissipation at 27 points in the vicinity of the breathing-zone was selected for examination under mesh refinement. The relative error norm is reported in Table 5 as a function of mesh refinement for each degree of freedom.

Subsequently, the other dependent variables were examined. The predicted transfer efficiencies are constant over the finest three meshes at a value of 0.81 for the 1/4 J nozzle and a value of 0.83 for the HVLP gun. The difference is due to a different mass distribution associated with the two different nozzles. The measured values of transfer efficiency for the 1/4 J atomizer (at a nozzle-to-plate distance of 0.203 m) range from 0.935–0.940 with a mean of 0.938. For the HVLP spray gun (at a nozzle-to-plate distance of 0.254 m) they range from 0.78–0.81 with a mean of 0.80. The superior agreement of the predicted transfer efficiency with the HVLP data is due in part to the fact that the nozzle-to-plate distances match exactly. Studies (Tan and Flynn [10]) have shown that transfer efficiency increases with decreasing distance to the plate, other factors being equal. In addition, the HVLP gun has fan air (serving to mix the particles more uniformly), subsonic discharge, and a nozzle area of 0.000033 m^2, resulting in a better scaling match with the simulation.

Due to the turbulent nature of the flow, and the discrete nature of particle size, there is a distribution of solutions for any given input. Figure 5 shows a plot of the dimensionless breathing zone concentration as a function of the number of trajectories per size interval for the finest meshes. Given the difference between the two finest meshes, results suggest that the predicted dimensionless concentration converges to a value of 0.38 ± 0.08, considerably above the measurement of 0.13 ± 0.02. However, the tendency for an extractive aerosol sampling methodology to underestimate the true mass concentration due to aspiration losses is well known (Vincent [11]), and has been examined for the types of filter cassettes used to collect the experimental data in this study. Using the numerically predicted velocity, and the empirical correction factors for open-face cassettes at a 90 deg sampling angle (Vincent [11]), the adjusted data in Table 7 are obtained. The adjusted value for the predicted dimensionless concentration is 0.13 ± 0.03, indistinguishable from the measured value.

Breathing-zone particle size distributions by mass were constructed, that were approximately lognormal. The unadjusted mass median diameter (MMD) was 23 μm with a geometric standard deviation (GSD) of 1.8. When adjusted for closed-face filter aspiration losses an MMD of 11 μm and a GSD of 2.0 were obtained. The corresponding measured values were an MMD of 25 μm and a GSD of 1.6. The summary of results is presented in Table 6 for the finest two meshes and the experimental data. The adjusted MMD predicted in the breathing zone, is about half the measured value.

Table 4 Mesh details

	NELX	NELY	NELZ	NELOF OBJECT FACE	NELCF CYLINDER FACE	TOTAL NODES
M1	32	10	40	24	18	61,698
M2	40	12	48	32	20	120,255
M3	50	14	56	40	24	225,572
M4	56	16	62	42	28	338,189
M5	66	18	68	46	36	581,132

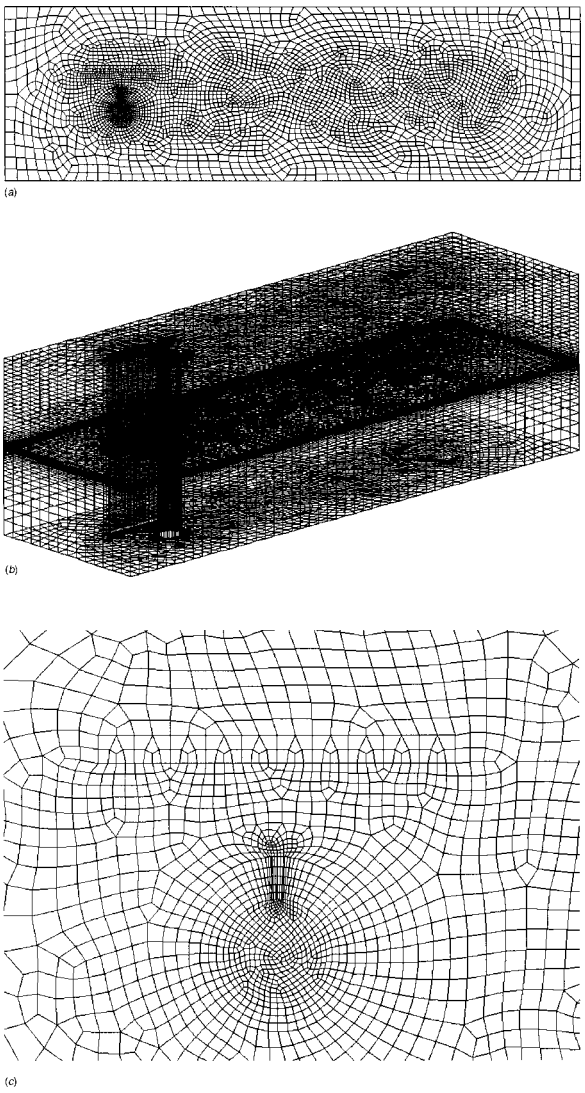

Fig. 4 Three views of computational grid m3: (*a*) top view, (*b*) 3D view, (*c*) details of the jet region.

There are many additional sources of uncertainty in this approach, including the adequacy of the geometric representation, and the turbulence model. A major approximation is representation of the small air nozzle as a larger equivalent-momentum jet. This introduces a violation of continuity since the jet and spray-nozzle do not have equal areas. The ratio of the air-jet mass flows (reality to simulation) is equal to the ratio of the jet velocity in the simulation, to the nozzle velocity in reality. This local error is significant; however spray airflow is a very small part of the total flow when the booth air is included. The global continuity error, for the simulation run here is negligible at 0.7 percent. The error approaches 2 percent if a 0.025 m (1 in.) square jet is used in the simulation.

Kim and Marshall [9], report the uncertainty in their prediction of mass median diameter as ±24.2 percent. Using this to define an upper and lower bound for the particle size uncertainty and recalculating the dependent variables produces the results in Table 7. The particle size distributions in the breathing zone are relatively unaffected by uncertainty in the input size distributions. Concentration and transfer efficiency vary inversely, but the dimensionless concentration remains essentially unchanged. This is examined further in the discussion section below.

Table 5 Relative error norms for solution variables as a function of mesh refinement

	U	V	W	k	e
M2-M3	0.186	0.046	0.427	0.359	0.224
M3-M4	0.093	0.034	0.230	0.038	0.049
M4-M5	0.100	0.025	0.156	0.017	0.009

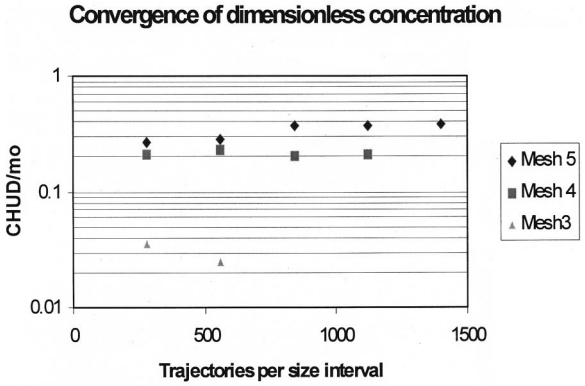

Fig. 5 Convergence of the dimensionless breathing-zone concentration as a function of the number of particle trajectories per size interval for the three finest meshes

Representation of the mannequin as a circular cylinder also introduces some uncertainty. The jet-to-plate distance and the appropriate spacing of the cylinder-to-plate cannot be simultaneously achieved without a ''virtual arm'' on the cylinder. The spacing selected, i.e., 0.254 m was a compromise. However, it is likely that some of the discrepancy in transfer efficiency is due to uncertainty in the spatial distribution of the particles. One study (Domnick et al. [16]) suggests that larger particles migrate to the periphery of the spray, resulting in perhaps an escape of more large particles than predicted. This is consistent with the differences in particle size distribution observed. This effect may be mitigated when fan air is used and perhaps part of the reason for the excellent agreement of transfer efficiency with the HVLP gun experiments.

Table 6 Comparison of numerical predictions to experimental data

Variable	Mesh 4 1120 particles per trajectory	Mesh 5 1400 particles per trajectory	Experiment
C mg/m^3 (unadjusted)	1128	2062	N/A
C mg/m^3 (adjusted)	372	699	225
Transfer efficiency	0.81 0.83	0.81 [0.73-0.86] 0.83 [0.77-0.88]	0.94 (1/4 J) 0.80 (HVLP)
¼ J over-spray generation rate kg/s	0.00054	0.00054	0.00017
CHUD/m_o (unadjusted)	0.21	0.38	N/A
CHUD/m_o (adjusted)	0.07	0.13	0.13
MMD (GSD) (unadjusted)	23.9 (1.9)	23.0 (1.8)	N/A
MMD(GSD) (adjusted)	12.0 (2.1)	11.0 (2.0)	25.0 (1.6)

Table 7 Sensitivity of predictions to uncertainty in the mass median diameter of the input particle size distribution

Variable	¼ J MMD=56 HVLP MMD=52	¼ J MMD=42 HVLP MMD=40	¼ J MMD=69 HVLP MMD=64
C mg/m^3 (¼ J) unadjusted	2062	2867	1523
Transfer efficiency ¼ J HVLP	 0.81 0.83	 0.73 0.77	 0.86 0.88
m_o (kg/s) (¼ J)	0.00054	0.00076	0.00040
CHUD/m_o (¼ J) unadjusted	0.38	0.37	0.37
MMD (GSD) ¼ J (adjusted)	11.0 (2.0)	11.6 (2.1)	11.2 (2.1)

Discussion

The direct proportionality between the over-spray generation rate and the breathing zone concentration makes the dimensionless concentration relatively insensitive to uncertainty in input particle size distribution. This is significant for occupational hygiene engineers using computational fluid dynamics as a tool for optimizing exposure control decisions. The dimensionless concentration is essentially a mixing factor, relating the generation rate to a local concentration, that is a function of the geometry and the momentum flux ratio. Engineers desiring to assess how ventilation design alterations e.g., air supply and extract locations, or work practices e.g., orientation, might affect this mixing pattern and reduce exposure can work with the dimensionless form of the concentration and incur less uncertainty. In addition, by combining the CFD predictions with measurements, or more accurate models (Tan and Flynn [10]), of spray gun transfer efficiency, excellent estimates of actual exposure are possible. For example, based on the predicted dimensionless breathing-zone concentration of 0.13 and a measured value for transfer efficiency of 0.94, a predicted exposure of 225 mg/m^3 is obtained, which matches the measurement.

This work suggests that accurate predictions of human exposure to toxic airborne contaminants are possible using CFD software and some simplifying approximations. Within the quantifiable uncertainties, the numerically predicted dimensionless concentration is in good agreement with experimental values measured in the wind tunnel. These data in turn were supported by field studies of actual human exposures. The numerical simulation of dimensionless concentration provides a powerful tool for occupational hygiene engineers to evaluate exposures a priori and to assist in optimization of control. Further refinements including a virtual arm, a representation of the filter sampling process, worker motion and the inclusion of volatile aerosols will help extend the power of such an approach. A significant limitation of the numerical method as it currently exists is the required post-processing of particle trajectory files. If this were an option within the CFD software, particle trajectories could be processed much more efficiently.

Acknowledgments

This work was supported by grant number R01/OH02858-06 from the U.S. National Institute of Occupational Safety and Health (NIOSH), and by the North Carolina Supercomputing Center (NCSC). Its contents are solely the responsibility of the authors and do not necessarily represent the official views of NIOSH or NCSC.

References

[1] Heinonen, K., Kulmala, I., and Saamanen, A., 1996, ''Local Ventilation for Powder Handling a Combination of Local Supply and Exhaust Air,'' Am. Ind. Hyg. Assoc. J., **57**, pp. 356–365.
[2] Kulmala, I., Saamanen, A., and Enbom, S., 1996, ''The Effect of Contaminant Source Location on Worker Exposure in the Near-Wake Region,'' Ann. Occup. Hyg., **40**, pp. 511–523.
[3] Flynn, M. R., and Sills, E., 2000, ''On the use of computational fluid dynamics in the prediction and control of exposure to airborne contaminants–an illustration using spray painting,'' Ann. Occup. Hyg., **44**, No. 3, pp. 191–202.
[4] Flynn, M. R., Gatano, B., McKernan, J. L., Dunn, K., Blazicko, B. A., and Carlton, G. N., 1999, ''Modeling Breathing-Zone Concentrations of Airborne Contaminants Generated During Compressed Air Spray Painting,'' Ann. Occup. Hyg., **43**, No. 1, pp. 67–76.
[5] Carlton, G. N., and Flynn, M. R., 1997, ''Field Evaluation of an Empirical-Conceptual Exposure Model,'' Appl. Occup. Environ. Hyg., **12**, No. 8, pp. 555–561.
[6] Heitbrink, W. A., Wallace, M. E., Bryant, C. J., and Ruch, W. E., 1995, ''Control of Paint Overspray in Autobody Repair Shops,'' Am. Ind. Hyg. Assoc. J., **56**, No. 10, pp. 1023–1032.
[7] Carlton, G. N., and Flynn, M. R., 1997, ''A Model to Estimate Worker Exposure to Spray Paint Mists,'' Appl. Occup. Environ. Hyg., **12**, No. 5, pp. 375–382.
[8] Carlton, G. N., and Flynn, M. R., 1997, ''Influence of Spray Painting parameters on Breathing Zone Particle Size Distributions,'' Appl. Occup. Environ. Hyg., **12**, No. 11, pp. 744–750.
[9] Kim, K. Y., and Marshall, J. R., 1971, ''Drop-Size Distributions from Pneumatic Atomizers,'' AIChE J., **17**, No. 3, pp. 575–584.
[10] Tan, Y., and Flynn, M. R., 2000, ''Experimental Evaluation of a Mathematical Model for Predicting Transfer Efficiency of a High Volume–Low Pressure Air Spray Gun,'' Appl. Occup. Environ. Hyg., **15**, No. 10, pp. 785–793.
[11] Vincent, J., 1995, *Aerosol Science for Industrial Hygienists*, Pergamon Press, New York, NY.
[12] Hicks, P. G., and Senser, D. W., 1995, ''Simulation of Paint Transfer in an Air Spray Process,'' ASME J. Fluids Eng., **117**, pp 713–719.
[13] Fluid Dynamics International, 1998, *FIDAP Manual*, Evanston III.
[14] Gosman, A. D., and Ioannides, E., 1981, ''Aspects of Computer Simulation of Liquid-Fuelled Combustors,'' AAIA 19th Aerospace Mtg., Paper No. 81-0323, St. Louis, MO.
[15] Heinsohn, R. J., 1991, *Industrial Ventilation: Engineering Principles*, Wiley Interscience, New York, NY.
[16] Domnick, J., Tropea, C., and Xu T. H., 1991, ''Measurements in Paint Sprays Using a Phase-Doppler Anemometer'' *Proceedings of the International Conference on Liquid Atomization and Spray Systems (5th)*, NTIS pb91-216838 pp. 129–138.

Gas-Liquid Distribution in the Developing Region of Horizontal Intermittent Flows

M. Fossa
DITEC, Dipartimento di Termoenergetica e Condizionamento Ambientale,
Università degli Studi di Genova,
Via all'Opera Pia 15a-16145 Genova, Italy
e-mail: mfossa@ditec.unige.it

Experiments have been carried out to analyze the evolution of the air/water flow structure along a horizontal 60 mm i.d. straight pipe. Plug and slug flow regimes were observed. In order to investigate the local structure of the flow, dynamic void fraction measurements have been performed by means of ring impedance probes. From dynamic void fraction measurements the mean void fraction values, the probability distributions of void, the liquid film height in the gas cavities and the slug frequencies have been evaluated. The analysis of the results showed that the flow structure deeply modifies along the pipe and that minor effects have to be ascribed to gas injection mode. The examination of the probability distribution function enabled the identification of the operating conditions at which the transition occurs, thus making it possible to propose a new objective criterion of identification. [DOI: 10.1115/1.1343108]

Keywords: Intermittent Flow, Impedance Probe, Slug Frequency, Flow Pattern Transition

1 Introduction

The flow of two-phase mixtures is a common situation in such industrial plants as chemical reactors, power generation units, oil wells, and pipelines. As it is well known, the flow configuration and the gas-liquid interactions in such systems are a complex function of the flow rates of the two phases, of their physical properties and of pipe geometry. Among the possible two-phase configurations, intermittent flow conditions are encountered for a wide range of gas and liquid superficial velocities. The intermittent flow in horizontal pipes can be described as the flow of liquid regions where the liquid bridges the whole pipe (plugs or slugs) separated by stratified flow regions. The repetitive structure of the flow introduces fluctuations in the flow properties (pressure, void fraction) that have to be accurately predicted in order to design pipelines and other two-phase flow industrial components.

Generally, the approach to predict the intermittent behavior of gas-liquid systems is to define a one-dimensional model based on the assumption that the flow can be described as a sequence of similar slug units travelling at assigned velocity. This is the method proposed first by Duckler and Hubbard [1], Nicholson et al. [2] and recently by Andreussi and co-workers [3,4]. Fabre et al. [5] proposed a multi-cell model based on a statistical distribution of the slug cell length.

Irrespective of the slug model chosen, some preliminary information (closure relationships) is required to apply the model and to obtain predictions of the flow. These relationships concern the evaluation of such flow parameters as the gas fraction in the slug body α_s, the translational velocity of the slug V_t, the frequency of the slug passage f, or the slug length l_s. In particular, the knowledge of the last two parameters is crucial to accurately predict the behavior of the two-phase flow.

Moreover, it is necessary to know the flow conditions at which the flow pattern transition from plug to slug flow occurs to account for the presence of gas in the liquid body (slug). There is a history of uncertainty over the correct location of the plug to slug boundary as can be noticed from the examination of different flow map and transition criteria (Mandhane et al. [6], Barnea [7], Lin and Hanratty [8], Ruder and Hanratty [9], Andreussi and Paglianti [10]). To date, it is even not clear whether the transition occurs at constant superficial gas velocity (as proposed by Mandhane et al., and Ruder and Hanratty) or whether it occurs at constant mixture superficial velocity.

Finally, it is important to know if the flow pattern is fully developed and if entrance effects are extinguished at the location where the flow parameters have to be evaluated. Since the entrance length (100 diameters and over) is usually greater than the characteristic length of several industrial components where a two-phase mixture is generated, it is essential to know to what extent the steady (or quasi-steady) configuration is suitable to describe the flow region immediately downstream the phase mixer, where the effects of the injection mode can appear.

The flow structure analysis is very important to understand the basic two-phase behavior and to develop, improve, and test the physical models of the intermittent flow. A fundamental quantity is the local void fraction, which allows the flow structure to be described efficiently when information is available in terms of space-time characteristics.

In this work, three void meters have been employed to control the flow evolution along the pipe and two gas injectors have been tested to study the effects of the injection mode. From dynamic void fraction measurements the mean void fraction values, the probability distributions of void (PDF), the liquid film height and the power spectra of void fraction fluctuations (PSD) have been evaluated.

2 Experimental Facility

2.1 Flow Loop. The experimental results presented in this paper have been obtained in a loop designed and assembled at Ditec, University of Genoa. The facility consists of a horizontal test section where air and water can be mixed to generate the two-phase flow under bubble, stratified and intermittent flow regimes near atmospheric pressure. Transparent pipes, carefully chosen to match the inner diameters at the tube ends, allow the inspection of the flow pattern; the test section is 12 m long and the pipe inner diameter is 60 mm.

In order to assess the effects of inlet conditions on the main flow parameters, two different phase mixers have been employed. Injector A was extensively employed: it is constituted by a holed drum (hole diameter 0.5 mm) where the gas phase is introduced

Contributed by the Fluids Engineering Division for publication in the JOURNAL OF FLUIDS ENGINEERING. Manuscript received by the Fluids Engineering Division April 5, 2000; revised manuscript received November 17, 2000. Associate Editor: J. Lasheras.

radially into the liquid stream. Injector B, employed to check the variations of the flow parameters to inlet condition variations, is a co-current phase injector where the gas phase is introduced from the top parallel to the liquid stream to create stratified flow conditions.

The gas and liquid superficial velocities covered in the experiments were $V_{sg}=0.3\sim4$ m/s and $V_{sl}=0.6$, 0.9, 1.1 and 2 m/s, respectively. Each run was repeated 5 times. Plug and slug flow regimes were observed during overall 130 test runs. The gas superficial velocities (and the gas volume fraction x_v) were calculated according to the pressure measurements collected 6 m downstream the phase mixer.

The test apparatus is equipped with resistive probes to measure the instantaneous void fraction at different locations from the mixer. The probes are located, respectively, at 33, 100, and 160 diameters from the injection. The test pipe is also equipped with 15 pressure taps to measure the pressure profiles along pipe. Further details on the test loop are available in Guglielmini and Soressi [11].

2.2 Void Meter Testing and Procedures. In the present work the instantaneous area-average void fraction measurement is performed by applying the conductance method by means of the device described by Fossa [12].

Many studies have been carried out on impedance void meters; impedance probes able to produce information on the area average void fraction were employed by Asali et al. [13], Andreussi et al. [14], Tsochatzidis et al. [15], Costigan and Whalley [16]. In particular, Andreussi, Tsochatzidis and co-workers described the response of resistive probes with ring electrodes flush mounted on the pipe internal wall on theoretical and experimental bases.

The void meters adopted in this investigation consists of ring electrode pairs placed on the internal wall of the cylindrical test duct, flush to the pipe surface. The calibration curve was obtained by means of the procedures described in detail in [12]. The assumption adopted here concerns the possibility to describe the structure of intermittent horizontal flows as if it were constituted of stratified regions separated by liquid regions where a few gas bubbles may be present.

As demonstrated, both theoretically and experimentally, by Andreussi et al. and as confirmed by the authors' measurements, the probe response is affected by the probe geometry and even more by the flow pattern: as a consequence, at the same mean void fraction, the mixture impedance changes with the phase distribution. In order to overcome this problem, the probe geometry was chosen to produce a probe response quite insensible to the changes between the uniformly dispersed (bubble) regime and the stratified regime. Based on preliminary tests, the probe aspect ratios D_e/D and s/D (D pipe diameter, D_e electrode spacing, s electrode width) have been chosen equal to 0.34 and 0.071, respectively. The selection of the proper electrode aspect ratios also resulted in small measuring volumes as compared with holdup spatial fluctuations.

Figure 1 shows the results of the calibration procedure in terms of dimensionless conductance. The data refer to the stratified and bubble flow configurations, different ring diameters but same aspect ratios. In order to avoid continuous checking of the electrical conductivity of the liquid during the runs, the measured two-phase conductance was normalized with respect to the conductance of the full-of-liquid test pipe at the beginning of the each test session, and then converted into void fraction data by means of the calibration curve. The reliability of the instrumentation adopted was confirmed by extensive comparisons with the void fraction measurements carried out with an optical fiber device as described by Arosio et al. [17].

The signal from each probe was picked up by the acquisition system at a sampling frequency of 100 Hz during a sampling period of 82 seconds. Each run was repeated 5 times. A repeatability investigation was performed over 50 test runs and at different probe locations: the standard deviation of the void fraction

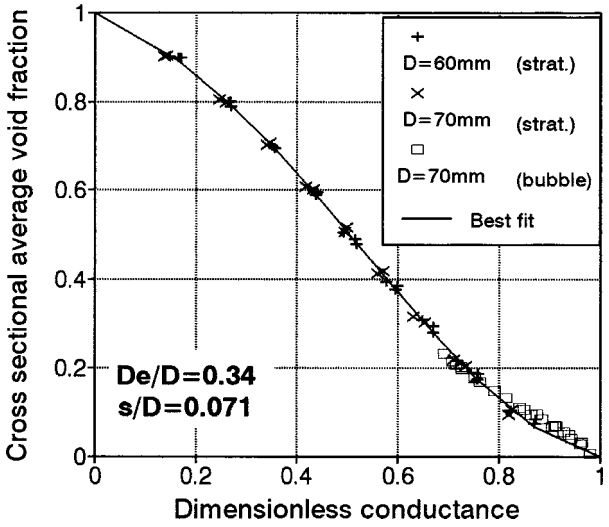

Fig. 1 Calibration of the impedance probe, according to the stratified and bubble phase distributions

measurements was found to be 1.5 percent. The statistical analysis of the data records allowed the time-average void fraction α and the void probability density function (PDF) to be inferred. The probability density profiles were employed to identify the flow pattern, as suggested by Jones and Zuber [18]. Furthermore, the analysis of the PDF profiles enabled the estimation of the void fraction in the stratified region between slugs from which the mean (i.e., most probable) liquid film height h and the minimum liquid film height $h_{\min}$ were inferred. The automated procedure consists in the analysis of the double peak profiles of the PDFs pertinent to intermittent flow: the peak at high void fraction is representative of the mean liquid level h while the right value of the void fraction where the PDF goes to zero can be associated to the minimum liquid level $h_{\min}$ (see Fig. 2). From the void fraction values the liquid level height has been calculated by solving a simple trigonometric problem.

The power spectral densities of the void sensor signal were obtained by the Fast Fourier Transform technique (FFT) according to the following procedure: 5 sets of records (82 seconds each) were collected and the final power spectrum was obtained from frequency averaging of the 5 power spectra resulting from each

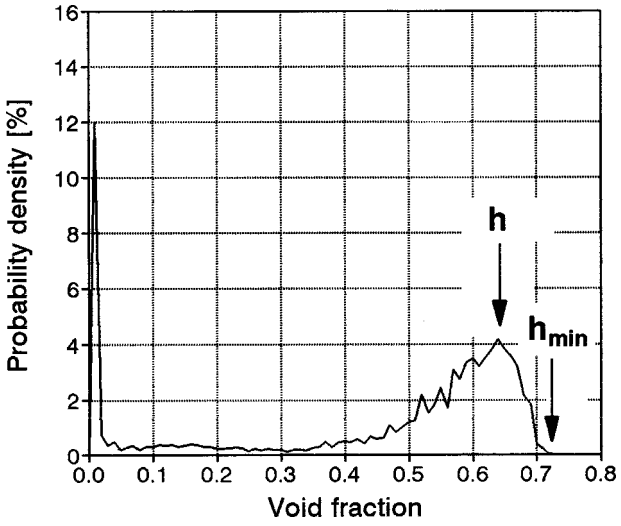

Fig. 2 Procedure to infer the liquid level values h and h_{min} from PDF profiles

data record (subjected to Welch type data windowing [19]). The frequency corresponding to the maximum of the power spectrum was assumed as the main frequency of the intermittent flow (slug frequency). More than 5 records (up to 10) were employed for some operating conditions to precisely detect the main frequency of the flow. This procedure yielded results in agreement with the classic criterion to infer the slug frequency, i.e., by counting the slug passages from the time histories of the probe signal.

3 Results and Discussion

3.1 Influence of the Inlet Conditions and Length for Flow Development. In order to investigate the effect of inlet conditions on the main flow parameters, a limited set of experiments have been duplicated by employing both the injection devices described in Section 2.1. The operating conditions considered for comparison cover the V_{sg} range 0.5–3 m/s and the liquid superficial velocities 0.6, 1.1, and 2.0 m/s: the overall number of runs was 30.

The influence of the injection mode on the measured flow parameters proved to be weak. As can be observed in Fig. 3 in terms of the ratios between void fraction values obtained with injectors A and B, the time average values were substantially the same for both inlet conditions. The values obtained with injector A were slightly higher (the average value of the ratio α_B/α_A is 0.986) but the differences between corresponding values turned out in the range of measurement uncertainty.

From the point of view of the time histories of the void signal, no considerable effects on the flow pattern have been observed due to the different injection mode at $x/D=100$, 160 and even near the mixer, at $x/D=33$. Similar conclusions can be drawn for the measured values of slug frequency and liquid film levels.

For what concerns the developing length to obtain a stable flow condition 150 diameters from injection are generally considered enough. As a confirmation, most of available data in literature have been collected at a distance from the phase mixer in the range 150–200 D. Even if the occurrence of a developed flow is a matter of definition (the pressure drops continuously affect the gas density and hence the mixture velocity), one important contribution is the study of Nydal et al. [20], where the question is deeply discussed. The authors demonstrated that a (cf. p. 444) ''well-defined statistical distribution of the slug holdup, with only one peak, may be regarded as a necessary condition for developed slug flow.'' Nydal and co-workers demonstrated that the entrance length depends on both gas and liquid superficial velocities and

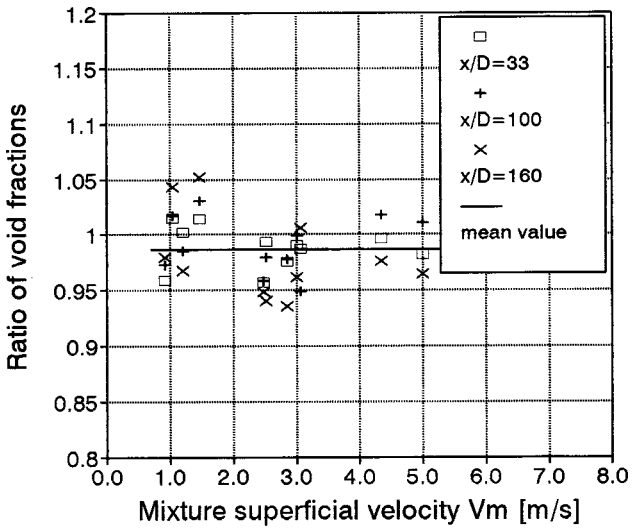

Fig. 3 Ratio of void fraction values α_B/α_A as obtained from different injector tests

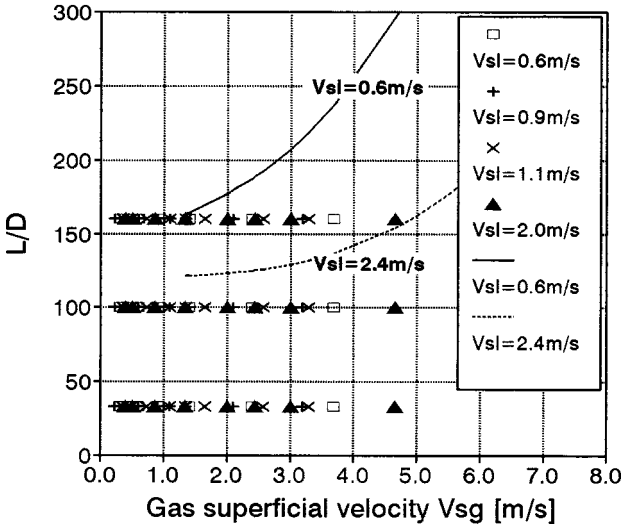

Fig. 4 Nydal map [20] for entry length and present operating conditions

that it ranges from 120 D to 400 D and over. Based on their own measurements they obtained a map of minimum length for developed slug flow. The operating conditions of present investigation have been plotted on Nydal map (Fig. 4): it can be observed that a length of 160 D generally accomplishes the developed flow criterion, while shorter distances such as 33 D and 100 D (the other measuring position in the present work) are in the entrance region of the flow.

3.2 Liquid Holdup Time Histories. The effects of the operating conditions on the local flow structure in two-phase horizontal intermittent flow have been investigated by recording the void fraction fluctuations in three locations along the test pipe. some typical time histories are shown in Figs. 5(*a*)–5(*f*), in terms of liquid holdup versus time. As can be observed, the flow pattern changes with the flow rates of gas and liquid and with the distance from the phase mixer thus making it possible to notice a few peculiar features.

The plug flow, defined as usual as a sequence of liquid packets free of gas bubbles bridging the whole pipe, is evidenced by the appearance of time intervals during which the holdup is equal to unity. As can be observed in Figs. 5(*a*) and 5(*b*), the plug flow is accompanied by step changes of the liquid level in the gas cavities between plugs when the liquid superficial velocity is low, namely for $V_{sl}=0.6$ m/s and $V_{sg}=0.9$ m/s. This phenomenon was observed and outlined by Ruder and Hanratty [9], who carried out experiments with a 0.095 m i.d. pipe and measured the liquid level during intermittent flows at 190 diameters from the injection. They concluded that the existence of staircase-like shape of the liquid level profile is an indicator of the plug flow regime. The examination of Fig. 5(*c*), which refers to $V_{sl}=1.1$ m/s, shows that the two-stage liquid level disappears as V_{sl} is increased at the same gas superficial velocity V_{sg} (around 0.4 m/s) as imposed for the test runs of Figs. 5(*a*) and 5(*b*). The analysis of the holdup records pertinent to $V_{sl}=2.0$ m/s confirms that plug flow can exist without step changes in the liquid level of the stratified regions. It is interesting to notice that at $V_{sl}>1$ m/s no two-stage liquid profiles were observed even at $x/D=100$, so that the possibility to ascribe the appearance of a two-stage liquid level to a flow development effect can be excluded. From the above experimental results and observations, it can be concluded that the phenomenon is peculiar of plug flow only at low liquid superficial velocities, namely at $V_{sl}<1$ m/s.

Figures 5(*d*) and 5(*e*) show two typical holdup records concerning slug flow: the holdup pertinent to the slug passages is gener-

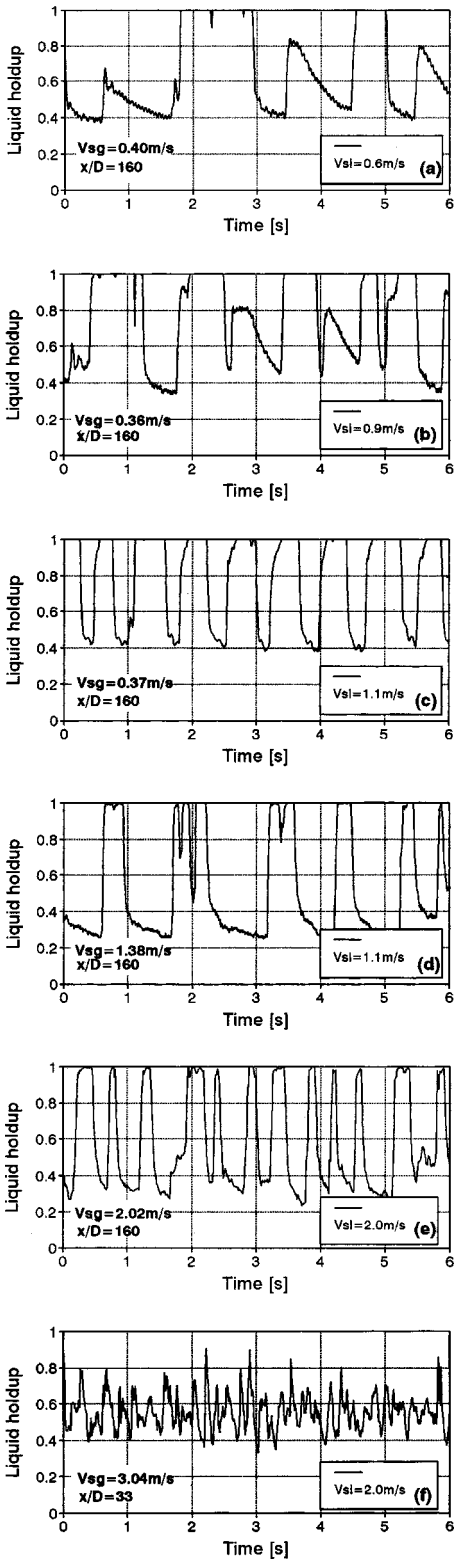

Fig. 5 Liquid holdup tracings at different locations along the test pipe and for different operating conditions

ally lower than the unity due to the presence of gas bubbles in the liquid core. It can be noticed that liquid height minimum (as indicated by the holdup trace with the assumption of no aeration of the liquid carpet) is associated with the slug front, as observed by Ruder and Hanratty.

Figure 5(*f*) shows typical holdup fluctuations near the phase mixer ($x/D=33$) at high values of V_{sg}. As can be noticed from the holdup records (and as confirmed by the visual observation of the flow), the structure of the intermittent flow disappears and the flow pattern assumes the features of a wavy stratified regime when V_{sg} is higher than 2.5 m/s for all the liquid flow rates here considered and irrespective of the phase mixer employed. Below this threshold value, even at $x/D=33$ an intermittent flow structure has been observed. This fact may suggest that the length needed to start the intermittent flow mainly depends on the gas flow rate, increasing as the gas flow rate is increased.

3.3 Time Average Void Fraction Along the Channel. Data on the time average void fraction α have been obtained from integration of time series such as those described above. The knowledge of the average void fraction during intermittent flows is important since it allows the velocity of the gas pockets V_b (or slug translational velocity V_t) to be evaluated, which is an unknown of the one-dimensional slug model. To this aim the relation of Nicklin et al. [21] can be generalized to evaluate the bubble velocity in plug/slug flow as a function of the mixture velocity $V_m=(V_{sg}+V_{sl})$, the velocity of a bubble in stagnant liquid v_0 (drift velocity) and a constant C_0:

$$V_b=C_0V_m+v_0 \tag{1}$$

According to Bendiksen [22] the the above relation may be interpreted by stating that the bubble moves at velocity v_0 relative to the centerline velocity of the liquid ahead of the bubble; when the flow is horizontal, the term v_0 can be neglected at high mixture velocities. According to Bendiksen [22], v_0 vanishes at liquid Reynolds numbers greater than 40,000. Woods and Hanratty [23] stated that v_0 contributes to bubble velocity only for $V_m<3$ m/s. At low mixture velocity, the drift velocity approaches the values suggested by Benjamin [24]:

$$v_0=0.542(gD)^{0.5} \tag{2}$$

A great number of studies have been devoted to the evaluation of the constant C_0 as reported in [22,23]. For horizontal flows the most significant results of such investigations is that the values of C_0 range from 1–1.35. According to Bendiksen, C_0 approaches value 1.2 at liquid Reynolds numbers greater than 50,000. With the assumptions of deaerated liquid regions and negligible drift velocity, it can be easily demonstrated that (1) can be written in terms of α as:

$$V_{sg}/\alpha=C_0V_m \tag{3}$$

which in turns, as C_0 is fixed at the value 1.2, coincides (if the pressure term is neglected) with the correlation of Armand and Treshchev [25]:

$$\alpha=0.833x_v+0.05\ln(10p) \tag{4}$$

where x_v is the volume gas fraction defined as V_{sg}/V_m and p is the pressure in MPa.

Data relative to the time average void fraction measured during our experiments for given values of gas and liquid superficial velocities are sketched in Figs. 6(*a*)–6(*d*) as a function of x_v with the dimensionless distance from injection x/D as a parameter. The reported values are the averages of those obtained for 5 repeated runs. The main result is the increase of the void fraction while moving in the streamwise direction. The void fraction values predicted by Armand-Treshchev correlation are attained in the measuring station located at 160 diameters while values up to 20 percent less have been measured upstream. At low liquid superficial velocities (i.e., $V_{sl}=0.6$ m/s) the void fraction values at $x/D=33$ and $x/D=100$ are very close to each other and the void fraction values at $x/D=160$ are lower than those expected by (4) as can be noticed from Fig. 6(*a*).

For higher liquid superficial velocities (Figs. 6(*b*), 6(*c*), 6(*d*)), the void fraction values at $x/D=33$ are generally lower than those measured at $x/D=100$ but the difference is reduced at $x_v>0.6\sim0.7$ ($V_{sg}>1.3$ m/s). The void fraction values at $x/D=160$ are

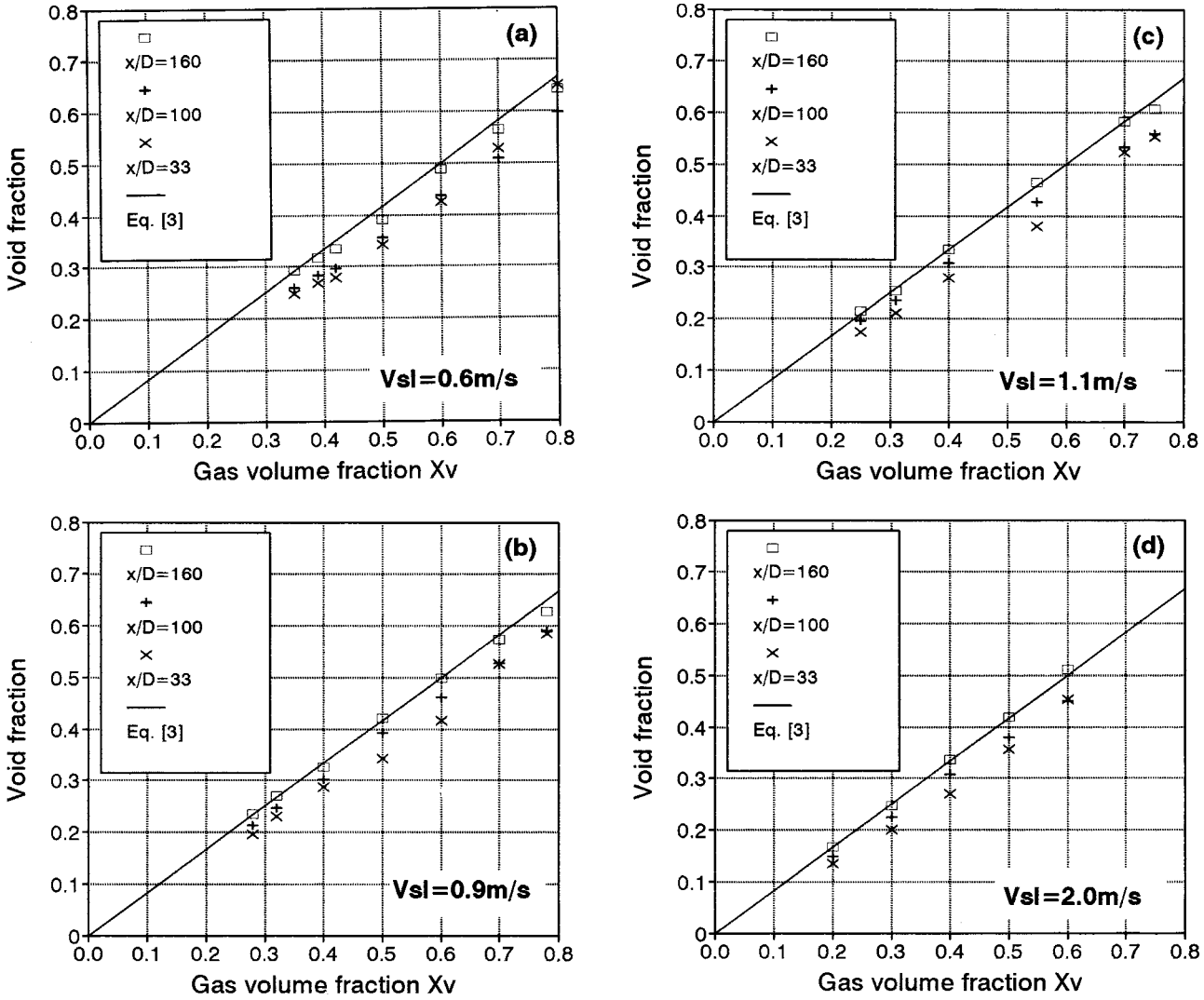

Fig. 6 Area average void fraction as a function of the gas volume fraction. Parameter: distance from the phase injection.

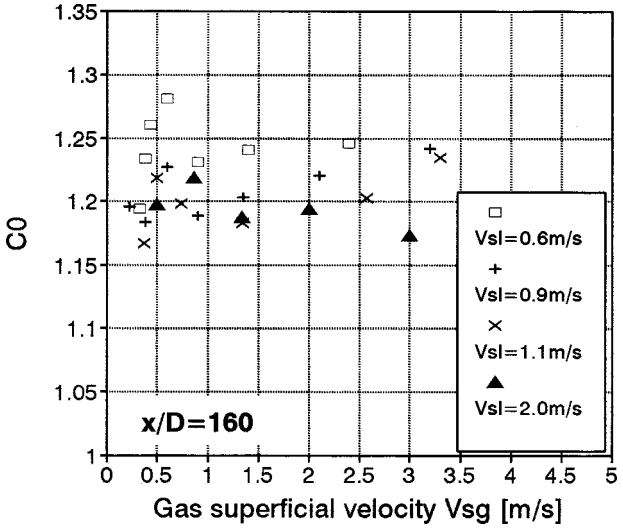

Fig. 7 Calculated values of the constant C_0 as defined in (3)

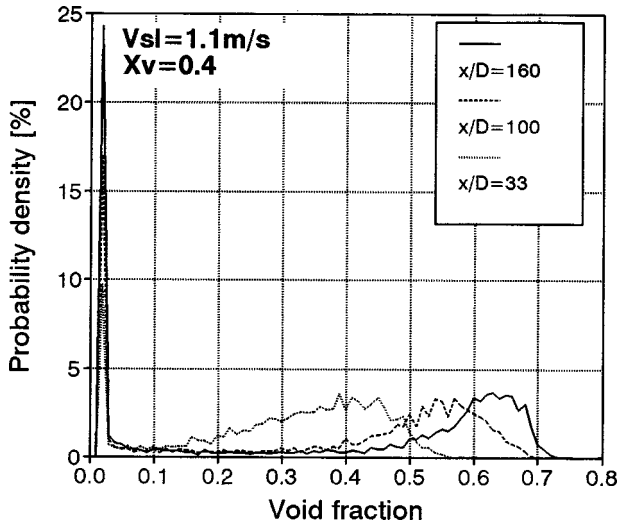

Fig. 8 PDF profiles at different locations along the test pipes

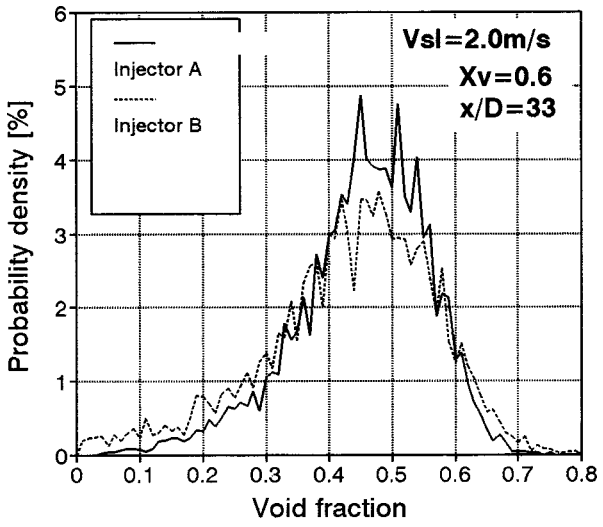

Fig. 9 Typical PDF profiles for stratified flow at the tube inlet ($x/D=33$) when $V_{sg}>2.5$ m/s

well fitted by (4): this fact may be a further indication that a (quasi) steady flow pattern has been reached at the downstream measuring location.

The measurements of the void fraction can be interpreted in terms of constant C_0 by (3). It can be deduced from Figs. 6(*a*)–6(*d*) that C_0 ranges from 1.20–1.50 for all the operating conditions and measuring locations. In particular, at $x/D=160$, the constant C_0 is around value 1.20 as can be noted in Fig. 7. A closer examination of the figure reveals the influence of the liquid flow rate, as already observed above in comments to Figs. 6(*a*)–6(*d*).

These results are in reasonable agreement with the measurements of Bendiksen [21] but it should be noted that the present results refer to liquid Reynolds numbers in the range 40,000–120,000 while Bendiksen's data correspond to lower Reynolds numbers.

3.4 Statistical Distribution of Void Fraction, Flow Pattern Transition and Liquid Film Level. The records of the instantaneous void fraction have been analyzed in terms of probability density function (PDF). Intermittent flow is associated with a twin-peaked PDF [18], where the low void fraction peak is pertinent to slug (plug) passage and the high void fraction peak is

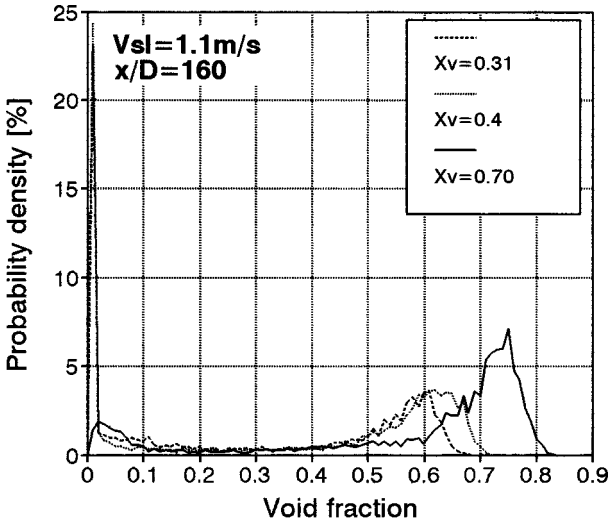

Fig. 10 PDF profiles at different gas flow rates

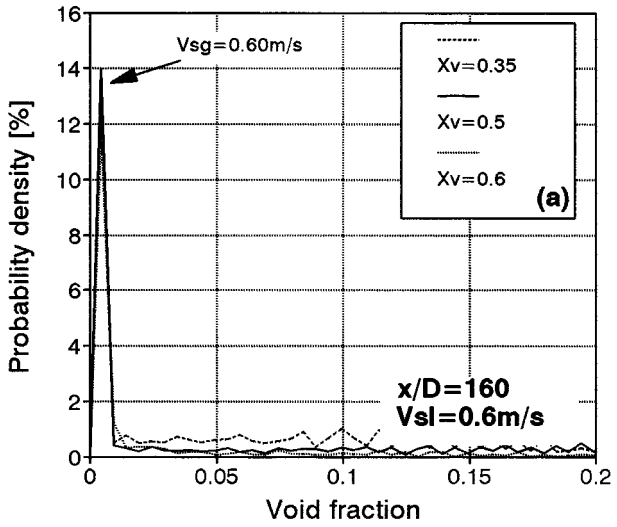

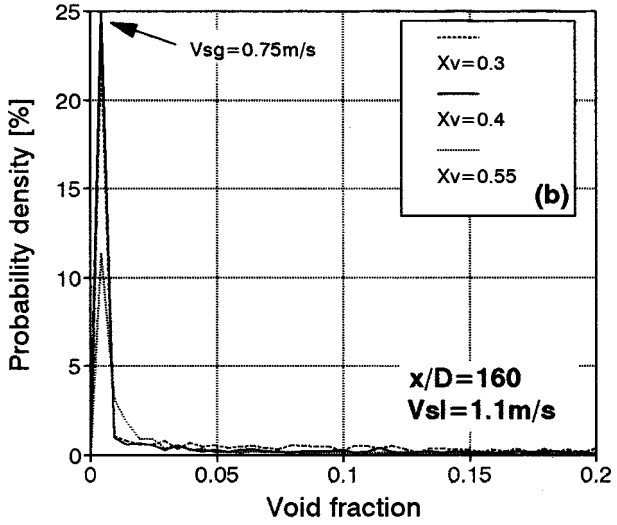

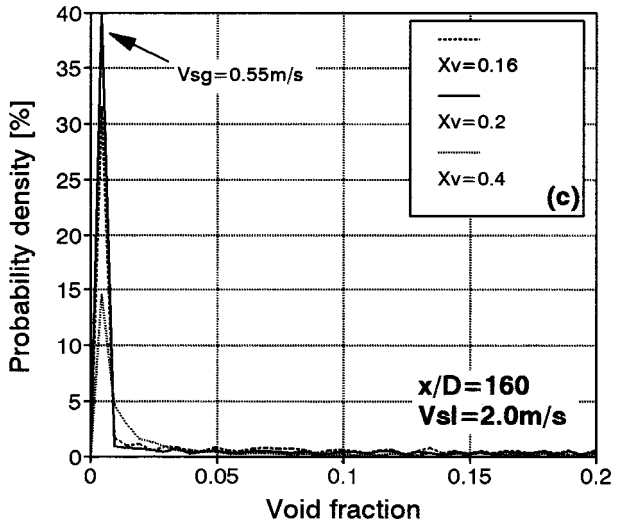

Fig. 11 Transition plug/slug flow by the analysis of PDF: the influence of the increasing gas flow rate on the height of the slug peak

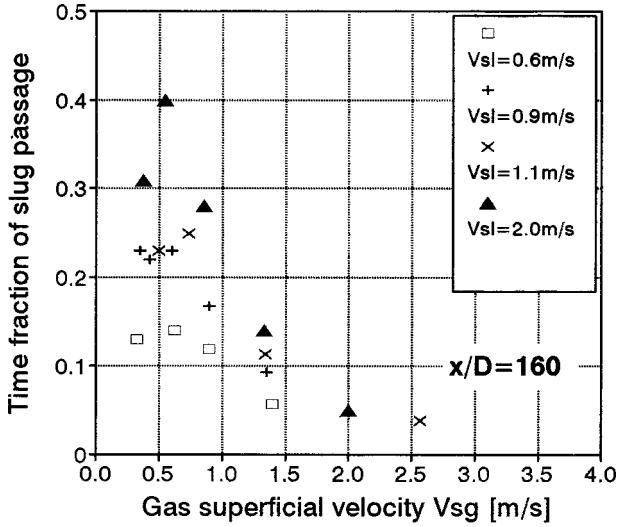

Fig. 12 Slug peak amplitudes for different values of V_{sg} and V_{sl}

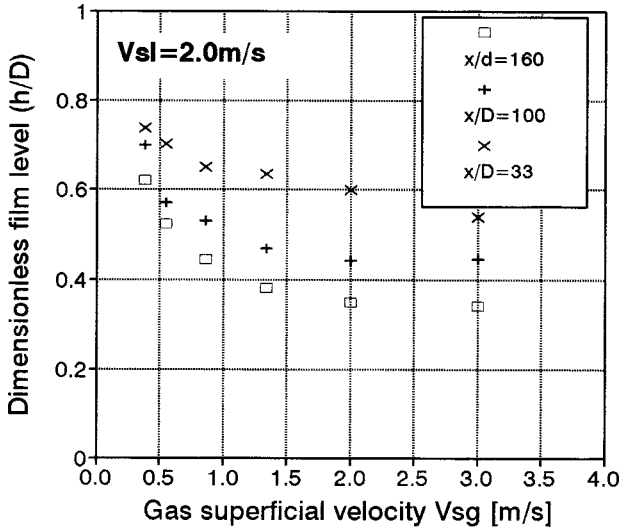

Fig. 13 Mean liquid levels evaluated from PDF analysis at different locations along the pipe

characteristic of separated phase regions (gas pockets). Typical PDF profiles reconstructed by means of the present data are shown in Figs. 8 and 9. Figure 8 shows the PDFs concerning the measurements at $x/D=33$, 100, and 160 for given gas and liquid flow rates. From Fig. 8 it is easy to detect the flow development along the channel: the height of the slug peak increases and the peak pertinent to the stratified regions moves to higher void fraction values as the distance from the injector is increased. The results of Fig. 8 correspond to a situation in which the time fraction pertinent to slug passage increases and the liquid film level in the separated phase regions reduces while moving along the streamwise direction. Figure 9 shows the PDF at $x/D=33$ at high values of the gas superficial velocity. The situation is described in Fig. 3(f). As can be observed, the PDF profile pertinent to $x/D=33$ collapses from double peak shape into single-peak shape as V_{sg} exceeds 2.5 m/s. In these conditions, the flow pattern can be classified as stratified and the void fraction at which the maximum of the PDF occurs is very close to the time average α. It should also be noted from Fig. 9 that the two injection devices here employed produce similar phase distributions.

The effect of gas flow rate on the flow pattern is shown in Fig. 10 at $x/D=160$. The main result is that the slug peak tends to disappear and the separated phase peak moves to the right and increases in height. A deeper analysis of the PDF profile as a function of the V_{sg} reveals a very interesting feature. Consider the PDFs reported in Figs. 11(a), 11(b), and 11(c) that correspond to different values of V_{sl}, namely 0.6 m/s, 1.1 m/s, 2.0 m/s; in all cases, the height of low void fraction peak (slug peak, which represents the time fraction pertinent to slug passage) goes through a maximum while the gas flow rate increases. The situation is summarized in Fig. 12, where the slug peak amplitude is plotted as a function of gas and liquid superficial velocities. Careful observation of the time histories of the void signal as well as of the PDF profiles themselves indicates, at gas superficial velocities greater than those pertinent to the occurrence of the peak height maximum, the presence of gas bubbles inside the slug body. From PDF profiles, it can be noted that, as the peak height passes beyond the maximum, the peak base enlarges to prove the inception of bubble entrainment in the slug core.

According to the standard definition of plug and slug flow regimes, the presence of bubbles is the indicator of the transition. Therefore, the existence of a maximum of the slug peak height can be utilized as a criterion to identify the transition from plug to slug flow regime. This criterion can be used as an objective and quantitative discriminator for the occurrence of flow pattern transition.

The examination of Figs. 11(a)–11(c), as well as of Fig. 12, reveals other interesting features. The first observation pertains to the slug residence time over the observation period: the time fraction of slug passage has a maximum, which increases with the liquid flow rate. Second observation: the flow pattern transition does not depend on the liquid flow rate but it depends only on the gas flow rate, as the Mandhane flow map suggested. The threshold V_{sg} value for transition is around 0.6–0.7 m/s for all the liquid flow rate investigated. This value matches that evaluated by Ruder and Hanratty (0.6 m/s [9]) according different criteria based on the inspection of the shape of the elongated bubbles. The transition value for V_{sg} is also close to the boundary on the Mandhane map ($V_{sg}=0.8-1$ m/s), while, on the contrary, is far from the values expected from Refs. [7], [10], according to which the transition occurs at constant mixture velocity ($V_m=2-2.5$ m/s).

The height of the liquid film in the stratified region between slugs was determined from the analysis of PDF curves of the type shown in Figs. 8–10. As described in Section 2.2, the average height h (most probable) of the liquid film was inferred from the

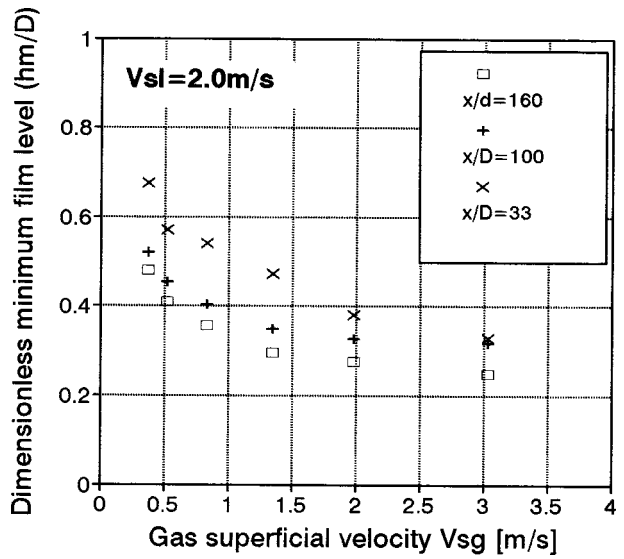

Fig. 14 Minimum liquid levels evaluated from PDF analysis at different locations along the pipe

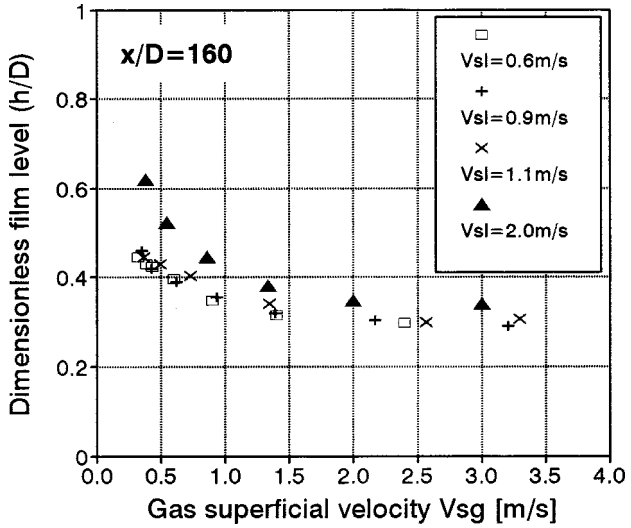

Fig. 15 Mean liquid levels evaluated from PDF analysis for different values of V_{sl}

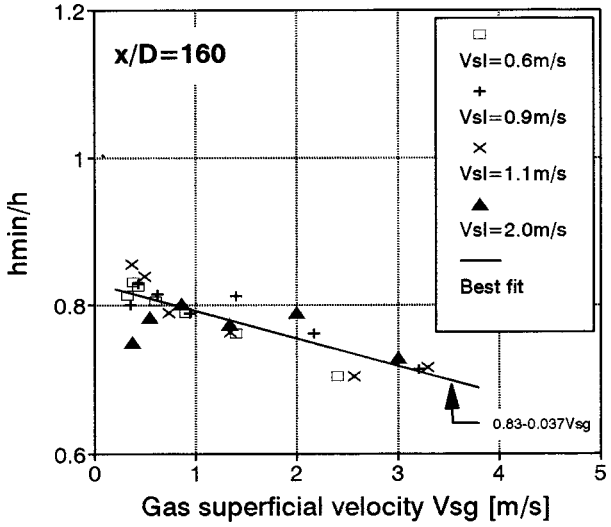

Fig. 17 The ratio between the minimum and the mean liquid levels at $x/D=160$

void fraction at which the maximum of the right peak occurs while the minimum liquid level $h_{\min}$ was associated with the right value of the void fraction where the PDF goes to zero.

Figures 13 and 14 show the dimensionless liquid level h/D and minimum liquid level $h_{\min}/D$ as a function of V_{sg} at different location along the pipe. As can be observed, the values of h and $h_{\min}$ decrease with the distance from the injection and with increasing gas flow rate.

The figures refer to $V_{sl}=2.0$ m/s; similar trends have been obtained at lower liquid flow rates. The effect of the increasing liquid flow rate is to increase the liquid depth (either h or $h_{\min}$) mainly at the tube inlet ($x/D=33$), where difference up to 30 percent have been observed at the same value of V_{sg}. Such differences decrease as the gas flow rate increases. It is worthwhile to notice that for $V_{sl}<1$ m/s the values of h as measured at $x/D=33$ are in reasonable agreement with the values expected from the stability criterion for the onset of intermittent flow as proposed by Lin and Hanratty [26].

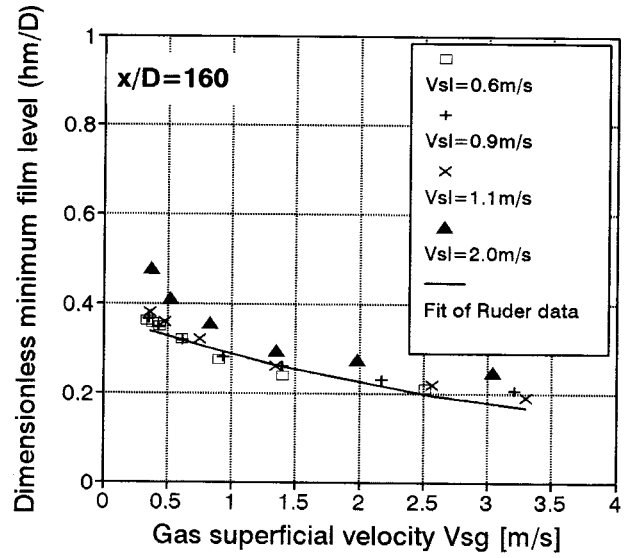

Fig. 16 Minimum liquid levels evaluated from PDF analysis for different values of V_{sl}

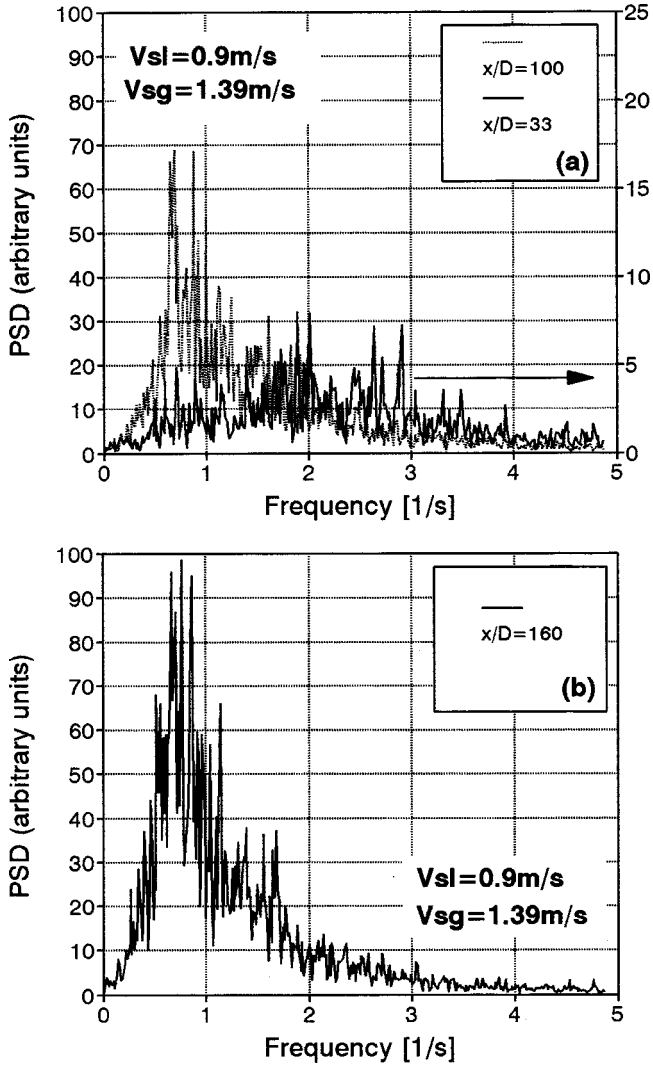

Fig. 18 Power spectral densities of void fraction fluctuations. Parameter: location along the pipe

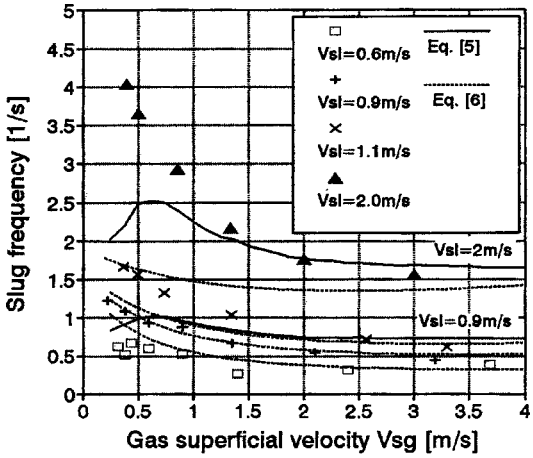

Fig. 19 Slug frequencies as inferred from FFT analysis and comparison with theoretical models

Near the tube outlet ($x/D=160$) the liquid levels h and $h_{\min}$ are not very sensitive to the changes in the liquid flow rate, as can be seen in Figs. 15 and 16. In particular, for V_{sl} in the range 0.6–1.1 m/s the experimental data lie on the same curve while the data pertinent to $V_{sl}=2.0$ m/s show values approximately 25 percent higher. These results are consistent with Ruder and Hanratty measurements that are summarized as continuous line in Fig. 16. The agreement between the two sets of data is good and confirms that the minimum film heights weakly depend on liquid flow rate for V_{sl} values up to 1 m/s. Over this value the increase of V_{sl} yields the liquid level to rise as demonstrated by the level profile pertinent to $V_{sl}=2.0$ m/s.

Finally, it has been observed that a linear relationship exists between the measured values of $h_{\min}$ and h. The ratio of the two quantities is about 0.65–0.8 and is quite insensible to the liquid flow rate variations: the effect of the gas superficial velocity on the $h_{\min}/h$ ratio is shown in Fig. 17 with reference to the measurements taken at $x/D=160$.

4.5 Power Spectral Densities and Slug Frequency. As previously discussed (cap. 1), one-dimensional models to predict intermittent flow behavior, require some preliminary information (closure relationships). These relationships concern the evaluation of such flow parameters as the frequency of the slug passage f or the slug length l_s. In what follows, some available relationships for slug frequency evaluation are considered for comparison with present data.

The analysis of probe signals in the frequency domain allowed the power spectral densities (PSD) of void fraction to be obtained by using the Fast Fourier Transform technique as described in Section 2.2. As an example, Figs. 18(*a*), 18(*b*) give the results obtained at 33, 100, and 160 diameters from the air injection, for $V_{sl}=0.9$ m/s and $V_{sg}=1.39$ m/s. The PSDs show the appearance of a dominant frequency that becomes more evident with the increase in the distance from the phase mixer. With reference to the measurements collected at $x/D=33$, it can be noticed that, although the spectrum is wide and no dominant frequency can be detected, the maximum of the PSD occurs at frequencies two or three times higher than those measured in the downstream locations.

This observation is consistent with the model proposed by Tronconi [27], who postulated that a linear relationship exists between the frequency of formation of superficial waves during the stratified flow and the slug frequency: the proposed model allows the slug frequency to be evaluated as a function of the flow parameters pertinent to the stratified flow configuration.

$$f=0.61\frac{\rho_g}{\rho_l}\left(\frac{V_g}{D-h}\right)_{\text{strat}} \tag{5}$$

In order to evaluate the slug frequency, the phase density ρ, the equilibrium liquid height h and the actual gas velocity V_g have to be estimated with reference to the stratified flow configuration. The author suggests the Taitel and Dukler model [28] to get the flow parameters at equilibrium for the stratified flow.

For comparison with present data the well-known correlation of Gregory and Scott [29] has also been considered. This dimensional correlation for slug frequency is based on experiments carried out in horizontal pipes at low liquid superficial velocities ($0.4<V_{sl}<1.3$ m/s):

$$f=0.0226\left[\frac{V_{sl}}{Dg}\left(\frac{19.75}{V_m}+V_m\right)\right]^{1.2} \tag{6}$$

The slug frequency results obtained from FFT analysis at $x/D=160$ are reported in Fig. 19 as a function of V_{sg} and V_{sl} together with the expected values from (5) and (6).

As can be observed, the experimental values and the predicted ones are in fairly good agreement at V_{sg} values greater than 2 m/s. In particular, the experimental results are in satisfactory agreement with the Gregory and Scott correlation at low values of V_{sl}($V_{sl}<1$ m/s); these are the conditions at which the correlation was developed. At high liquid superficial velocity (2.0 m/s in this study) the Gregory and Scott correlation underestimates the slug frequency with an error up to 120 percent for $V_{sg}<0.5$ m/s. In this range, no reliable predictions can be obtained with Tronconi model, since the error is around 50 percent. It can be noticed that the Tronconi model, which remains a simple but powerful tool based on a realistic description of the flow, exhibits a through-a-maximum profile at low V_{sg} which does not correspond to the trend of the measured values. As the gas superficial velocity increases the error reduces: at $V_{sg}=3$ m/s the difference between the values predicted by (5) and the measured ones is around 15 percent.

5 Conclusions

The impedance method was adopted to measure the area average instantaneous void fraction in two-phase flows developing in a horizontal pipe. The investigated flow conditions cover the plug and slug flow regimes. The analysis of the results shows that the flow structure deeply modifies along the pipe and that minor effects have to be ascribed to the gas injection mode. The main results are the following:

1 The examination of the time histories of void fluctuations showed some peculiar features: in particular it was observed that at low liquid superficial velocities ($V_{sl}<1$ m/s) the plug flow is associated with appearance of step changes of the liquid level in the gas cavities between plugs. The examination of void records which refer to $V_{sl}=1.1$ m/s and 2.0 m/s, showed that the two-stage liquid level disappears as V_{sl} is increased at the same gas superficial velocity V_{sg}.

2 The time average void fraction increases along the pipe: in the downstream region ($x/D=160$) the measured values agree with those predicted by the correlation of Armand and Treshchev while upstream ($x/D=33$,100) up to 20 percent less values have been measured.

3 The variation of PDF profile as a function of the gas flow rate shows that the height of the slug peak goes through a maximum that may be associated with the flow conditions at which the transition between plug and slug flow regimes occurs. Thus the examination of the probability distribution function enables the identification of the operating conditions at which the transition occurs. When the possibility to vary the flow rate exists, this criterion can be used as an objective and quantitative discriminator

for the occurrence of flow pattern transition. According to this procedure, the transition occurs at constant V_{sg} at a value around $0.6 \sim 0.7$ m/s.

4 Far from the injection ($x/D = 160$) the liquid levels h and $h_{\min}$ are not very sensitive to the changes in the liquid flow rate, while the influence is stronger at the inlet ($x/D = 33$). In particular, for V_{sl} in the range 0.6–1.1 m/s the experimental data lie on a single curve while the data pertinent to $V_{sl} = 2.0$ m/s show values approximately 25 percent higher. The h-over-$h_{\min}$ ratio ranges from 0.8–0.6 as V_{sg} increases in the range of investigated values.

5 The slug frequencies inferred from power spectra showed that a lack in the prediction capability of different correlations exists at $V_{sl} > 1$ m/s especially for low gas superficial velocities, namely at $V_{sg} < 0.5$ m/s, where the error is at least 50 percent.

Acknowledgments

The author is grateful to Professor Giovanni Guglielmini for his helpful suggestions and assistance. The author also acknowledges the financial support of ''MURST, PRIN 1999, tecniche per l'incremento dell'efficienza dei processi termofluidodinamici.''

Nomenclature

C_0 = coefficient for bubble velocity expression
D = pipe diameter
D_e = electrode spacing
f = frequency
g = acceleration of gravity
h = liquid depth
$h_{\min}$ = minimum liquid depth
$\dot{m}$ = mass flow rate
p = pressure
s = electrode width
v_0 = drift velocity
V = velocity
V_s = superficial velocity
x = distance from the injection
x_v = gas fraction of volume flow
α = void fraction
ρ = density
σ = Area contraction ratio

Subscripts

b = bubble
g = gas
l = liquid
m = mixture

References

[1] Dukler, A., and Hubbard, M. G., 1975, ''A Model for Gas-Liquid Slug Flow in Horizontal and Near Horizontal Tubes,'' Ind. Eng. Chem. Fundam., **14**, pp. 337–347.
[2] Nicholson, M. K., Aziz, K., and Gregory, G. A., 1978, ''Intermittent Two Phase Flow in Horizontal Pipes: Predictive Models,'' Can. J. Chem. Eng., **56**, pp. 653–663.
[3] Andreussi, P., Bendiksen, K. H., and Nydal, O. J., 1993, ''Void Distribution in Slug Flow,'' Int. J. Multiphase Flow, **19**, pp. 817–828.
[4] Andreussi, P., Minervini, A., and Paglianti, A., 1993, ''Mechanistic Model of Slug Flow in Near Horizontal Pipes,'' AIChE J., **39**, pp. 1281–1291.
[5] Fabre, J., Ferschneider, G., and Masbernat, L., 1983, ''Intermittent Gas Liquid Flow in Horizontal or Weakly Inclided Pipes,'' *Proc. Int. Conf. on Physical Modelling of Multiphase Flow*, Coventry, U.K.
[6] Mandhane, J. M., Gregory, G. A., and Aziz, K., 1974, ''A Flow Pattern Map for Gas-Liquid Flows in Horizontal Pipes,'' Int. J. Multiphase Flow, **1**, pp. 537–553.
[7] Barnea, D. A., 1987, ''A Unified Model for Predicting Flow-Pattern Transitions for the Whole Range of Pipe Inclinations,'' Int. J. Multiphase Flow, **13**, pp. 1–12.
[8] Lin, P., and Hanratty, T. J., 1987, ''The Effect of the Pipe Diameter on the Flow Patterns for Air-Water Flow in Horizontal Pipes,'' Int. J. Multiphase Flow, **13**, pp. 549–563.
[9] Ruder, Z., and Hanratty, T. J., 1990, ''A Definition of Gas-Liquid Plug Flow in Horizontal Pipes,'' Int. J. Multiphase Flow, **16**, pp. 233–242.
[10] Andreussi, P., and Paglianti, A., ''The Boundary of Slug Flow in Near Horizontal Pipes,'' 1995, *Proc. Int. Conf. on Multiphase Flow in Industrial Plants*, Amalfi, Italy.
[11] Guglielmini G., and Soressi, E., 1996, ''Experimental Data of Two-Phase Pressure Drop Across Sudden Area Contractions in Horizontal Flow,'' *Proc. 5th Int. Conf. Multiphase Flow in Industrial Plants*, Amalfi, Italy.
[12] Fossa, M., 1998, ''Design and Performance of a Conductance Probe for Measuring the Liquid Fraction in Two-Phase Gas-Liquid Flows,'' J. Flow Meas. Instrum., **9**, pp. 103–109.
[13] Asali, J. C., Hanratty, T. J., and Andreussi, P., 1985, ''Interfacial Drag and Film Height for Vertical Annular Flow,'' AIChE J., **31**, pp. 895–902.
[14] Andreussi, P., Di Donfrancesco, A., and Messia, M., 1988, ''An Impedance Method for the Measurement of Liquid Hold-Up in Two Phase Flow,'' Int. J. Multiphase Flow, **14**, pp. 777–785.
[15] Tsochatzidis, N. A., Karapantios, T. D., Kostoglou, M. V., and Karabelas, A. J., 1992, ''A Conductance Method for Measuring Liquid Fraction in Pipes and Packed Beds,'' Int. J. Multiphase Flow, **5**, pp. 653–667.
[16] Costigan, G., and Whalley, P. B., 1997, ''Slug Flow Regime Identification from Dynamic Void Fraction Measurement in Vertical Air-Water Flows,'' Int. J. Multiphase Flow, **23**, pp. 263–282.
[17] Arosio, S., Bertola, V., and Fossa, M., 1999, ''Comparative Analysis of Intermittent Air-Water Flow Structure by Means of Different Measurement Techniques,'' *Proc. 2nd Int. Symp. Two-Phase Flow Modelling and Experimentation*, Pisa, Italy.
[18] Jones, O. C., and Zuber, N., 1975, ''The Interrelation between Void Fraction Fluctuations and Flow Patterns in Two-Phase Flow,'' Int. J. Multiphase Flow, **2**, pp. 273–306.
[19] Press, W. H., Teukolsky, S. A., Vetterling W. T., and Flannery, B. P., 1994, *Numerical Recipes in Fortran*, Cambridge Univ. Press, pp. 545–550.
[20] Nydal, O. J., Pintus, S., and Andreussi, P., 1992, ''Statistical Characterization of Slug Flow in Horizontal Pipes,'' Int. J. Multiphase Flow, **3**, pp. 439–453.
[21] Nicklin, D. J., Wilkes, J. O., and Davidson, J. F., 1962, ''Two-Phase Flow in Vertical Tubes,'' Trans. Inst. Chem. Eng., **40**, pp. 61–68.
[22] Bendiksen, K. H., 1984, ''An Experimental Investigation of the Motion of Long Bubbles in Inclined Tubes,'' Int. J. Multiphase Flow, **6**, pp. 467–483.
[23] Woods, B. D., and Hanratty, T. J., 1996, ''Relation of Slug Stability to Shedding Rate,'' Int. J. Multiphase Flow, **22**, pp. 809–828.
[24] Benjamin, T. B., 1968, ''Gravity Current and Related Phenomena,'' J. Fluid Mech., **31**, pp. 209–248.
[25] Armand, A. A., and Treshchev, G., 1959, ''Investigation of the Resistance during the Movement of Steam-Water Mixtures in Heated Pipe at High Pressure,'' *AERE Lib/Trans*, Vol. 81.
[26] Lin, P. Y., and Hanratty, T. J., 1986, ''Prediction of the Initiation of Slugs with Linear Stability Theory,'' Int. J. Multiphase Flow, **12**, pp. 79–98.
[27] Tronconi, E., 1990, ''Prediction of Slug Frequency in Horizontal Two-Phase Slug Flow,'' AIChE J., **36**, pp. 701–709.
[28] Taitel, Y., and Dukler, A., 1976, ''A Theoretical Approach to the Lochart-Martinelli Correlation for Stratified Flow,'' Int. J. Multiphase Flow, **2**, pp. 591–605.
[29] Gregory, G. A., and Scott, D. S., 1972, ''Correlation of Liquid Slug Velocity and Frequency in Cocurrent Horizontal Gas-Liquid Slug Flow,'' Ind. Eng. Chem. Proc. Des. Dev., **11**, pp. 317–318.

Rotating Probe Measurements of the Pump Passage Flow Field in an Automotive Torque Converter

Y. Dong

B. Lakshminarayana

Center for Gas Turbine and Power,
The Pennsylvania State University,
153 Hammond Building,
University Park, PA 16802

The relative flow in an automotive torque converter pump passage was measured at three locations inside the passage (mid-chord, 3/4-chord, and 4/4-chord) using a miniature high-frequency response five-hole probe in the pump rotating frame. A custom-designed brush-type slip-ring unit is used in the rotating probe system to transmit the amplified signal from the probe in the rotating frame to the stationary frame. At speed ratio of 0.6, a weak ''jet-wake'' flow pattern is observed at the pump mid-chord. High flow loss is observed in the core-suction corner due to the ''wake'' flow caused by the flow separation. A strong clockwise secondary flow is found to dominate the flow structure at the pump mid-chord. The Coriolis force and the through flow velocity deficit near the core at the pump inlet are the main reasons for this secondary flow. The jet-wake flow pattern at the 3/4-chord is enhanced by the upstream secondary flow. A jet-wake flow pattern is also observed at the pump 4/4-chord, with concentration of the flow near the passage pressure side. The secondary flow changes its direction of rotation from the 3/4-chord to 4/4-chord. This is mostly caused by the passage meridional curvature and the flow concentration. High loss is found in the core-suction corner wake flow due to a low kinetic energy flow accumulation and the flow separation. Finally, the pump flow field is assessed through the mass-averaged total pressure and relative pressure loss parameter. The data are also analyzed to assess the effect of the speed ratio on the flow field.
[DOI: 10.1115/1.1341202]

Keywords: Torque Converter, Pump, Flow Measurement, Rotating Probe, Secondary Flow

Introduction

The automotive torque converter is a hydrodynamic, closed-loop, multi-component turbomachine. Compared with the conventional turbomachine, the torque converter flow field is more complex mainly due to: (1) the differing rotational speed of each element; (2) 360 deg flow turning in the meridional plane; (3) the large blade turning angles (turbine and stator); (4) the wide range of operating conditions; (5) the high viscosity of the working fluid; and (6) the closely coupled system with substantial rotor-stator, rotor-rotor interaction.

In an automatic transmission, the output torque and power of the engine is imparted to the transmission oil by the pump of the torque converter. The pump provides the pressure rise and increases the angular momentum of the oil through the rotation and the flow turning. In order to study the torque converter fluid dynamics and to investigate the loss mechanisms, it is very important to understand the flow field inside the pump passage. This knowledge will greatly help designers to improve the torque converter performance. The objective of this paper is to study the flow field inside the pump passage through a rotating probe measurement and provide a thorough understanding of the flow feature and loss mechanisms of the pump flow.

There have been several investigations of the pump flow field in recent years. By and Lakshminarayana [1] measured the pressure on the pump blade surface. The static pressure was found to be well behaved near the shell and poorly behaved near the core. Gruver et al. [2] measured three components of velocity in the pump at three streamwise planes (inlet, mid-chord, and exit) using LDV. The velocity distribution was found to be highly three-dimensional at speed ratio 0.8 and 0.065. The flow was well behaved near the shell and at the mid-span, but very poorly behaved near the core. The jet-wake flow dominates the flow structure in the pump passage. The jet-wake flow is a typical flow pattern observed in centrifugal impeller blade passages. The flow concentration on the pressure side of the passage looks like a ''jet.'' On the suction side of the passage, a low momentum flow with high flow disturbance exists. This looks like a wake. This is mainly caused by the rotation and curvature effects. The LDV measurement indicates a strong secondary flow at the mid-chord and the exit. The rotation of the secondary flow is reversed from the mid-chord to exit [3]. The steady and unsteady flow field at the pump exit of a GM 245 mm torque converter was measured using a high-frequency response five-hole probe [4]. The dominant feature of the flow field is the mass flow concentration on the shell and pressure side, and a strong clock-wise (radically inward on the suction side and outward on the pressure side) secondary flow. A core-suction corner flow separation and an intense flow-mixing region with very high flow unsteadiness were observed at the pump exit. The centrifugal effect, not the blade turning, dominates the flow feature in the pump passage. Dong et al. [5] performed the steady flow measurement at the stator exit (the pump inlet). The measurement at the stator exit indicates the presence of a large axial velocity deficit near the core at the speed ratio 0.6, and the strong secondary flow causes large exit flow angle variations from the core to the shell at the pump inlet. The flow at the stator exit was found to be highly turbulent.

A new rotating probe system (both mechanical and electrical systems) was designed and fabricated for the same GM 245 mm torque converter. A miniature high-frequency response five-hole probe, which was developed earlier at Penn State [6], was employed to measure the pump passage flow field in the rotating frame. The flow field at three chordwise locations of the pump passage was measured at five speed ratios. For brevity, only the

Contributed by the Fluids Engineering Division for publication in the JOURNAL OF FLUIDS ENGINEERING. Manuscript received by the Fluids Engineering Division June 6, 2000; revised manuscript received October 3, 2000. Associate Technical Editor: Y. Tsujimoto.

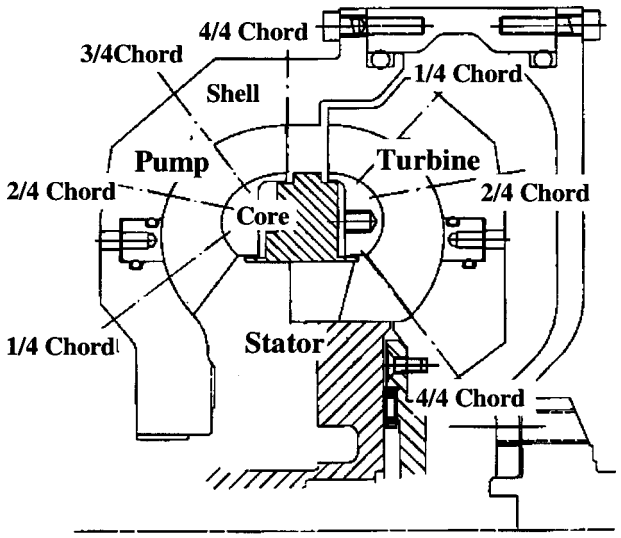

(a)

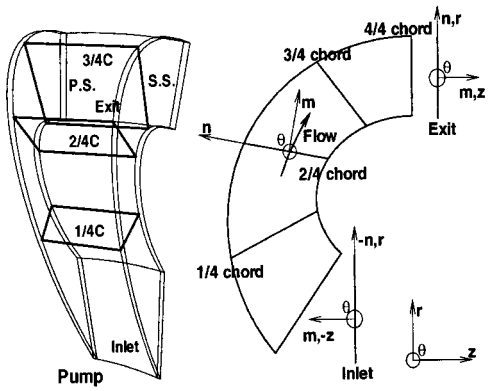

(b)

Fig. 1 Cross-section of the pump rotating probe measurement test unit and coordinate system. (*a*) Cross-section of test unit; (*b*) pump blade passage and coordinate system.

data at speed ratio of 0.6 are presented and interpreted in this paper. The comprehensive data at all speed ratios can be found in [7].

Rotating Probe System and Measurement Technique

The experimental investigation was accomplished using the Torque Converter Research Facility at the Pennsylvania State University. The facility consists of six main components: drive motor, absorb dynamometer, control system, hydraulic system, test unit, and data acquisition system. A detailed description of this torque converter test dynamometer is given by Dong [7]. A schematic of the test section and the cross section of the pump are shown in Figs. 1(*a*) and 1(*b*), respectively. The newly developed rotating probe system is described in this section.

The pump has 32 blades with 1 mm constant blade thickness. The pump inlet blade angle is −30 deg and the outlet blade angle is 10 deg. The turbine has 36 blades with 1 mm constant blade thickness. The inlet blade angle is 61.4 deg and the outlet blade angle is −62.6 deg. The stator has 17 blades with aerodynamic profile. The inlet and outlet blade angles are 27 and 70 deg. The flow field was measured at five different operating conditions, speed ratios (defined as n_t/n_p) 0.8, 0.6 (design point), 0.4, 0.2, and 0.065. Only the data at the design speed ratio of 0.6 are presented and interpreted in this paper. The test speed of the pump is 1160 rpm, and the turbine speed is 696 rpm at a speed ratio 0.6. At this condition, the torque converter has a 75.6 percent overall efficiency and a 1.26 torque ratio on the Penn State facility. Details of the high-frequency five-hole probe used in this investigation is described in [4].

The rotating probe measurement system designed, developed, and used in this research consists of (1) a probe traversing mechanism to measure the flow field at various chordwise and tangential locations, (2) a signal conditioner (amplifiers and battery) mounted on the rotating probe casing, (3) electrical conduits to transmit the data to slip-ring unit, and (4) a slip-ring unit. The probe design and data acquisition and processing systems in the stationary system are identical to those described in earlier publications.

During the design, one of the most difficult problems encountered was the probe traverse system. The probe must be traversed both tangentially and radially relative to the blade passage. The probe is designed to be mounted on the pump shell at some specified location (percentage of the blade chord length, as shown in Fig. 1). The radial traverse of the probe is accomplished by a sliding sleeve, which has a series of index holes on its outer diameter. The sleeve can be translated (shell-to-core) in the pump shell and be fixed in incremental positions by a set screw, which engages the holes on the sleeve. The guide holes for the probe sleeve are manufactured at the specified locations on the pump shell and are aligned with the local blade angle. To carry out the tangential traverse, the blade system was designed to rotate relative to the pump shell. The contour of the shell is manufactured to match perfectly with the contour of the blade tip to keep the tip leakage flow to be negligible. The angular position of blade relative to the probe is determined by a group of index holes, which are accurately drilled by a CNC machine. Once the probe tangential position is fixed, the shell and blade parts are held together by eight bolts. The pump cover is redesigned into two pieces; an annular ring and a flat plate cover. The electrical wires used to transfer the signal to the slip-ring unit are connected through two small holes in the pump cover from the pump shell to the pump shaft. All test parts mentioned above were manufactured by CNC machining, and the pump blade part was made by five-axis CNC milling machine. Complete details of the design and hardware can be found in [7].

The error in the rotating probe measurement is strongly dependent on the noise of the electronic system. The Kulite pressure transducers, which are used in the high-frequency response probe, require a very stable voltage DC power supply. The output signals of these transducers need to be amplified by low noise amplifiers. These amplifiers are powered by a powerful DC power supply. For the rotating frame measurement, the signal has to be transferred from the rotating frame to the stationary frame, which is then processed through a data acquisition system (DAS-50 and 486 PC). The contribution to the electronic noise comes from the pressure transducer, the amplifier, the power supply, and the data acquisition system.

A slip-ring unit was used to transfer the electrical signal from the rotating frame to the stationary frame. This slip-ring unit is a custom-designed, high quality, brush-type unit. It has 37 channels, and is made of gold alloy for brushes and rings. For the speed range from 0–1500 rpm, the noise level of this slip-ring unit is about 5–7 mV for a 3–5 V level signal. This represents a signal noise ratio of 0.10 percent–0.25 percent. For the flow measurement, this noise level is acceptable after amplification, where the DC signal is about 3–5 V and the AC signal is about 20–50 mV. However, before amplification this noise is not acceptable, because it is even higher than the flow signal, and will be amplified by the amplifier gain (250 in this system). Therefore, the amplifier and the transducer power supply have to be installed in the rotating frame before the signal transmitting through the slip-ring unit.

A schematic of the electronic system of the rotating five-hole probe is shown in Fig. 2. Two groups consisting of a rechargeable battery and a voltage regulator are used as the transducer power

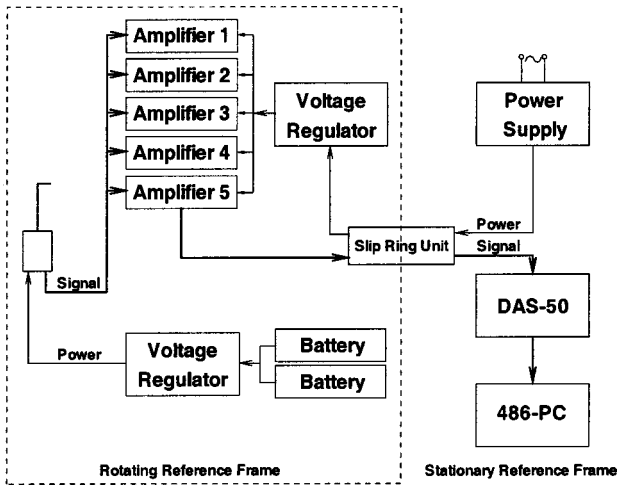

Fig. 2 Schematic of electrical system used for rotating probe measurements.

supply. The DC power supplies (+12V, −12V) for the five amplifiers are transmitted through the slip-ring unit by five parallel channels each. Two voltage regulators are used in the rotating frame to reduce the noise of these power supplies due to the slip-ring unit. All the above electronic units and five signal amplifiers are custom-designed miniature parts. They are mounted on the pump shell, rotating with the pump passage. The output signal from each transducer of the probe is transmitted to the stationary frame through four parallel channels of the slip-ring unit in order to reduce the noise due to the slip-ring unit. Seven slip-ring channels were parallel connected to the common ground. The measured noise of this system is low, total about 5–6 mV, which is the same level as that measured in the stationary five-hole probe system. Since the probe is in the rotating frame, the transducers are not located at the same radius as the tip of the probe, the measured pressures were corrected for the centrifugal force effect. The accuracy of the centrifugal force correction depends on the spatial error in measuring the location of the probe tip and the transducer sensors.

The accuracy of the steady flow measurement of this rotating probe system is ±0.7 kPa (±0.1 psi) of the pressure, ±0.2 m/s of the velocity, and ±1.5 deg of the flow angle. The dynamic performance of the high frequency response probe has been discussed in earlier publications [4,7]. The maximum frequency response is 9 kHz; the probe's natural frequency is 6 kHz. The accuracy of the probe positioning is ±0.15 mm in position and ±0.15 deg in angle alignment. The flow field inside the pump passage was measured at three cross sections; the mid-chord section (50 percent chord length from the pump inlet), 3/4-chord section (75 percent chord length from the pump inlet), and 4/4-chord section (pump blade trailing edge section inside the passage), as shown in Fig. 1. At the pump mid-chord, the probe was traversed on a grid of 8×7, which covers about 49 percent of the passage area. At the pump 3/4-chord, the probe was traversed on a grid of 9×7, and covers 65 percent of the flow area. At the pump 4/4-chord, the probe was traversed on a grid of 8×7, and covers 59 percent of the flow area. Compared with the conventional turbomachinery measurement, these grid cover much less percentage of the passage area because of the size of the torque converter. The mass averaged (or passage-averaged) flow parameters have some inaccuracy; this can be determined only through nonintrusive measurement technique such as Laser Doppler Velocimeter.

In consistent with the earlier publications of the Penn State group, the velocities and pressures presented in this paper are normalized using the following equations:

$$v_{\text{norm.}}=\frac{V}{V_{\text{ref}}},\quad V_{\text{ref}}=\pi D\frac{n_p}{60}\sqrt{1-\frac{n_t}{n_p}} \tag{1}$$

where the V_{ref} is called reference velocity of a given speed ratio, which is found to be approximately proportional to the averaged through flow velocity.

$$P_{\text{norm.}}=\frac{P-P_{\text{hub}}}{P_{\text{ref}}},\quad P_{\text{ref}}=\frac{1}{2}\rho V_{\text{ref}}^2 \tag{2}$$

P_{hub} is the static pressure measured at the stator hub.

The secondary velocity in the relative frame (W_{sec}) is calculated as follows:

$$\vec{W}_{\text{sec}}=\vec{W}_{\text{measured}}-\vec{W}_{\text{ideal}} \tag{3}$$

$$\vec{W}_{\text{sec}}=(W_{\theta\ \text{measured}}-W_{\theta\text{ideal}})\vec{i}_{\theta}+(W_{\text{nmeasured}}-W_{\text{nideal}})\vec{i}_{n} \tag{4}$$

where the W_{ideal} is the ideal flow velocity that exists in an inviscid or primary flow field.

$$W_{\theta\ \text{ideal}}=W_{m\ \text{measured}}\tan\beta_b \tag{5}$$

$$W_{n\text{ideal}}=0 \tag{6}$$

where β_b is the local blade angle.

In the pump rotating system, the relative total pressure loss parameter is defined as:

$$P_1=(P_0)_p-\frac{1}{2}\rho U^2 \tag{7}$$

where U is the local blade speed, equal to ωr, and the $(P_0)_p$ is the relative total pressure in the rotating frame, defined as follows:

$$(P_0)_p=P+\frac{1}{2}\rho W_0^2 \tag{8}$$

where P is the static pressure and W_0 is the relative total velocity. In some publications, the relative total pressure loss parameter (P_1) is called rothalpy, or Bernoulli constant in the rotating frame. The physical meaning of this parameter is explained below.

In a rotating reference frame, the value of P_1 is constant along the streamline for incompressible and inviscid flow [8]. For the viscous flow, the change in this parameter between two points on the same streamline is the viscous loss. For the rotating probe measurement, the relative total pressures $(P_0)_p$ is measured directly by the five-hole probe because the probe is in the same rotating frame as the flow. Therefore, the loss information can be obtained by comparing the upstream and downstream distributions of the relative total pressure loss parameter.

The pump is located downstream of the stator inside the torque converter. Thus, the stator exit flow controls the pump inlet flow condition. The stator exit steady flow field of GM 245 mm torque converter was measured by a stationary conventional five-hole probe.

Results and Discussion

Typical spectrum of the rotating five-hole probe signal (channel 1) at one typical location is shown in Fig. 3. The signal from the probe center hole (No. 1) at the center of the cross section is presented. It is clear that the pump shaft frequency ($f_{p,s}$) is the dominant periodic signal at all locations. This is mostly due to the gravity force. Because the facility is set horizontally, the rotating probe senses different pressure at different angular position due to the gravity force. At the pump mid-chord location, the probe is located at the smallest radius among these three pump measurement locations (2/4, 3/4, and 4/4; Fig. 1), and the pressure difference between the top and bottom positions of the probe is the smallest. The pump shaft frequency periodic signal has the smallest value at mid-chord and the highest value at the trailing edge (Fig. 3). When a pressure correction for the gravity force is ap-

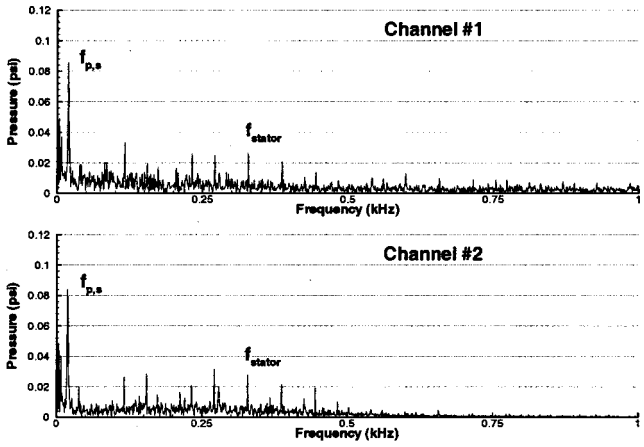

(a)

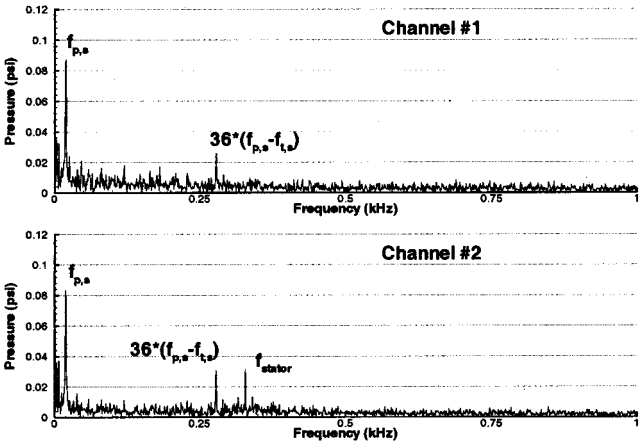

(b)

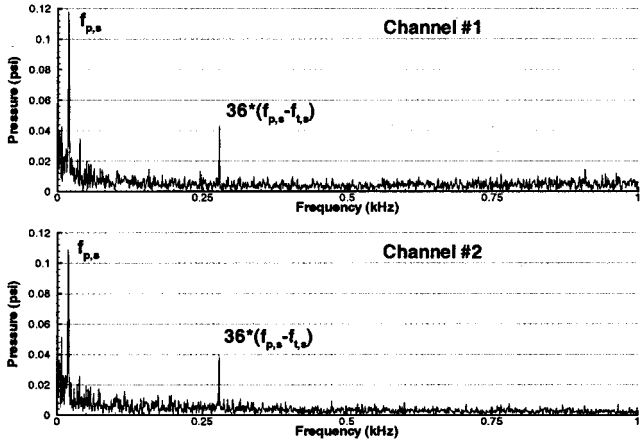

(c)

Fig. 3 Spectrums of the rotating five-hole probe signal at center of passage (SR=0.6). (*a*) Pump mid-chord; (*b*) pump 3/4-chord; (*c*) pump 4/4-chord.

plied in the data processing, the periodic signal at pump shaft frequency disappears. Other factors that could also generate the periodic shaft frequency are misalignment of the test section, unbalance weight, mechanical vibration, and electrical noise of the dynamometer and control system. However, compared with the gravitational force, all these signals are very weak at the shaft frequency.

The other periodic signals shown in the spectrum are the stator blade frequency (f_{stator}) and the turbine blade frequency 36 $\times(f_{p,s}-f_{t,s})$. At the pump mid-chord, only the stator blade frequency can be seen in the spectrum. This implies that the stator blade periodic flow, such as the blade wake, has not been decayed completely at the pump mid-chord location. However, the magnitude of this signal is very weak; only about 1/3 of the pump shaft frequency signal. At the pump 3/4-chord, both the stator blade frequency signal and the turbine blade frequency signal can be seen in the spectrum. This indicates that both the upstream stator blade periodic flow and the downstream turbine blade periodic interaction are sensed by the probe. At the pump 4/4-chord, only the turbine blade periodic signal is measured by the probe. From the pump mid-chord to the 4/4-chord, the stator blade periodic signal decreases as the upstream periodic flow decays, and the turbine blade periodic signal increases as the effect of downstream flow interaction increases. Furthermore, compared with the periodic flow signal, the broad-band signal (random flow signal) is very small. This means that the random unsteadiness of the relative flow inside the pump passage is small. This also indicates that the electronic noise of the rotating probe system is also very small.

The Flow Field at the Pump Inlet. The pump inlet flow is measured at the stator exit using a conventional five-hole probe [5]. Only the passage-averaged (circumferentially mass averaged from the pressure to the suction surface) flow properties (in pump rotating frame) are presented in Fig. 4 to facilitate interpretation of the pump passage flow data. At the speed ratio 0.6, the most significant feature of the pump inlet flow is the axial and total velocity deficit near the core (Fig. 4(*b*) and (*c*)). A higher mass flow rate is found near the shell region. The reason for this radial redistribution is partly due to the axial velocity deficit at the stator inlet near the core, and partly due to the radial mass transport by the secondary flow inside the stator passage. A large velocity deficit is also observed in the relative total velocity (Fig. 4(*b*)) due to the non-uniform through flow profile. The stator pressure variation is small, except at idle conditions (SR=0.065, Fig. 4(*a*)).

The pump has a −30 deg inlet angle. At the speed ratio 0.6, the relative flow yaw angle at the pump inlet is −15 deg near the shell, and −67 deg near the core (Fig. 4(*d*)). This implies that the pump inlet has a 52 deg incidence change from shell to core; 15–37 deg. It is clear that the axial velocity deficit is one of the major reasons for such a large variation in the pump incidence. The presence of strong secondary flow at the stator exit and the presence of convex curvature (core) and the concave curvature (shell) are possible causes for such inlet conditions. The automotive torque converters use the sheet metal as the pump blade, and these are sensitive to the inlet flow angle. Even a small incidence will cause flow separation near the leading edge, resulting in large inlet flow losses. Therefore, the secondary flow and the radial mass transport in the stator passage, as well as the flow separation inside the stator passage, have an adverse effect on the pump inlet condition, leading to large inlet flow losses.

Flow Field at the Pump Mid-Chord. At the speed ratio 0.6, the static pressure contours at the pump mid-chord location (Fig. 5(*a*)) show that the pressure has the highest value in the shell-pressure surface corner, and the pressure gradient is from the shell-pressure corner to the core-suction surface corner. This is because the shell has a larger radius than the core, and the pressure increases from the core to the shell. The pump torus curvature also causes the pressure gradient in the same direction. The tangential pressure gradient is from the pressure side to the suction side, which has about the same magnitude as the radial pressure gradient because the contours are inclined at about 45 deg.

The relative total velocity vectors are shown in Fig. 6(*a*). The jet-wake flow structure is not very strong. The velocity is low at the core-suction corner and high near the shell and at the center of the passage. The through flow velocity contours (Fig. 7(*a*)) show

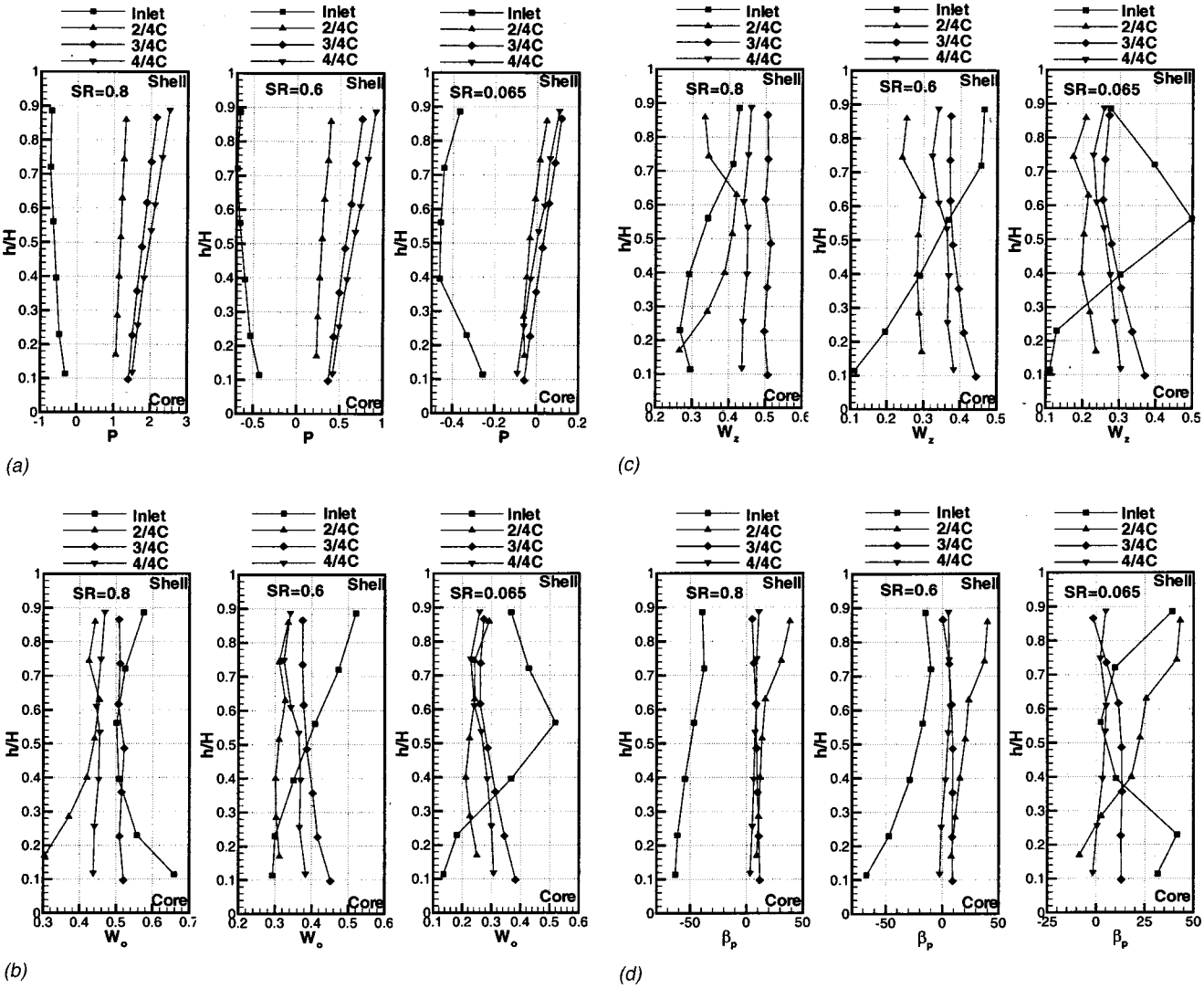

Fig. 4 Radial distribution of mass averaged pump flow parameters (in pump rotating frame). (*a*) Static pressure; (*b*) Relative total velocity; (*c*) Through flow velocity; (*d*) Relative flow yaw angle in degrees.

the mass flow deficit in two regions; the core-suction corner and the shell-pressure corner. The low through flow velocity at the core-suction corner is due to the tendency for flow separation in the wake flow region. The mass flow deficit at the shell-pressure corner is caused by the secondary flow, which will be discussed later.

At the speed ratio 0.6, a strong clockwise (looking from downstream to upstream) secondary flow is found at the pump mid-chord location (Fig. 8(*a*)). The flow is highly underturned in the upper half of the passage, since the relative tangential velocity is from the suction side to the pressure side. A large radial inward velocity (shell to core) is observed near the pressure side. It should be noted that the secondary flow velocity near the shell-pressure side is about the same order of magnitude as the through flow velocity (Fig. 7(*a*)). The relative flow angle is about 40 deg to 50 deg in this area.

The detailed secondary flow analysis for general radial turbomachinery is given by Lakshminarayana [8]

$$\left(\frac{\omega_s}{\rho W}\right)_1^2 = \int_1^2 \frac{2\omega_n}{\rho W R'} ds - \int_1^2 \frac{2(\vec{\Omega}\times\vec{\omega})\cdot\vec{s}}{\rho W^2} ds \qquad (9)$$

where ω_s is the streamwise vorticity, ω_n is the normal vorticity, W is the relative velocity, and Ω is the rotor speed. R' is the radius of curvature of the flow path. For a centrifugal/radial turbomachinery, three sources of secondary flow can be recognized from the above equation. The first source of secondary flow is the meridional curvature in the presence of ω_n. The second source is the blade chamber, again in presence of ω_n. The third source is caused by the direct effect of rotation (last term in the equation).

According to this theory, several reasons could be attributed to this strong clockwise secondary flow at the torque converter pump mid-chord. These reasons are: (1) the direct effect of rotation through meridional curvature induces secondary flow as shown in Fig. 8(*a*) [8]. (2) In the first half of the pump passage (from the inlet to the mid-chord), the effect of rotation transports blade boundary layer flow towards the core due to a higher radius at the core. It is believed that these are two main causes of the secondary flow. (3) The meridional curvature of the blade passage is another reason for the secondary flow. From the stator exit, where the flow is in the axial direction, to the pump mid-chord, where the flow is nearly in the radial direction, the pump blade passage has a 100 deg turning in meridional plane. The radial inward flow (shell to core) along the pressure side is partly caused by this flow turning. (4) The pump inlet incidence also causes the secondary flow. As mentioned earlier, the pump inlet has a 20 deg incidence near the shell and -37 deg near the core. An inlet flow separation prob-

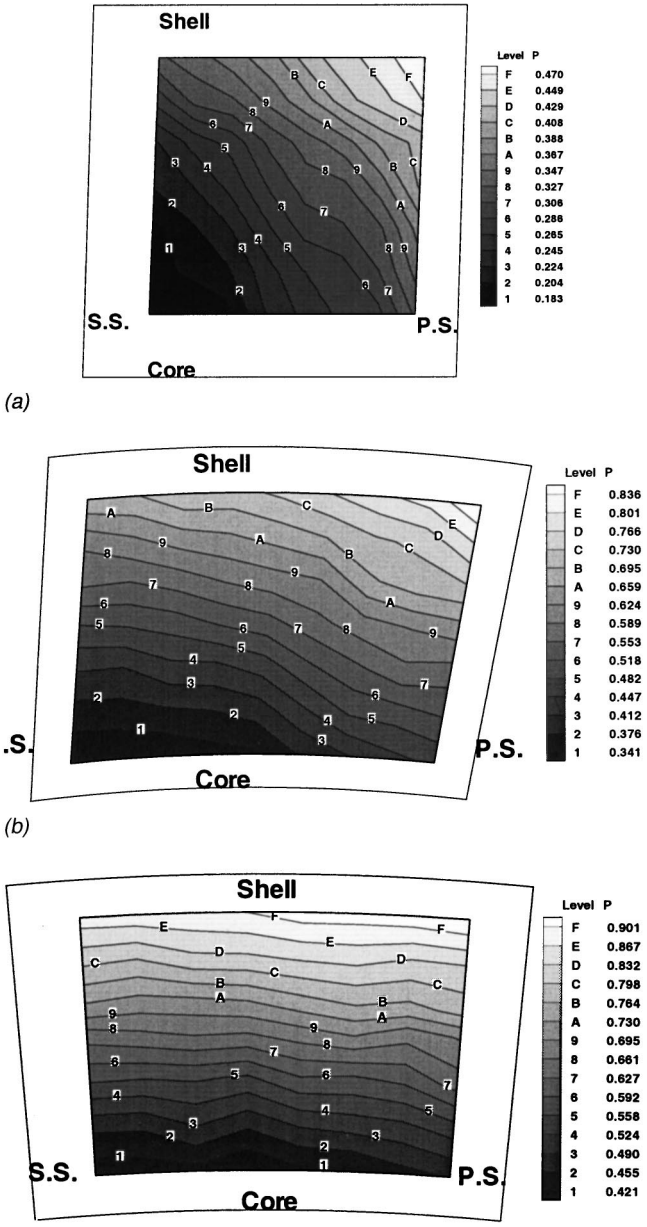

Fig. 5 Static pressure contours of the pump passage flow at speed ratio 0.6. (*a*) Pump mid-chord; (*b*) pump 3/4-chord; (*c*) pump 4/4-chord.

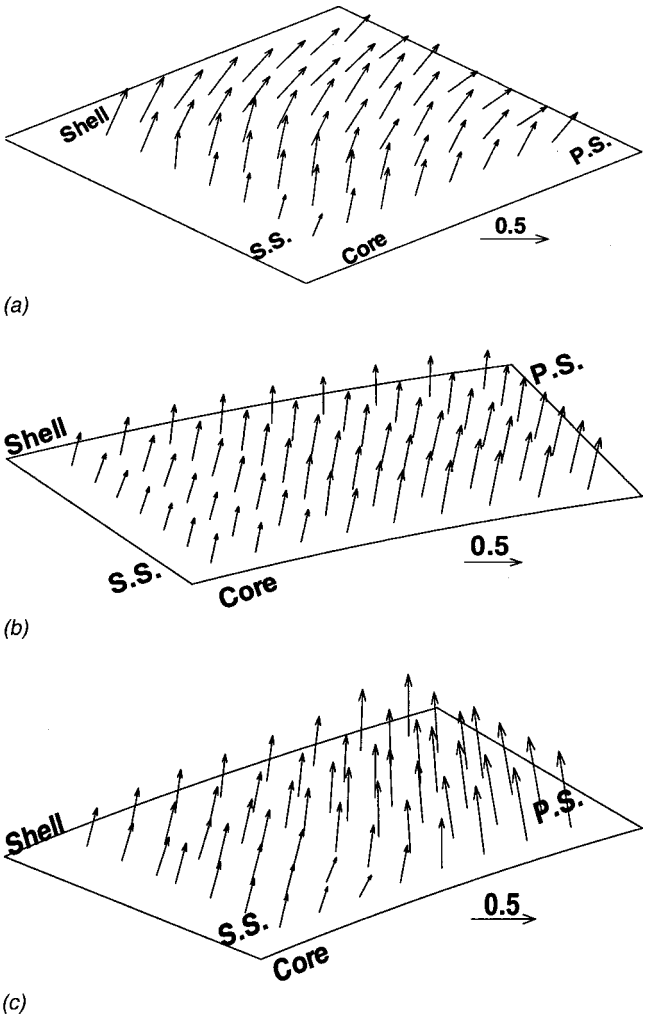

Fig. 6 Total velocity vectors of the pump passage flow at speed ratio 0.6. (*a*) Pump mid-chord; (*b*) pump 3/4-chord; (*c*) pump 4/4-chord.

ably exists on the core suction side of the pump blade. The fluid is forced to move to the pressure side by the blockage effect of the flow separation. Likewise, due to a high negative incidence near the pump inlet on the shell side, an inlet flow separation probably exists on the shell pressure side of the blade. The fluid is transported to the core along the pressure side by the blockage of the flow separation. Hence, two major sources of secondary flow are the rotation and flow separation near the leading edge of the pump.

It is noticed that a large radial redistribution of mass, momentum and energy occurs inside the pump passage as the flow progresses from the inlet to the mid-chord. The radial redistribution of averaged through flow velocity shows that only a small velocity deficit exists near the shell at the mid-chord location (Fig. 4(*c*)). However, a large through flow deficit is found near the core at the inlet (Fig. 4(*c*)). It is believed that the secondary flow (Fig. 8(*a*)) causes this migration of shell flow towards core. This accounts for the large radial inward flow observed on the pressure side of the passage. The blockage effect of the inlet flow separation near the shell-pressure side is another reason for this mass flow redistribution. The radial distribution of averaged relative total velocity shows the same trend as the through flow velocity (Fig. 4(*b*)). Similarly, the flow angle has become nearly uniform (Fig. 4(*d*)) at this location. This seems to indicate that the secondary flow, even though increases losses, has a beneficial effect in reducing large variations in flow properties in the spanwise direction through intense mixing.

The absolute total pressure contours at the pump mid-chord location are shown in Fig. 9(*a*). It is clear that the flow near the shell has a higher pressure rise because of the higher rotating speed and larger radial pressure gradient. The lowest absolute total pressure is found in the core-suction corner region. This is partly because of the lowest static pressure and partly because of the highest flow losses in this corner. The relative total pressure loss parameter contours are shown in Fig. 10(*a*). The jet-wake flow structure can be easily seen in this figure. The difference in the loss parameter between the inlet and mid-chord represents the flow losses in the first half of the pump passage. It is noticed that the flow losses are low near the pressure side and high near the suction side. The maximum loss is near the core-suction corner. The core-suction wake flow has a larger loss due to the flow separation. The possible inlet flow separation on the core suction

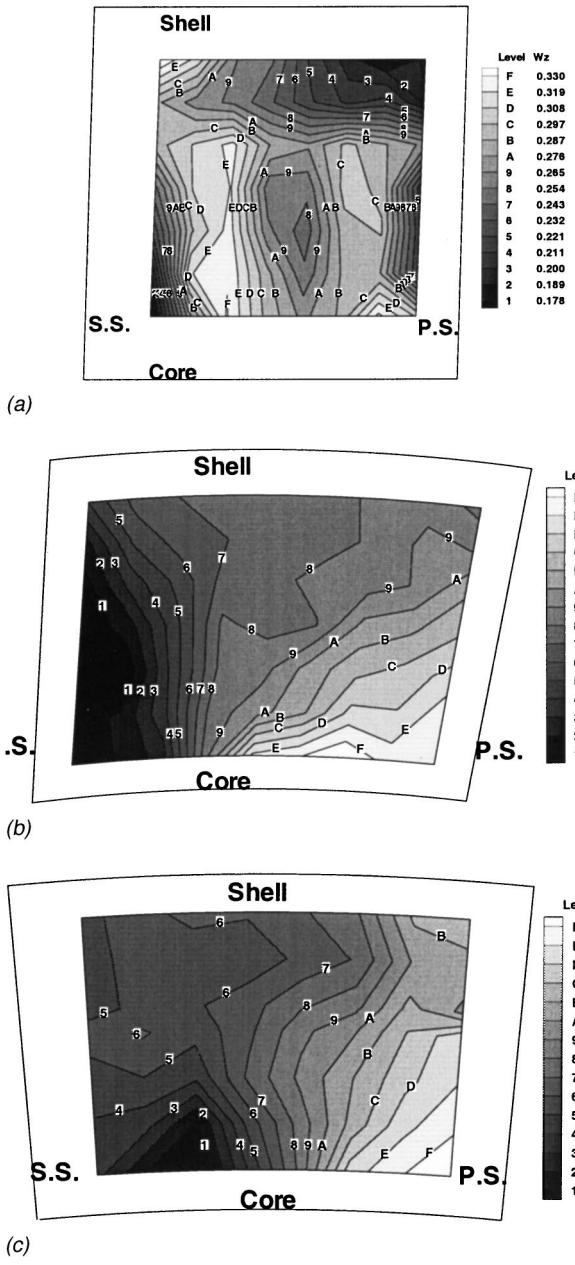

Fig. 7 Through flow velocity contours of the pump passage flow at speed ratio 0.6. (*a*) Pump mid-chord; (*b*) pump 3/4-chord; (*c*) pump 4/4-chord.

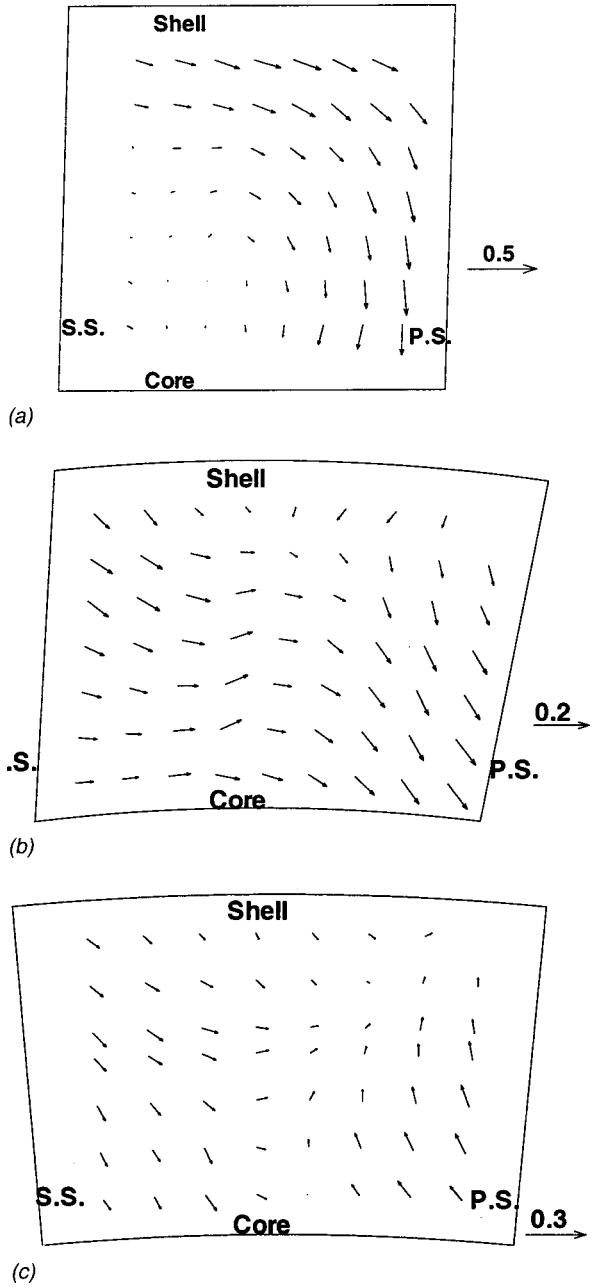

Fig. 8 Secondary flow vectors of the pump passage flow at speed ratio 0.6. (*a*) Pump mid-chord; (*b*) pump 3/4-chord; (*c*) pump 4/4-chord.

side of the pump blade is another reason for the high losses in the core-suction corner. The secondary flow vectors show that the cross section velocity (tangential and radial velocity) is very low in the core-suction corner.

At the speed ratio 0.6, the radial distribution of the mass-averaged static pressure is nearly linear, with the highest value occurring near the shell and the lowest value near the core (Fig. 4(*a*)). The absolute total pressure has a similar trend (Fig. 11). It is important to note that at the speed ratio 0.6, the first half of the pump passage has the most (76 percent) total pressure rise of the pump. The radial distributions of the relative total pressure loss parameter are shown in Fig. 12. Only a small amount of flow loss (27 percent) occurs in the first half of the pump passage.

In summary, the flow field in the first half of the passage (inlet to mid-chord) has complex flow characteristics. The secondary flow and associated mixing reduces large variations in flow properties observed at inlet. The static pressure gradient (shell-to-core) is reversed from inlet to mid-chord. Highest static and stagnation pressure rise (Figs. 4(*a*) and 11, respectively) occurs from the inlet to the mid-chord. Furthermore, the largest losses occur near the shell region (Fig. 12). Part of these losses can be attributed to the migration of low energy fluid from the core toward the shell due to the secondary flow. Most of the flow turning from mid-span to core region occurs from inlet to mid-chord (Fig. 4(*d*)).

Flow Field at the Pump 3/4-Chord. At the speed ratio 0.6, the static pressure distribution at pump 3/4-chord location (Fig. 5(*b*)) has the same trend as that at the pump mid-chord location (Fig. 5(*a*)). The pressure near the shell is higher than the pressure near the core. Unlike the pump mid-chord, the radial pressure gradient is larger than the tangential pressure gradient. Since the pump 3/4-chord location has a 49.5 deg angle with the pump shaft

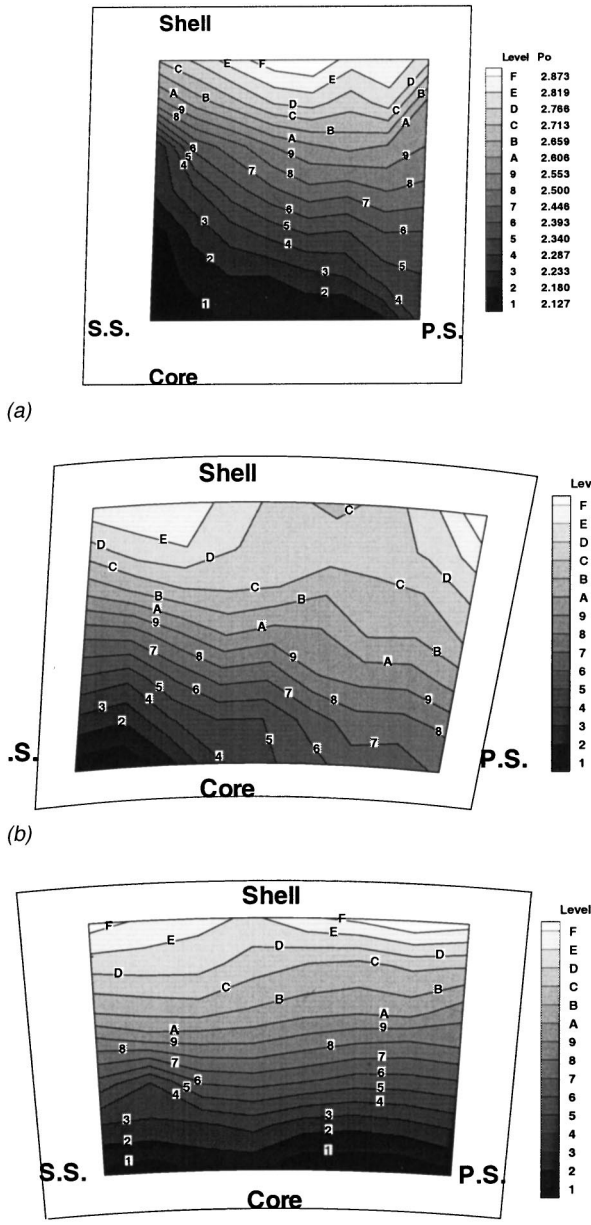

Fig. 9 Absolute total pressure contours of the pump passage flow at speed ratio 0.6. (*a*) Pump mid-chord; (*b*) pump 3/4-chord; (*c*) pump 4/4-chord.

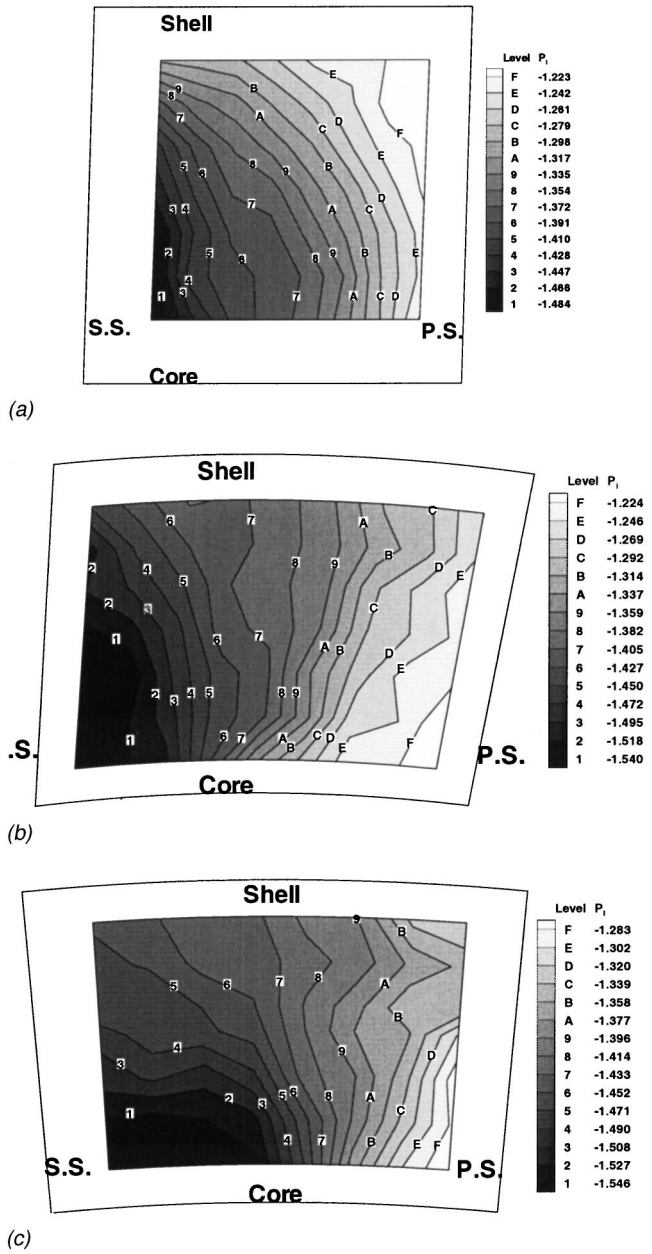

Fig. 10 Pressure loss parameter (P_1) contours of the pump passage flow at speed ratio 0.6. (*a*) Pump mid-chord; (*b*) pump 3/4-chord; (*c*) Pump 4/4-chord.

(Fig. 1), the centrifugal force at this location is larger than that in the pump mid-chord. Furthermore, most of the static pressure rise due to flow turning occurs before this chordwise location. The passage-average static pressure (Fig. 4(*a*)) shows that the shell region has higher static pressure rise and the spanwise gradient has increased from mid-chord to this location. As mentioned earlier, this is due to the centrifugal force.

The jet-wake flow structure is also present at the pump 3/4-chord (Figs. 6(*b*) and 7(*b*)), which is enhanced by the upstream secondary flow. No flow separation is found on the suction side (Fig. 7(*b*)). The size and the location of the wake region can be clearly seen from the through flow velocity contours (Fig. 7(*b*)) and relative total pressure loss parameter contours (Fig. 10(*b*)).

The most important feature of the flow field at the pump 3/4-chord is the mass flow concentration on the pressure side of the passage (Fig. 7(*b*)). The through flow velocity near the suction side is only about 60 percent of that near the pressure side. The relative total velocity vectors also show the same feature (Fig. 6(*b*)); the velocity is high near the pressure side and core-pressure corner and low near the suction side. The strong secondary flow observed at the pump mid-chord is the direct reason for this flow feature. The fluid is transported from the suction side to the pressure side and from the shell-pressure corner to core-pressure corner by the strong secondary flow (Fig. 8(*a*)).

The secondary flow at the pump 3/4-chord is still in the clockwise direction (Fig. 8(*b*)). The flow is highly underturned in most of the passage area, from the suction side to the pressure side. The radial inward flow is still found near the pressure side. Moreover, a weak radial inward flow is observed near the suction side and a radial outward flow is observed in the middle of the passage. The reasons for this secondary flow were explained earlier. The pump 3/4-chord plane has a 49.5 deg angle with the pump shaft (Fig. 1). The magnitude of the tangential component of the Coriolis force

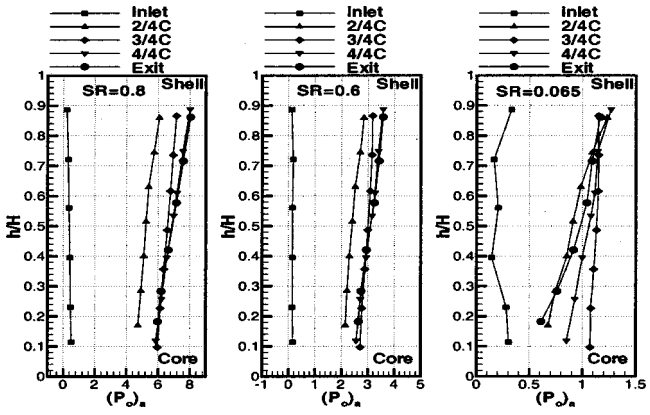

Fig. 11 Radial distribution of mass averaged absolute total pressure of the pump flow

is smaller than that at the pump mid-chord because of the smaller absolute radial velocity component. The influence of the Coriolis force has less dominant influence on the secondary flow at the pump 3/4-chord than that at the pump mid-chord.

The absolute stagnation pressure shown in Fig. 9 indicates that the pressure rise is highest in the shell region and lowest in the core-suction corner. The spanwise distribution of average stagnation pressure rise is nearly linear in the spanwise direction (Fig. 11).

The relative total pressure loss parameter contours show that the flow losses are concentrated near the passage suction side (Fig. 10(*b*)). The contours are approximately in the radial direction. The value of the loss parameter in the ''wake'' flow is much lower than that in the ''jet'' flow. The flow near the pressure side is more efficient. The relative total pressure loss parameter reaches the highest value near the core-pressure corner, indicating lowest losses. Compared with the loss parameter contours at the pump mid-chord (Fig. 10(*a*)), it is found that the high value region has been transported from the shell-pressure corner to the core-pressure corner due to the radial transport of the secondary flow. The high loss region near the suction-core corner has increased substantially from the mid-chord to the 3/4-chord.

In summary, the flow redistribution from mid-chord to 3/4-chord is again due to strong secondary flow. The average through flow and total velocities are higher near the core than the shell, and the flow turning from the mid-chord to the 3/4-chord is much smaller than that which occurs between the leading edge and mid-chord. In spite of this, an appreciable static and stagnation pressure rise occurs between these two locations (Figs. 4(*a*) and 11),

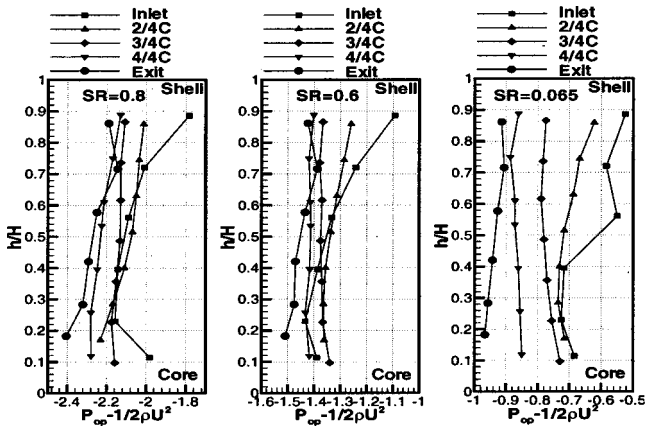

Fig. 12 Radial distribution of mass averaged relative total pressure loss parameter of the pump flow

and this is caused by centrifugal forces and not flow turning. But, substantial pressure losses are observed near the shell region. This is again due to transport of mass, momentum, and energy by the secondary flow.

Flow Field at the Pump 4/4-Chord. At the speed ratio 0.6, the static pressure contours (Fig. 5(*c*)) and the mass-averaged static pressure distribution (Fig. 4(*a*)) at the pump 4/4-chord show that the static pressure gradient in the tangential direction is negligible and the radial gradient is substantial. The measurement plane at the pump 4/4-chord is a radial plane, perpendicular to the axis of the pump shaft (Fig. 1). The flow is dominated by radial pressure gradient, mainly caused by the centrifugal force. The static pressure rise from 3/4-chord to 4/4-chord is very small compared to other locations. Furthermore, the static pressure rise in the first half of the flow path is nearly double the static pressure rise from the mid-chord to the trailing edge.

The relative total velocity vectors (Fig. 6(*c*)) show that the flow field at the pump 4/4-chord still exhibits the jet-wake flow structure. The size and location of the wake flow can be clearly seen from the axial velocity contours (Fig. 7(*c*)) and the relative pressure loss parameter contours (Fig. 10(*c*)), but is not as strong as those observed at 3/4-chord. The jet-wake flow structure dominates the flow field in the second half of pump passage. It is enhanced by the strong secondary flow in the pump passage.

It is important to note that the secondary flow changes the direction of the rotation (Fig. 8(*b*) and 8(*c*)). A counter-clockwise secondary flow is observed at the pump 4/4-chord. The flow is radial inward on the suction side and radial outward on the pressure side. This is much clearer in the data acquired with a stationary probe at the pump exit [4]. The causes of this secondary flow were explained earlier.

Lakshminarayana [8] provided an analysis of the relative order of magnitude of the meridional curvature effect and the rotation effect in the generation of secondary flow. The ratio of the last two terms in Eq. (9) can be written approximately as $W/R'\Omega$, where R' is the principal radius of curvature of the relative streamline. If W is approximated as Ωr, this ratio is equal to r/R'. Hence, secondary flow due to meridional curvature dominates if the (r/R') is large, the rotation dominates the secondary flow development if this ratio is small. For the torque converter pump, the passage curvature R' is about the same from the inlet to the exit. In the first half of the passage (inlet to mid-chord), r is small and the ratio r/R' is small. The pump rotation has a dominant effect in the generation of secondary flow. In the second half of the passage (mid-chord to exit), r is large and the ratio r/R' is large. The passage meridional curvature probably has a larger effect than the rotation; hence, the secondary flow reverses direction.

As the flow path changes from the radial (at the mid-chord) to the axial direction (at the 4/4-chord), the Coriolis force changes direction from the tangential direction to the radial direction. However, since the pump exit blade angle is only 10 deg, the relative tangential velocity component is very small. The magnitude of the Coriolis force is also small at or near the exit, and is much less than that at the pump mid-chord and 3/4-chord. Hence, the Coriolis force is not the cause of the secondary flow at the pump 4/4-chord.

As the pump blade has only a 12.7 deg turning angle from the 3/4-chord to the 4/4-chord, hence the turning would not cause a dramatic change in the secondary flow. The secondary flow caused by the blade turning should result in overturning near the two end-walls. Only a small overturning is found near the shell. Hence, the pump blade turning angle between 3/4-chord and 4/4-chord is not a contributor to the secondary flow. At the pump 4/4-chord, the relative rotation eddy is in the clockwise direction. However, the secondary flow is in the counter-clockwise direction. This means the relative eddy is not the cause of this secondary flow.

It is clear that the secondary flow pattern in the first half of the pump passage depends mainly on the pump inlet flow condition and rotation effect. In the second half, the secondary flow is mainly affected by the rotation effect and the torus curvature effect. It is very difficult to show such complex three-dimensional secondary flow pattern in one illustration. However, the velocity vectors at three cross sections (Fig. 8) do show the main features.

The relative total pressure loss parameter contours at the pump 4/4-chord are shown in Fig. 10(*c*). The flow loss contour is consistent with the presence of the jet-wake flow. It is noted that the loss in the wake region has been transported from the blade suction side at the 3/4-chord to the core at the 4/4-chord. This is caused by the radial inward secondary flow along the suction side. When comparing the radial distribution of the mass-averaged flow loss parameter at different pump sections (Fig. 12), it is clear that higher losses are found near the core from the mid-chord to the 4/4-chord. It is believed that the core-suction wake flow is the main reason for this loss.

The radial distribution of the mass-averaged static pressure shows that the pump 4/4-chord has the largest radial pressure gradient in all pump measurement sections (Fig. 4(*a*)). This is mainly because the 4/4-chord is a radial plane and it has the largest radius, the centrifugal force has the highest value. The radial distribution of the mass-averaged relative flow yaw angle is nearly linear. This means that the deviation angle, which is exit blade angle (10 deg) minus the relative flow angle, also has a linear distribution of 4.5 deg at the shell and 12.2 deg at the core (Fig. 4(*d*)).

Effect of Speed Ratio. At the speed ratio 0.8, the flow field inside the pump passage is very similar to that at the speed ratio 0.6, because of the similar pump inlet (stator exit) flow structure [4]. The jet-wake flow structure dominates the pump passage flow. The secondary flow is even stronger, it also changes the direction of the rotation from 3/4-chord to 4/4-chord. The radial distributions of the absolute total pressure (Fig. 11) and the relative total pressure loss parameter (Fig. 12) are also very similar to those of the speed ratio 0.6. The first half of the passage has the most of the total pressure rise (73 percent), and the second half of the passage has the most of the flow losses (70 percent). However, the axial velocity deficit near the core is reduced (Fig. 4(*b*)). Unlike the speed ratio 0.6, the pump inlet flow has a positive incidence. The relative flow yaw angles are 39 deg at the shell and 63 deg at the core (Fig. 4(*d*)). The jet-wake flow structure inside the pump passage becomes stronger [7] due to the enlarged inlet flow separation on the blade suction side.

At the speed ratio 0.065, the first half of the pump passage has a considerable deviation as compared to that at the speed ratio 0.6 because of the dramatic change of pump inlet (stator exit) flow condition (Fig. 4). It has a -41.6 deg incidence angle (flow coming towards the suction side). The inlet flow separation switches to the pressure side of the blade. At the pump mid-chord, a very low through flow velocity is observed near the pressure side [7]. The jet-wake flow structure is much weaker at the speed ratio 0.065. The secondary flow is still very strong, and the radial and tangential transport of mass flow is also very strong (Fig. 4(*c*)). Most of the total pressure rise (95 percent) is accomplished in the first half of the pump passage.

The mass-averaged and area-averaged total pressure loss of each element is shown in Fig. 13. These losses are based on the stationary probe data at the exit. At the peak efficiency condition, the stator flow has the highest total pressure loss. This is believed mainly due to the positive incidence at the stator inlet. An improved design of the stator flow will improve the peak efficiency of the torque converter. At the design condition and other low-speed ratio conditions, the turbine flow has the highest total pressure loss. Thus, an improvement in turbine flow field would lead to increased torque converter efficiency. Hence, major improvements in performance can be gained through proper matching of pump-turbine and stator, and by redesigning the turbine and stator to reduce losses.

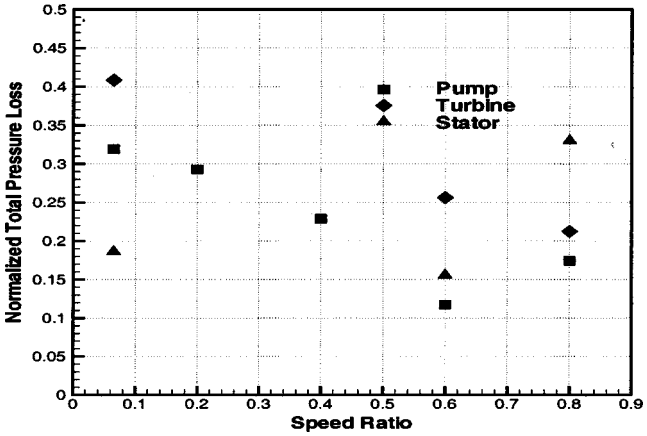

Fig. 13 Normalized mass average total pressure loss across elements versus speed ratio

Conclusions

The following conclusions are drawn from this investigation:

1 A rotating high-frequency response five-hole probe system has been successfully designed, fabricated, and used in the present research. The electronic noise of this system is small. The accuracy of the flow measurement is about the same as that in the stationary frame.

2 The most significant feature of the pump inlet flow is the axial velocity deficit near the core, caused by the secondary flow and the axial velocity deficit at the stator exit. At the speed ratio 0.6, the pump inlet has a 52 deg incidence angle variation along the blade span.

3 A strong secondary flow is found to dominate the flow structure at the pump mid-chord. The Coriolis force and the direct effect of rotation are the main causes for the secondary flow. A large radial transport of mass flow is observed in the first half of the pump passage due to the secondary flow.

4 The flow field at the pump 3/4-chord location is dominated by the mass flow concentration on the pressure side. The jet-wake flow pattern is enhanced by the upstream secondary flow. Relative high flow losses are found in the core-suction corner between the pump mid-chord and 3/4-chord.

5 The flow field measured at the pump 4/4-chord location using the rotating probe is similar to that measured at the pump exit downstream location using the stationary high-frequency response five-hole probe. The mass flow concentration on the pressure side of the passage still dominates the flow field because of the upstream secondary flow. Low kinetic energy fluid is found in the core-suction corner.

6 The secondary flow changes the direction of circulation from the pump 3/4-chord to the pump 4/4-chord, mainly caused by the torus meridional curvature and the flow concentration near the pressure side.

7 The first half of the passage has the most total and static pressure rise and the second half (mid-chord to exit) has the most losses.

Acknowledgments

This project was sponsored by the Powertrain Division of the General Motors Corporation with D. G. Maddock as the technical monitor. The authors wish to express their acknowledgment to Mr. Donald G. Maddock for his support, encouragement, and as-

sistance. The probe traversing mechanisms and test sections were designed by Mr. Maddock. Assistance by J. Burningham in the data acquisition is also acknowledged.

Nomenclature

D = diameter of torque converter (245 mm)
$f_{p,s}$ = pump shaft frequency ($n_p/60$)
$f_{t,s}$ = turbine shaft frequency ($n_t/60$)
f_{pump} = pump blade passing frequency ($N_p \times f_p$)
f_{stator} = stator blade passing frequency
f_{turb} = turbine blade passing frequency ($N_t \times f_t$)
h = probe radial height, mm
H = blade height, mm
h/H = relative radial location
i = incidence angle
n_p = pump rotating speed, rpm
n_t = turbine rotating speed, rpm
N_p = number of pump blade (32 in this paper)
N_t = number of turbine blade (36 in this paper)
P = static pressure
$P_0, (P_0)_a$ = absolute stagnation pressure
$P_{op}, (P_0)_p$ = relative stagnation pressure in rotating frame
P_1 = relative total pressure loss parameter (Eq. (7))
P.S. = pressure side of the passage
SR = speed ratio, n_t/n_p
S.S. = suction side of the passage
U = pump blade tip rotating speed
V = absolute velocity
W_m = relative normal velocity (through flow velocity, Fig. 1(b)
W_n = relative bi-normal velocity (Fig. 1(b))
W_0 = relative total velocity
W_s = secondary flow velocity in relative frame (Eq. (3))
W_θ = relative tangential velocity
α_p = relative flow pitch angle (core-to-shell direction) in pump rotating frame
β_p = relative flow yaw angle (blade-to-blade direction) in pump rotating frame
δ = deviation angle
ρ = oil density, kg/m^3

Subscripts

r, θ, z = components in the radial, tangential and axial locations (Fig. 1(b))
ref = reference velocity (Eq. (1))

References

[1] By, R., and Lakshminarayana, B., 1995, ''Measurement and Analysis of Static Pressure Field in a Torque Converter Pump,'' ASME J. Fluids Eng., **117**, pp. 109–115.
[2] Gruver, J., Flack, R., and Brun, K., 1994, ''Laser Velocimeter Measurement in the Pump of a Torque Converter Part I—Average Measurements,'' ASME 94-GT-47.
[3] Brun, K., and Flack, R., 1994, ''Secondary Flow Measurement in a Mixed Flow Pump Using Laser Velocimetry,'' Seventh International Symposium on Applications of Laser Techniques to Fluid Mechanics, Lisbon, Portugal.
[4] Dong, Y., Lakshminarayana, B., and Maddock, D., 1998, ''Steady and Unsteady Flow Field at Pump and Turbine Exit of a Torque Converter,'' ASME J. Fluids Eng., **120**, pp. 538–548.
[5] Dong, Y., and Lakshminarayana, B., 1999, ''Experimental Investigation of the Flow Field in an Automotive Torque Converter Stator,'' ASME J. Fluids Eng., **121**, pp. 788–797.
[6] Marathe, B. V., Lakshminarayana, B., and Maddock, D. G., 1997, ''Experimental Investigation of Steady and Unsteady Flow Field Downstream of Automotive Torque Converter Turbine and Inside the Stator,'' ASME J. Turbomach., **119**, pp. 624–645.
[7] Dong, Y., 1998, ''An Experimental Investigation on Fluid Dynamics of An Automotive Torque Converter,'' Ph.D. thesis, The Pennsylvania State University, State College, PA.
[8] Lakshminarayana, B., 1996, *Fluid Dynamics and Heat Transfer of Turbomachinery*, Wiley-Interscience Publication, New York, NY.

Amos Ullmann
Department of Fluid Mechanics
and Heat Transfer,
Faculty of Engineering,
Tel-Aviv University,
Ramat-Aviv 69978, Israel

Ilan Fono
Micro Infusion Ltd,
2a Katzir Street,
Tel-Hashomer,
Ramat Gan 52656, Israel

Yehuda Taitel
Department of Fluid Mechanics
and Heat Transfer,
Faculty of Engineering,
Tel-Aviv University,
Ramat-Aviv 69978, Israel

A Piezoelectric Valve-Less Pump-Dynamic Model

A complete dynamic model for the simulation of the valve-less piezoelectric pump performance is presented. In this model the piezoelectric action is considered as a periodic force acting on a pumping membrane. The natural frequency of the pump is calculated as well as its performance as a function of the driving frequency. The effect of the deviation of the driving frequency from the natural frequency on the pump performances is clearly shown. Also, it is demonstrated that the effect of the liquid mass in the pump nozzles on the natural frequency of the system is very high owing to the high acceleration of the fluid in the nozzles. Comparison with experiments shows a very good agreement with a minimal number of adjusting parameters. [DOI: 10.1115/1.1343459]

Keywords: Valve-Less Pump, Piezoelectric

1 Introduction

A piezoelectric valve-less pump is an attractive device to be used as a micro pump for law flow rates. The pump converts the reciprocating motion of a diaphragm activated by a piezoelectric disk to a pumping action similarly to the conventional piston reciprocating pumps (Shuchi and Esashi [1]). The conventional valves that direct the flow from low pressure to high pressure are replaced here with nozzle/diffuser elements that have a preferential flow direction. That is, the resistance to flow is higher in one direction than in the other direction. Thus, a pump can be constructed utilizing these nozzles instead of conventional valves thereby eliminating moving parts that are not easy to construct, especially for very small pump assembly. Several papers were published recently on the design and fabrication of such micropumps by various etching technologies (Gerlach et al. [2], Olsson et al. [3], Heschell et al. [4] and Olsson et al. [5]).

A simple analytic model to predict the maximum flow (at zero pump pressure) and the maximum pump pressure (at zero pump flow) was presented by Stemme and co-workers (Stemme and Stemme [6], Olsson et al. [7]). The model is based on the continuity consideration and requires an input of the pumping membrane displacement volume and frequency. The analysis using the continuity equation was extended (Ullmann [8]) to predict the temporal pressure and output flow rate during a single cycle of pumping and the overall (integrated) pressure behavior (e.g., flow rate versus pressure) of the pump. However, the performance, which is based on the kinematic knowledge of the displacement, is limited in its realistic simulation since it lacks the ability to follow the true dynamic behavior of the pump and its response as a function of the piezoelectric driving frequency. A lumped mass model was recently presented by Olsson et al. [9], which is based on subdivision of the complete pump into lumped mass elements with simple analytic relations between them. The resonance frequency of the pump is estimated via a spring—mass analogy and a simulation of the pump performance was presented.

In this work, a dynamic model is presented, which is simpler and different in many details than that of Olsson et al. [9]. New experimental data for the pump behavior with frequency and the pump performance is included.

Although valve-less pump is usually associated with the piezoelectric way of activating reciprocal motion, obviously the analysis here is not restricted only to the piezoelectric pump and it is valid for any type of reciprocal motion applied to the valve-less pump assembly.

2 Pump Model

2.1 The Natural Frequency of the Piezoelectric Pump. A schematic configuration of a single chamber piezoelectric pump is shown in Fig. 1. The performance of the pump is based on the unique quality of the ''diffuser nozzles'' to have lower resistance for flow from left to right (in the figure) than from right to left. Consequently, a reciprocating piezoelectric disc motion results in a net flow from left to right and can be used to pump fluid from a lower inlet pressure P_{in} to a higher outlet pressure P_{out}.

The piezoelectric pump works best near the natural frequency of the pump (Stemme and Stemme [6]). This natural frequency is greatly affected by the liquid in the pump, in the nozzles and in the leading inlet and outlet pipes and it is much lower than the natural frequency of the disk/piezoelectric device assembly without the liquid.

For the purpose of calculating the natural frequency we use a mass spring analogy to represent the system (similarly to Olsson et al. [7]). The spring is presented by the elastic properties of the diaphragm and the piezoelectric element and the mass by the diaphragm mass and the effective mass of the fluid in the pumping chamber, the nozzles and the inlet and outlet tubes. The piezoelectric pump chamber is considered as a cylinder that contains m_L mass of liquid (see Fig. 2). The two nozzles are represented by two short pipes with a constant diameter, which is the average of the nozzles' variable diameter. Each nozzle contains a mass of liquid m_N. The leading inlet and outlet pipes contain m_{P1} and m_{P2} masses of liquid. The piezoelectric membrane device, com-

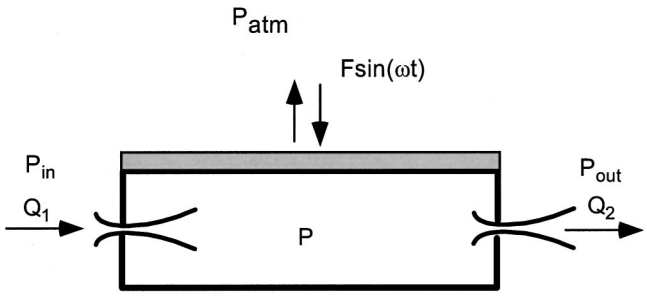

Fig. 1 Schematic valve-less pump structure

Contributed by the Fluids Engineering Division for publication in the JOURNAL OF FLUIDS ENGINEERING. Manuscript received by the Fluids Engineering Division December 30, 1999; revised manuscript received November 1, 2000. Associate Editor: J. Katz.

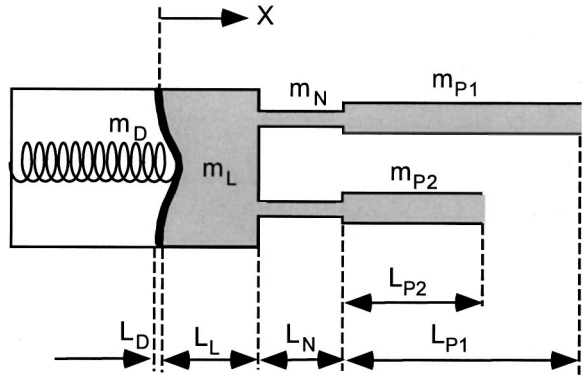

Fig. 2 The valve-less pump, schematic description for the calculation of the natural frequency

posed of a stainless-steel disk or any other metal substrate, on which the piezoelectric device is glued, is considered as a clamped or a supported disk (two options). The driving voltage on the piezoelectric device is assumed to be converted into force acting on the center of the disk. It will cause a deflection of the disk as follows (Timoshenko [10]):

For a clamped disk the deflection is

$$x=\frac{Fr^2}{8\pi D}\ln\frac{r}{R}+\frac{F}{16\pi D}(R^2-r^2) \tag{1a}$$

where x is the local deflection, R the disk radius, D the flexural rigidity, r is the local radius and F is the central force applied at the center of the disk. For a supported disk:

$$x=\frac{Fr^2}{8\pi D}\ln\frac{r}{R}+\frac{F}{16\pi D}\frac{3+\nu}{1+\nu}(R^2-r^2) \tag{1b}$$

where

$$D=\frac{\mathrm{E}L_D^3}{12(1-\nu^2)} \tag{2}$$

E is the Young modulus of elasticity, ν is the Poisson's ratio, and L_D is the disk thickens. Substituting for $\nu=0.3$ yields, for the central disk deflection X,

$$X=\frac{0.217R^2}{\mathrm{E}L_D^3}F \tag{3a}$$

for a clamped disk, or

$$X=\frac{0.55\,R^2}{\mathrm{E}L_D^3}F \tag{3b}$$

for a supported disk.

Equation (3) shows that the disk acts as an elastic spring with spring coefficient k

$$F=-kX \tag{4}$$

where

$$k=\frac{\mathrm{E}L_D^3}{0.217R^2} \tag{5a}$$

for a clamed disk and

$$k=\frac{\mathrm{E}L_D^3}{0.55R^2} \tag{5b}$$

for a supported disk.

The potential energy of the disk is therefore

$$\mathrm{E}_P=\tfrac{1}{2}kX^2 \tag{6}$$

The Kinetic energy of the Piezoelectric disk and the liquid is (see Fig. 2):

$$\mathrm{E}_K=\frac{1}{2}K_Dm_D\dot{X}^2+\frac{1}{2}m_L\left[\frac{K_VA_D}{A_L}\dot{X}\right]^2+2\times\frac{1}{2}m_N\left[\frac{K_VA_D}{2A_N}\dot{X}\right]^2+\frac{1}{2}m_{P1}\left[\frac{K_VA_D}{2A_{P1}}\dot{X}\right]^2+\frac{1}{2}m_{P2}\left[\frac{K_VA_D}{2A_{P2}}\dot{X}\right]^2 \tag{7}$$

Equation (7) shows that the kinetic energy can be expressed in the form:

$$\mathrm{E}_k=\tfrac{1}{2}M\dot{X}^2 \tag{8}$$

where M is the equivalent mass

$$M=K_Dm_D+m_L\left(\frac{A_DK_V}{A_L}\right)^2+2m_N\left(\frac{A_DK_V}{2A_N}\right)^2+m_{P1}\left(\frac{A_DK_V}{2A_{P1}}\right)^2+m_{P2}\left(\frac{A_DK_V}{2A_{P2}}\right)^2 \tag{9}$$

In Eqs. (6) and (7) the liquid displacement and velocity is given in terms of the maximum deflection X and $\dot{X}$. Due to continuity considerations, the velocities in the nozzles and the leading pipes (see Fig. 2) are determined by the ratio of the areas of the nozzles, A_N, (or pipes, A_P) and the area of the disk, A_D. However, an additional correction should be made since X is the maximum central deflection, the volumetric displacement is less than $A_D\times X$. This is done by the correction coefficient K_V, thus, the volumetric rate displacement is $\dot{V}=A_D\times\dot{X}\times K_V$ where

$$K_V=\frac{\int_0^R x2\pi r\,dr}{X\pi R^2} \tag{10}$$

Using Eq. (1) we obtain

$$K_V=2\int_0^1[2y^2Ln(y)+(1-y^2)]y\,dy=4[0.25y^2-0.1875y^4+0.25y^4Ln(y)]_0^1=0.25 \tag{11a}$$

for a clamped disk and

$$K_V=2\int_0^1\left[\frac{2}{2.53846}y^2Ln(y)+(1-y^2)\right]y\,dy=0.4 \tag{11b}$$

for a supported disk where $y=r/R$.

A similar correction is required for the term of the disk's kinetic energy in Eq. (7). The kinetic energy of the disk is the sum (integral) of its local kinetic energy. Thus, the kinetic energy of the disk with reference to the central deflection velocity is expressed by Eq. (12).

$$\mathrm{E}_{K,D}=\frac{1}{2}\int\dot{x}^2dm=\frac{1}{2}K_Dm_D\dot{X}^2 \tag{12}$$

This equation defines the coefficient K_D, which is a correction factor for the mass of the disk (that contains the piezoelectric device).

Using Eqs. (1a) and (1b) yields, for the clamped disk:

$$K_D=2\int_0^1[2y^2Ln(y)+(1-y^2)]^2y\,dy=0.13 \tag{13a}$$

and for the supported disk:

$$K_D=2\int_0^1\left[\frac{2}{2.53846}y^2Ln(y)+(1-y^2)\right]^2y\,dy=0.235 \tag{13b}$$

As for a spring-mass system the sum of the kinetic energy and the potential energy is constant, equal to the maximum potential energy when the central deflection X is maximal. Thus,

$$\tfrac{1}{2}M\dot{X}^2+\tfrac{1}{2}kX^2=\tfrac{1}{2}kX_{\max}^2 \tag{14}$$

that yields the following differential equation:

$$\dot{X}+\sqrt{\frac{k}{M}}\sqrt{X_{\max}^2-X^2}=0 \tag{15}$$

Solution of this equation yields:

$$X=X_{\max}\cos\left(\sqrt{\frac{k}{M}}t\right) \tag{16}$$

Thus, the natural frequency of the system is:

$$f_0=\frac{\sqrt{\frac{k}{M}}}{2\pi} \tag{17}$$

2.2 Dynamic Pump Performance. The general dynamic pump performance can be calculated from a complete differential equation that includes the piezoelectric force and the pressure forces on both sides of the disk. The piezoelectric device is assumed to produce a sinusoidal force of amplitude F_{amp} on the clamped/supported disk center, thus,

$$M\frac{d^2X}{dt^2}=F_{\text{amp}}\sin(\omega t)-kX-(P-P_{\text{atm}})A_DK_P \tag{18}$$

The constant K_P is a correction factor that converts the continuous pressure force $(P-P_{\text{atm}})$ to a central force, thus

$$K_P=\frac{X_{\text{continuous}}}{X_{\text{central}}} \tag{19}$$

For a clamped disk and a central force, X is given by Eq. (3*a*). For a continuous force, X is given by (Timoshenko [10]),

$$X=\frac{0.171PR^4}{\mathrm{E}L_D^3} \tag{20a}$$

that yields $K_P\approx 0.25$.

For a supported disk and a central force, X is given by Eq. (3*b*). For a continuous force, X is

$$X=\frac{0.696PR^4}{\mathrm{E}L_D^3} \tag{20b}$$

which yields $K_P\approx 0.40$. Note that K_P is equal to K_V. This can be easily verified by comparing the work done by a uniform force with the work of a central force.

The pressure loss in the nozzle is conventionally expressed in terms of a loss coefficient K as (Stemme and Stemme [6]),

$$\Delta P=\tfrac{1}{2}K\rho_L U^2 \tag{21}$$

where U is the velocity at the throat of the nozzle. This can be written in the form:

$$Q=C\sqrt{\Delta P} \tag{22}$$

where Q is the flow rate, equals to $U\times A_{\min}$ and C, the conductivity coefficient is:

$$C=\frac{A_{\min}}{\sqrt{\tfrac{1}{2}K\rho_L}} \tag{23}$$

$A_{\min}$ is the minimum nozzle cross sectional area (the throat area). The loss coefficient K is low for the flow from left to right and high from right to left (see Fig. 1). C is just the opposite. Based on the above relations, the pressure in the pump's chamber, P, can be expressed as a function of the conductivity coefficients, the central disk deflection, and the inlet and outlet pressures.

For $\mathbf{P>P_{out}>P_{in}}$

$$\begin{aligned} Q_1&=-C_L\sqrt{P-P_{\text{in}}}\\ Q_2&=C_H\sqrt{P-P_{\text{out}}}\end{aligned} \tag{24}$$

Mass balance requires that:

$$Q_2-Q_1=\dot{V} \tag{25}$$

where $\dot{V}=\dot{X}A_DK_V$.

Substituting Q_1 and Q_2 into (25) yields:

$$C_H\sqrt{P-P_{\text{out}}}+C_L\sqrt{P-P_{\text{in}}}=\dot{V} \tag{26}$$

Equation (26) is solved for P to yield

$$P=P_{\text{out}}+\left[\frac{C_H\dot{V}-C_L\sqrt{(C_H^2-C_L^2)\Delta P+\dot{V}^2}}{(C_H^2-C_L^2)}\right]^2 \tag{27}$$

where $\Delta P=P_{\text{out}}-P_{\text{in}}$.

The range of $P>P_{\text{out}}>P_{\text{in}}$ takes place when $\dot{V}>C_L\sqrt{P_{\text{out}}-P_{\text{in}}}$ (Eq. 26)

For $\mathbf{P<P_{in}<P_{out}}$

$$\begin{aligned} Q_1&=C_H\sqrt{P_{\text{in}}-P}\\ Q_2&=-C_L\sqrt{P_{\text{out}}-P}\end{aligned} \tag{28}$$

Substituting into Eq. (25) the solution for P is:

$$P=P_{\text{out}}-\left[\frac{C_L\dot{V}+C_H\sqrt{(C_H^2-C_L^2)\Delta P+\dot{V}^2}}{(C_H^2-C_L^2)}\right]^2 \tag{29}$$

This range of $P<P_{\text{in}}<P_{\text{out}}$ takes place when $\dot{V}<-C_L\sqrt{P_{\text{out}}-P_{\text{in}}}$ (Eqs. (25), (28))

For $\mathbf{P_{in}<P<P_{out}}$

$$\begin{aligned} Q_1&=-C_L\sqrt{P-P_{\text{in}}}\\ Q_2&=-C_L\sqrt{P_{\text{out}}-P}\end{aligned} \tag{30}$$

and the solution for P is:

$$P=P_{\text{out}}-\left[-\frac{1}{2}\frac{\dot{V}}{C_L}+\frac{1}{C_L}\sqrt{\frac{1}{2}C_L^2\Delta P-\frac{1}{4}\dot{V}^2}\right]^2 \tag{31}$$

The range of $P_{\text{in}}<P<P_{\text{out}}$ takes place when $-C_L\sqrt{P_{\text{out}}-P_{\text{in}}}<\dot{V}<C_L\sqrt{P_{\text{out}}-P_{\text{in}}}$.

The expression for P is substituted into Eq. (18), which is integrated numerically to yield the displacement X and the pressure P as a function of time. Once P is obtained, the temporal flow rates Q_1 and Q_2 can be calculated and the average inlet and outlet flow rates are obtained by the numerical integration of Q_1 or Q_2 during one pumping cycle after reaching a periodic ''steady state'' at time t

$$\overline{Q}_{1,2}=\frac{1}{\tau}\int_t^{t+\tau}Q_{1,2}dt \tag{32}$$

where τ is the cycle time. Obviously $\overline{Q_1}=\overline{Q_2}$.

3 Experimental

3.1 Test Device and Experimental Setup. An experimental pump was assembled as shown in Fig. 3. The pump has the following parameters:

The loss coefficients K_H and K_L were obtained using simple steady-state ''static'' experiments. Namely, allowing flow of water by gravity through the valves in one direction and then in the opposite direction and measuring the hydrostatic head and the flow rate. The values of K_H and K_L are average values. The dependence of the loss coefficient on the Reynolds number was relatively weak and the use of constant values seems to be a reasonable engineering approach.

Two sets of experiments were conducted both for 100 volts driving voltage. The first is a set where the flow output was recorded as a function of the driving frequency for the case of zero pressure difference ($P_{out}=P_{in}=P_{atm}$). In the second set of experiments, the maximum pressure difference ($P_{out}-P_{in}$) at the limit of the pumping action was measured. Namely, the pressure difference at the point where the output flow rate is zero.

3.2 Experimental Results. The results of this experiment are shown in Figs. 4 and 5. The comparison of the theoretical model with the experiments is not completely independent and some of the parameters used in the modeling have to be calibrated based on the experimental results.

In the model the membrane disk is considered as it is composed of a single material. In practice, the membrane is composed of the piezoelectric device attached to a stainless steel disk. A theoretical way for calculating the effective Young modulus is beyond the scope of this work. The effective Young modulus in the current experiments is obtained by recording the natural frequency of an empty pump. Thus, the first model calibration was done by matching the calculated natural frequency of the disk with the frequency of an empty pump by adjustment of the Young modulus. The experimental natural frequency was about 16500 Hz and the Young modulus that gives this value is $E=13.0\times10^{10}$ Pa. This value, by the way, is very close to the average of the stainless steel Modulus and the Young modulus of the piezoelectric ceramic material. Note also that in this work we presented two basic arrangements of disk attachments to the pump, namely a supported disk and a clamped disk. Based on the experimental results we found that the supported disk better fits our experimental data. Nevertheless, for the sake of generality we do include these two options in the analysis.

The theoretical natural frequency of the pump with water, using Eq. (17) with the aforementioned Young modulus and the parameters reported in Table 1, is 550 Hz, which corresponds very closely to the experimental results. The natural frequency of the pump with the fluids is much lower than the natural frequency in free air.

As one can observe from Eq. (9), the equivalent mass of the system is comprised of the mass of the membrane, the mass of the liquid in the chamber (both of which can be neglected), the mass of the fluid in the nozzles and the leading pipes multiplied by the cross sectional area ratio squared. Obviously, the effect of the mass is to lower the natural frequency. The main contribution to this is the mass of the liquid in the nozzles that moves with the highest velocity and acceleration due to the very low cross-sectional area of the nozzles as also reported by Olsson et al. [7].

As we do not have a way to translate the driving voltage into a driving force acting on the membrane we had to obtain this force by calibrating the model using a single experimental result. This was done by matching the central force amplitude to obtain about the same flow rate as the experimental one, at the natural fre-

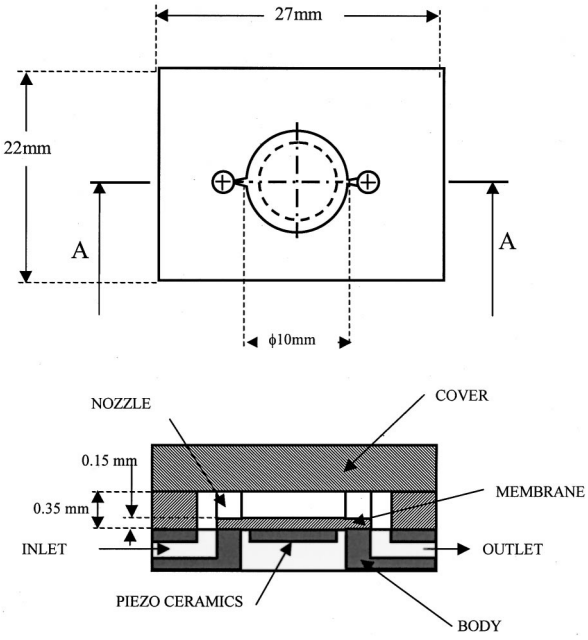

Fig. 3 Detailed design of the piezoelectric valve

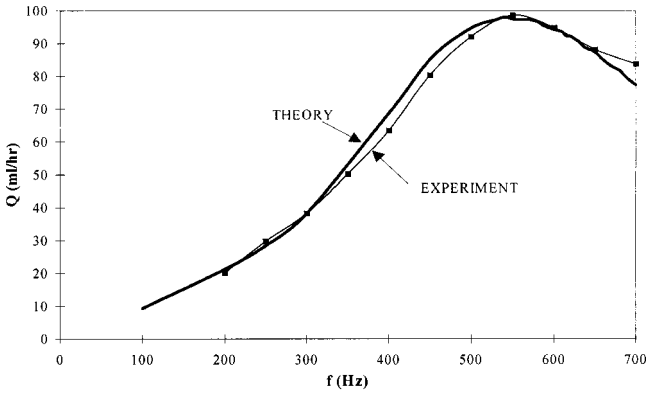

Fig. 4 Flow rate against the driving frequency, comparison with experiments

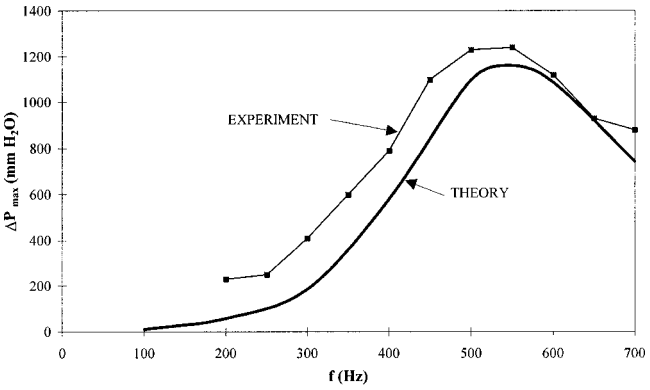

Fig. 5 Maximum pressure against the driving frequency, comparison with experiments

Table 1 Pump parameters

Disk (membrane) material	−stainless steel
Disk diameter	−10 mm
Disk thickness	−0.15 mm
Disk density	−7850 kg/m^3
Disk Young elastic modulus	-19.0×10^{10} Pa
Piezoelectric device diameter	−8 mm
Piezoelectric device thickness	−0.25 mm
Piezoelectric Young modulus	-6.6×10^{10} Pa
Chamber diameter	−10 mm (equal to disk diameter)
Chamber depth	−0.20 mm
Liquid density (water)	−1000 kg/m^3
Nozzles length	−4.2 mm
Nozzles average diameter	−0.29 mm
Nozzles minimum diameter	−0.15 mm
Diameter of inlet and outlet pipes	−1.8 mm
Length of inlet and outlet pipes, about	−100 mm
High loss coefficient	$-K_H=0.8$
Low loss coefficient	$-K_L=0.4$

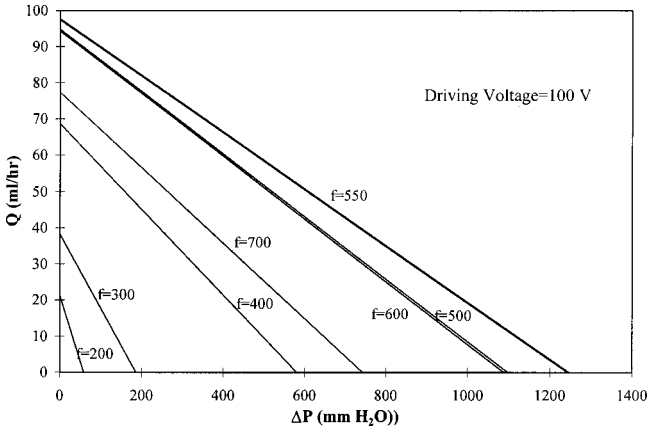

Fig. 6 Pump performance, theoretical

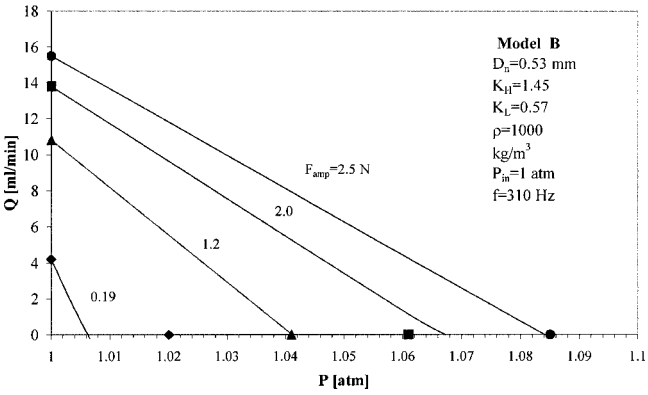

Fig. 8 Pump performance, comparison with experiment, Stemme and Stemme [6] Model B

quency. The value of $F_{amp}=1.4$ N was found to be valid for this case. The theoretical prediction of this force is also beyond the scope of this work.

With these two adjustments, that are the Young modulus E and the force amplitude F_{amp} the theory can now be used. The comparison between the experiments and the predicted flow rates and maximum pressure as a function of the driving frequency is shown in Figs. 4 and 5. The comparison is excellent for the flow rate at zero pressure difference and it is satisfactory for the maximum pressure (zero flow rate).

Note that, since it was shown before (Olsson et al. [7] and Ullmann [8]) that the flow rate versus pressure is very close to a linear line, one can draw the anticipated performance for the different frequencies as shown in Fig. 6. As can be observed, the maximum pump performance is obtained at the calculated resonance frequency.

Figure 7 shows the calculated variation with time of the central membrane deflection (Eq. (18)) for three different driving frequencies, 50, 550, and 2000 Hz. The amplitude is normalized with respect to the static amplitude (X_{sta}), that is with respect to the central displacement subject to a constant force equals to F_{amp}. The time is normalized with respect to the time period of one natural cycle. The natural frequency is $f_0=550$, and, as expected the amplitude is maximal when the driving frequency is identical to the natural frequency. For the case of 50 Hz one can clearly observe the super imposed natural frequency of 550 Hz on the 50 Hz driving frequency. For the case of driving frequency of 2000 Hz we can observe an imposed 550 Hz just at the beginning. At some later time the driving frequency of 2000 Hz is the dominant one. The amplitude for this case is, however, very low. The initial condition for all cases is zero for both the deflection and the velocity. As one can observe, a periodical steady state is achieved after a short time of the order of a few periods of the natural frequency.

3.3 Comparison With Previous Experimental Results Figures 8 and 9 show the comparison of the theoretical model prediction with the experimental results obtained by Stemme and Stemme [6] for two models of pumps, models A and B. The pump dimensions and required input variables were taken from Stemme and Stemme [6] and Olsson et al. [9]. Two adjustments were made in this comparison. The first adjustment is of the Young modulus to obtain the experimental natural frequency of model B at 310 Hz. The result obtained for the Young modulus is $E=11.5\times10^{10}$ Pa. The second adjustment is of the force amplitude so that the flow rate, Q for zero pressure difference is the same as in the experiments. With these two adjustments the theoretical model was used to predict the maximum pressure at zero flow rate and the amplitude of the membrane center. The performance curve, Q versus ΔP, as mentioned above, can be approximated as a straight line connecting the points at $\Delta P=0$ and at $Q=0$. Figure 8 is a comparison of the theory with the results for model B, where the marks are the experimental results. Obviously, the experimental data coincide with the theory at $\Delta P=0$. The results at $Q=0$ matched quite close the experimental data except for the case of $F_{amp}=0.19$N. This is probably an anomaly of the experimental results since this case yields a slope that is contrary to the trends of the other curves. Note also that Olsson et al. [9] observed this anomaly.

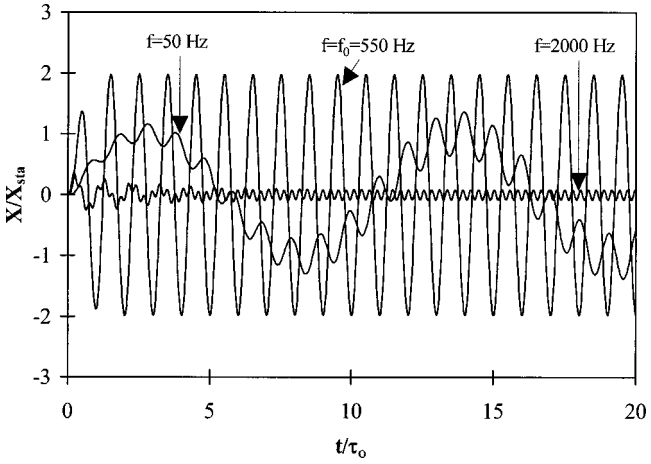

Fig. 7 Central amplitude of the piezoelectric membrane

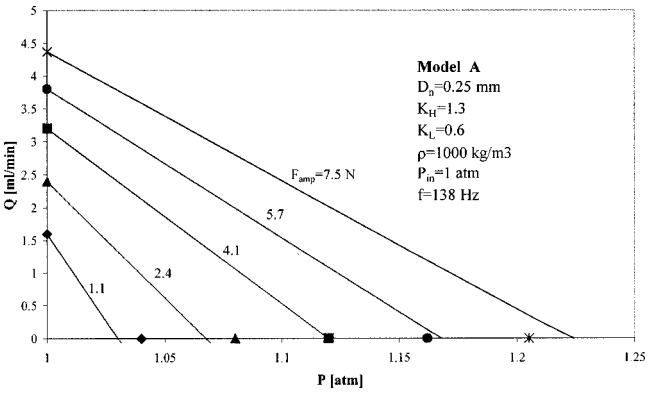

Fig. 9 Pump performance, comparison with experiment, Stemme and Stemme [6] Model A

Table 2 Membrane deflection amplitude (μm), Model B

	F_{amp}=0.19 N	F_{amp}=1.2 N	F_{amp}=2.0 N	F_{amp}=2.5 N
Experimental	5.6	8.2	11.3	13
Theory at $\Delta P=0$	4.33	11.30	14.23	15.98
Theory at $Q=0$	3.93	9.12	11.07	12.06

Table 3 Membrane deflection amplitude (μm), Model A

	F_{amp}=1.1 N	F_{amp}=2.4 N	F_{amp}=4.1 N	F_{amp}=5.7 N	F_{amp}=7.5 N
Experimental	4.8	7.2	9.2	11	12.5
Theory at $\Delta P=0$	4.43	6.63	8.82	10.44	12.04
Theory at $Q=0$	3.15	3.82	3.90	3.62	3.00

The results for the membrane deflection amplitude are presented in Table 2. The experimental results are given as a single number. Our analysis shows a difference for the case of $Q=0$ and the case of $\Delta P=0$. As can be seen, the theoretical results are quite close to the experiment (much closer than those reported by the model presented by Olsson et al. [9]).

Figure 9 is our comparison with the experimental results for model A pump. Note that since we used for model A the same value of the Young modulus, the natural frequency is not an adjusted value. Thus, the model predicted a natural frequency $f_0=138$ Hz instead of the experimental 110 Hz. The discrepancy is considered acceptable for our approximate model (note again that Olsson et al. [9] got 165 Hz in their calculations and used a frequency of 160 Hz in the simulation). Following the same procedure as before, Fig. 9 yields the performance curves and Table 3 the deflection amplitude. The agreement of the model with the data is quite good.

4 Summary and Conclusions

In the present work a dynamic model is developed capable of predicting the performance of the piezoelectric valve-less pump as a function of the frequency.

It is shown that the natural frequency of the pump with water is much less than the natural frequency in air. This is primarily due to the high virtual mass of the liquid in the nozzles that results from the high acceleration in the nozzle throat.

The piezoelectric element is assumed to act as a central periodic force on the membrane center. Two options are considered for the disk (1) a clamped disk and (2) a supported disk. The supported disk approximation seems to yield better results when compared with experimental data.

Two empirical adjustments are used here in the application of this model (1) The equivalent Young modulus of the membrane disk assembly and (2) The amplitude of the central cyclic force. The equivalent Young modulus is obtained by a single test of the natural frequency of the membrane assembly. The conversion of the voltage applied to the piezoelectric disk into a central force is obtained by matching the pump output at one operational point.

An experimental pump was built and tested. Data of flow rate and maximum pressure were plotted versus frequency. The agreement between the experiment and the theory was quite good. In addition, comparison with previous work shows good agreement with the results of the present model.

It is demonstrated that, in spite of the complexity of the physical behavior of the valve-less pump, the simplified model presented here, predicts many of the true features of the valve-less pump behavior and can be employed as a useful design tool.

Nomenclature

A = cross sectional area
C = conductivity coefficient
D = flexural rigidity
E = Young modulus
E_P = potential energy
E_K = kinetic energy
f = frequency
f_0 = natural frequency
F = force
k = spring constant
K = loss coefficient
K_H, K_L = high and low loss coefficients
K_V = volumetric correction factor
K_D = disk mass correction factor
K_P = correction factor for the pressure force
L = length
m = mass
M = equivalent mass
P = pressure
Q = flow rate
r = radial coordinate
R = disk radius
t = time
U = velocity at the nozzle throat
V = volume
x = local deflection
X = central deflection
y = r/R
V = volume
ν = Poisson's ratio
ρ = density
ω = angular frequency
τ = cycle time

Subscripts and Superscripts

amp = amplitude
atm = atmosphere
central = based on a central load model.
continuous = based on a continuous load model.
D = disk
H = high
in = at inlet
L = liquid, also low
N = nozzle
out = at outlet
P = pipe
sta = static

References

[1] Shuchi, S., and Esashi, M. E., 1994, ''Microflow devices and systems,'' J. Micromech. Microeng., **4**, pp. 157–171.

[2] Gerlach, T., Schuenemann, M., and Wurmus, H., 1995, ''A new micropump principle of the reciprocating type using pyramidic micro flow channels as passive valves,'' J. Micromech. Microeng., **6**, pp. 199–201.

[3] Olsson, A., Enoksson, P., Stemme, G., and Stemme, E., 1996, ''A valve-less planar pump isotropically etched in silicon,'' J. Micromech. Microeng., **6**, pp. 87–91.
[4] Heschell, M., Müllenborn, M., and Bouwstra, S., 1997, ''Fabrication and characterization of truly 3-D diffuser/nozzle microstructures in silicon,'' J. Microelectromech. Syst., **6**, pp. 41–46.
[5] Olsson, A., Enoksson, P., Stemme, G., and Stemme, E., 1997, ''Micromachined flat-walled valveless diffuser pumps,'' J. Microelectromech. Syst., **6**, pp. 161–166.
[6] Stemme, E., and Stemme, G., 1993, ''A valveless diffuser/nozzle-based fluid pump,'' Sens. Actuators A, **39**, pp. 159–167.
[7] Olsson, A., Stemme, G., and Stemme, E., 1995, ''A valve-less planar fluid pump with two pumps chambers,'' Sens. Actuators A, **46/47**, pp. 549–556.
[8] Ullmann, A., 1998, ''The piezoelectric valve-less pump-Performance enhancement analysis,'' Sens. Actuators A, **69/1**, pp. 97–105.
[9] Olsson, A., Stemme, G., and Stemme, E., 1999, ''A numerical design study of the valveless diffuser pump using a lumped-mass model,'' J. Micromech. Microeng., **9**, pp. 34–44.
[10] Timoshenko S., 1940, *Theory of Plates and Shells*, McGraw-Hill, New York.

David Jeffrey[1]
Penske Research Student

Xin Zhang[2]
Professor in Aerodynamics

School of Engineering Sciences,
University of Southampton,
Southampton SO17 1BJ, United Kingdom

David W. Hurst
Senior Lecturer
Department of Aerospace Engineering,
Glasgow University,
Glasgow, United Kingdom

Some Aspects of the Aerodynamics of Gurney Flaps on a Double-Element Wing

Gurney flaps of different heights have been fitted to a generic double-element wing, and the effects at two typical flap angles have been observed using force and pressure measurements, and by performing flow surveys using Laser Doppler Anemometry. At a low flap setting angle of 20 deg the suction-surface flow remains attached to the trailing edge of the flap, and vortex flow features and perturbation velocities are all similar to those observed when Gurney flaps are fitted to single element wings. At a high flap deflection of 50 deg there is an extensive region of separated flow over the flap, yet the Gurney flap still alters the flow structure. The measurements suggest that the wake flow behind the Gurney flap consists of a von Karman vortex street of alternately shed vortices. The effects of the Gurney flap on the lift, zero-lift drag, and pressure distributions are reported, and the differences between the trends observed for single-element wings are discussed.
[DOI: 10.1115/1.1334376]

Introduction

By fitting a short strip perpendicular to the pressure-surface trailing-edge of a wing it is possible to increase both the C_L generated at a given incidence, and the maximum C_L, at the expense of an increase in zero-lift drag. This mechanically simple device is known as the Gurney flap, and it is used extensively on various aerodynamic devices, e.g., race car wings. A typical Reynolds number for race car applications is 1.5×10^6.

The overall effect of Gurney flaps on the lift and drag of single- and double-element wings has been extensively documented, for example by Liebeck [1], Papadakis et al. [2,3], and Myose et al. [4]. Recent work by the authors (Jeffrey [5] and Jeffrey et al. [6]) has investigated the effect of Gurney flaps on single-element airfoils, using techniques including force and pressure measurements, and flow surveys performed using Laser Doppler Anemometry (LDA). The results indicate that fitting a Gurney flap to a wing introduces a street of alternately shed vortices directly downstream of the trailing edge. This enhances the suction acting on the downstream face of the Gurney flap, and hence at the trailing-edge of the suction surface of the wing. The upstream face decelerates the flow on the pressure-surface of the airfoil, resulting in an increase in pressure at the trailing edge on this surface. In combination, these two effects introduce a pressure difference across the trailing edge of the airfoil that induces an increase in circulation around the wing. The increase in zero-lift drag is largely caused by the pressure drag acting across the upstream and downstream faces of the Gurney flap.

In some engineering applications, Gurney flaps can be found on multi-element wings, usually consisting of a main element and flaps on which the Gurney flaps are attached. The aim of the research presented in this paper is therefore to investigate the effect of Gurney flaps as fitted to a generic double-element high-lift airfoil, and to compare these effects to those previously reported for single-element wings. The understanding of the aerodynamics of the Gurney flaps on a double-element wing is augmented by a flow physics study using LDA.

[1]Now, Aerodynamicist, British American Racing.
[2]Corresponding author.

Contributed by the Fluids Engineering Division for publication in the JOURNAL OF FLUIDS ENGINEERING. Manuscript received by the Fluids Engineering Division February 3, 2000; revised manuscript received August 28, 2000. Associate Editor: D. Williams.

Description of Experiments

In this paper, results are presented for a generic wing of finite span that has the double-element airfoil illustrated in Fig. 1. The flap was attached to the main element using four brackets: one at each tip and a pair mounted inboard at 275 mm (37 percent semi-span) either side of the centerline. Further details of this airfoil can be found in Jeffrey [5]. Results are presented here for two flap angles, $\delta_f=20$ degrees, and $\delta_f=50$ degrees. The overlap and gap were optimized with no Gurney flap fitted, at a flap angle of 50 degrees, to give the maximum C_L possible at a main wing incidence of $\alpha=0$ degree (it was found that the Gurney flap had little effect on this optimum flap position).

The reference chord of the model, c, was taken to be 0.32 m while the span, b, was 1.6 m. This span and reference chord were used to provide consistency with earlier single-element wing tests (Jeffrey et al. [6]). The coordinates plotted in Fig. 1 have been nondimensionalized using the reference chord, and hence the positions of the trailing edge of the flap extend beyond $x/c=1.0$.

The model is supported, pressure surface uppermost, by two vertical supports, located at 57 percent semi-span from the wing centerline, and by a third strut located on the centerline, downstream of the wing. The model had 26 chordwise tappings on the main element, and 16 on the flap, located 50 mm from the centerline of the wing ($\eta=0.0625$), and a total of 10 spanwise tappings on each surface at quarter reference chord from the leading edge.

Full-span Gurney flaps of $h/c=0.5$ percent, 1 percent, 2 percent, and 4 percent were manufactured. The Gurney flaps were fitted normal to the local curvature, on the pressure surface of the flap.

LDA surveys around the flap and the trailing-edge of the main element were performed using the three-component system installed in the University of Southampton's $3.5\,\text{m}\times2.5\,\text{m}$ wind tunnel. The spatial resolution of the measurement points was 3 mm in the regions of interest rising to 25 mm in the surrounding areas. Further details of the tests are provided in Jeffrey [5]. The freestream turbulence intensity for these experiments was of the order of 0.3 percent. Force and pressure measurements were obtained with the same model in the University's $2.1\,\text{m}\times1.7\,\text{m}$ wind tunnel, which has a freestream turbulence intensity of the order of 0.2 percent. The blockage produced by the wing was acceptable in both facilities.

The experiments were performed at a freestream velocity of

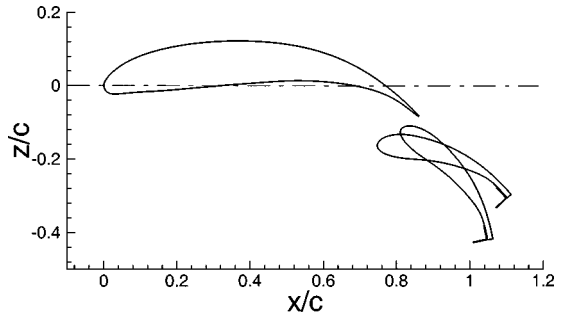

Fig. 1 Double-element generic airfoil with 4 percent Gurney fitted at $\alpha = 0$ deg, $\delta_f = 20$ and 50 deg

$U_\infty = 30$ m/s, which gave Reynolds numbers in the range $R_c = 0.55 - 0.69 \times 10^6$. (The variation in Reynolds number was caused by variations in ambient pressure and temperature.) For all of these tests, transition was not forced on either surface.

All the quoted incidences and setting angles (the latter measured across the pressure surface of the flap, not including the Gurney flap) are measured relative to the $z/c = 0.0$ axis shown in Fig. 1. The force results, measured from the overhead balance, have been corrected to free-air wind-axes coefficients. Incidence corrections derived from the force measurements have also been applied to the incidences in the surface pressure tests, but no other corrections have been made to the measured pressures, nor have any been made to the LDA results.

Uncertainties in force balance readings, data-acquisition system, and incidence settings all contributed to the overall uncertainties in the measurements of C_L and C_D. An uncertainty analysis gives typical uncertainties of ± 0.0087 in the lift-coefficient and ± 0.00078 in the drag coefficient. The surface pressures were measured using a Scanivalve system by averaging 20 samples taken over 0.5 s, and a ZOC system averaging 270 samples taken over 7 s. An uncertainty analysis gives a typical total uncertainty of ± 0.0013 in C_p. Uncertainties in the measurements of the mean velocities are ± 0.002 in $\overline{u}/U_\infty$ and ± 0.006 in $\overline{w}/U_\infty$. The positional accuracy of the LDA traverse is ± 0.1 mm, while the width of the measurement volume is typically 0.3 mm. An inclinometer with a setting accuracy of ± 0.1 deg was used to set the incidence of the wings.

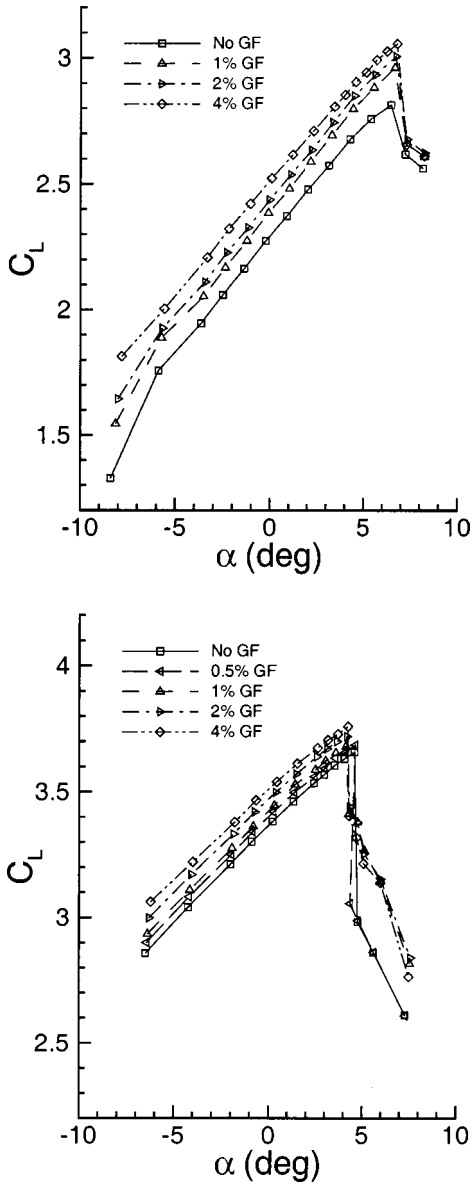

Fig. 2 Forces: C_L versus α. (*a*) $\delta_f = 20$ deg, (*b*) $\delta_f = 50$ deg.

Results

Forces. Figures 2(*a*) and 2(*b*) present C_L versus α curves for the two different flap angles. The Gurney flaps increase C_L for a given incidence-with the smaller devices generating disproportionately large increments in C_L but have only a weak effect on the stalling incidence. These increments in C_L reduce as the flap angle is increased, and are notably lower than those for the two single-element wings tested earlier in the research program.

Drag polars for the double-element wing at the two flap settings are presented in Figs. 3(*a*) and 3(*b*). The Gurney flaps increase the drag coefficient across most of the unstalled C_L range.

Surface Pressures. Figures 4(*a*) and 4(*b*) present typical chordwise loadings at an incidence of $\alpha = 3.0$ degrees for a range of device heights fitted to the flap set at $\delta_f = 20$ degrees and 50 degrees, respectively. The most striking feature of these figures is that the Gurney flaps result in relatively small changes in loading, which are not as distinct as the larger increases found with single-element wings.

Fitting a Gurney flap to the flap results in an overall increase in main-element and flap suctions, with only minor changes in the overall shape. The increases in suction generated by the Gurney flaps at the trailing edge of the main element are relatively small, and although the increments in trailing-edge suction on the flap are more significant, they are still under half those found for the single-element wings.

At the lower flap setting, the trailing-edge camber of the main element generates a large downwash onto the flap, causing the stagnation point for this element to occur on the suction surface. On the pressure surface, this results in a sudden deceleration of the flow just downstream of the flap leading-edge, which, at most incidences and Gurney flap heights, causes the flow to separate. The Gurney flaps do increase the loadings on the flap pressure surface, but these increments are less ordered than found for the suction surface. This is probably caused by the large extent of separated flow on the pressure surface of the flap at this setting angle.

The chordwise distributions for $\delta_f = 50$ degrees indicate that there is a large region of separated flow on the suction surface of the flap, even when no Gurney flap is fitted. Despite this, the Gurney flaps continue to generate small increases in the suctions acting over this surface. The Gurney flaps also increase the loading on the pressure surface of the flap at this angle. When the 4 percent Gurney flap is fitted, the trailing-edge pressure of the flap

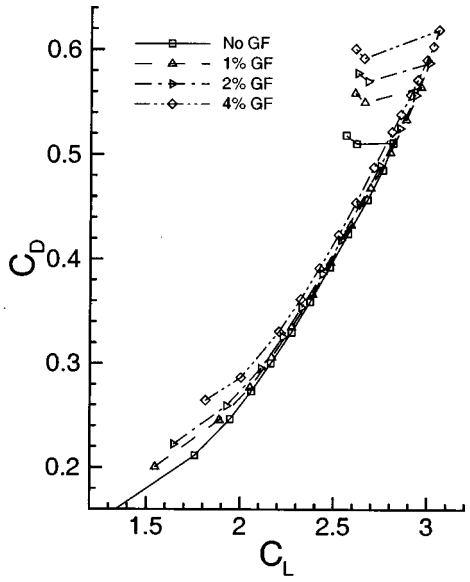

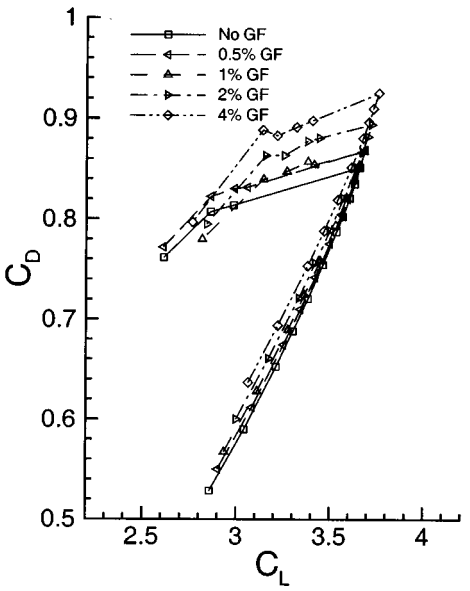

Fig. 3 Forces: C_D versus C_L. (*a*) δ_f=20 deg, (*b*) δ_f=50 deg.

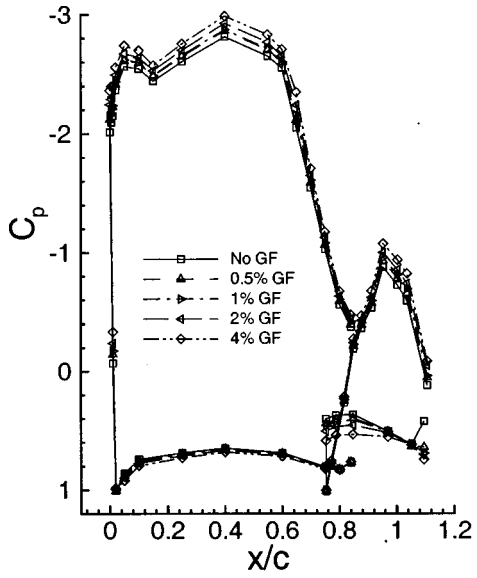

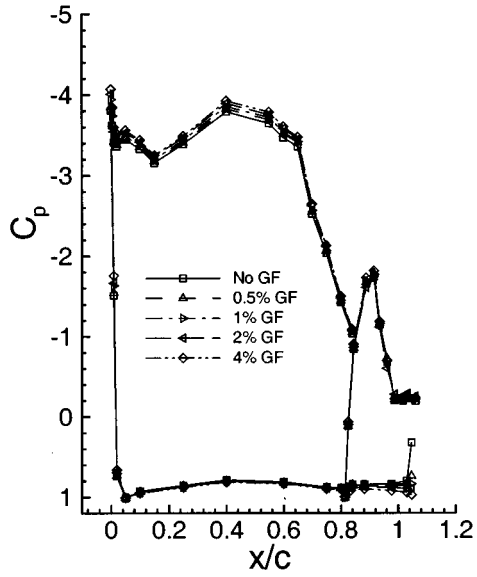

Fig. 4 Chordwise pressure at α=3 deg. (*a*) δ_f=20 deg, (*b*) δ_f =50 deg.

is very close to stagnation across the incidence range. The smaller device heights also increase the trailing-edge pressure, by an amount disproportionate to their height.

LDA Measurements. Typical mean-velocity and turbulent kinetic energy distributions from the LDA surveys are presented in Figs. 5–8, which are for the two flap setting angles, both at $\alpha = -5$ degrees, with and without a 4 percent Gurney flap fitted. These LDA measurements were obtained at the same spanwise station as the surface pressures.

The results have been plotted so that the flap is always in the same position, so the main element position and the incidences of the freestream velocity appear different for the two setting angles. The coordinates have been nondimensionalized such that $x/c = 1$, $z/c = 0$ is at the trailing edge of the flap suction surface. Note that the perturbation velocities were measured in the tunnel axis system, and do not represent the components in the rotated axis system used in Figs. 5 and 7.

The streamline data were produced using the TECPLOT software routines.

20 Degree Flap. Velocity vectors and streamlines near the trailing edge at the lower flap angle for the wing with and without a 4 percent Gurney flap fitted are given in Fig. 5. The clean wing results show that there is no flow separation on the flap upper surface. The same applies to the case with Gurney. The mean velocity vectors and the streamlines show two distinct counter-rotating vortices directly downstream of the Gurney flap, and an off-surface stagnation point where the streamlines bounding the vortex region meet to form the wake. This pattern and the dimensions of this flowfield are very similar to those found for single-element wings.

In the turbulent kinetic energy (TKE) distribution (the normal stress distributions are similar to each other and are therefore not shown), two distinctly high concentrations are observed (Fig. 6). The first high TKE concentration follows the trailing edge of the main element, which is the result of the turbulent boundary layer on the main wing. Fitting a 4 percent Gurney flap introduces another, high TKE concentration downstream of the Gurney flap. This is formed by the flow separating at the trailing edge and around the Gurney flap edge. The highest value occurs near the off-surface stagnation point where the streamlines bounding the

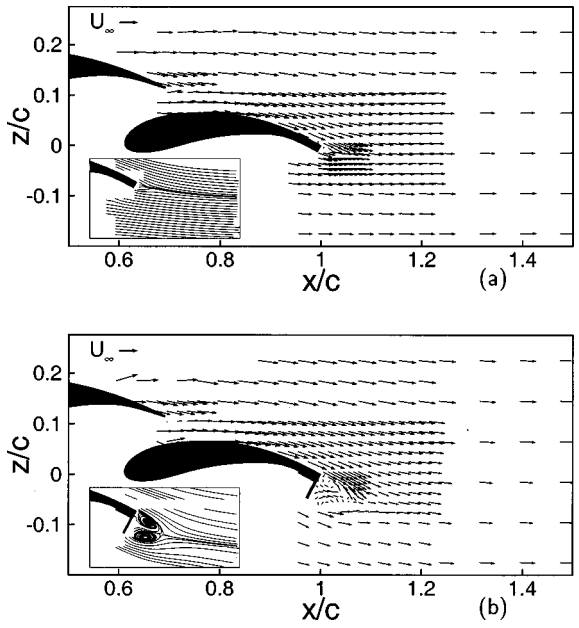

Fig. 5 Mean velocity vectors and streamlines at $\delta_f = 20$ deg and $\alpha = -5$ deg: (*a*) clean wing and (*b*) 4 percent Gurney

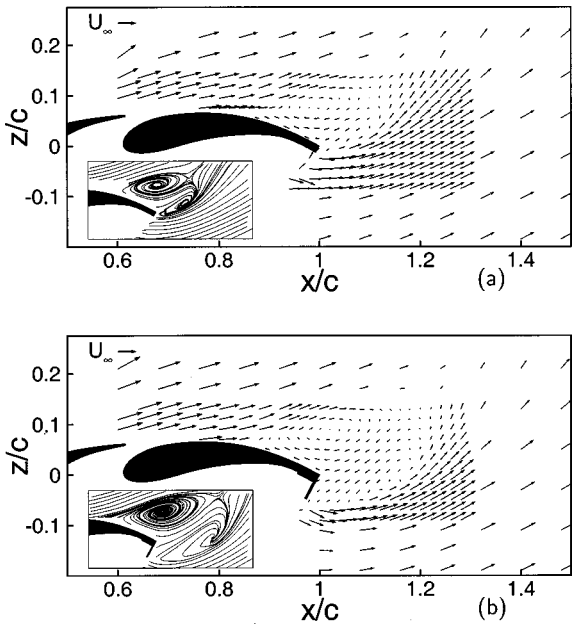

Fig. 7 Mean velocity vectors and streamlines at $\delta_f = 50$ deg and $\alpha = -5$ deg: (*a*) clean wing and (*b*) 4 percent Gurney

vortex region meet to form the turbulent wake flow (see Fig. 5(*b*)). The distribution is broadly similar to that for single-element wings, and is consistent with alternate vortex shedding (Jeffrey et al. [6]). Reducing the height of the Gurney flap has a relatively weak effect on the maximum values of the perturbation velocities.

50 Degree Flap. In Fig. 7, mean velocity vectors and streamlines are presented for the flap set at $\delta_f = 50$ degrees, with and without a 4 percent Gurney flap fitted. The mean velocity vectors reveal a large region of flow reversal over the flap, while the streamlines show that this separated flow forms two counter-rotating vortices, with an off-surface stagnation point. The vortices are formed through separations on the suction surface of the flap and at the edge of the Gurney flap. A similar pattern is also evident when no Gurney flap is fitted: the location of the separation point on the flap surface is relatively unchanged, but the Gurney flap displaces the off-surface stagnation point, and the points of zero velocity in the vortices, and increases the extent of the vortex shed off the pressure surface. The observed vortex flow pattern offers an insight to the effectiveness of the Gurney even with the presence of flow separation on the suction surface. The existence of the single large vortex behind the Gurney flap would still enhance the suction acting on the downstream face of the Gurney flap, and hence at the trailing-edge of the suction surface of the wing.

In the contours of vorticity for the $\delta_f = 50$ degree setting (not shown), the recirculating flow over the flap results in distinct contours of positive and negative vorticity. Fitting a 4 percent Gurney flap has a negligible effect on the maximum values, but does move the concentration of positive contours from the trailing edge of the flap to the off-surface edge of the Gurney flap.

The turbulent kinetic energy (TKE) distribution (Fig. 8) shows two distinctly high concentrations from the flow separation on the flap: one from the suction surface and another from the edge of the Gurney flap. These two high TKE concentrations merge near the off-surface stagnation point (Fig. 7(*b*)) to form the trailing wake flow. The measured maximum normal stresses (Table 1) are smaller than those at $\delta_f = 20$ degree setting. This is caused by the weaker vortex shedding.

Vortex Shedding Frequencies. It has been observed that the time-dependent flow consists of alternative shedding of vortices downstream of the Gurney flap (Jeffrey et al. [6]). The Lomb periodgram method was used to derive the power spectra, as this is specifically designed for randomly-spaced data (Press et al. [7]).

There are no distinct peaks in the power spectra when no device is fitted. In contrast, the spectra for the wings with Gurney flaps fitted have clear single peaks, at periodic frequencies, f_p, that remain broadly constant in a region downstream of the trailing

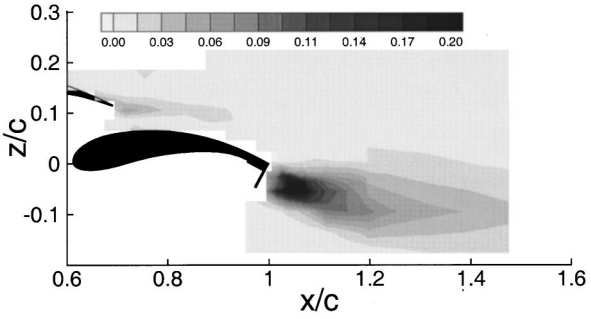

Fig. 6 Turbulent kinetic energy (TKE) distribution at $\delta_f = 20$ deg and $\alpha = -5$ deg, with 4 percent Gurney

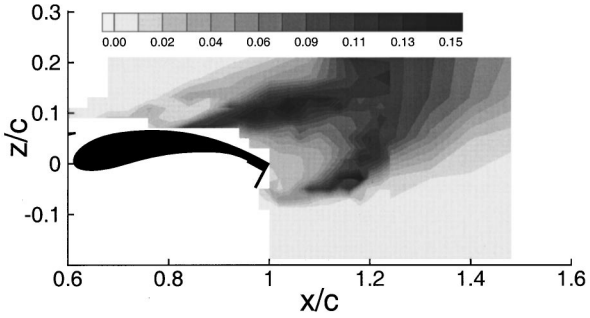

Fig. 8 Turbulent kinetic energy (TKE) distribution at $\delta_f = 50$ deg and $\alpha = -5$ deg, with 4 percent Gurney

Table 1 LDA and spectral data

δ_f (deg)	GF (h/c)	$\zeta c/U_\infty$ Min	$\zeta c/U_\infty$ Max	$\overline{u'^2}$max/ U_∞^2	w'^2max/ U_∞^2	f_p (Hz)	St
20	None	−36.0	+55.6	0.077	0.051	–	–
20	2%	−84.0	+78.5	0.222	0.281	505	0.162
20	4%	−73.4	+59.3	0.203	0.285	305	0.157
50	None	−34.7	+38.0	0.115	0.150	–	–
50	4%	−32.8	+37.0	0.124	0.145	475	0.244

edge. Table 1 lists f_p for the different cases tested, which represents the statistical mode of f_p for the measurement points inside the periodic flow. This table also includes estimates of the Strouhal number, $\mathrm{St}=f_p d/U_\infty$, where d is the base dimension (i.e., measured normal to the $z/c=0.0$ chordline, and including the trailing-edge thickness).

At the lower flap angle, fitting a Gurney flap does introduce a distinct principal frequency, which reduces as the height of the device is increased. These values of f_p yield values of Strouhal number, which at around $\mathrm{St}=0.16$ are broadly consistent with flat plates, which have Strouhal numbers of the order of $\mathrm{St}=0.135$ (Roshko [8]). They also lie within the range $0.13\leqslant \mathrm{St}\leqslant 0.17$ found for 4 percent and 2 percent Gurney flaps fitted to single-element airfoil (Jeffrey [5]).

At the lower flap setting, the region where distinct principal frequencies were observed was quite large, and fanned downstream from the whole extent of the Gurney flap. In contrast, at $\delta_f=50$ degrees this region is much shorter and narrower, and is largely confined to a region downstream of the off surface edge of the Gurney flap, broadly coincident with the time-averaged streamlines that bound the pressure-surface edge of the vortical flow in Fig. 7. The frequency for this region of periodic flow is between the values for the 2 percent and 4 percent Gurney flaps at the lower flap angle.

Discussion of Results

Trailing-Edge Pressure. Results published by Good and Joubert [9] for flat plates immersed perpendicular to a turbulent boundary layer show that the maximum pressure measured upstream of a plate increases with the height of the disturbance, with the smaller plates causing a relatively large increase in pressure. It has already been hypothesized by the authors (Jeffrey et al. [6]) that the upstream face of the Gurney flap acts in a similar manner, with small Gurney flaps giving a disproportionately large increase in pressure.

This is also evident here, in the results at the higher flap setting, where the 0.5 percent Gurney flap gives an increase in pressure at the trailing-edge of the flap from $C_p\approx 0.3$–$C_p\approx 0.7$, while the 4 percent Gurney flap increases the pressure from $C_p\approx 0.3$ to near $C_p\approx 1$. These increases, however, are higher than were observed for the single-element wings. It is hypothesized here that this is because, when attached, the pressure-surface boundary layer on the flap will be much thinner than for the single-element wings. This will increase the height of the Gurney flap relative to the boundary-layer thickness, resulting in increases in trailing-edge pressure.

Effect on Lift. The increases in C_L due to the Gurney flap observed for the lower flap setting are typically half those for the single-element wings. The values of trailing-edge suction show differences of a similar order, so it seems likely that the lower increments in C_L stem directly from the lower values of trailing-edge suction.

The increments in C_L are even less at the higher flap angle. Despite the large increases in trailing-edge pressure, the flow separations mean that the Gurney flaps have only a weak effect on the trailing-edge suction, and this is reflected in the reduced increments in C_L.

Effect on Zero-Lift Drag. When fitted to the flap at the lower angle, the Gurney flaps do not cause consistently higher increments in drag than when fitted to the single-element wings, because of the large region of separated flow on the pressure surface of the flap.

At the higher flap setting, the flow remains attached on the pressure surface of the flap. This means that the boundary layer on this surface is thinner than found in the comparable single-element experiments. As a result, the increments in zero-lift drag are greater than those found for the single-element wings.

Conclusions

The overall effects of a Gurney flap are broadly similar whether it is fitted to a single-element or to the flap of a double-element wing. The Gurney flap introduces a vortex street and the vortex shedding enhances the base suction, but the increments in this can be lower than found for single-element wings, possibly because of an interaction with the wake of the main element. The vortex shedding, and increases in trailing-edge suction, pressure, and lift coefficient, are still observed even after the flow has largely separated from the flap, even though the mean flow patterns are altered.

On the pressure surface, the upstream face of the flap decelerates the flow, in a manner similar to that of a flat plate immersed in a turbulent boundary layer. On a double-element wing with attached flow the boundary layer at the very trailing edge will be thinner than for a single-element wing, and this results in a greater increase in trailing edge pressure, and in zero-lift drag.

The overall increases in circulation are lower than found for single-element wings, and reduce with flap angle. These two trends may partly be caused by the interaction between flap and main element, and partly by flow separations on the flap.

Acknowledgments

The authors would like to thank Penske Cars Ltd, of Poole, Dorset, U.K. for funding this research program.

Nomenclature

b = wing span
c = reference chord
d = base height
C_D = drag coefficient
C_L = lift coefficient
C_p = pressure coefficient
f_p = vortex shedding frequency
GF = Gurney flap
h = Gurney flap height
$\mathrm{R_c}$ = Reynolds number based on c
St = Strouhal number, $f_p d/U_\infty$
SP = pressure surface
SS = suction surface
TKE = normalized turbulent kinetic energy, $1/2(\overline{u'u'}+\overline{v'v'}+\overline{w'w'})/U_\infty^2$
u, v, w = velocity components in x, y, z axes system
U_∞ = freestream velocity
x, y, z = coordinate system: $x+ve$ downstream, $y+ve$ to starboard, $z+ve$ up
α = incidence
δ_f = flap deflection
η = nondimensional span: $\eta=|2y/b|$
ζ = vorticity, $(\partial w/\partial x-\partial u/\partial z)c/U_\infty$

References

[1] Liebeck, R. H., 1978, ''Design of subsonic airfoils for high lift,'' AIAA J. Aircraft, **15**, No. 9, Sept., pp. 547–561.

[2] Papadakis, M., Myose, R. Y., Heron, I., and Johnson, B. L., 1996, ''An experimental investigation of Gurney flaps on a GA(W)-2 airfoil with 25% slotted flap,'' AIAA Paper 96-2418, June.

[3] Papadakis, M., Myose, R. Y., and Matallana, S., 1997, ''An experimental investigation of Gurney flaps on a two element general aviation airfoil,'' AIAA Paper 97-0728, Jan.

[4] Myose, R., Papadakis, M., and Heron, I., 1998, ''Gurney flap experiments on airfoils, wings, and reflection plane model,'' AIAA J. Aircraft, **35**, No. 2, Mar.–Apr., pp. 206–211.

[5] Jeffrey, D., 1998, *An Investigation Into the Aerodynamics of the Gurney Flap*, Ph.D. thesis, University of Southampton, July.

[6] Jeffrey, D., Zhang, X., and Hurst, D. W., 2000, ''Aerodynamics of Gurney flaps on a single-element high-lift wing,'' AIAA J. Aircraft, **37**, No. 2, Mar.–Apr., pp. 295–301.

[7] Press, W., Teukolshy, A. S., Vetterling, W., and Falnnery, B. P., 1992, *Numerical Recipes in FORTRAN*, Vol. 1, Cambridge University Press, pp. 569–577.

[8] Roshko, A., 1954, ''On the drag and shedding frequency of two-dimensional bluff bodies,'' NACA TN 3169, July.

[9] Good, M. C., and Joubert, P. N., 1968, ''The form drag of two-dimensional bluff-plates immersed in turbulent boundary layers,'' J. Fluid Mech., **31**, Part 3, Feb., pp. 547–582.

The Force and Pressure of a Diffuser-Equipped Bluff Body in Ground Effect

Andrea E. Senior
Ph.D student

Xin Zhang[1]
Professor in Aerodynamics

Department of Aeronautics and Astronautics,
School of Engineering Sciences,
University of Southampton,
Southampton SO17 1BJ, United Kingdom

The force and pressure behavior of a generic diffuser in ground effect were investigated. The diffuser model is a bluff body with a rear diffuser at 17 deg to the horizontal, and side-plates. Measurements were conducted in a low speed wind tunnel equipped with a moving ground facility. Techniques employed were force balance, pressure taps, and surface flow visualization. The diffuser flow in ground effect was characterized by vortex flow and three-dimensional flow separation. Four types of force behavior were observed: (a) down-force enhancement at high ride heights characterized by an attached symmetric diffuser flow, (b) maximum down-force at moderate ride heights characterized by a symmetric diffuser flow and separation on the diffuser ramp surface, (c) down-force reduction at low ride heights characterized by an asymmetric diffuser flow and flow separation, and (d) low down-force at very low ride heights, also characterized by an asymmetric diffuser flow and flow separation. The down-force reduction near the ground is attributed to flow separation at the diffuser inlet and subsequent loss of suction in the first half of the diffuser. [DOI: 10.1115/1.1340637]

Introduction

A region of upsweep on the underbody surface of an otherwise symmetrical body gives the body camber, which leads to negative lift (down-force). If the aerodynamic body is placed near a moving ground, a diffuser is formed with additional fluid flow mechanisms, leading to changes in the pressure field. The fluid flow in a diffuser in ground effect represents a complex fluid dynamic problem with features such as flow separation, vortex flow, and flow reversal. An understanding of the major flow physics is important in developing flow control methods and assisting in the development of theoretical and numerical predictive methods. This type of flow is important in the automobile and aeronautical industries, and it has implications in performance and safety.

Current understanding of the diffuser flow in ground effect is limited. There are only a small number of studies published in open literature [1–4]. Sovran [3] suggested that as the diffuser delivers flow to a fixed exit pressure such as the base pressure of a vehicle, its pressure recovery appears as a depression in pressure at the diffuser inlet, the diffuser has ''pumped down'' the underbody pressures below that which would occur on a flat bottomed model, the underbody flow rate increases and the result is a greater down-force. Cooper et al. [4] found that for any one diffuser angle, the down-force exerted on the model increased as the model was lowered from a freestream ride height to near the ground until a maximum was reached. Below this ride height down-force reduced sharply. They surmised that at this critical height the sum of the boundary layer thickness under the body and over the ground became a substantial fraction of the ride height. They also documented a difference in the down-force curves between smaller and larger diffuser angles below a certain ride height, the latter showed a reversal in the consistent trend in down-force seen in all the curves above this ride height. George [1] observed a leeside vortex pair on the upsweep surface of a diffuser which appeared to keep the flow attached to the surface and thus maintain down-force. Streamwise corner vortices are a well known feature of secondary flows in rectangular ducts (see e.g., Brundrett and Barnes [5]). In tests on a venturi-type model George and Donis [2] found that flow entrainment underneath the side-skirts resulted in a separated shear layer from which a vortex pair formed. They observed a loss of down-force and asymmetric diffuser surface patterns with the model skirts sealed to the ground, attributing the phenomenon to the absence of the vortices originating from the skirt edges. At low ride heights an unsteady vertical oscillation of the model led to suspicion of either vortex breakdown inside the diffuser, or an association with a small separated region of fluid found on the ground plane, thought to be a flow away from the ground up toward the model induced by the vortices. Due to the broad nature of the study these findings were not probed further. Furthermore, the observations were made with a fixed ground and should not necessarily be applied to flows with a moving ground, particularly in the force reduction region.

Thus for a given angle, fluid flow in a diffuser appears to operate in several different modes in ground effect. It is also clear that there are still gaps in the current understanding of this important flow, in particular, the major flow physics affecting the down-force reduction. It is by no means clear that boundary layer interaction is the dominant factor.

In the present study an attempt was made to establish the flow features governing the variation in force behavior of the diffuser with proximity to the ground and to investigate the major physics. For this purpose, model tests in wind tunnels were employed. By combining flow visualization with pressure and force measurements, it was possible to give a better explanation of the force reduction phenomenon.

Experimental Arrangement

Tests were conducted in one of the University of Southampton's low speed closed circuit wind tunnels, which has a test section of $2.1\,\mathrm{m}\times1.5\,\mathrm{m}$. The tunnel is equipped with a moving ground 3.5 m in length and 1.5 m in width. The freestream turbulence level in the tunnel is 0.2 percent. Tests were run at a wind and belt speed of 20 m/s and at a Reynolds number of 1.8×10^6. A system is located upstream of the belt (moving ground) for removal of the boundary layer that grows along the floor of the wind tunnel. The boundary layer is sucked away through a slot and a perforated plate. With the boundary layer suction applied, the velocity reaches the freestream value less than 2 mm above the moving ground, corresponding to $h_r/d<0.013$. A more detailed description of the moving belt system can be found in Burgin et al. [6].

[1]Corresponding author.

Contributed by the Fluids Engineering Division for publication in the JOURNAL OF FLUIDS ENGINEERING. Manuscript received by the Fluids Engineering Division April 27, 2000; revised manuscript received October 3, 2000. Associate Editor: K. Zaman.

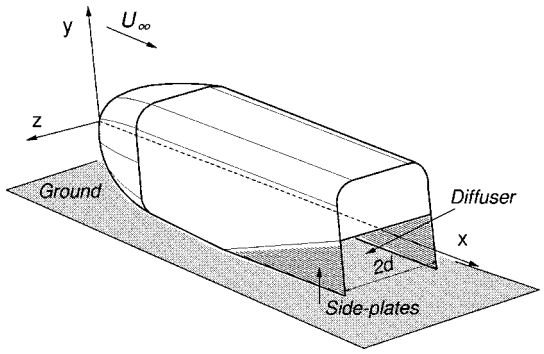

Fig. 1 A perspective view of the model setup

A view of the wind tunnel test model is given in Fig. 1 where a coordinate system is also shown. The model is a bluff body with a rounded nose, a rear diffuser at 17 deg to the horizontal, and side-plates. The diffuser angle has been chosen with a view of controlling flow separation inside the diffuser in later tests. The model is 1.315 m in length, 0.324 m in height, and 0.314 m in width. The diffuser inlet is at $x=0.777$ m. Installation in the tunnel was via adjustable struts allowing the model to be placed over a moving ground plane at heights varying from 0.01 m to 0.199 m above the ground. Transition to turbulent flow on the model was fixed by a wire of 0.4 mm in diameter fastened around the nose at a distance of $x=100$ mm from the nose tip. This ensured that transition occurred at the same location for each test. The model was placed in the middle of the moving ground.

Tests performed include surface hypodermic pressure taps, surface flow visualization, and force balance measurements. The pressure taps were arranged to give the centerline pressures and the spanwise pressures at several stations on the diffuser ramp, along the bottom surface, and over the model base. A total of 111 taps were used. The majority of the taps were connected to a ZOC system, and the remainder to a Scanivalve system. Visualization of the surface flow in and around the diffuser was obtained using an oil streak method with a mixture of titanium dioxide and light oil. The forces, measured from the overhead balance, have been corrected to free-air wind-axes coefficients. The values given have also been corrected for installation tares.

Uncertainties in the measurements taken during each test were evaluated using the procedure described by Moffat [7]. The model ride height was set to an accuracy of ± 0.5 mm. During the test runs no belt-lifting was observed. The yaw angle was set to within ± 0.05 deg. The belt speed was maintained to within 0.25 percent of the wind speed at a wind speed of 20 m/s. In the force balance measurements, 8 runs were made at each ride height, each with 75 samples. The forces were then averaged from these measurements. The uncertainties in C_L and C_D measurements were ± 0.044 and ± 0.014, respectively, for a model ride height of $h_r/d=0.223$. The uncertainty in the surface pressure coefficients was estimated using the above parameters as well as the quoted accuracy of the equipment and aquisition software, and was calculated as ± 0.012 for a C_p of -2.0.

Results and Discussion

Force Enhancement and Reduction Process. The influence of a moving ground is illustrated by the force behavior as the ride height is reduced (see Fig. 2). Also given in the figure are results for the fixed ground and at two other Reynolds numbers. For clarity the fixed ground results are not included in Fig. 2(*b*). It can be observed that the condition of the ground has a large effect on the flow and down-force behavior; both the magnitude and the height for the maximum force are different. Results obtained using a fixed ground cannot be applied to the moving ground study. The Reynolds number is seen to have relatively little effect on the down-force behavior. This will help to explain the physics of the force reduction phenomenon (see later discussion). As expected, the drag coefficient reduces with the Reynolds number.

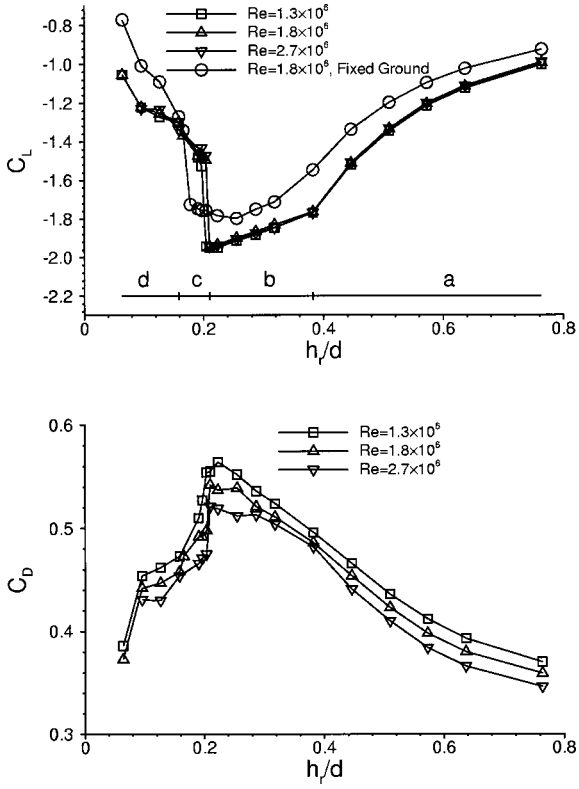

Fig. 2 Force coefficients. (*a*) C_L versus h_r/d; (*b*) C_D versus h_r/d

Based on the force measurements and the surface flow visualization, four distinct regions can be identified: down-force enhancement in *region-a* ($h_r/d \geq 0.382$), maximum down-force in *region-b* ($0.21 \leq h_r/d < 0.382$), down-force reduction in *region-c* ($0.159 \leq h_r/d < 0.21$), and low down-force in *region-d* as the ride height is lowered toward the ground ($h_r/d < 0.159$).

The down-force in the force enhancement region (*region-a*) is relatively weak at $h_r/d=0.764$, increasing smoothly with decreasing ride height until a limiting height of $h_r/d=0.382$. Between these two heights, the magnitude of C_L is increased from -0.993 to -1.763. C_D is also increased from 0.359–0.486. A change in the gradient of the down-force curve occurs around $h_r/d=0.382$, suggesting the introduction of new flow physics due to the proximity of the ground. Between this height ($h_r/d=0.382$) and $h_r/d=0.21$ is the maximum down-force region (*region-b*), highlighted by a ''plateau'' in the down-force versus ride height curve where the gradient of the force curve is reduced, and the flow around the model appears to maintain a constant character. The peak down-force occurs at $h_r/d=0.21$. In this region the drag coefficient continues to rise. The plateau is terminated by a sharp drop in the down-force. In the force reduction region (*region-c*), the down-force coefficient experiences a rapid reduction within a short ride height range, from -1.943 at $h_r/d=0.21$ to -1.297 at $h_r/d=0.159$. In the process the majority of the down-force gain in the force enhancement region is lost. In *region-d* a relatively low down-force level is maintained and the down-force continues to reduce.

The drag force maximum occurs at the same ride height as the maximum down-force, and tends to fall with a similar trend to down-force either side of the limiting height of $h_r/d=0.21$. It should be mentioned here that, while in the force reduction region

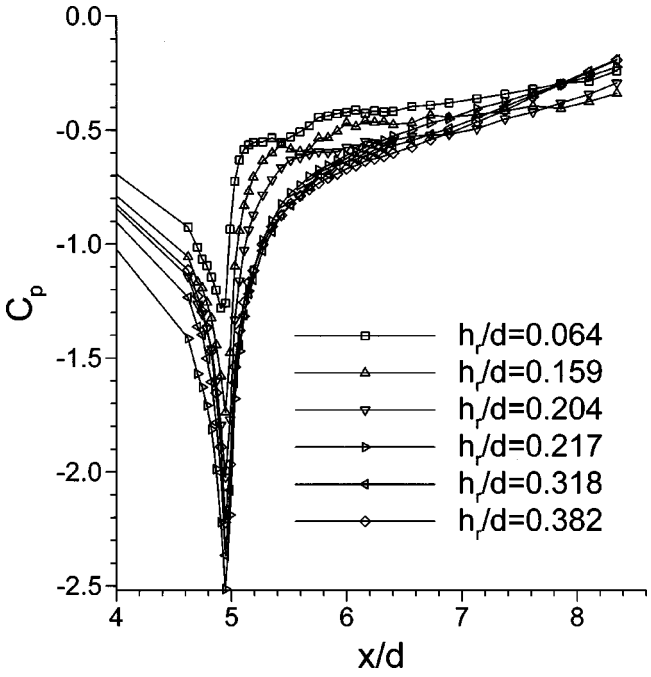

Fig. 3 Surface pressure coefficients underneath the diffuser along the centerline. Diffuser inlet at $x/d=4.95$

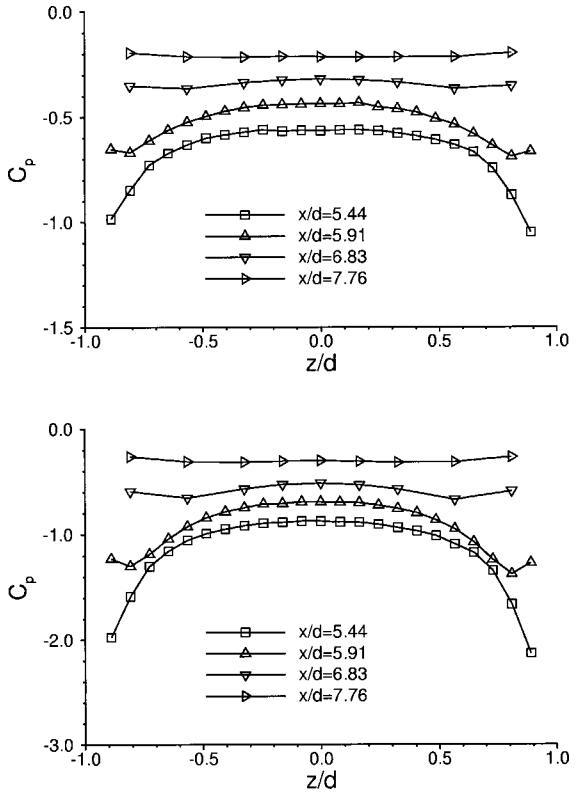

Fig. 4 Spanwise C_p distributions on the diffuser ramp in the force enhancement region. (*a*) $h_r/d=0.764$; (*b*) $h_r/d=0.382$

C_L measurements point to a new flow feature appearing at $h_r/d=0.159$, C_D results show a consistent reduction in value with the ride height reduction.

Surface pressure coefficients underneath the model on the centerline are given at six typical heights in Fig. 3. It can be seen that the flow underneath the model accelerates at all the heights up to the inlet of the diffuser. At all heights the suction peak appears at the inlet. Once the flow enters the diffuser the streamwise pressure distributions on the ramp surface show that the flow encounters an adverse pressure gradient. The behavior and/or ability of the flow in resisting the adverse pressure gradient would define the characteristics of the diffuser flow and ultimately the force characteristics. In Fig. 3 the exit pressure is seen to be slightly negative due to a separated flow behind the diffuser base.

While the suction peak appears at the inlet (Fig. 3), the highest suction peak does not occur at the lowest ride height. The suction level at the inlet is seen to increase as the ride height is reduced in the force reduction region, until the ride height reaches a limiting value of $h_r/d=0.21$ where the highest suction level is observed. As the ride height is reduced further and the flow enters in the force reduction region, the suction level at the inlet decreases. The suction level at the inlet defines the suction upstream of the diffuser as well as in the first part of the diffuser, which sets the overall level of down-force. In Fig. 3 it can be seen that as the flow approaches the diffuser exit, the suction level is higher at the lowest ride heights in the force reduction region (*region-c* in Fig. 2(*a*)) than those in the force enhancement region (*region-a*) and the maximum force region (*region-b*), reversing the trend at the inlet. In later sections this is attributed to the appearance of a single, large streamwise vortex. Below the ride height of $h_r/d=0.21$, C_p distributions in Fig. 3 show signs of flow separation in the first half of the diffuser.

The surface flow visualization (see Figs. 5, 7, and 9 in following sections) revealed that at all ride heights, flow is entrained underneath the model from the sides by the low pressure between the diffuser and the ground. Although there is evidence of slight flow convergence toward the centerline on the surface immediately upstream of the diffuser inlet, the flow appears to be relatively uniform across the span of the model. Flow is also entrained underneath the side-plates. Separation occurs along the plate edges forming streamwise vortices (see also George and Donis [2]).

Force Enhancement. In the force enhancement region (*region-a*), the flow is symmetric about the center-plane ($z=0$) of the diffuser. The symmetric nature of the flow is illustrated in Fig. 4 where the spanwise pressure distributions at four streamwise locations on the diffuser ramp surface at $h_r/d=0.764$ and 0.382 are plotted. The presence of two streamwise vortices is identifiable by points of low pressure near the side-plates. At $h_r/d=0.382$ the peak C_p appears at $x/d=5.44$, $z/d=\pm 0.89$. It is likely the suction peaks could be at $z/d>\pm 0.89$ beyond the position of the last pressure tap. At $x/d=5.91$ the suction peaks occur at $z/d=\pm 0.8$. The influence of the vortices, albeit somewhat weakened, can still be seen at $x/d=6.83$, but is not a feature of the flow on the ramp surface at $x/d=7.76$. At this position, the presence of the vortex pair is no longer apparent, leaving an almost flat pressure distribution across the ramp surface.

Surface flow visualization in *region-a* reveals more of the flow features. In Fig. 5 the surface flow pattern is symmetric about the model center-plane ($z=0$). A small separation region is present across the inlet to the ramp except at the sides. Counter-rotating streamwise vortices are detectable at either side of the ramp in the upper third of the ramp as weak 'S' shaped lines [8]. The spanwise location of the suction peak of each vortex lies close to the point of inflexion of these S-lines. The suction peak can be seen to move slightly toward the diffuser centerline downstream. The curvature of the lines weakens as the flow decelerates to the base of the model. Observation of the surface flow on the side-plates suggests that the vortices actually become detached from the surface. Secondary separations are apparent at the sides of the ramp as indicated by the surface flow. As the ride height is reduced, the S-lines of the surface flow extend much further down the ramp and are more pronounced indicating increased vortex strength.

(a)

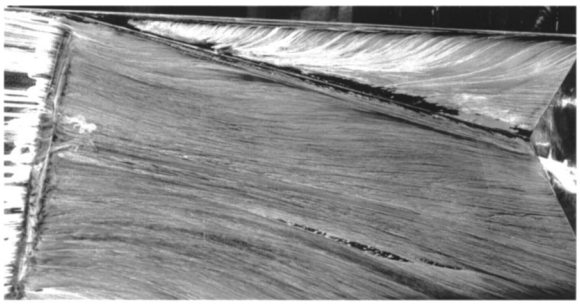

(b)

Fig. 5 Surface flow pattern in the force enhancement region. $h_r/d=0.764$. Flow from left to right. (*a*) Surface flow on the ramp; (*b*) surface flow on the side-plate

Maximum Force. In the down-force enhancement region, the flow is symmetric about the center-plane of the model. This feature of the flow is retained in the maximum force region to a large extent, as indicated by both surface pressure measurements (Fig. 6) and flow visualization (Fig. 7). The defining feature of the flow and the cause of the sudden decrease in the gradient of the down-force curve (Fig. 2(*a*)) in this regime is the flow separation and a separation bubble seen in the center of the diffuser. The main flow features are similar to those found by Morel [9] on base-slant flows.

The flow separation on the ramp surface is also the likely explanation for the difference in the down-force curves between smaller and larger angle diffusers below a certain ride height found by Cooper et al. [4].

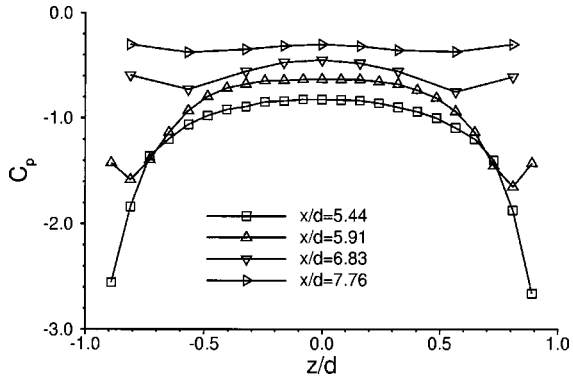

Fig. 6 Spanwise C_p distributions on the diffuser ramp in the maximum force region. $h_r/d=0.217$

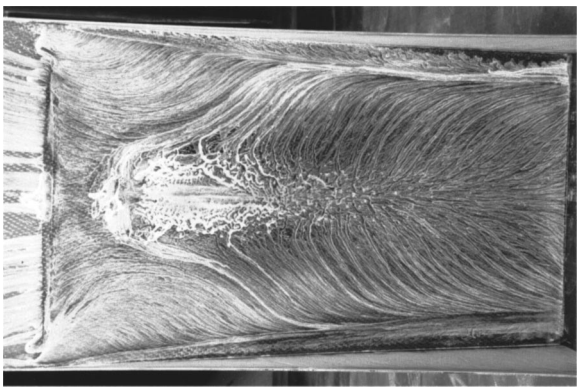

Fig. 7 Surface flow pattern in the maximum force region. $h_r/d=0.217$. Flow from left to right

The first clear sign of the existence of the separation in these tests appears at $h_r/d=0.318$, although the beginning of a separation could be inferred from the surface flow patterns at the end of the ramp at $h_r/d=0.382$. Its presence is governed by the limiting pressure at the diffuser exit and following low pressure in the diffuser. At a ride height typical of the flow in the force enhancement region there is a relatively smaller acceleration beneath the model and under-body flow rates do not increase greatly, thus the suction level remains lower than that in the maximum force region and the pressure gradient between the diffuser inlet and exit remains weaker. Although the flow deceleration and loss of momentum occur immediately downstream of the inlet, the adverse pressure gradient is small enough for the flow to remain attached over the ramp surface. However, as the ride height is reduced, the under-body flow rate increases and the pressure recovery of the diffuser is seen as a stronger suction at the inlet.

The adverse pressure gradient along the diffuser becomes increasingly steep as the ride height is reduced until at a critical height separation occurs, producing a bubble and a primary separation line seen in Fig. 7. With the reducing ride height, the primary separation line moves forward up the ramp as both the down-force and the adverse pressure gradient rise. The separation bubble may be identified in the spanwise pressure distributions of Fig. 6 as a flat constant pressure region between $z/d=0$ and $z/d \approx \pm 0.3$, at $x/d=5.91$. Further downstream the flow seen in the surface flow pattern is dominated by the increasingly enlarged counter-rotating vortices (or a swirling flow), and the central portions of the spanwise distributions accordingly become gentle curves.

From the surface flow it appears that the streamwise primary vortex flow meets the secondary separated flow at junctions either side of the ramp centerline. The primary separation line includes the separation line of the bubble. The line is then seen to run toward the secondary separation line, after which the primary vortex flow is no longer present on the ramp surface. It appears that the vortex has detached from the surface due to the adverse pressure gradient. The flow patterns downstream of the primary separation line are the result of recirculating fluid from the bubble re-attaching to the diffuser surface and then being entrained outboard towards the low pressure associated with the presence of the near-surface primary vortices.

The spanwise pressure distributions across the diffuser at these heights exhibit similar characteristics, the pressures staying almost the same at ride heights between $h_r/d=0.217$ and 0.318 over the majority of the ramp. The down-force increase is created by the higher levels of suction experienced at the inlet, and at the sides of the diffuser where the maximum suction on the model occurs due to the streamwise vortices attached to the surface. At $h_r/d=0.318$, the peak C_p at is -2.332 at $x/d=5.44$, $z/d=\pm 0.89$, reducing to -1.282 at $x/d=5.91$. At $h_r/d=0.217$, the value is

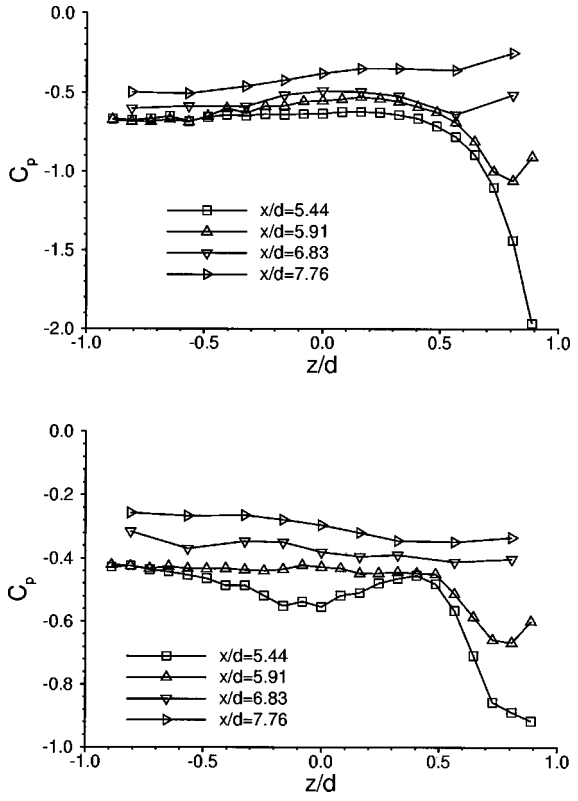

Fig. 8 Spanwise C_L distributions on the diffuser ramp in the force reduction region. (*a*) $h_r/d=0.191$; (*b*) $h_r/d=0.064$

-2.66 at $x/d=5.44$, reducing to -1.429 at $x/d=5.91$. The increase in suction is reflected in the increased curvature of the surface flow, the curvature being greatest at $h_r/d=0.21$.

Force Reduction and Low Down-Force. The maximum down-force occurs between $h_r/d=0.21$ and 0.217. During the model tests it was found that the height at which the maximum down-force occurred varied between these two heights. The switch between the maximum down-force and the onset of the loss of down-force appeared in a random fashion, and on occasion the flow switched between a *region-b* flow (maximum force) and a *region-c* flow (force reduction) between wind tunnel runs without apparent variations in model settings.

Figure 8 gives surface pressures on the diffuser surface typical of flows in the force reduction region (*region-c*) and the low force region (*region-d*). On the down-force curve, the two regions are not clearly marked. However, there is a discernible difference in the slope of the curve. Figure 8(*a*) was taken at $h_r/d=0.191$, and shows the flow in a region where the down-force experiences a rapid reduction. Figure 8(*b*) gives spanwise pressures at $h_r/d=0.064$. The loss of down-force is accompanied by the appearance of an asymmetric flow in the diffuser. The flow is now separated at the inlet on one side. The separation bubble has collapsed and the primary separation line is now difficult to identify from the surface flow visualization (see Fig. 9). In Fig. 9, the surface flow is no longer symmetric about the diffuser center-plane. Instead, it runs from the bottom left corner of the ramp diagonally towards the center-plane, where the separation causes the detachment of the vortex on the top side as in the maximum force region. Although the top side vortex rolls up as normal, the bottom side flow has begun to reverse back up the ramp, indicating a separated flow and the collapse of the vortex at this side of the diffuser.

The asymmetry of the flow is unlikely to be caused by errors in setting the model height. Its appearance occurs at random, during

Fig. 9 Surface flow pattern in the force reduction region. $h_r/d=0.191$. Flow from left to right

pressure measurement tests a switching of the side of the reverse flow was observed. The distribution seen in Figs. 8(*a*) and 8(*b*) was reversed at $h_r/d=0.204$. The causes could be a slight deviation in aligning the model to zero yaw angle, and/or slight imperfections in the model surface as found by researchers in slender body and missile aerodynamics. The occurrence of stall phenomenon in the flow region is in close agreement with the transitory stall behavior found by Kline and his co-workers (see Reneau et al. [10]) in 2D diffusers close to the conditions of maximum pressure recovery, as is the case here, and is an inherently unsteady flow. The flow in *regions c* and *d* may well also be unsteady.

In *region-c*, as the model is lowered to the ground, the suction at the inlet increases, leading to flow entrainment from both sides of the model. The boundary layer on the surface underneath of the model is three-dimensional (3D) in nature. The 3D effect is increased as the ride height is reduced. Another factor in determining the diffuser flow is the boundary layer approaching the inlet, the thickness of which is 15 mm($0.096\,d$) just before the inlet when the model is in freestream. Although it will not create a ''blockage'' effect at a height in the maximum force region, it does enhance the suction at the inlet as the effective ride height is reduced, leading to a high adverse pressure gradient in the diffuser. At a limiting height ($h_r/d=0.21$ for the present flow), separation finally occurs at the inlet instead of on the diffuser ramp surface. The asymmetric nature of the 3D boundary layer separation produces the apparent collapse of one of the counter-rotating vortices.

The asymmetry found with skirts sealed to a *fixed ground* by George and Donis [2] was attributed to the absence of the vortices, however it seems possible that as in these tests, the pressure gradient over the diffuser surface was too large to be contained by a separation bubble, thus the separation occurred at the inlet.

The above observation of the force reduction phenomenon is at variance with the assertion that boundary layer merging was the cause of the force reduction phenomenon. Support for this argument comes from down-force curves plotted at various freestream Reynolds numbers shown in Fig. 2(*a*). Down-force characteristics are very similar for each curve. At Re numbers of 1.8×10^6 and 2.7×10^6 the maximum down-force occurs at the same ride height, while at $\mathrm{Re}=1.3\times10^6$ it occurs at a slightly lower ride height (a difference of 1 mm). The boundary layer thickness at a lower Re is expected to be larger than that at a higher Re. If the maximum down-force and the subsequent stall depended upon a blockage at the inlet of the diffuser, as a result of merging of the boundary layers, stall at a lower Re would be expected to occur at a higher ride height.

The boundary layer merging is more likely to be the dominant feature of the flow in *region-d*. In this region, the down-force maintains a low level, being relatively insensitive to the ride

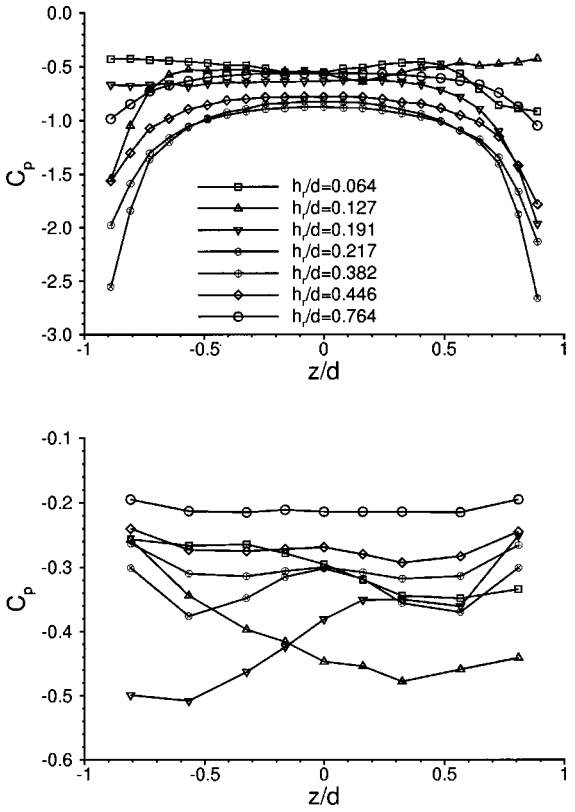

Fig. 10 Spanwise pressure distribution on the diffuser ramp. (*a*) $x/d=5.44$; (*b*) $x/d=7.86$

height change. The size of the boundary layer ($O(0.096d)$) suggests a merging of boundary layers on the model and the ground is likely to lead to a reduction in the flow entering the diffuser, hence the low level of down-force in this region. The basic flow features, though, remain similar to those in *region-c*. In Fig. 2, the down-force level and drag at the lowest ride height ($h_r/d=0.064$) show a further reduction. From the surface pressure measurement (Fig. 3) and flow visualization (not included), it can be surmised that, at this height, the flow entrainment in front of the diffuser inlet is reduced substantially, leading to the very low levels of down-force and drag.

Further Discussions. The mean flow behavior exhibits different characteristics in the four main flow regimes over the ride heights tested. For flows in the force enhancement region, surface flow visualization and pressure measurements suggest that a major part of the down-force is produced across the diffuser inlet due to the ''diffuser pumping'' [3] and near the sides of the diffuser where the additional suction is created by the streamwise vortices near the diffuser surface. This feature of the flow can be seen in the surface pressure distributions (e.g., Figs. 4 and 10(*a*)). With the suction peak at a fixed ride height occurring at the inlet of the diffuser, the suction level in the first part of the diffuser is constrained by the suction peak and varies accordingly, which contributes to a large part of the overall down-force.

At a critical height near to the ground the pressure gradient between the diffuser inlet and the fixed exit pressure becomes too large to prevent the 3D boundary layer separation on the ramp surface inside the diffuser and the vortex detachment from the surface. Even so, in the maximum down-force region, down-force increases in the presence of the separated flow as h_r is reduced. Although the region of separated flow inside the diffuser becomes larger, the under-body pressures become increasingly negative in localized areas of the diffuser before the vortex pair detach from the surface. This is sufficient to continue the generation of an overall, larger down-force on the model.

The increase in down-force is terminated at very low model ride heights when the 3D flow separation occurs at the inlet. This 3D flow separation is asymmetric, leading to the apparent collapse of one of the counter-rotating vortices. As a result the suction level at the inlet is reduced. Although the large single vortex still generates a high suction level near the diffuser exit as seen in Fig. 10(*b*), the overall down-force is reduced.

Conclusion

A study of a generic diffuser-equipped bluff body in ground effect was performed, using correct ground conditions. The study established the major flow features and provided an insight into the flow physics, particularly the force reduction phenomenon at low ride heights. Four flow regions were identified.

Based on the results discussed, the following conclusions can be drawn:

1 In the force enhancement region, the diffuser flow is characterized by a pair of counter-rotating streamwise vortices formed from separation at the edges of the side-plates. The diffuser flow remains attached to the ramp of the diffuser. The vortices detach from the surface towards the exit of the diffuser due to flow deceleration and adverse pressure gradient.

2 In the maximum force region, flow separates on the ramp of the diffuser. However, the flow remains symmetric about the center-plane of the diffuser, and the suction level at the diffuser inlet continues to rise as the ride height is reduced, leading to a high down-force level.

3 Increasing down-force is terminated at a critical ride height due to 3D flow separation at the diffuser inlet, leading to the apparent collapse of one of the counter-rotating vortices and asymmetric flow in the diffuser.

4 At lower ride heights still, a low level of down-force exists, which could be indicative of a boundary layer blockage at the diffuser inlet at very low ride heights.

5 Correct ground conditions should be used in investigating the force behavior in the proximity of ground, in particular the force reduction phenomenon.

Certain issues were not covered by the present study, but nevertheless could be important. For example, the diffuser flow is likely to be unsteady as one of the two large counter-rotating vortices collapses (or a flow reversal occurs). If the flow is indeed unsteady then the flow physics would be of both fundamental and practical importance.

Acknowledgments

Andrea Senior wishes to thank British American Racing for providing a scholarship, and the authors would like to thank Willem Toet and Professor G. M. Lilley for their advice and suggestions.

Nomenclature

C_D = drag coefficient, $D/q_\infty S$
C_L = down-force (lift) coefficient, $L/q_\infty S$
C_p = pressure coefficient, p/q_∞
d = model half width
D = drag
h = model height
h_r = ride height (ground clearance)
l = model length
L = down-force (lift)
p = pressure
q_∞ = dynamic head, $\rho_\infty U_\infty^2/2$
Re = Reynolds number, $\rho U_\infty l/\mu$
S = frontal area of the model

U_∞ = freestream flow speed
x, y, z = cartesian coordinates: x + ve downstream, y + ve up, z + ve to starboard
μ = viscosity
ρ_∞ = freestream air density

References

[1] George, A., 1981, ''Aerodynamic effects of shape, camber, pitch and ground proximity on idealized ground-vehicle shapes,'' ASME J. Fluids Eng., **103**, Dec., pp. 631–638.

[2] George, A., and Donis, J., 1983, ''Flow patterns, pressures, and forces on the underside of idealized ground effect vehicles,'' *Proceedings of the ASME Fluids Engineering Division Symposium on Aerodynamics of Transportation-II*, Vol. 7, Dec., pp. 69–79.

[3] Sovran, G., 1994, ''The kinematic and fluid-mechanic boundary conditions in underbody flow simulation,'' *Proceedings of the CNR-Pininfarina Workshop on Wind Tunnel Simulation of Ground Effect*, Turin, Italy, May.

[4] Cooper, K., Bertenyi, T., Dutil, G., Syms, J., and Sovran, G., 1998, ''The aerodynamic performance of automotive underbody diffusers,'' SAE Paper 98-0030, Jan.

[5] Brundrett, E., and Baines, W., 1964, ''The production and diffusion of vorticity in duct flow,'' J. Fluid Mech., **19**, pp. 375–394.

[6] Burgin, K., Adey, P. C., and Beatham, J. P., 1986, ''Wind tunnel tests on road vehicle models using a moving belt simulation of ground effect,'' J. Wind. Eng. Ind. Aerodyn., **22**, pp. 227–236.

[7] Moffat, R., 1988, ''Describing the uncertainties in experimental results,'' Exp. Therm. Fluid Sci., **1**, pp. 3–17.

[8] Maltby, R., and Keating, R., 1962, ''Flow visualization in wind tunnels using indicators,'' AGARDDoraph, Apr. pp. 29–38.

[9] Morel, T., 1978, ''The effect of base slant on the flow pattern and drag of three-dimensional bodies with blunt ends,'' *Aerodynamic Drag Mechanisms of Bluff Bodies and Road Vehicles*, Plenum Press, New York, pp. 191–226.

[10] Reneau, L., Johnston, J., and Kline, S., 1967, ''Performance and design of straight two-dimensional diffuser,'' ASME J. Basic Eng., **89**, pp. 141–150.

Near Wall Measurements for a Turbulent Impinging Slot Jet

(Data Bank Contribution)[1]

Jiang Zhe
Graduate Research Assistant

Vijay Modi
Associate Professor

Department of Mechanical Engineering,
Columbia University,
New York, NY 10027

The velocity field in the vicinity of a target surface with a turbulent slot jet impinging normally on it is examined. The impingement region is confined by means of a confinement plate that is flush with the slot and parallel to the impingement plate. The distance H of the impingement wall from the slot is varied from 2 to 9.2 slot widths. Jet Reynolds numbers (based on slot width B) of 10,000–30,000 are considered. Mean velocity and root mean square velocity measurements are carried out using hot-wire anemometry. A boundary layer probe is utilized in order to obtain measurements at a wall distance as close as 110 microns (0.0028B). This corresponds to a distance of approximately $y^+ \sim 2-4$ *in wall units and is found to be adequate in order to permit an estimate of wall shear under most conditions. The problems of hot wire interference with the wall and calibration at low velocities are solved by calibrating the probe in a known Blasius flow. With the exception of the stagnation region where shear could not be evaluated, it is found that velocity profiles follow a linear behavior in the viscous sublayer everywhere along the wall. Results indicate that the peak in normal stress occurs at* $y/B \sim 0.025$ *to 0.04 at a distance six to eight jet widths away from the jet-axis.*
[DOI: 10.1115/1.1343085]

Keywords: Slot-Jet Impingement, Turbulence, Fluid-Flow Measurement, Friction Coefficient

Introduction

Impinging jets are widely used in materials processing, manufacturing and electrochemical deposition because of their high heat and mass transfer rates. This has led to numerous studies of heat transfer characteristics in jet impingement systems [1]. Webb and Ma [2] presented a detailed review of the experimental studies on heat transfer of single-phase liquid jet impingement. Studies that examine the flow field experimentally are however few despite the obvious importance of the flow field to heat transfer. In particular, the shear at the impingement wall has been rarely measured. Velocity field as well as shear data in these systems are also useful because of the increasing reliance on computational fluid dynamics for predicting heat and mass transfer in turbulent flows. In impingement flows where flow curvature, separation and stagnation are common features, experimental data are particular important to establish validity of the turbulence models and associated wall functions. The validation of flow field and shear can allow the analyst to uncouple the effects of flow modeling approximations from those of scalar transport approximations. Many physical processes require the knowledge of shear, either indirectly because of its relevance to heat and mass transfer or directly for its relevance to forces exerted on a wall or particle removal from a wall.

Direct measurement of the local wall shear force is difficult because of the low level of shear involved. For a system with a jet width of O(1 cm) if a spatial resolution of 1 mm is desired, one would require an ability to measure a force of 0.1 μNewtons on a 1 mm by 1 mm plate for Reynolds numbers of $O(10^4)$. Hot-film sensors flush mounted on the wall or mass transfer sensors have been employed to estimate wall shear. This approach, however, relies on a prior knowledge of the relationship between mass/heat transfer and shear, something that is not always available except in boundary layer flows.

Alternatively, one could deduce shear from a near wall velocity measurement using a hot-wire, provided this measurement is made within the viscous sublayer. Such a measurement is however difficult for several reasons. The difficulties are: (i) hot-wire interference with the wall, (ii) measurement of the distance of the hot-wire from the wall, (iii) calibration of the hot-wire at low velocities, and (iv) corruption of wire data with a nondominant velocity component. In the present paper, we have overcome the first three of the difficulties allowing shear measurement in a region where the fourth effect is small.

Structure of the Flow Field

The flow regions associated with the discharge of a gas jet (into otherwise stagnant surroundings) that impinges on a target surface are shown in Fig. 1. One of the applications where this geometry is of particular interest is electrochemical deposition using fountain platers, where the knowledge of shear on the impingement wall is important to the understanding of mass transfer. These reactors are usually enclosed systems and the present location of the confinement wall is a simple means to achieve this enclosure without introducing additional geometrical parameters. Immediately after discharge from the slot, the jet behaves as a free jet, until the flow is influenced by the target surface. Within the free jet is a potential core where the velocity is uniform and equal to the exit velocity. The length of the potential core can be quantified by the distance from the slot, $(H-y)/B$, where the jet velocity diminishes to 95% of the exit velocity and, for a slot jet, this length is between 4.7–7.7, depending on the slot conditions [1]. Downstream of the potential core region, the jet behaves as a free jet and spreads while the peak axial velocity decreases with increasing distance from the slot. If H/B is larger than this distance, this behavior continues until the flow is influenced by the target surface. In this region, called the stagnation region, the flow decelerates sharply in the direction along the jet axis while accelerating in the x-direction. Acceleration in the x-direction cannot

[1]Data have been deposited to the JFE Data Bank. To access the file for this paper, see instructions on p. 171 of this issue.

Contributed by the Fluids Engineering Division for publication in the JOURNAL OF FLUIDS ENGINEERING. Manuscript received by the Fluids Engineering Division May 26, 2000; revised manuscript received November 17, 2000. Associate Editor: K. Zaman.

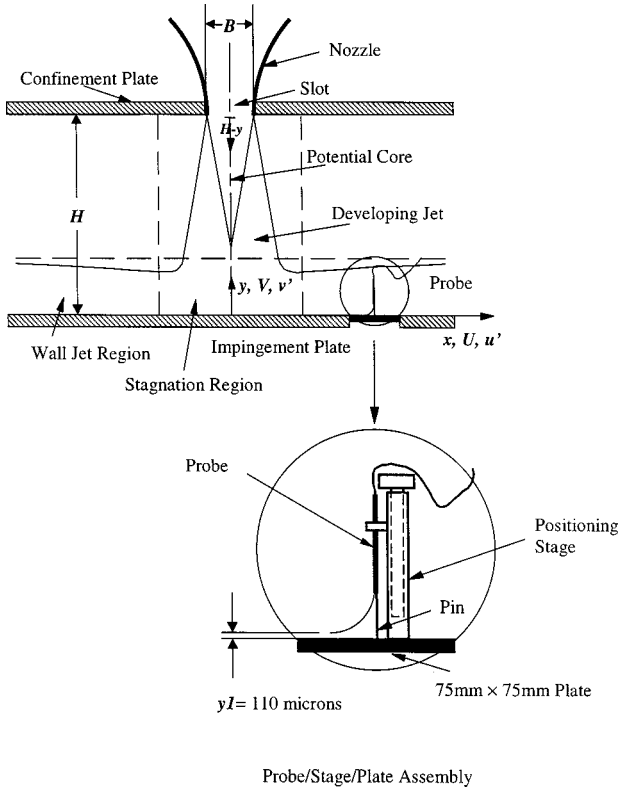

Fig. 1 Impinging slot jet configuration and hot wire probe with probe/stage/plate assembly

continue since the flow entrains low-momentum fluid from the ambient. Further downstream the flow behavior is similar to that of a wall jet, with deceleration of the bulk velocity and spreading in the y-direction [1].

Literature Review

The literature relevant to the present study can be classified as experimental or numerical. Numerical studies that address heat or mass transfer do need to compute fluid flow as well and hence frequently report the skin friction coefficient on the wall. Experimental studies that measure heat or mass transfer rates at the wall in impingement systems normally do not provide velocity or shear data. There are very few studies that measure fluid flow in a confined slot jet impingement system. The numerical studies are reviewed first, followed by experimental studies of heat/mass transfer and fluid flow.

Numerical/Theoretical. Behnia et al. [3,4] applied the k-ε-v^2 (where v^2 might be regarded as the velocity fluctuation normal to the streamlines) model to unconfined and confined circular jets impinging on a plane wall. They showed that the model captured Reynolds number effects. The importance of near-wall modeling was addressed. The comparisons were however largely to surface heat transfer since they note there is paucity of flow field data. Craft et al. [5] examined four different turbulence models for the numerical prediction of the circular turbulent impinging jets measured by Cooper et al. [6]. These models consisted of one k-ε model and three second-moment closure based models. The numerical predictions, obtained with an extended version of the finite-volume TEAM code indicate that the k-ε model and a widely used Reynolds stress model (Gibson and Launder [7]) led to too large levels of turbulence near the stagnation point. Two second-moment closures tailored to impingement flow did much better in predicting the flow field characteristics. None of the schemes is entirely successful in predicting the effect of Reynolds number. The stagnation point anomaly was addressed by Durbin [8]. A mathematical bound on the turbulent time-scale was derived. Some other studies that carried out two-equation modeling with limited success are those of: Dianat et al. [9] with a standard k-ε turbulence model; Heyerichs and Pollard [10] with a k-ω model of Wilcox [11] and several versions of k-ε models; and Chen and Modi [12], who also employ a k-ω model but in addition compute high-Schmidt number mass transfer.

Experimental. Hot-wire velocity field measurements were reported by Cooper et al. [7] for an unconfined turbulent circular jet impinging orthogonally onto a large plane surface. They examined jet Reynolds numbers of 23,000 and 70,000 for slot heights above the plate ranging from two to eight diameters. They measured mean velocity and root mean square velocity in the vicinity of the plate surface. While the data point closest to the wall is at a distance of 130 microns ($y/D=0.005$ where D is the jet diameter), it is not clear whether their hot-wire data have been corrected for near wall effects even though the ratio of wall distance to wire diameter is 26. The same problem exists with the recent work of Ashforth-Frost et al. [13] where the ratio of wall distance to wire diameter is 20. The wall material used in their experiments is 10 mm thick Perspex. They report measurements of velocity and turbulence characteristics in an identical geometry as in the present study at a single jet Reynolds number of 20,000 and two H/B ratios of 4 and 9.2. In the velocity range of 1 to 3 m/s typical of their first point away from the wall, failure to correct the hot-wire data for wall interference could lead to erroneous measurements. In the current study mean and root mean square velocity measurements near the wall are carried out over a wide H/B range (2–9.2) for Reynolds numbers of 10,000–30,000.

Experimental Apparatus

Setup. The exit section of a small wind tunnel was modified to produce a slot jet. Air supplied from a centrifugal fan driven by a 2 H.P. motor passes through a flow-straightening honeycomb section followed by a two-stage diffusion section that expands the flow cross-section to 600 mm×600 mm without flow separation, followed by several fine wire meshes and a long settling chamber. A contraction with a ratio of 6:1 designed to keep boundary layer growth to a minimum leads the flow to the slot where a uniform y-direction normalized root mean square velocity of 0.9 percent is observed.

The slot jet width B was 40 mm in the experimental setup. The slot jet width in most practical applications is much smaller, but the scale up in the present experiment ensures that the data point nearest to the wall is sufficiently within the viscous sublayer. The slot jet dimension in the z-direction was six times the slot width extending in either direction to $z/B=\pm 3$. The confinement and impingement plates extend in the z direction to $z/B=\pm 4$ and in the x direction to $x/B=\pm 13$. Both the confinement and the impingement plates were made of polymethyl methacrylate or PMMA. The confinement plate is integrated with the nozzle so that it is flush with the slot and parallel to the impingement plate. The distance between the confinement and the impingement plates was designed to permit H/B to be varied from 2–13. All experimental data reported in the present paper are obtained at the $z=0$ plane. Two experiments were carried out to ensure that the effects of three-dimensionality are absent. The first experiment ensured that the measurements at the slot jet exit as well as on the impingement plate did not vary with z within $z/B=\pm 2$. The second experiment was carried out to determine whether fluid leaving the flow domain from the open boundaries at $z/B=\pm 4$ altered the near-wall measurements. Additional confinement plates were placed at $z/B=\pm 4$ to close off the otherwise open boundaries. Measurements made at $z=0$ with this modification did not show any significant differences. Hence the results reported in the present study can be considered to be representative of a two-dimensional slot jet flow. The measurements reported in this paper

(with the exception of those needed to qualify the jet conditions) were carried out in the $z=0$ plane in the region defined by $x/B = \pm 13$ and $y/B=0$ to 0.35.

Instrumentation. Velocity was measured with a TSI 1051-2 constant temperature hot wire anemometer and a TSI 1218AF-T1.5 hot wire boundary layer probe designed for near wall measurements. The hot wire is 1.27 mm long with a diameter of 3.8 microns. The probe was attached using a rigid aluminum rod (so that the rod is downstream of the flow) to a DAEDAL-3900 precision ball bearing positioning stage. The stage permitted control of position in the y-direction with a resolution of 5 μm (see Fig. 1). The positioning stage was in turn attached to a small 75 mm by 75 mm polished aluminum plate that was flush mounted to the impingement plate with care to ensure that the flow was not disturbed. The entire probe/stage/plate assembly permits the distance from the probe to the wall to be maintained constant during three different events: during measurement of the distance between the probe and the wall, during calibration of the probe and during actual measurement. When this assembly is used for actual measurements, its position relative to the jet could be varied, to permit measurements at several locations along the x-direction.

The uncertainty in the location of the first wire position away from the wall is of critical importance to the determination of shear. This measurement is also important because all other wire position measurements are referenced to this distance. In order to ensure an accurate estimate of this distance, a CCD camera with a magnification ratio of 800 was used to measure the distance from the wall. The uncertainty in this measurement was 10 μm, with a 95% confidence level. For the wire position nearest to the wall where the nominal distance is 110 μm, this corresponds to an uncertainty of 9%.

A pitot tube and a Datametrics (Model 1173) Barocel electronic manometer were employed for the determination of the free stream velocity in the calibration procedures described below. A separate experiment carried out to test the linearity of the electronic manometer with the use of a conventional micromanometer confirmed that the electronic manometer demonstrated linear behavior over the pressure range of interest. A 12-bit MetraByte DAS-8PGA board with 2.44 mV resolution interfaced to a personal computer was used for data acquisition.

Calibration of the Hot Wire. The conventional means of hot-wire calibration is to place the wire in a free stream where a uniform velocity profile exists and measure the velocity by a reliable alternate means such as a pitot tube. Such a calibration is however inappropriate in the present study. First, at the distances from the wall at which we wish to carry out the measurements (nearest to the wall being 110 μm), hot-wire interference with the wall may alter the response from that in a free stream. Second, it is difficult to calibrate a hot-wire at low velocities of interest here. The effect of wall interference on the hot-wire response has been examined by several investigators such as Wills [14], Collis and Williams [15], Lange et al. [16], Durst et al. [17], Bhatia et al. [18]. These studies addressed the determination of the correction due to the wall by means of numerical, analytical or experimental techniques. There is no clear agreement among the studies, however, on the means to correct the hot-wire response for wall interference. In the present study, a technique was adopted that bypassed the need to apply a correction based on an experimental correlation or numerical analysis. The wire calibration in the present study was carried out in the exact same position as in the actual measurements. Moreover, as pointed out by Bhatia et al. [18], wire interference also depends upon the wall material. In the present study, the wire calibration was carried out with the same probe/stage/plate assembly ensuring that the wall material in the vicinity of the wire is the same during the calibration and the actual measurements. Further details of the procedures adopted are given below.

A separate calibration was carried out at each probe distance away from the wall. This calibration procedure is described next. The probe/stage/plate assembly with a finely polished leading edge attached flush to the plate (see Fig. 2) was placed in a free-stream to create a laminar boundary layer flow over a flat plate with a zero pressure gradient. The leading edge is also made of aluminum. The maximum Reynolds number based on the distance from the leading edge is 24,000 ensuring a laminar flow over a flat plate resulting in a boundary layer flow with a Blasius velocity profile. The variation of the streamwise velocity with distance from the wall in such a flow is known analytically. Thus from a manometric measurement of the free stream velocity, the velocity within the boundary layer at any known distance from the wall can be established. This permits the hot wire to be calibrated at much lower velocities than would be possible if both the wire and the pitot tube were in the free stream flow. More important, however, is the ability to account for the wall interference effect using such an approach.

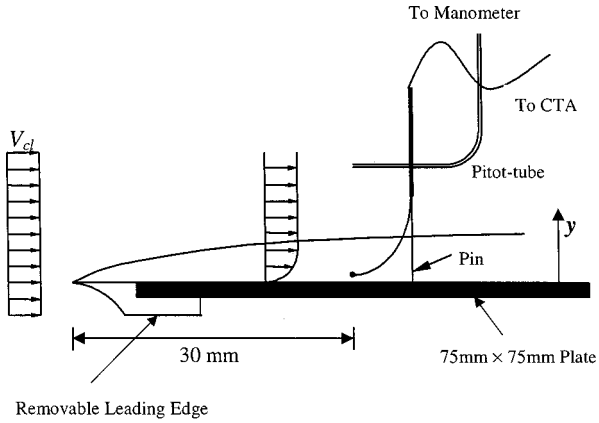

Fig. 2 Configuration during calibration of the probe/stage/plate assembly along with a removable leading edge

During a single calibration run for a fixed position of the probe from the wall, the free stream velocity was altered and at least 8 data points within the expected range of velocities were acquired. A least-square curve was fitted to the voltage-velocity data using King's law (Goldstein [19]). This calibration procedure was repeated for each position of the hot-wire away from the wall, since the wall interference effect depends upon the wire distance from the wall. The calibration was redone after obtaining the measurements to ensure that the results were not significantly different. A new calibration was also done if a new series of experiments were carried out 8 hours after the original calibration. This procedure, in principle, is similar to that of Khoo et al. [20] even though the flow they utilize for calibration was laminar channel flow.

Mean and root mean square velocities were evaluated from 5,000 samples gathered at 1000 samples per second. The mean velocity recorded by a single hot-wire probe with the wire oriented along the z-direction is $q=(U^2+V^2)^{0.5}$. Near the wall, this quantity is however very nearly equal to U, the mean velocity being parallel to the impingement plate except at $-1 \leqslant x/B \leqslant 1$. Hence except in this region, the measured values of q are utilized to determine wall shear.

Experiment Flow Conditions. The near-wall flow field has been examined at x/B locations ranging from 1–9. The experiments encompass H/B ratios from 2–8 in increments of 1 and $H/B=9.2$ and Reynolds numbers of 10,000, 20,000, and 30,000. For $H/B>4$, only a single Reynolds number of 20,000 was considered. The investigation focused on near-wall measurements, with the smallest wall-probe distance being $y/B=0.0028$ and the largest y/B about 0.35, where y is the normal distance from the impingement plate. In order to characterize the flow field outside of the slot, velocity and turbulence profiles across the slot were

also obtained at $(H-y)/B=0.3$, 1.0 and 5.4, where $(H-y)$ is the distance measured from the slot and along the jet axis.

Uncertainty Analysis. A detailed uncertainty analysis using Moffat's [21,22] computer-based data-reduction method 'JITTER' as well as Kline's [23] method was carried out. Uncertainty in the determination of the mean and root square velocity is considered first. These factors arise due to the fitting of data to King's law, due to deviation from linearity of the electronic manometer and due to uncertainty in position during calibration. This uncertainty is 4% and 3% in the mean and root mean square velocity respectively for hot-wire distances from the wall larger than 510 μm, where typical velocities are greater than 3 m/s. At these distances the contribution from a 10 μm uncertainty in hot-wire position to velocity calibrations is small. The same factors, however, lead to an uncertainty of 11% in the mean velocity and 6% in the normalized root mean square velocity, for the smallest wall distance of 110 μm. The much higher uncertainties at this distance are due to a higher contribution from uncertainty in position to velocity calibration. For wall distances between 110 μm and 510 μm the uncertainty lies somewhere in between the two extreme sets of values provided above. At these distances the typical absolute velocities are less than 3 m/s.

With an uncertainty of 11% in mean velocity and 9% in distance (both uncertainties corresponding to the measurement point with the smallest wall distance) the uncertainty in shear is estimated to be 14%. Hence for typical nominal C_f values of 0.005, the reported shear measurements should be considered to be 0.0050 ± 0.0007.

Experimental Results

Single component experimental velocity data are obtained in the free jet region and the near wall region ($y/B<0.35$). A single component measurement is adequate in these two regions because the *x*-component velocity is insignificant in the free jet region and the *y*-component velocity is insignificant in the wall jet region. This was ensured by traversing the flow regions of interest with a tuft for flow visualization.

One exception to the above occurs for the near wall region at $x/B=1$. At this position, for y/B values between 0.1 and 0.35, the single component mean velocity data are contaminated by the presence of a *V*-velocity component. The largest contamination occurs at $y/B=0.35$ and at this location the *V*-component may be as large as 14% of the measured velocity. This is based on a somewhat simplistic visual estimate of the flow angle using a tuft. At y/B of 0.1, the contamination was estimated to be as large as 5%. It is difficult to estimate the flow angle at positions closer to the wall than $y/B=0.1$, but one would expect the *V*-component to be smaller than that at $y/B=0.1$. This systematic error would lead to a higher uncertainty of 19% in the C_f values reported for $x/B=1.0$.

Based on visual observations, the data at all the other x/B positions for all H/B values was found to be free of *V*-component contamination. Contamination of root mean square velocity measurements, or $\langle u'u'\rangle^{0.5}/V_{cl}$ data due to $\langle v'v'\rangle^{0.5}/V_{cl}$ is negligible since the $\sqrt{(U+u')^2+(V+v')^2}\approx U+u'$ when *U* is much larger than *V* in the near-wall region.

Free Jet Velocity and Turbulence Profiles. Experimental data were first acquired in the absence of the impingement wall. The mean and root mean square velocity distributions across the width of the jet just after the flow emerges from the slot are shown in Fig. 3 for three different downstream distances given by $(H-y)/B=0.3$, 1.0, and 5.4. Data immediately downstream of the slot show a symmetric top hat profile with velocity uniform over $-0.4\leqslant x/B\leqslant 0.4$ to within 2% of the maximum. The normalized root mean square velocity reported here is $\langle v'v'\rangle^{0.5}/V_{cl}$, because the flow is entirely in the *y*-direction near the slot. Further downstream as the jet spreads and the potential core diminishes, the centerline velocity begins to decay accompanied by a dramatic

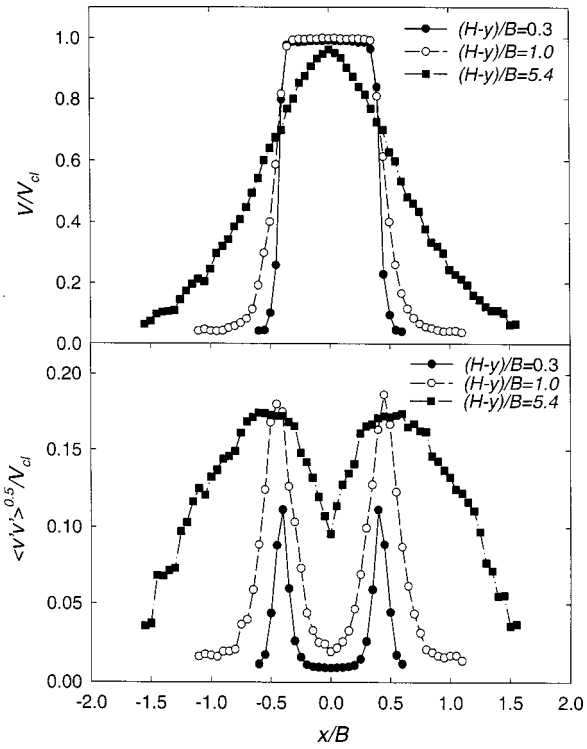

Fig. 3 Variation of mean velocity V/V_{cl} and normalized root mean square velocity $\langle v'v'\rangle^{0.5}/V_{cl}$ with x/B across the slot at $(H-y)/B$ values of 0.3, 1.0, and 5.4

growth in normalized root mean square velocity. Data at $(H-y)/B=5.4$ show this behavior with normalized root mean square velocity nearly 10 times as large as that at $(H-y)/B=0.3$. The peak values of root mean square velocity at $(H-y)/B=0.3$, 1 and 5.4 range from 12%–18%.

Velocity Measurements. The primary goal of the present paper is to obtain the variation of *x*-direction velocities and root mean square velocities with distance from the impingement wall. For the smallest impingement wall spacing of $H/B=2$, these data are shown in Fig. 4 for Re=10,000, 20,000, and 30,000. We note here once again that the unusually rapid increase in U/V_{cl} with y/B near the wall for $x/B=1$ is indicative of a *y*-direction velocity component contamination. This observation is consistent with continuity considerations and the measurements of Ashforth-Frost et al. [13]. At $x/B=2$ and 3, the maximum near-wall velocity is observed to be $U/V_{cl}=0.98$ at y/B values of about 0.08. At larger values of x/B, a decrease in the maximum velocity is observed with the point of maximum velocity moving to larger y/B values, behavior typical of a wall jet. The U/V_{cl} data at $x/B=2$ and 3 for Re=20,000 and 30,000 show that the peak U/V_{cl} values are the same as those for Re=10,000 but occur at lower y/B values. The dependence of the flow field on Reynolds number shows similar behavior at larger H/B values as well. Hence the flow field variation with H/B at higher H/B values is shown only for Re =20,000, while the data at Re=10,000 and 30,000 is placed in the data bank.

Velocity profiles at Re=20,000 for $H/B=3$, 4, 5, 6, 7, 8, and 9.2 are shown in Figs. 5(*a*)–(*g*), respectively. The data show that the maximum mean velocity exceeds 0.96 for all H/B values up to 5, but begins to drop after that from 0.92 to 0.76 as H/B increases from 6–9.2. This behavior reflects the fact that when $H/B=5$ or lower the impingement wall is located within the potential core (95% criterion) of the jet. At larger H/B values the impingement wall is outside the potential core region of the jet

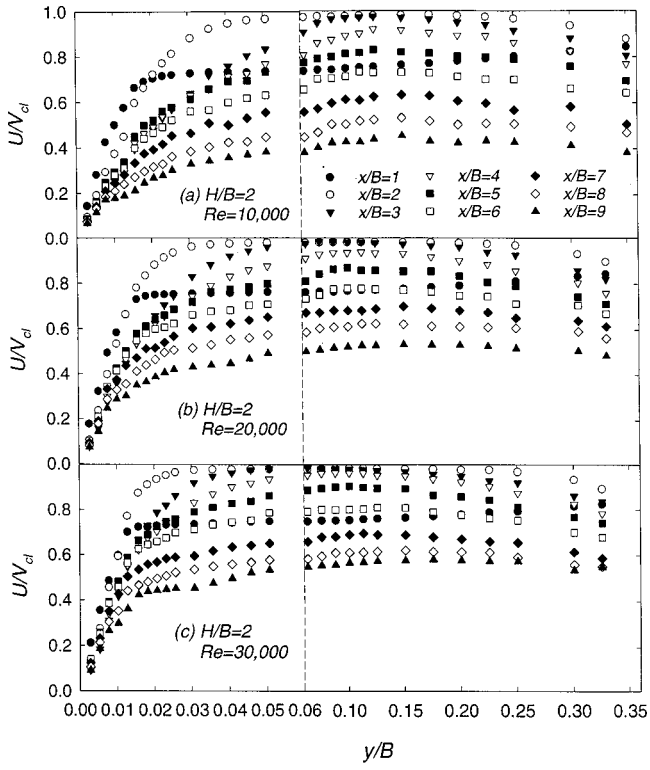

Fig. 4 Variation of mean velocity U/V_{cl} with y/B along impingement wall for $H/B=2$, (*a*) Re=10,000, (*b*) Re=20,000, and (*c*) Re=30,000

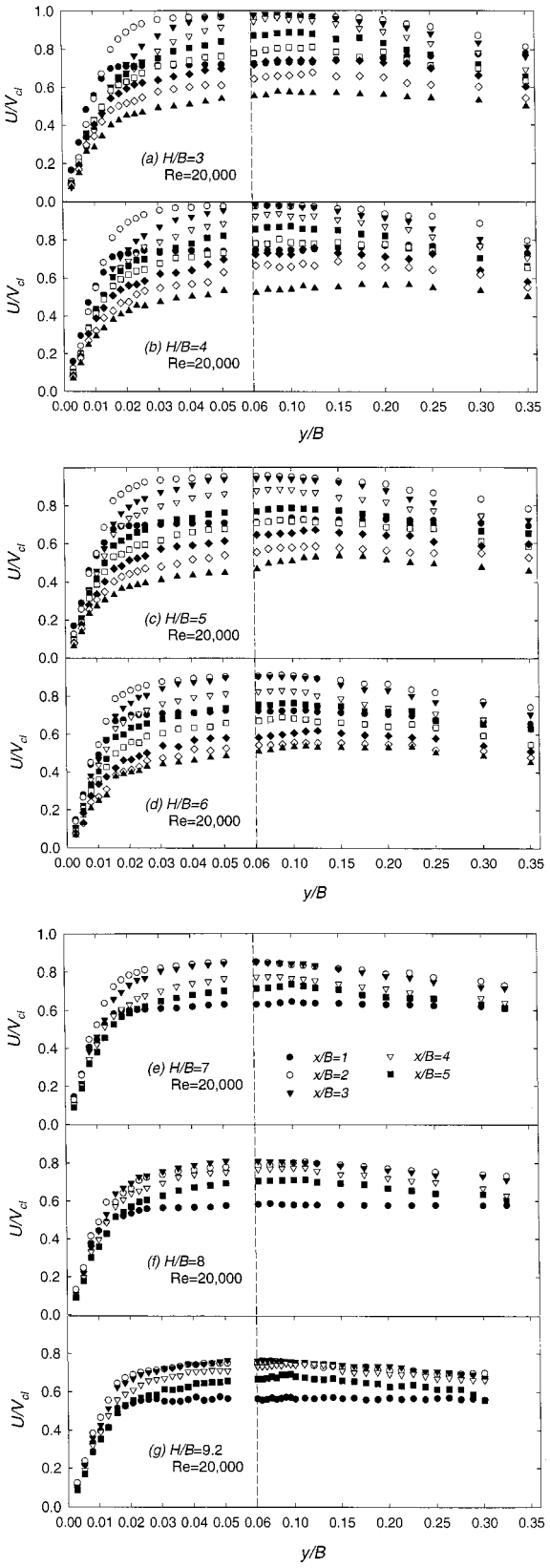

Fig. 5 Variation of mean velocity U/V_{cl} with y/B along impingement wall for Re=20,000 (*a*) $H/B=3$, (*b*) $H/B=4$, (*c*) $H/B=5$, (*d*) $H/B=6$, (*e*) $H/B=7$, and (*f*) $H/B=8$, and (*g*) $H/B=9.2$ symbols as in Fig. 4

and the speed with which the jet impinges on the surface begins to reduce even before the presence of the wall is felt.

Normal Stress $\langle u'u'\rangle/V_{cl}^2$ Measurements. The root mean square velocity data are shown in the form of the normal stress $\langle u'u'\rangle/V_{cl}^2$ in Figs. 6(*a*)–(*c*) for $H/B=2$ at Re=10,000, 20,000, and 30,000. For clarity of presentation, only the data from $y/B=0$ to 0.06 is shown, and the remaining data from 0.06–0.35 are placed in the Databank. As seen from the figure, the normal stress $\langle u'u'\rangle/V_{cl}^2$ data are largely uninfluenced by Reynolds number. For this $H/B=2$, the peak $\langle u'u'\rangle/V_{cl}^2$ value is about 0.04 and occurs at $y/B=0.03\sim0.04$, roughly six to seven jet widths downstream from the jet axis. The characteristic near-wall rise in $\langle u'u'\rangle^{0.5}/u_\tau$ is shown in Fig. 6(*d*) at $x/B=4$ for three Reynolds numbers of 10,000, 20,000 and 30,000 and $H/B=2$. The absence of a significant decrease in normal stress beyond the wall jet region in the experimental results is due to the inevitable presence of low frequency unsteady motion in the quiescent region. Hence any comparison of $\langle u'u'\rangle/V_{cl}^2$ or $\langle u'u'\rangle^{0.5}/u_\tau$ data reported here with turbulence modeling results should be limited to the region near the wall.

The effect of H/B on the normal stress is shown in Figs. 7(*a*)–(*d*) where $\langle u'u'\rangle/V_{cl}^2$ is plotted for $H/B=3,4,5,6$ at a single Re =20,000. The peak $\langle u'u'\rangle/V_{cl}^2$ level reduces from about 0.038 to 0.027 as H/B increases from 2–6. Moreover, location of the peak shifts further downstream from about six jet widths to eight jet widths. The normal stress level as well as the off-axis location of its peak may be important features that may help discriminate between turbulence models [3,4]. Measurement data acquired at Re=10,000 and 30,000, are not shown here for brevity and are placed in the data bank instead. For a single Reynolds number of 20,000 data was also acquired for $H/B=7$, 8 and 9.2 and these are placed in the data bank.

Accurate measurement of turbulence level requires that the sen-

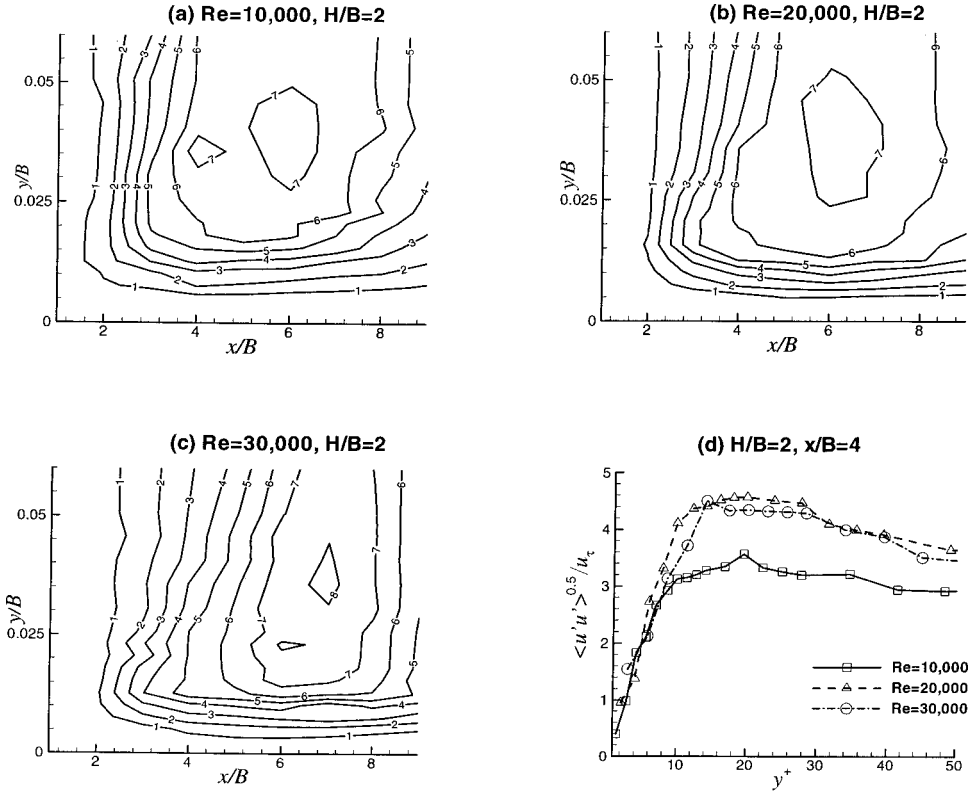

Fig. 6 Normal stress $\langle u'u'\rangle/V_{cl}^2$ contours for $H/B=2$ (*a*) Re=10,000, (*b*) Re=20,000, and (*c*) Re=30,000. Contour 1 through 8 correspond to stress levels from 0.005 to 0.04 in increments of 0.005. (*d*) Variation of $\langle u'u'\rangle^{0.5}/u_\tau$ with y^+ at $x/B=4$ for $H/B=2$. Wall units are defined using shear stress at each Re=10,000, 20,000, and 30,000.

sor, in our case a hot-wire, be smaller than the smallest length scales present. In a detailed study of turbulence within the viscous sublayer using hot-wire probes of length l^+ (wire length in wall units) from 3.3–60, Ligrani and Bradshaw [24,25] found that a wire length l^+ less than 20–25 is required to prevent contamination of the data due to the so-called ''eddy-averaging effect.'' In addition, they also found that the wire length/diameter ratio l/d should be greater than 200. In a similar study Khoo et al. [20] found the turbulence level to be independent of wire lengths for l^+ less than 22. In the present work, the wire length/diameter ratio is 334. The wire length in the present work was 1.27 mm, corresponding to l^+ of 16–21 for Re=10,000, 21–29 for Re=20,000 and 32–45 for Re=30,000. Hence the turbulence levels and the normal stresses at Re=20,000 and 30,000 are likely to be contaminated by the eddy averaging effect. The error due to this contamination is however not likely to be significant since the fraction of the energy contained within the range of length scales that are not captured is likely to be small. In the viscous sublayer this can be further confirmed from Fig. 6(*d*) where the variation of the normal stress with distance from the wall is shown in wall units. The normal stress distributions in the viscous sublayer for all three Reynolds numbers (10,000, 20,000, and 30,000) are nearly the same even though the wire length l^+ varied from 16–45. The stress levels in this region are also in good agreement with the data of Khoo et al. [20] in the boundary layer of a fully developed channel turbulence flow, acquired with much smaller wire lengths l^+ from 3–22.

Law of the Wall and Wall Shear. We are not aware of any experimental studies that have examined the applicability of the law of the wall on the target surface of a slot jet impingement flow. Such studies do, however, exist for wall jet flows, a configuration that is similar to the present one, at least away from the stagnation region. Measurements of fully developed turbulent wall jets by Kamemoto [26], Bradshaw and Gee [27], and Wygnanski et al. [28] do show that the mean velocities follow the law of the wall accurately to y^+ values of at least up to 50. With the objective of examining the law of the wall hypothesis for the present configuration, data were acquired sufficiently close to the wall to ensure that at least two points would be within the viscous sublayer everywhere along the target surface except in the stagnation region. The experimental data were plotted in wall units based on an assumption that the first point away from the wall (110 μm) is within the viscous sublayer and can be used to determine the wall shear. This assumption was indeed borne out to be correct as shown in the subsequent discussion.

The experimental data for Re=20,000 and $H/B=4$ are shown at four different downstream positions $x/B=2$, 4, 7, and 9 in Fig. 8, along with the law of the wall given by:

$$u^+=y^+ \quad \text{for} \quad y^+\leqslant 5, \quad u^+=-3.05+5\ln(y^+) \quad \text{for} \quad 5\leqslant y^+\leqslant 26$$

and

$$u^+=5.0+2.44\ln(y^+) \quad \text{for} \quad y^+>26$$

where a buffer layer has been assumed between the viscous sublayer and the log-law region. The results for $x/B=2$, 4, 7, and 9 shown in Fig. 8 indicate that expected linear behavior in the viscous sublayer is observed up to $y^+\sim 4$. This linear behavior in the viscous sublayer is observed at all x/B values for all Reynolds numbers and H/B ratios at least up to y^+ values of 4. This behavior is similar to the behavior observed by Ligrani [29] for a turbulent boundary layer over a flat plate in the absence of a pressure gradient. Due to the few numbers of data points in the viscous sublayer, it is difficult to establish the precise location at which deviation from this linear behavior occurs. The agreement

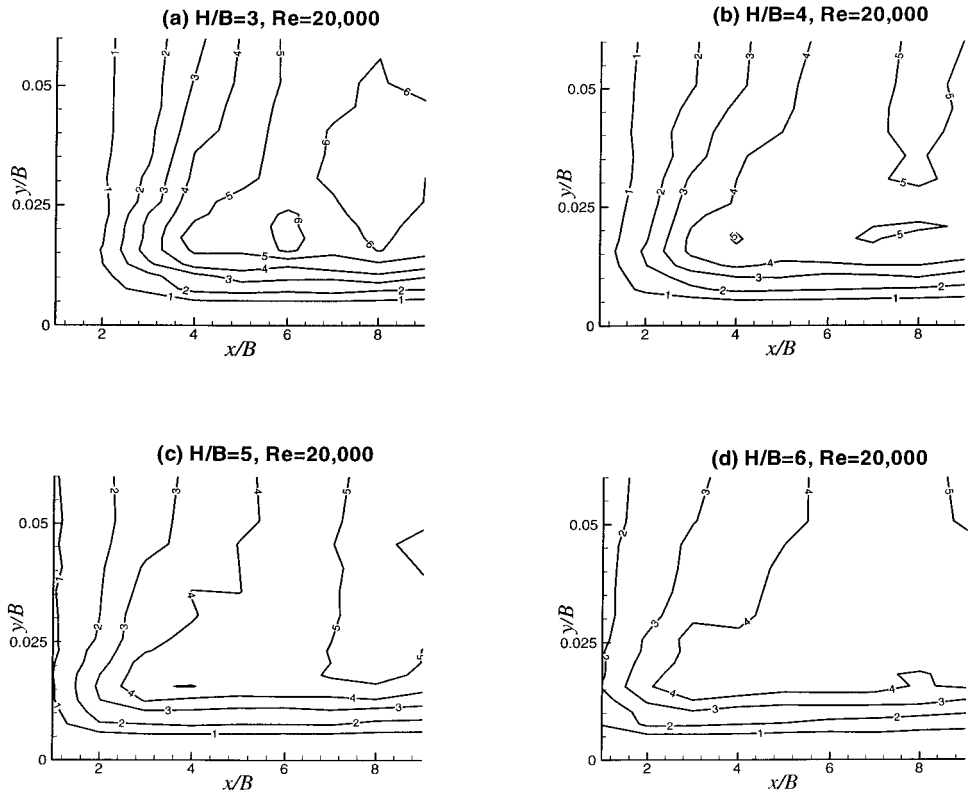

Fig. 7 Normal stress $\langle u'u' \rangle / V_{cl}^2$ contours at Re=20,000 (*a*) $H/B=3$, (*b*) $H/B=4$, (*c*) $H/B=5$, and (*d*) $H/B=6$. Contour 1 through 8 correspond to stress levels from 0.005 to 0.04 in increments of 0.005.

with the law of wall beyond the linear region is found to improve with increasing downstream distance x/B. At the largest x/B value of 9 examined, the experimental data follows the law of the wall up to y^+ of about 50. These observations are also valid at other Reynolds numbers and H/B ratios examined in the present study.

Having ensured that at least the first two points in all data sets are within the viscous sublayer, it is possible to estimate wall shear from the first data point at $y/B=0.0028$, corresponding to a y^+ value between 1.4 and 3.8 in most cases. The wall shear data are computed in the form of a friction coefficient defined as:

$$C_f = \frac{\tau_w}{0.5\rho V_{cl}^2} = \frac{2}{\mathrm{Re}} \left. \frac{d(U/V_{cl})}{d(y/B)} \right|_{y=0}$$

The skin friction coefficient distribution (for each of the three Re=10,000, 20,000, and 30,000) along the *x*-direction is shown in Figs. 9(*a*), (*b*), and (*c*) at $H/B=2$, 3, and 4, respectively. A collapse of the C_f data for Re=20,000 and 30,000 is observed in Figs. 9(*a*)–(*c*) and hence a single dashed line is shown through the mean of these two data sets. Representative error bars about this dashed line at only a few x/B positions are also shown for clarity. As discussed earlier, the results for $x/B=1$ cannot be relied upon for estimate of shear with the same certainty as other x/B values. Moreover, the skin friction coefficients for H/B values of 2, 3, and 4 are also nearly the same and not dependent on the target wall to slot distance to within experimental uncertainty of 14%. This is better seen in Fig. 10(*a*) for Re=20,000. While not shown here a similar collapse also occurs for Re=10,000 and 30,000.

The skin friction coefficients C_f for higher H/B values of 5 through 9.2 are shown in Fig. 10(*b*) for a single Re=20,000. A notable feature of the low H/B data in Fig. 10(*a*) is the presence of a secondary peak in the skin friction coefficient. As shown in computations by Chalupa et al. [30], while the presence of the recirculation region at the confinement wall can lead to a secondary peak, the actual V component near the impingement wall is never significant compared to the U component. One observes that the secondary peak is clearly absent from the data at H/B values of 5 and larger. It appears that the location of the confinement wall does not alter wall shear at the impingement wall at these larger values of H/B. These trends in skin friction with H/B

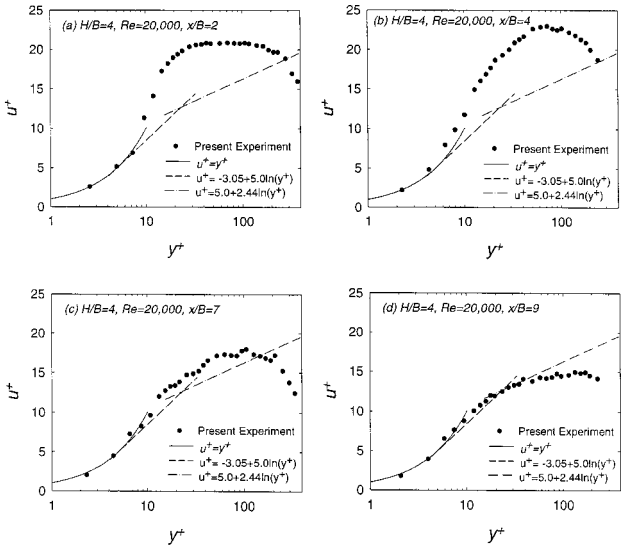

Fig. 8 Variation of mean velocity u^+ for $H/B=4$, Re=20,000 with y^+ at four streamwise locations (*a*) $x/B=2$, (*b*) $x/B=4$, (*c*) $x/B=7$, and (*d*) $x/B=9$. The law of the wall is also shown.

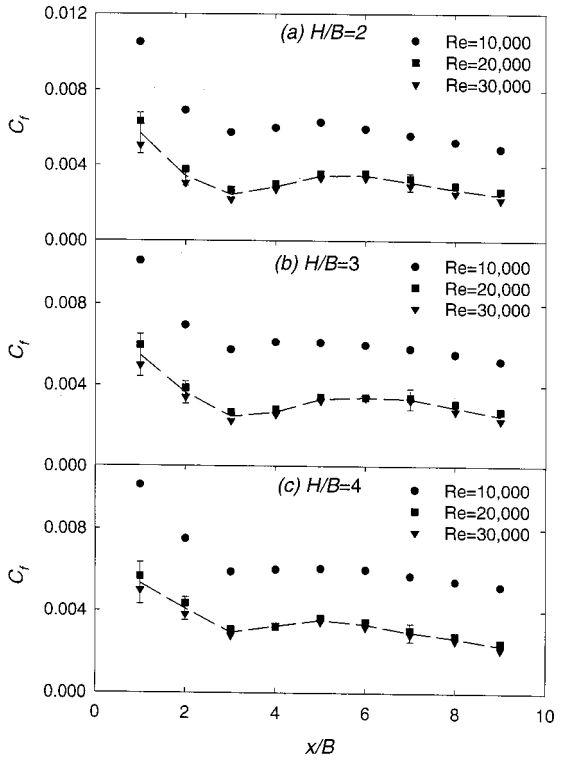

Fig. 9 Variation of skin friction coefficient along the impingement wall for Re=10,000, 20,000, and 30,000 (*a*) *H*/*B*=2, (*b*) *H*/*B*=3, and (*c*) *H*/*B*=4

mimic the Nusselt number heat transfer behavior reported by Gardon and Akfirat [31] from their measurements of local heat transfer coefficient under similar conditions.

The mean velocity data of Ashforth et al. [13] can also be utilized to determine skin friction coefficient. The so determined skin friction coefficient values are, however, consistently higher than those reported here. Their velocity profiles in the viscous sublayer do not follow a linear behavior. Conversion to wall units was carried out using their velocity data at the first point away from the wall to determine shear. It is however difficult to establish whether this discrepancy is solely due to the lack of correction for wall interference since the wall material used by Ashforth et al. [13] is of considerably different thermal properties than that used here.

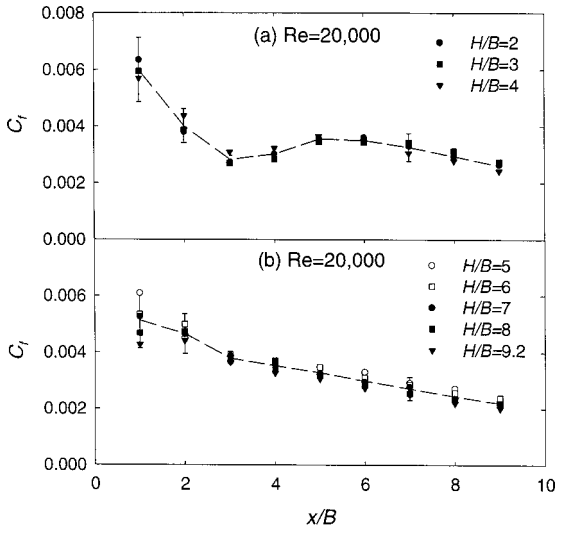

Fig. 10 Variation of skin friction coefficient along impingement wall for Re=20,000 (*a*) *H*/*B*=2, 3, 4 and (*b*) *H*/*B*=5, 6, 7, 8, 9.2

Conclusions

An experimental investigation of a turbulent slot jet impinging orthogonally onto a flat plate has been carried out. Hot-wire anemometry was employed to measure mean velocity and root mean square velocity data with particular attention paid to the near-wall region. It was found imperative to account for the effect of wall interference on the near wall hot-wire data. In the present study, this was done by carrying out a calibration of the hot-wire by placing the entire probe/stage/plate assembly in a known flow before measurement in the flow of interest.

The study provides experimental mean velocity data suitable for validating fluid flow in slot impingement systems at Reynolds numbers of 10,000, 20,000, and 30,000 for H/B ratios from 2–9.2. This data could be useful in developing and assessing turbulence models in such systems without reliance on heat and mass transfer data, which would require additional assumptions regarding scalar transport. The peak value of normal stress near the wall is found at $y/B \sim 0.025-0.04$, at a distance six to eight jet widths away from the jet axis. The normal stress data for Re=10,000 are likely to be free of eddy averaging error. At the two higher Reynolds numbers of 20,000 and 30,000, the wire length in wall units, l^+ is between 21 to 45, larger than a recommended length of 22–25 [20,24,25] leading to possible eddy averaging error. It is shown by comparison with [20] that the contribution due to this error may be small at least in the viscous sublayer.

With the exception of the stagnation region where shear could not be evaluated, it is found the velocity profiles follow the linear behavior of the law of wall in the viscous sublayer. Skin friction coefficients seem to have become Reynolds number independent at a Reynolds number somewhere between 10,000 and 20,000. Skin friction behavior at the target surface in slot impingement systems depends upon the distance of the target surface from the slot, however the variation among the three H/B values of 2, 3, and 4 was found to be small. Moreover, the shear for these low H/B configurations shows a clear secondary peak that is absent at higher H/B values.

JFE Data Bank

The full set of experimental data is presented in the file ''jzexp.xls'' using Microsoft Excel version 7.0.

Acknowledgments

The authors would like to thank Dr. Xuanhui Lu and Mr. Mark Angelov for their supports during the experiments. Partial support for this work was provided by the National Science Foundation through grant number CTS-9706824.

Nomenclature

B = slot width
C_f = $\tau_w/0.5\rho V_{cl}^2$, skin friction coefficient
d = diameter of hot-wire
D = diameter of circular jet in [7]
H = distance from the slot and the impingement plate
l = length of hot-wire
l^+ = length of hot-wire in wall units
q = $(U^2+V^2)^{0.5}$
Re = Reynolds number based on slot width
U = time-averaged mean x direction velocity
u' = root mean square velocity in x direction
$\langle u'u' \rangle^{0.5}/V_{cl}$ = nondimensional root mean square velocity in x direction

$\langle u'u' \rangle / V_{cl}^2$ = nondimensional normal stress
u^+ = U/u_τ, mean x-direction velocity in wall units
u_τ = $(\tau_w/\rho)^{0.5}$, friction velocity
V = time-averaged mean velocity in y direction
v' = root mean square velocity in x-direction
V_{cl} = time-averaged mean velocity at slot exit
$\langle v'v' \rangle^{0.5} / V_{cl}$ = nondimensional root mean square velocity in y direction
x = coordinate along impingement wall
y = coordinate in the direction normal to the impingement wall
y_1 = distance of the nearest measurement point from the impingement wall
y^+ = yu_τ/ν, distance from wall in wall units
z = coordinate normal to the x-y plane
ρ = density
ν = kinematic viscosity
τ_w = wall shear stress

References

[1] Livingood, J. N. B., and Hrycak, P., 1973, ''Impingement heat transfer from turbulent air stream jets to flat plates: A Literature Survey,'' NASA TM X-2778.
[2] Webb, B. W., and Ma, C. F., 1995, ''Single-phase liquid jet impingement heat transfer,'' Adv. Heat Transfer, **26**, pp. 105–217.
[3] Behnia, M., Parneix, S., and Durbin, P. A., 1998, ''Prediction of heat transfer in an axisymmetric turbulent jet impinging on a flat plate,'' Int. J. Heat Mass Transf., **41**, pp. 1845–1855.
[4] Behnia, M., Parneix, S., Shabany, Y., and Durbin, P. A., 1999, ''Numerical study of turbulent heat transfer in confined and unconfined impinging jets,'' Int. J. Heat Fluid Flow, **20**, pp. 1–9.
[5] Craft, T. J., Graham, L. J. W., and Launder, B. E., 1993, ''Impinging jets studies for turbulence model assessment-II. An examination of the performance of four turbulence models,'' Int. J. Heat Mass Transf., **36**, pp. 2685–2697.
[6] Cooper, D., Jackson, D. C., Launder, B. E., and Liao, G. X., 1993, ''Impinging jets studies for turbulence model assessment-I. Flow-field experiments,'' Int. J. Heat Mass Transf., **36**, pp. 2675–2684.
[7] Gibson, M. M., and Launder, B. E., 1978, ''Ground effects on pressure fluctuations in the atmospheric boundary layer,'' J. Fluid Mech., **86**, pp. 491–511.
[8] Durbin, P. A., 1996, ''On the k-ε stagnation point anomaly,'' J. Heat Fluid Flow, **17**, pp. 89–90.
[9] Dianat, M., Fairweather, M., and Jones, W. P., 1997, ''Predictions of axisymmetric and two-dimensional impinging turbulent jets,'' Int. J. Heat Fluid Flow, **17**, pp. 530–538.
[10] Heyerichs, K., and Pollard, A., 1996, ''Heat transfer in separated and impinging turbulent flows,'' Int. J. Heat Mass Transf., **39**, pp. 2385–2400.
[11] Wilcox, D. C., 1993, *Turbulence Modeling for CFD*, DCW Indus. Inc, La Canada, CA.
[12] Chen, Q., and Modi, V., 1999, ''Mass transfer in turbulent impinging slot jets,'' Int. J. Heat Mass Transf., **42**, pp. 873–887.
[13] Ashforth-Frost, S., Jambunathan, K., and Whitney, C. F., 1997, ''Velocity and turbulence characteristics of a semiconfined orthogonally impinging slot jet,'' Exp. Therm. Fluid Sci., **14**, pp. 60–67.
[14] Wills, J. A. B., 1962, ''The correction of hot-wire readings for proximity to a solid boundary,'' J. Fluid Mech., **12**, pp. 388–396.
[15] Collis, D. C., and Williams, M. J., 1959, ''Two-dimensional convection from heated wires at low Reynolds numbers,'' J. Fluid Mech., **6**, pp. 357–384.
[16] Lange, C. F., Durst, F., and Breuer, M., 1999, ''Correction of hot-wire measurements in the near-wall region,'' Exp. Fluids, **26**, pp. 475–477.
[17] Durst, F., Kikura, H., Lekakis, I., Jovanovic, J., and Ye, Q., 1996, ''Wall shear stress determination from near-wall mean velocity data in turbulent pipe and channel flows,'' Exp. Fluids, **20**, pp. 417–428.
[18] Bhatia, J. C., Durst, F., and Jovanovic, J., 1982, ''Correction of hot-wire ameometer measurements near walls,'' J. Fluid Mech., **122**, pp. 411–431.
[19] Goldstein, R. J., 1983, *Fluid Mechanics Measurements*, Hemisphere Publishing, NY.
[20] Khoo, B. C., Chew, Y. T., and Li, G. L., 1997, ''Effects of imperfect spatial resolution on turbulence measurements in the near-wall viscous sublayer region,'' Exp. Fluids, **22**, pp. 327–335.
[21] Moffat, R. J., 1982, ''Contribution to the theory of single-sample uncertainty analysis,'' ASME J. Fluids Eng., **104**, pp. 250–260.
[22] Moffat, R. J., 1988, ''Describing the uncertainties in experimental results,'' Exp. Therm. Fluid Sci., **1**, pp. 3–17.
[23] Kline, S. J., 1985, ''The purpose of uncertainty analysis,'' ASME J. Fluids Eng., **107**, pp. 153–160.
[24] Ligrani, M. P., and Bradshaw, P., 1987, ''Spatial resolution and measurement of turbulence in the viscous sublayer using subminiature hot-wire probes,'' Exp. Fluids, **5**, pp. 407–417.
[25] Ligrani, M. P., and Bradshaw, P., 1987, ''Subminiature hot-wire sensors: development and use,'' Journal of Physics, **20**, pp. 323–332.
[26] Kamemoto, K., 1974, ''Investigation of turbulence jets over logarithmic spiral surface (2nd Report, Properties of flow near wall),'' Bull. JSME, **17**, No. 105, pp. 343–350.
[27] Bradshaw, P., and Gee, M. T., 1960, ''Turbulent wall jets with and without an external stream,'' Aeronautical Research Council-R. & M., Great Britain, 3252.
[28] Wygnanski, I., Katz, Y., and Horev, E., 1992, ''On the applicability of various scaling laws to the turbulent wall jet,'' J. Fluid Mech., **234**, pp. 669–690.
[29] Ligrani, M. P., 1988, ''Structure of the turbulence boundary layers,'' *Aerodynamics and Compressible Flows, Encyclopedia of Fluid Mechanics*, N. Cheremisinoff, ed., Vol. 8, Gulf Publishing, Houston, pp. 111–189.
[30] Chalupa, R., Chen, M., Modi, V., and West, A. C., 2000, ''High Schmidt mass transfer in a turbulent impingement slot jet,'' submitted to *International Journal of Heat and Mass Transfer*.
[31] Gardon, R., and Akfirat, J. C., 1996, ''Heat transfer characteristics of impinging two-dimensional air jets,'' ASME J. Heat Transfer, **108**, pp. 101–108.

Plane Turbulent Surface Jets in Shallow Tailwater

S. A. Ead
Assistant Professor,
Ain Shams University, Cairo, Egypt;
Currently, Research Associate,
Department of Civil and Environmental Engineering,
University of Alberta,
Edmonton, Alberta, Canada, T6G 2G7

N. Rajaratnam
Professor,
Department of Civil and Environmental Engineering,
University of Alberta,
Edmonton, Alberta, Canada, T6G 2G7

This paper presents a theoretical and laboratory study of plane turbulent surface jets in shallow tailwater. The main objective was to show that when the depth of tailwater is finite, the momentum flux in the forward flow in the surface jet decays appreciably with the distance from the nozzle producing the surface jet. This decay is shown to be due to the entrainment of the return flow which has negative momentum and an increase in the tailwater depth further away from the nozzle produces this return flow. An extensive set of experiments, with different Froude numbers and offset ratios, was conducted to observe and quantify the growth of the surface jet, the decay of the velocity scale, and the momentum flux and the variation of the volume flux. On the whole, the results from this study highlight the effect of the tailwater depth on the behavior of plane turbulent surface jets when the ambient fluid has a limited extent. [DOI: 10.1115/1.1331556]

Keywords: Turbulent Jets, Limited Ambient, Free Turbulent Flows, Water Flow, Hydraulics

Introduction

For turbulent jets discharged from slots or orifices in walls into large ambients at rest, it has been generally assumed (Albertson et al. [1], Schlichting [2], and Rajaratnam [3]) that the momentum flux would be preserved. In some experimental investigations (Miller and Comings [4]; Goldschmidt and Eskinazi [5]; Heskestad [6], and Kotsovinos [7]), it has been noticed that the momentum flux decayed to some extent at large distances from the origin of the jets. Kotsovinos [8] noticed that the momentum flux could decay to about 80 percent of that at the source at a longitudinal distance equal to 100 b_o for plane turbulent jets where b_o is the slot width. Kotsovinos [8] attributed this loss of momentum flux to the negative momentum carried by the entrained fluid which approached the jet at an angle of about $\pi/4$ radians from the forward direction of the jet. Based on an approximate integral analysis, Kotsovinos [8] developed an equation to describe the variation of the momentum flux with the longitudinal distance from the nozzle producing the jet. Schneider [9] attempted to explain this decay of momentum flux by combining the analysis of the jet with the flow in the region surrounding the jet. Schneider coupled the jet and the induced outer flow through momentum and volume balances.

Swean Jr. et al. [10] studied the variation of momentum and mass fluxes as well as the growth for plane turbulent surface jets with limited depth of tailwater. They conducted ten experiments to study the effect of the finite depth of tailwater on the characteristics of the surface jet and to observe the variation of the momentum and volume fluxes and the breakdown of the surface jet due to the limited depth of the ambient. They also used the experimental results of Vanvari and Chu [11] and Rajaratnam and Humphries [12]. Their results showed a momentum decay and a break down (or variation from that of jets in infinite ambient) in the velocity and length scales due to the jet confinement. The study of Swean Jr. et al. [10] provides a general understanding of the problem of surface jets with a finite depth of tailwater. Their analysis did not consider the adverse pressure gradient in the momentum balance. As the depth of flow increases gradually in the longitudinal direction, it is important to include the excess pressure due to this increasing depth.

This paper presents the results of a theoretical and experimental study of turbulent surface jets with finite depth of tailwater. It was conducted to understand the nature of the jet growth, the decay of the maximum velocity, the variation of the momentum and volume fluxes in the forward flow region of the surface jet, and the effect of the depth of tailwater on these properties. Further, since the authors have recently suggested the use of supercritical surface jets for energy dissipation below certain types of hydraulic structures (Ead and Rajaratnam [13]), it was necessary to understand the effect of tailwater depth on the behavior of these surface jets.

Theoretical Considerations

Assume a plane turbulent surface jet of thickness b_o with a flow rate per unit width of Q_o, and momentum flux per unit width of M_o entering a rectangular channel horizontally at a height of Z_o above the bed of the channel as shown in Fig. 1(*a*). Let U_o be the velocity of the jet at the nozzle. The downstream control gate is adjusted so that the depth of flow at the nozzle is equal to $(Z_o + b_o)$ and that the surface jet enters the channel horizontally. Our experimental observations (presented later) have shown that the water surface rises gradually as the distance x from the gate or nozzle increases and this increase becomes important for flows with finite depth of tailwater. Assume that δ_∞ is the maximum rise in the water surface elevation (see Fig. 1(*a*)) and that δ_x is the corresponding rise at a section located at a longitudinal distance of x from the gate. The maximum value of δ_x is δ_∞ which occurs at the section where the jet attaches to the bed. Assuming that the pressure distribution is hydrostatic in the vertical direction, a longitudinal adverse pressure gradient is created to produce the return flow underneath the surface jet, for the jet entrainment.

Assuming hydrostatic pressure distribution on the wall containing the nozzle and at the downstream section I-I (see Fig. 1(*a*)) and that the velocity distribution at the nozzle and the downstream section is uniform (see Fig. 1(*b*)) and neglecting the integrated bed shear stress between the two sections, the continuity and the momentum equations could be written as

$$U_o b_o = V(Z_o + b_o + \delta_\infty) \tag{1}$$

$$M_o - M_\infty = \gamma \delta_\infty (Z_o + b_o) + 0.5 \gamma \delta_\infty^2 \tag{2}$$

where V and M_∞ are, respectively, the uniform velocity and the momentum flux at the downstream section and M_o is the momentum flux at the nozzle.

Multiplying Eq. (1) by ρV and rearranging, Eq. (1) is rewritten as

Contributed by the Fluids Engineering Division for publication in the JOURNAL OF FLUIDS ENGINEERING. Manuscript received by the Fluids Engineering Division September 27, 1999; revised manuscript received September 8, 2000. Associate Editor: P. Bearman.

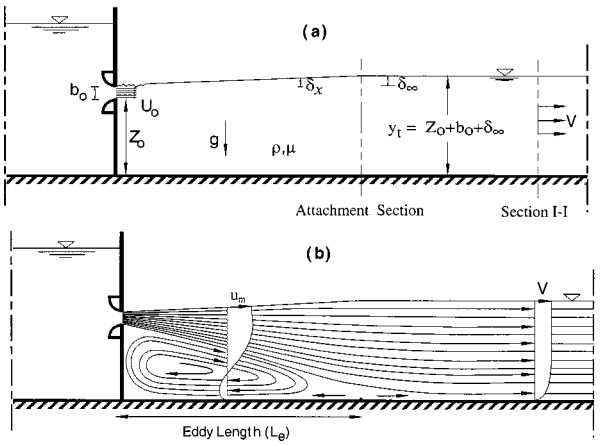

Fig. 1 (*a*) Definition sketch; (*b*) flow pattern

$$\frac{M_\infty}{M_o} = \frac{1}{(1 + Z_o/b_o + \delta_\infty/b_o)} = \frac{1}{(1+\eta)+\theta} \tag{3}$$

Where $\eta = Z_o/b_o$ and $\theta = \delta_\infty/b_o$.

Dividing Eq. (2) by M_o and rearranging, Eq. (2) becomes

$$1 - \frac{M_\infty}{M_o} = \frac{2\theta(1+\eta)+\theta^2}{2F_o^2} \tag{4}$$

Solving Eqs. (3) and (4) we obtain a cubic equation in θ as

$$\theta^3 + 3(1+\eta)\theta^2 + 2[(1+\eta)^2 - F_o^2]\theta - 2\eta F_o^2 = 0 \tag{5}$$

Equation (5) has three real roots, one is positive and the other two are negative. Since all the experiments had positive values for δ_∞, the positive root of Eq. (5) was only considered as the relevant solution. However, the negative roots (that represent a depression in the water elevation) may be relevant for other problems. The positive root of Eq. (5) can be written as

$$\theta = \left[\frac{2}{\sqrt{3}} \sqrt{(1+\eta)^2 + 2F_o^2} \cos(\phi/3) - (1+\eta) \right] \tag{6}$$

where ϕ is a function of η and the Froude number F_o at the nozzle equal to $[U_o/\sqrt{g b_o}]$ and is described by the equation

$$\phi = \tan^{-1}\left(\sqrt{\frac{[(1+\eta)^2 + 2F_o^2]^3}{27F_o^4}} - 1 \right) \tag{7}$$

With the exception of relatively small values of η ($\eta < 10$ as shown in Fig. 2), ϕ was found to be equal to $\pi/2$. Using this value of ϕ, Eq. (6) reduces to

$$\theta = [\sqrt{(1+\eta)^2 + 2F_o^2} - (1+\eta)] \tag{8}$$

Further, M_∞ can be evaluated by combining Eq. (3) and Eq. (8) as

$$\frac{M_\infty}{M_o} = ((1+\eta)^2 + 2F_o^2)^{-1/2} \tag{9}$$

It is interesting to note that substituting in Eq. (5) with $\eta = 0$, (the supercritical jet is on the bed), results in a quadratic equation. Solving this quadratic equation

$$\theta = 0.5(\sqrt{1 + 8F_o^2} - 3) \tag{10}$$

which is closely related to the well-known Belanger equation.

Based on these theoretical formulations, the variation of θ, which is equal to the maximum rise in the water surface elevation in terms of the slot width, with the offset ratio η, is shown in Fig. 3 as solutions of Eq. (8) for the jet Froude number F_o varies from 1.6–7.2. Figure 3 shows that for any given Froude number, θ decreases as the offset ratio increases. For the offset ratio equal to 100, θ decreases from about 0.5 for $F_o = 7.2$ to almost zero for $F_o = 1.6$.

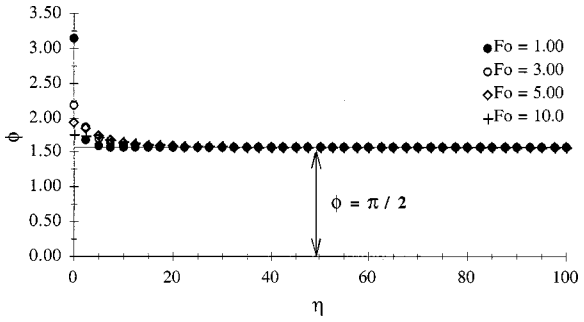

Fig. 2 Variation of (ϕ) with the offset ratio (η)

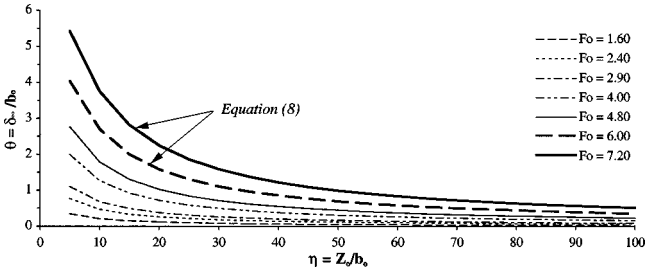

Fig. 3 Variation of (θ) with the offset ratio (η) for different Froude numbers

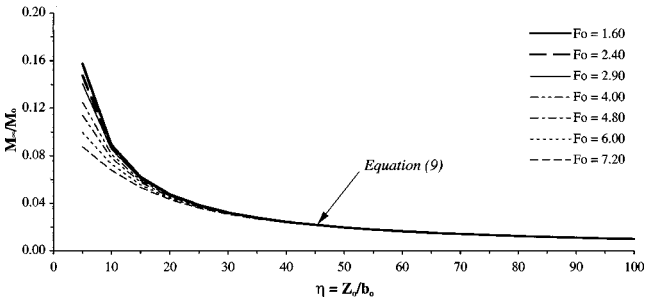

Fig. 4 Variation of (M_∞/M_o) with the offset ratio (η) for different Froude numbers

Equation (9) was plotted in Fig. 4 to show the variation of the dimensionless momentum flux with the offset ratio η for the different Froude numbers. Figure 4 shows that the Froude number F_o appears to have no effect on the momentum decay for η greater than about 30. Figure 4 also shows that the momentum flux in terms of that at the nozzle is equal to 0.04, 0.02, 0.013, and 0.01, respectively, for η equal to 25, 50, 75, and 100.

Experimental Study

The surface jets were produced in a flume, 0.446 m wide, 0.60 m deep, and 7.6 m long, with aluminum bottom and Plexiglas sides. Two pumps were used to supply the head-tank feeding the flume. The discharge was measured by a magnetic flowmeter located in the supply line. Water entered the flume through an opening between two aluminum gates, provided with streamlined entrances thereby producing an uniform jet with a thickness of b_o. A tailgate was used to control the tailwater depth in the flume. In all the experiments, the tailgate was adjusted so that the jet issued from the slot horizontally. False floors of different heights were used to produce the required offset distance Z_o.

Table 1 Primary details of experiments

Exp. (1)	b_o (mm) (2)	Z_o (mm) (3)	y_g (mm) (4)	W(mm) (5)	U_o (m/s) (6)	F_o (7)	Z_o/b_o (8)	$(y_g-Z_o)/b_o$ (9)	R (x 10^3) (10)
1	5	500	505	446	1.60	7.2	100	1.00	8.00
2	10	500	510	446	0.75	2.4	50	1.00	7.50
3	10	500	510	446	1.50	4.8	50	1.00	15.00
4	10	500	510	446	2.25	7.2	50	1.00	22.50
5	10	300	310	446	1.88	6.0	30	1.00	18.80
6	20	500	520	446	2.13	4.8	25	1.00	42.60
7	10	200	210	446	0.90	2.9	20	1.00	9.00
8	10	100	110	446	1.25	4.0	10	1.00	12.50
9	10	50	60	446	0.50	1.6	5	1.00	5.00

A Prandtl tube with an external diameter of 3.0 mm was used to measure the time-averaged longitudinal velocity u. Velocity distributions of the forward and backward flows were measured along vertical sections at different longitudinal distances from the nozzle producing the jet. Velocity measurements were also taken, when needed, downstream of the line of the jet attachment to the bed. All the measurements were taken in the middle third of the flume. One transducer, of the Validyne model (DP45-16), was used in the experiments to measure the pressure difference indicated by the Prandtl tube. The output of the transducer was connected to a Macintosh IIfx computer. When the pressure difference was outside the transducer range ($\pm$25.4 mm), the pressure connections were switched to a manometer board. The computer displayed the results on a strip chart on the screen in real time. When the required number of samples (usually 5000) were recorded at each point with a sampling rate of 40 samples/s, the computer processed all the samples to obtain the mean value and the standard deviation for each variable and saved the results in an open file. The computer programs used in the experiments were written in Lab View Language. The method introduced by Kline and McClintock [14] and Kline [15] was used to estimate the accuracy of the velocity measurements in our experiments. It was found that the relative error in velocity was equal to $\pm$0.06 percent and $\pm$6 percent for u equal to 1 and 0.1 m/s. It was estimated that the error due to viscous effects (Chue [16]) was about 1 percent for a velocity as low as 0.1 m/s.

A total of nine experiments were conducted and the primary details of these experiments are shown in Table 1. The values of the various parameters (b_o, Z_o, U_o) were selected to achieve a wide range of the offset ratio and the Froude number. Seven offset ratios of 5, 10, 20, 25, 30, 50, and 100 were used. Experiments were conducted for Froude numbers equal to 1.6, 2.4, 2.9, 4.0, 4.8, 6.0, and 7.2. The Reynolds number of the jet was in the range of 5000–43000.

Analysis of Results

As soon as the jet issues from the slot, a recirculating-flow region starts to develop between the jet and the bed of the flume (see Fig. 1(*b*)). Figures 5(*a*)–(*c*) show velocity profiles for offset ratios of 50, 30, and 5, respectively, with $F_o = 7.2$, 6.0, and 1.6. These typical velocity profiles show the forward and backward flows. The bottom of the forward flow was estimated from these velocity profiles. For the profiles shown in Fig. 5(*a*), the jet attached to the bed at a distance of approximately 3.2 m from the wall and this location was found using dye injection. For the cases shown in Figs. 5(*b*)–(*c*), the jet attached to the bed at distances of 2.0 m and 0.5 m, respectively. Several complete velocity profiles at different *x*-stations from the gate were used to check for the validity of the two-dimensional continuity equation. By integrating these velocity profiles, a maximum error of about 8 percent was obtained (with most of the errors not exceeding 5 percent) indicating that the assumption of a two dimensional model was reasonable.

If L_e is the length of the recirculating region (or the eddy length), it could be written that

$$L_e = f_1[U_o, b_o, \nu, Z_o] \tag{11}$$

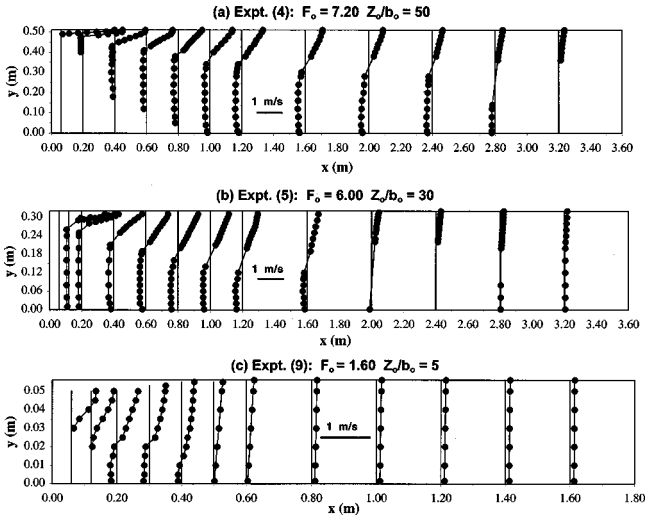

Fig. 5 (*a*)–(*c*) Typical velocity profiles

wherein gravitational effects are neglected and this assumption was well substantiated by our experiments. (It should be pointed out that if there is significant surface wave activity near the jet, the acceleration due to gravity g will have to be included in Eq. (11).) Using the Pi theorem, it can be shown that

$$\frac{L_e}{b_o} = f_2\left[\frac{Z_o}{b_o}, \frac{U_o b_o}{\nu}\right] \tag{12}$$

For large values of the Reynolds number, viscous effects may be neglected and Eq. (12) reduces to

$$\frac{L_e}{b_o} = f_3\left[\frac{Z_o}{b_o}\right] \tag{13}$$

The experimental results are shown plotted in Fig. 6 with L_e/b_o versus Z_o/b_o. Figure 6 shows a linear relationship between the eddy length L_e and the offset distance Z_o. The best-fit linear equation shows that L_e is 6.5 times Z_o. Rajaratnam [17] found this constant to be approximately 7.5.

The velocity measurements in the surface-jet zone show that the maximum velocity u_m occurs at or very near the free surface. To test for the similarity of the forward-flow velocity distributions, the maximum velocity, u_m, at any station was chosen as the velocity scale. The length scale, b, is the distance between the point of u_m and that of $0.5u_m$. Figure 7 shows the velocity distribution in the partially-developed flow region. In this figure, u/u_m was plotted against $(y_o - y)/b$ where y_o is the depth of flow at any station and y is the height above the flume bed, of the point under consideration. This plot represents a station located approximately in the middle of the developing region (at $x/b_o = 6$). Within the potential core, the velocity is constant whereas outside the potential core, the distribution of the velocity is almost linear.

Velocity distributions in the fully-developed flow region ($x/b_o \geq 12$) for the nine experiments are shown in Fig. 8. A study of these profiles established that the velocity distributions are similar. The similarity profile is almost linear. This linear velocity distribution has been observed earlier by Wu and Rajaratnam [18] and can also be observed in the results of Swean Jr et al. [10]. There is some scatter in the data near the bottom of the forward flow region and this could be due to the interaction with the backward flow and the resulting turbulence.

Having found that the velocity profiles in the forward flow are similar, it is necessary to study the variation of the velocity scale, u_m, and the length scale, b, with the distance x. Figure 9(*a*) shows the decay of the maximum velocity u_m at any section in terms of the velocity of the jet at the nozzle U_o with the normalized dis-

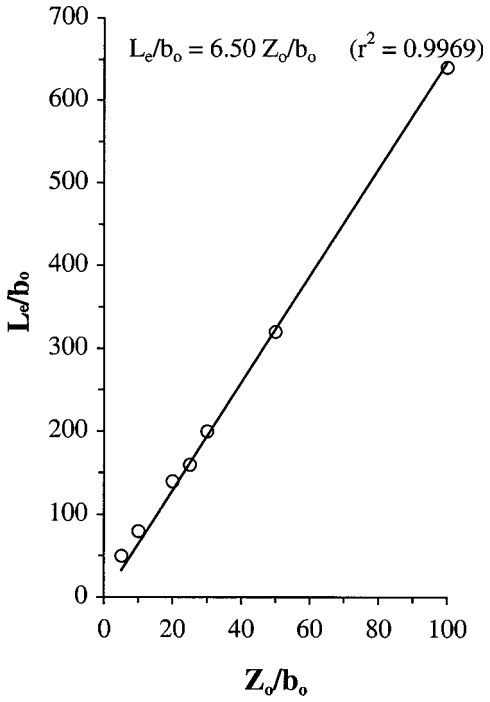

Fig. 6 Variation of the eddy length with the offset ratio

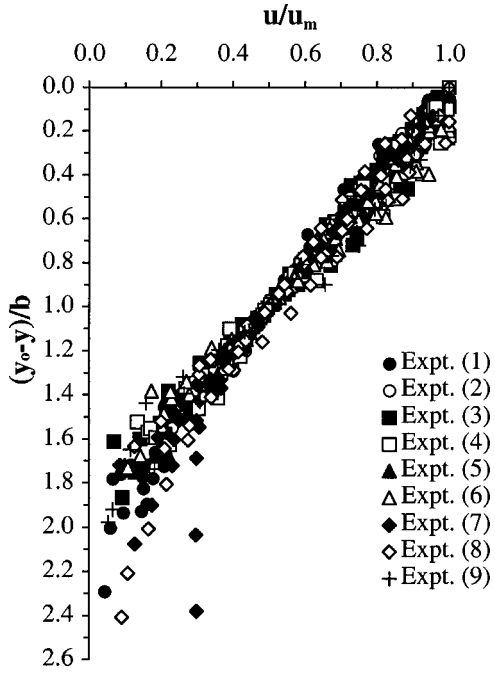

Fig. 8 Velocity distribution in fully-developed flow ($x/b_o \geq 12$)

tance from the gate x/b_o. The decay of the maximum velocity shows the existence of two stages. The first stage represents the plane surface jet with large depth of tailwater and starts at the end of the development region. The decay of the normalized velocity scale in this region can be described by the following equation

$$\frac{u_m}{U_o} = \frac{4.20}{\sqrt{x/b_o}} \tag{14}$$

The second stage of the velocity decay starts at a distance x_o from the gate, where the observations begin to deviate from the curve describing Eq. (14) and the maximum velocity decays more rapidly. The value of x_o, varies with the offset ratio as shown in Fig. 9(*b*). These considerations show that as the tailwater depth decreases, the length of the first stage of decay decreases and the maximum-velocity decay will be more rapid. It was also found that the Froude number does not have any noticeable effect on the velocity decay.

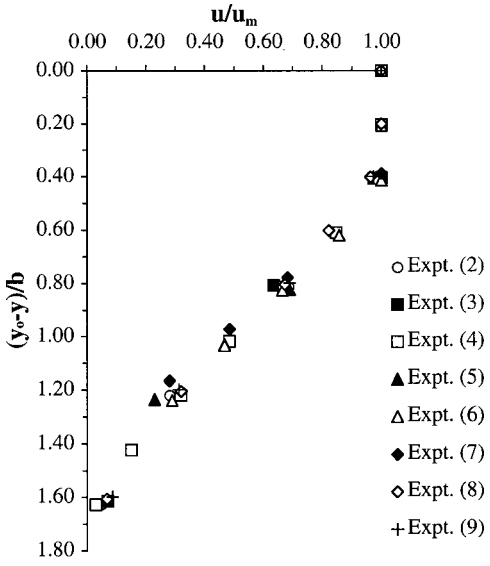

Fig. 7 Velocity distribution in partially-developed flow ($x/b_o = 6$)

A breakdown in the growth of the length scale, *b*, occurred in all the nine experiments, as shown in Fig. 10. The location of this breakdown, where the rate of growth begins to deviate from the linear growth rate of surface jets in deep tailwater, was very close to the location where the corresponding breakdown occurred in the velocity scale variation. The original growth rate of the jet half-width was 0.065, which is somewhat smaller than the value of 0.07 found by Rajaratnam and Humphries [12]. After the breakdown, the jet half-width grew at a rate which varied from 0.007–0.033.

It may be observed from Figs. 5(*a*)–(*c*) that at any *x*-station the mean velocity u_r in the reverse flow below the surface jet is almost uniform except near the bed. The variation of the mean velocity u_r with distance *x* was found to depend only on the offset ratio Z_o/b_o. The maximum value of the reverse-velocity, u_{rm}, was found to decrease as the offset ratio increased and can be described by the equation

$$\left(\frac{u_{rm}}{U_o}\right) = 11^{*}10^{-4}\left[\left(\frac{Z_o}{b_o}\right) - 175\right] \quad (r^2 = 0.95) \tag{15}$$

If x_{rm}, is the value of *x* where u_{rm} occurs, x_{rm}/b_o was found to increase with the offset ratio and can be described by the equation

$$\left(\frac{x_{rm}}{b_o}\right) = 2.65\left[\left(\frac{Z_o}{b_o}\right) + 7.65\right] \quad (r^2 = 0.99) \tag{16}$$

Equations (15) and (16) show that for an offset ratio equal to 5 and 100, the normalized maximum reverse velocity is 0.19 and 0.08, respectively, and the normalized locations of these values are about 33.50 and 285.25, respectively.

Then for every experiment, at each section where velocity observations were made, the forward flow rate *Q* and momentum flux *M* per unit width were calculated as the sum of the fluxes through thin strips (of thickness varying from 2.5–20 mm). Figure 11 shows the variation of the relative discharge Q/Q_o in the

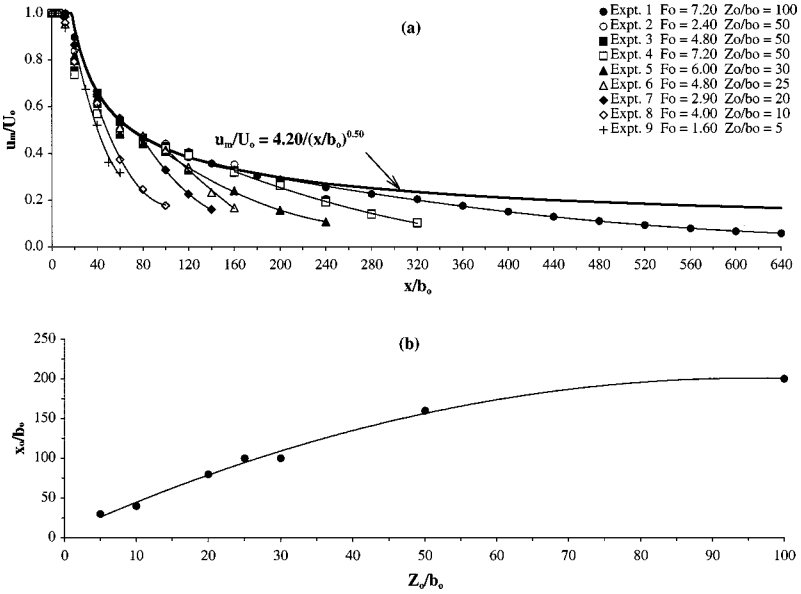

Fig. 9 (*a*) Variation of the maximum jet velocity with distance; (*b*) effect of the offset ratio on the breakdown distance

surface jet with distance x/b_o and a number of interesting observations could be made from a study of Fig. 11. First, the relative discharge increases with the relative distance at the same rate as that of the surface jet with large tailwater up to a certain section and then deviates from it, to reach eventually the value of one.

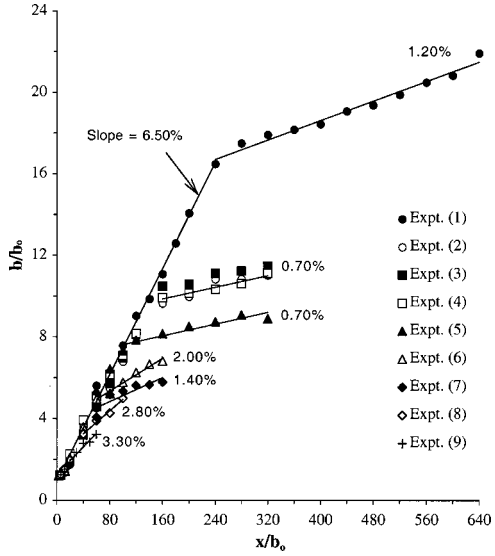

Fig. 10 Variation of the jet half-width with distance

Second, the maximum value of the relative discharge decreases from about 4 for $Z_o/b_o=100$ to 1.5 for $Z_o/b_o=5$. Third, the discharge variations in experiments 2, 3, and 4 were almost identical confirming the independency of the jet characteristics of the Froude number. If x_{Qm}, is the longitudinal distance where the relative discharge reaches the maximum value, x_{Qm}/b_o decreases from about 200 for $Z_o/b_o=100$–about 20 for $Z_o/b_o=5$. For a surface jet with very large value of Z_o/b_o, the variation of Q/Q_o with x/b_o should be independent of the offset ratio and for such a jet, $Q/Q_o=\text{constant}(x/b_o)^{0.50}$. This equation is shown plotted in Fig. 11 with the value of the constant chosen as 0.35. Detailed correlations for the various characteristics of the jet can be found in Ead [19].

It was mentioned earlier that the surface jet loses a substantial portion of the momentum flux as it travels downstream when the depth of tailwater is relatively shallow. Figure 12 shows the variation of the normalized momentum flux of the surface jet with the normalized distance from the nozzle for different offset ratios. A relatively simple equation was found to describe this variation and is written as

$$\frac{M}{M_o}=\cos\left[\left(\frac{\pi}{\varepsilon}\right)\cdot\left(\frac{x}{b_o}\right)\right] \tag{17}$$

where ε is a function of the offset ratio and is given by the equation

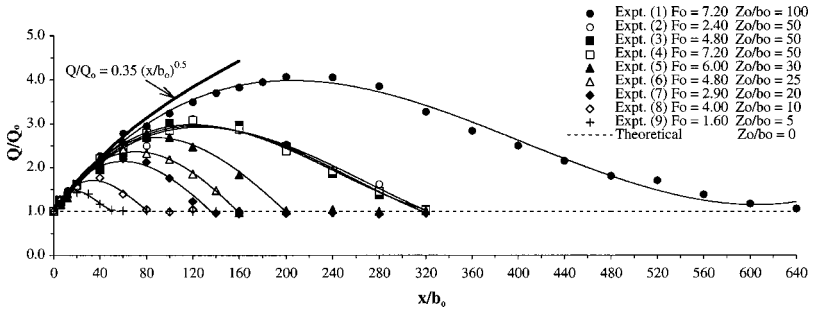

Fig. 11 Variation of the surface jet discharge with distance

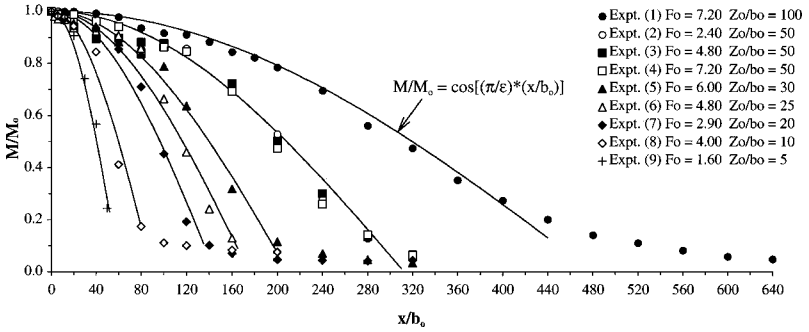

Fig. 12 Variation of the surface jet momentum flux with distance

Table 2 Measured and calculated momentum fluxes

Z_o/b_o	L_e/b_o (Measured)	M/M_o (Measured at x_r/b_o)	x_r/b_o	M/M_o (Equation 9)
100	640	0.05	640	0.01
50	320	0.06	320	0.02
30	200	0.03	320	0.03
20	140	0.05	200	0.05
10	80	0.08	160	0.08

$$\varepsilon = 8.80\left(\frac{Z_o}{b_o} + 13.40\right) \quad (r^2 = 0.98) \tag{18}$$

It can be seen also from Fig. 12 that the Froude number has no effect on the momentum-distribution profiles. It should be remembered that the great percentage of the momentum that is lost is converted into pressure in the form of a water depth increase. Table 2 shows a comparison between the measured and calculated momentum fluxes. For offset ratios equal to 100, 50, 30, 20, and 10, the measured values of M/M_o are equal to 0.05, 0.06, 0.03, 0.05, and 0.08 while the calculated values are equal to 0.01, 0.02, 0.03, 0.05, and 0.08, respectively. Also shown in Table 2 are the locations of the attachment sections and the locations where the momentum flux was measured. For offset ratios $\leqslant$30, the momentum was measured in the uniform flow region (at section I-I or further downstream) while for offset ratio equal to 100 and 50, the momentum flux was measured at the attachment section. This is the reason why the measured momentum fluxes for these two offset ratios are relatively higher than the model values. Based on the above results, it may be concluded that this model is quite efficient in calculating the momentum flux in the uniform flow region for surface jets in shallow tailwater.

Conclusions

For turbulent surface jets in shallow tailwater, it was shown theoretically and experimentally that the momentum flux is not preserved. In the theoretical study, the momentum loss and the pressure increase were evaluated at a section downstream of the line of the jet attachment to the bed. The experimental results showed that the length of the return-flow region is about 6.5 times the offset distance. The velocity profiles in the surface jet were found to be similar, in the developing as well as in the developed regions. Two stages were seen to exist in the decay of the maximum velocity. The rate of the velocity decay in the first stage was independent of the relative depth of the tailwater whereas the faster rate in the second stage depended on it. The length of the first stage of decay was directly proportional to the offset ratio. The length scale of the jet grew at a rate of 0.065 in the early stage and the rate of growth was much smaller in the second stage. The volume flux in the surface jet with limited tailwater was affected significantly. The decay of the momentum flux in the surface jet with the distance from the nozzle was observed and correlated with the offset ratio and the relative longitudinal distance. On the whole, the results from this study highlight the effect of limited tailwater depth on the behavior of plane turbulent surface jets.

Acknowledgment

This research work was performed in the T. Blench Graduate Hydraulics Laboratory of the University of Alberta, Edmonton, with the financial support of the Natural Sciences and Engineering Research Council of Canada. The authors are thankful to S. Lovell for his help in the construction and maintenance of the experimental arrangement.

Nomenclature

b = length scale for surface jet
b_o = slot width
F_o = supercritical Froude number at the slot
g = acceleration due to gravity
L_e = length of backward flow region (eddy length)
M = surface-jet momentum flux at any station
M_∞ = momentum flux in the uniform flow region
M_o = surface-jet momentum flux at the slot
Q = surface-jet discharge per unit width
Q_m = maximum value of Q
Q_o = value of Q at the slot
r^2 = correlation coefficient
R = Reynolds number
u = time-averaged velocity at any point
u_m = maximum value of u
U_o = velocity issuing from the slot
u_r = depth-averaged reverse velocity
u_{rm} = maximum value of u_r
V = uniform velocity of the flow when the jet occupies the whole depth
x = longitudinal distance measured from the wall
x_o = the distance at which the velocity and length scales breakdown
x_{Qm} = distance at which the surface-jet discharge is maximum
x_{rm} = the distance at which the maximum reverse velocity occurs
y = height above the bed
y_g = water depth at the gate$=Z_o+b_o$
y_o = the depth of flow (equals to $Z_o+b_o+\delta_x$)
Z_o = height of the lower edge of the slot above the bed
δ_x = increase of water surface elevation at a section of x distance from the wall
δ_∞ = maximum value of δ_x
ε = function of the offset ratio
ϕ = function of the offset ratio and the Froude number
γ = specific weight of water
η = Z_o/b_o
μ = dynamic viscosity
ν = kinematic viscosity
θ = δ_∞/b_o
ρ = density of water

References

[1] Albertson, M. L., Dai, Y. B., Jensen, R. A., and Rouse, H., 1950, ''Diffusion of submerged jets,'' Trans. Am. Soc. Civ. Eng., **115**, pp. 639–664.

[2] Schlichting, H., 1960, *Boundary Layer Theory*, 4th edition, McGraw-Hill, New York.

[3] Rajaratnam, N., 1976, *Turbulent Jets*, Elsevier, The Netherlands.

[4] Miller, D. R., and Comings, E. W., 1957, ''Static pressure distribution in the free turbulent jet,'' J. Fluid Mech., **3**, No. 10, pp. 1–16.

[5] Goldschmidt, V., and Eskinazi, S., 1966, ''Two phase turbulent flow in a plane jet,'' ASME J. Appl. Mech., **33**, No. 4, pp. 735–747.

[6] Heskestad, G., 1965, ''Hot wire measurements in a plane turbulent jet,'' ASME J. Appl. Mech., **32**, No. 4, pp. 721–734.

[7] Kotsovinos, N. E., 1975, ''A Study of the Entrainment and Turbulence in a Plane Turbulent Jet,'' W. M. Keck Lab. Hydr. Water Resources, Calif. Inst. Technical Report No. KH R-32.

[8] Kotsovinos, N. E., 1978, ''A note on the conservation of the axial momentum of a turbulent jet,'' J. Fluid Mech., **87**, No. 7, pp. 55–63.

[9] Schneider, W., 1985, ''Decay of momentum flux in submerged jets,'' J. Fluid Mech., **154**, No. 5, pp. 91–110.

[10] Swean, T. F. Jr., Ramberg, S. E., Plesniak, M. W., and Stewart, M. B., 1989, ''Turbulent surface jet in channel of limited depth,'' J. Hydraul. Engr., Am. Soc. Civ. Eng., **115**, No. 12, pp. 1587–1606.

[11] Vanvari, M. R., and Chu, V. H., 1974, ''Two-Dimensional Turbulent Surface Jets of Low Richardson Number,'' Technical Report No. 74-2 [FML], Fluid Mech. Lab., Dept. of Civ. Engrg. and Appl. Mech., McGill Univ., Montreal, Canada.

[12] Rajaratnam, N., and Humphries, J. A., 1984, ''Turbulent non-buoyant surface jet,'' J. Hydraul. Res., **22**, No. 2, pp. 103–115.

[13] Ead, S. A., and Rajaratnam, N., 1998, ''A double leaf gate for energy dissipation below regulators,'' J. Hydraul. Engr., Am. Soc. Civ. Eng., **124**, No. 11, pp. 1134–1145.

[14] Kline, S. J., and McClintock, F. A., 1953, ''Describing uncertainties in single-sample experiments,'' Mech. Eng. (Am. Soc. Mech. Eng.), **75**, pp. 3–8.

[15] Kline, S. J., 1985, ''The purposes of uncertainty analysis,'' ASME J. Fluids Eng., **107**, pp. 153–160.

[16] Chue, S. H., 1975, ''Pressure probes for fluid measurement,'' Prog. Aerosp. Sci. **16**, No. 2, pp. 147–223.

[17] Rajaratnam, N., 1969, ''Diffusion of a supercritical stream on a stagnant pool,'' Trans. Eng. Inst. Canada, **12**, No. A-1, pp. 1–5.

[18] Wu, S., and Rajaratnam, N., 1995, ''Effect of baffles on submerged flows,'' J. Hydraul. Div., Am. Soc. Civ. Eng., **121**, No. 9, pp. 644–652.

[19] Ead, S. A., 1998, ''Plane Turbulent Jets in Shallow Tailwater and Their Application to Energy Dissipation,'' Ph.D. thesis, University of Alberta, AB, Canada.

Espen S. Johansen
Graduate Research Assistant,
Department of Mechanical Engineering,
Texas A&M University,
College Station, TX 77843-3141

Othon K. Rediniotis
Associate Professor,
Department of Aerospace Engineering,
Texas A&M University,
College Station, TX 77843-3141

Greg Jones
Research Scientist,
Flow Modeling and Control Branch,
NASA Langley Research Center,
Hampton, VA 23681-0001

The Compressible Calibration of Miniature Multi-Hole Probes

This work presents the development of a data reduction algorithm for non-nulling, multihole pressure probes in compressible, subsonic flowfields. The algorithm is able to reduce data from any 5- or 7-hole probe and generate very accurate predictions of the velocity magnitude and direction, total and static pressures, Mach and Reynolds number and fluid properties like the density and viscosity. The algorithm utilizes a database of calibration data and a local least-squares interpolation technique. It has been tested on four novel miniature 7-hole probes that have been calibrated at NASA Langley Flow Modeling and Control Branch for the entire subsonic regime. Each of the probes had a conical tip with diameter of 1.65 mm. Excellent prediction capabilities are demonstrated with maximum errors in angle prediction less than 0.6 degrees and maximum errors in velocity prediction less than 1 percent, both with 99 percent confidence.
[DOI: 10.1115/1.1334377]

Introduction

The multi-hole pressure probe is a cost effective, robust and accurate method for determining three-dimensional velocity vector and fluid properties such as density and viscosity in any unknown flowfield. For steady-state measurements, 5- and 7-hole probes are capable of resolving flow angularities up to approximately 75 degrees and predict the flow conditions with high accuracy. The use of measurement techniques such as Laser Doppler Velocimetry (LDV) and Particle Image Velocimetry (PIV) have a number of disadvantages compared to multi-hole probes. LDV and PIV require the use of costly components, such as lasers and optical equipment. Both methods are complex and require painstaking alignment of the lasers and optical equipment to achieve accurate flow predictions, and it is often impossible to get good results outside the laboratory environment.

A calibrated probe can be inserted into an unknown flowfield and accurately predict the velocity vector by recording the port pressures and comparing them with a calibration database through a set of nondimensional coefficients. By interpolation of the recorded angles and pressure coefficients in the calibration database the velocity vector is accurately predicted. The development of a high-accuracy data reduction algorithm for 5- and 7-hole pressure probes is described herein.

Historically, a number of different calibration techniques have been utilized for multi-hole probes, all with their own advantages and difficulties. A commonly used method for hemispherical probe tips has been to apply the potential flow equations for a sphere to relate the flow angle velocity magnitude with the pressure differentials measured by the probe. Kjelgaard [1] used this technique on a hemispherical tipped 5-hole probe. The potential flow calibration method is a direct calculation of properties from a theoretical probe model. This approach is very sensitive to construction defects of the probe tip. Multi-hole probes are generally desired to be small such that the flow disturbance caused by the probe can be kept to a minimum. When minimizing the probe tip, construction imperfections become increasingly inevitable, and the relative impact of the imperfections is increasing. Thus, a theoretical model will be inaccurate because of discrepancies between the theoretical probe geometry and the physical probe. To compensate for the manufacturing defects, each probe has to be calibrated individually using extensive calibration routines. To account for compressibility and viscous effects, probes are also often calibrated over a range of Mach and Reynolds number.

Multi-hole probes are typically calibrated by inserting the probe into a flowfield of known magnitude and direction. The probe is then rotated and pitched through a range of known angles, to simulate every possible measurable velocity inclination. For each of the specific angles the pressures from all the pressure ports are recorded and stored in a database. Angle increments are typically in the range of 0.5–5 degrees yielding a database with several thousand data points, each with a pressure signature that is unique for that angle inclination and velocity magnitude. Unless the probe is physically damaged, it will keep its characteristics and only one calibration is required for the lifetime of the probe.

Several methods of comparing the measured pressures from an unknown flowfield with the calibration database have been developed. Bryer and Pankhurst [2] applied relationships derived from a set of pressure coefficients over the different flow regions of the probe. On a 5-hole probe the measuring regions on the probe were divided into one low angle regime and four high angle regimes corresponding to the center port and each of the peripheral ports, respectively. The calibration data was used to derive empirical relationships representing the relative angle inclinations and the magnitude of the velocity vector in terms of the measured pressure coefficients. Using the calibration data points, polynomial curve fits were generated that described the variation of the angle and pressure coefficients throughout the calibration domain. Rediniotis et al. [3] derived polynomial fits for calibration data for conical 7-hole probes. Further they divided the port specific regions into several sections thus increasing the number of regions for which polynomials were used to describe the calibration coefficients. They created 8 regions describing the low angle flow (where the center port senses the highest pressure) and 12 high angle regions (where one of the 6 peripheral ports senses the highest pressure). The method of subdividing the regions increased the agreement of the polynomial fit through the calibration points, but did not necessarily ensure well-behaved calibration surfaces between data points.

The polynomial fit techniques mentioned are global in nature, that is: they generate polynomial fits for relatively large sectors or regions. Though Rediniotis et al. [3] reduced the region size by subdividing the sectors, the individual regions were still large and could, depending on the density of the calibration data, contain hundreds of data points. Using polynomial fits for large regions can cause the overall prediction accuracy to decline because of the large number of calibration points the fit tries to model. Zilliac [4] calibrated conical tipped 7-hole probes for use in flowfields with high angularity. For each of the calibration points, the seven port

Contributed by the Fluids Engineering Division for publication in the JOURNAL OF FLUIDS ENGINEERING. Manuscript received by the Fluids Engineering Division February 22, 2000; revised manuscript received September 6, 2000. Associate Editor: K. Zaman.

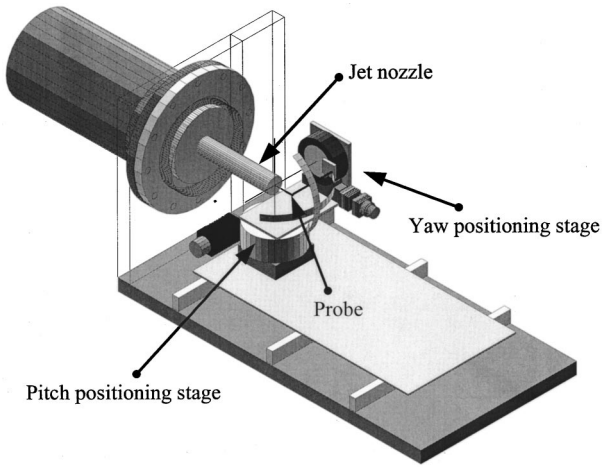

Fig. 1 Probe calibration tunnel configuration for 7-hole probe calibration

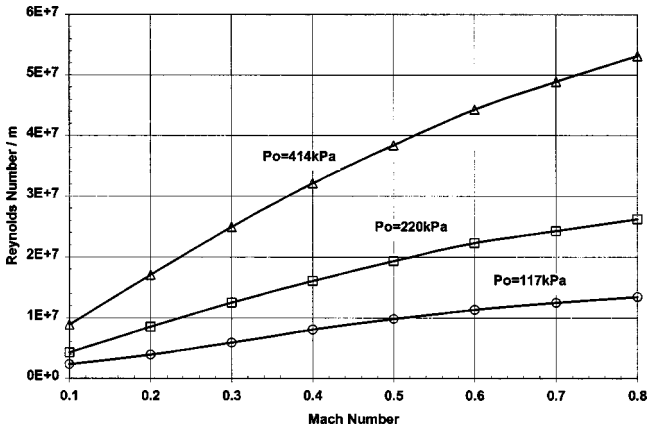

Fig. 2 Seven-hole probe test envelope, shows Mach and Reynolds number distribution in the calibration database for total pressures of 117, 220, and 414 kPa

pressures, the total pressure and the known pitch and roll angles were recorded in a database. Sets of nondimensional angle and pressure coefficients were also stored in the calibration database. For a calibrated probe in an unknown flowfield the seven port pressures were recorded and the nondimensional coefficients calculated. The sector is determined by the maximum recorded pressure and the corresponding pressure coefficients in the database were identified. Rather than using a sector wide curve-fitting approach, he used an Akima interpolation (IMSL subroutine) of the calibration data and thus approximate flow conditions were identified.

Applying the two different approaches described above, the regional polynomial fit and the quasi-local data point interpolation, a method is derived to calculate a polynomial interpolation that is local in nature. Using only a few selected data points that have similar coefficients as the measured coefficients, a low-order polynomial fit is created. Using this method the calibrated probe can be inserted into an unknown flowfield at a known location and angle relative to the test area coordinate system. The port pressures from the probe are recorded and compared with the port pressures in the calibration file through the independent nondimensional pressure coefficients. When the N most similar pressure signatures are located in the calibration database, four low-order least-squares polynomials (pitch and roll angle, total and static pressure coefficient) are created using the data points and independent coefficient values found in the calibration database. From the total and static pressure coefficients the local total and static pressures are determined. The predicted angles of the unknown flow is relative to the probe coordinate system. To get the angles relative to the test area coordinate system a simple transformation is performed using the probe mounting geometry. The velocity magnitude is calculated from the total and static pressure coefficients using perfect gas laws. Thus the velocity vector, both magnitude and direction can be found for any unknown subsonic flowfield. Four miniature 7-hole probes have been calibrated at NASA Langley Flow Modeling and Control Branch, and the data results presented herein are from the calibration and data reduction using these probes.

Experimental Facility Description

The NASA LaRC Probe Calibration Tunnel (PCT) is a variable density, pressure tunnel that can independently control Mach number, Reynolds number, and total temperature. The PCT configuration for 7-hole probe calibration is shown in Fig. 1. This open return tunnel is supplied from a 3400 kPa bottle field and exhausts into either a baffled atmospheric trench or vacuum sphere. The air is preheated with a steam heater to compensate for the gross Joule Thompson temperature effects. A secondary electric heating system is used to set the final tunnel total temperature. The interaction of the temperature and pressure systems is dependent on the mass flow through the system. The tunnel operator selects the mode of operation to maintain Mach number variations less than 1 percent of set value, tunnel pressure variations less than 0.7 kPa, and tunnel temperature variations less than 0.5°C. If at any time the tunnel conditions deviate more than these boundaries the probe data acquisition system is paused then resumed when the conditions are reestablished. The test envelope for this test is shown in Fig. 2. At each of the conditions in the test envelope the probe is calibrated in increments of 2 degrees in both the pitch and yaw angle.

Local Least-Squares Data Reduction Algorithm

Description of the Calibration Method. Multi-hole probes are generally calibrated by inserting the probe into a flowfield of known magnitude and direction. The probe is mounted on a traversing system capable of pitching and rolling the probe. While the flow magnitude and direction stays constant, the probe is pitched and rolled through a set of known angles relative to the flow direction, keeping the location of the probe tip fixed. For each of these sets of angles all of the port pressures from the probe are recorded. A typical system consists of two stepper motors that can vary the probe angles θ (pitch/cone) and φ (roll) within the ranges 0–90 and −180 to 180 degrees, respectively. Using high stepping resolutions the entire calibration domain is covered and up to several thousand discrete calibration points describe every possible angle inclination for the probe. The standalone probe positioning system is shown schematically in Fig. 3. The physical construction and geometric properties of the calibration rig will dictate the type of angles that are recorded in the calibration process. Depending on the type of probe used (whether straight, L-shaped or other) and the setup of the probe calibration facility, the relative angle between the flow and the probe tip can be defined in a number of ways. There are two typical angle conventions widely used, both applicable to the probe calibration facility shown in Fig. 1. When a straight probe is calibrated in the probe calibration facility shown in Fig. 3 the recorded angles are the cone and the roll angles. The roll angle is the roll of the probe around its longitudinal (stem) axis and the cone angle indicates the angle between the flow and the probe tip. When an L-shaped probe calibrated in the same facility the angles recorded will be the pitch and yaw angle of the probe relative to the flow. The two different systems of angles are also used to describe low angularity and high angularity flow, respectively (Gerner and Maurer

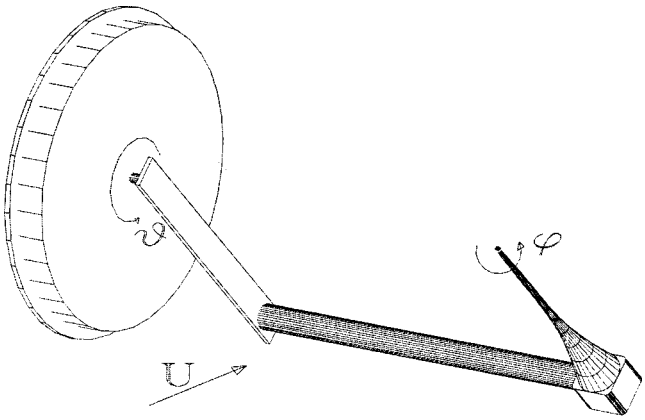

Fig. 3 Schematic drawing of typical probe positioning assembly

[5]). The four probes used in the current analysis (Fig. 4) are ''L-shaped'' and most conveniently calibrated using pitch and yaw angles (α, β). See Fig. 5.

Data Reduction Algorithm. The data reduction algorithm is designed to handle a wide variety of probe types and calibration configurations. The user creates a probe profile that describes the angle orientation for the calibrated probe, port orientation, calibration file format and the units of the data values. Thereafter the calibration files are analyzed and the nondimensional angle and pressure coefficients are calculated. The conversion from the pitch and yaw angles (used for low angularity flow) to the cone and roll angles (used for high angularity flow) is (Figs. 5 and 6):

$$\theta = \cos^{-1}(\cos\alpha\cos\beta) \tag{1}$$

$$\phi = \tan^{-1}\left(\frac{\sin\alpha}{\tan\beta}\right) \tag{2}$$

It is not necessary to use the two distinct coordinate systems internally in the calibration routine, however both the high angle notation and low angle notation will be included in this discussion for completeness. The reference to low angle and high angle coordinates systems is based on notation found in literature. The developed algorithm uses the pitch and yaw angle system internally due to simplicity and uniqueness of the angles (there is no discontinuity at 0 or 360 degrees roll).

Each sector on the face of the probe (Figs. 7 and 8) is identified by the pressure port that senses the highest pressure for all possible flow inclinations within that sector. The flow over a 5- or 7-hole probe is divided into low-angle and high-angle flow re-

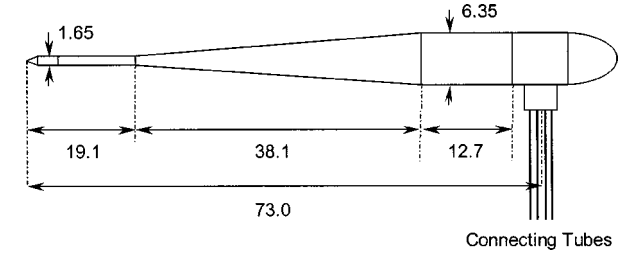

Fig. 4 Schematic of 7-hole conical tip probe used by NASA Langley (all dimensions in mm)

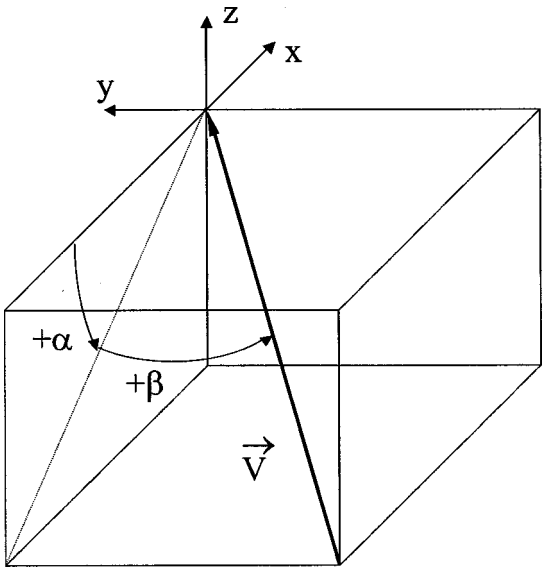

Fig. 5 Pitch and yaw angle definitions

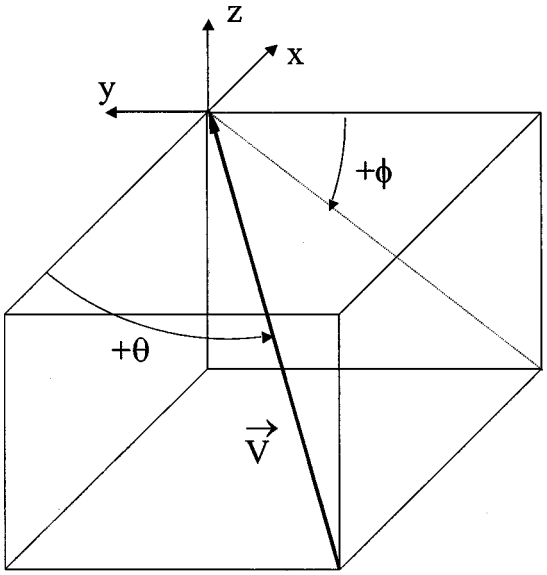

Fig. 6 Cone and roll angle definitions

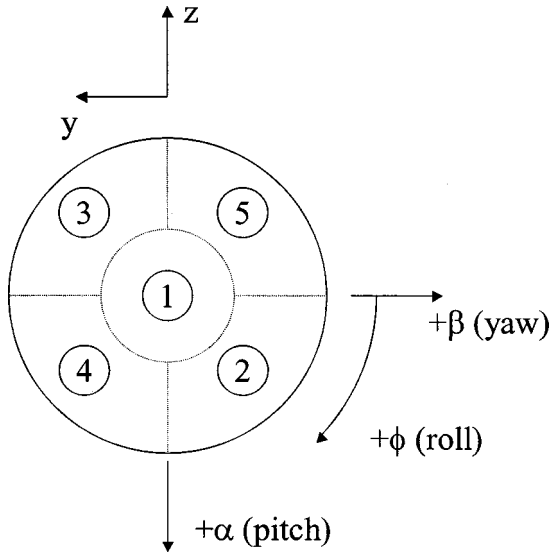

Fig. 7 Sector view of a 5-hole probe

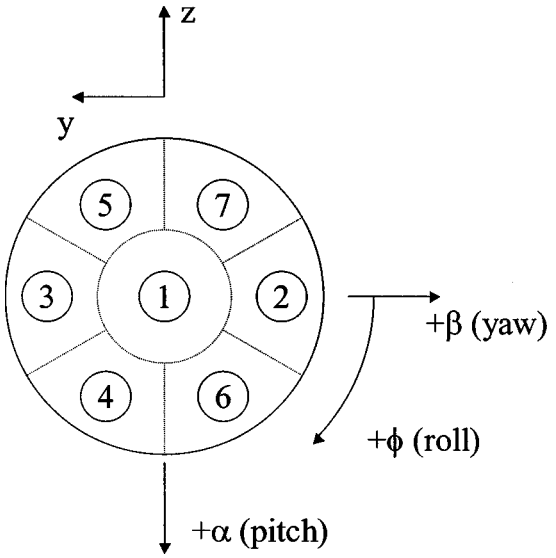

Fig. 8 Sector view of a 7-hole probe

gimes. Low-angle flow is identified when pressure port 1, the central port, has the highest pressure. High-angle flow is identified when the highest pressure is recorded in one of the peripheral ports 2–5 for a 5-hole probe and ports 2–7 for a 7-hole probe.

The local velocity vector at any measurement location can be fully characterized by four variables. For low-angle flow these variables are: pitch angle α, yaw angle β, total pressure coefficient A_t and static pressure coefficient A_s. For high-angle flow the variables are: cone angle θ, roll angle ϕ, A_t, and A_s. These quantities are determined as functions of two non-dimensional pressure-coefficients formed from the 5 or 7 measured pressures: b_α, b_β for low-angle flow and b_θ, b_ϕ for high-angle flow (Rediniotis et al., [3] Everett et al. [6]).

For a 5-hole probe in the low angle flow regime (sector 1) the following definitions are used

$$b_\alpha=\frac{(p_2+p_4-p_5-p_3)}{2\cdot q} \tag{3a}$$

$$b_\beta=\frac{(p_5+p_2-p_3-p_4)}{2\cdot q} \tag{3b}$$

$$A_t=\frac{(p_1-p_t)}{q} \tag{3c}$$

$$A_s=\frac{q}{(p_t-p_s)} \tag{3d}$$

The pseudo dynamic pressure, q, is defined as

$$q=p_1-\frac{(p_2+p_3+p_4+p_5)}{4} \tag{3e}$$

For a 5-hole probe in the high angle flow regime (sector 2–5) the following definitions are used

$$b_\theta=\frac{(p_i-p_1)}{q} \tag{4a}$$

$$b_\phi=\frac{(p^+-p^-)}{q} \tag{4b}$$

$$A_t=\frac{(p_i-p_t)}{q} \tag{4c}$$

$$A_s=\frac{(p_i-p_s)}{q} \tag{4d}$$

The pseudo dynamic pressure, q, is defined as

$$q=p_i-\frac{(p^+-p^-)}{2} \tag{4e}$$

For a 7-hole probe in the low angle flow regime (sector 1) the following definitions are used

$$b_\alpha=\frac{1}{\sqrt{3}}\cdot\frac{(p_6+p_4-p_7-p_5)}{q} \tag{5a}$$

$$b_\beta=\frac{(p_2-p_3)}{q}+\frac{(p_6+p_7-p_4-p_5)}{2\cdot q} \tag{5b}$$

$$A_t=\frac{(p_1-p_t)}{q} \tag{5c}$$

$$A_s=\frac{q}{(p_t-p_s)} \tag{5d}$$

The pseudo dynamic pressure, q, is defined as

$$q=p_1-\frac{(p_2+p_3+p_4+p_5+p_6+p_7)}{6} \tag{5e}$$

For a 7-hole probe in the high angle flow regime (sector 2–7) the following definitions are used

$$b_\theta=\frac{(p_i-p_1)}{q} \tag{6a}$$

$$b_\phi=\frac{(p^+-p^-)}{q} \tag{6b}$$

$$A_t=\frac{(p_i-p_t)}{q} \tag{6c}$$

$$A_s=\frac{q}{(p_t-p_s)} \tag{6d}$$

The pseudo dynamic pressure, q, is defined as

$$q=p_i-\frac{(p^+-p^-)}{2} \tag{6e}$$

In the previous definitions p_i is the highest measured pressure (at the ith port). Looking into the probe tip: p^+ and p^- are the pressures measured by the peripheral holes adjacent to port i, in the clockwise and counterclockwise direction respectively. The input coefficients b_α,b_θ will be referred to as $b1$ and b_β,b_ϕ will be referred to as $b2$ in the remainder of this text because many of the processes described below use both high and low angle definitions in the same manner. In the description of the local least-squares data reduction algorithm, the 7-hole definitions will be used however the same principles apply to the 5-hole probe definitions.

In the preprocessing scheme the probe calibration files are used to create a new calibration database that contains for all velocity inclinations all of the dependent and independent non-dimensional coefficients described in Eqs. (5*a*)–(6*e*). A scaling factor, $\Delta b2/\Delta b1$, is introduced to bring the input coefficient scales on the same scale and thus simplify 2D interpolation of values based on Euclidean distances. This factor is defined using the maximum and minimum values of the independent coefficients found in the calibration file, and is stored in the calibration database:

$$\frac{\Delta b2}{\Delta b1}=\frac{(b2_C)_{\max}-(b2_C)_{\min}}{(b1_C)_{\max}-(b1_C)_{\min}} \tag{7}$$

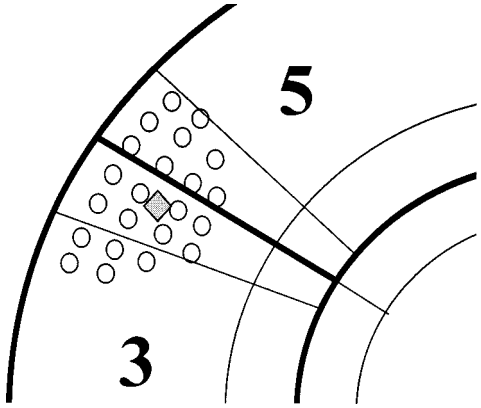

Fig. 9 Typical local distribution of calibration point

Data Reduction Procedure. The calibrated probe is ready to be used to determine the flow conditions in an unknown flowfield. When the probe is inserted into an unknown flowfield seven port pressures are recorded and the independent non-dimensional coefficients $b1$ and $b2$ are calculated. That is: b_α and b_β for low angle flow (center port senses the highest pressure) and b_θ and b_ϕ for high angle flow (one of the peripheral ports senses the highest pressure). The second step is to find the closest values of the independent coefficients in the calibration file compared to the test values. The closest data points are found in terms of Euclidean distance

$$d_j = \sqrt{\left(\frac{\Delta b2}{\Delta b1}((b1_C)_j - b1_T)\right)^2 + ((b2_C)_j - b2_T)^2} \qquad (8)$$

where the index j is the calibration point number and d_j is the Euclidean distance from the independent coefficients of the tested point $(b1_T, b2_T)$ to the scaled (using Eq. (7) independent coefficients in the calibration file $(b1_C, b2_C)_j$.

The coefficient definitions for $b1$ and $b2$ are sensitive to which sector senses the highest pressure. For a test point lying close to the boundary between sectors, a method of selecting points from both the sector with highest pressure (the primary sector) and up to two adjacent sectors is introduced. The adjacent sectors use the nondimensional coefficient definitions in the primary sector to make the independent coefficients $(b1_C, b2_C)$ from the different sectors comparable. The overlap or sub-sector size is chosen as percentage of the maximum port pressure of the test point. Each calibration point is given a three-digit number to identify the primary sector and any adjacent sectors. The algorithm will search the calibration database for calibration points that have the same or a specific combination of the three-digit code for the test point. Example: Port 3 has the maximum pressure of 10.0 and we use a multi-region overlap percentage of 25 percent. Say port #5 has a pressure of 8.0 (within 25 percent of max pressure) and all other ports have pressures less than 7.5 (not within 25 percent of max pressure).

In Fig. 9 the diamond indicates the test point and the circles indicate the calibration points. The algorithm will in this case consider calibration points from sectors 3 and 5 for the local interpolation.

It is necessary that the selected calibration points $(b1_C, b2_C)$ be distributed around the test point $(b1_T, b2_T)$ to obtain a well-behaved polynomial surface and allow for interpolation rather than extrapolation. A procedure will check if the closest calibration points in triplets form a triangle around the test point in the $b1$-$b2$ plane. The original ranking of the closest points based on Euclidean distance, d_j, can be altered to ensure that (if at all possible) the combination of the three overall closest calibration points forms a triangle around the test point. Alternatively, four sides or more could also be used.

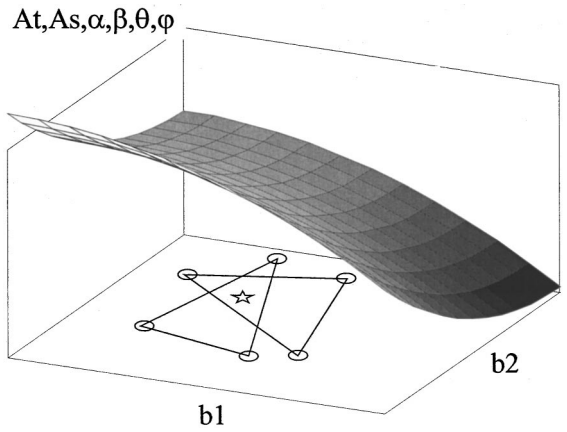

Fig. 10 Local least-squares interpolation surface with triangulation in the *b*1-*b*2 plane

In Fig. 10 the star indicates the test point $(b1_T, b2_T)$ and the circles at the corners of the triangles indicate the closest selected calibration points $(b1_C, b2_C)$ that are also checked for the triangulation requirement. The triangles are calculated by finding the direction of the vectors $\hat{n}_1$, $\hat{n}_2$ and $\hat{n}_3$. See Fig. 11.

$$\hat{n}_1 = \vec{AP} \times \vec{AC} \qquad (9a)$$

$$\hat{n}_2 = \vec{CP} \times \vec{CB} \qquad (9b)$$

$$\hat{n}_3 = \vec{BP} \times \vec{BA} \qquad (9c)$$

where P is the test point $(b1_T, b2_T)$ and A, B, C are three calibration points $(b1_C, b2_C)_j$. $\hat{n}_1$, $\hat{n}_2$ and $\hat{n}_3$ are directional vectors normal to the $b1$-$b2$ plane. If all the three vectors have the same direction the test point P is within the triangle, otherwise P is outside the triangle.

Calibration points far from the tested point (in the $b1$-$b2$ plane) are assumed to have little or no influence on the calculation. Therefore, a local interpolation scheme is used and only calibration points close to the test point are used in the evaluation. A least-squares surface fit technique is used to calculate the two flow angles and the two pressure coefficients as functions of the independent input variables.

$$\alpha = \alpha(b1, b2) \qquad (10)$$

Similarly for β, θ, ϕ, A_t, and A_s. The selected closest and triangulation-checked calibration points (minimum number determined by the order of the polynomial surface) are used to calculate four separate interpolation surfaces. Each surface is calculated using a polynomial with coefficients calculated by a least-squares approximation method. For a first-order surface the following polynomial is used

$$f(b1, b2) = a_0 + a_1 \cdot b1 + a_2 \cdot b2 \qquad (11)$$

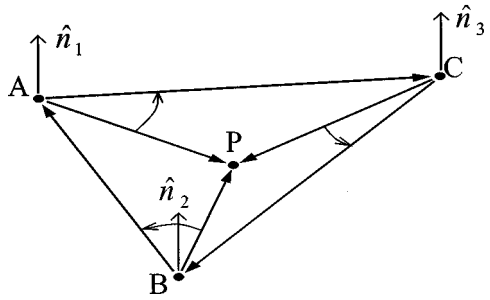

Fig. 11 Triangulation scheme in the *b*1-*b*2 plane

where f can be any of the dependent variables α, β, θ, ϕ, A_t, A_s and a_0, a_1, a_2 are the least-squares polynomial coefficients. The coefficients are calculated using the least-squares criterion described by

$$S=\sum_{i=1}^{N}\sigma_i^2=\min \tag{12}$$

where N is the number of calibration points used in the approximation and σ_i is the distance from each separate calibration point (e.g., $(\alpha_C, b1_C, b2_C)_j$) to the closest point on the calculated surface. The procedure will find the polynomial coefficients (a_0, a_1, and a_2) that minimize the sum of the square of the distances, σ_i. By entering the measured input coefficients ($b1_T, b2_T$) into the calculated function $f(b1,b2)$, interpolated values for α_T, β_T, θ_T, ϕ_T, $(A_t)_T$ and $(A_s)_T$ are obtained. The angle or pressure coefficient surfaces for the probe is assumed to be smooth locally and not exhibit any large gradients or discontinuities. The local least-squares method generates a surface that does not directly go through all the calibration data points, but is rather an average surface. A standard polynomial surface fit can exhibit large fluctuations because the surface is required to go through all the data points. The least-squares surface will moderate the effect of a badly selected or measured point and create the best overall surface fit.

The angles (α_T, β_T) for low angle flow, or (θ_T, ϕ_T) for high-angle flow, and the pressure coefficients $(A_t)_T$, $(A_s)_T$ are given directly by the least-squares interpolation. The total pressure and static pressure are calculated from the nondimensional pressure coefficients $(A_t)_T$, $(A_s)_T$

$$p_t=p_i-(A_t)_T\cdot q_T \tag{13a}$$

$$p_s=p_t-\frac{q_T}{(A_s)_T} \tag{13b}$$

In Eqs. (13*a*) and (13*b*) the pressure p_i is the port with maximum pressure and q_T is the pseudo dynamic pressure at the test point (from Eq. (8*e*) or (9e)). The velocity magnitude and the flow conditions are calculated using adiabatic, perfect gas relationships for air [7]. Mach number from total pressure and static pressure:

$$M=\sqrt{5\cdot\left(\left(\frac{p_t}{p_s}\right)^{2/7}-1\right)} \tag{14}$$

Temperature and velocity magnitude are calculated from

$$T=\frac{T_t}{(1+M^2/5)} \tag{15}$$

$$U=M\cdot\sqrt{\gamma\cdot R\cdot T} \tag{16}$$

The Cartesian velocity components are calculated from the following equations

$$u=U\cdot\cos\alpha\cdot\cos\beta \tag{17a}$$

$$v=U\cdot\sin\beta \tag{17b}$$

$$w=U\cdot\sin\alpha\cdot\cos\beta \tag{17c}$$

The viscosity is calculated from the Sutherland law:

$$\mu=\mu_0\cdot\left(\frac{T}{T_0}\right)^{3/2}\cdot\left(\frac{T_0+S}{T+S}\right) \tag{18}$$

where S is the Sutherland constant. For air: $S=111\,\mathrm{K}$, $\mu_0=1.1716E-5\,\mathrm{m^2/s}$ and $T_0=273\,\mathrm{K}$. Reynolds number per unit length

$$\frac{\mathrm{Re}}{1}=\frac{U\cdot\rho}{\mu} \tag{19}$$

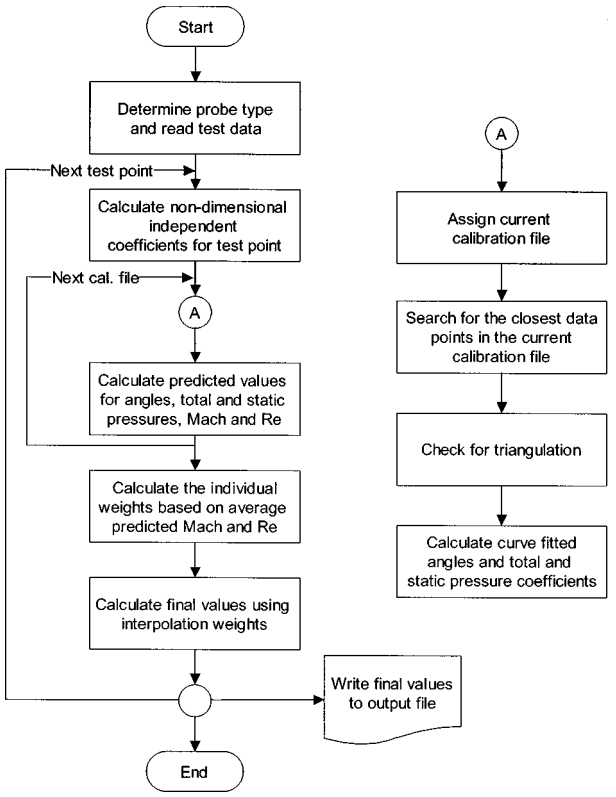

Fig. 12 Data reduction process

The data reduction procedure described above is repeated for each separate test data point. The flowchart in Fig. 12 shows an overview of the process.

Compressibility and Viscosity Effects

The nondimensional coefficients have a slight dependence on Mach and Reynolds number (Krause and Dudzinski [8], Ainsworth et al. [9], Dominy and Hodson [10]. Since the dependence is small, the pressures measured by the probe in an unknown flowfield can be used with a calibration file from any Mach and Reynolds number to estimate the angles within a few degrees and the velocity magnitude within a few percent. Approximate Mach and Reynolds number for the flow is also obtained. Reducing test data with a calibration file from the same flow conditions will yield the most accurate predictions, thus to obtain high prediction accuracy throughout the entire subsonic regime, it is necessary to calibrate the probe over a wide range of Mach and Reynolds number. By reducing test data from an unknown flowfield with a range of calibration files, it is possible to find the best-predicted flow conditions by proper interpolation between the results from the separate files. Everett et al. [6] introduced a compressibility coefficient to correct for the Mach number effects. A similar approach was attempted using a compressibility coefficient in conjunction with the interpolation based on the dependent coefficients $b1$ and $b2$. No consistent prediction accuracy was achieved with this method. Thus, in the luxury of having the probes calibrated at a wide range of Mach and Reynolds numbers in small increments, a data reduction based solely on the dependent coefficients $b1$ and $b2$ was chosen. The four probes were calibrated at Mach numbers equal 0.1–0.8, with total pressure (P_t) at 117, 220 and 414 kPa which yields a Reynolds number range from $2.5\cdot10^6\,\mathrm{m^{-1}}$ to $52\cdot10^6\,\mathrm{m^{-1}}$. Each of the dotted lines represents a different wind tunnel total pressure during the calibration (Fig. 2).

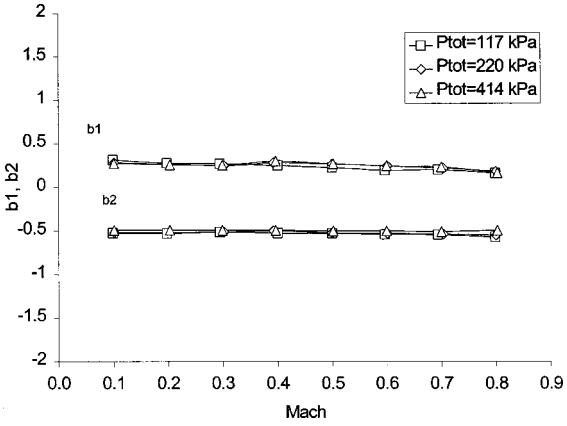

Fig. 13 High angle *b*1 and *b*2 coefficients versus Mach number for total pressures of 117, 220 and 414 kPa

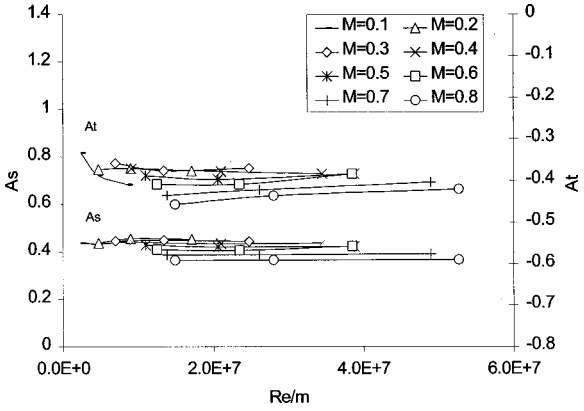

Fig. 16 High angle A_t and A_s coefficients versus Reynolds/m at discrete Mach numbers

The nondimensional coefficients dependence on Mach and Reynolds number are shown in Figs. 13–16. The observed ranges of values for the independent angle coefficients, $b1$ and $b2$, are 0 to 1.7 and -2 to 2, respectively, and the ranges for the dependent pressure coefficients, A_t and A_s, are -0.8 to 0 and 0 to 1.4, respectively. The scales for the nondimensional coefficients are in the figures adjusted to these ranges. The specific calibration point analyzed has cone angle of 25 degrees and a roll angle of 84 degrees, however similar plots can be obtained at any angle within the measurable regime.

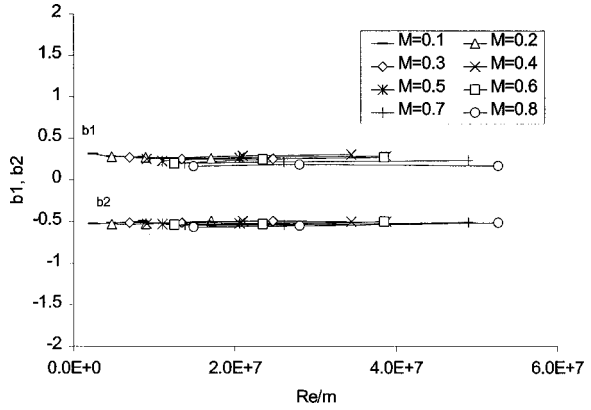

Fig. 14 High angle *b*1 and *b*2 coefficients versus Reynolds/m at discrete Mach number

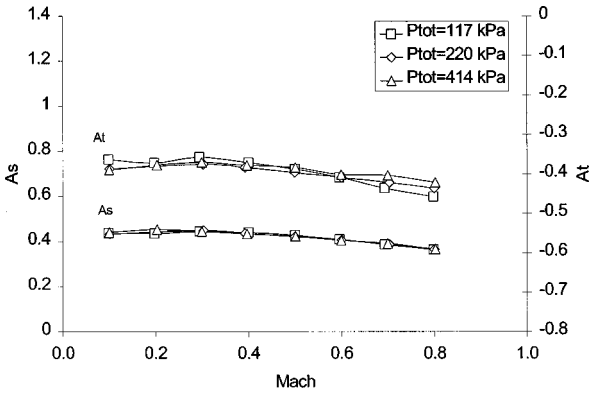

Fig. 15 High angle A_t and A_s coefficients versus Mach number for total pressures of 117, 220, and 414 kPa

The algorithm creates a probe specific database using any number of calibration files, and will reduce a test point from an unknown flowfield with all of the calibration files provided in the database and store the predicted values from each of these. Average predicted Mach and Reynolds number are calculated and the differences between these and the Mach and Reynolds number in the individual calibration files are used to calculate an interpolation function. This function will give the final results based on interpolation between the predicted values from the closest files in terms of Mach and Reynolds number. The interpolation function is given by

$$w_i = \frac{\prod_{i=1}^{N} d_{j\neq i}^{P}}{\sum_{k=1}^{N}\prod_{j=1}^{N} d_{j\neq k}^{P}} \tag{20a}$$

where N is the number of files used in the interpolation, w is the individual weights for each of the N files, d_j is the Euclidean distance between the average predicted Mach and Reynolds number and the Mach and Reynolds in each of the separate files. P is an exponent to increase the sensitivity and enforce mostly use of the files that are closest in terms of the Euclidean distance. The final values are calculated by using the individual weights multiplied with the predicted values from each of the closest N files

$$f_{\text{final}} = \sum_{i=1}^{N} (w_i \cdot f_i) \tag{20b}$$

where f_{final} is any of the final estimates for the angles and pressures, w_i is the individual weights and f_i is the predicted quantities from each of the N closest files.

Uncertainty Analysis

Overview of Uncertainty Analysis. All measured values have errors, all instruments have errors and all calculations using experimental data have errors. Error is defined as the difference between the measured value and the true value. It is often necessary to estimate the error to be able to determine the confidence that the measured or predicted result is within a specified range of the true value. The expected errors from a measurement or prediction will be referred to as the uncertainty and can be estimated in several ways. Example: A calculation, $Z(X,Y)$, depends on two measurements, X and Y, that have associated random errors. The maximum values of the two variables due to these uncertainties are X max and Y max, respectively. Thus, there is a possibility that the result from the calculation will be $Z(X\,\text{max}, Y\,\text{max})$, however it is very unlikely that the maximum errors of the two vari-

Table 1 Determining the uncertainties of multi-hole pressure probe measurements

Procedures
Investigate all sources of error
A combined analytical and numerical analysis of how uncertainties in the pressure measurements propagate through the algorithm
Evaluation of the LLS surface fitting procedure
Evaluating uncertainty (standard deviation) of the algorithm using data verification test files

ables will occur at the same time. A more realistic measure for the uncertainty is the most probable error [11]. In statistical calculations the standard deviation can be a measure for the most probable error or uncertainty. The standard deviation is for multiple samples defined as

$$\sigma = \sqrt{\frac{1}{N}\sum_{i=1}^{N}(x_i - \overline{x})^2} \tag{21}$$

where N is the number of samples, x_i is the individual sample estimate, $\overline{x}$ is the average of all the estimates and σ is the standard deviation of the data. If the measurement errors have a near Gaussian distribution, the probability that the measurement is within one standard deviation value ($\overline{x} \pm \sigma$) is approximately 0.67 or 67 percent. This probability will in many cases be too low for an experimenter to have any confidence in the data. By increasing the uncertainty of the error to two times the standard deviation ($\overline{x} \pm 2\sigma$) a probability of 95 percent is achieved. It is important to get a reasonable estimate for the uncertainty, since it can be just as unfortunate to overestimate the uncertainty as it is to underestimate the uncertainty. An underestimation can cause false security, while an overestimation can discard good data as being bad. For many engineering purposes one standard deviation will describe the uncertainty in the data and measurements that fall outside of three standard deviations are considered unacceptable and should be discarded. In multiple-sample theory where a large number of data is recorded under the same conditions, the uncertainty is reported as the mean value $\pm$ the standard deviation with given odds or probability. However, in the case of finding the uncertainty of pressure probe data, only one recording is done under a particular set of conditions. The uncertainty of such systems can be estimated using single-sample theory and is reported as the uncertainty with odds only (Moffat [12]).

Uncertainty Analysis of Local Least-Squares Algorithm. To find the uncertainties of the local least-squares data reduction algorithm an extensive analytical and numerical analysis was performed. The procedures to find and determine the uncertainties of the algorithm are shown in Table 1.

Attention should also be directed to the problem of bias or systematic error, which is error that is roughly constant throughout the sampling of the data. Such errors can be due to errors in the reading of the reference manometer, hysteresis and temperature drift of pressure sensors and probe positioning and measurement. Bias errors are ignored in this analysis because the experimenter should identify them and they can be accounted for. Errors due to nonlinearity and the averaged sequential recording of pressures are summed up in an uncertainty in the pressure reading. The errors analyzed are errors due to the data reduction technique and the interpolation routines Analysis of Error Propagation through the Algorithm

There are two different ways to analyze the uncertainty, the worst-case approach or the constant odds approach. The uncertainty of a function R, that depends on a number of independent variables x_i, with associated uncertainty δx_i, can be described as:

Worst case:

Table 2 Low angle perturbed coefficient expressions

Expressions for low angle flow
$\delta b_\alpha(p_1..p_7, \delta p_1..\delta p_7, p_{\text{static}}, \delta p_{\text{static}}, p_{\text{total}}, \delta p_{\text{total}})$
$\delta b_\beta(p_1..p_7, \delta p_1..\delta p_7, p_{\text{static}}, \delta p_{\text{static}}, p_{\text{total}}, \delta p_{\text{total}})$
$\delta A_{t\ \text{low angle}}(p_1..p_7, \delta p_1..\delta p_7, p_{\text{static}}, \delta p_{\text{static}}, p_{\text{total}}, \delta p_{\text{total}})$
$\delta A_{s\ \text{low angle}}(p_1..p_7, \delta p_1..\delta p_7, p_{\text{static}}, \delta p_{\text{static}}, p_{\text{total}}, \delta p_{\text{total}})$

$$\delta R = \left|\frac{\partial R}{\partial x_1}\delta x_1\right| + \left|\frac{\partial R}{\partial x_2}\delta x_2\right| + \cdots + \left|\frac{\partial R}{\partial x_n}\delta x_n\right| \tag{22a}$$

Constant odds:

$$\delta R = \left[\left(\frac{\partial R}{\partial x_1}\delta x_1\right)^2 + \left(\frac{\partial R}{\partial x_2}\delta x_2\right)^2 + \cdots + \left(\frac{\partial R}{\partial x_n}\delta x_n\right)^2\right]^{1/2} \tag{22b}$$

The general form for constant odds uncertainty predictions was shown by Kline and McClintock [13] to estimate the uncertainty in R with good accuracy. The constant odds uncertainty prediction requires that each of the x_i's are independent variables and that they have a Gaussian error distribution.

Each of the coefficients ($R = b_\alpha$, b_β, b_θ, b_ϕ, A_t, and A_s) were differentiated with respect to all the pressure terms ($x_i = p_i$). Eight expressions are derived from the constant odds equation shown above (Wenger and Devenport [14]). Perturbed values for each of the pressure dependent coefficients are found from (Tables 2 and 3):

These expressions are used to create a modified version of the local least-squares data reduction algorithm. It is assumed that the error introduced by the pressure transducer is normally distributed. To simulate perturbed pressure values a random Gaussian distribution of pressure perturbations is created. The data reduction algorithm uses six local calibration data points to estimate one test point. The 7 port pressures from each of these points are perturbed using random values from the perturbation file. Also, for each calibration data point the four non-dimensional coefficients: b_1, b_2, A_t, and A_s are calculated. A second set of perturbed coefficients is calculated from the expressions derived above (Tables 2 and 3) using random perturbation pressure values. All the six calibration data points are perturbed in this manner, resulting in randomly perturbed non-dimensional coefficients and interpolation surfaces. The reduction is executed and the results from the perturbed analysis are compared to the results from an unperturbed analysis. The uncertainty is defined as one standard deviation of the difference between the results obtained from the unperturbed surface and the results from the perturbed surface (Table 4).

Surface Fit Evaluation. An estimation of the errors induced from using a linear least-squares interpolation technique was per-

Table 3 High angle perturbed coefficient expressions

Expressions for high angle flow
$\delta b_\theta(p_1..p_7, \delta p_1..\delta p_7, p_{\text{static}}, \delta p_{\text{static}}, p_{\text{total}}, \delta p_{\text{total}})$
$\delta b_\phi(p_1..p_7, \delta p_1..\delta p_7, p_{\text{static}}, \delta p_{\text{static}}, p_{\text{total}}, \delta p_{\text{total}})$
$\delta A_{t\ \text{high angle}}(p_1..p_7, \delta p_1..\delta p_7, p_{\text{static}}, \delta p_{\text{static}}, p_{\text{total}}, \delta p_{\text{total}})$
$\delta A_{s\ \text{high angle}}(p_1..p_7, \delta p_1..\delta p_7, p_{\text{static}}, \delta p_{\text{static}}, p_{\text{total}}, \delta p_{\text{total}})$

Table 4 Calculated standard deviation using the analytical constant odds approach

Data	Standard deviation	Units
Pitch/Cone	0.1369	[deg]
Yaw/Roll	0.1972	[deg]
Velocity	0.3212	[%]

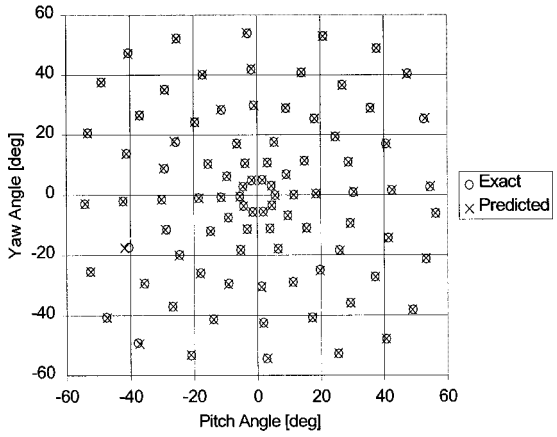

Fig. 17 Exact and predicted pitch and yaw angles for test verification data

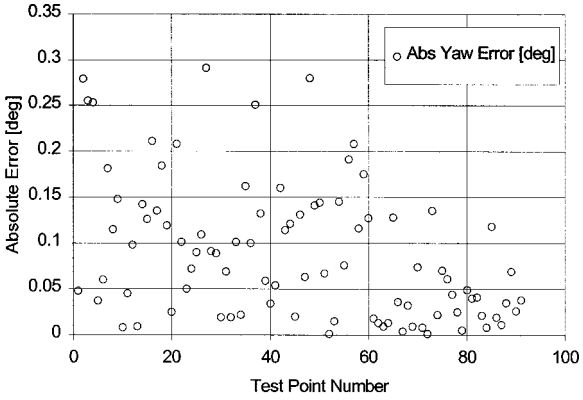

Fig. 19 Absolute yaw angle error in degrees. Mean error: 0.0888, max error: 0.291, standard deviation: 0.0742

formed. The surface fitting procedure in many conventional data reduction algorithms is found to be one of the greatest sources of error. A global surface fitting procedure will complicate the structure of the surface because the probe tip surface on a small probe usually contains irregularities that will be reflected in the measured pressures and non-dimensional coefficients. Even smaller sector sized surfaces have these problems when trying to fit an interpolation surface to all calibration points in that sector. A local least-squares approach can be more accurate, because the surface is only covering a small segment of the probe and uses few data points. A linear local least-squares surface can create a very good approximation to the actual data assumed that there is dense grid of calibration data.

A procedure to validate the accuracy of the LLS routine was performed using a known model surface. For each of the separate sectors on a 7-hole probe a surface was created using all the calibration data points belonging to that sector. A second-order polynomial surface was created using surface fitting software. The resultant error (R^2) of approximating a second order surface over all the calibration data points in each sector was reasonably good. The second-order surface will now be regarded as a model surface because it contains similar characteristics as would an actual calibration surface. Because the polynomial expression is known for the surface, a grid of angle coefficients is created with corresponding exact values for the angles. The new grid is created to have similar density and distribution of data points as the actual surface. For the created range of test points the exact values for the pressure coefficients and the angles are known through the four model surface polynomials. The new test file is reduced using a modified version of the LLS algorithm that only reads the test data coefficients and finds the closest (by Euclidean distance) six coefficients in the calibration file and interpolates the value for the test data angle. The error is calculated as the difference of the LLS calculated angle and the exact angle calculated by the polynomial expression for the model surface. The data reduction also selects which calibration points to use in the data reduction such that this method can also serve as a measure for the quality of the data point search routine.

As described the surface fit is most probably not a smooth second-order polynomial surface over an entire sector and the surface might exhibit larger curvature locally. Several ''worst case'' examples were analyzed by fitting a higher curvature surface through fewer data points. However, the results from this analysis found that the contributing errors due to the local least-squares surface fit are negligible. Discrepancies between the fitted surface and the model surface were on the order of 10^{-5} degrees for angle calculations and 10^{-3} percent for velocity calculations.

Evaluating the LLS Algorithm Using Test Verification Files. When calibrating multi-hole pressure probes, a common practice is to record a separate test file using noncoinciding data points. The pressures and the angles for the test file are recorded in the same sequence as the calibration data file such that it can be used as a verification of the quality of the calibration and the data reduction algorithm. Several verification files from probes calibrated in laboratory conditions at NASA Langley are used to give a measure of the uncertainties expected when reducing an actual test data file. The following error histograms were calculated for Probe 1 using a data verification test file. The data verification file is recorded at Mach number 0.5 and a Reynolds number of about

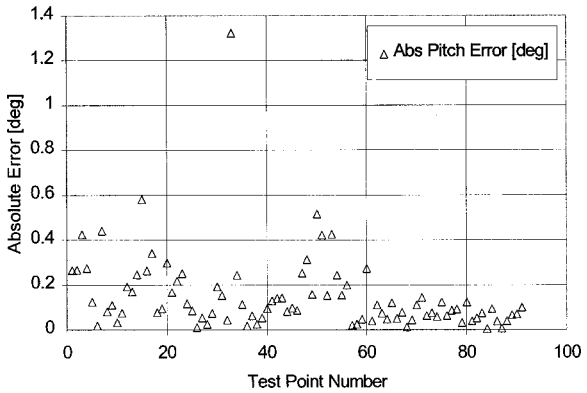

Fig. 18 Absolute pitch angle error in degrees. Mean error: 0.151, max error: 1.32, standard deviation: 0.173

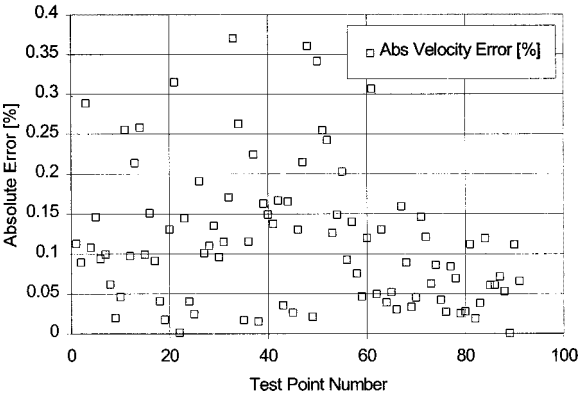

Fig. 20 Absolute velocity error in percent. Mean error: 0.116, max error: 0.370, standard deviation: 0.0862

Table 5 Average standard deviations of a number of experimental test verification files

Data	Standard deviation	Units
Pitch/Cone	0.1465	[deg]
Yaw/Roll	0.1855	[deg]
Velocity	0.3426	[%]

$11 \cdot 10^6\ \mathrm{m}^{-1}$. See also Fig. 2 for the range of calibration files (in terms of Mach and Reynolds number) used in the data reduction.

The quality of the calibration and the data reduction is measured using the discrepancies between the angles and velocity in the verification file and the predicted angles and velocity (Figs. 17–20).

As seen from Tables 4 and 5 there is good correspondence between the calculated uncertainty and the measurement errors from the data verification files.

Conclusions

The multi-hole pressure probe is a cost effective, robust and accurate method for determining three-dimensional velocity vector and fluid properties such as density and viscosity in any unknown subsonic air flowfield. For steady-state measurements, 5- and 7-hole probes are capable of resolving flow angularities up to 75 degrees and successfully predict flow conditions with high accuracy.

The nondimensional angle and pressure coefficients used internally in the data reduction algorithm have a very slight dependence on Mach and Reynolds number. A test point at a certain Mach and Reynolds number can be reduced with calibration data taken at completely different Mach and Reynolds number and still predict the velocity vector, both magnitude and direction with reasonable accuracy. However reducing test data with a calibration file at the same Mach and Reynolds number will yield the most accurate predictions. Thus to obtain high prediction accuracy throughout the entire subsonic regime, it is necessary to calibrate the probe at a wide range of Mach and Reynolds number. By reducing test data from any unknown subsonic flowfield with a range of calibration files, it is possible to find the best-predicted flow conditions by interpolation between the results from the separate files.

An uncertainty analysis of the expected errors from 7-hole probe measurements was performed. Three different approaches to determine the uncertainty were utilized: Evaluation of the LLS surface fitting procedure. A combined analytical and numerical analysis of how uncertainties in the pressure measurements propagate through the algorithm and evaluation of the uncertainty of the algorithm using data verification files. The results from the surface fit analysis found that the contributing errors due to the local least-squares surface fit are negligible. Discrepancies between the fitted surface and the model surface were on the order of 10^{-5} degrees for angle calculations and 10^{-3} percent for velocity calculations. Both the analysis of the error propagation through the algorithm and the uncertainty evaluation with test verification files gave similar results. Angles can be predicted to within 0.6 degrees and velocity can be predicted to within 1.0 percent both with 99 percent confidence.

Nomenclature

a = polynomial constant calculated by least-squares method
A_t, A_s = nondimensional dependent pressure coefficient
b = nondimensional independent input coefficient
$b1$ = nondimensional independent pitch or cone coefficient
$b2$ = nondimensional independent yaw or roll coefficient
C_p = nondimensional pressure coefficient
d = Euclidean distance from calibration point to test point
l = length
M = Mach number
$\hat{n}$ = directional vector
N = number of calibration points used by local least-squares approximation
p = pressure
q = pseudo dynamic pressure
R = universal gas constant
Re = Reynolds number
S = local least-squares residual
T = temperature
U = velocity magnitude
u, v, w = Cartesian velocity components
w = interpolation weight
$\overline{x}$ = average predicted value
α = pitch angle
β = yaw angle
ϕ = roll angle
θ = cone angle
λ = offset angle for port orientation
ρ = density
σ = distance from calibration point to the least-squares surface
μ = viscosity, Gaussian distribution bias

Subscripts

α, β = pitch, yaw
θ, ϕ = cone, roll
C = calibration
compr = compressible
i = port with maximum pressure
j = calibration point number in calibration database
s = static
t = total
T = test

Superscripts

$+$ = in the clockwise direction looking into the probe
$-$ = in the counter-clockwise direction looking into the probe

Abbreviations

LDV = Laser Doppler Velocimetry
LLS = Local Least-Squares
PIV = Particle Image Velocimetry
PCT = Probe Calibration Tunnel

References

[1] Kjelgaard, S. O., 1988, ''Theoretical Derivation and Calibration Technique of a Hemispherical-Tipped, Five-Hole Probe,'' NASA Technical Memorandum 4047.
[2] Bryer, D. W., and Pankhurst, R. C., 1971, ''Pressure-Probe Methods for Determining Wind Speed and Flow Direction,'' Her Majesty's Stationary Office/National Physics Laboratory, The Campfield Press, St. Albans.
[3] Rediniotis, O. K., Hoang, N. T., and Telionis, D. P., 1993, ''The Seven-Hole Probe: Its Calibration and Use,'' Forum on Instructional Fluid Dynamics Experiments, **152**, June, pp. 21–26.
[4] Zilliac, G. G., 1989, ''Calibration of Seven-Hole Probes For Use in Fluid Flows With Large Angularity,'' NASA Technical Memorandum 102200, Dec.
[5] Gerner, A. A., and Maurer, C. L., 1981, ''Calibration of Seven-Hole Probes Suitable for High Angles in Subsonic Compressible Flows,'' United States Air Force Academy-TR-81-4.
[6] Everett, K. N., Gerner, A. A., and Durston, D. A., 1983, ''Seven-Hole Cone Probes for High Angle Flow Measurements: Theory and Calibration,'' AIAA J. **21**, No. 7, July, pp 992–998.
[7] Ames Research Staff, 1953, ''Equations, Tables and Charts for Compressible Flow,'' NACA Report 1135.
[8] Krause, L. K., and Dudzinski, T. J., 1969, ''Flow Direction Measurement with Fixed Position Probes in Subsonic Flow over a Range of Reynolds Number,'' Proceedings for 15th International Aerospace Symposium, Las Vegas, Nevada, pp. 217–223.
[9] Ainsworth, R. W., Allen, J. L., and Batt, J. J., 1995, ''The Development of

Fast Response Aerodynamic Probes for Flow Measurement in Turbomachinery,'' ASME J. Turbomach. **117**, pp 625–634.
[10] Dominy, R. G., and Hodson, H. P., 1993, ''An Investigation of Factors Influencing the Calibration of Five-Hole Probes for Three Dimensional Flow Measurement,'' ASME J. Turbomach. **115**, July, pp. 513–519.
[11] ''Assessment of Wind Tunnel Data Uncertainty,'' 1995, AIAA Standard S-071-1995.
[12] Moffat, R. J., 1982, ''Contributions to the Theory of Single-Sample Uncertainty Analysis,'' ASME J. Fluids Eng. **104**, June, pp. 250–260.
[13] Kline, S. J., and McClintock, F. A., 1953, ''Describing Uncertainties in Single-Sample Experiments,'' Mech. Eng. (Am. Soc. Mech. Eng.) **75**, Jan., pp 3–88.
[14] Wenger, C., and Devenport, W., 1998, ''A Seven-Hole Pressure Probe Measurement System and Calibration Method Utilizing Error Tables.'' AIAA Paper No. 98-0202, 36th AIAA Aerospace Sciences Meeting, Reno, Nevada, Jan.

Investigation on Turbulent Expansion-Corner Flow With Shock Impingement

Kung-Ming Chung
Associate Research Fellow,
Aerospace Science
and Technology Research Center,
National Cheng Kung University,
711, Tainan, Taiwan, ROC

Experiments are performed to study the interaction of an impinging shock wave and an expansion fan in a Mach 1.280 flow. The expansion fan neutralizes the pressure rise induced by the impinging shock wave. The mean surface static pressure shows a linear combination of the effect of both perturbations. Surface pressure fluctuations, which are associated with the characteristics of the perturbed boundary layer, indicate a transitional behavior. This is related to a nonlinear phenomenon arising the simultaneous action of the impinging shock wave and the expansion fan. The level of downstream pressure fluctuation depends on the overall inviscid interaction strength.
[DOI: 10.1115/1.1343084]

1 Introduction

There has been considerable research in compressible turbulent boundary layers including shock wave and turbulent boundary layer interactions (e.g., Morris et al. [1]; Zheltovodov [2], Bur et al. [3]; Unalmis and Dolling, [4]; Gibson et al. [5]) and Prandtl-Meyer expansion flows (e.g., Adamson [6], Bloy [7], Goldfeld [8], Chung and Lu [9]). However, there are few studies on the effect of an expansion corner on a shock wave interaction with a boundary layer (Chew [10], Hawbolt et al. [11]; Chung and Lu [12]; White and Ault [13]). Another way of viewing the effects of shocks and expansions is in terms of the rates of strain imposed on the turbulent flow (Bradshaw [14]). Examples of the extra rates of strain include longitudinal curvature, bulk compression, longitudinal pressure gradient and streamline divergence. Previous studies (Smits et al. [15], Smits and Wood [16]; Degani and Smits [17], Smith and Smits [18], Neves and Moin [19]) are mainly concerned with a single perturbation on the boundary layer, and simultaneous influence of different extra rates of strain needs to be further studied. Bradshaw further noted that the effect of multiple perturbations may be not just the simple summation of the effects of the individual perturbations.

In this investigation, experiments are conducted to study the behavior of a supersonic turbulent boundary layer subjected to an impinging shock wave and an expansion corner, Fig. 1. Surface pressure measurements and limited Pitot pressure surveys are performed. Although the mean surface static pressure distributions reveal little about the flow away from the model surface, they are footprint signatures of the flow. In addition, surface pressure fluctuations are related to the volume integral over the whole turbulent boundary layer, and the amplitude is coupled with the local skin friction (Kistler and Chen [20]). Distributions of surface pressure fluctuation can indicate regions of flow unsteadiness induced by multiple perturbations.

2 Experiment. Experiments are performed in the ASTRC/NCKU transonic wind tunnel. The incoming boundary layer is developed naturally along a flat plate with an expansion corner located 500 mm from the leading edge. Expansion corner angle α is 5, 10, or 15 deg, while shock wave (wedge angle $\beta=1$, 3, or 5 deg) impinges at the corner. In the present experiments, expansion-corner angle is equal to or larger than the angle of shock generator ($\alpha \geqslant \beta$). The physical boundary condition requires that the flow would be parallel to the wall downstream of corner. Thus there would be no inviscid shock reflection under present test conditions.

2.1 Transonic Wind Tunnel. ASTRC/NCKU transonic wind tunnel is a blowdown type. Its operating Mach number ranges from 0.2–1.4. A detailed description of the tunnel is given by Chung [21]. Major components of the facility include compressors, air dryers, cooling water system, storage tanks and the tunnel. The dew point of high-pressure air through the dryers is maintained at -40°C under normal operation conditions. A rotary perforated sleeve valve controls the stagnation pressure (p_0). The high-pressure air is discharged into the stilling chamber through flow spreaders. Inside the stilling chamber, acoustic baffles, screens and a honeycomb are used to absorb control valve noise and to reduce the flow turbulence. The test section is 600 mm square and 1500 mm long ($1/h=2.5$). In the present study, the test section is assembled with solid sidewalls, perforated top and bottom walls. Downstream of the test section, a model support strut is installed for sting mounted Pitot probe surveys.

2.2 Data Acquisition Systems. A NEFF 620 data acquisition system and LeCroy waveform recorders are available for the experiments. The NEFF 620 system is used to record the test conditions, while a host computer, Digital Equipment Corporation (DEC) Micro VAX 3500 minicomputer, controls the setup of the NEFF system through high-speed interfaces. For surface pressure measurements, LeCroy model 6810 waveform recorders are used. The sampling rate in the present study is 200 ksamples/s. All input channels are triggered simultaneously, either externally or by using an input channel as trigger source. Signals from pressure transducers are digitized and stored in model 6810 modules, while a Twinhead 486 host computer with CATALYST software controls the setup of model 6810 modules through a LeCroy 8901A interface. Also, external amplifiers (Ecreon model E713) are used. With a gain of 20, the roll-off frequency (3 dB) is about 140 kHz.

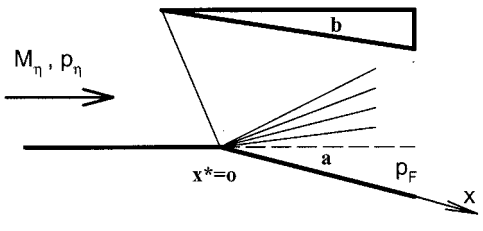

Fig. 1 Test configuration

Contributed by the Fluids Engineering Division for publication in the JOURNAL OF FLUIDS ENGINEERING. Manuscript received by the Fluids Engineering Division August 25, 1999; revised manuscript received November 17, 2000. Associate Editor: D. Williams.

Each data record possesses 131,072 data points for statistical analysis. The data are divided into 32 blocks. Mean and standard deviation (or fluctuating) values of each block (4,096 data points) are calculated. Variation of the blocks is estimated to be 0.43 and 0.13 percent for C_p and $C_{\sigma p}$, values respectively, which are considered as the uncertainty of the experimental data. In addition, a study of Lagnelli et al. [22] examine the available data of surface pressure fluctuations in both incompressible and compressible flows. It is found that σ_p/q_∞ varies with local Mach number and wall temperature ratio. For the present test condition, σ_p/q_∞ for the flat plate case is about 1.8 percent, which is higher than that predicted by Lagnelli et al. ($\sigma_p/q_\infty \approx 0.6$ percent). This is considered due to the background noise with the presence of perforated walls in a transonic wind tunnel (Dods and Hanly [23]). The reasonable estimate on the true level of pressure fluctuations may be obtained by extracting the known tunnel noise sources.

2.3 Models and Instrumentation. The test model consists of a flat plate and an instrumentation plate. The flat plate, with a 4 deg sharp leading edge, is 150 mm wide by 450 mm long, and is supported by a single sting mounted on the bottom of tunnel. For surface pressure measurements, four instrumentation plates (150-mm square) with 0, 5, 10 or 15 ± 0.1 deg expansion angle are fabricated. The instrumentation plate and flat plate are butted tightly together with O-ring material sealing the end faces. One row of 19 pressure taps along the centerline of the plate is drilled perpendicularly to the test surface from 39 mm upstream of the corner to 69 mm downstream ($-5.57 \leqslant x^* \leqslant 9.86$). All pressure taps are 6 mm apart and 2.5 mm in diameter. In addition, an external shock generator consists of a sharp-edged plate and an angle-of-attack adapter. The plate is tightened to the adapter to obtain the desired shock generator angle of 1, 3, or 5 ± 0.1 deg. The shock generator assembly is mounted on the sting support of the tunnel. Further, the position of shock generator is adjusted so that the inviscid shock impinges at the expansion corner.

For surveying the incoming boundary layer, a Kulite pressure transducer (Model XCS-093-25A) is installed inside the Pitot probe at 20 mm from the tip to ensure a fast response. The flattened intake is 2.0 mm wide by 0.3 mm high to minimize the displacement effect. A one-dimensional traversing mechanism is used to move the Pitot probe vertically to build a detailed boundary layer profile. For surface pressure measurements, the same type of Kulite pressure transducers is used. The diameter is 2.36 mm, and the pressure sensitive sensor is 0.97 mm in diameter. The natural frequency of the pressure transducers is 200 kHz as quoted by the manufacturer. The pressure transducers are flush-mounted and potted using silicone rubber sealant. The resolution of the pressure fluctuations is limited by the finite size of pressure transducer, i.e., there is high-frequency damping due to the transducer size. According to Corcos's criterion (Corcos [24]), the maximum measurable frequency ($f_{\max} = U_c/2\pi r$, where r is the radius of pressure sensor) for the present test conditions is about 87 kHz, assuming the convection velocity $U_c = 0.65U_\infty$. However, the perforated screen of the Kulite pressure transducer may reduce the frequency response (Perng [25]).

2.4 Test Conditions. In the present experiments, the test Mach number is 1.28 ± 0.01 for all the test cases. Stagnation pressure and temperature are 193 ± 0.7 kPa and room temperature, respectively. The Reynolds number based on the incoming boundary layer thickness Re_δ is 1.8×10^5. The undisturbed boundary layer measurements are conducted at 485 mm from the leading edge of the flat plate (or 15 mm upstream of the expansion corner). The incoming boundary layer thickness δ is estimated to be 7.0 ± 0.2 mm, which is used as the scaling parameter for the streamwise distance along the centerline of the instrumentation plates. Further, the normalized velocity profile appears to be full ($n \approx 9$ for the velocity power law, Fig. 2), and no transformed velocity profile is presented due to the limited resolution of Pitot pressure survey near the wall. However, the study of Miau et al. [26] showed that the transition region under the present test condition is close to the leading edge the flat plate. This indicates a turbulent flow at measurement locations.

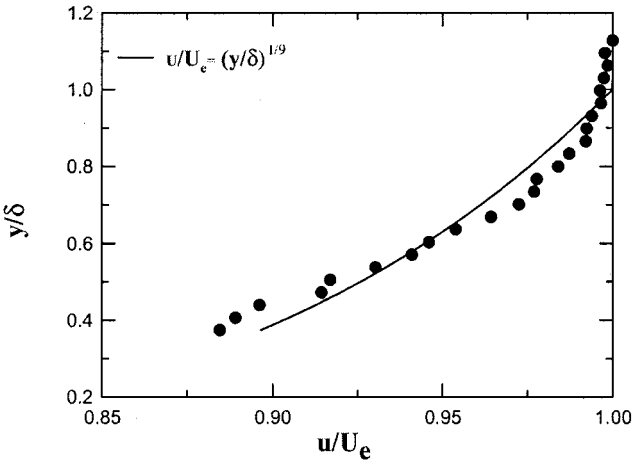

Fig. 2 Normalized incoming boundary layer velocity profile

3 Results and Discussions

3.1 Surface Static Pressure Distributions. Surface static pressure distributions (p_w/p_0) for the three impinging shock strengths are plotted in Fig. 3. The surface pressure is normalized by the stagnation pressure. The inviscid static pressure distributions are also shown as solid lines for comparison. For the weaker impinging shock wave ($\beta = 1$ deg, Fig. 3(*a*)), the agreement of surface static pressure with inviscid static pressure distributions is fair, particularly at higher α. The upstream influence x_u^* ($= x_u/\delta$) at $\alpha = 5$ deg ($x_u^* \approx 1-2$) is considerably higher than that

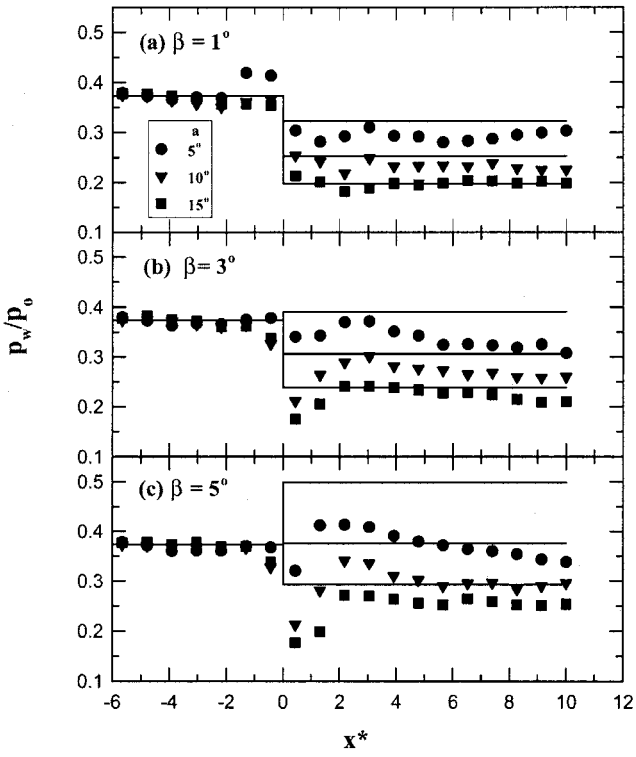

Fig. 3 Mean surface pressure distributions, expansion corner effect

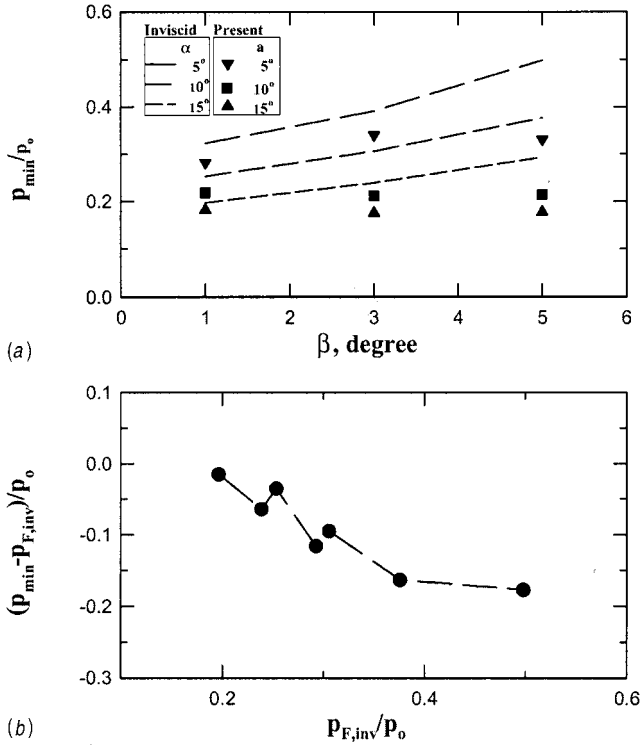

Fig. 4 Surface pressure at immediate downstream of corners

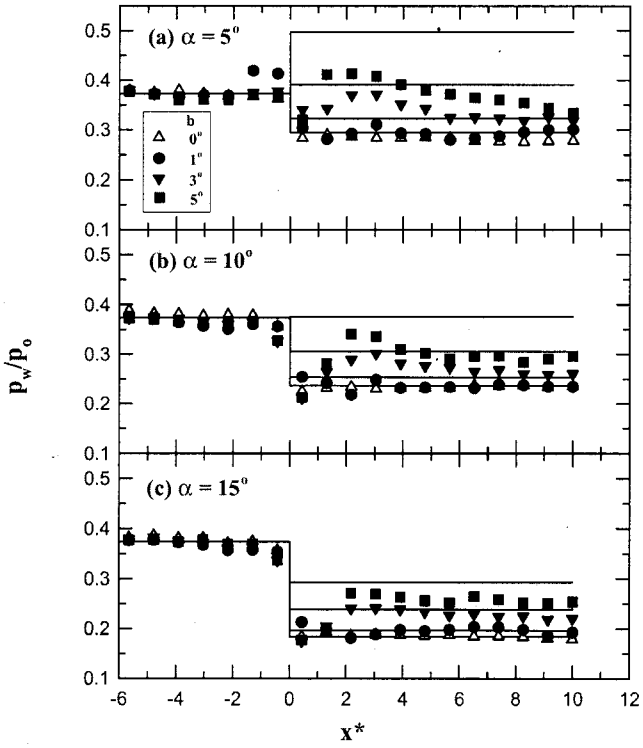

Fig. 5 Mean surface pressure distributions, impinging shock effect

of $\alpha=10$ or 15 deg ($x_u^*<0.5$). Downstream of the corner, the flow is over-expanded. The over-expansion is more pronounced at higher α. This indicates the dominant effect of the expansion fan for the cases of weaker shock strength. For stronger impinging shock waves ($\beta=3$ or 5 deg, Figs. 3(*b*) and 3(*c*)) the upstream influence for $\alpha=10$ and 15 deg increases ($x_u^*\approx 1-2$) although the upstream influence for $\alpha=5$ deg is less pronounced. This implies that the interaction region may depend on the overall interaction strength (or inviscid pressure ratio $p_{F,\mathrm{inv}}/p_0$) induced by the impinging shock wave and the expansion fan. Downstream of the corner, over-expansion of the flow is also observed for the test cases of $\beta=1$ deg.

Further, the minimum surface static pressure $p_{\min}$ downstream of the corner is summarized in Figs. 4(*a*) and 4(*b*). Inviscid conditions are also shown as short-dash lines for comparison. It can be seen that the deviation from inviscid conditions is more significant as β increases. The over-expansion pressure ratio $((p_{\min}-p_{F,\mathrm{inv}})/p_0)$ is replotted against the overall interaction strength. It can be seen that over-expansion downstream of the corner is more significant with larger overall interaction strength, up to eighteen percent of the stagnation pressure. At a location further downstream, the surface pressure approaches equilibrium and the mutual influence of the impinging shock wave and the expansion fan is clearer. For stronger expansion cases ($\alpha=15$ deg), an equilibrium pressure is observed at about $2\delta_0$ downstream of the corner. However, a pressure-drop induced by the expansion flow begins to reappear further downstream for weaker expansion cases ($\alpha=5$ deg), in which a lower downstream equilibrium pressure is obtained. This lower downstream equilibrium pressure could be due to a mixing loss associated with the interaction (Chew [10]).

Surface static pressure data are replotted to show the relative effect of impinging shock wave on expansion flows, where $\beta=0$ deg represents expansion flow without shock impingement. For a weaker expansion flow ($\alpha=5$ deg), Fig. 5(*a*), it can be seen that the agreement with the inviscid distribution is fair for $\beta=1$ deg but not for $\beta=3$ and 5 deg. The interaction region, including upstream and downstream influence, increases with the shock strength. As the expansion-corner angle increases, Figs. 5(*b*) and 5(*c*), the impinging shock wave is ''neutralized'' by the expansion fan and the flows approach new equilibrium conditions at a few boundary layer thicknesses downstream of the corner. The downstream equilibrium surface pressure with respect to inviscid conditions $C_{p,F}((p_F-p_{F,\mathrm{inv}})/q_\infty)$ is shown in Fig. 6(*a*). Deficit of downstream equilibrium pressure is shown for different expansion angles. It is noted that the flows for $\beta=5$ deg may not

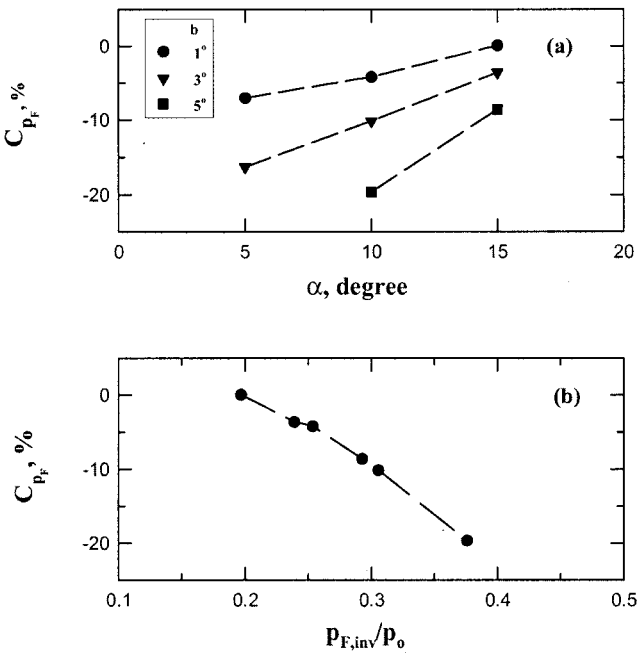

Fig. 6 Deficit of downstream equilibrium surface pressure

reach equilibrium conditions within the measurement region and the data are shown only for reference. Correlation of the data indicates that the downstream equilibrium pressure for a given expansion-corner angle falls further below the inviscid pressure level as the shock strength increases. This phenomenon is more pronounced at lower α. As mentioned above, this phenomenon might be due to a mixing loss associated with the interactions and neutralization of the impinging shock wave with presence of the expansion corner. Further, the pressure deficit is correlated with the overall interaction strength, Fig. 6(*b*). It can be seen that the downstream equilibrium pressure falls further below the inviscid pressure with increasing $p_{F,\mathrm{inv}}/p_0$. This clearly shows the mutual influence of the impinging shock wave and the expansion fan on the interaction.

3.2 Unsteadiness of the Interactions. Distributions of surface pressure fluctuations are shown in Fig. 7. The surface pressure fluctuation σ_p is normalized by the dynamic pressure q_∞. For $\beta=1$ deg (Fig. 7(*a*)), the surface pressure fluctuation coefficients $C_{\sigma p}$ decrease upstream of the corner and reach a maximum near the corner. Damping of upstream pressure fluctuations is considered to be due to modification of the approaching boundary layer by the interactions which increase the local Mach number near the corner. The peak pressure fluctuation is due to an intermittent behavior associated with the impinging shock. Downstream of the corner, damping of pressure fluctuation reappears and an increase in the pressure fluctuations at $3-4\,\delta_0$ is observed. This indicates that the boundary layer is recovering to a new equilibrium state. It is also observed that the level of downstream pressure fluctuation is considerably lower than that of the incoming flow. The attenuation is considered due to the favorable pressure gradient induced by the expansion corner (Chung and Lu [9]). As the shock strength increases, Figs. 7(*b*) and 7(*c*), the basic characteristic shape of the surface pressure fluctuation distribution is similar to that of weaker shock strength. However, the damping of upstream pressure fluctuation is less pronounced. In addition, the peak pressure fluctuation $C_{\sigma p,\max}$ increases in magnitude and its location moves downstream of the corner $(0.5-1.5\delta_0)$, which is considered due to the presence of expansion corner on actual shock impingement location and local flow field. $C_{\sigma p,\max}$ for all the cases is summarized in Fig. 8. It can be seen that $C_{\sigma p,\max}$ for flat plate and 15 deg expansion corner is about the same for different β and increases with shock strength for the weaker expansion. Particularly for $\alpha=5$ and 10 deg at $\beta=5$ deg, the amplitude of the peak surface pressure fluctuations is considerably higher than that of other test cases. This higher peak pressure fluctuation is associated with a stronger shock strength and related to the intermittent behavior of the interaction. Moreover, it is also observed that the amplitude of the downstream equilibrium pressure fluctuation at a given shock strength decreases at larger α. In other words, the damping of the pressure fluctuations downstream of the corner is more significant for stronger expansion flows. The downstream equilibrium pressure fluctuations $C_{\sigma p,F}$ of all the test cases are summarized in Fig. 9. It can be seen that the downstream equilibrium pressure fluctuation for the flat plate flow with shock impingement increases for higher β. However, the level of the pressure fluctuations at a given expansion-corner angle shows only slight variation with β. This means that the presence of the expansion corner reduces the flow unsteadiness inherent in the shock wave and boundary layer interaction. The data is further correlated with overall interaction strength, Fig. 10. The basic feature of the correlation is a roughly constant downstream equilibrium pressure fluctuation ($C_{\sigma p,F}\approx 0.009$) at $p_{F,\mathrm{inv}}/p_0<0.249$, a gradual increase within $p_{F,\mathrm{inv}}/p_0=0.249-0.398$ and a new equilibrium level at $p_{F,\mathrm{inv}}/p_0>0.398$($C_{\sigma p,F}\approx 0.011$). This transitional behavior indicates the dominant effect of impinging shock wave or expansion fan on the interactions, which also implies a nonlinear effect of the perturbations on the boundary layer at different overall interaction strength.

Further, examples of PDF (probability density function) are plotted in Figs. 11. For $\alpha=5$ deg and $\beta=1$ deg (Fig. 1(*a*)), the

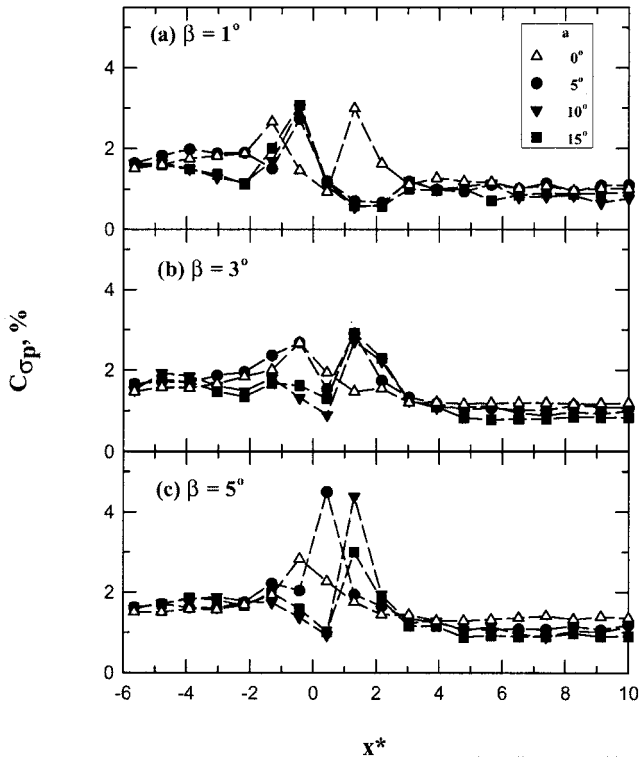

Fig. 7 Surface pressure fluctuations

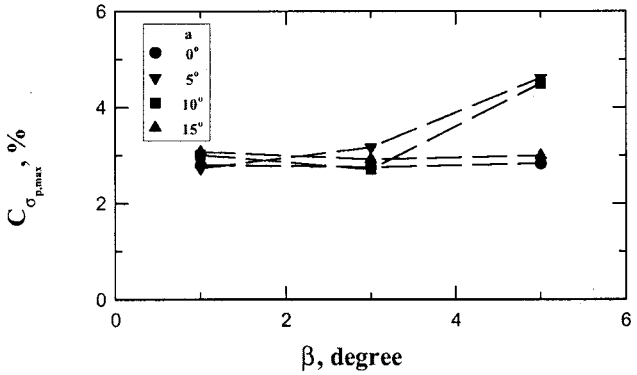

Fig. 8 Peak surface pressure fluctuations

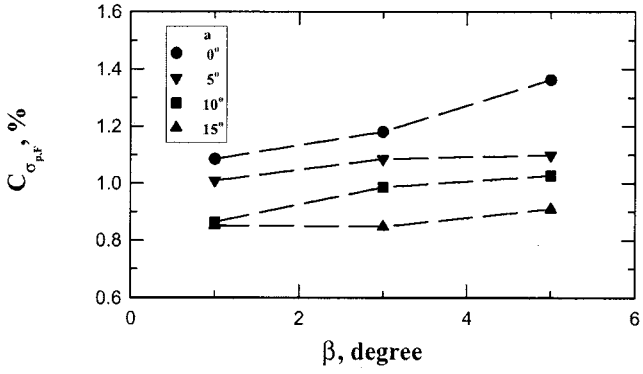

Fig. 9 Downstream surface pressure fluctuations

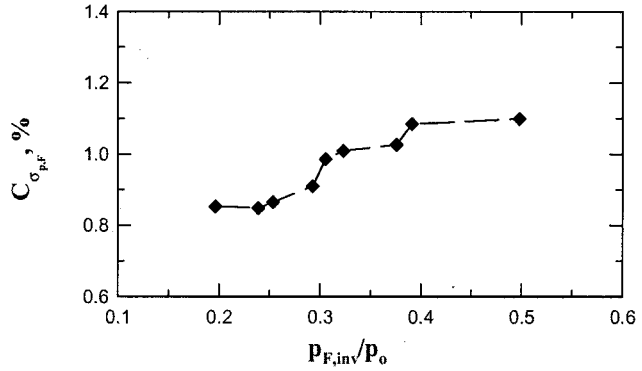

Fig. 10 Downstream surface pressure fluctuations as a function of inviscid pressure ratio

PDF shows a highly skewed signal at $x^*=0.43$ downstream of the corner. This corresponds to the intermittent nature of the signal at the measured location. Also at $\beta=3$ deg (Fig. 11(*b*)), the skewness of the signal is observed at $x^*=1.30$. However, for the case of $\beta=5$ deg (Fig. 11(*c*)), the PDFs are near Gaussian distributions at all measured locations, which indicate the random nature of the signals. For $\beta=1$ deg at $\alpha=10$ or 15 deg, the PDFs show the similar feature of random signals. Furthermore, the $\alpha=10$ deg and $\beta=3$ deg case, the PDFs show mildly skewed signals at further downstream locations. The interaction spreads over a wider region. Also, the PDFs of $\beta=5$ deg at $\alpha=10$ or 15 deg show intermittency at $x^*=1.30$. Based on the above observation, the PDFs data indicates two important features of the signals. First, the skewness of the signals is observed only for some cases, in which $p_{F,\mathrm{inv}}/p_0=0.249-0.398$. As mentioned above, the downstream equilibrium pressure fluctuation increases within this pressure range. This transitional behavior indicates that the flow is basically dominated by either the expansion fan or the impinging shock wave at lower and higher p_F/p_0. Second, skewness is observed only at certain measured locations, e.g., $x^*=0.43$ or 1.30. Thus the intermittent nature of the flow is only a localized phenomenon, which corresponds to the discrete peak pressure fluctuations associated with impinging shock wave.

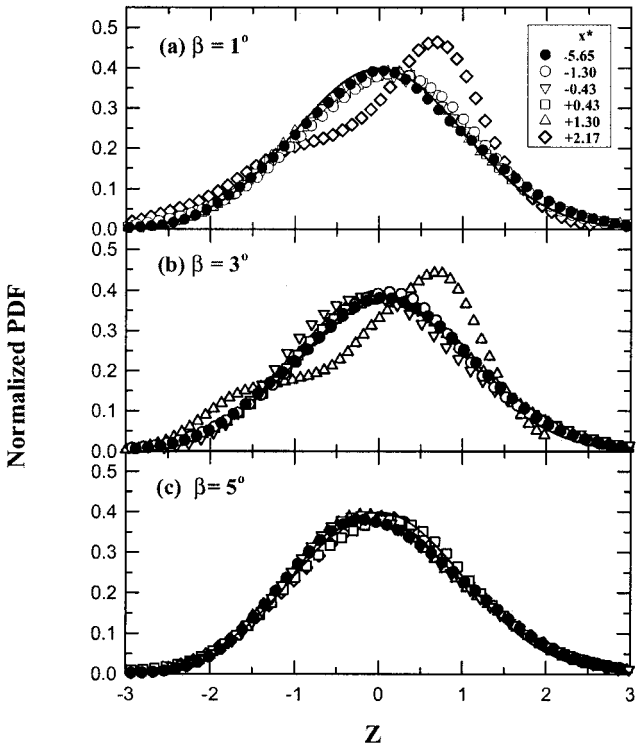

Fig. 11 Probability density functions, $\alpha=5$ deg

4 Conclusions

The presence of an expansion corner in a shock wave/boundary layer interaction has a strong effect on the upstream influence, downstream pressure and flow unsteadiness. The coupling between impinging shock wave and expansion fan on the interactions depends on the overall interaction strength, in which attenuation of the downstream pressure and peak surface pressure fluctuation at a given shock strength are more pronounced at higher expansion-corner angle.

Acknowledgment

The research was supported by the National Science Council (88-2612-E-006-004). The support is gratefully acknowledged. The author also thanks Prof. Frank K. Lu of the University of Texas at Arlington for many helpful comments with the manuscript.

Nomenclature

$C_{\sigma p}$ = fluctuating pressure coefficient, σ_p/q_∞
C_p = pressure coefficient, $(p_w-p_\infty)/q_\infty$
$C_{p,F}$ = pressure coefficient, $(p_F-p_{F,\mathrm{inv}})/q_\infty$
M = Mach number
p = pressure
q_∞ = dynamic pressure
U_c = convection velocity
x = distance measured along test surface, Fig. 1
x^* = normalized streamwise distance x/δ_0
x_u^* = normalized upstream influence, x_u/δ_0
α = expansion corner angle, Fig. 1
β = external wedge angle, Fig. 1
δ = incoming boundary layer thickness
σ_p = standard deviation of pressure fluctuations
Z = standardized variable, $(p_w-p_{w,\mathrm{avg}})/\sigma_p$

Subscripts

F = downstream equilibrium condition
inv = invicid condition
0 = stagnation condition
∞ = incoming condition

References

[1] Morris, M. J., Sajben, M., and Kroutil, J. C., 1992, ''Experimental Investigation of Normal Shock and Turbulent Boundary Layer Interactions with and without Mass Removal,'' AIAA J., **30**, No. 2, pp. 359–366.
[2] Zheltovodov, A. A., 1996, ''Shock Waves/Turbulent Boundary Layer Interactions—Fundamental Studies and Applications,'' AIAA Paper 96-1977.
[3] Bur, R., Corbel, B., and Delery, J., 1998, ''Study of Passive Control in a Transonic Shock Wave/Boundary Layer Interaction,'' AIAA J., **36**, No. 3, pp. 394–400.
[4] Unalmis, O. H., and Dolling, D. S., 1998, ''Experimental Study of Cause of Unsteadiness of Shock-Induced Turbulent Separation,'' AIAA J., **36**, No. 3, pp. 371–378.
[5] Gibson, T. M., Babinsky, H., and Squire, L. C., 2000, ''Passive Control of Shock Wave-Boundary Layer Interactions,'' The Aeronautical J., Paper No. 2411, Mar., pp. 129–140.
[6] Adamson, T. C., Jr., 1967, ''Effect of Transport Properties on Supersonic Expansion Around a Corner,'' Phys. Fluids, **10**, No. 5, pp. 953–962.
[7] Bloy, A. W., 1975, ''The Expansion of a Hypersonic Turbulent Boundary Layer at a Sharp Corner,'' J. Fluid Mech., **53**, Part 1, pp. 647–655.
[8] Goldfeld, M. A., 1985, ''On the Reverse Transition of Compressible Turbulent Boundary Layer in a Transverse Flow around a Convex Corner Configuration,'' IUTAM Symposium on Laminar-Turbulent Transition, Novosibirsk, USSR, edited by V. V. Kozlov, Springer-Verlag, Berlin, pp. 515–520.
[9] Chung, K., and Lu, F., 1993, ''Damping of Surface Pressure Fluctuations in Hypersonic Flow past an Expansion Corner,'' AIAA J., **31**, pp. 1229–1234.
[10] Chew, Y. T., 1979, ''Shock Wave and Boundary Layer Interaction in the Presence of an Expansion Corner,'' Aeronaut. Q., **XXX**, pp. 506–527.
[11] Hawbolt, R. J., Sullivan, P. A., and Gottlieb, J. J., 1992, ''Experimental Study

of Shock Wave and Hypersonic Boundary Layer Interactions Near a Convex Corner,'' AIAA Paper 93-2980.
[12] Chung, K., and Lu, K., 1995, ''Hypersonic Turbulent Expansion-Corner Flow with Shock Impingement,'' J. Propul. Power, **11**, No. 3, pp. 441–447.
[13] White, M. E., and Ault, D. A., 1995, ''Hypersonic Shock Wave/Turbulent Boundary Layer Interactions in the Vicinity of an Expansion Corner,'' AIAA Paper 95-6125.
[14] Bradshaw, P., 1973, ''Effects of Streamline Curvature on Turbulent Flows,'' AGARDograph 169.
[15] Smits, A. J., Eaton, J. A., and Bradshaw, P., 1979, ''The Response Turbulent Boundary Layers to Lateral Divergence,'' J. Fluid Mech., **94**, Part 2, pp. 243–268.
[16] Smits, A. J., and Wood, D. H., 1985, ''The Response of Turbulent Boundary Layers to Sudden Perturbations,'' Annu. Rev. Fluid Mech., **17**, pp. 321–358.
[17] Degani, D., and Smits, A. J., 1989, ''Response of a Compressible Turbulent Boundary Layer to a Short Region of Surface Curvature,'' AIAA J., **27**, No. 1, pp. 23–28.
[18] Smith, D. R., and Smits, A. J., 1991, ''The Rapid Expansion of a Turbulent Boundary Layer in a Supersonic Flow,'' Theor. Comput. Fluid Dyn., **2**, pp. 319–328.
[19] Neves, J. C., and Moin, P., 1994, ''Effects of Convex Traverse Curvature on Wall Bounded Turbulence. Part 2. The Pressure Fluctuations,'' J. Fluid Mech., **272**, pp. 383–406.
[20] Kistler, A. L., and Chen, W. S., 1963, ''Fluctuation Measurements in a Supersonic Turbulent Boundary Layer,'' J. Fluid Mech., **16**, Part 1, pp. 41–64.
[21] Chung, K., 1995, ''Development and Calibration of ASTRC/NCKU 600 mm $\times$600 mm Transonic Wind Tunnel,'' AIAA Paper 95-0238.
[22] Laganelli, A. L., Martellucci, A., and Shaw, L. L., 1983, ''Wall Pressure Fluctuations in Attached Boundary-Layer Flow,'' AIAA J., **21**, No. 4, pp. 495–502.
[23] Dods, J. B., Jr., and Hanly, R. D., 1972, ''Evaluation of Transonic and Supersonic Wind-Tunnel Background Noise and Effects of Surface Pressure Fluctuation Measurements,'' AIAA Paper 72-1004.
[24] Corcos, G. M., 1963, ''Resolution of Pressure in Turbulence,'' J. Acoust. Soc. Am., **35**, pp. 192–199.
[25] Perng, S., 1996, ''Passive Control of Pressure Oscillation in Hypersonic Cavity Flow,'' PhD dissertation, The University of Texas at Austin.
[26] Miau, J., Cheng, J., Chung, K., and Chou, J., 1998, ''The Effect of Surface Roughness on the Boundary Layer Transition,'' 7th Inter. Symp. in Flow Modeling and Turbulent Measurement, National Cheng Kung University, Oct. 5–8, Tainan, Taiwan, ROC, ISFMTM98', pp. 609–616.

Shock Wave Reflections in Dust-Gas Suspensions

G. Ben-Dor
Professor

O. Igra
Professor

L. Wang
Visiting Researcher

Pearlstone Center for Aeronautical Engineering Studies,
Department of Mechanical Engineering,
Ben-Gurion University of the Negev,
Beer Sheva, Israel 84105

The reflection of planar shock waves from straight wedges in dust-gas suspensions is investigated numerically. The GRP shock capturing scheme and the MacCormac scheme are applied to solve the governing equations of the gaseous and solid phases, respectively. These two schemes have a second-order accuracy both in time and space. It is shown that the presence of the dust significantly affects the shock-wave-reflection-induced flow field. The incident shock wave attenuates and hence unlike the shock wave reflection phenomenon in a pure gas, the flow field in the present case is not pseudo steady. The presence of the dust results in lower gas velocities and gas temperatures and higher gas densities and gas pressures than in dust-free shock wave reflections with identical initial conditions. It is also shown that the smaller is the diameter of the dust particle the larger are the above-mentioned differences. In addition, the smaller is the diameter of the dust particle the narrower is the width of the dust cloud behind the incident shock wave. Larger dust velocities, dust temperatures and dust spatial densities are obtained inside this dust cloud for smaller dust particles. The results provide a clear picture of whether and how the presence of dust particles affects the shock-wave-reflection-induced flow field. [DOI: 10.1115/1.1331558]

Introduction

Two of the more intensively investigated shock wave related phenomena in the past two decades have been the reflection of oblique shock waves and the propagation of shock wave in dust-gas suspensions. These two subjects were summarized, respectively, in Ben-Dor's [1] book and Igra and Ben-Dor's [2] review that was recently updated by Ben-Dor [3].

As shown by Ben-Dor [1] there are four major types of shock wave reflection wave configurations in pseudo-steady flows. They are regular reflection-RR, single-Mach reflection-SMR, transitional-Mach reflection-TMR, and double-Mach reflection-DMR.

Surprisingly, to the best of the authors' knowledge, only one study, a numerical one, by Kim and Chang [4] has been published on the combined phenomenon of oblique shock wave reflections in dust-gas suspensions. Unfortunately, their TVD-based numerical study was limited to only one case, a single-Mach reflection (SMR) that resulted from the reflection of a planar incident shock wave having a Mach number $M_i = 2.03$ over a compressive wedge having an angle $\theta_w = 27$ deg. They did, however, investigate this case quite thoroughly and conducted a parametric study in which they numerically investigated the influence of the solid particle diameter, d_p, and the loading ratio, η, on the resulted flow field. These facts motivated us to complement their study and conduct a comprehensive numerical investigation of this phenomenon.

Present Study

The Assumptions. It is a common practice to employ the following assumptions in studies of shock waves in dusty laden gases: (1) The flow field is two-dimensional and unsteady. (2) The gaseous phase behaves as a perfect gas. (3) The solid particles, which are identical in all their physical properties, are rigid spherical and inert. They are uniformly distributed in the gaseous phase. (4) The number density of the solid particles is high enough so that the solid phase could be considered as a continuous medium. (5) The solid particles do not interact with each other. As a result, their partial pressure in the suspension is negligibly small. (6) The volume occupied by the solid particles is negligibly small. (7) The heat capacity of the solid particles is constant. (8) The dynamic viscosity, the thermal conductivity, and the specific heat capacity at constant pressure of the gaseous phase depend solely on its temperature. (9) Beside the momentum and energy exchanges between the solid and the gaseous phases, the gaseous phase is assumed to be an ideal fluid, i.e., inviscid and thermally nonconductive. (10) The weight of the solid particles and the buoyancy force are negligibly small compared to the drag force acting on them. (11) The solid particles are too large to experience a Brownian motion. (12) The temperature within the solid particles is uniform.

In addition to the above general assumptions, the following more specific assumptions will also be used:

1 When a dust particle hits the wedge surface it sticks to it and does not bounce back into the flow field.

2 The incompressible drag coefficient is sufficient to calculate the drag force applied by the gaseous phase on the solid phase. The validity of this assumption will be discussed subsequently.

The Governing Equations. In the following, the governing equations for the considered flow as developed based on the above assumptions are presented.

The two-dimensional unsteady compressible governing equations for the gaseous and the solid phases expressed in a Cartesian coordinates system, in a vector form, are

$$\frac{\partial \mathbf{Q}_i}{\partial t} + \frac{\partial \mathbf{F}_i}{\partial x} + \frac{\partial \mathbf{G}_i}{\partial y} = \mathbf{S}_i \tag{1}$$

where $i \equiv g$ and $i \equiv s$ indicate the gaseous and the solid phases, respectively. Here $\mathbf{Q}_i$ is the vector of the conservation variables, $\mathbf{F}_i$ and $\mathbf{G}_i$ are the flux-vectors and $\mathbf{S}_i$ is the source term. Equation (1) can be rewritten as follows

$$\frac{\partial}{\partial t}\begin{bmatrix} \rho_i \\ \rho_i u_i \\ \rho_i v_i \\ e_i \end{bmatrix} + \frac{\partial}{\partial x}\begin{bmatrix} \rho_i u_i \\ \rho_i u_i^2 + p_i \\ \rho_i u_i v_i \\ u_i(e_i + p_i) \end{bmatrix} + \frac{\partial}{\partial y}\begin{bmatrix} \rho_i v_i \\ \rho_i u_i v_i \\ \rho_i v_i^2 + p_i \\ v_i(e_i + p_i) \end{bmatrix} = \begin{bmatrix} 0 \\ \pm D_x \\ \pm D_y \\ \pm q \pm u_p D_x \pm v_p D_y \end{bmatrix} \tag{2}$$

Contributed by the Fluids Engineering Division for publication in the JOURNAL OF FLUIDS ENGINEERING. Manuscript received by the Fluids Engineering Division November 5, 1999; revised manuscript received September 6, 2000. Associate Editor: J. Eaton.

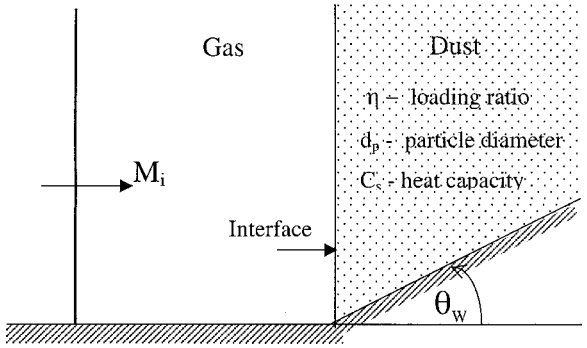

Fig. 1 Schematic illustration of the flow field to be solved and definition of some parameters. The interface separates the dust-free and the dusty-gas.

Table 1 Initial conditions for obtaining the various shock-wave reflection configurations

Type of reflection	M_i	θ_w
Regular reflection-RR	2.03	60 deg
Single-Mach reflection-SMR*	2.03	27 deg
Transitional-Mach reflection-TMR	3.00	27 deg
Double-Mach reflection-DMR	6.00	35 deg

*Identical to Kim and Chang [4].

The plus (+) and the minus (−) signs in the r.h.s. of Eq. (2) are for the gaseous and the solid phases, respectively, ρ_i is the spatial density, p_i is the partial pressure of phase i (note that based on the assumptions $p_s=0$ and hence p_g is also the suspension pressure, p), u_i, and v_i, are the x- and y-components of the velocity of the gaseous phase, D_x and D_y are the x- and y-components of the drag force exerted, per unit volume, by the gaseous phase on the dust particles, q is the heat convected, per unit volume, from the gaseous phase to the dust particles. The total energy of the gaseous phase is given by

$$e_g=\frac{p_g}{\gamma-1}+\frac{1}{2}\rho_g(u_g^2+v_g^2) \tag{3}$$

Here, $\gamma=C_p/C_v$ is the ratio of the specific heat capacities. The total energy of the dust phase is given by

$$e_p=\frac{\gamma}{\gamma-1}\frac{C_s}{C_p}\rho_p T_p+\frac{1}{2}\rho_p(u_p^2+v_p^2) \tag{4}$$

Here, C_s is the specific heat capacity of the dust particles and T_p is the temperature of the dust phase. Finally, the equation of state for the gaseous phase is

$$p=\rho_g R T_g=(\gamma-1)\rho_g e_g \tag{5}$$

where R is the specific gas constant of the gaseous phase and T_g is the gaseous phase temperature.

In order to have a set of governing equations that can be integrated, the source terms in the r.h.s. of Eq. (2) should be expressed in terms of either known parameters or the dependent parameters. This is presented in the following.

Momentum is exchanged between the gaseous and the solid phases by means of the drag force, **D**, which can be expressed in terms of the drag coefficient, C_D

$$\begin{vmatrix}D_x\\D_y\end{vmatrix}=\frac{3}{4}\frac{\rho_g\rho_p}{\rho_s d_p}C_D\begin{vmatrix}u_g-u_p\\v_g-v_p\end{vmatrix}[(u_g-u_p)^2+(v_g-v_p)^2]^{1/2} \tag{6}$$

The drag coefficient C_D is usually expressed as a function of the dust particle Reynolds number, Re_p. In the present study, the correlation proposed by Clift et al. [5] was adopted.

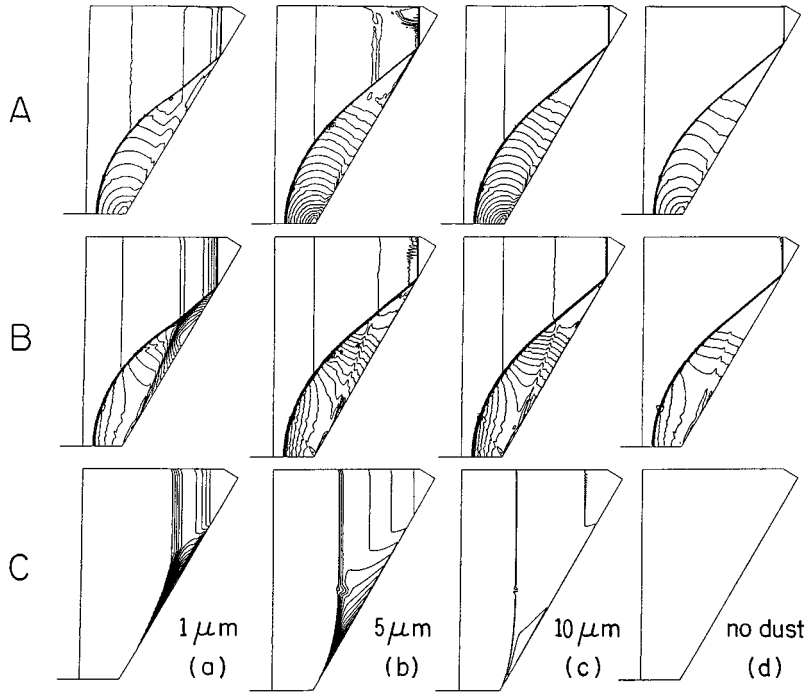

Fig. 2 The flow fields (A-constant flow Mach number contours, B-constant gaseous phase density contours, and C-constant dust phase spatial density contours) and the wave configurations of a regular reflection (RR) for different diameters of the dust particles: (*a*) $d_p=1\ \mu$m, (*b*) $d_p=5\ \mu$m, (*c*) $d_p=10\ \mu$m, and (*d*) dust-free

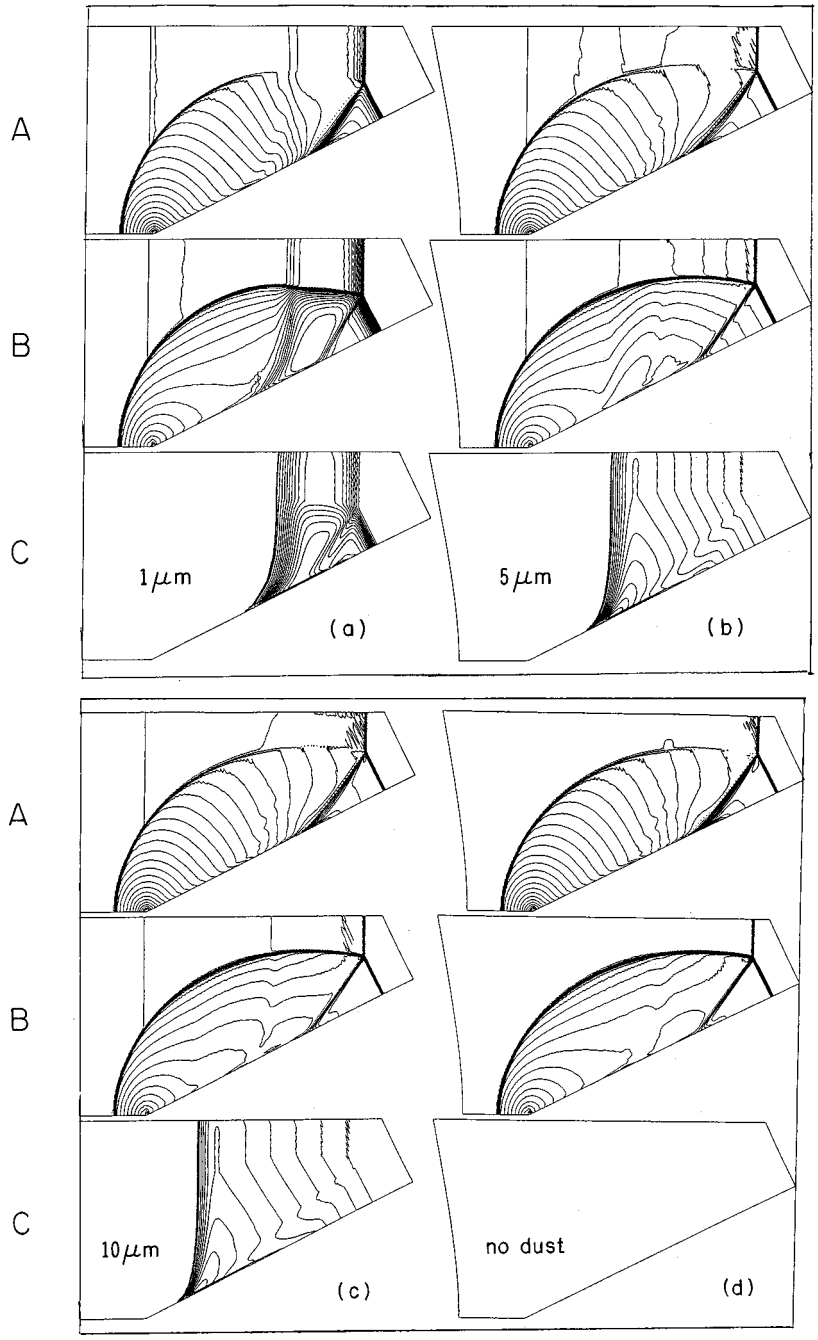

Fig. 3 The flow fields (A-constant flow Mach number contours, B-constant gaseous phase density contours, and C-constant dust phase spatial density contours) and the wave configurations of a single-Mach reflection (SMR) for different diameters of the dust particles: (*a*) $d_p=1\ \mu$m, (*b*) $d_p=5\ \mu$m, (*c*) $d_p=10\ \mu$m, and (*d*) dust-free

$$C_D=\left|\begin{array}{l}\dfrac{24}{\mathrm{Re}_p}(1+0.15\,\mathrm{Re}_p^{0.687}) \\ \dfrac{24}{\mathrm{Re}_p}(1+0.15\,\mathrm{Re}_p^{0.687})+\dfrac{0.42}{(1+42500\,\mathrm{Re}_p^{-1.16})}\end{array}\right| \quad \text{for} \left|\begin{array}{l}\mathrm{Re}_p\leqslant 800 \\ \mathrm{Re}_p> 800\end{array}\right| \tag{7}$$

It should be noted here that Igra and Ben-Dor [6,2] showed numerically that the use of ''compressible drag coefficients'' (i.e., drag coefficients which account for compressibility) does not result in significant changes from results obtained by the use of ''incompressible drag coefficients'' for flow Mach numbers that are considered in this study. Had the flow Mach numbers been higher ''compressible drag coefficients'' must have been used. The experimental study of Kurian and Das [7] justified this approach. In that study, they compared their experimental results to the predictions of a general attenuation law that was developed by Olim et al. [8] using the ''incompressible drag coefficient'' given by Eq. (7). The good agreement between the experimental results and the empirical predictions clearly indicates that the use of an ''incompressible drag coefficient'' is sufficient. In addition, it

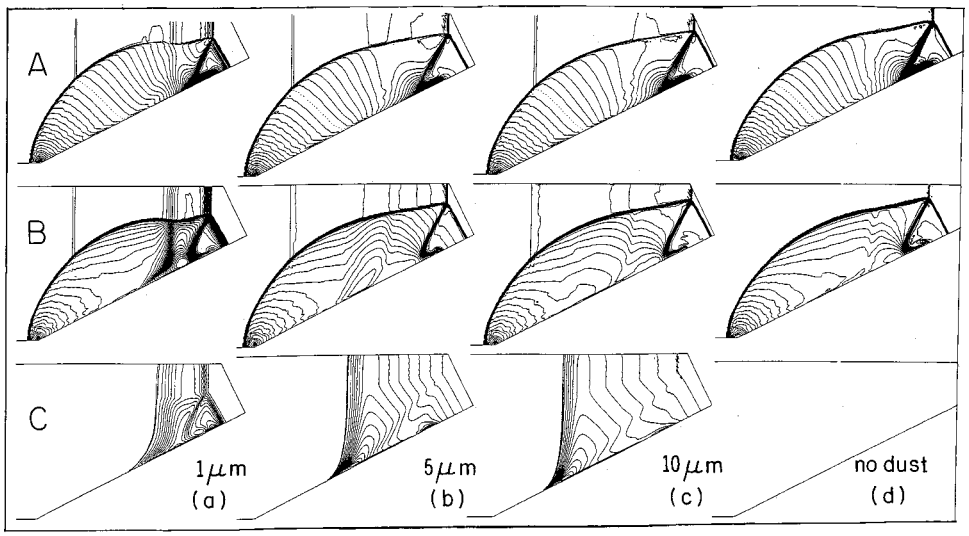

Fig. 4 The flow fields (A-constant flow Mach number contours, B-constant gaseous phase density contours, and C-constant dust phase spatial density contours) and the wave configurations of a transitional-Mach reflection (TMR) for different diameters of the dust particles: (*a*) $d_p=1\ \mu$m, (*b*) $d_p=5\ \mu$m, (*c*) $d_p=10\ \mu$m, and (*d*) dust-free

should be noted that the present study is a phenomenological one, it presents for the first time comprehensive results of the reflection of oblique shock waves in dust-gas suspensions. Since experimental data of this phenomenon do not exist we cannot compare our numerical results with experiments and hence the known insignificant contribution of accounting for compressibility in the drag coefficient can justify its neglection. Consequently, in spite the fact that the flow under consideration is compressible an ''incompressible drag coefficient'' has been used.

The dust particle Reynolds number, Re_p, is defined as

$$\mathrm{Re}_p=\frac{\rho_g[(u_g-u_p)^2+(v_g-v_p)^2]^{1/2}d_p}{\mu_g} \tag{8}$$

Here, the dynamic viscosity of the gaseous phase, μ_g, is calculated using the following correlation proposed by Mazor et al. [9]

$$\mu_g=\mu_{g_r}\left(\frac{T_g}{T_{g_r}}\right)^{0.65} \tag{9}$$

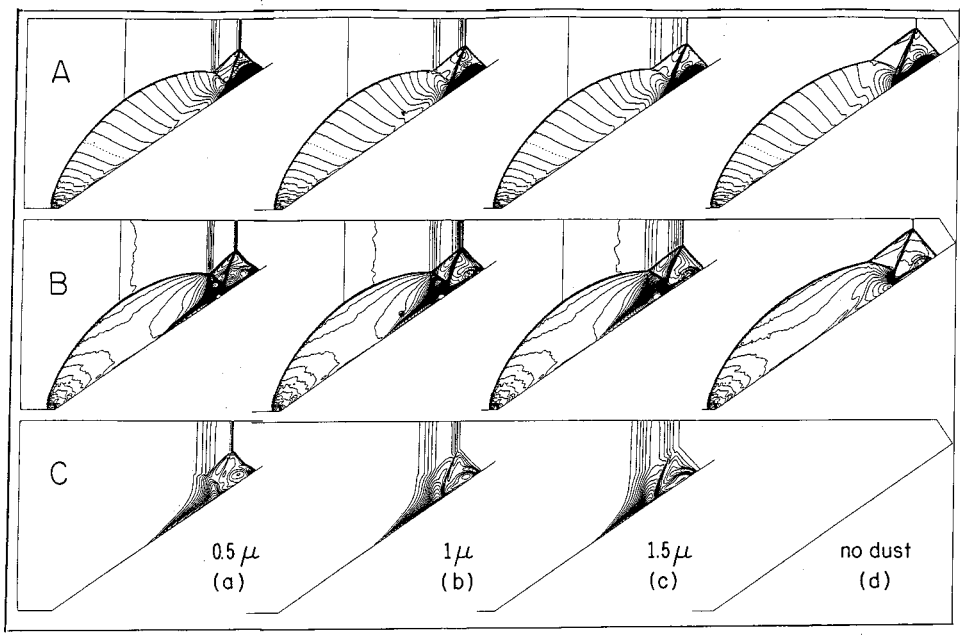

Fig. 5 The flow fields (A-constant flow Mach number contours, B-constant gaseous phase density contours, and C-constant dust phase spatial density contours) and the wave configurations of a double-Mach reflection (DMR) for different diameters of the dust particles: (*a*) $d_p=0.5\ \mu$m, (*b*) $d_p=1.0\ \mu$m, (*c*) $d_p=1.5\ \mu$m, and (*d*) dust-free

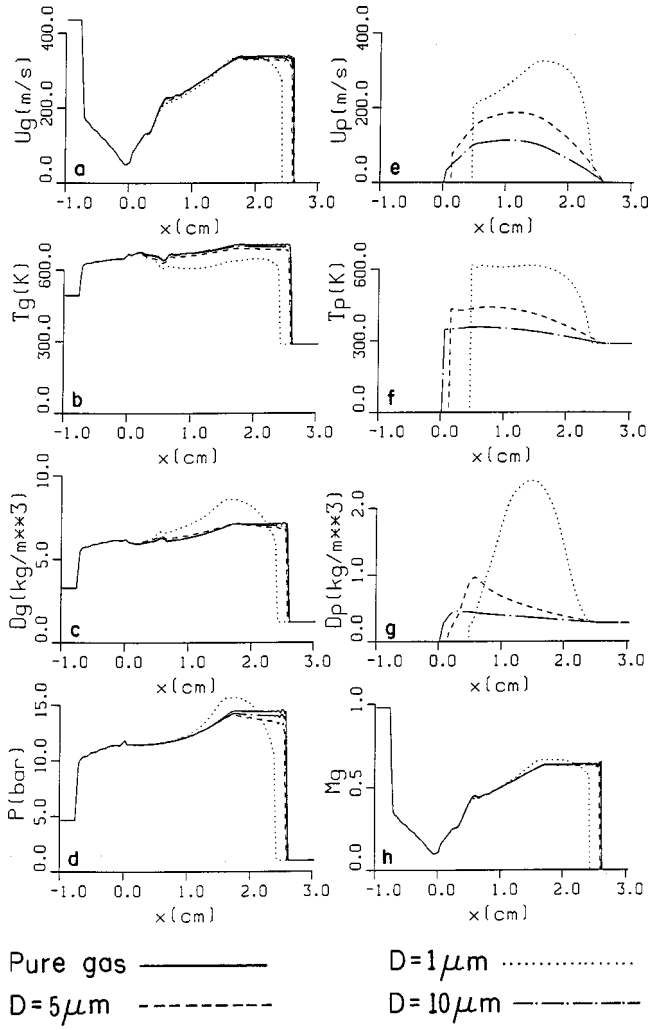

Fig. 6 The distributions of various suspension properties along the reflecting wedge surface in the case of a regular reflection (RR) for a dust-free case and three suspensions having dust particles with d_p=1 μm, d_p=5 μm, d_p=10 μm

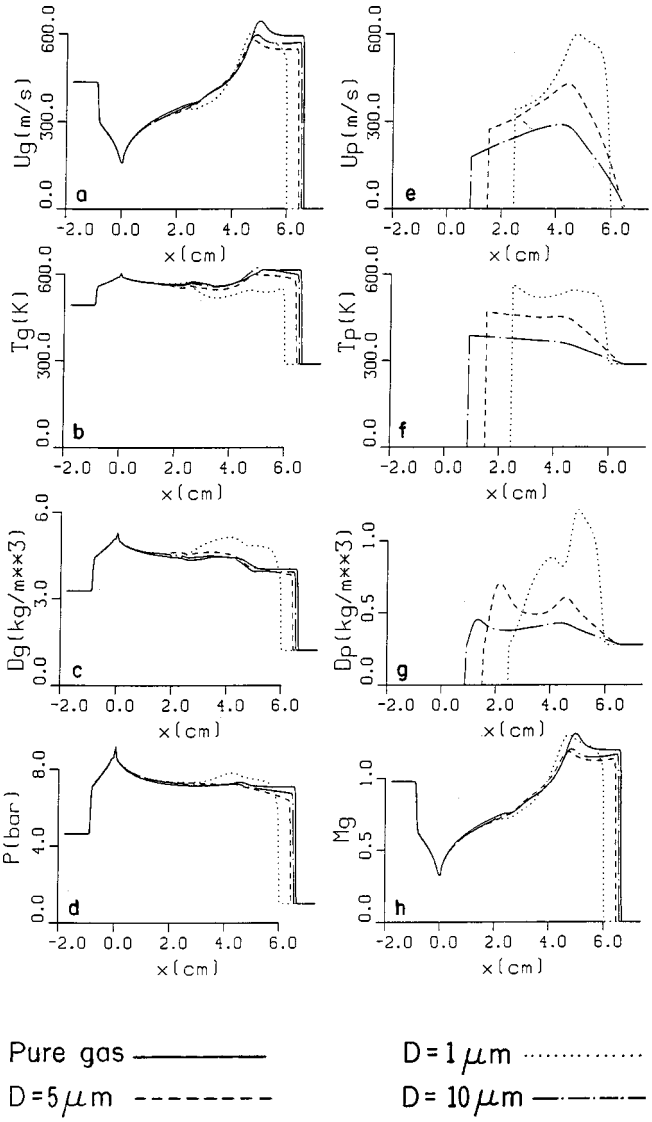

Fig. 7 The distributions of various suspension properties along the reflecting wedge surface in the case of a single-Mach reflection (SMR) for a dust-free case and three suspensions having dust particles with d_p=1 μm, d_p=5 μm, d_p=10 μm

where μ_{g_r} is the dynamic viscosity at the reference temperature T_{g_r}.

Energy is exchanged between the gaseous and the solid phases by means of heat convection. It can be expressed in terms of the Nusselt number $\mathrm{Nu}=hd_p/\mu_g$ (h is the coefficient of heat convection), in the following way

$$q=\frac{6\mathrm{Nu}\,C_p\mu_g\rho_p}{\mathrm{Pr}\,d_p^2\rho_s}(T_g-T_p) \tag{10}$$

The Nusselt number here can be expressed in terms of the dust particles Reynolds number, Re_p, and the Prandtl number, Pr, in the following way

$$\mathrm{Nu}=2+0.459\,\mathrm{Re}_p^{0.55}\,\mathrm{Pr}^{0.33} \tag{11}$$

The Prandtl number was considered to be constant, Pr=0.71.

The Numerical Method of Solution. The Generalized Riemann Problem (GRP) shock capturing scheme and the MacCormac [10] scheme are applied to the equations of the gaseous and solid phases, respectively. These two schemes have a second order accuracy both in time and space.

A comprehensive description of the used GRP scheme can be found in Falcovitz and Ben-Artzi [11]. The way in which the solid phase (dust) is incorporated into the GRP scheme is outlined in Wang et al. [12]. A ''Mathematical'' validation, i.e., verification of convergence and accuracy of solutions with grid refinement, has in fact been done by us on the GRP scheme, as well as by other researchers on similar conservation laws schemes. A ''physical'' validation, aimed at the validity and accuracy of the two-phase modeling, has been conducted with respect to shock tube experiments where a planar shock wave has been driven into a dusty gas suspension (Sommerfeld [13]). Given the serious difficulties in setting up controlled experiments in dusty gas suspensions, we have to rely on planar shock configurations as the sole experimental validation data. As for pure gas 2-D flows a detailed ''physical'' validation can be found in Igra et al. [14]. The GRP scheme is based on a Reimann problem solver and it is especially suitable for handling flow discontinuities. Therefore, there is no need to employ artificial viscosity for smoothing solutions near discontinuities.

The Numerical Results. A schematic drawing of the flow field under investigation is shown in Fig. 1. An incident shock wave having a Mach number M_i is propagating from left to right toward a compressive corner having a wedge angle θ_w. The dust

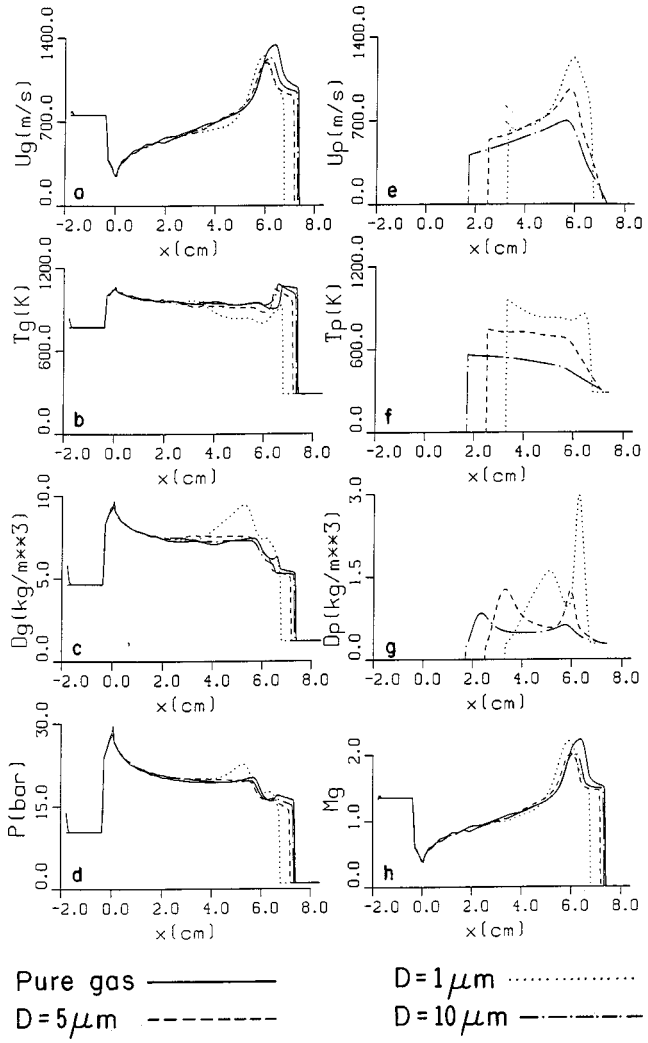

Fig. 8 The distributions of various suspension properties along the reflecting wedge surface in the case of a transitional-Mach reflection (TMR) for a dust-free case and three suspensions having dust particles with $d_p=1\ \mu$m, $d_p=5\ \mu$m, $d_p=10\ \mu$m

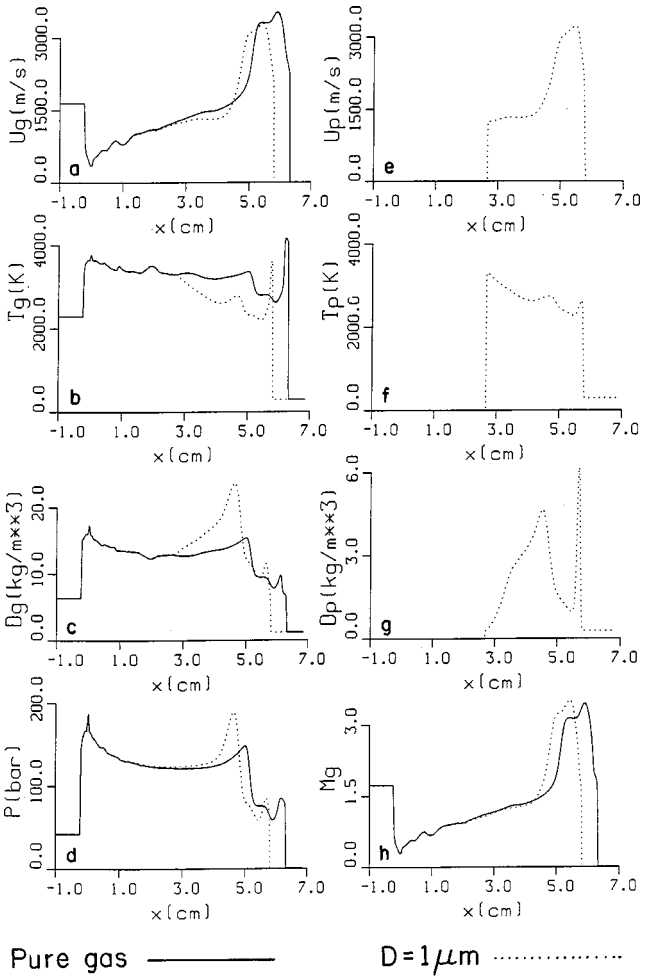

Fig. 9 The distributions of various suspension properties along the reflecting wedge surface in the case of a double-Mach reflection (DMR) for a dust-free case and a suspension having dust particles with $d_p=1\ \mu$m

suspension extends downstream from the leading edge of the reflecting wedge. The dust-loading ratio is η, the diameter of the dust particles is d_p, their specific heat capacity is C_s, and their material density is ρ_s.

The numerical results will be presented in the following. First, the results which are common to all the four shock-wave reflection configurations, RR, SMR, TMR, and DMR will be presented, then results which are specific to each of these four configurations will be presented, and finally some results regarding the influence of the dust on the RR↔MR transition will be given. The incident shock wave Mach numbers and the reflecting wedge angles that were used to obtain the four shock-configurations are summarized in Table 1.

The loading ratio in all the above cases was $\eta=0.23$. In addition, in all the calculations the specific heat capacity of the dust particles and their material density were kept constant at $C_s=1.38$ kJ/(kgK) and $\rho_s=4000$ kg/m^3, respectively. These values were chosen in order to enable us to compare our dusty-SMR calculations with those of Kim and Chang [4]. The comparison indicated that the flow-field predictions of our code, which was based on the GRP method, were very similar to those of their code, which was based on the TVD method.

The Flow Fields Associated With the Shock Wave Reflection Configurations. Constant flow Mach number contours (A), constant gas density contours (B), and constant dust spatial density contours (C) are shown in Figs. 2, 3, 4, and 5 for RR, SMR, TMR, and DMR, respectively. Each of these figures consists of four parts. Parts (*a*) to (*c*) show the numerical results of the entire flow field for three different dust particle diameters ($d_p=1$, 5, and 10 μm in the RR-, SMR-, and TMR-cases and $d_p=0.5$, 1.0, and 1.5 μm in the DMR-case). Owing to the high compressions associated with the DMR smaller particle diameters had to be used in order not to violate the assumptions. For comparison purposes the above-mentioned contours for a similar dust-free case are shown in part (*d*) of Figs. 2–5.

Comparing the constant dust spatial density contours [parts C of Figs. 2(*a*)–2(*c*) (RR), 3(*a*)–3(*c*) (SMR), 4(*a*)–4(*c*) (TMR) and 5(*a*)–5(*c*) (DMR)] clearly indicates that the smaller the diameter of the dust particles the further they are carried away by the gas. This is a direct result of the fact that their inertia is smaller and hence their acceleration is higher. In addition, the constant gas density contours [parts B of Figs. 2(*a*)–2(*c*) (RR), 3(*a*)–3(*c*) (SMR), 4(*a*)–4(*c*) (TMR) and 5(*a*)–5(*c*) (DMR)] indicate that the interaction of the interface, separating the rear edge of the dust cloud and the pure gas downstream of the incident shock wave, with the reflected shock wave generates a disturbance that becomes stronger as the dust particle diameter decreases. It is also evident that as the diameter of the dust particles decreases the

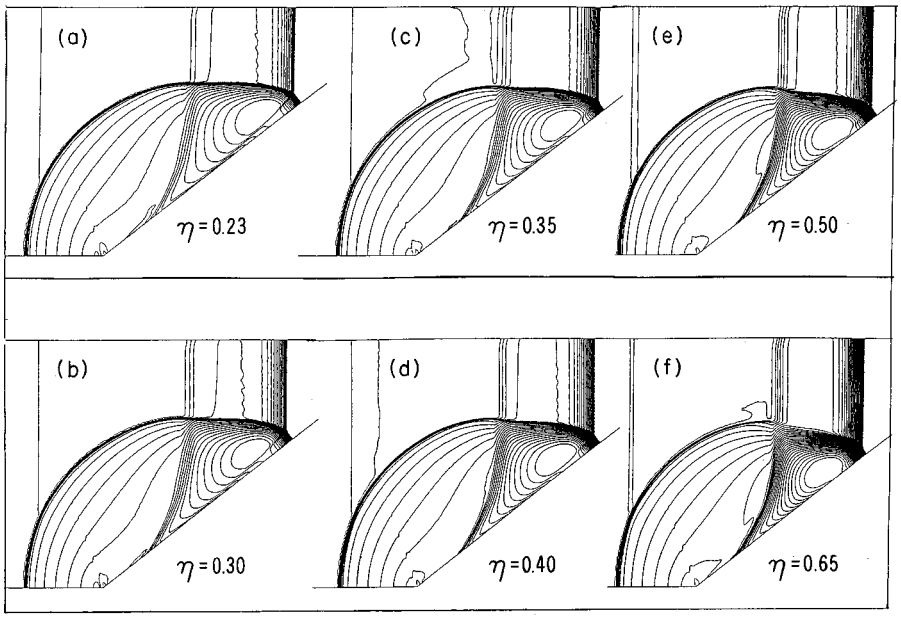

Fig. 10 The gaseous phase density contours and the wave configurations of a single-Mach reflection (SMR) with six different loading ratios (M_i=1.5, θ_w=38°, d_p=1 μm)

disturbance causes the reflected shock wave to develop a reversal of curvature [see parts B of Figs. 2(*a*) (RR), 3(*a*) (SMR), 4(*a*) (TMR), and 5(*a*) (DMR)]. As a result the wave configuration of the SMR (see Fig. 3(*a*)) looks similar to that of a TMR and the wave configuration of the TMR (see Fig. 4(*a*)) looks similar to that of a DMR. It is also of interest to note that in the case of a DMR (see part B in Fig. 5(*a*)) the presence of the dust causes the lower part of the Mach stem to be pushed forward and to develop a bulge. The bulge is more pronounced when the dust particles are smaller. This phenomenon will be discussed in more details subsequently.

The Distribution of the Suspension Properties Along the Reflecting Wedge Surface. The distributions of various suspension properties along the reflecting wedge surface are shown in Figs. 6, 7, 8, and 9 for RR, SMR, TMR, and DMR, respectively. Each of these figures consists of the following eight parts: (*a*) the gaseous phase velocity, (*b*) the gaseous phase temperature, (*c*) the gaseous phase density, (*d*) the gaseous phase pressure (recall that owing to the assumptions this is also the suspension pressure), (*e*) the dust particles velocity, (*f*) the dust particles temperature, (*g*) the dust particles spatial density, and (*h*) the gaseous phase Mach number. Figures 6, 7, and 8 for RR, SMR, and TMR, respectively, show the numerical results for three different dust particle diameters (d_p=1, 5, and 10 μm) and Fig. 9 for DMR shows the numerical results for d_p=1.0 μm only. For comparison purposes the distributions of the above-mentioned gas properties for a similar dust-free case are also shown with solid lines.

The following is evident from the results shown in Figs. 6–9.

1 The smaller the diameter of the dust particles is the larger is the attenuation of the incident shock wave.

2 The uniform flow region that exists in a dust-free RR (see the

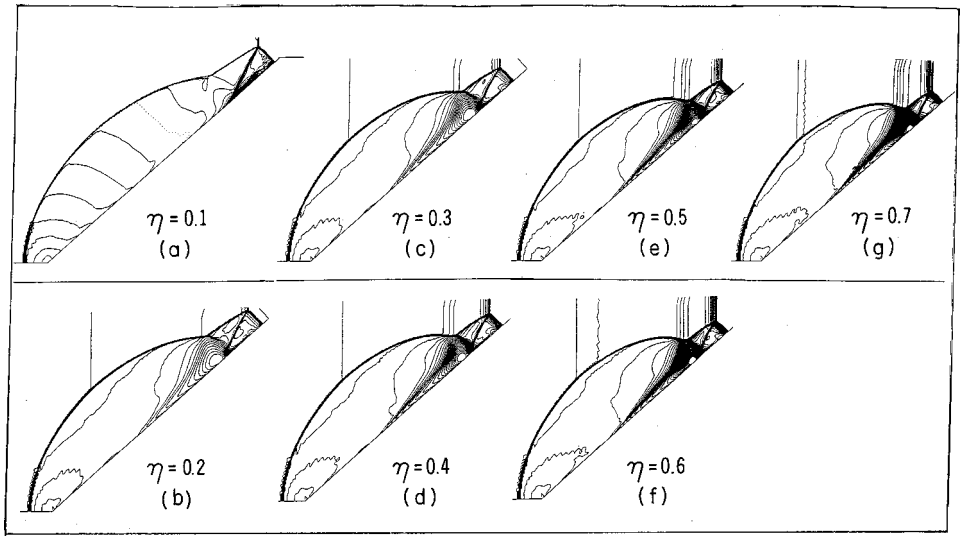

Fig. 11 The gaseous phase density contours and the wave configurations of a double-Mach reflection (DMR) with seven different loading ratios (M_i=3, θ_w=42°, d_p=1 μm)

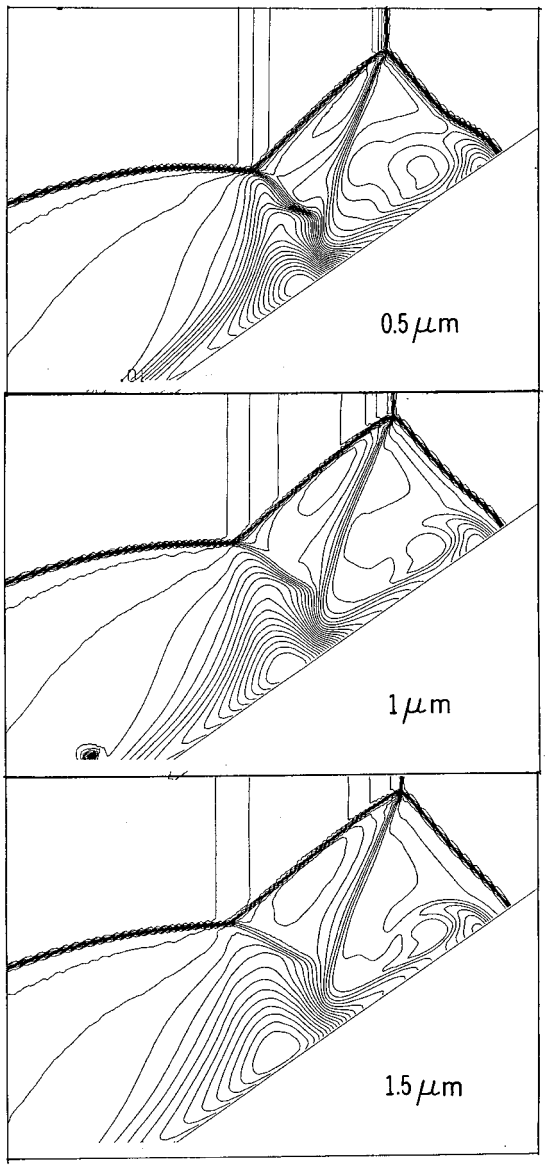

Fig. 12 Blow-ups of the constant density contours (part B in Fig. 5) illustrating the interaction between the wall jet and the foot of the Mach stem in the case of a double-Mach reflection (DMR)

plateau following the initial jump across the reflection point in Figs. 6(*a*)–6(*d*) and 6(*h*)) vanishes as the diameter of the dust particles become smaller.

3 Parts (*a*) of Figs. 6–9 indicate that the presence of the dust reduces the gaseous phase velocity. This is a direct result of the momentum transferred from the gaseous to the solid phase. It should also be noted that while the diameter of the dust particles has no significant effect on the gaseous phase velocities in the RR-case, in the SMR-, TMR-, and DMR-cases the dust particle diameter has a noticeable influence on both the gaseous phase velocity (parts (*a*) of Figs. 7–9). The smaller the dust particle is, the smaller is the gaseous phase velocity.

4 Parts (*b*) of Figs. 6–9 indicate that the presence of the dust reduces the gaseous phase temperature. This is a direct result of the energy transferred from the gaseous to the solid phase. It should be also noted that the smaller the diameter of the dust particle is, the lower is the gaseous phase temperature.

5 The above-mentioned reductions in both the gaseous phase

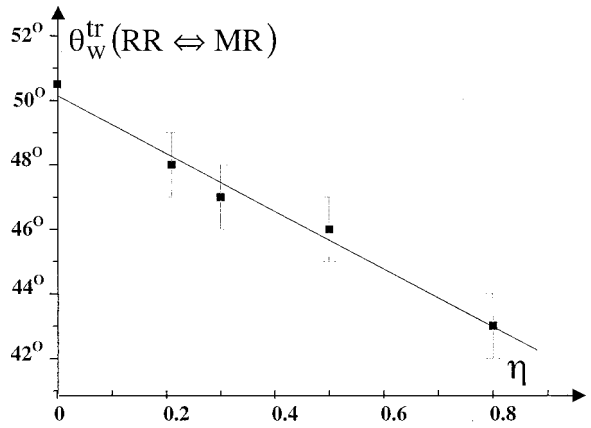

Fig. 13 Dependence of the RR↔MR transition wedge angle on the dust-loading ratio for M_i=1/5 and d_p=1 μm

velocities and temperatures result in a situation in which the gaseous phase Mach numbers (see parts (*h*) of Figs. 6–9) are not much different from those of the dust-free gas.

6 Parts (*c*) and (*d*) of Figs. 6–9 indicate that the presence of the dust increases the gaseous phase densities and pressures. It is clearly seen that the smaller is the diameter of the dust particles the larger are the densities (parts (*c*)) and the pressures (parts (*d*)), reached by the gaseous phase.

7 Parts (*e*)–(*g*) of Figs. 6–9, in which the distribution of some properties of the dust phase are shown, clearly indicate that the smaller the diameter of the dust particle is, the narrower is the dust cloud.

8 Parts (*e*)–(*g*) of Figs. 6–9 also indicate that the smaller the diameter of the dust particle is, the larger are the velocities, the temperatures and the spatial densities that are reached by the dust particles.

9 It is also important to note that the dust phase spatial density profiles in the SMR-, TMR-, and DMR-cases (parts (*g*) of Figs. 7–9) resemble a double peak shape in which the minimum is associated with the point where the slipstream reaches the reflecting wedge surface.

Loading Ratio Influence on SMR and DMR. The SMR wave configurations that result from the reflection of an incident shock wave, $M_i=1.5$, over a compressive wedge, $\theta_w=38$ deg, in dust-gas suspensions having six different loading ratios, $\eta=0.23$, 0.30, 0.35, 0.40, 0.50, and 0.65 are shown in Figs. 10(*a*)–10(*f*), respectively. The diameter of the dust particles was $d_p=1$ μm. It is clearly evident from these simulations that as the loading ratio increases the reflected shock wave and the slipstream become fuzzier until they become completely dispersed (compare Fig. 10(*a*) where a sharp slipstream is clearly seen with Fig. 10(*f*) where a slipstream is not visible at all). It is also seen that the width of the dust cloud decreases as the loading ratio increases. This implies larger dust concentrations inside the dust cloud. In return stronger disturbances at the interaction point of the rear edge of the dust cloud with the reflected shock wave are evident.

The DMR wave configurations that results from the reflection of an incident shock wave, $M_i=3$, over a wedge, $\theta_w=42$ deg, in suspensions having seven different dust loading ratios, $\eta=0.10$, 0.20, 0.30, 0.40, 0.50, 0.60, and 0.70 are shown in Figs. 11(*a*)–11(*g*), respectively. The diameter of the dust particles was $d_p=1$ μm. It is evident from these simulations that as the dust-loading ratio increases the reversal of curvature of the part of the reflected shock wave, just downstream of the second triple point becomes more pronounced. While it is hardly seen for $\eta=0.1$ (Fig. 11(*a*) an almost 90 deg kink is seen for $\eta=0.7$ (Fig. 11(*g*).

It is also evident from Figs. 10 and 11 that the parts of the SMR- and DMR-wave configurations that are downstream of the

dust cloud are practically unaffected by the dusty phase. For example, the parts of the reflected shock waves that extend from the point where they interact with the interface, which separates between the rear edge of the dust cloud and the pure gas downstream of it, to the point where they terminate on the horizontal surface, are practically identical. Finally, it is important to note that the triple point trajectory angles of the SMR simulations shown in Figs. 10(*a*)–10(*f*), and the DMR simulations shown in Figs. 11(*a*)–11(*g*), were found to be the same. Hence, it is concluded that the loading ratio does not affect the Mach stem height of an SMR and a DMR. A similar finding should be expected in the case of a TMR, which is an intermediate reflection between an SMR and a DMR.

The Jetting Effect. Figures 12(*a*)–12(*c*) are blow-ups of the DMR wave configurations shown in parts B of Figs. 5(*a*)–5(*c*), respectively. The above-mentioned bulge development process is clearly seen in these figures to be a result of a jetting effect, similar to the one observed in low γ gases (e.g., Li and Ben-Dor [15]). In the case of the larger particles, $d_p = 1.5\ \mu$m (Fig. 12(*c*) the front edge of the jet is seen to be lagging slightly behind the Mach stem whose foot is already pushed forward. In the case of the medium size particles, $d_p = 1\ \mu$m (Fig. 12(*b*)) the front edge of the jet has caught up with the foot of the Mach stem. In the case of the smaller particles, $d_p = 0.5\ \mu$m, (Fig. 12(*a*) the bulge developed by the front edge of the jet is much more pronounced.

The RR↔SMR Transition

The dependence of the RR↔SMR transition wedge angle-θ_w^{tr} on the dust loading ratio-η for an incident shock wave with $M_i = 1.5$ propagating into a dust-gas suspension of particles having a diameter of $d_p = 1\ \mu$m, a specific heat capacity of $C_s = 1.38$ kJ/(kgK) and a material density of $\rho_s = 4000$ kg/m^3, is summarized in Fig. 13. As can be seen the transition wedge angle decreases in a close to a linear fashion as the loading ratio increases.

Conclusions

The four possible types of shock wave reflection configurations: i.e., regular reflection (RR), single-Mach reflection (SMR), transitional-Mach reflection (TMR) and double-Mach reflection (DMR), that result when planar shock waves reflect over compressive straight wedges in dusty gas suspensions were investigated numerically.

A second-order accurate, in space and time, Godunov based scheme was used for solving the governing equations that describe the investigated flow fields. The dependence of the flow fields on the loading ratio of the dust and the diameter of the dust particles was investigated.

It was found that the presence of the dust caused the incident shock wave to attenuate. The smaller the dust particle was the larger was the attenuation. As a result unlike the reflection of planar shock waves over straight wedges in pure gases, the reflection phenomenon in the dusty-gas case is not pseudo-steady.

The resulted flow field was found to strongly depend on the diameter of the dust particles. Decreasing the dust particles resulted in an increase in the density and pressure of the gaseous phase and a decrease in its temperature and velocity.

A jetting effect was discovered in the case of a double-Mach reflection for small dust particle diameters. As a result of this jetting effect, a bulge developed on the Mach stem at its foot near the reflecting wedge surface.

It was found that the interaction between the interface, separating the dust-free and the dusty-gas regions behind the incident shock wave, with the reflected shock wave resulted in a clear disturbance that became more pronounced for smaller dust particles. This disturbance manifested itself as a kink (i.e., a change in curvature) in the reflected shock wave.

Finally, it was found that the RR↔MR transition wedge angle decreases linearly when the loading ratio increases.

References

[1] Ben-Dor, G., 1991, *Shock Wave Reflection Phenomena*, Springer-Verlag, New York, N.Y.

[2] Igra, O., and Ben-Dor, G., 1988, ''Dusty Shock Waves,'' Appl. Mech. Rev., **41**, No. 11, pp. 379–437.

[3] Ben-Dor, G., 1996, ''Dusty Shock Waves-Update,'' Appl. Mech. Rev., **49**, No. 10/2, pp. S141–S146.

[4] Kim, S.-W., and Chang, K.-S., 1991, ''Reflection of Shock Wave from a Compression Corner in a Particle-Laden Gas Region,'' Shock Waves, **1**, No. 1, pp. 65–73.

[5] Clift, R., Grace, J. R., and Weber, M. E., 1978, *Bubbles, Drops and Particles*, Academic Press, NY.

[6] Igra, O., and Ben-Dor, G., 1980, ''Parameters Affecting the Relaxation Zone Behind Normal Shock Waves in a Dusty Gas,'' Isr. J. Technol., **18**, No. 3/4, pp. 159–168.

[7] Kurian, J., and Das, H. K., 1997, ''Studies of Shock Wave Propagation in Gas-Particle Mixtures,'' *Shock Waves*, A. P. F. Houwing et al., eds., Panther Publishing & Printing, **11**, pp. 953–958.

[8] Olim, M., Ben-Dor, G., Mond, M., and Igra, O., 1990, ''A General Attenuation Law of Moderate Planar Shock Waves Propagating into Dusty Gases with Relatively High Loading Ratios of Solid Particles,'' Fluid Dyn. Res., **6**, No. 3–4, pp. 185–200.

[9] Mazor, G., Ben-Dor, G., and Igra, O., 1986, ''A Simple and Accurate Expression for the Viscosity of Non-polar Diatomic Gases up to 10000 K,'' AIAA J., **23**, No. 4, pp. 636–638.

[10] MacCormac, R. W., 1969, ''The Effect of Viscosity in Hyperbolic Impact Cratering,'' AIAA Paper 69-354.

[11] Falcovitz, J., and Ben-Artzi, M., 1995, ''Recent Developments of the GRP Method,'' JSME Int. J., **B**, No. 38, pp. 497–517.

[12] Wang, B. Y., Wu, Q. S., Wang, C., Igra, O., and Falcovitz, J., 1999, ''Shock Wave Diffraction by a Square Cavity Filled with Dusty Gas,'' *22nd International Symposium on Shock Waves*, London, UK.

[13] Sommerfeld, M., 1995, ''The Unsteadiness of Shock Waves Propagating Through Gas-Particles Mixtures,'' Exp. Fluids, **3**, p. 197.

[14] Igra, O., Falcovitz, J., Reichenbach, H., and Heilig, W., 1996, ''Experimental and Numerical Study of the Interaction Between a Planar Shock Wave and a Square Cavity,'' J. Fluid Mech., **313**, p. 105.

[15] Li, H., and Ben-Dor, G., 1999, ''Analysis of Double-Mach-Reflection Wave Configurations with Convexly Curved Mach Stems,'' Shock Waves, **9**, No. 5, pp. 319–326.

Journal of Fluids Engineering

Technical Briefs

The Computation of a Two-Dimensional Turbulent Wall Jet in an External Stream

R. Tangemann
Assistant

W. Gretler
Professor
e-mail: F321gret@mbox.tu-graz.ac.at

Institute of Fluid Mechanics and Heat Transfer, Graz Technical University, Graz, A-8010 Austria

[DOI: 10.1115/1.1331557]

Introduction

An extended expression for the primary turbulent shear stress combined with an algebraic Reynolds-stress model is applied to the computation of a two-dimensional turbulent wall jet. This model predicts the region with negative production of turbulent kinetic energy between the points of maximum velocity and vanishing shear stress, which is a characteristic feature of turbulent wall jets. The computed results are compared with measurements and results obtained with a k-ε model and a full Reynolds-stress closure.

The numerical simulation of turbulent wall jets is very important because of various engineering applications. Film-cooling has to be mentioned, as well as all principles of boundary-layer control by blowing. Other applications can be found in the paper and aeroplane industry. Even the flow over an automotive wind shield is a type of wall-jet flow when the demister is activated. Furthermore, the wall jet is a very important test case for turbulence models because it is a turbulent shear flow which is influenced by a free stream and by a wall.

Reviews on measurements of turbulent wall jets are given by Abrahamsson [1], Tangemann [2], and Launder and Rodi [3]. In this work, only two-dimensional wall jets in an external stream are considered. The flow configuration is shown in Fig. 1. The turbulent wall jet is characterized by the slot-width b, the jet velocity u_j, and the external stream velocity u_e.

Many experimental investigations of turbulent wall jets have shown that near the velocity maximum there exists a small region where the velocity gradient and the turbulent shear stress have opposite signs. In this region energy is transferred back from the fluctuation velocities to the mean flow. Abrahamsson [1] has shown that even in a fully developed three-dimensional wall jet the leading production term $P=-\overline{u'v'}\partial\overline{u}/\partial y$ becomes negative in this region. This behavior can only be shown if a relationship for the calculation of the turbulent shear stress is used, which does not predict vanishing shear stress at the point of maximum velocity. Computations applying a Reynolds-stress model can show the negative production of turbulent kinetic energy, however, with a comparatively higher computational effort.

Fundamental Equations

In this work the following relationship for the turbulent shear stress by Gretler and Meile [4]

$$-\overline{u'v'}=\Gamma_t\left[\left(1+\frac{L}{2}\frac{\partial^2 L}{\partial y^2}\right)\frac{\partial\overline{u}}{\partial y}+L\frac{\partial L}{\partial y}\frac{\partial^2\overline{u}}{\partial y^2}\right] \tag{1}$$

is combined with an algebraic eddy-viscosity model using transport equations for the kinetic energy k and dissipation rate ε. Here, and in the following equations, x and y denote the coordinate along and perpendicular to the wall, and $\overline{u}$ and $\overline{v}$ are the respective mean velocity components in these directions. The model of Andreasson and Svensson [5] is obtained when the term with the second derivative of L in Eq. (1) is neglected. The eddy viscosity Γ_t and the turbulent length scale L are related to the eddy viscosity ν_t and the Prandtl-Kolmogorov length scale l, which are used in the standard k-ε model.

The authors are aware of the fact that this new model is not frame invariant and that this limits the applicability of the model. However, this shear-stress expression has been successfully used for the computation of channel flow with unequal rough walls and rotating channel flow (Gretler and Meile, [4]) and turbulent Couette-Poiseuille flows (Gretler and Meile [6]). The computation of curved flows is possible with a slightly modified shear-stress expression (Gretler and Baltl, [7], Baltl [8]).

Wall jets in an external stream have a dominant flow direction and therefore it is sufficient to solve the Reynolds averaged momentum equations in their partially parabolic form.

$$\overline{u}\frac{\partial\overline{u}}{\partial x}+\overline{v}\frac{\partial\overline{u}}{\partial y}=-\frac{1}{\rho}\frac{\partial p}{\partial x}+\nu\frac{\partial^2\overline{u}}{\partial y^2}+\frac{\partial}{\partial y}(-\overline{u'v'}) \tag{2}$$

$$\overline{u}\frac{\partial\overline{v}}{\partial x}+\overline{v}\frac{\partial\overline{v}}{\partial y}=-\frac{1}{\rho}\frac{\partial p}{\partial y}+\nu\frac{\partial^2\overline{v}}{\partial y^2}+\frac{\partial}{\partial y}(-\overline{v'^2}) \tag{3}$$

These equations have the advantage that a very fast and stable forward-marching solution procedure can be used for the computations.

The k- and ε-equations are used in a low-Reynolds-number version proposed by Shih and Lumley [9].

$$\overline{u}\frac{\partial k}{\partial x}+\overline{v}\frac{\partial k}{\partial y}=\frac{\partial}{\partial y}\left(\left[\frac{\nu_t}{\sigma_k}+\nu\right]\frac{\partial k}{\partial y}\right)+P-\varepsilon \tag{4}$$

Contributed by the Fluids Engineering Division of THE AMERICAN SOCIETY OF MECHANICAL ENGINEERS. Manuscript received by the Fluids Engineering Division July 14, 1999; revised manuscript received September 11, 2000. Associate Editor: P. Bradshaw.

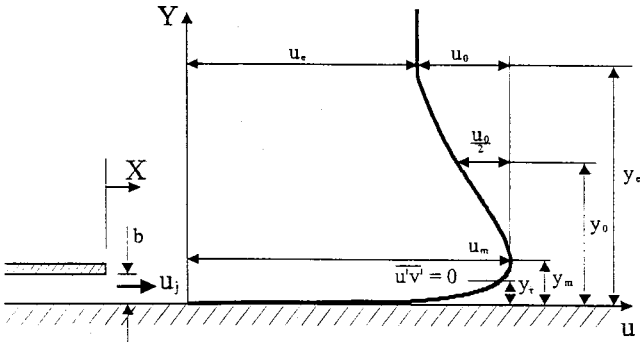

Fig. 1 Two-dimensional wall jet in an external stream

$$\overline{u}\frac{\partial\varepsilon}{\partial x}+\overline{v}\frac{\partial\varepsilon}{\partial y}=\frac{\partial}{\partial y}\left(\left[\frac{\nu_t}{\sigma_\varepsilon}+\nu\right]\frac{\partial\varepsilon}{\partial y}\right)+c_{\varepsilon1}f_1\frac{\varepsilon}{k}P-c_{\varepsilon2}f_2\frac{\varepsilon^2}{k}+\nu\nu_t\left(\frac{\partial^2\overline{u}}{\partial y^2}\right)^2 \tag{5}$$

$$f_1=1,\quad f_2=1-0.22\exp\left(-\frac{\mathrm{Re}_t^2}{36}\right) \tag{6}$$

$$\nu_t=c_\mu f_\mu\frac{k^2}{\varepsilon} \tag{7}$$

$$f_\mu=[1-\exp(a_1\,\mathrm{Re}_k+a_3\,\mathrm{Re}_k^3+a_5\,\mathrm{Re}_k^5)]^{1/2} \tag{8}$$

$$\mathrm{Re}_t=\frac{k^2}{\nu\varepsilon},\quad \mathrm{Re}_k=\frac{k^{1/2}y}{\nu} \tag{9}$$

The high-Reynolds-number model is obtained when all the damping functions f_1, f_2, f_μ are set to unity and the extra term $\nu\nu_t(\partial^2\overline{u}/\partial y^2)^2$ is neglected.

Equation (1) is used for the computation of the turbulent shear stress. The description of the algebraic Reynolds-stress model, which has been used for the calculation of the turbulent normal stresses, can be found in Ljuboja and Rodi [10]. A complete description of the boundary conditions and the numerical solution procedure can be found in Tangemann [2]. All model constants are summarized in Table 1. The length scale L must be related to a length scale determined within the turbulence model. From the equation for the kinetic energy of turbulence with the simplifications valid in the inertial sublayer, we can obtain the following well-known relation between the mixing length ℓ_m and the Prandtl-Kolmogorov length scale ℓ

$$l_m=c_\mu^{-1/4}\ell \tag{10}$$

Table 1 Model constants

		k-ε	ARS
eddy-viscosity concept	c_μ	0.09	0.09
	σ_m	⋯	1.18
	κ	⋯	0.43
k-equation	σ_k	1.0	1.0
ε-equation	σ_ε	1.3	1.3
	$c_{\varepsilon1}$	1.44	1.44
	$c_{\varepsilon2}$	1.92	1.92
pressure-strain term	c_1	⋯	1.8
	c_1'	⋯	0.6
	c_2	⋯	0.6
	c_2'	⋯	0.3
near-wall turbulence model	a_1	$-1.5\,10^{-4}$	$-1.5\,10^{-4}$
	a_3	$-10.0\,10^{-9}$	$-10.0\,10^{-9}$
	a_5	$-5.0\,10^{-10}$	$-5.0\,10^{-10}$

where c_μ denotes a model constant. Introducing the usual model assumptions for the dissipation ε together with

$$L=l_m=\kappa y \tag{11}$$

leads to the following relation for the unknown length scale L

$$L=c_\mu^{3/4}\frac{k^{3/2}}{\varepsilon} \tag{12}$$

If von Kármán's similarity hypothesis

$$L=\kappa\left|\left(\frac{\partial\overline{u}}{\partial y}\right)\Big/\left(\frac{\partial^2\overline{u}}{\partial y^2}\right)\right| \tag{13}$$

is applied in a small region near the maximum velocity, it follows that $L\propto|y-y_m|$ is a suitable approximation, where y_m denotes the location of the velocity maximum. This can be verified by differentiating (13) with respect to y. In the resulting formula, the term containing the first derivative of the mean velocity can be neglected, which leads to $\partial L/\partial y\approx\kappa$.

The eddy viscosity Γ_t can be obtained if one compares the expanded and the standard shear-stress expression in the region of the wall jet near the point of maximum velocity, where a negative shear stress and a positive mean velocity gradient may cause the negative production of turbulent kinetic energy. Applying the above-mentioned expressions for L and $\partial L/\partial y$ it follows that

$$-\overline{u'v'}=\Gamma_t\frac{\partial\overline{u}}{\partial y}(1+\kappa^2)=\nu_t\frac{\partial\overline{u}}{\partial y} \tag{14}$$

$$\Gamma_t=\frac{\nu_t}{1+\kappa^2}=\frac{\nu_t}{\sigma_m} \tag{15}$$

Here, the constant σ_m can be interpreted as a turbulent Prandtl number for momentum transport. Furthermore, it should be noted here that in order to reproduce the logarithmic law with Eq. (1), the value of σ_m should be $(1-\kappa^2)$ in the constant-stress layer. However, the higher value $\sigma_m=1+\kappa^2$ yields significantly better results in this region, compared with the experiments. So, for applications using the logarithmic law as a boundary condition, the use of two different values of σ_m can be proposed. However, when using a low-Reynolds-number model, this possible subdivision into an inner region and an outer region with different values of σ_m seems not to be necessary.

In the following transport equation, $\mathrm{Diff}(\overline{u'v'})$ denotes the diffusion of the turbulent shear stress and f is a dimensionless wall function. A description of all included terms can be found in Ljuboja and Rodi [10].

$$\frac{D\overline{u'v'}}{Dt}=\mathrm{Diff}(\overline{u'v'})-\overline{v'^2}\frac{\partial\overline{u}}{\partial y}-c_1\frac{\varepsilon}{k}\overline{u'v'}\left(1+\frac{3}{2}\frac{c_1'}{c_1}f\right)+c_2\overline{v'^2}\frac{\partial\overline{u}}{\partial y}\left(1-\frac{3}{2}c_2'f\right) \tag{16}$$

For a fully developed flow, the convection terms in Eq. (16) can be neglected. Under the assumption of local equilibrium near the wall, the wall function f must reach unity. Then a comparison with Eq. (1) yields $(\Gamma_t L/2\partial^2 L/\partial y^2\partial\overline{u}/\partial y$ vanishes under these assump-

tions)

$$\Gamma_t = \frac{\nu_t}{\sigma_m} = \frac{c_\mu}{\sigma_m}\frac{k^2}{\varepsilon}$$

$$-\overline{u'v'} = \overbrace{\frac{2}{3}\frac{c_1 - 1 + c_2(1-2c_2')}{c_1 + 2c_1'}\frac{1 + \frac{3}{2}c_2c_2' - c_2}{c_1\left(1 + \frac{3}{2}\frac{c_1'}{c_1}\right)}\frac{k^2}{\varepsilon}\frac{\partial \bar{u}}{\partial y}}$$

$$\underbrace{-\frac{1}{c_1\left(1 + \frac{3}{2}\frac{c_1'}{c_1}\right)}\frac{k}{\varepsilon}\mathrm{Diff}(\overline{u'v'})}_{\Gamma_t L \frac{\partial L}{\partial y}\frac{\partial^2 \bar{u}}{\partial y^2}} \qquad (17)$$

The term with the mean velocity gradient represents the standard eddy-viscosity formulation. The second term can be interpreted as the modelling of the diffusion of the turbulent shear stress. Therefore, the authors are of the opinion that the shear stress is treated more realistically than in the standard k-ε model.

Comparison With Experiments

In order to show the performance of the turbulence model given in the preceding section, calculations for several test cases have been carried out. The results are compared with measurements and computations with the standard k-ε model and a full Reynolds-stress closure using the commercial code ''FIRE'' [11]. The Reynolds-stress model of this code is based on a concept by Speziale et al. [12].

The development of the mean velocity $\bar{u}$ for different slot distances x/b for the wall jet of Zhou and Wygnanski [13] is shown in Fig. 2. For increasing distances from the slot the velocity maximum decreases and its location moves farther away from the wall. The two vertical lines indicate the points of maximum velocity and vanishing shear stress; the latter is always located nearer to the wall. In between these two locations, which have been obtained with computations with the expanded shear-stress formulation, there is the region with the negative production of turbulent kinetic energy. The extent of this region is growing with increasing distances from the slot. Only the results of the present turbulence model are shown because with all three turbulence models very similar velocity predictions are obtained.

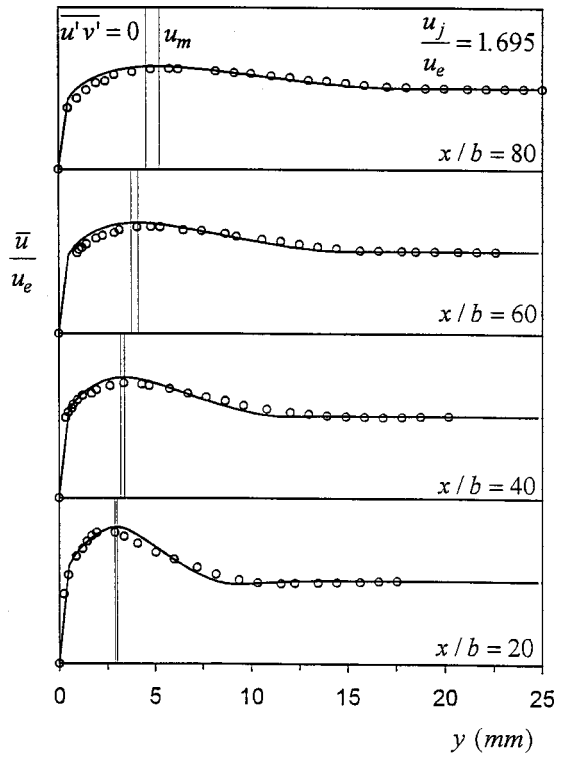

Fig. 2 Velocity profiles $\bar{u}$ for the wall jet of Zhou and Wygnanski [13] (○ measurements, —— present model).

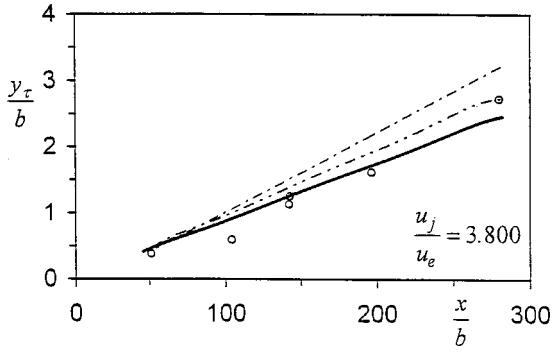

Fig. 3 Location y_τ of vanishing shear stress for the wall jet of Kruka and Eskinazi [14] (○ measurements, —— present model, —·—·—·— RMS[12], –··– standard k-ε model).

The location y_τ of vanishing shear stress for the wall jet of Kruka and Eskinazi [14] is shown in Fig. 3. The computation with the expanded shear-stress formulation gives better results than the other two turbulence models. The standard k-ε model and the Reynolds-stress closure tend to predict zero shear stress too far away from the wall.

Figure 4 displays the production P over the dissipation ε of turbulent kinetic energy k for the wall jet of Kacker and Whitelaw [15]. Only the points of vanishing shear stress and maximum velocity can be compared with available measurements. The two vertical lines indicate the locations of zero shear stress and maximum velocity as obtained with the present turbulence model and from the measurements, respectively. The extent of the region with negative production of turbulent kinetic energy shows very good agreement with the experiments. The standard $k-\varepsilon$ model cannot show this behavior. The result obtained with the Reynolds-stress model exhibits a region with negative production of turbulent kinetic energy; however, at incomparably higher cost and less accuracy.

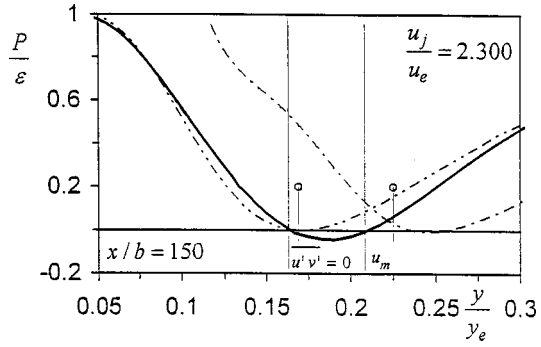

Fig. 4 Production P over the dissipation ε of turbulent kinetic energy for the turbulent wall jet of Kacker and Whitelaw [15] (○ measurements, —— present model, —·—·—·— RMS [12], –··– standard k-ε model).

Conclusions

A combined algebraic stress model is proposed in order to improve the predictions obtained with two-equation turbulence models. This model, the standard k-ε model and a full Reynolds-stress model, has been used for the numerical analysis of two-dimensional wall jets in an external stream. The following conclusions can be drawn.

1 The results obtained with the combined ARS model and the second moment closure show better agreement with the measurements than those obtained with the standard k-ε model. Computations with the Reynolds-stress model are more costly in computing time than those with the k-ε models.

2 With the combined ARS model and the Reynolds-stress model it is possible to show the existence of a region with negative production of turbulent kinetic energy k. Better results concerning the extent of this region are obtained with the combined ARS model than with the Reynolds-stress model of Speziale et al., [12]. Linear and nonlinear k-ε models cannot show this physical property.

3 The term with the second derivative of the mean velocity $\overline{u}$ in the extended shear-stress expression can be interpreted as the modelling of the diffusion term. This results in a more realistic modelling of the turbulent shear stress $\overline{u'v'}$ in the present model and in better results in comparison with the k-ε model. However, from an engineering viewpoint the k-ε model shows good performance when the region of negative production of turbulent kinetic energy is small.

References

[1] Abrahamsson, H., 1997, ''On turbulent wall jets,'' Ph.D. thesis, Chalmers University of Technology, Göteborg.

[2] Tangemann, R., 1997, ''Berechnung von turbulenten Wandstrahlen mit verschiedenen Turbulenzmodellen,'' Dissertation, Institut für Strömungslehre und Gasdynamik, Technische Universität Graz; VDI-Fortschrittsbericht 7/327.

[3] Launder, B. E., and Rodi, W., 1981, ''The turbulent wall jet,'' Progress in Aerospace Sciences, **19**, pp. 81–128.

[4] Gretler, W., and Meile, W., 1994, ''Shear-stress calculation in asymmetric turbulent flows: a combined ARS-Model,'' Fluid Dyn. Res., **14**, pp. 289–311.

[5] Andreasson, P., and Svensson, U., 1992, ''A note on a generalized eddy viscosity hypothesis'' ASME J. Fluids Eng., **114**, pp. 463–466.

[6] Gretler, W., and Meile, W., 1997, ''Calculation of plane turbulent Couette-Poiseuille flow with a modified k-ε model,'' Fluid Dyn. Res., **21**, pp. 263–283.

[7] Gretler, W., and Baltl, M., 1999, ''Modifiziertes $k-\varepsilon$ Modell zur Berechnung der turbulenten Strömung in gekrümmten Kanälen,'' Z. Angew. Math. Mech., **79**, pp. 683–684.

[8] Baltl, M., 1999, ''Berechnung turbulenter Strömungen in gekrümmten Kanälen,'' Dissertation, Institut für Strömungslehre und Wärmeübertragung, Technische Universität Graz.

[9] Shih, T.-H., and Lumley, J. L., 1993, ''Kolmogorov behaviour of near-wall turbulence and its application in turbulence modelling,'' International Journal of Computational Fluid Dynamics, **1**, pp. 43–56.

[10] Ljuboja, M., and Rodi, W., 1980, ''Calculation of turbulent wall jets with an algebraic Reynolds-stress model,'' ASME J. Fluids Eng., **102**, pp. 350–356.

[11] 1996, ''FIRE Turbulence models for computational fluid dynamics,'' A course for the FIRE users-V.6.2.a.

[12] Speziale, C. G., Sarkar, S., and Gatski, T. B., 1991, ''Modelling the pressure-strain correlation of turbulence: an invariant dynamical systems approach,'' J. Fluid Mech., **227**, pp. 245–272.

[13] Zhou, M. D., and Wygnanski, I., 1993, ''Parameters govering the wall jet in an external stream,'' AIAA J., **31**, pp. 848–853.

[14] Kruka, V., and Eskinazi, S., 1964, ''The wall-jet in a moving stream,'' J. Fluid Mech., **20**, pp. 555–579.

[15] Kacker, S. C., and Whitelaw, J. H., 1971, ''The turbulence characteristics of two-dimensional wall-jet and wall-wake flows,'' ASME J. Appl. Mech., **37**, pp. 239–252.

Flow in a Channel With Longitudinal Tubes

C. Y. Wang

Visiting Professor, Mem. ASME, Department of Mechanical Engineering, National University of Singapore, Singapore, 119260 and Professor, Departments of Mathematics and Mechanical Engineering, Michigan State University, East Lansing, MI 48824

[DOI: 10.1115/1.1335496]

Laminar flow in a channel with internal tubes occurs in shell and tube heat exchangers, dialysis machines, and the cooling of nuclear reactor rods (e.g., Johannsen [1]). Existing solutions for the flow in ducts with cores have been tabulated in handbooks by Shah and London [2] and Blevins [3]. The methods used include conformal mapping, boundary collocation, and numerical integration.

The present Note considers the flow in a channel containing a periodic series of longitudinal circular tubes. We are particularly interested in the flow decrease caused by the tubes, and the singular behavior as the tube radii shrink to zero.

Figure 1(a) shows the cross section. The height of the channel is $2H$, the tubes are of radius bH, centrally placed with a period of $2\lambda H$. For this geometry, conformal mapping is almost impossible, and numerical integration would have serious difficulties when b is small. We shall use domain decomposition and collocation to solve the problem.

Normalize all lengths by H and the longitudinal velocity by (pressure gradient) H^2/(viscosity). The governing equation for the velocity is

$$\nabla^2 w = -1 \tag{1}$$

Figure 1(b) shows two different domain decompositions, depending whether λ is greater or smaller than unity. Region II is square with a circular cylinder at the center, Region I is rectangular which complements Region II. The two regions are in series for $\lambda > 1$ and is parallel for $\lambda < 1$. The separate coordinate systems for each region are shown.

First consider the $\lambda > 1$ case. The solution to Eq. (1) satisfying the symmetry conditions and zero on the top and bottom plates is

$$w_I(x,y) = (1-y^2)/2 + \sum_1^N A_n \cos(\alpha_n y)(e^{\alpha_n(x-c)} + e^{-\alpha_n(x+c)}) \tag{2}$$

where we have truncated the infinite series to N terms, A_n are coefficients to be determined and $\alpha_n = (n-1/2)\pi$. The solution for Region II satisfying Eq. (1) and zero on the cylinder is

$$w_{II}(r,\theta) = (b^2 - r^2)/4 + B_0 \ln(r/b) + \sum_1^{2N-1} B_n \cos(2n\theta)(r^{2n} - b^{4n} r^{-2n}) \tag{3}$$

where B_0, B_n are unknown coefficients. Now choose $2N$ points on 1/4 of the square boundary to be matched. Let $\theta_j = (j-0.5)\pi/4N$, $j = 1$ to $2N$. We need no-slip on the top, and continuity on the sides, i.e.,

Contributed by the Fluids Engineering Division of THE AMERICAN SOCIETY OF MECHANICAL ENGINEERS. Manuscript received by the Fluids Engineering Division July 18, 2000; revised manuscript received September 7, 2000. Associate Editor: S. Tsujimoto.

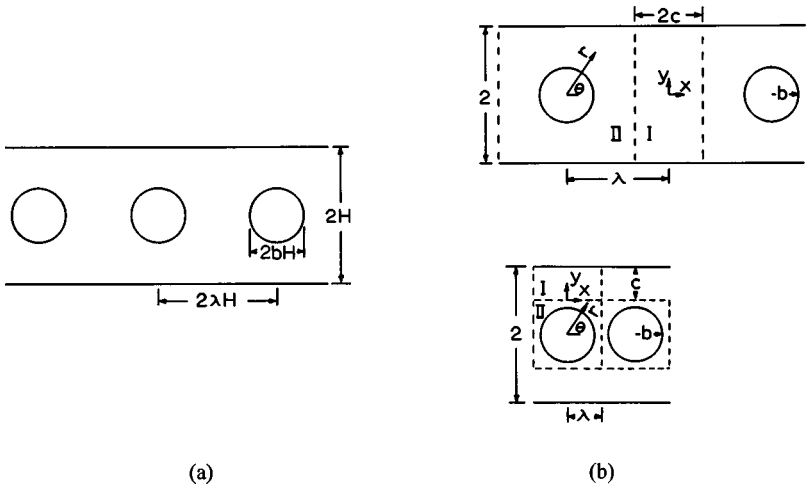

Fig. 1 (*a*) Cross section of the channel flow (*b*) domain decompositions

$$w_{II}(\csc\theta_j,\theta_j)=0,\quad j=N+1\ \text{ to }\ 2N \tag{4}$$

$$w_{II}(\sec\theta_j,\theta_j)=w_I(-c,\tan\theta_j),\quad j=1\ \text{ to }\ N \tag{5}$$

$$\left[\left(\cos\theta\frac{\partial}{\partial r}-\frac{\sin\theta}{r}\frac{\partial}{\partial\theta}\right)w_{II}\right](\sec\theta_j,\theta_j)=\left[\frac{\partial}{\partial x}w_I\right](-c,\tan\theta_j),\quad j=1\ \text{ to }\ N \tag{6}$$

where $c=|1-\lambda|$. Equations (4)–(6) represent a set of $3N$ linear equations which can be solved for the $3N$ coefficients. In general, $N=10$ assures a three-digit accuracy.

Let F be the flow rate per period, normalized by (pressure gradient) H^2/(viscosity). Then

$$F=4(I_1+I_2+I_3) \tag{7}$$

where

$$I_1=\int_0^1\int_{-c}^0 w_I\,dx\,dy=\frac{c}{3}+\sum_1^N A_n\frac{(-1)^{n+1}}{\alpha_n^2}(1-e^{-2\alpha_n c}) \tag{8}$$

$$I_2=\int_0^{\pi/4}[J(\sec\theta,\theta)-J(b,\theta)]\,d\theta \tag{9}$$

$$I_3=\int_{\pi/4}^{\pi/2}[J(\csc\theta,\theta)-J(b,\theta)]\,d\theta \tag{10}$$

and

$$J(r,\theta)\equiv\frac{r^2}{8}\left(b^2-\frac{r^2}{2}\right)+B_0\left[\frac{r^2}{2}\ln\left(\frac{r}{b}\right)-\frac{r^2}{4}\right]+B_1\left(\frac{r^4}{4}-b^4\ln r\right)\cos(2\theta)+\sum_2^{2N-1}B_n\left(\frac{r^{2n+2}}{2n+2}-b^{4n}\frac{r^{-2n+2}}{-2n+2}\right)\cos(2n\theta) \tag{11}$$

For the $\lambda<1$ case we supplant Eq. (2) by

$$w_I(x,y)=\frac{c^2-y^2}{2}+C_0(c-y)+\sum_1^{N-1}C_n\cos(\gamma_n x)(e^{\gamma_n(y-2c)}-e^{-\gamma_n y}) \tag{12}$$

where $\gamma_n=n\pi/\lambda$ while the form of w_{II} and θ_j remain the same. The boundary conditions are

$$\left[\left(\cos\theta\frac{\partial}{\partial r}-\frac{\sin\theta}{r}\frac{\partial}{\partial\theta}\right)w_{II}\right](\lambda\sec\theta_j,\theta_j)=0\quad j=1\ \text{ to }\ N \tag{13}$$

$$w_{II}(\lambda\csc\theta_j,\theta_j)=w_I(\lambda\cot\theta_j,0),\quad j=N+1\ \text{ to }\ 2N \tag{14}$$

$$\left[\left(\sin\theta\frac{\partial}{\partial r}+\frac{\cos\theta}{r}\frac{\partial}{\partial\theta}\right)w_{II}\right](\lambda\csc\theta_j,\theta_j)=\left[\frac{\partial}{\partial y}w_{II}\right](\lambda\cot\theta_j,0),\quad j=N+1\ \text{ to }\ 2N \tag{15}$$

After obtaining the $3N$ coefficients, the flow per period is

$$F=4(K_1+K_2+K_3) \tag{16}$$

where

$$K_1=\int_0^c\int_0^\lambda w_I\,dx\,dy=\lambda c^2\left(\frac{c}{3}-\frac{C_0}{2}\right) \tag{17}$$

$$K_2=\int_0^{\pi/4}[J(\lambda\sec\theta,\theta)-J(b,\theta)]\,d\theta \tag{18}$$

$$K_3=\int_{\pi/4}^{\pi/2}[(J(\lambda\csc\theta,\theta)-J(b,\theta)]\,d\theta \tag{19}$$

Figure 2(*a*) shows the constant velocity lines for a large period. The maximum velocity is on the symmetry axis of the channel. Figure 2(*b*) shows the location of the maximum velocity is shifted to the sides when the period is small. Of interest is the large effect on the flow even for very small cylinder radii such as $b=0.01$ (Fig. 2(*c*)).

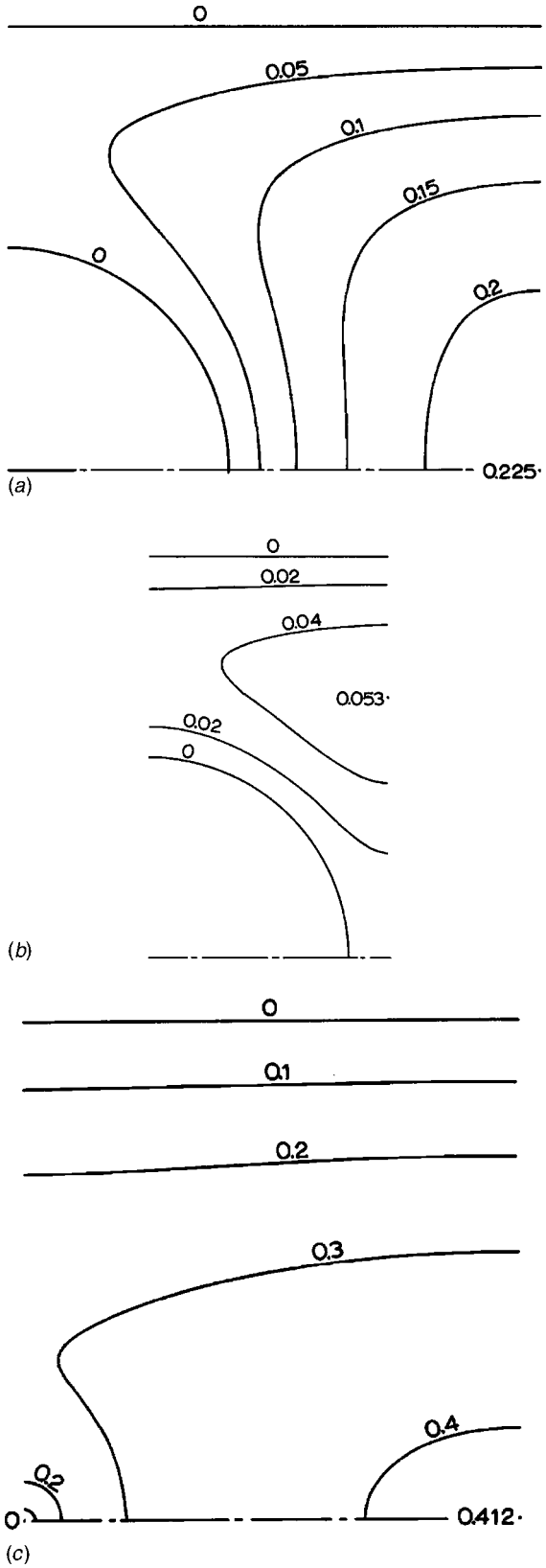

Fig. 2 (*a*) Constant velocity lines $\lambda=1.2$, $b=0.5$, (*b*) $\lambda=0.6$, $b=0.5$, (*c*) $\lambda=1$, $b=0.01$

Instead of flow per period F, the flow per width Q may be useful, related by $Q=F/2\lambda$. Figure 3 shows Q as a function of half period λ for various constant cylinder radius b. For $b=0$ ($\lambda\neq 0$), $Q=2/3$ which is the Poiseuille flow rate without the cylinders. If $\lambda=b$ the cylinders are touching, indicated by the open circles. When $\lambda=b=0$ the cylinders form a bisecting thin plate and the flow is 1/6. In general flow increases as λ is increased, and is asymptotic to $Q=2/3$.

Let S be the decrease in flow due to a single cylinder. Then

$$S=\frac{4}{3}\lambda-F, \quad \lambda\gg 1 \tag{20}$$

where the first term on the right-hand side of Eq. (20) is the Poiseuille flow in one period. Our computation shows S approaches a limit when $\lambda\geqslant 5$, which is equivalent to the case of a single cylinder. Figure 4 shows S increases with b, but the increase is singular when $b\approx 0$, indicating the relatively large effect on the flow rate for small cylinders. We shall investigate this situation further.

The exact solution for the flow in an annulus with outer radius 1 and inner radius b is

$$F=\frac{\pi}{8}\left[1+\frac{(1-b^2)^2}{\ln b}-b^4\right] \tag{21}$$

where the effect of the inner cylinder is of order $(-\ln b)^{-1}$ as $b\to 0$. Let $\eta=(-\ln b)^{-1}\ll 1$. For our case we plotted S/η against η for $b=10^{-2}$ to $b=10^{-15}$ in Fig. 5. It is seen that the curve is almost linear. This suggests an expansion

$$S=c_1\eta+c_2\eta^2+\ldots \tag{22}$$

A linear extrapolation on Fig. 5 yields $c_1=1.57$ and $c_2=-0.37$. Thus a semi-empirical formula for small b is

$$S=\frac{1.57}{(-\ln b)}-\frac{0.37}{(-\ln b)^2}+O((-\ln b)^{-3}) \tag{23}$$

This approximation is accurate for $b\leqslant 0.1$ as seen from Fig. 4. The single cylinder formula can also be used for sparsely spaced periodic cylinders by the relation

$$Q=2/3-S/2\lambda \tag{24}$$

Figure 3 shows such an approximation is valid for small b or large λ values.

Our method of domain decomposition and collocation worked well. The convergence of the collocation method can be proven for circular boundaries, and our square boundary is the rectangle-closest to the circle. Numerical integration can also be used, however serious scaling difficulties would be encountered when b is as small as 10^{-2}, not to say the 10^{-15} used in this paper. The necessary double numerical integrations for the flow rate would further compromise the accuracy.

Our Fig. 3 for multiple cylinders and Fig. 4 for the single cylinder would be useful in the design of channel flow with internal tubes.

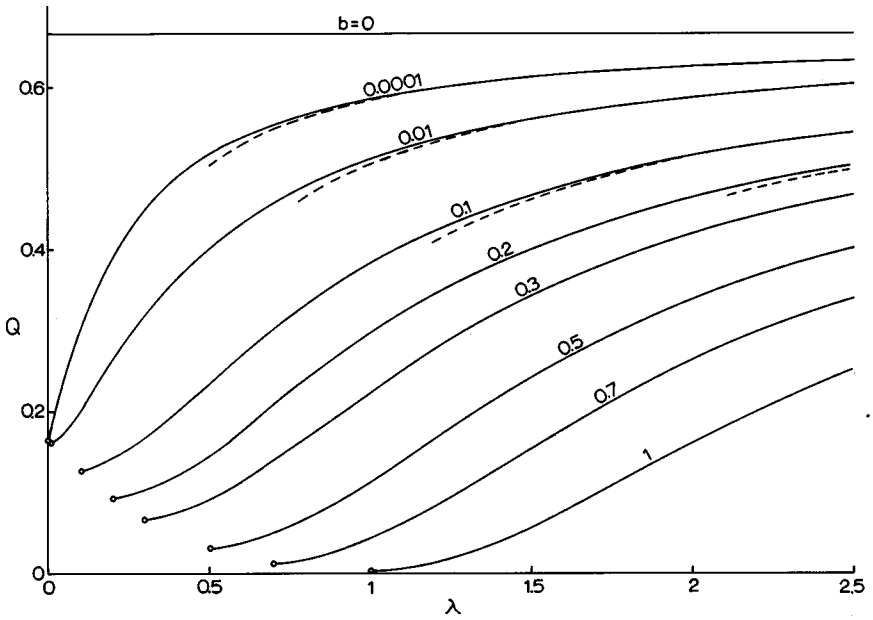

Fig. 3 Flow per width *Q* versus half period λ. Dashed lines are from Eq. (24). Circles are touching cases.

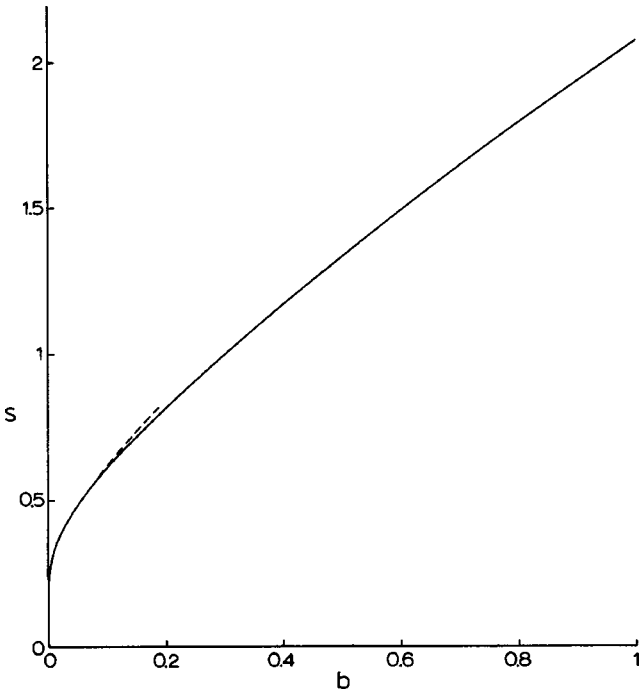

Fig. 4 Decreased flow *S* due to a single cylinder. Dashed line is from Eq. (23).

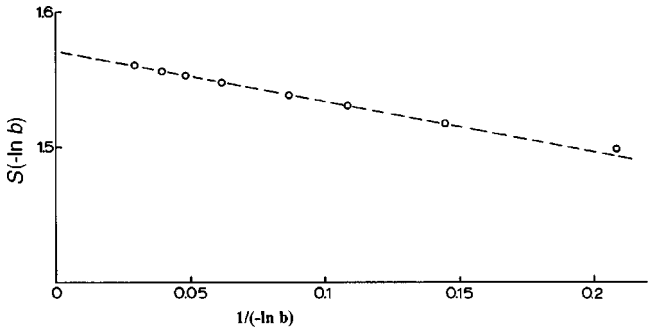

Fig. 5 Extrapolation for small *b*. Circles from right: $b=10^{-2}$, 10^{-3}, 10^{-4}, 10^{-5}, 10^{-7}, 10^{-9}, 10^{-11}, 10^{-15}.

References

[1] Johannsen, K., 1983, ''Longitudinal flow over tube bundles,'' *Low Reynolds Number Flow Heat Exchangers*, S. Kakac, R. K. Shah, and A. E. Bergles, eds., Hemisphere, Washington, pp. 229–273.

[2] Shah, R. K., and London, A. L., 1978, *Laminar Flow Forced Convection in Ducts*, Academic, New York.

[3] Blevins, R. D., 1984, *Applied Fluid Dynamics Handbook*, Van Nostrand, New York.